eman ta zabal zazu
Universidad del País Vasco
Euskal Herriko Unibertsitatea

UNIVERSITY OF THE BASQUE COUNTRY

DEPARTMENT OF CHEMICAL ENGINEERING

Advanced technologies for the reduction of the carbon footprint in the reforming of bio-oil over $NiAl_2O_4$ derived catalyst

DOCTORAL THESIS

Leire Landa Bilbao

2023

Tras finalizar el trabajo realizado durante estos últimos 4 años, es momento de echar la vista atrás. Son muchas las personas que, de una forma u otra, me han acompañado y ayudado a llevar a cabo esta Tesis, lo que sin lugar a duda ha resultado en un proceso de aprendizaje tanto a nivel profesional como personal.

En primer lugar, quiero agradecer a mis directores, a la Prof. Ana Gayubo y al Dr. Aingeru Remiro, por brindarme la oportunidad de emprender este viaje y por la confianza depositada en mí en todo momento. Gracias por vuestra implicación, paciencia, apoyo y consejos. Vuestros conocimientos y vuestra experiencia han ayudado a dar forma a este trabajo en numerosas ocasiones. Al Prof. Javier Bilbao, por su esfuerzo y trabajo constante, así como por las valiosas ideas, conocimientos y aportaciones que han sido fundamentales para este trabajo, y al Prof. Andrés Aguayo, por su constante disposición para prestar ayuda cuando era necesario.

En el entorno del laboratorio quisiera hacer una mención especial a la Dra. Naiara García, quien tuvo la paciencia de guiarme y enseñarme durante mis inicios en la experimentación, con la elaboración de mi Trabajo de Fin de Grado y de Máster, e iniciarme experimentalmente en el mundo del bio-oil. Zenbat momentu on pasatu doguzan batera (la limpieza de la U y los tubos posteriores han dado mucho de sí). Al Dr. José Valecillos, por su contribución a este trabajo, tus consejos y aportaciones han sido de gran a ayuda. A la Dra. Beatriz Valle, por su apoyo a lo largo de estos años. Y como no a Sergio, mi relevo en el reformado del bio-oil (bio-oil/etanol), por todos los momentos vividos en el laboratorio codo con codo (sobre todo aquellas maravillosas tardes reparando el Micro GC o cambiando el Genie), por tus consejos, charlas y apoyo.

Agradecer también al resto de compañeros de trabajo, por hacer más ameno aquellos momentos donde la locura o la desesperación afloran. Anderri, alkarregaz bizitako momento on guztiengaitik, beti be laguntzeko prest egoteagaitik eta sortzen dozun giro onagaitik. A Hector, por poder contar contigo en todo momento, tanto en lo profesional como en lo personal, has sido un gran apoyo a lo largo de todos estos años. A Zuria, mi compañera en paralelo en esta aventura,

por tu disposición para escuchar, ayudar y apoyar en todo lo que en tus manos estuviera. Gracias al resto del grupo ProCat-Vares, os deseo lo mejor en el futuro.

I am also very thankful to Prof. Peter Clough for accepting me into his group during my research stay at Cranfield University and to his great work team (Serap, Siqi, Ziqi, Jude) for their kindness and helpfulness, they treated me as one of them from the first day. A Andoni, Willy, Juan, Koke, Luis, Oihane y Kerman, por todos los buenos momentos vividos en Cranfield.

Laborategitik kanpo, unibertsitateko lagunei eta Sondikako lagunei, betikoei, eskerrik asko beti entzuteko eta laguntzeko prest egoteagaitik, askotan be zertaz berba egiten neban ulertzen ez bazenduen be. Egindako planak, bidaiak eta irriak ezinbestekoak izan dira.

Amaitzeko, Aita, Ama eta Naia aipatu gurako nebazan, eskerrik asko emondako baloreengaitik, erabakiak hartzerako orduan erabateko askatasuna eta laguntza emoteagaitik. Gaur egun nazana izatera heldu banaz, zeuei esker izan da.

Eta Josebari, bidelagun eta ekipo bat izateagaitik. Beti irri bat ateratzeko prest egoteagaitik eta bidea errazteagaitik. Zeure babesa ezinbestekoa izan da urte hauetan zehar.

Leire Landa Bilbao

Amomari,

zagozan tokian zagola ni zaintzeagaitik

CONTENTS

LIST OF FIGURES

LIST OF TABLES

SUMMARY

This Doctoral Thesis has been carried out in the ProCat-Vares group (Catalytic Processes and Waste Valorization, CPWV) of the University of the Basque Country as part of a broad line of research within the large bio-refinery concept, for the production of fuels and high value added products from biomass, promoting the development of a sustainable economy. In this framework, the production of hydrogen and/or syngas by catalytic reforming of biomass-derived feedstocks continues to attract considerable scientific interest as a sustainable route due to the growing demand of H_2 as a fuel and of H_2 or syngas as a raw material. This has been one of the main lines of research of the ProCat-Vares group for more than a decade, with 8 previous Doctoral Theses and a high production of high impact articles derived from them. This line of research has addressed the reforming of simple feedstocks consisting of individual oxygenated compounds, such as DME (derived from biomass via synthesis gas) [1, 2] or ethanol (obtained by fermentation) [1, 3], as well as complex feedstocks, such as bio-oil (produced by fast pyrolysis of lignocellulosic biomass). Given the complexity of the bio-oil feedstock, the initial studies carried out by the group considered the reforming of its aqueous fraction [4], although in recent years the effort has focused on the reforming of the complete bio-oil [5–8]. In this way, significant progress has been made in the knowledge of the effect of operating conditions on the behaviour of Ni and Rh supported catalysts in the reforming of bio-oil aqueous fraction [4] or complete bio-oil [5, 6, 8], in the development of a kinetic model for the Ni/La_2O_3-αAl_2O_3 supported catalyst [5], in the understanding of the coke deposition mechanisms on these supported catalysts in steam reforming [7, 8] and oxidative steam reforming [6] of bio-oil, and in the different reforming strategies to mitigate catalyst deactivation by conditioning the bio-oil by phenol extraction or by using a system with two catalytic steps in series (pre-reforming with a low-cost catalyst and steam reforming with a Ni catalyst) [8].

With this background, the focus of the Thesis was to progress in this research line by studying strategies to minimise the carbon footprint in bio-oil reforming. Firstly, we approached the sorption enhanced steam reforming (SESR) process from three perspectives, minimising CO_2 emissions by in situ CO_2 capture, which enhances hydrogen production. The experiments were performed in a continuous reaction system with two in-line units: a thermal treatment unit at 500 °C for raw bio-oil volatilization and controlled deposition of pyrolytic lignin, and a packed-bed or fluidized-bed reactor for the steam reforming (SR) or SESR of the remaining oxygenates. First of all, the effect of sorbent type (dolomite or CaO/mayenite), catalyst type (Ni/Al_2O_3 obtained upon reduction of a $NiAl_2O_4$ spinel or Ni/CeO_2 prepared by wet-impregnation) and sorbent/catalyst mass ratio (4, 10 and 20) were studied in a packed-bed reactor under selected conditions (600 °C, space time of 0.15 $g_{catalyst}{\cdot}h/g_{oxygenates}$, steam-to-carbon (S/C) molar ratio of 3.4 and time on stream of 300 min). Secondly we have compared the performance (conversion, product yields and deactivation) of packed-bed and fluidized-bed reactors using the $NiAl_2O_4$ spinel derived catalyst for the H_2 production from raw bio-oil via SR and SESR. The experiments were carried out with dolomite as CO_2 sorbent and under the same previous selected conditions, with dolomite/catalyst ratio of 10 in the SESR runs. Finally, the effect of operating conditions on the performance of the $NiAl_2O_4$ spinel derived catalyst+dolomite system in the SESR in a fluidized-bed reactor was studied. The SESR conditions were: 550-700 °C, space time of 0.15 and 0.30 $g_{catalyst}{\cdot}h/g_{oxygenates}$, dolomite/catalyst mass ratio of 10 and 20, S/C ratio of 3.4 and time on stream of 50 and 300 min. In addition, the reproducibility of operating in reaction-regeneration cycles (with joint regeneration of the catalyst and dolomite) has also been analysed at 600 °C, space time of 0.30 $g_{catalyst}{\cdot}h/g_{oxygenates}$, dolomite/catalyst mass ratio of 10, S/C ratio of 3.4 and time on stream of 120 min. The regeneration step was carried out in an external oven at 850 °C for 4 h in air atmosphere (enough time for the complete removal of the coke deposits and CO_2). In all cases, the different causes responsible for catalyst deactivation have been identified, analysing the content, nature and morphology of the coke, as well as the change in the structural properties of the catalyst.

On the other hand, the second strategy to reduce the carbon footprint is the CO_2 valorization by combined steam/dry reforming (CSDR) of bio-oil as an efficient route for jointly valorize the CO_2 and the produce syngas (mixture of H_2+CO), which can be used as raw material in different catalytic processes. The viability of the process for the scale-up requires the selection of suitable operating conditions. To this end, a thermodynamic study of a simulated bio-oil was carried out, with the aim of demonstrating the theoretical feasibility of the process and providing a preview for further research. The calculations were performed by Gibbs energy minimisation with ProII software, considering a mixture of 6 typical compounds in a raw bio-oil (acetic acid, 2-methoxyphenol (guaiacol), hydroxyacetone, acetone, furfural and ethanol). Firstly, the effect on the equilibrium composition of reaction temperature (300-900 °C) and feed composition referred to C in the bio-oil at the reactor inlet (S/C ratio in the 0.5-3 range and CO_2-to-carbon (CO_2/C) molar ratio in the 0.5-5 range) was studied. In this study, the emphasis was placed on the capacity of the CSDR of bio-oil for the valorization of CO_2 and, with this objective in mind, special attention was paid to delimiting the conditions that allow positive values of CO_2 conversion and/or the reduction of CO_2 emissions compared to the conventional SR process (without CO_2 in the feed). The operating conditions that maximise the yield of syngas as well as those required for producing a syngas with a targeted H_2/CO ratio of 1 and 2 (of interest for its use as a feedstock for the synthesis of fuels and chemicals) were also delimited. Moreover, the energy requirements of the unit were assessed for all the scenarios presented, because the viability of the process for the industrial scale implementation requires the production of syngas with a reasonable energy requirement. Additionally, an experimental study of the CSDR of a real bio-oil with the Ni/Al_2O_3 catalyst derived from $NiAl_2O_4$ spinel was carried out. The experiments were performed in a fluidized-bed reactor with a space time of 0.125 or 0.250 $g_{catalyst}{\cdot}h/g_{oxygenates}$ and time on stream of 360 min, in the range of temperature (600-800 °C) and feed composition (CO_2/C ratio of 0 (conventional SR), 0.6 and 1.1 and S/C ratio of 0.5 (corresponding to the water contained in the bio-oil feed), 1.2 and 1.7) selected from the previous thermodynamic study. The conditions that maximise syngas production and

catalyst stability were delimited. The effect of the operating conditions on the location, nature and morphology of the coke and the structural and physical properties of each used catalyst sample has also been examined.

Since most of this Thesis is based on a Ni/Al_2O_3 catalyst derived from $NiAl_2O_4$ spinel, proposed in a previous project [6], with high activity and H_2 selectivity in the raw bio-oil reforming and fully regenerable under suitable conditions, as a preliminary step to better understand the results obtained with the previous strategies (SESR and CSDR) on catalyst deactivation, we further studied the role of individual oxygenated compounds in bio-oil reforming, both thermodynamically and experimentally with the Ni/Al_2O_3 catalyst. Firstly, the yield of H_2 and by-products and the energy requirements in the reforming of different oxygenates present in bio-oil (acetic acid, levulinic acid, acetaldehyde, vanillin, hydroxyacetaldehyde, acetone, hydroxyacetone (or acetol), cyclohexanone, phenol, catechol, guaiacol and mannose) were compared by thermodynamic analysis, focusing on different reforming strategies (steam reforming and autothermal reforming). The study was performed by minimisation of Gibbs energy method with ProII software, under a wide range of operating conditions (temperature, 300-1000 °C; S/C ratio, 0.5-16; N_2 co-feeding, 0-10 kmol/h) in order to stablish the optimal conditions in each case. Secondly, the influence of oxygenates composition in bio-oil on the deactivation by coke of a $NiAl_2O_4$ spinel-derived catalyst was approached by studying the individual SR of a wide range of model oxygenates with different functionalities (acetic acid, acetone, ethanol, acetaldehyde, acetol, 1,2-benzenediol, 2-methoxyphenol and levoglucosan). The fluidized-bed reactor was used in the following conditions: 600 and 700 °C; S/C ratio, 3 (6 for levoglucosan); space-time, 0.034 $g_{catalyst}{\cdot}h/g_{oxygenate}$ (0.080 $g_{catalyst}{\cdot}h/g_{oxygenate}$ for levoglucosan) (low enough to favour the rapid catalyst deactivation) and time on stream, 300 min

Chapter 1

INTRODUCTION AND OBJECTIVES

This Chapter introduces the topic for the scope of this Thesis, focusing mainly on the reduction of CO_2 emissions in the reforming of raw bio-oil for the production of hydrogen and/or syngas. The background of this work is based on the current energy framework and the transition towards a sustainable model, where renewable hydrogen is a priority goal in the global economic and political strategies for carbon neutrality and for a rapid transition to clean energy. A brief overview of the different hydrogen production technologies (from fossil fuels and renewable sources) is presented, followed by a detailed description of the main feedstock used in this work (raw bio-oil). A bibliographic review of the steam reforming of individual oxygenated compounds or their mixtures, raw bio-oil or bio-oil aqueous fraction is also provided. Likewise, a strategy to enhance hydrogen production by sorption enhanced steam reforming (SESR) with in situ CO_2 capture and different CO_2 valorization routes, focusing on combined reforming (with steam and CO_2), are also addressed, with a brief discussion of several studies reported in the literature. Finally, the main causes of catalyst deactivation and different regeneration methods are described. Based on the literature review, the aim and objectives of the Thesis are presented at the end of the chapter.

1.1. ENERGY FRAMEWORK

Energy plays a fundamental role in human development and is a driving force in our progress. Overdependence on and high demand for fossil fuels such as oil, coal and natural gas, linked to environmental, social, political and economic factors, has caused a number of challenges and problems.

Global energy demand has been steadily increasing due to population growth, industrial development, technological progress and rising living standards. This has led to a deficit in the balance of energy production and consumption. In addition, the extraction and combustion of fossil fuels has serious environmental consequences. Greenhouse gas (GHG) emissions from the combustion of fossil fuels are one of the main causes of climate change. The problems associated with climate change are numerous and very serious, with dangerous impacts on nature and people in every region of the world, including the rise of temperature in the planet, which result in heatwaves and extreme weather events (hurricanes, droughts, wildfires and floods), sea-level rise and coastal zones (caused by thermal expansion of the oceans and melting of glaciers and the Antarctic ice sheet), loss of biodiversity (changes in habitats and migratory patterns of plant and animal species), agriculture and food insecurity and health impacts [9, 10].

Therefore, to ensure a liveable and sustainable future for all, a deep, rapid and sustained reductions in GHG emissions are required. Energy is at the core of GHG emissions. According to the World Resource Institute, the energy consumption accounts for more than 75 % of the GHG emissions. The rest originates from industrial processes (6.1 %), agriculture (11.6 %), land use change and forestry (3.3 %), and waste (3.3 %) [11]. Climate change is therefore essentially an energy challenge. Based on data reported by the United Nations Framework Convention on Climate Change (UNFCCC), CO_2 is the major GHG worldwide (75.7 %), followed by CH_4 (13.9 %) and N_2O (7.2 %). We will therefore focus on CO_2 emissions within the energy sector, as this represents the majority of emissions and is relevant to the objective of this Thesis. Figure 1.1 shows the energy-related CO_2 emissions for the period 1900-2021.

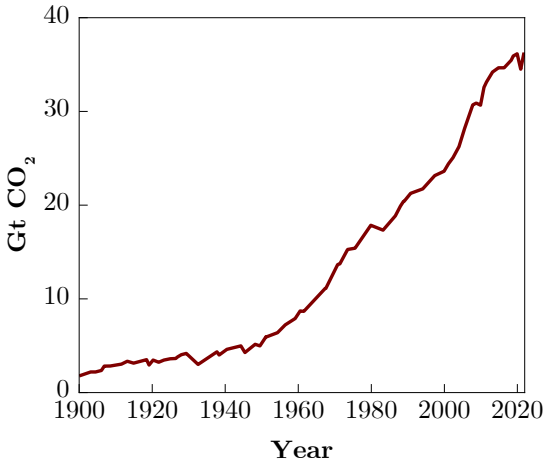

Figure 1.1. CO_2 emissions from energy combustion and industrial processes, 1900-2021 [12].

In 2020, global CO_2 emissions from fuel combustion recorded an unprecedented decline of almost 6 % as the COVID-19 pandemic reduced global energy demand, with a slowdown in transport, trade and economic activity worldwide [13]. COVID-19 has created the biggest and most multidimensional impact on our lives, not only socially but also in the energy and industrial sectors. The total lockdown executed by most of the countries reflected a 25 % reduction in weekly energy consumption [14]. However, with the rapid recovery of the global economy, energy consumption and associated emissions rebounded again. Thus, energy-related CO_2 emissions grew to 36.3 Gt in 2021, above pre-pandemic levels. Emissions increased by over 2.0 Gt from 2020 levels [15, 16].

China and the United States together are responsible for 45 % of the global fuel combustion emissions, followed by European Union, India, Russian Federation and Japan [17, 18].

Therefore, the current context of climate emergency highlights the need to consider the recommendations of the Intergovernmental Panel on Climate Change (IPCC) and to meet the targets set out in various international agreements (Kyoto Protocol, Paris Agreement). These agreements emphasize the need to reduce GHG emissions, primarily CO_2 emissions, and to limit global warming to

below 1.5 °C above pre-industrial levels. Thus, for a liveable climate, net emissions must be reduced by 43 % by 2030 and reach net zero by 2050 in order to stabilize global temperature. To achieve this goal of net zero emissions by 2050, the 44 participating countries and the European Union will have to make significant changes to their current energy model, which is mainly based on fossil fuels [19, 20].

Besides the environmental impacts, dependence on fossil fuels also has socio-economic and political implications. Fossil fuel prices are volatile and subject to fluctuations in international markets, which can affect the economic stability of countries. Moreover, reliance on external energy sources can create political dependency and energy vulnerability, leading to geopolitical conflicts. The most recent international conflict is the ongoing war between Russia and Ukraine, which has had a major impact on the global energy system, disrupting supply and demand patterns and fracturing long-standing trade relationships. Russia's invasion of Ukraine has led to a period of extraordinary turbulence in energy markets, especially for natural gas [21, 22].

As an alternative to the exposed dependence on fossil fuels and increasingly stricter environmental policies aimed at mitigating net CO_2 emissions, research and development of alternative and clean technologies using renewable and clean energy sources as raw materials is a top priority [23]. Thus, a new, less carbon-intensive energy economy is emerging based on the increased use of renewable sources (wind, solar, hydro, biomass, geothermal), driven by political action, technological innovation and the growing urgency to address climate change.

Similarly, the electrification of certain sectors, starting with land transport (mainly cars) and the residential sector by replacing gas boilers with heat pumps, is of great importance. In this process of large-scale electrification of industry and transport, energy storage systems are essential due to the seasonal nature of the main energy sources. Batteries and other systems designed to fulfil this function, such as pumped hydroelectric and solar thermal installations, therefore play a key role. It is also essential to shift electricity demand to daytime hours, when the contribution of photovoltaic solar energy is assured. However, electrification

is not technically feasible in energy-intensive industries such as steel and cement. There are also significant limitations in the maritime and aviation sectors due to the high energy density requirements that cannot met by current batteries. In this scenario, hydrogen has an important role to play, not forgetting the current and future demand for H_2 as a reagent in the chemical industry (currently petrochemicals) [24–28].

1.2. HYDROGEN

Hydrogen (H_2) has the potential to provide economically viable, socially advantageous and energy-efficient solutions to the problems associated with the world's growing energy demand, including global warming [29], and is considered a key pillar in the energy transition towards a sustainable and environmentally friendly model [30]. It is the most abundant element in the universe and, due to its high reactivity, is only found bound to other elements, such as in water and organic compounds. It is non-toxic and much lighter than air, so it dissipates quickly when released. H_2 is an odourless, flammable and colourless gas that poses safety concerns, particularly if a leak is not detected and the gas accumulates in a confined area, as it can ignite and cause an explosion. However, as with other fuels, the safe use of H_2 focuses on preventing situations where all the combustion factors (ignition, oxidant and fuel) are present.

Unlike oil, natural gas or coal, hydrogen is considered an energy vector, like electricity, that can be used to convert, store and release energy [24, 31]. It is an environmentally pleasant and beneficial fuel, with water as the only by-product in the conversion to energy. Likewise, it has a high energy storage capacity, 120 MJ/kg, more than double of most conventional fuels (47 MJ/kg natural gas, 43 MJ/kg conventional gasoline and diesel, 23 MJ/kg coal, 20 MJ/kg methanol and 27 MJ/kg ethanol) [32]

1.2.1. Current situation of H_2

Global H_2 demand reached 94 Mt in 2021 (74 Mt of pure H_2 production and about 20 Mt H_2 mixed with carbon-containing gases in methanol production and steel

manufacturing), an increase of 5 % compared to 2020 demand, mainly driven by the recovery of activity in the chemical and refining sectors [33, 34]. However, it is currently produced from fossil fuel technologies. These routes are incompatible with the zero carbon footprint objective due to the significant associated CO_2 emissions, more than 900 Mt CO_2 in 2021 [35–37].

The actual distribution of H_2 production is shown in Figure 1.2. Natural gas without CCUS (Carbon Capture, Usage and Storage) is the main route for 62 % of H_2 production, 19 % from coal and less than 1 % from oil. Besides, 18 % of global supply is "by-product" H_2, which comes from facilities and processes primarily designed to produce something else. This by-product H_2 often requires dehydration or other forms of purification, and can then be sent to a variety of hydrogen-using processes and facilities (hydrocracking, desulphurisation). Low emission H_2 production was less than 1 Mt (0.7 %), almost all from fossil fuels with CCUS, and only 35 kt H_2 was obtained from water electrolysis [34].

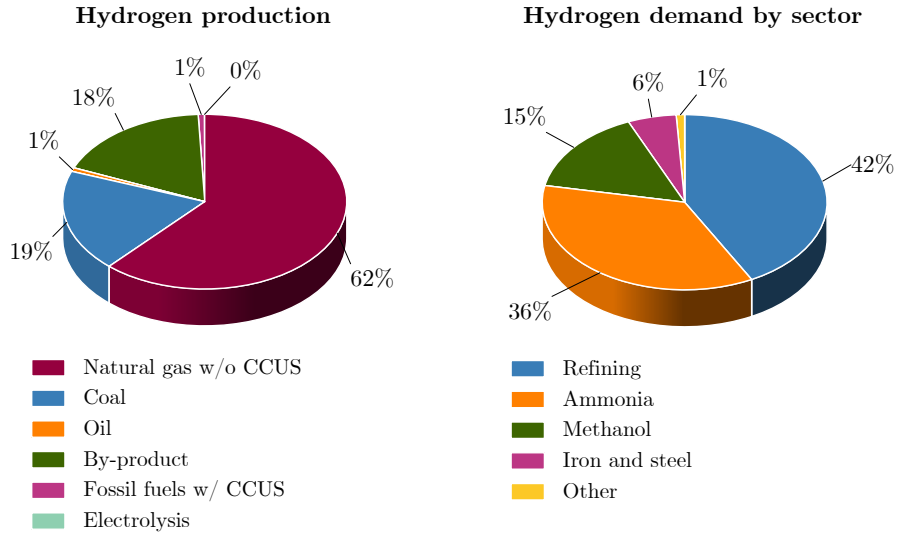

Figure 1.2. H_2 production and demand by sector distribution in 2021 [34, 38].

Global H_2 demand by sector is also shown in Figure 1.2. As observed, most of the H_2 produced goes mainly to three industries whose purpose is the production of existing raw materials: refining, chemicals (ammonia and methanol) and iron and

steel. Hence, the overall H_2 consumption is distributed as follows: 42 % for refinery processes such as hydrocracking or hydrotreating (39.8 Mt H_2), 36 % for ammonia production for urea and other fertilizers (33.8 Mt H_2), 16 % for methanol synthesis and derivatives (14.6 Mt H_2), 5 % for iron and steel (5.2 Mt H_2) and 1 % for other (0.9 Mt H_2), which includes other industrial uses and new applications such as transport, power generation, buildings and high temperature heat in industry [38].

Hence, in order to move towards a net zero emissions future scenario, the world should move away from the fossil fuel economy to a much cleaner H_2 future, known as the Hydrogen Economy, proposed back in the early 1970s [39]. Interest in this technology is not new, and has gone through several waves in recent decades. Like all emerging technologies, the Hydrogen Economy has followed the hype cycle [40]. In the 1970s, with the oil price shocks, oil shortages and concerns about pollution, H_2 was considered as a long-term alternative, especially in the transport sector. The Hydrogen Economy reached its major peak in the 1990s. Concerns about climate change prompted further H_2 studies, with a focus on carbon capture and storage (CCS), renewable energy and transport. During this period, many car manufacturers exposed H_2 cars at motor shows, driven by rapid advances in fuel cell technology. In the early 2000s, concerns about climate change began to translate into renewed political action directed at the transport sector, and concerns about peak oil resurfaced [41]. In 2003, the International Partnership for Hydrogen and Fuel Cells in the Economy (IPHE) was formed by 19 member countries and the European Commission, with the mission to facilitate and accelerate the transition to clean and efficient mobility and energy systems, using H_2 and fuel cell technologies for different applications and sectors [37]. In 2010, expectations for H_2 fell with the retreat of the peak oil narrative, uncertainty in climate policy development and the progress of battery electric vehicles, whose initial infrastructure needs are less costly compared to those of H_2 [41].

Today we are in a period of technological growth and consolidation, leading to a period of productivity, with large-scale production and valorization of H_2 from

sustainable sources and technologies expected around 2030. Nonetheless, there are barriers to overcome in order to fully develop the Hydrogen Economy. Some of these challenges include reducing the cost of H_2 production and storage, and developing adequate distribution infrastructures [24, 32].

1.2.2. Colours of H_2

Hydrogen technologies are classified based on different colours to provide information about how the H_2 is produced, the energy sources used and the climate neutrality of the H_2. The main colours are grey, brown, blue, turquoise, green, pink and yellow [31, 42, 43].

Grey hydrogen is produced by steam reforming of natural gas without CCUS, which is currently the largest amount of H_2 produced. The main drawback of this process is the significant CO_2 emissions into the atmosphere, estimated at around 830 Mt CO_2 per year [44].

Brown hydrogen is produced by coal gasification, another major H_2 production process. It is similar to grey hydrogen as it is produced from fossil fuels without CCUS technologies. Here, too, the production of H_2 generates large amounts of GHG emissions.

Blue hydrogen is also produced from fossil fuels (steam reforming of natural gas or coal gasification), but incorporates CCUS technologies to reduce or offset the associated carbon emissions.

Turquoise hydrogen is produced through methane pyrolysis (thermal decomposition), with solid carbon as a by-product. Unlike other processes that use fossil fuels as a feedstock, this process produces H_2 without emitting CO_2. The solid carbon produced as a by-product can be stored or used for further production processes in industry and for soil amendments, providing benefits for the circular economy.

Green hydrogen is produced using renewable energy sources such as solar, hydro or wind power, followed by water electrolysis. Electrolysis splits water into

H_2 and O_2, and when renewable electricity is used, the process is emission-free and environmentally friendly. This makes green hydrogen the most sustainable and climate-neutral form of H_2 production.

Pink hydrogen refers to H_2 produced using nuclear power as the energy source for the electrolysis process. Nuclear power is a low-carbon and highly efficient primary energy source. The production of H_2 from nuclear energy has the advantage of producing no GHG, using water as the raw material.

Yellow hydrogen is produced by electrolysis using a mixed-source electricity grid: the mix of renewable and fossil power actually flowing through the grid.

An overview of all H_2 production processes is given in Figure 1.3.

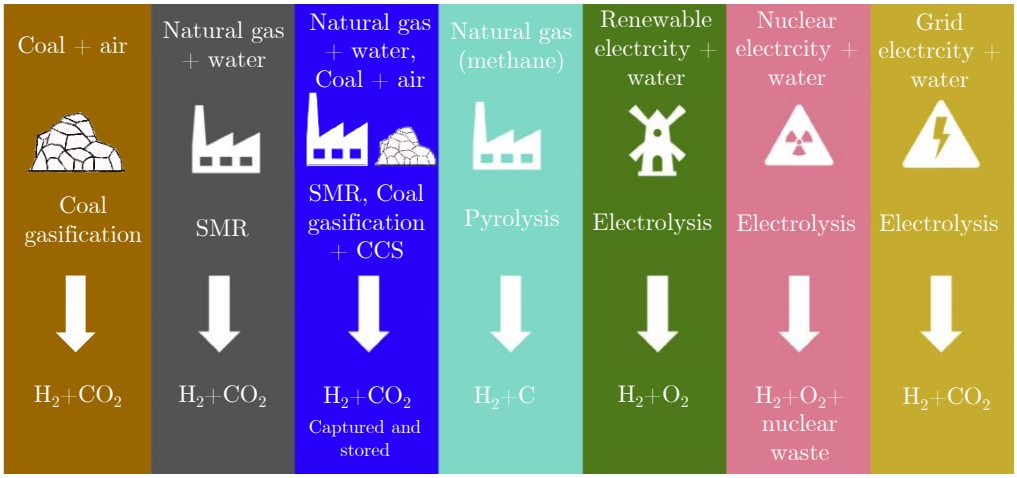

Figure 1.3. Summary of H_2 production routes and colours (adapted from [31]).

1.2.3. H_2 production technologies

H_2 production technologies can be classified into two main groups based on the feedstock used: fossil fuels and renewable sources. Figure 1.4 summarises a schematic overview of the different hydrogen production technologies.

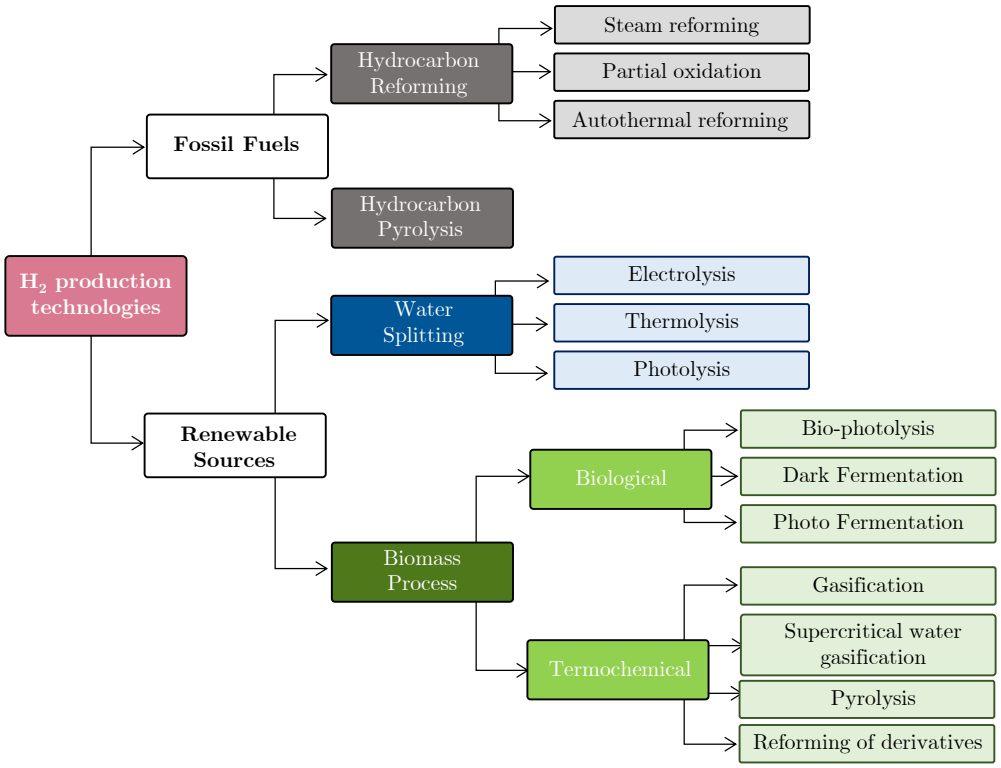

Figure 1.4. Hydrogen production technologies.

1.2.3.1. Fossil fuels

Fossil fuels (natural gas, oil and coal) are currently the primary source for hydrogen production. The two most developed and widely used techniques are hydrocarbon reforming and pyrolysis.

Hydrocarbon reforming is the process where a hydrocarbon fuel gas is converted into hydrogen through certain reforming techniques (varying the reactant). Therefore, besides hydrocarbon, the other reactant can be steam (steam reforming (SR), endothermic reaction), oxygen (partial oxidation (POX), exothermic reaction) or both (oxidative steam reforming (OSR) and autothermal reforming (ATR), which is a thermoneutral reaction) [24, 37, 45, 46].

- *Steam reforming (SR)* is one of the most widely used, comprehensive and mature catalytic process for H_2-rich syngas production. It is an endothermic reaction in which hydrocarbon and steam are catalytically converted into H_2 and CO. Mostly, natural gas is the main raw material, and thus the process is generally called methane steam reforming (MSR). MSR is the most common and developed method used for large-scale H_2 production, with conversion efficiency between 74-85 %. This process requires high operating temperatures (700-900 °C) and pressures (3-25 bar) [24, 37, 45, 46].

  MSR consists of three steps: (i) reforming or syngas (H_2+CO) production (Eq. (1.1)); (ii) water-gas-shift (WGS) reaction (increasing H_2 content ratio of syngas) (Eq. (1.2)); and (iii) gas purification (CO_2 separation) [24, 37, 45, 46].

$$C_nH_m + nH_2O \rightarrow nCO + \left(n + \frac{1}{2}m\right)H_2 \tag{1.1}$$

$$CO + H_2O \leftrightarrow CO_2 + H_2 \tag{1.2}$$

- *Partial oxidation (POX)* consists of converting a hydrocarbon feedstock to H_2 and CO (Eq. (1.3)) in the presence of oxygen (or air). This technique can be done non-catalytically (thermal partial oxidation, TPOX) or catalytically (catalytic partial oxidation, CPOX). The non-catalytic process operates at 1300-1500 °C with feedstocks such as methane, heavy oil and coal, whereas the catalytic process occurs at about 950 °C with feedstocks ranging from methane to naphtha [37, 46].

$$C_nH_m + \frac{1}{2}nO_2 \rightarrow nCO + \frac{1}{2}mH_2 \tag{1.3}$$

  In this process, after sulphur removal, pure O_2 is used for partial oxidation of the hydrocarbon feedstock and the syngas produced is further treated in the same manner as the product gas of the SR process. However, in the POX route less H_2/CO ratio is obtained compared to SR. The conversion of CO with steam (WGS reaction, Eq. (1.2)) complements the process producing H_2 and CO_2 [24, 45].

POX is the most appropriate technology to produce H_2 from heavier feedstock such as heavy oil residues and coal [37].

- *Oxidative steam reforming (OSR)* is a combination of the endothermic SR and the exothermic POX reactions. Partial exothermic oxidation is used to provide the heat and endothermic steam reforming to increase the hydrogen production. In the OSR process, steam and oxygen (or air) are fed into the reformer and the reforming and oxidation reactions occur simultaneously (Eq. (1.4)). When the steam/oxygen ratio is adjusted suitably, a thermoneutral process or autothermal reforming (ATR) can be achieved [24, 37, 45].

$$C_nH_m + \frac{1}{2}nH_2O + \frac{1}{4}nO_2 \rightarrow nCO + \left(\frac{1}{2}n + \frac{1}{2}m\right)H_2 \qquad (1.4)$$

  The process has lower investment costs (around 25 %) than MSR because, although SR has a higher efficiency and a low CO content, it is an endothermic process and the energy required must be supplied from outside [24, 37].

Hydrocarbon pyrolysis involves the thermal decomposition of the sole source (the hydrocarbon itself) under specific conditions for the production of H_2, as shown in Eq. (1.5).

$$C_nH_m \rightarrow nC + \frac{1}{2}mH_2 \qquad (1.5)$$

Thermo-catalytic decomposition of light hydrocarbons (boiling point, 50-200 °C) produces H_2 and elemental C, whereas in the case of the heavy hydrocarbon fraction (boiling point, $>$ 350 °C) H_2 production occurs in two steps: hydrogasification and CH_4 cracking [24, 37, 45]. In the case of methane, produced at 980 °C and atmospheric pressure, the energy required per mole of H_2 produced (37.6 kJ/mol) is lower than the energy required in the MSR (63.3 kJ/mol). In addition, pyrolysis technology does not require any waste gas sequestration or CO_2 removal steps [37].

1.2.3.2. Renewable sources

Although hydrocarbons are the main feedstock used for industrial H_2 production, the need to increase the integration of technologies that use renewable energy sources and do not contribute to CO_2 generation is unavoidable in a near future. Next, the methods of H_2 production from renewable sources are summarised. Firstly, the different water-based techniques are described, followed by the biomass-based processes.

Water splitting

Water is one of the most abundant raw materials on the planet and can be used as a resource for H_2 production. Water splitting is the hydrolysis of water into H_2 and O_2. The overall reaction is:

$$H_2O \rightarrow H_2 + \frac{1}{2}O_2 \qquad (1.6)$$

This technique is a promising, clean and environmentally benign route. Three water splitting pathways are currently in practice [37, 47]:

- *Electrolysis* is a well established endothermic process that splits water molecules using electrical energy. As this is a thermodynamically unfavourable process, an energy input is required to drive it [48]. If the electrical energy is provided by renewable energy sources such as solar, wind or hydro, electrolysers will play a fundamental role in the transition towards the Hydrogen Economy, as the H_2 produced is the cleanest energy carrier. In this way, water electrolysis offers a sustainable and cost-effective method [37].

  The electrolyser unit consists of a cathode (positively charged) and an anode (negatively charged) in an electrolyte, and when an electric current is applied, water splits, producing H_2 at the cathode and O_2 at the anode [45]. There are three main routes to water electrolysis: alkaline electrolysis (AE), proton exchange membrane electrolysis (PEM) and solid-oxide electrolysis (SOE). Alkaline electrolysis stands out among the other technologies as it is the most mature and commercially available. AE and PEM are known as low

temperature electrolysers (LTE), whereas SOE is known as high temperature electrolyser (HTE) [49, 50].

Currently, hydrogen production via electrolysis is the only large-scale renewable process. It is the most effective technique of the three water splitting processes to date, achieving an efficiency of 60 % [51]. Nevertheless, although the purity of the H_2 produced by water electrolysis is extremely high, this process cannot compete with other large-scale H_2 production technologies due to the high electrical energy consumption of the electrolysers (~ 40 kWh per kg of H_2). Consequently, production costs are the factors limiting competition with other available technologies [37, 52, 53].

- *Thermolysis* or thermochemical water splitting, is a high temperature technique in which water is heated until decomposed into H_2 and O_2 in a direct step. Although it is a simple technique, the decomposition of water is not effective until the temperature is high enough, around 2500 °C, due to its high Gibbs energy [47, 54, 55]. The yield of the process increases proportionally with temperature, with a maximum of 50 % at around 5000 °C [56]. Therefore, the stability of the materials at these high temperatures and the scarcity of sustainable heat sources (extremely high energy demand is required) are the challenges of this technology [56]. Besides, the maximum reported efficiency is 40 % [51].

  To make this technology more sustainable, several thermochemical cycles with Cu-Cl or SnO_2-based catalysts have been proposed, operating at lower temperatures (maximum temperature range 500-530 °C) and using solar flux or nuclear energy as a renewable source [37, 45, 57, 58].

- *Photolysis* splits water molecules by the charge generated in a semiconductor electrode by the absorption of visible light, using a system of photoelectrochemical photon collection. The photoelectrodes, typically made of TiO_2, IrO_2 and RuO_2, once exposed to sunlight and submerged in the aqueous electrolyte, generate the electrical energy necessary to drive the reaction that splits the water [51, 52]. The photolysis process, as well as

thermolysis, requires chemical catalysts such as ZnO, SnO, ZrO_2 and other semiconductor sulphur oxides. The production technology is still in the experimental stage [51].

Biomass processes

Biomass is a promising and available renewable resource derived from energy crops (herbaceous and woody), wastes (animal, wastewater and sludge, and industrial) and residues (agricultural and forestry) [59], which has attracted attention for H_2 production due to its abundance and low cost [36]. The interest in the conversion of biomass into fuels and raw materials is growing because of the sustainable and CO_2 neutral lifecycle, because the CO_2 released during the biomass-derived process is used for plant growth during photosynthesis [60, 61]. Biomass can be used for H_2 production through biological and thermochemical processes:

Biological

Biological processes use microbial metabolism to produce H_2. The main biological processes used for H_2 production are direct and indirect bio-photolysis, dark fermentation and photo fermentation due to their low energy-consumption.

- *Direct and indirect bio-photolysis* uses the photosynthesis process to dissociate water using organisms such as photosynthetic bacteria, macro- and microalgae and cyanobacteria [51]. It consists mainly of the decomposition of water using photons (from sunlight) with biological catalysts, known as water photolysis [62]. Bio-photolysis can be direct or indirect. In the *direct bio-photolysis*, green algae or cyanobacteria split water molecules into hydrogen ions and O_2 via photosynthesis in the presence of solar energy (Eq. (1.7)), and hydrogen ions are then converted to H_2 gas by hydrogenase enzyme (Eq. (1.8)) [24, 62, 63].

$$H_2O + \text{light energy} \rightarrow \frac{1}{2}O_2 + 2H^+ + 2e^- \quad (1.7)$$

$$2H^+ + 2e^- + \text{hydrogenase} \rightarrow H_2 \quad (1.8)$$

In the *indirect bio-photolysis*, the H_2 production from water by cyanobacteria or blue-green algae takes place in two steps: (i) first, glucose is produced with O_2 by photosynthesis (Eq. (1.9)), and then, (ii) CO_2 and H_2 are produced from glucose and water through two enzymes: hydrogenase and nitrogenase (Eq. (1.10))[45, 62].

$$6H_2O + 6CO_2 + \text{solar energy} \rightarrow 6O_2 + C_6H_{12}O_6 \tag{1.9}$$

$$C_6H_{12}O_6 + 6H_2O + \text{solar energy} \rightarrow 6CO_2 + 12H_2 \tag{1.10}$$

- *Dark fermentation* is one of the most studied processes for H_2 production using biological approaches [64]. Dark fermentation or anaerobic fermentation is a process that occurs in the absence of light and involves the anaerobic decomposition of organic materials by certain bacteria. Microorganisms, such as *Clostridium, Enterobacter, Bacillus and Escherichia coli* species, ferment organic substrates, such as simple sugars (glucose, sucrose, lactose), waste material (food industry waste or agricultural waste) or wastewater, and produce H_2 gas along with other metabolic by-products, such as CO_2 and volatile fatty acids (acetic acid or butyric acid) [62, 65, 66].

  Using glucose as a model organic substrate, a maximum of 4 and 2 moles of H_2 are generated per 1 mol of glucose in acetate and butyrate type fermentation, respectively, as shown in Eqs. (1.11) and (1.12) [67].

$$C_6H_{12}O_6 + 2H_2O \rightarrow 2CH_3COOH + 4H_2 + 2CO_2 \tag{1.11}$$

$$C_6H_{12}O_6 + 2H_2O \rightarrow CH_3CH_2CH_2COOH + 2H_2 + 2CO_2 \tag{1.12}$$

- *Photo fermentation* involves H_2 production by purple non-sulphur (PNS) bacteria from various carbon sources using solar energy under deficient nitrogen. Photosynthetic bacteria converts organic acids (butyric acid, lactic acid, acetic acid), waste from various industrial processes or wastewater into CO_2 and H_2 in the presence of nitrogenase enzyme [62, 68].

Thermochemical

Thermochemical conversion is the most advanced technology for H_2 production from biomass, faster than the biological processes and with a higher stoichiometric H_2 yield [24]. The four main thermochemical routes are gasification, supercritical water conversion, pyrolysis and reforming of derivatives technology.

- Biomass *gasification* is the thermochemical conversion route of biomass into H_2-rich gas, mostly containing H_2, CO_2, CO, CH_4 and hydrocarbons, at temperatures between 700 and 1200 °C (endothermic process). The quality and composition of the gas depends on the gasifying agent: air, oxygen, steam or a combination of these [69]. O_2 is often the preferred gasification agent because it produces a gas with moderate heating value, with high level of H_2 (high purity), no nitrogen and less tar and char in the outlet stream. Nonetheless, its use as gasifying agent makes the process too expensive as it requires an O_2 separation process. Air is an inexpensive and widely used gasification agent, but the nitrogen content affects negatively to the heating value of the fuel [70]. Therefore, steam gasification is used as a compromise between O_2 and air gasification. It is a well established and efficient method for H_2 production (higher H_2 yield than air biomass gasification and avoids O_2 separation steps), with a H_2-rich syngas with high calorific value [36].

  The general process consists of several stages: drying, pyrolysis, combustion and reduction. In the drying step, an endothermic evaporation of compounds takes place at a low temperature, around 100 °C, with the aim of removing moisture from the feedstock. The dried biomass undergoes thermal decomposition by pyrolysis at a temperature between 125 and 500 °C. Gases, condensable products and char are the main outputs [70]. Combustion (or oxidation) takes place at 700-1500 °C, oxidising the fuel and causing exothermic reactions, a large amount of heat is released in this step. The final process is a reduction reaction which occurs at 800-1100 °C and involves endothermic reactions [71].

- *Supercritical water gasification* is an alternative thermochemical technology for the conversion of high moisture content biomass (moisture > 35 %), as the implementation of a drying step makes any conversion process economically unviable. Supercritical steam is used as a gasification agent and also as a catalyst, at pressures above 22.1 MPa and temperatures above 374 °C (supercritical conditions). Organic compounds and gases are miscible in supercritical water at high temperatures, which facilitates their conversion. However, maintaining such operating conditions (high temperature and pressure) requires high energy input, which increases the operating cost of the process and makes it difficult to scale-up [36, 72].

- Biomass *pyrolysis* is the thermal decomposition of biomass in the absence of O_2 or air. It is one of the most energy-efficient and cost-effective processes for producing fuels from a renewable source [73]. It is an endothermic process that typically occurs at temperatures between 400 and 800 °C. A liquid fraction (tar or bio-oil), a solid residue (char) and a fraction of non-condensable gases (H_2, CO_2, CO, CH_4 and hydrocarbons) are obtained from this thermochemical process [36, 69].

  Based on the operating temperature, the process can be divided into three main types [36, 72, 74]: conventional (or slow) pyrolysis, fast pyrolysis and flash pyrolysis. The distribution of product yield therefore varies according to the type of pyrolysis and its operating conditions. Conventional or slow pyrolysis, whose main purpose is to produce char (gas and liquid fuels are also produced as by-products), is carried out at moderate temperatures (below 450 °C) and heating rates (< 1°C/s) and long residence times (> 5 min) [36, 74]. In this process, H_2 production is low but it increases with increasing temperature and heating rate [72]. Under fast pyrolysis conditions (medium temperature, 450-600 °C; high heating rates, around 300 °C/min; and short residence times) [36], the liquid fraction is the main product, with bio-oil yields between 60 and 75 wt%, which can be valorised latter by reforming processes to produce H_2 as the main product (more detailed description in section 1.4) [69]. Flash pyrolysis is similar to fast pyrolysis but it takes place at higher

temperatures (above 600 °C) and heating rates (1000 °C/s) and with shorter residence times (below 1 s). Despite the production of H_2 in the product gas stream of the process, fast pyrolysis and/or flash pyrolysis do not aim for efficient H_2 production, unlike other thermochemical pathways such as gasification [36].

- *Reforming of derivatives technologies:* H_2 production from the reforming of biomass-derived oxygenates has received much attention in the literature, due to its sustainability and promising progress towards scale-up. There are two main routes: (i) a decentralised (two separate systems) production of storable oxygenates, such as bio-ethanol (produced by biomass fermentation), methanol and dimethyl ether (DME) (produced from biomass via syngas), or bio-oil (produced by biomass fast pyrolysis), their transport and subsequent reforming in the bio-refinery; and (ii) a centralised system (a single coupled system within the bio-refinery) consisting of biomass pyrolysis and in-line reforming of the pyrolysis volatiles or biomass gasification and in-line reforming.

  Biomass pyrolysis and in-line reforming of the volatiles has received great attention among centralised processes, while reforming of bio-oil (produced by fast pyrolysis of biomass) is the most studied and developed technology among decentralised processes [69].

  Section 1.4 describes various existing reforming technologies for H_2 production from bio-oil or individual oxygenated compounds, object of this Thesis

1.3. BIO-OIL

1.3.1. Production, composition and properties

The most commonly used method for the production of bio-oil is the fast pyrolysis of biomass. This is a thermal decomposition in the absence of O_2 (or air) or with an O_2 concentration lower than that required for the complete combustion of the biomass, producing solid (char), liquid (bio-oil) and gaseous products (as detailed

explanation in section 1.2.3.2). Typical process yields are: 60-75 wt% bio-oil, 15-25 wt% char and 10-20 wt% gas [75, 76].

Bio-oil is a dark brown, viscous, polar, hydrophilic liquid with a characteristic odour, composed of a complex mixture of components derived from the fragmentation and depolymerisation reactions of biomass components (cellulose, hemicellulose and lignin). Its average molecular weight is between 100-1000 g/mol. It is composed of water and a mixture of oxygenated hydrocarbons (>300) from different families: acids, alcohols, ketones, aldehydes, ethers, esters, phenols, sugars, furans, nitrogen compounds and other oxygenates [77]. These compounds confer to the bio-oil an acidic (pH $\approx$ 2-3), corrosive (especially at high temperatures) and unstable nature. Hence, its high heating value (HHV) is about 16-19 MJ/kg, almost 2.7 lower than that of typical fossil diesel fuel [78, 79].

The water content in bio-oil is a key factor in its physical and chemical properties and is usually determined by Karl-Fischer titration method. Water is the most abundant compound in bio-oil, which comes from the original moisture in bio-oil and the dehydration reactions in pyrolysis, and its content varies between 15-30 wt%, depending on the type of biomass and the conditions of the production process (lower for wood and higher for agroforestry residues [80]). The oxygen content of bio-oil depends on the water content and varies between 35-40 wt% [81, 82]. Oxygen is present in almost all the organic compounds in bio-oil, which are mainly responsible for its polarity and low miscibility with fossil fuels (non-polar). In addition, the high oxygen content results in a biofuel with a low heating value, high corrosivity and instability [83, 84].

Bio-oil also contains ash (combustion residues) whose content varies between 0.004-0.30 wt%. The ASTM D-7544 standard suggests that the content of these solids should not exceed 0.25 wt%, as high levels can cause high wear in pumps and injectors, and corrosion and deposition problems in combustion equipment, due to the alkali metals contained in the ash [76].

The viscosity of bio-oil is another relevant property to consider, as it is important for the design of equipment and chemical reactors. Its value ranges from 40-100

cP at 50 °C, depending on the biomass and pyrolysis conditions, and can be reduced by moderate preheating (< 80 °C) to facilitate pumping and atomisation, without significantly modifying its composition [81].

Bio-oil has a tendency to polymerise over time (aging) due to the presence of phenolic oligomers derived from the lignin of the biomass and aldol-type reactions promoted by acids. The addition of alcohols (mainly methanol and ethanol, around 10 wt%) has been shown to have a significant stabilising effect on the bio-oil during storage, not only preventing aging reactions but also reducing the increase in viscosity [85].

It is interesting to note that the properties and composition of the bio-oil change depending on the pyrolysis conditions, the reactor configuration and the origin and characteristics of the biomass used [82, 86].

1.3.2. Upgrading routes

The aforementioned properties of bio-oil limit its direct use as a biofuel or as a raw material in various processes, and therefore usually require processes to upgrade its composition. The main valorization routes for bio-oil include direct, physical and catalytic upgrading.

The ***direct valorization*** of bio-oil is due to its great potential for heat and energy generation as a fuel at industrial level, in boilers, furnaces, kettles or turbines [87], although its use requires certain modifications to improve the efficiency of the equipment, such as the installation of particle retention systems (filters or cyclones) and the removal of carbonaceous deposits. There are a number of strict standards that must be followed for its direct use, which are clearly defined in the ASTM D-7544 standard.

The use of bio-oil as a transport fuel in automotive vehicles involves the physical blending (***physical upgrading***) of bio-oil with conventional fuels. Bio-oil/diesel has been the most studied mixture [80]. However, the low miscibility of the two phases requires emulsification using low cost surfactants or chemical emulsifiers (alcohols such as octanol or butanol) to achieve or maintain a more or less

homogeneous emulsion between them. Bio-oil/diesel emulsion combustion has the advantage of reducing particulate matter and NOx emissions compared to diesel combustion [88].

Valorization by catalytic conversion of bio-oil has been addressed in the literature by several routes: hydrotreating/hydrodeoxygenation (HDO), catalytic cracking, esterification and steam reforming. This latter will be extensively described in section 1.4.

- *Hydrotreating/hydrodeoxygenation (HDO)* aims to reduce the O, N and S content of heterogeneous streams to improve their fuel properties. In the case of bio-oil, nitrogen and sulphur are not present in significant quantities, but oxygen is abundant. Therefore, hydrodeoxygenation (HDO) treatment is needed for the elimination of oxygen. In this process, oxygen is removed as H_2O, CO_2 and CO through dehydration, decarboxylation and decarbonylation reactions. HDO is carried out under high pressure (20-200 bar) and high temperature (250-400 °C) conditions with a H_2 supply. The result is a highly deoxygenated liquid product with a residual oxygen content of less than 5 wt% [80, 89].

- *Catalytic cracking* involves the deoxygenation of bio-oil using acid catalysts, at atmospheric pressure and without H_2 feed, so it has lower operating costs than HDO. It consists of dehydration reactions, hydrocarbon cracking, hydrogen production and consumption reactions, and production of larger molecules by C-C bonding [76]. The most commonly used catalysts are zeolites, which have a large specific surface area and high adsorption capacity, the most commonly used being H-ZSM-5, H-Beta and H-USY [80, 90].

- The *esterification* process converts organic acids (such as acetic acid, formic acid, propionic acid) into esters, thereby improving the quality of the bio-oil (stabilising the bio-oil by neutralising its acidity) [91]. This reaction is accompanied by the acetylation of aldehydes, ketones and sugars [92]. This process requires the addition of alcohols (ethanol, methanol, glycerol), moderate temperatures (60-120°C) and the use of strongly acidic catalysts [93].

1.4. HYDROGEN PRODUCTION THROUGH REFORMING OF BIO-OIL AND OXYGENATED COMPOUNDS

As discussed earlier in this Thesis, reforming is one of the processes with the greatest potential for sustainable H_2 production. Among the different alternatives, steam reforming (SR) of bio-oil receives great attention as it is a promising and economically viable thermochemical technology for the production of clean H_2, with a low environmental impact due to its neutral CO_2 balance. Additionally, the steam reforming process avoids the costly step of separating water from the bio-oil, for its use as a fuel, and allows the joint valorization of the complex mixture of oxygenated compounds [94].

The overall reaction for the SR of oxygenated hydrocarbons ($C_nH_mO_k$) (Eq. (1.13)) involves reforming reaction to produce syngas ($CO+H_2$) (Eq. (1.14)) and the subsequent water-gas-shift (WGS) reaction (Eq. (1.15)).

$$C_nH_mO_k + (2n - k)H_2O \rightarrow nCO_2 + \left(2n + \frac{m}{2} - k\right)H_2 \quad (1.13)$$

$$C_nH_mO_k + (n - k)H_2O \rightarrow nCO + \left(n + \frac{m}{2} - k\right)H_2 \quad (1.14)$$

$$CO + H_2O \leftrightarrow CO_2 + H_2 \quad (1.15)$$

The high endothermicity of the reforming reaction (Eq. (1.14)) requires a high operating temperature, which shifts the WGS reaction (Eq. (1.15)) (exothermic reaction) towards the formation of CO and H_2O (reverse-WGS) [95].

According to the global stoichiometry (Eq. (1.13)), the maximum H_2 yield for the SR of oxygenated hydrocarbons is $(2n + m/2 - k)$mol H_2/mol$_{oxygenates}$. However, the real yield is lower due to the thermodynamic limitations of the WGS reaction and the existence of parallel secondary reactions, such as decomposition/cracking of oxygenates (Eq. (1.16)), steam reforming of decomposition products (CH_4 and light hydrocarbons (C_aH_b), Eq. (1.17) and Eq. (1.18), respectively) and interconversion of oxygenates (Eq. (1.19))

$$C_nH_mO_k \rightarrow C_xH_yO_z + \text{gas (CO, } CH_4\text{, } CO_2\text{, } C_aH_b\text{, } H_2\text{, ...)} + \text{coke} \quad (1.16)$$

$$CH_4 + H_2O \leftrightarrow CO + 3H_2 \quad (1.17)$$

$$C_aH_b + aH_2O \rightarrow aCO + (a + b/2)H_2 \quad (1.18)$$

$$C_nH_mO_k \rightarrow C_xH_yO_z \quad (1.19)$$

Moreover, the catalyst undergoes rapid and severe deactivation mainly due to coke deposition, whose amount depends on the relative importance of the reactions for its formation (decomposition/cracking of oxygenates, methane decomposition and Boudouard reaction, Eqs. (1.16), (1.20) and (1.21), respectively) and gasification (Eq. (1.22)).

$$CH_4 \leftrightarrow 2H_2 + C \quad (1.20)$$

$$2CO \leftrightarrow C + CO_2 \quad (1.21)$$

$$C + H_2O \rightarrow CO + H_2 \quad (1.22)$$

The complexity of the reaction system makes it difficult to design a selective catalyst for the reforming reactions of oxygenates and hydrocarbons (by-product), WGS and coke gasification, while inhibiting methanation and coke formation reactions [96, 97]. The most studied catalysts for the reforming process are Ni-based catalysts [96, 98], Mg-doped catalysts [99, 100] and noble metal-loaded catalysts (Pd, Pt, Pu and Rh) [77, 97]. Ni-based catalysts are widely used for steam reforming of bio-oil due to their cost effectiveness and high C-C bond breaking activity. Noble metal-based catalysts are generally more effective than Ni-based catalysts and exhibit less carbon deposition, but they are not commonly used in practical applications due to their high cost [97].

The main challenge of bio-oil SR is to mitigate catalyst deactivation, mainly due to coke deposition. The co-feeding of O_2 (oxidative steam reforming, OSR) is effective in promoting the partial combustion of coke precursors and attenuating their formation, although it decreases the H_2 yield, according to the ideal stoichiometry (Eq. (1.23)) [95, 101]. Furthermore, the heat generated in the combustion reactions in the OSR partially satisfies the energy requirement, and

a thermo-neutral regime (autothermal reforming, ATR) can be achieved with an adequate O_2/steam/bio-oil ratio.

$$C_nH_mO_k + aO_2 + (2n - 2a - k)H_2O \rightarrow nCO_2 + \left(2n + \frac{m}{2} - k - 2a\right)H_2 \qquad (1.23)$$

1.4.1. Steam reforming of oxygenated compounds

The handling of raw bio-oil (as obtained) presents important problems/challenges due to the presence of highly reactive oxygenates (mainly phenolic compounds) which easily repolymerise at moderate temperatures to form a solid residue (pyrolytic lignin, PL) whose deposition causes problems in the bio-oil feed (even blocking the flow in the reaction system) and rapidly deactivates the catalyst. Therefore, due to the complexity of raw bio-oil, many bio-oil SR studies have been approached in the literature with model compounds, representative of the main families of components present in raw bio-oil, such as acetic acid (the most studied as it is one of the main components of bio-oil) [102, 103, 112–121, 104, 122, 123, 105–111], acetone [103, 111, 120, 121, 124–128], acetol [105, 110, 113, 115, 129], some alcohols (ethanol, methanol, butanol) [110, 113, 120, 121, 124, 129–132] or phenols [115, 133–135].

1.4.1.1. Acetic acid

Acetic acid is considered representative of the carboxylic acid family, one of the major families of bio-oil. Wang et al. [115] studied the SR of acetic acid with 15 %Ni/nano-Al_2O_3 catalyst, steam-to-carbon (S/C) molar ratio of 9.2 and weight hourly space velocity (WHSV) of 3 h^{-1}, obtaining high conversions and H_2 yields that increase with temperature from 82.9 % conversion and 80.4 % H_2 yield at 500 °C to 98.5 % conversion and 87.4 % H_2 yield at 800 °C.

Zhang et al. [119] studied the SR of acetic acid over Ni/γ-Al_2O_3 catalysts with different nickel contents (5, 10, 15, 20 wt%), at 600 °C, S/C molar ratio of 1.5 and liquid hourly space velocity (LHSV) of 7.2 h^{-1}, with a duration of 5 h. The catalyst with 5 wt% Ni showed very low reforming activity and rapid

deactivation, with H_2 yield below 20 %. Increasing the nickel loading improved the stability of the catalysts, so that with 20 wt% Ni both the conversion (~ 100 %) and the product distribution were very stable throughout the reaction.

Li et al. [120] compared the catalytic behaviour of catalysts based on Mn, Fe, Co, Ni, Cu and Zn in the SR of methanol, acetic acid and acetone. The SR of acetic acid was studied with Ni, Ni/Al_2O_3, Co and Co/Al_2O_3 catalysts (at 500 °C, S/C ratio of 1.5, time on stream (TOS) of 5 h and LHSV of 12.7 h^{-1}). Low acetic acid conversion (40 %) and H_2 yield of 20 % were obtained with the unsupported Ni catalyst, although no evidence of deactivation was observed under the experimental conditions. On the contrary, the Ni/Al_2O_3 catalyst, which was more active at the beginning of the reaction, was progressively deactivated until a conversion of 70 % and a H_2 yield of 50 % were obtained. For the unsupported Co catalyst, although the conversion remained stable (55 %), the hydrogen evolution decreased from 30 % to about 22 %. Similar to the supported Ni catalyst, the Co/Al_2O_3 catalyst suffered a clear deactivation with the reaction time, obtaining a conversion of 80 % and a H_2 yield of 43 %. Thus, this work concluded that the alumina support has a significant influence on the catalytic stability of the catalyst.

1.4.1.2. Acetone

Acetone is also a widely studied model compound as it is an intermediate in the reforming of acetic acid and ethanol. Due to its high reactivity, most studies have been carried out using low cost Ni and Co catalysts.

Navarro et al. [125] investigated the SR of acetone with Ni catalysts and bimetallic Pt-Ni catalysts supported on modified Al_2O_3. La, Ce and Mg oxides were used as support modifiers to neutralise acidity and/or increase water adsorption and OH- surface mobility of the Al_2O_3 support. At 600 °C, S/C ratio of 2, TOS of 10 h and gas hourly space velocity (GHSV) of 10180 h^{-1}, full acetone conversion was obtained with all the catalysts used.

Elias et al. [126] used a Ni/ZnO catalyst for the SR of acetone and analysed the effect of the incorporation of CeO_2 on the catalytic behaviour and carbon deposit formation. The CeO_2 phase, either as a pure support or as part of a mixed oxide mixture, is traditionally a widely used support for catalysts, due to its good redox properties and high oxygen storage capacity, which promotes the combustion of coke and its precursors [136, 137]. The authors studied the SR of acetone at 600 °C, S/C ratio of 1 and GHSV of 7800 h^{-1}, and concluded that Ni/xCeZnO catalysts (x=10, 20, 30 CeO_2 wt%) performed better than Ni/ZnO catalyst, with higher acetone conversion: 75 % (Ni/ZnO) versus 81 % (Ni/30CeZnO). Similarly, a higher H_2 yield was obtained, 9.8 % (Ni/ZnO) versus 30.7 % (Ni/30CeZnO). In addition, the amount of carbonaceous deposits on the used catalyst and their graphitic nature was lower for Ni/xCeZnO than for Ni/ZnO, and the amount of carbonaceous deposits decreases with CeO_2 content.

Basu and Pradhan [127] studied the SR of acetone over NiCoMgAl mixed oxide catalysts obtained from hydrotalcite precursors with varying Ni/Co ratios (0.33, 1 and 3), in the 450-550 °C range, with a steam/acetone molar ratio of 4-10 and a space time of 10-24 $kg_{catalyst}{\cdot}h/kmol_{acetone}$. These authors obtained about 99 % acetone conversion over all the catalysts employed and a maximum hydrogen selectivity of ~ 80 % over NiCoMgAl (0.33). The stability of the catalyst (NiCoMgAl (0.33)) was studied for 4 h at 500 °C and with a steam/acetone molar ratio of 6. The conversion remained constant throughout the test.

1.4.1.3. Hydroxyacetone (Acetol)

Hydroxyacetone or acetol, formed from carbonyl and hydroxyl functional groups, is studied as a model compound for the ketone and alcohol families. Medrano et al. [113] studied the SR of acetol, butanol, ethanol and acetic acid in a fluidized-bed reactor at 650 °C, S/C ratio of 7.64, $u/u_{mf} = 6$ and methane-equivalent gas hourly space velocity ($G_{C1}HSV$) of 30000 h^{-1} with NiMgAl catalyst (29.3 wt% Ni and Mg/Al=0.26 molar ratio). The catalyst showed high stability in the SR of alcohols, although the carbon to gas conversion was low (76.4 % and 88.3 % for butanol and ethanol, respectively). In the SR of acetol and acetic acid, acetol was

significantly more reactive, reaching a carbon to gas conversion of 91.7 %, and in both cases a decrease in carbon to gas conversion was observed with time, more significant in the case of acetic acid. In the SR of butanol, ethanol and acetic acid the H_2 selectivity remained stable at a value corresponding to the equilibrium conditions, whereas in the SR of acetol a steady decrease of H_2 selectivity was observed, resulting in a selectivity far from thermodynamic equilibrium.

Wang et al. [115] investigated the SR of acetol over a 15 %Ni/nano-Al_2O_3 catalyst, S/C ratio of 9.2 and WHSV of 3 h^{-1}. Both, acetol conversion and H_2 yield increase with temperature: at 500 °C, 72.8 % conversion and 71.3 % H_2 yield; at 700 °C, 98.7 % conversion and 97.2 % H_2 yield; and at 800 °C, 99 % conversion and 97 % H_2 yield.

1.4.1.4. Phenols

Some phenols and derivatives, such as furfural, cresol, guaiacol and toluene, have been studied as representative model compounds for tar (organic fraction of bio-oil) [138–141]. One of the main problems in the SR of phenol is the formation of some by-products such as carbon, which leads to catalyst deactivation and can cause problems for continuous SR and sustainable hydrogen production [134].

Matas Güell et al. [133] compared the SR of phenol over Ni/K-La-ZrO_2 and Ni/Ce-ZrO_2 catalysts at 700 °C, S/C ratio of 20, GHSV of 950000 h^{-1} and TOS of 22 h. The conversion of phenol with Ni/K-La-ZrO_2 catalyst was ~ 85 %, remaining relatively stable during the whole reaction. However, the product distribution varied with time. The H_2 and CO_2 yields decreased from 90 % to 78 % and from 86 % to 65 %, respectively. In contrast, the CO yield increased from 20 % to 32 %. The Ni/Ce-ZrO_2 catalyst also showed high initial activity (~ 80 % phenol conversion), with H_2 and CO_2 yields around 88 % and 79 %, respectively, CO yield ~ 21 % and no CH_4 was detected throughout the experiment. The changes in product distribution were less than for Ni/K-La-ZrO_2: H_2 and CO_2 decreased from 85 % to 71 % and from 78 % to 68 % respectively, whereas CO remained fairly constant.

Wang et al. [115], under the same conditions used for the SR of acetic acid and acetol (15 %Ni/nano-Al_2O_3 catalyst, S/C ratio of 9.2 and WHSV of 3 h^{-1}), also observed an increase in phenol conversion and H_2 yield with temperature: at 500 °C, 700 °C and 800 °C the conversion was 64.8 %, 84.2 % and 92.2 %, whereas the H_2 yield was 64.8 %, 69 % and 74.4 %, respectively.

Nabgan et al. [134] analysed the influence of Ni-Co ratio supported on ZrO_2 (Ni_xCo_y/ZrO_2 x = 0, 1, 2, 3 where x + y = 4) on phenol SR at 600 °C, water/phenol molar ratio of 10 and 6 h. No significant variation with time was observed for phenol conversion and H_2 and CO yield for the Ni_2Co_2 and Ni_3Co_1 catalysts. However, both phenol conversion and H_2 and CO yields decreased slowly with time for the Ni_4 and Co_4 catalysts. On the other hand, the CO_2 yield increased progressively with time for all catalysts. Overall, the work concluded that the Ni_3Co_1 catalyst had the highest activity and stability compared to the others (phenol conversion of 53.5 % and H_2 yield of 50.4 %).

Hu and co-workers extensively studied the SR of guaiacol over different Ni-based catalysts [142–145]. The authors investigated the effect of the support (Al_2O_3 and SBA-15) with two Ni-based catalysts (both with 20 wt% of Ni) in a fixed-bed reactor with S/C ratio of 5 and LHSV of 21.2 h^{-1} at 300-600 °C temperature range for 30 min on stream [142]. Both catalysts were not active below 400 °C, but significant activity was observed for guaiacol SR at 600 °C, with initial values of conversion and H_2 yield of ~ 92 % and 80 %, respectively, for Ni/SBA-15 catalyst and of ~ 75 % and ~ 30 % for Ni/Al_2O_3 catalyst. Ni/SBA-15 catalyst also showed superior stability at 600 °C for 300 min in spite of its higher amount of coke deposited (38.6 %) compared to Ni/Al_2O_3 (10.2 %), which was explained because the coke in the Ni/Al_2O_3 catalyst was mainly of amorphous nature, whereas in the Ni/SBA-15 catalyst carbon nanotubes were the main form of coke. These authors also studied the SR of guaiacol over a Ni/SiO_2 catalyst (20 wt% Ni) modified with Na, Mg and La [143], under similar operating conditions. The La-Ni/SiO_2 catalyst reached the highest activity (complete guaiacol conversion and ~ 80 % of H_2 yield at 600 °C) and stability, whereas the strong alkalinity caused

by the addition of Na or Mg to Ni/SiO_2 led to a noticeable decrease in the initial catalytic activity and a higher deactivation rate.

These researchers also investigated the SR of a series of organic molecules with different molecular structures derived from bio-oil (methanol, formic acid, ethanol, acetic acid, acetaldehyde, acetone, furfural and guaiacol) over a Ni-La/Al_2O_3 catalyst (15 wt% of Ni and 2 wt% of La) in a fixed-bed reactor at 600 °C, S/C ratio of 1.5 and LHSV of 12.7 h^{-1} for 240 min on stream [144]. The reforming of methanol and formic acid was relatively easy because they do not contain a carbon (C-C) chain to be cracked in their structures and thus, coke formation was insignificant, so the catalyst showed a stable catalytic performance. A progressive deactivation was observed with time on stream in the SR of the other reactants (acetic acid, ethanol, acetaldehyde and acetone), which were more difficult to be reformed and coking was significant (mainly amorphous coke), especially for acetone and acetaldehyde. However, the catalyst was unable to convert the high molecular weight reactants furfural and guaiacol under the reaction conditions employed in that study and a significant amount of coke (mainly carbon nanotubes) was formed. These results showed that the structures of the feedstock affect their reaction behaviour in the steam reforming and, in particular, their tendencies to coke formation.

Moreover, the SR of acetic acid and guaiacol over Ni/attapulgite (natural mineral) catalyst (25 wt% of Ni) and the effect of attapulgite activation with KOH on the catalytic behaviour of Ni/attapulgite catalyst were investigated [145]. The reaction runs were carried out in a fixed-bed reactor, S/C ratio of 5, LHSV of 10.4 h^{-1} (for acetic acid SR) and 21.1 h^{-1} (for guaiacol SR), KOH/attapulgite mass ratio of 0 and 2, at 700 °C for 300 min on stream. For acetic acid SR, no deactivation was observed in any case (KOH/attapulgite 0 and 2). For guaiacol SR, the Ni/attapulgite (no KOH activation) catalyst deactivated rapidly with time on stream, but the Ni/KOH-attapulgite (ratio of 2) catalyst was much more stable. In both cases, the initial catalyst activity was higher with KOH activation due to the higher metallic nickel dispersion and alkalinity of the KOH activated Ni/attapulgite catalysts.

Wu and Liu [146] studied the SR of m-cresol with Ni/MgO-Al_2O_3 catalyst in a fixed-bed reactor at 850 °C, S/C ratio of 5 and space time of 1 $g_{catalyst}{\cdot}h/g_{m\text{-}cresol}$ for 3 h on stream. After the experimental run, two conventional carbon elimination methods (combustion with air and gasification with steam) were applied and the m-cresol was steam reformed again on the regenerated samples to investigate possible activity changes. Although catalyst activity decreased slightly after regeneration (mainly due to loss of active metal), with H_2 yield decreasing from 84 % to 81.3 % for the combustion method and to 82.9 % for steam gasification method, the overall performance of the regenerated catalysts was similar to that of the fresh catalyst, achieving $>$ 81 % H_2 yield, and $>$ 97 % carbon conversion

1.4.2. Steam reforming of bio-oil

As discussed previously, steam reforming of raw bio-oil is an experimental challenge due to the complex composition of the bio-oil. However, in order to progress towards the scale-up of this process, it is required the study with real bio-oil feeding, since the catalyst performance in the reforming of the model compounds may differ significantly from that observed in the reforming of a real bio-oil, in which the possible synergies between its components could impact on the catalyst performance. Moreover, real bio-oils have a large amount of heavy oxygenates with a lower expected SR reactivity and higher coking tendency than light oxygenates. Unfortunately, SR studies with real bio-oil or with bio-oil aqueous fraction are limited.

The studies over catalyst development and reaction conditions (temperature, S/C ratio and space time) in bio-oil SR have mainly been performed with Ni-based catalysts over different supports and with packed-bed reactors. The results evidence operating problems due to the rapid catalyst deactivation by coke, and even gas flow blockage when the feed is raw bio-oil [147, 148]. Considering the relevance of catalyst deactivation by coke, it is required to be regenerable, recovering its activity after coke combustion. It has been demonstrated that a catalyst prepared by reduction of $NiAl_2O_4$ is completely regenerable [149] and its

good performance in the reforming of bio-oil (with high activity, H_2 selectivity and stability) is due to the presence of highly dispersed and uniformly distributed Ni sites within the catalyst particle.

The scale-up of raw bio-oil SR (as well as other catalytic processes with high reaction heat and rapid catalyst deactivation) recommends the use of a fluidized-bed reactor [150] to avoid bed blockage problems [151, 152] and the complex design and operation of packed-bed multitube reactors [153]. Thus, the free movement of the catalyst particles facilitates temperature control (uniform throughout the reactor and without cold spots). Moreover, the high velocity of heat transport between phases facilitates external heat input (necessary because the reaction is highly endothermic). The movement of the catalyst in the fluidized-bed reactor would also facilitate the future operation of a reactor-regenerator system, with circulation of the catalyst between the two units, maintaining a constant catalyst activity in the reactor and continuously regenerating the catalyst (and the sorbent in the sorption enhanced steam reforming (SESR) operation, process explained in section 1.4.3). Papalas et al. [154] have simulated such a system for CH_4 reforming.

For the purpose of attenuating catalyst deactivation by coke, lower coke deposition has been observed in the fluidized-bed reactor compared to the packed-bed reactor in the steam reforming of biogas [155], acetic acid [156], aqueous fraction of bio-oil [151, 157, 158] and raw bio-oil [148], and in the oxidative reforming of ethanol [159]. The reason seems to be that the mixing regime of the catalyst particles, at a high temperature (above 600 °C in the experiments reported in the literature) and with the appropriate catalyst, promotes the gasification of the coke from bed particles and also delays the evolution of the coke towards structures that encapsulate the Ni sites.

However, results in the literature (in laboratory equipment or by simulation) show the negative effect of bubble presence in the gas-solid contact [160]. Thus, for the SR of methane [161], methanol [162], aqueous fraction of bio-oil [151, 158] and raw bio-oil [148] the conversion is lower in the fluidized-bed reactor than in the packed-bed reactor. Fernández et al. [163] have studied the reforming of

volatiles from biomass fast pyrolysis on a commercial Ni-Ca/Al_2O_3 catalyst and attributed the higher coke deposition rate in the fluidized-bed reactor to the higher-concentration of unreacted oxygenates [164].

Overall, numerous articles in the literature summarise the general aspects of the SR reaction, such as the effect of the feed, catalyst, reactor type and operating conditions on hydrogen production [77, 79, 165, 166].

To mitigate catalyst deactivation, Remiro et al. [167, 168] proposed a two-step in-line (thermal and catalytic) reaction system (Figure 1.5) for the SR of bio-oil aqueous fraction or complete bio-oil. The first reactor (a U-shaped stainless steel tube) retains the carbonaceous solid (pyrolytic lignin) formed by the repolymerization of certain oxygenated components of the bio-oil (mainly phenolic compounds). The volatile compounds leaving this unit (treated bio-oil+gases) are reformed (by catalytic steam reforming) in a fluidized-bed reactor (unit 2). This reaction system minimises the operational problems caused by pyrolytic lignin deposition and attenuated catalyst deactivation. Therefore, under suitable conditions (700 °C, S/C ratio of 9 and $G_{C1}HSV$ of 8000 h^{-1}), H_2 and CO yields were 95 % and 6 %, respectively, with slow catalyst deactivation, leading to a minimal decrease (about 2 %) in H_2 yield over 100 min of reaction [167].

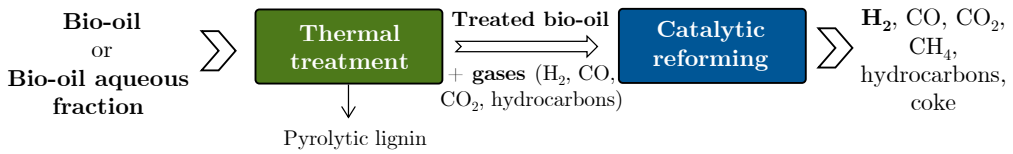

Figure 1.5. Two step process for the steam reforming of bio-oil or bio-oil aqueous fraction [167, 168].

Bimbela et al. [169] studied the catalytic steam reforming of three different aqueous fractions of bio-oil (with 83-84 wt% of H_2O) using Ni/Mg-Al (28 wt% of Ni) catalysts modified with Ce (0-5 wt% of Ce), by different preparation methods (co-precipitation, impregnation and thermal decomposition of the precursor salts) in a packed-bed reactor at 650 °C and $G_{C1}HSV$ of 13000 h^{-1}. Overall, the addition

of Ce to the Ni/Mg-Al catalyst improved the carbon conversion to gas, H_2 yield and catalyst stability in the SR process. The best preparation method was impregnation and the optimum Ce content was 0.5 wt% (resulting in a significant reduction of carbon deposits compared to the unpromoted Ni/Mg-Al catalyst) with a carbon conversion to gas of 78.7 % and 70.8 vol.% of H_2. Regarding the effect of the aqueous fraction fed, the two aqueous fractions derived from pine produced much higher initial carbon conversion to gas and initial H_2 yield than that derived from poplar. However, the latter provided a more stable carbon conversion to gas and H_2 production.

Valle et al. [170, 171] investigated the influence of temperature, space time and S/C molar ratio in the SR of raw bio-oil over Ni/La_2O_3-αAl_2O_3 (10 wt% of Ni) catalyst in a fluidized-bed reactor. The influence of temperature was studied in the 550-700 °C range with S/C ratios of 1.5 and 6, and space time in the 0.04-0.38 $g_{catalyst}·h/g_{bio\text{-}oil}$ range. Bio-oil conversion and H_2 yield were significantly improved by increasing the temperature. Above 650 °C, S/C ratio of 6 and space time higher than 0.10 $g_{catalyst}·h/g_{bio\text{-}oil}$, a H_2 yield higher than 88 % was obtained with low catalyst deactivation [170]. On the other hand, the effect of space time (0.04-0.38 $g_{catalyst}·h/g_{bio\text{-}oil}$) and S/C molar ratio (1.5, 3 and 6) were also studied at 700 °C over the same catalyst [171]. The increase of both space time and S/C ratio contributes to increase the yield of H_2 and decrease the yield of CO, CH_4 and light hydrocarbons (C_2-C_4). In addition, catalyst deactivation is attenuated by the increase of space time due to the lower deposition of encapsulating coke (amorphous carbon), which blocks Ni sites and causes rapid deactivation. However, space time has no effect on the formation of filamentous coke (with lower impact on deactivation). Regarding the S/C ratio, it has less influence than space time on the total coke content. Therefore, at 700 °C with the highest space time (0.38 $g_{catalyst}·h/g_{bio\text{-}oil}$) and S/C ratio (6) studied, a hydrogen-rich gaseous outlet stream is obtained, with an initial H_2 yield of 93 %, which decreased to 70 % after 7 h of reaction due to low catalyst deactivation.

Bizkarra et al. [172] analysed the SR of a real bio-oil (obtained from pine sawdust with $C_{2.7}H_{6.7}O_{3.7}$ chemical composition) in a packed-bed reactor with catalysts

based on Ni supported on alumina (Ni/Al_2O_3, 13 wt% of Ni), modifying the Al_2O_3 support with CeO_2 (8 wt%) (Ni/CeO_2-Al_2O_3) and La_2O_3 (6 wt%) (Ni/La_2O_3-Al_2O_3) at 800 °C, atmospheric pressure, S/C ratio of 5 and space time of 1.45 $g_{catalyst}{\cdot}h/g_{bio\text{-}oil}$ for 3 h. Initially all the catalysts presented high H_2 yields (about 90 % for Ni/Al_2O_3 and Ni/CeO_2-Al_2O_3 catalysts and about 75 % for Ni/La_2O_3-Al_2O_3 catalyst), but they rapidly decreased to H_2 yields of ~ 35-40 %. The bare alumina supported catalyst (Ni/Al_2O_3) showed the fastest deactivation, while Ni/CeO_2-Al_2O_3 maintained the initial activity for a longer time, being more resistant to deactivation. Therefore, Ni/CeO_2-Al_2O_3 catalyst was selected for further studies under the same operating conditions but promoted by noble metals (Rh, Pt and Pd, with 1 wt% of each promoter). Although Pt- and Pd-containing catalysts showed high initial H_2 yields (around 70 %), they rapidly lost catalytic activity, resulting in a decrease in H_2, CO_2 and CO yields. For the Rh-Ni/CeO_2-Al_2O_3 catalyst, the initial H_2 yield (around 60 %) was lower compared to the other bimetallic catalysts and Ni/CeO_2-Al_2O_3, but remained stable up to 3 h, without showing any deactivation. The latter is therefore a promising catalyst for obtaining a hydrogen-rich gas from the SR of bio-oil.

Remiro et al. [173] studied the deactivation mechanism of Rh/CeO_2-ZrO_2 (with 2 wt% of Rh) catalyst in raw bio-oil SR in a fluidized-bed reactor at 700 °C, S/C ratio of 6 and space time of 0.15 $g_{catalyst}{\cdot}h/g_{bio\text{-}oil}$, up to 6 h on stream. Considering the evolution with time of the results, five catalyst deactivation states can be distinguished, with two sharp changes in bio-oil conversion and product yields (as shown in Figure 1.6). The initial period corresponds to thermodynamic equilibrium, with constant values of the reaction indices (complete bio-oil conversion and 95 % of H_2 yield). Subsequently, a rapid deactivation occurs (first sharp change), which is followed by a new pseudo-stable period (stage 3) with 95 % of bio-oil conversion and H_2 yield of ~ 70 %. In this first deactivation period (stage 2), CH_4 and hydrocarbons (HCs) yields increase due to catalyst deactivation for their reforming. From the pseudo-stable state (period 3), a second rapid deactivation period begins (second sharp change, stage 4), where the bio-oil conversion and H_2 and CO_2 yields decreased significantly, faster than in the first deactivation period, and the yield of hydrocarbons increases in parallel. Once

the catalyst has undergone a high deactivation level, the change in the reaction indices takes place slowly (stage 5), reaching values corresponding to the thermal routes, when the catalyst is completely deactivated. According to the authors, the first deactivation period is the result of a structural change in the catalyst (support aging), which is irreversible and occurs quickly at the beginning of the run, whereas the second deactivation stage is associated with encapsulating coke deposition, which is reversible and develops more slowly.

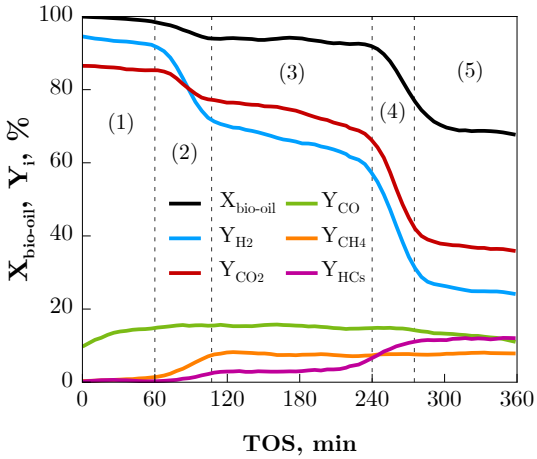

Figure 1.6. Evolution with TOS of bio-oil oxygenates conversion and yields of products and deactivation stages in the SR of bio-oil with Rh/CeO_2-ZrO_2 catalyst (adapted from [173]).

García-Gómez et al. [96] studied the effect of reaction conditions (temperature, space time and S/C molar ratio) on the deactivation of a Ni/Al_2O_3 catalyst (obtained by reduction of $NiAl_2O_4$ spinel, with 33 wt% of Ni) in the SR of bio-oil. The runs were carried out in a fluidized-bed reactor with prior separation of the pyrolytic lignin (Figure 1.5). The effect of reaction temperature was analysed at 600, 650 and 700 °C for a space time of 0.15 $g_{catalyst}$·h/$g_{bio-oil}$ and S/C ratio of 3. Initially, bio-oil conversion increased with increasing temperature, reaching complete conversion at 650 and 700 °C, while the initial yields of H_2 and CO_2 reached a maximum at 650 °C (around 90 %). Regarding the catalyst stability, bio-oil conversion and the yield of H_2 and CO_2 decreased with time, indicating

that the catalyst underwent deactivation, in the following order: 650 °C > 700 °C > 600 °C. Catalyst deactivation was practically complete after 4 h and 4.5 h at 650 °C and 700 °C, respectively, whereas at 600 °C, the catalyst maintained high activity after 4.5 h. The influence of space time (of 0.075, 0.15 and 0.25 $g_{catalyst}·h/g_{bio\text{-}oil}$, varying catalyst weight) was assessed at 700 °C and S/C ratio of 3. Complete conversion and fairly similar product yields were observed at zero time on stream for the different space time values due to the high reaction temperature used (at 700 °C). The deactivation rate decreased significantly with increasing space time and therefore, the variations of the reaction indices were slower at higher space time values. Finally, the effect of S/C molar ratio (1.5, 3 and 4.3) was studied at 700 °C and space time of 0.25 $g_{catalyst}·h/g_{bio\text{-}oil}$. Initial bio-oil conversion and H_2 and CO_2 yields increased with increasing S/C ratio, indicating that the excess of water favours SR and WGS reactions. Besides, the deactivation rate was attenuated with increasing S/C ratio.

Moreover, these authors also investigated the effect of bio-oil composition for H_2 production by SR process in fluidized-bed reactor over the same $NiAl_2O_4$ derived catalyst [174], using (i) raw bio-oil, or modifying raw bio-oil composition by (ii) removal of phenolic compounds by liquid-liquid extraction method or (iii) with a pre-reforming step using dolomite as a low-cost guard and pre-reforming catalyst. The experiments were performed at 600 and 700 °C, S/C ratio of 3 (for raw bio-oil and pre-reformed bio-oil) and 6 (for the treated bio-oil by removal of phenolic compounds) and space time of 0.14 $g_{catalyst}·h/g_{bio\text{-}oil}$. For the raw bio-oil SR, the catalyst stability was higher at 600 °C (with 13 h duration run) compared to 700 °C (7.5 h duration). At both temperatures, the oxygenate conversion was complete at zero time and the H_2 yield was around 90 %, slightly higher at 700 °C. In the case of the bio-oil treated by phenol extraction, the conversion was complete at 700 °C but not at 600 °C, and the H_2 yield was significantly lower at 600 °C (72 %) than at 700 °C (92 %). Contrary to the SR of raw bio-oil, for the treated bio-oil, the stability of the catalyst was higher at 700 °C and remains practically constant for almost 3 h, after which a moderate decrease was observed. For the pre-reformed bio-oil, although complete oxygenate conversion was achieved at both temperatures, the yield of H_2 was higher at 700 °C (80 %) than

at 600 °C (60 %), and temperature also affected catalyst stability, so that at 600 °C the conversion of oxygenates decreased with time more slowly than at 700 °C, remaining practically constant after 4 h with a conversion of 75 % and a H_2 yield of 42 %. Hence, when comparing the three bio-oil feeds, the catalyst stability at 600 °C was in the following order: raw bio-oil > pre-reformed bio-oil >> treated bio-oil, whereas at 700 °C the order was: treated bio-oil >> raw bio-oil > pre-reformed bio-oil.

1.4.3. Intensification in hydrogen production by in situ CO_2 sorption

The SR process allows obtaining higher H_2 yields from bio-oil than other reforming alternatives, such as dry reforming (DR) or combined steam/dry reforming (CSDR) (explained in more detail in section 1.4.4) and oxidative steam reforming (OSR), but it produces a high CO_2 yield. In this framework, the ***sorption enhanced steam reforming (SESR)*** (Chapter 4) is an attractive and more efficient technology that improves the traditional SR [175–177]. The use of a CO_2 sorbent in the catalytic bed in the SESR process allows for attaining a higher H_2 production, since CO_2 capture (Eq. (1.24)) shifts the equilibrium of WGS (Eq. (1.15)) and methane SR (Eq. (1.17)) reactions. Moreover, SESR also contributes to making CO_2 sequestration easier, as it is released almost pure when the sorbent is regenerated, which has a remarkable techno-economic interest to contribute to energy decarbonisation and reduction of emission taxes [178]. Besides, the exothermic carbonation reaction (ΔH_{298} = -178 kJ/mol, Eq. (1.24)) partially provides the energy required by the endothermic reforming reactions, contributing to mitigate its high-energy demand.

$$CaO + CO_2 \leftrightarrow CaCO_3 \tag{1.24}$$

Therefore, the selection of a suitable CO_2 sorbent is essential for the efficient implementation of the SESR process. For that purpose, a good sorbent should have the following properties: thermal stability at operating conditions, high CO_2 capture capacity, long-term cyclic stability and durability, attrition resistance and mechanical strength, good CO_2 sorption kinetics, availability, reasonable production cost and easiness of regeneration [179, 180]. CaO-based sorbents

derived from natural precursors, such as limestone and dolomite, are commonly used in the SESR process. Their main advantages are a high sorption capacity, fast sorption kinetics according to a random pore model [181], low cost and wide availability in nature, although they show lower reactivity after multiple carbonation/calcination cycles and weak mechanical resistance [175, 182, 183]. To overcome these drawbacks, synthetic CaO-based materials have received intense consideration [16]. It has been widely reported that dispersing CaO particles into inert supports such as Al_2O_3 improves the CO_2 capture capacity as well as the stability of the sorbent due to the formation of mayenite ($Ca_{12}Al_{14}O_{33}$) [180, 184–186]. According to Li et al. [186], the CaO/mayenite sorbent has high stability under multiple carbonation/calcination cycles.

Regarding the SESR strategy, it can be distinguished [177]: (i) the integration of the CO_2 sorbent material into the particle of a hybrid catalyst; and ii) the physical mixing of sorbent and catalyst particle. Antzaras and Lemonidou [187] analysed the main advances in the development of materials and processes for the production of blue H_2 from natural gas, considering chemical looping reforming (CLR) and SESR processes. They also considered several hybrid processes that combine the advantages of the mentioned [154] and incorporate multifunctional materials (sorbent/catalyst) [188] and other technologies, such as the membrane reactor, to increase conversion and reduce energy requirements. Sorption enhanced chemical looping steam reforming (SE-CLSR) has also been studied for pure oxygenates such as ethanol [189, 190] and glycerol [191].

The SESR of bio-oil has been approached in the literature mainly with pure or mixtures of oxygenated compounds (such as acetic acid, acetone, ethanol, phenol, glycerol), which are representative of the main families of components present in raw bio-oil [192–200]. In general, Ni-based catalysts have been used and different materials containing CaO or bifunctional composites (generally based on Ni over CaO and with different modifications) have been used as CO_2 sorbents [201, 202]. The objectives of these works have focused on the optimisation of the catalyst composition and the reaction conditions, although the results are different and the appropriate conditions to obtain a H_2 purity above 95 % depend on the nature

of oxygenates. Therefore, the nature of oxygenates has a great influence on the stability of the catalysts, which has also been established in the SR of oxygenates in bio-oil [174]. Unfortunately, SESR studies with real raw bio-oil or with bio-oil aqueous fraction are also limited [192, 203–207].

Considering the interest of activity recovery by catalyst regeneration for the viability of the SESR process, Acha et al. [200] have verified the importance of the Ni catalyst support and the composition of the dolomite used as sorbent for the activity recovery of both materials used in the SESR of acetic acid and a mixture of oxygenates. The results highlight the importance of a support that minimises sintering and coke deposition, while dolomites lose their capture capacity upon reactivation. Li et al. [192] investigated the SESR of acetic acid and poplar sawdust bio-oil in a packed-bed reactor, with good results for $Ni/Ce_{1.2}Zr_1Ca_5$ hybrid catalyst (Ce/Ca ratio of 0.24), with an initial H_2 purity up to 95 % for the SESR of acetic acid (550 °C, S/C ratio of 4, and LHSV of 0.48 mL/g·h) (even after 15 consecutive cycles). Under the same operating conditions, more than 90 % H_2 could also be obtained by SESR of bio-oil. Nevertheless, carbon deposits and Ni particles sintering were found on the surface, which could be the cause of deactivation of this catalyst.

Xie et al. [203] analysed the SESR of raw bio-oil in a packed-bed reactor with Ni-Ce/Co catalyst supported on Al_2O_3 and with CaO powder as a sorbent (at 650-850 °C, S/C ratio of 9-15, molar ratio of CaO and carbon in the bio-oil in the feed (CaO/C) of 3, LHSV of 0.15 h^{-1} over 30 min). Among the results, the increase of the H_2 yield in the SESR process with respect to the SR process ($>$ 85 % and 75-80 %, respectively, between 750 °C and 800 °C) and the verification of an optimal value of 12 for the S/C ratio in the SESR process stand out.

Yan et al. [207] investigated the influence of temperature (500-700 °C) and water/bio-oil ratio (1-4/1, by weight) in the SESR of bio-oil aqueous fraction in a bench-scale packed-bed reactor using a commercial Ni-based catalyst (Z417) and calcined dolomite as a sorbent. The authors set 600 °C as the optimum temperature, since the sorption capacity of the sorbent decreases above this

temperature, and a water/bio-oil ratio of 1/1. Under these operating conditions, the hydrogen yield was maximised and reached 75 %.

In the SESR of bio-oil aqueous fraction, with a Ni/La_2O_3-Al_2O_3 catalyst and calcined dolomite as sorbent, Remiro et al. [204] reported a significant role of the catalyst/dolomite mass ratio, due to the active role of dolomite for both cracking and reforming reactions. A suitable balance between the reforming and WGS reactions on the one hand, and the cracking and coke formation reactions on the other hand, was stricken at 600 °C for catalyst/dolomite mass ratios ≥ 0.17. At this temperature and space time of 0.45 $g_{catalyst}$·h/$g_{bio\text{-}oil}$, the bio-oil was fully converted and the H_2 yield was around 99 % throughout the CO_2 capture step. Dou et al. [189] also observed a limit on the sorbent/catalyst ratio to avoid a decrease in H_2 in SE-CLSR of ethanol with NiO/Al_2O_3 oxygen carrier catalyst, due to the role of CaO based sorbent (with > 96 % CaO) in secondary reactions to SR, such as dehydration and cracking of ethanol. These authors obtained the highest H_2 selectivity and ethanol conversion at a Ca/Ni ratio of 3.0.

1.4.4. Combined steam/dry reforming for valorization of CO_2

To ensure a sustainable future, a rapid reductions in GHG emissions (mainly CO_2) are required. Consequently, CO_2 valorization routes are receiving a great deal of attention in the literature, as part of the CCUS strategy framework [208–210]. Figure 1.7 summarises the different routes for CO_2 valorization: oxidative coupling (OC), oxidative dehydrogenation (OD), dry reforming (DR) or combined steam/dry reforming (CSDR) and chemical production [211]. We will focus on the combined steam/dry reforming process, which is object of this Thesis (Chapter 5).

As aforementioned, the main gaseous by-product of the steam reforming reactions is CO_2, which motivates the interest in the ***combined steam/dry reforming (CSDR)*** process, with the objective of reducing CO_2 emissions by forming CO (through reverse-WGS reaction, reverse of Eq. (1.15)) and thus producing syngas. This process is in line with the philosophy of CO_2 valorization for the production of fuels and chemicals of commercial interest [212, 213]. It has as a close reference

the development of DR of CH_4 for the production of syngas [214, 215], whose use for the production of fuels and chemicals (methanol, DME, gasoline, olefins, or aromatics, among others) is well established [216–218].

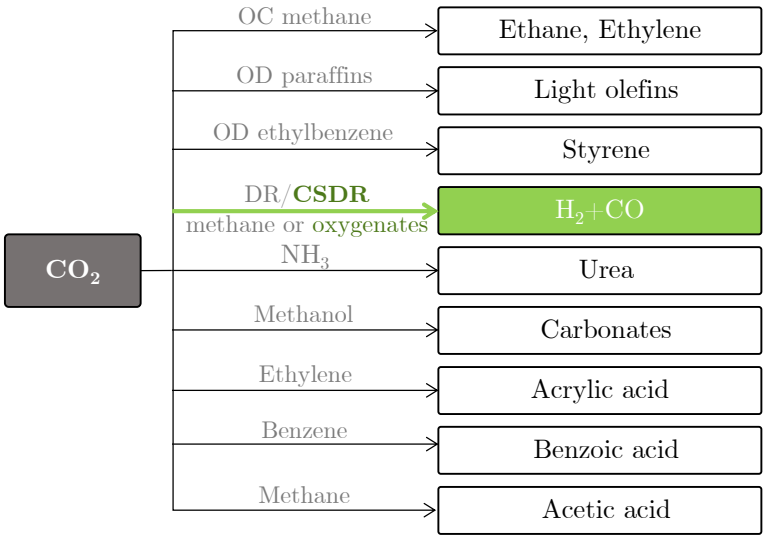

Figure 1.7. Routes for CO_2 conversion (adapted from [211]).

The main reactions for the CSDR process of bio-oil, apart from Eqs. (1.13)-(1.22), are DR of oxygenates and CH_4, Eqs. (1.25) and (1.26), respectively:

$$C_nH_mO_k + xCO_2 \rightarrow (n+x)CO + \left(\frac{m}{2}-x\right)H_2 + (x+k)H_2O \quad (1.25)$$

$$CH_4 + CO_2 \leftrightarrow 2CO + 2H_2 \quad (1.26)$$

DR and CSDR technologies have been extensively studied experimentally for methane/biogas, in a process usually called bi-reforming of methane (BRM) [219, 220, 229, 221–228], but studies with other H_2 sources are limited to ethanol [230, 231], glycerol [232, 233], toluene [234] and light hydrocarbons [235, 236]. The DR and CSDR of bio-oil has also been addressed in the literature, but mainly with mixtures of oxygenated compounds (such as phenol, ethanol, acetic acid, acetone, acetaldehyde, glycol, formic acid, methanol, formaldehyde) [237–242]. The results reveal that the main disadvantage of DR of oxygenates (Eq. (1.25)) is obtaining

a syngas with a reduced H_2/CO ratio (too low for its conversion to fuels and chemicals in the corresponding catalytic processes). Nevertheless, the CSDR process combines the advantages of the SR and DR processes, and limits the disadvantages of the DR process due to the presence of H_2O in the inlet stream (something inherent in real bio-oil). As a result, the CSDR of oxygenates enables producing a syngas with a H_2/CO ratio suitable for some applications (2 for methanol and Fischer-Tropsch synthesis; 1 for DME, acetic acid or ethanol synthesis and oxo-synthesis [243–247]). Nevertheless, when syngas is directly used as a fuel for power generation (in gas turbines, internal combustion engines or fuel cells) a H_2 rich gas (H_2/CO ratio ≥ 50) is required [248]. The feed composition (amount of CO_2 and H_2O referred to C in the bio-oil, CO_2/C and S/C molar ratios, respectively) and reaction temperature will determine the H_2/CO ratio in the product stream resulting from the CSDR of a real bio-oil.

Thermodynamic studies could bring important guidance toward the use of different process strategies, demonstrate their theoretical feasibility and provide a preview for further research. Thermodynamic analysis for the CSDR has focused on methanol [249], propane [250], methane [251, 252], methane-ethane-glycerol mixture [253]. Nonetheless, Xie et al. [241] investigated the thermodynamics of CSDR of bio-oil (empirical formula of $C_{1.8}H_{4.2}O_{1.4}$) with the perspective of using the waste heat from blast furnace slag to satisfy the energy requirement. The study was based on a simulated bio-oil composed of a mixture of 8 typical model oxygenates, limited to C_1-C_3 compounds, including carboxylic acids, ketones, aldehydes and alcohols, which corresponds to the typical aqueous fraction of the bio-oil. The authors concluded that the H_2 and CO yields are higher than in the SR and DR processes, with a lower coke yield at a lower reforming temperature. A feed with a H_2O/CO_2/C in bio-oil ratio of 3/0.5/1 allowed achieving a H_2/CO ratio of 3 (adequate for methanation) at 804 °C, with a H_2 yield of over 90 %.

Hu and Lu [254] introduced the idea of coupling the most common bio-oil reforming technologies (SR, POX and OSR) with CO_2 reforming (DR) to produce a useful syngas for chemical synthesis and, additionally, as an environmentally friendly and efficient method for CO_2 valorization. Recently, other authors have

addressed the DR or CSDR of bio-oil, either with thermodynamic works [241] or experimental studies with model compounds of bio-oil or their mixtures (simulated bio-oil) [237, 239, 242] and, more rarely, with real bio-oil [238, 240].

Xu et al. [237] studied the combined reforming (steam and dry) of bio-oil model compounds (consisting of phenol, ethanol, acetic acid and acetone, each at 25 wt% and a composition of $CH_{1.9}O_{0.43}$) with Ni/Al_2O_3 catalyst under different operating conditions (S/C ratio, CO_2/C ratio and temperature). The results showed that at the condition of 700 °C and bio-oil:CO_2:H_2O of 1:0.5:1.5 the H_2 yield, syngas yield and H_2/CO ratio were 60.23 %, 81.97 % and 2.77, respectively. Fu et al. [239] examined the DR of bio-oil model compounds (mixture of acetic acid, phenol, ethanol and acetone with a mass ratio of 1:1:1:1) over Ni/Al_2O_3 catalyst and studied the effect of reaction conditions such as temperature, WHSV and CO_2/C molar ratio. Their results showed a H_2 yield of 88.2 % and bio-oil model compounds conversion of 97 % under optimum reaction conditions of 700 °C, CO_2/C ratio of 0.75 and WHSV of 0.9 h^{-1}. Moreover, the authors concluded that high temperature (> 600 °C) and high CO_2/C ratio (> 0.75) are good for carbon elimination. Besides, the forms of carbon deposits on Ni/Al_2O_3 catalyst were mainly filamentous carbon and graphitic carbon. Regarding real bio-oil studies, Xu et al. [238] researched the catalyst deactivation and regeneration during CO_2 reforming of bio-oil ($CH_{1.57}O_{0.41}$, 58.83 wt% C, 7.68 wt% H, 32.50 wt% O, 0.99 wt% N). The activity and stability of Ni/Al_2O_3 catalyst (20 wt% of Ni prepared by impregnation method) for CO_2 reforming of bio-oil was tested in a packed-bed reactor at 700 °C with CO_2/C ratio of 0.75 and WHSV of 0.9 h^{-1}. Although the catalyst displayed a good stability within 1 h, with 74 % of H_2 yield, the catalyst stability was reduced progressively and after 4 h, the H_2 yield dropped remarkably, reaching a stable value around 39 % subsequent to 7 h. Catalyst deactivation was a combination of carbon deposition (amorphous and filamentous carbon) and sintering. Yao et al. [240] investigated bio-oil ($CH_{2.07}O_{0.65}$ with 13.24 wt% of water content) dry reforming under different operating conditions using the waste heat of granulated blast furnace slag in a packed-bed setup. According to the authors, the optimum operating conditions were 800 °C, CO_2/C ratio of 0.85 and LHSV of 0.45 h^{-1}, reaching 90.15 % of bio-oil conversion,

and 34.43 % and 40.17 % of H_2 and CO gas composition, respectively (H_2/CO ratio of 0.85).

1.5. DEACTIVATION AND REGENERATION OF REFORMING CATALYSTS

Catalyst deactivation is an undesirable and unavoidable phenomenon in bio-oil reforming. Continuous efforts are being made to develop new reaction technologies and new catalysts to minimise, delay and/or reverse deactivation so that the catalyst can be regenerated and recover the initial activity of the fresh catalyst. Deactivation is caused by a series of physicochemical phenomena, such as coke deposition/formation, metal sintering, metal oxidation, aging or thermal degradation of the support, poisoning and attrition. The causes and mechanisms of catalyst deactivation depend on the catalyst composition (metal, support and metal-support interaction) and the reaction medium: feed composition, operating conditions, reactor type [255].

There are several reviews in the literature that report advances in the understanding of catalyst deactivation and regeneration [77, 79, 255–257].

1.5.1. Coke formation and deposition

Coke deposition is the major cause of deactivation in the SR of bio-oil and its formation is inevitable in any catalytic process with hydrocarbon and/or oxygenated feeds. It consists of a physical deposition of an unwanted carbonaceous species from the fluid phase onto the catalyst surface, which blocks the active sites and/or pores, causing a loss of activity [257]. Coke deposition occurs by several pathways: (i) carbon chemisorption (as a monolayer: metal carbide) or physisorption (in multilayers), hindering the access of reactants; (ii) total encapsulation of the active site (metal particle), which completely deactivates the particle; (iii) plugging of micro- and/or mesopores, which blocks the access of reactants to the active sites in the inner pores; (iv) advanced coke growth (strong carbon filaments can form), which can lead to changes and/or disintegration of the catalyst structure and reactor plugging.

Overall, in processes affected by coke deposition, the properties and effects of coke are described based on four main characteristics: (i) content; (ii) location; (iii) morphology; and (iv) chemical nature.

The coke content depends mainly on the operating conditions (temperature, space time, feed composition). In reforming reactions, too low temperatures ($<$ 550 °C in bio-oil steam reforming) favour coke deposition, as secondary reactions are promoted instead of reforming and coke gasification [255]. However, several works show that increasing the reaction temperature (in the 500-800 °C range) decreases the total coke content [164, 168]. Similarly, as the space time increases, less coke is deposited because secondary reactions are minimised. Besides, the increase of steam (S/C ratio) and oxygen (O_2/C ratio) (in the SR and OSR, respectively) favours the gasification and combustion of coke precursors and coke itself [96, 168, 171, 258].

Several types of coke can be distinguished in terms of their location: (i) coke deposited on or near the metal sites, which facilities its combustion/gasification; (ii) coke deposited on the metal-support interface; and (iii) coke deposited over the support, whose combustion is not catalysed. Based on coke morphology, three different types of coke can be identified [255, 257]: (i) encapsulating coke; (ii) filamentous coke; and (iii) pyrolytic coke. Encapsulating coke covers the surface of the active site, hindering the access to the reactants. Its combustion temperature is low ($<$ 500 °C) and is considered responsible for significant catalyst deactivation. This type of coke is formed from the oxygenates decomposition/cracking or polymerization. Filamentous coke (usually carbon nanotubes and/or carbon fibres, whose length and thickness depend on the reaction medium and catalyst) burns at higher temperatures ($>$ 500 °C) and is located far away from the metal sites. It is mostly formed in the reforming of pure oxygenates and has little impact on deactivation [259–262]. Pyrolytic coke is formed at high reaction temperatures ($>$ 600 °C) and mostly in the reforming of bio-oil or under severe reforming conditions, with high impact on deactivation [164, 255, 263–266]. This coke is deposited indifferently over the catalyst surface, forming a coke layer and causing a total encapsulation. The origin of long and

heterogeneous carbon filaments can be attributed to CH_4/hydrocarbons decomposition and Boudouard (CO disproportion) reactions, whereas pyrolytic coke is formed by thermal cracking of hydrocarbons or oxygenates.

Regarding the chemical nature of coke, the fraction deposited near the active site is more hydrogenated (higher proportion of aliphatics compared to aromatics, higher H/C ratio) and/or more oxygenated (higher O/C ratio), easily combusted and/or gasified. Conversely, the coke fraction deposited further from the metal sites evolves into a more condensed and graphitic-like structure (higher proportion of aromatics), with lower H/C and O/C ratios and therefore, a higher combustion temperature is required [79, 164].

Interestingly, there is no direct relationship between the amount of coke and the deactivation rate [142, 145, 255, 260, 267, 268]. Other characteristics of the coke (such as, morphology, structure and location) have higher incidence on deactivation rather than its content.

1.5.2. Metal sintering

Metal sintering is a thermally activated phenomenon that results in a loss of active surface area due to the particle size growth and agglomeration. The sintering mechanism involves: (i) particle migration over the support followed by coalescence with other metals, (ii) atomic migration (known as Ostwald ripening) where the metal atom migrates over the support or in the vapour phase and is captured by larger crystallites, and (iii) vapour transport, which occurs at very high temperatures [256, 257, 269].

Several factors influence metal sintering (atmosphere, metal type, metal dispersion, promoters, support surface area, texture and porosity), but temperature is the most common [256]. The sintering rate increases exponentially with temperature. Metal sintering occurs above their Tamman temperature, which is half of the melting temperature, because above this temperature metal atoms become mobile. The Tamman temperature for Ni is 590 °C and therefore sintering is unavoidable under typical reforming conditions ($>$ 600 °C) [95, 257].

Sehested et al. [269–274] extensively investigated the sintering of Ni-based catalysts. In a steam/hydrogen atmosphere, the sintering of $Ni/MgAl_2O_4$ and Ni/Al_2O_3 catalysts was studied at high (40 bar) and low (1 bar) pressures. The authors concluded that above 600 °C at 40 bar and around 700 °C at 1 bar, the sintering rate increased significantly and was dominated by Ostwald ripening sintering mechanism [274]. Moreover, at high pressures of steam and hydrogen (31 bar and steam/hydrogen=10/1), potassium promotion increased the sintering rate. Similarly, sulphur poising also increased the sintering rate at high pressures, but the effect is less than that of potassium [271]. Remiro et al. [258] compared the performance of Ni-based (Ni/La_2O_3-αAl_2O_3) and Rh-based (Rh/CeO_2-ZrO_2) catalysts in the OSR of raw bio-oil at 700 °C, with metal sintering being the main responsible for the rapid deactivation of the Ni supported catalyst compared to Rh catalyst. Likewise, sintering is also accelerated by a high steam content in the SR process [257, 275].

1.5.3. Others causes of deactivation

In addition to coke deposition and metal sintering, which are the main causes of catalyst deactivation in the reforming processes, other phenomena can lead to catalyst deactivation, such as metal oxidation, aging or thermal degradation of the support, poisoning and attrition.

The *oxidation of metal particles* in the catalyst surface is detrimental to catalytic activity and stability, as the metal phase is normally the active one. Among the most commonly used reforming catalysts, noble metals (Rh, Pt, Pd, Ru) and Ni, the latter is the most susceptible to deactivation under typical reforming conditions. However, metal oxidation is often ruled out as a deactivation cause due to the highly reducing atmosphere along the SR reactions [79].

Thermal degradation or aging of the catalyst can lead to a loss of support area through support sintering and/or collapse of the porous structure, blocking the access to the reactants [257]. Remiro et al. [173] observed structural changes (support aging) over a Rh/CeO_2-ZrO_2 catalyst in the SR of raw bio-oil.

Poisoning consists of strong chemisorption of reactants, products or impurities onto metal sites, blocking sites for catalytic reactions. Sulphur poisoning, when present in the feed, is a difficult problem in many catalytic processes, such as steam reforming. Under reforming conditions, sulphur is converted to H_2S and the sulphur atom in H_2S then binds strongly to the metal [79, 256, 257].

Attrition refers to the mechanical degradation of catalyst particles due to physical forces such as collision, abrasion or mechanical stress. When catalyst particles undergo attrition, they can break into smaller fragments, leading to a decrease in particle size and surface area. As a result, the available catalytic sites are reduced, leading to a decline in catalytic activity. This is a difficult problem in the operation of reactors with continuous particle mobility, such as fluidized-bed, moving-bed or slurry-bed reactors [257].

1.5.4. Catalyst regeneration

In the literature, great emphasis is usually placed on the need to minimise the deactivation of the reforming catalysts. However, little attention is generally paid to regeneration, despite its importance for the industrial viability of the process [276, 277].

As mentioned above, carbon deposition is the main deactivation mechanism in bio-oil reforming. Therefore, catalyst regeneration requires the removal of coke, which can be achieved either by combustion with air [149] or by gasification with steam [278] or with CO_2 (reverse-Boudouard reaction) [279]. Each regeneration method has its advantages and disadvantages [238, 276]: combustion with air generally requires a lower temperature than gasification with steam, but can lead to sintering of the catalyst due to hot spot formation, as it is strongly exothermic, and generates significant CO_2 emissions. On the other hand, steam gasification has a remarkable energy consumption, but is attractive due to its reduced CO_2 emissions and sintering. Alenazey et al. [280] have used a mixture of air and CO_2 to remove coke from Ni-Co catalysts used in the propane reforming in order to achieve the autothermal regime by coupling the exothermic oxidation reaction in air with the endothermic reverse-Boudouard reaction. Wu and Liu [146] studied

the regeneration of Ni/MgO-Al_2O_3 catalyst by combustion (with air at 600 °C) or gasification (with steam at 850 °C) and reported that the regenerated catalysts had similar performance to the fresh catalyst in the SR of m-cresol. Recently, Xu et al. [238] have compared coke removal with air, steam and CO_2 for regeneration of a deactivated Ni/Al_2O_3 catalyst in CO_2 reforming of bio-oil. In addition to a slight irreversible deactivation in all three cases (attributed to sintering in the reaction stage), they observed a recovery of activity in the order of steam > air > CO_2, emphasizing in the case of CO_2 (in addition to the reduction of CO_2 emission) the interest in CO production.

Some researchers have prepared spinel-structured catalysts to overcome the sintering problem in the regeneration process [149, 281–283]. Remiro et al. [149] compared the performance of Ni/La_2O_3-α-Al_2O_3 (prepared by impregnation) and $NiAl_2O_4$ spinel (prepared by co-precipitation) catalysts in a reaction-regeneration cycle during the OSR of bio-oil at 700 °C. The causes of deactivation were coke deposition and slight sintering of Ni (more pronounced on the supported catalyst, Ni/La_2O_3-α-Al_2O_3). Therefore, for the complete recovery it was necessary to remove the formed coke, but also to restore the original $NiAl_2O_4$ spinel structure. The $NiAl_2O_4$ spinel derived catalyst recovered its initial activity after the ex situ combustion at 850 °C, since the initial spinel is completely reconstructed under these regeneration conditions and its subsequent reduction allows achieving a good redispersion of the Ni particles on the Al_2O_3 support, recovering the activity of the fresh Ni/Al_2O_3 and without negligible loss of Ni particles on the catalyst surface [282]. Wang et al. [283] also studied the regenerability of two Co-based catalysts (15 wt%) supported on Al_2O_3 and sepiolite (spinel phase in both cases) during the SR of a simulated bio-oil (mixture of ethanol, acetic acid, acetone and phenol) at 700 °C with a S/C molar ratio of 2 for 20 h. The regeneration step consisted of coke combustion with air at 900 °C for 4 h. Only the Co/Sepiolite catalyst recovered its initial activity and was partially regenerated by coke combustion after five consecutive reaction-regeneration cycles.

1.6. AIM AND OBJECTIVES

As mentioned above, the overall objective of this Thesis project is to reduce the carbon footprint in bio-oil reforming. For this purpose, two alternative strategies have been considered: i) sorption enhanced steam reforming (SESR) of bio-oil, minimising CO_2 emissions by in situ CO_2 capture, which enhances hydrogen production, and ii) CO_2 valorization by combined steam/dry reforming process (CSDR), for the production of syngas. As a preliminary step to better understand the results obtained in these previous chapters on catalyst deactivation, we have deepened our knowledge by studying the role of individual oxygenated compounds with different functionalities (present in bio-oil) in coke deposition and deactivation behaviour, through thermodynamic and experimental studies.

The following specific objectives were set in order to achieve this main goal. These individual objectives are addressed in an orderly manner in each of the chapters of the Thesis.

Role of individual oxygenates in the steam reforming of bio-oil

1. Improve the information on the effect of the different functionalities in bio-oil (acids, ketones, aldehydes, phenols and saccharides) in their reforming by thermodynamic analysis, providing the necessary information to understand the reforming of raw bio-oil. To this end, a wide range of operating conditions (temperature, S/C molar ratio, N_2 co-feeding) will be addressed. Likewise, the effect of oxygenates composition on the energy requirement of the unit will also be assessed.

2. Delve into the clarification of deactivation by coke of a catalyst derived from $NiAl_2O_4$ spinel in the SR process by studying the behaviour of individual oxygenated compounds with different functional groups present in bio-oil. In this way, the aim is to determine which of the bio-oil components are mainly responsible for its deactivation, as well as to identify the main causes of deactivation, primarily the coke characteristics.

Sorption enhanced steam reforming (SESR) of raw bio-oil

3. Selection of the most suitable sorbent/catalyst pair and optimum amount of sorbent and catalyst to maximise H_2 yield and catalyst stability, by comparing two Ni-based catalysts (derived from $NiAl_2O_4$ and supported on CeO_2), two sorbents (natural dolomite and CaO/mayenite) and two sorbent/catalyst mass ratios.

4. Compare the behaviour of packed-bed and fluidized-bed reactors with a Ni/Al_2O_3 catalyst derived from $NiAl_2O_4$ spinel and dolomite as sorbent.

5. Determine the optimum operating conditions (temperature, space time, sorbent/catalyst mass ratio, time on stream) for the selected sorbent/catalyst pair in order to maximise H_2 yield and purity and to attain stable operation in reaction-regeneration cycles.

Combined steam/dry reforming (CSDR) of raw bio-oil

6. Determine the right conditions to maximise syngas production or CO_2 conversion in combined reforming through thermodynamic analysis of a simulated bio-oil. The effect of reaction temperature and feed compositions (S/C and CO_2/C molar ratios) on the equilibrium composition will be studied and from these results the operating conditions that maximise the yield of syngas as well as those required to produce a syngas with a target H_2/CO ratio will be delimited. The energy requirements of the unit will also be evaluated for all the scenarios presented.

7. Selection of suitable conditions (temperature, CO_2/C molar ratio and S/C molar ratio) for maximising syngas production and catalyst stability in the CSDR of bio-oil over a Ni/Al_2O_3 catalyst derived from $NiAl_2O_4$ spinel.

Chapter 2

EXPERIMENTAL

This Chapter provides detailed information on the materials (feedstocks: pure oxygenated compounds and raw bio-oil; catalysts and sorbents), equipment and analyses used in the reforming processes. Here, the characterization of the raw bio-oil, a description of the synthesis methods used for the preparation of the catalysts and sorbents, the techniques used for their characterization (fresh and used samples), the reaction equipment and the reaction procedure (fluid dynamics and operating conditions), the analytical equipment used for the analysis of the outlet streams (reaction products) and the reaction indices used to quantify the kinetic behaviour of the catalysts are detailed.

2.1. FEEDSTOCKS

2.1.1. Pure oxygenated compounds

In section 3.1 of this Thesis, the reforming of different oxygenates in bio-oil (acids, ketones, aldehydes, phenols and saccharides) was compared by thermodynamic analysis using ProII software. Table 2.1 shows the 12 model oxygenates considered to represent the families of bio-oil components. The selection of components with different carbon numbers and with different functional groups allows to analyse the effect of these characteristics of the bio-oil composition on the equilibrium composition and the energy requirement of the reformer. It should be noted that the choice of the saccharide model (mannose) was conditioned by the limitations of the database of components of this family in the software used.

Table 2.1. Oxygenated compounds used as feed in the thermodynamic study of SR process.

Compound family	Compound	Formula
Carboxylic acids	Acetic acid	$C_2H_4O_2$
	Levulinic acid	$C_5H_8O_3$
Aldehydes	Acetaldehyde	C_2H_4O
	4-hydroxy-3-methoxybenzaldehyde (vanillin)	$C_8H_8O_3$
	Hydroxyacetaldehyde	$C_2H_4O_2$
Ketones	Acetone	C_3H_6O
	Hydroxyacetone (Acetol)	$C_3H_6O_2$
	Cyclohexanone	$C_6H_{10}O$
Phenols	Phenol	C_6H_6O
	1,2-benzenediol (Catechol)	$C_6H_6O_2$
	2-methoxyphenol (Guaiacol)	$C_7H_8O_2$
Saccharides	Mannose	$C_6H_{12}O_6$

Besides, Table 2.2 shows the stoichiometry of the SR of each one of the oxygenates, the corresponding stoichiometric steam/carbon molar ratio, $(S/C)_{st}$, and the number of moles of H_2 that can be obtained stoichiometrically for each C mol fed (H_2^0).

Table 2.2. Global reactions of SR of oxygenates, stoichiometric S/C molar ratio and stoichiometric H_2/C molar ratio.

Compound	Stoichiometry	$(S/C)_{st}$	$H_2{}^0$
Acetic acid	$C_2H_4O_2+2H_2O\rightarrow 2CO_2+4H_2$	1	2
Levulinic acid	$C_5H_8O_3+7H_2O\rightarrow 5CO_2+13H_2$	1.4	2.6
Acetaldehyde	$C_2H_4O+3H_2O\rightarrow 2CO_2+5H_2$	1.5	2.5
Vanillin	$C_8H_8O_3+13H_2O\rightarrow 8CO_2+17H_2$	1.62	2.12
Hydroxyacetaldehyde	$C_2H_4O_2+2H_2O\rightarrow 2CO_2+4H_2$	1	2
Acetone	$C_3H_6O+5H_2O\rightarrow 3CO_2+8H_2$	1.67	2.66
Acetol	$C_3H_6O_2+4H_2O\rightarrow 3CO_2+7H_2$	1.33	2.33
Cyclohexanone	$C_6H_{10}O+11H_2O\rightarrow 6CO_2+13H_2$	1.83	2.16
Phenol	$C_6H_6O+11H_2O\rightarrow 6CO_2+14H_2$	1.83	2.33
Catechol	$C_6H_6O_2+10H_2O\rightarrow 6CO_2+13H_2$	1.67	2.16
Guaiacol	$C_7H_8O_2+12H_2O\rightarrow 7CO_2+16H_2$	1.71	2.26
Mannose	$C_6H_{12}O_6+6H_2O\rightarrow 6CO_2+12H_2$	1	2

Additionally, an experimental study of the SR was carried out (section 3.2) with a wide range of model oxygenates with different functionalities, representative of the major families of oxygenates in bio-oil, including: acetic acid (Romil LTD, purity $>$ 99.9 %), acetaldehyde (Merck KGaA, purity $\geq$ 99 %), acetone (AppliChem GmbH, purity $\geq$ 99.9 %), acetol (hydroxyacetone, Alfa Aesar GmbH, purity of 95 %), ethanol (Merck KGaA, purity $\geq$ 99.9 %), 1,2-benzenediol or catechol (Sigma-Aldrich, purity $\geq$ 99 %), levoglucosan (1,6-anhydro-β-D-glucopyranose, Acros Organics, purity $>$ 99 %), and 2-methoxyphenol or guaiacol (Alfa Aesar GmbH & Co, purity $>$ 98 %) dissolved in 50 wt% of ethanol due to its low solubility in water. Acetone, acetaldehyde, catechol and guaiacol are representative of relevant families of compounds in bio-oils such as ketones, aldehydes and phenols (among these, mainly guaiacols and catechols) [82, 86]. Acetic acid, levoglucosan and acetol are present in remarkable concentrations in the bio-oil obtained from the pyrolysis of pine sawdust [167, 266]. The study of

the catalyst behaviour in the SR of ethanol is interesting because it can be co-fed with bio-oil for its stabilisation and because the SR of bio-oil/bio-ethanol mixture is an interesting route for sustainable H_2 production from two biomass derived feeds [284].

2.1.2. Bio-oil

The raw bio-oil reformed in Chapter 4 and Chapter 5 (section 5.2) was supplied by BTG Bioliquids BV (The Netherlands) and synthetized from fast pyrolysis of pine sawdust in a plant provide with a conical rotatory reactor (RCR) with a capacity to operate continuously with 5 t/h of biomass, with a bio-oil yield of 70 % (the remaining products are char and gases). The rotating conical reactor, invented at the University of Twelve and developed by BTG [87], allows rapid heating and a short residence time of the solids. No carrier gas is needed, which reduces the cost and the dimensions of the reactor, producing pyrolysis products at high concentrations [285].

The raw bio-oil was characterized by different analytical techniques to determine its complex composition and properties.

Physicochemical features. The water content was determined by Karl Fischer volumetric valorization in a *Metrohm KF Titrino Plus 870* apparatus, which operates at room temperature and pressure according to ASTM E-203. The instrument requires calibration with deionised water. The viscosity measurement was carried out in a *Brookfield DV2T Ametek* with a rotational speed of 5 rpm at two different temperatures, 20 and 40 °C.

Elemental analysis. The elemental analysis (C, H, O, N, S) was performed in an *EA Flash 2000 (Thermo Fisher Scientific)* with a TCD detector and *Mettler Toledo XP6 Microbalance*. Organic and inorganic substances are converted by combustion into elemental gases which, after further reduction, are separated on a chromatographic column and transferred to a thermal conductivity detector. The furnace temperature is 900 °C and the carrier gas (He) flow rate is 140 ml/min. It is also used as a reference gas (100 ml/min) and the O_2 flow rate is

250 ml/min. The standards used were sulphanilamide, cysteine and methionine in a tin capsule and 1000-2000 mg of sample were measured. The C, H and N contents were measured directly and the O content was calculated by difference. The empirical formula and the higher heating value (HHV) were obtained from the elemental analysis, the latter being calculated from the approach in Eq. (2.1) [286], which is suitable for calculation in biofuels [287] and bio-oil [288].

$$\text{HHV (MJ/kg)} = 0.3491\text{C} + 1.1783\text{H} + 0.1005\text{S} - 0.1034\text{O} - 0.0151\text{N} - 0.0211\text{Ash} \quad (2.1)$$

Composition. The composition of bio-oil was determined by gas chromatography-mass spectrometer (GC/MS) analysis on a Shimadzu GC/MS-QP2010S provided with a BPX-5 column, with a length of 50 m, diameter of 0.22 mm and thickness of 0.25 µm, and a mass selective detector. The analytical equipment is capable of operating up to 370 °C and of detecting trace amounts of polar and non-polar compounds. The heating program for the separation of the volatile compounds is as follows: i) 2 min at 50 °C; ii) linear heating rate of 10 °C/min up to 300 °C; and iii) 3 min at 300 °C. The oxygenated compounds of bio-oil are grouped in the following families: acids, ketones (linear and cyclic), esters, furans and furanones, alcohols, aldehydes, ethers, saccharides (levoglucosan) and phenols (alkyl phenols, guaiacols, catechols, syringols and others). The identification of compounds was carried out by comparison with pattern spectra available in NIST 147 and NIST 27 data libraries. Due to the complexity of the compounds analysed, it is not possible to carry out a direct quantification of each compound by the usual calibration of their peak areas. Thus, the relative proportion of each compound was determined using a semi-quantitative method based on the percentage of the chromatographic area. This analytical technique is limited in the detection of heavy oligomeric compounds with a molecular weight above 320 g/mol [289].

The main properties of the raw bio-oil are summarised in Table 2.3 (physicochemical properties), Table 2.4 (elemental analysis, empirical formula and HHV) and Table 2.5 (detailed composition of raw bio-oil and treated bio-oil

(volatile oxygenates leaving Unit 1 of the reaction equipment, explained in more detail in section 2.3.1)).

The physicochemical properties are consistent with those of bio-oils obtained by fast pyrolysis of lignocellulosic biomass [290, 291], more specifically from pine [292] and pine sawdust [81, 293], although with a lower water content than the latter. Both density and viscosity are a function of water content [292, 294].

Table 2.3. Physicochemical properties of raw bio-oil.

Physicochemical properties	
Water content, wt%	24
Density, g/ml	1.201
pH	2.5-3.5*
Viscosity at 20 °C, cP	950
Viscosity at 40 °C, cP	250

* provided by BTG Bioliquids BV.

According to the elemental composition in Table 2.4, the raw bio-oil used in this Thesis is in the range of compositions analysed by Czernik and Bridgwater [290] for bio-oil from lignocellulosic biomass (54-58 % C, 5.5-7.0 % H, 35-40 % O) and by Oasmaa et al. [292] in the case of biomass from pine (53.3 % C, 6.5 % H, 40.2 % O). For the HHV, the value is in line with those of the literature [83, 295, 296].

Table 2.4. Elemental analysis, empirical formula and HHV of raw bio-oil.

Elemental analysis, wt% (dry basis)	
Carbon	55.4
Hydrogen	6.2
Oxygen	38.4
Nitrogen	-
Sulphur	-
Empirical formula	$C_{4.6}H_{6.2}O_{2.4}$
HHV, MJ/kg	22.7

As shown in Table 2.5, the composition of the raw bio-oil is similar to the bio-oil analysed by Bertero et al. [293] from pine sawdust, with the main compounds being acetic acid (16.6 wt%), levoglucosan (11.1 wt%), guaiacol (11.1 wt%) and acetol (9.4 wt%).

Table 2.5. Composition (wt%) of raw bio-oil and treated bio-oil (oxygenates stream at the outlet of the thermal treatment (Unit 1) at 500 °C used for bio-oil volatilization and controlled deposition of pyrolytic lignin).

Compound	**Raw bio-oil**	**Treated bio-oil**
Acids	19.5	28.8
Acetic acid	16.6	20.8
Ketones	21.4	26.4
Linear	17.1	20.7
Acetone	*5.2*	*1.0*
Acetol	*9.4*	*15.4*
Cyclic	4.3	5.7
Esters	11.3	1.1
Furans/Furanones	5.0	4.4
Alcohols	3.2	2.0
Aldehydes	6.8	6.4
Ethers	0.8	1.2
Saccharides	13.7	19.0
Levoglucosan	11.1	13.8
Phenols	18.4	10.6
Alkyl phenol	1.4	0.7
Guaiacol	11.1	2.6
Catechol	0.9	3.5
Syringol	0.5	0.0
Others	4.5	3.8

Moreover, in section 5.1 the thermodynamic analysis of the combined steam/dry reforming of a simulated bio-oil was performed. The simulated bio-oil is composed of 6 typical compounds representing the main families components in raw bio-oil, and its composition (Table 2.6), with an empirical formula of $C_{3.4}H_{5.5}O_{1.8}$ (54.3 wt% C, 7.3 wt% H and 38.3 wt% O, on a water-free bases), is representative of the raw bio-oil used in this Thesis (Table 2.4).

Table 2.6. Oxygenate compounds constituting the simulated bio-oil for the thermodynamic study of the CSDR process.

Compound family	Compound	wt%
Carboxylic acids	Acetic acid ($C_2H_4O_2$)	28.0
Aldehydes	Furfural ($C_5H_4O_2$)	9.8
Alcohols	Ethanol ($C_2H_6O_1$)	4.6
Ketones	Acetone (C_3H_6O)	11.0
	Hydroxyacetone ($C_3H_6O_2$)	19.9
Phenols	2-methoxyphenol ($C_7H_8O_2$)	26.7

2.2. CATALYSTS AND SORBENTS

2.2.1. Synthesis of catalysts and sorbents

In this Thesis, two Ni-based catalysts were tested in the experimental runs: Ni/Al_2O_3 derived from $NiAl_2O_4$ spinel and Ni/CeO_2 prepared by wet impregnation.

The $NiAl_2O_4$ spinel structure (with a nominal Ni content of 33 wt%) was prepared by the co-precipitation method, using adequate amount of aqueous solutions of hexahydrated nickel nitrate ($Ni(NO_3)_2{\cdot}6H_2O$, Scharlau, purity of 98 %) and aluminium nitrate nonahydrate ($Al(NO_3)_3{\cdot}9H_2O$, Honeywell Fluka, purity of 98 %) and adding a 0.6 M solution of ammonium hydroxide (NH_4OH, 5 M, Honeywell Fluka) as the precipitating agent. The precipitation was carried out at 25 °C until the pH was packed at 8. After aging for 30 min, the precipitate was filtered and washed with distilled water to remove the remaining ammonium

ions. The recovered precipitate was dried at 110 °C for 24 h, calcined at 850 °C for 4 h with a heating ramp of 10 °C/min and finally, crushed and sieved to obtain particle sizes in the range of 150-250 µm. Prior to each reaction, the Ni spinel derived catalyst was reduced in situ at 850 °C for 4 h, thus obtaining the active Ni metallic particles deposited on the alumina support (Ni/Al_2O_3 catalyst) (Figure 2.1).

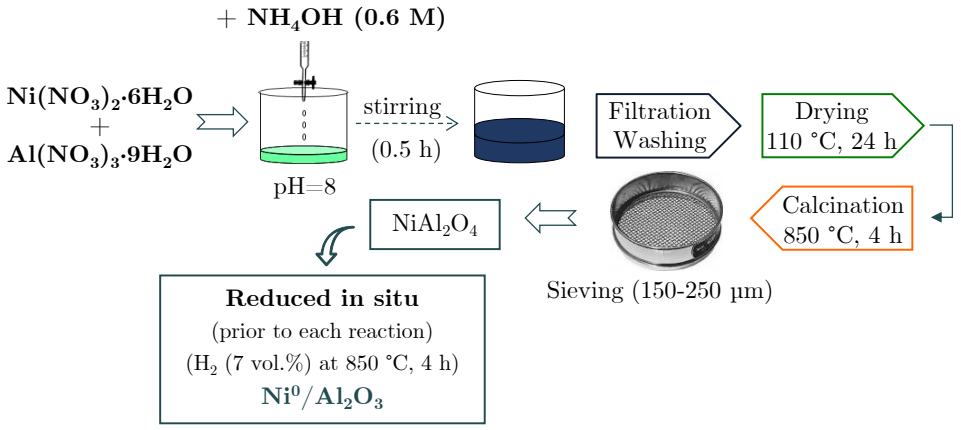

Figure 2.1. Flowchart of the procedure for the synthesis of Ni/Al_2O_3 catalyst derived from $NiAl_2O_4$ spinel.

The Ni/CeO_2 catalyst was synthetized in the laboratories of Professor Wu at Queen's University Belfast. The CeO_2 was prepared by precipitating ammonia cerium nitrate with urea in an aqueous solution (Figure 2.2). Typically, 60 g of $(NH_4)_2Ce(NO_3)_6$ (Sigma-Aldrich, purity > 99 %) and 200 g of urea (Sigma-Aldrich, purity > 99 %) were dissolved into 2000 ml distilled water, and the mixture was heated to 90 °C under stirring and kept at this temperature for 27 h. After filtration and washing with water, the precipitate was dried at 130 °C overnight. The CeO_2 was calcined at 650 °C for 5 h with a heating rate of 5 °C/min. The Ni/CeO_2 catalyst with 10 wt% of Ni was prepared using a wet impregnation method. In general, 5.0 g of CeO_2 powder and 2.75 g $Ni(NO_3)_2{\cdot}6H_2O$ (Sigma-Aldrich, purity > 99 %) were suspended in 30 ml distilled water and stirred at room temperature for 2 h. Then, the slurry was vapored and dried at 130 °C overnight and ground to powder (particle size around 50 µm). The sample

was reduced in 100 ml/min of 5 vol.% H_2 in N_2 in a tube furnace with a heating rate of 5 °C/min and kept at 650 °C for 1 h. Subsequently, it was cooled down to room temperature in H_2 atmosphere.

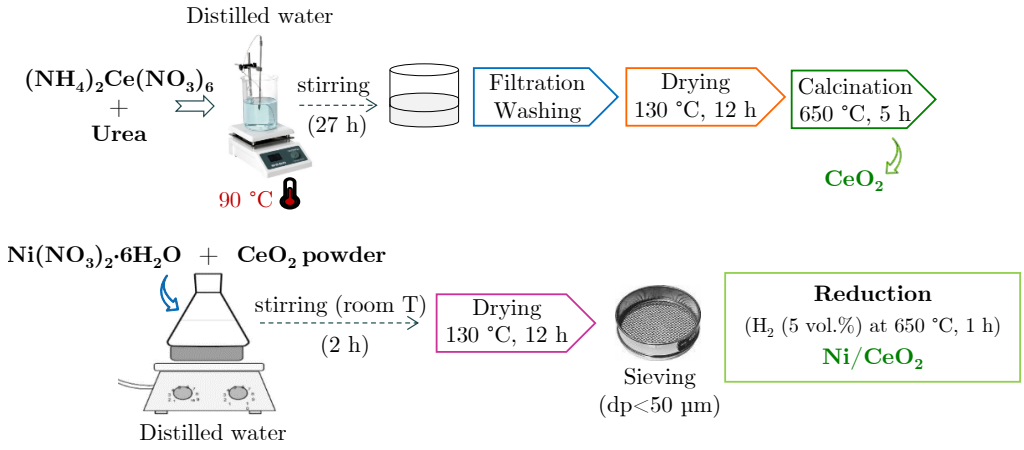

Figure 2.2. Flowchart of the procedure for the synthesis of Ni/CeO_2 catalyst.

In the SESR runs, two sorbents were studied: dolomite ($CaMg(CO_3)_2$) and CaO/mayenite ($CaO/Ca_{12}Al_{14}O_{33}$) (denoted Ca-M hereafter).

The natural dolomite was provided by Calcinor S.A. (Cantabria, Spain). Prior to each experiment the sorbent was sieved between 90-125 µm and dried at 110 °C for 12 h. Then, it was calcined at 850 °C for 5 h with a heating rate of 10 °C/min, to decompose into CaO and MgO [297]. Afterwards, it is sieved again to ensure a particle size between 90-125 µm, since during the calcination step the particles decrease in size due to decrepitation caused by the loss of CO_2 from the carbonates (Figure 2.3).

The procedure used for synthesizing Ca-M sorbent (Figure 2.4) was based on the work of Li et al. [186] and consisted, first, of calcining pure CaO at 900 °C for 2 h with a heating rate of 5 °C/min, in order to remove possible impurities. Then, calcium oxide powder (26.2 g) and aluminium nitrate nonahydrate ($Al(NO_3)_3$ $9H_2O$) (28.27 g) were added into a mixture of distilled water (760 ml) and 2-propanol (130 ml), previously heated at 75 °C. The solution was stirred for 1 h

at 75 °C and dried at 120 °C for 24 h before it was calcined at 500 °C for 3 h (5 °C/min) in air. This way, nitric acid, water and 2-propanol were evaporated from the solution. Distilled water was then slowly added to the paste obtained and was stirred until homogeneous. This solution was dried at 120 °C for 24 h and calcined in air at 900 °C for 1.5 h. The mixed powder was ground to a particle size below 50 µm due to the poor mechanical strength of the synthesized Ca-M.

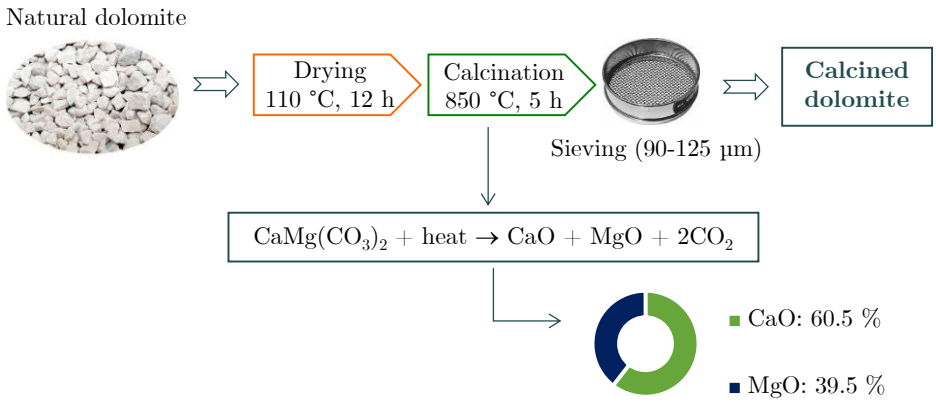

Figure 2.3. Flowchart of the procedure for preparation of natural dolomite sorbent.

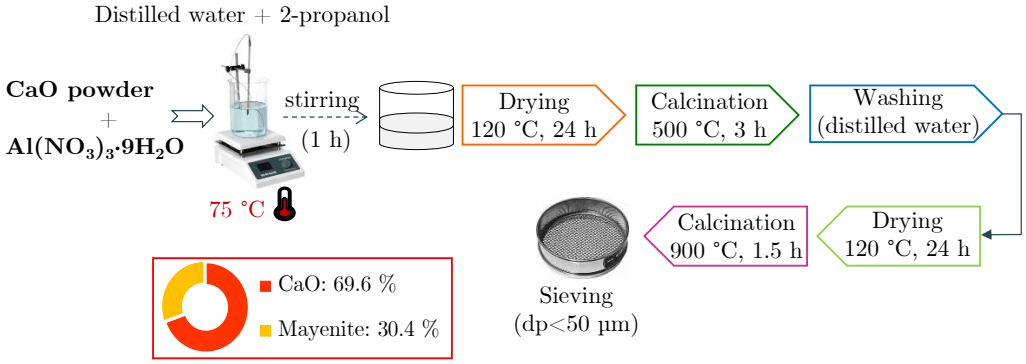

Figure 2.4. Flowchart of the procedure for the synthesis of Ca-M sorbent.

2.2.2. Characterization of catalysts and sorbents

Hereby, the different techniques used for the characterization of fresh, used and regenerated catalysts and sorbents are described, which allow to determine their

physical, chemical and metallic properties. Furthermore, special emphasis was put on the analysis of the features of coke deposited (content, morphology, location).

2.2.2.1. N_2 adsorption-desorption

The specific surface area and porous properties (pore volume and average pore diameter) of the catalysts and sorbents were determined by N_2 adsorption-desorption at N_2 liquid temperature (-196 °C) in a *Micromeritics ASAP 2010* apparatus. The experimental procedure consists of degasifying the sample (~ 100 mg) at 150 °C and under vacuum (10^{-3} mmHg) for 8 h in order to remove any impurity and adsorbed water in the pores. Subsequently, N_2 adsorption-desorption is carried out in multiple equilibrium steps (different N_2 relative pressures) until sample saturation at cryogenic temperature (liquid N_2). From the N_2 isotherms, information of the specific surface area was obtained with the Brunauer-Emmett-Teller (BET) method, which uses the adsorbed monolayer volume at relative pressures between 0.05-0.20 [298]. Besides, pore volume and pore diameter were determined from the pore size distribution by the Barrett-Joyner-Halenda (BJH) method proposed in 1951 [299], increasing the pressure until the sample saturation at cryogenic temperature.

Figure 2.5 and Figure 2.6 show the N_2 adsorption-desorption isotherms and BJH pore volume distribution of the fresh-reduced catalyst and sorbent samples used in this Thesis, respectively. Likewise, the textural properties of the solids (BET surface area, pore volume and average pore diameter) are displayed in Table 2.7 for the catalysts and in Table 2.8 for the sorbents.

Table 2.7. Physical properties of fresh-reduced catalysts.

Catalyst	$\mathbf{S_{BET}}$**, m²/g**	$\mathbf{V_{pore}}$**, cm³/g**	$\mathbf{d_{pore}}$**, nm**
Ni/Al_2O_3	65.1	0.234	13.1
Ni/CeO_2	23.1	0.073	9.3

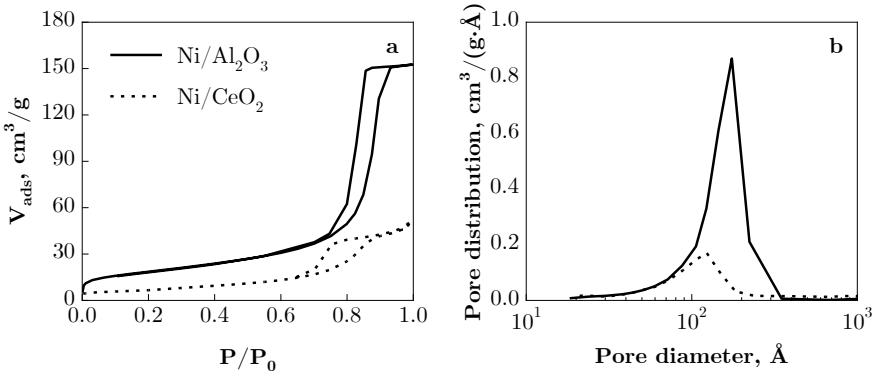

Figure 2.5. N_2 adsorption-desorption isotherms (a) and BJH pore volume distribution (b) of the fresh-reduced Ni/Al_2O_3 (solid line) and Ni/CeO_2 (dashed line) catalysts.

All the solids have an isotherm of type IV according to IUPAC classification, typical of mesoporous materials, whose hysteresis loop is associated with the occurrence of capillary condensation in the pores. The isotherm of the Ni/Al_2O_3 catalyst presents a hysteresis of type H2, attributed to disordered materials in which the pore size and shape distribution are not well-defined. Conversely, a H3-type hysteresis cycle is observed for the Ni/CeO_2 catalyst and for dolomite and Ca-M sorbents, associated with aggregates of plate-like particles that gives rise to slit-shaped pores with non-uniform size and/or shape [300, 301].

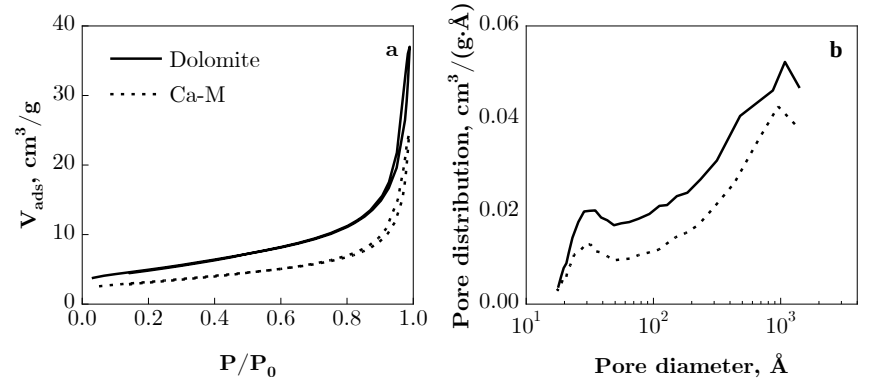

Figure 2.6. N_2 adsorption-desorption isotherms (a) and BJH pore volume distribution (b) of the fresh-calcined dolomite (solid line) and Ca-M (dashed line) sorbents.

Table 2.8. Physical properties of fresh-calcined sorbents.

Sorbents	S_{BET}, m^2/g	V_{pore}, cm^3/g	d_{pore}, nm
Dolomite	17.5	0.058	13.2
Ca-M	11.3	0.023	13.9

2.2.2.2. Temperature programmed reduction (TPR)

The optimum reduction temperature and the reducibility of the metal species of the fresh catalysts were determined by TPR analysis in a *Micromeritics Autochem II 2920* system. The experimental procedure consist in an initial treatment of the sample (100-200 mg) contained in a U-shape quartz reactor at 200 °C (with a heating ramp of 10 °C/min) for 1 h with a 40 ml/min He stream to desorb impurities. The sample is then cooled to 30 °C and stabilised at room temperature with a reducing flow rate (30 ml/min) of H_2-Ar, 10 % H_2 in volume. Finally, the sample is heated up to 950 °C with a heating ramp of 5 °C/min. The hydrogen consumption is determined by thermal conductivity detector (TCD) between the H_2 stream passing through the reactor and another stream of similar characteristics which does not pass through the sample. The temperature and signal data from the TCD detector are recorded every second and the water formed during the reduction is retained in a cold trap, located between the sample and the detector to avoid interference in the TCD signal.

Figure 2.7 shows the TPR profiles corresponding to the two Ni-based catalysts used in this Thesis, which were essential to establish the temperature needed for their reduction prior to their use in the reforming runs. The TPR profile of the $NiAl_2O_4$ spinel catalyst shows a main reduction peak at around 800 °C, corresponding to the reduction to Ni^0 of the Ni^{2+} ions incorporated in the spinel structure and subsequent formation of Al_2O_3, which require high temperatures for breaking the strong bonds [282, 302, 303].

The TPR profile of the Ni/CeO_2 catalyst shows a major peak in the 400-450 °C range, assigned to the reduction of NiO species with strong interaction with the CeO_2 support. In addition, the possible reduction of the CeO_2 support at a

temperature close to 500 °C, whose peak could overlap with the NiO reduction peak, should be considered [304].

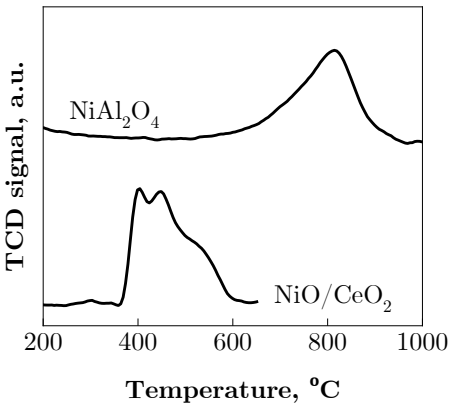

Figure 2.7. TPR profiles of the $NiAl_2O_4$ spinel and NiO/CeO_2 catalysts.

Based on the TPR results, the reduction temperature of these catalysts was set at 850 °C for 4 h for the $NiAl_2O_4$ spinel catalyst and at 650 °C for 1 h for the NiO/CeO_2 catalyst.

2.2.2.3. X-ray diffraction (XRD)

The structural properties of the fresh-reduced and used catalyst (crystalline phases, crystalline state of coke deposits and dynamics of sintering of Ni crystals) were analysed by X-ray diffraction (XRD) analysis. The structural phases detected by XRD were identified using the database of the International Centre for Diffraction Data by matching with the appropriate Powder Diffraction File (PDF).

In this technique, a monochromatic X-ray beam hits the crystalline sample and the intensity of the elastically dispersed (diffracted) beam is measured as a function of the diffraction angle (2θ). The equation proposed by Debye-Scherrer in 1918, Eq. (2.2), is used to determine the average crystal size of the metal present in the active phase of the catalyst:

$$\tau = \frac{K \cdot \lambda}{\beta \cdot \cos\theta} \tag{2.2}$$

where τ is the average crystallite size; K is a factor whose common value is 0.9; λ is the wavelength of the employed radiation; β is the width at half height of the diffraction peak of the sample, which is corrected considering the contribution of the measuring equipment (0.08 °); θ is the position of the diffraction peak corresponding to the analysed metal.

The measurements were performed by technicians at the Advanced Research Facilities (SGIker) in the University of the Basque Country. The used diffractometer was an automatic *Philips X'Pert PRO* operating at 40 kV and 40 mA, in theta-theta configuration and equipped with a secondary monochromator with Cu-Kα1 radiation (wavelength, 1.5318 Å) and a PIXcel solid state detector (active length in 2θ, 3.347 °). Data was collected at room temperature from 10 to 80 ° in the 2θ range (step size, 0.026°; time per step, 90 s). Additionally, a fixed divergence and anti-scattering slit were used, giving constant lighting volume to the sample.

The XRD diffractograms of the fresh and reduced catalysts are presented in Figure 2.8. The presence of different phases is identified. For $NiAl_2O_4$ spinel catalyst (Figure 2.8a), in the fresh (oxidized) sample a single $NiAl_2O_4$ phase is observed (intense peaks at 2θ = 37.2, 45.2 and 65.7 °, PDF-00-010-0339), whereas the reduced sample presents two phases, Ni^0 (2θ = 44.6, 51.8 and 76.3 °, PDF 04-010-6148) and Al_2O_3 (2θ =37.5, 45.9 and 66.9 °, PDF 04-005-4662). For NiO/CeO_2 catalyst (Figure 2.8b), in the fresh (oxidized) sample signals corresponding to NiO (2θ = 37.5, 43.6 and 63.3 °, PDF 01-080-5508) and CeO_2 (2θ = 28.7, 33.2, 47.7, 56.6, 59.3, 69.6, 76.3 and 79 °, PDF 01-078-0694) phases are identified, whereas the reduced sample confirms the presence of CeO_2 and reduced Ni species.

The XRD diffractograms of the fresh-calcined dolomite and Ca-M sorbents are shown in Figure 2.9. The XRD pattern of the calcined dolomite shows different peaks attributed to the presence of CaO (PDF 00-043-1001) and MgO (PDF 00-

045-0946), while the diffractogram of the fresh Ca-M sorbent presents signals corresponding to CaO and $Ca_{12}Al_{14}O_{33}$ (mayenite) (PDF 01-070-2144). In both cases, a small presence of the $Ca(OH)_2$ phase is also observed (PDF 01-076-0570).

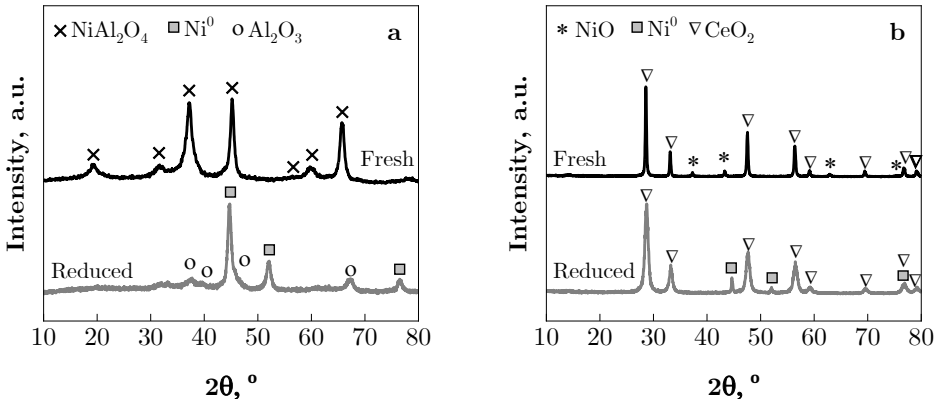

Figure 2.8. X-ray diffractograms of fresh and reduced $NiAl_2O_4$ spinel (a) and NiO/CeO_2 (b) catalysts.

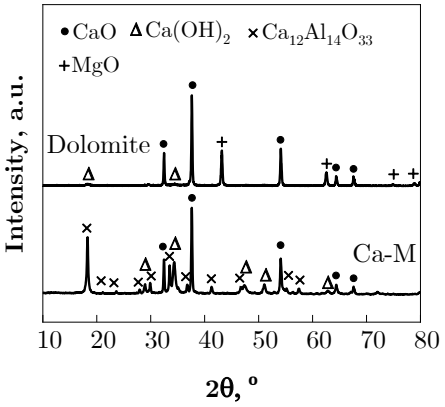

Figure 2.9. X-ray diffractograms of fresh-calcined dolomite and Ca-M sorbents.

2.2.2.4. X-ray fluorescence (XRF)

The X-ray fluorescence (XRF) was used to determine the composition of the prepared sorbents. The measurements were performed by technicians from SGIker in the University of the Basque Country, using a wavelength dispersive X-ray fluorescence spectrometer (*PANAnalytical, AXIOS*). The sample preparation consisted of melting sorbent powder (dolomite or Ca-M) with lithium borate

(Merck, Spectromelt A12) in a 1:20 proportion, using an induction melting microfurnace at 1200 °C. The XRF spectra were collected on the resulting glass pearl containing the sorbent sample, and they are compared with several elemental parents in order to determine the composition of each sorbent sample.

The quantitative composition of calcined dolomite is 60.5 wt% CaO and 39.5 wt% MgO, while for the Ca-M sorbent it is 69.6 wt% CaO and 30.4 wt% $Ca_{12}Al_{14}O_{33}$ (mayenite).

2.2.2.5. X-ray photoelectron spectroscopy (XPS)

The atomic composition of the surface species present in the catalyst samples was determined by X-ray photoelectron spectroscopy (XPS). This technique is based on the quantic interpretation of the photoelectric effect: the kinetic energy of the emitted electrons in a photoemission process (E_k) is calculated by the difference between the energy of the incident photon ($h\upsilon$) and the binding energy of the electrons in the sample (E_B):

$$E_k = h\upsilon - E_B \tag{2.3}$$

The binding energy of an electron is characteristic of a certain atom and the orbital in which the emitted electron was before. XPS is a superficial analysis and thus, only species found on the outlet layers of the sample surface can be analysed.

The measurements of the XPS spectra were carried out at SGIker in the University of the Basque Country with a *SPECS* system (Berlin, Germany) equipped with a Phoibos 150 1D-DLD analyser and an Al Kα monochromatic radiation (1486.6 eV). An initial analysis was carried out, with low resolution, to gather information on the type of elements present on the solid surface of the catalyst: energy increase of 1 eV, residence time of 0.1 s and an energy leap of 80 eV. Afterwards, detailed analyses, high-resolution local spectra (detailed scans), were done to get information on the composition and chemical status of the elements found on the solid surface. The high-resolution spectra were obtained under the following conditions: energy increase of 0.1 eV, residence time of 0.1 s, energy leap of 30 eV and an angle of 90 ° for the exiting electrons. The binding

energies were referenced to the C 1s peak, established at 284.6 eV, to correct the charge effect after calibrating the spectrometer with the $3d_{5/2}$ peak of Ag (368.28 Ev). The spectra were fitted with CasaXPS 2.3.16 software, which models the Gauss-Lorentzian contributions, after a Shirley subtraction of the background.

2.2.2.6. Scanning electron microscopy (SEM)

The morphology of the fresh-reduced and used catalyst samples as well as the morphology and location of the coke deposited (encapsulating or fibrillar nature) were analysed by scanning electronic microscopy (SEM) images at SGIker in the University of the Basque Country, using a *FEG-SEM Hitachi S-4800 N* field emission gun scanning electron microscope with an accelerating voltage of 5 kV and secondary electron detector (SE-SEM), and a *SEM Hitachi S-3400N* microscope with 15 kV accelerating voltage and backscatter electron detector (BSE-SEM). For the metallic coating of the non-conductive samples, a layer of about 15 nm of gold was deposited using an Emitech K550X ion sputter.

The SE-SEM provides a high-resolution image, while the BSE-SEM is used to distinguish between different compounds in the surface, as the brightness in the BSE-SEM images depends on the atomic number of the compound.

The SE-SEM images of the fresh-reduced $NiAl_2O_4$ spinel derived catalyst and Ni/CeO_2 catalyst are shown in Figure 2.10a and Figure 2.10b, respectively. A uniform granular texture (rough and porous structure) is observed in Figure 2.10a, which is expected for porous alumina phases [305]. Similarly, the Ni/CeO_2 catalyst shows a porous surface (Figure 2.10b), as typically expected for this catalyst [306].

The BSE-SEM images of the fresh-reduced $NiAl_2O_4$ spinel derived catalyst and Ni/CeO_2 catalyst are shown in Figure 2.11. The high brightness intensity in these figures indicate the presence of heavy elements (Ni, Al and Ce) constituting the catalyst phases (Ni crystals, Al_2O_3 and CeO_2).

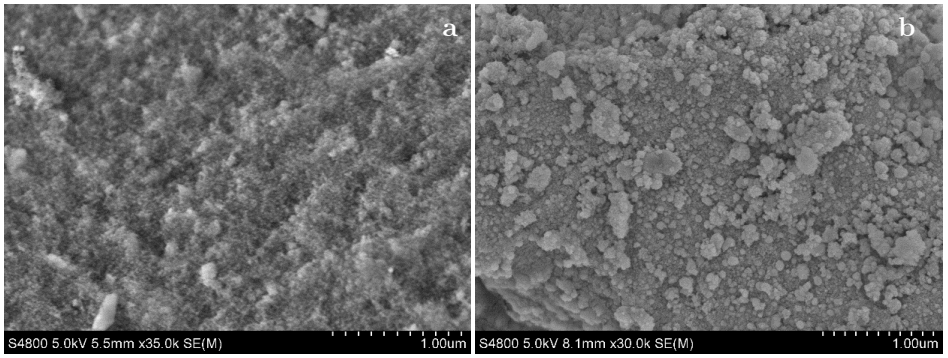

Figure 2.10. SE-SEM images of fresh Ni/Al_2O_3 catalyst (a) and Ni/CeO_2 catalyst (b).

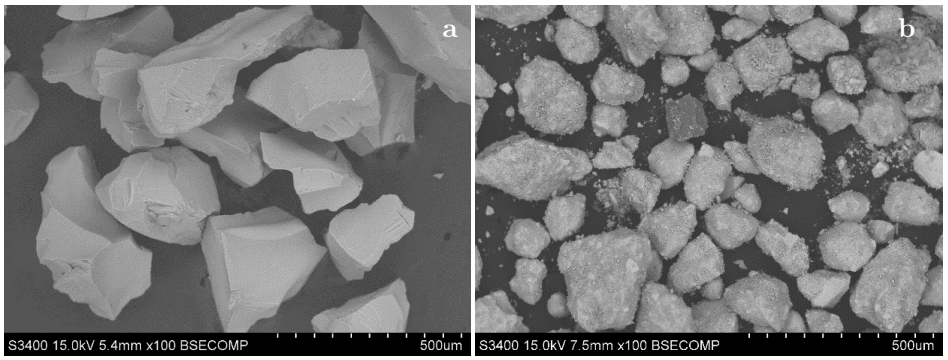

Figure 2.11. BSE-SEM images of fresh Ni/Al_2O_3 catalyst (a) and Ni/CeO_2 catalyst (b).

2.2.2.7. Transmission electron microscopy (TEM)

The transmission electron microscopy (TEM) images were obtained at SGIker in the University of the Basque Country in a *Phillips SuperTwin CM-200* microscope equipped with a LaB6 filament and *EDAX EDX* microanalysis system using an accelerating voltage of 200 kV. Firstly, the samples submitted to analysis were dispersed in ethanol, keeping the suspension in an ultrasound bath for 5 min. Subsequently, a drop of the suspension was deposited on a TEM copper sieve (300 Mesh) covered by carbon film.

2.2.2.8. Raman spectroscopy

Raman spectroscopy is a technique used to study the vibrational, rotational and other low-frequency modes of a material. It provides structural information about the materials, because the vibrational information is specific to the chemical bonds of the molecules. The technique is based on inelastic dispersion or Raman dispersion of the monochromatic light, which usually comes from a laser in the visible region, near infrared region or near ultraviolet region. The Raman spectra were carried out on a *Renishaw In Via* confocal microscope at SGIker in the University of the Basque Country, using an excitation wavelength of 514 nm, taking a spectrum in several areas of the sample for assuring reproducibility.

2.2.2.9. Temperature programmed oxidation (TPO)

The amount and nature of coke deposited on used catalyst/saturated sorbent samples was determined by Temperature programmed oxidation (TPO) in a *TA-Instruments TGA-Q5000IR* thermobalance, coupled in line with a mass spectrometer (*Thermostar Balzers Instrument*) for monitoring the CO_2 signal.

Usually, the deposited coke measurement is determined by the difference between the initial and the final sample mass during TPO experiment. Nonetheless, this method is unfeasible for samples that increase their mass during combustion. The metals of these type of catalysts react with oxygen, in parallel to the combustion of coke, as in the case of the Ni metallic catalysts used in this Thesis. Thus, the coke content was quantified from the CO_2 spectroscopic signal, because oxidation of Ni crystals during the combustion process might mask the thermogravimetric signal.

The experimental procedure consists on introducing 20-25 mg of sample in the cresol and stabilizing the TG signal at 50 °C with an air flow (20 ml/min) for 5 min. Subsequently, the coke combustion is started by heating the sample up to 800 °C with a heating ramp of 5 °C/min, maintaining this value for 10 min to ensure a complete combustion of the coke deposited. During the heating process, values of temperature and sample mass were registered as well as the exiting gas

composition, by means of the m/z 14, 18, 32 and 44 signals, corresponding to N_2, H_2O, O_2 and CO_2, respectively.

For the determination of the coke and CO_2 content in the saturated sorbent samples, an additional CO_2 desorption step (combustion+CO_2 desorption) was included after the combustion of the coke with air. First, the sample is stabilised at 50 °C with an air stream (20 ml/min) for 5 min and then the combustion step is carried out, heating up to 550 °C with a heating ramp of 5 °C/min and keeping it constant for 15 min. The CO_2 adsorbed during the SESR runs is then desorbed by heating with a N_2 stream of 20 ml/min to a maximum temperature of 800 °C, maintaining the isotherm for 10 min. In this way, $CaCO_3$ is decomposed into CaO and the adsorbed CO_2 is removed. In this case, both the content and nature of the coke and the amount of CO_2 captured by the sorbents were determined directly from the thermogravimetric signals (TG, DTG).

2.3. REACTION EQUIPMENT, OPERATING CONDITIONS AND PRODUCT ANALYSIS

This section describes each of the elements of the reaction equipment (section 2.3.1), the different operating conditions studied and the fluid dynamic conditions required in the fluidized-bed reactor (section 2.3.2), and the analysis procedure for each of the products (section 2.3.3). Besides, the calculation procedure of the equilibrium composition (for thermodynamic studies with ProII software) (section 2.3.4) and the reaction indices used to quantify the kinetic behaviour of the catalysts are defined (section 2.3.5).

2.3.1. Reaction equipment

The steam reforming (SR), sorption enhanced steam reforming (SESR) and combined steam/dry reforming (CSDR) runs were performed in an automated reaction equipment *(MicroActivity-Reference, PID Eng & Tech)* provided with two units in series (Figure 2.12), for thermal treatment of raw bio-oil (Unit 1) and catalytic reforming (Unit 2) of treated bio-oil (fluidized- or packed-bed reactor). The system can operate up to approximately 900 °C and with gaseous

and/or liquids feeds. The equipment is highly automatized and allows programming consecutive sequences varying any operating condition or even operating in reaction-regeneration cycles. It has a high security level, with an anti-failure system of the electric current, several alarm system for temperature, pressure, liquid level and gas flows and automatic sessions that stop the experiment when one of the alarms is activated.

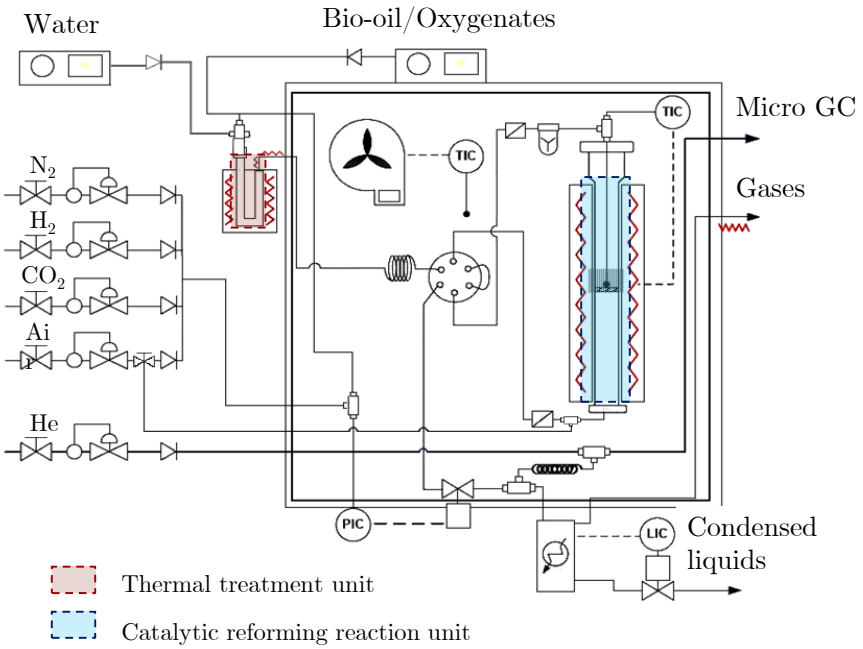

Figure 2.12. Scheme of the experimental set-up with two units in series.

The different elements of the reaction equipment are described below.

2.3.1.1. Liquid feeding system

The equipment has two liquid feed lines: (i) for bio-oil or oxygenated model compounds and (ii) for water. An injection pump (*Harvard Apparatus 22*) was used for feeding the bio-oil or individual oxygenates in a 100 ml *Harvard Apparatus* injection syringe (diameter, 34.9 mm) and a *307 Gilson HPLC* pump for co-feeding the additional water required according to the desired S/C ratio.

2.3.1.2. Gas feeding system

The gas distribution network used for the reduction, reaction, sweep, regeneration and in-line analysis steps consists of five gas lines: inert gas for the reactor (N_2), reducing gas (H_2), CO_2 for the CSDR reaction runs, synthetic air for the catalyst regeneration (coke combustion) and auxiliary carrier gas for the chromatograph (He). The gas feed lines are controlled by *Bronkhosrt High-Tech* mass flow meters. At the exit of the controllers the stream of inert, reducing and CO_2 gases (the latter only in the combined process) are jointly preheated in the hot box (300 °C) and fed into the thermal treatment. The synthetic air stream, after exiting the mass flow controller, can be routed via a valve to the thermal treatment unit (same route as the N_2, H_2 and CO_2 lines) or directly to the reactor to avoid combustion of oxygenates in the thermal stage when performing an OSR run. This last configuration has not been used in this Thesis. The He stream joins a sample of reforming products (collected by a loop), carrying and diluting it into the chromatographic analysis.

2.3.1.3. Thermal treatment unit (Unit 1)

The first unit is a U-shaped steel tube (Figure 2.13) (inner diameter of 15.9 mm) at 500 °C for vaporization of bio-oil and controlled deposition of a solid residue (pyrolytic lignin, PL) formed by repolimerization of oxygenates (mainly phenolic compounds), which is responsible for rapid catalyst deactivation [307]. The composition of pyrolytic lignin is suitable for use as fuel [308], which is interesting to provide the energy required for the process, achieving an integral valorization of the bio-oil. Therefore, the catalyst deactivation is noticeably attenuated using this reaction system with two steps in series (Figure 1.5) [171]. The temperature is measured with a K-type thermocouple located in the outlet branch and controlled by a *Toho TTM-005 Series* digital controller. In a previous work [309], it was proved that 500 °C is the thermal treatment temperature that allows obtaining a better compromise between the yield of liquid volatiles susceptible to be reformed in subsequent Unit 2 (treated bio-oil), of solid deposited as PL and of gases. With the bio-oil feed used in this work, the yield (dry basis) of treated

bio-oil, PL and gases is 75 wt%, 15 wt% and 10 wt%, respectively. The composition of the treated bio-oil is detailed in Table 2.5 (section 2.1.2). The gases consist mainly of CO (56.1 wt%) and CO_2 (25.5 wt%) resulting from oxygenates decarbonylation/decarboxylation reactions, and with low concentration of H_2 (1.3 wt%), CH_4 (7.7 wt%) and C_2-C_3 hydrocarbons (9.5 wt%) resulting from decomposition/cracking reactions of the oxygenates.

The volatile oxygenates leaving Unit 1 constitute the treated bio-oil and together with the inert gas and the vaporized water are fed into the reforming step through a heated line (500 °C) to avoid condensation of heavy oxygenates.

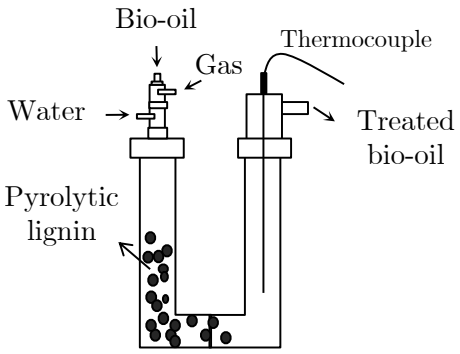

Figure 2.13. Scheme of the U-shaped reactor configured for the thermal treatment unit.

2.3.1.4. Reforming reaction unit (Unit 2)

The second unit is a stainless-steel tube (22 mm of internal diameter, total length of 460 mm and effective reaction length of 116 mm), for the reforming of the volatiles exiting unit 1 (treated bio-oil), which is operated with downwards (packed-bed reactor, PBR) or upwards (fluidized-bed reactor, FBR) flux. The catalytic bed is located over a layer of quartz wool and consists of the catalyst mixed with inert solid (silicon carbide (SiC) with particle size of 75 µm, Fisher Scientific), in order to improve the isothermal condition (in packed-bed) and the fluid dynamics (in the fluidized-bed) of the bed. The temperature is measured with a K-type thermocouple and controlled by a *Toho TTM-005 Series* digital controller. The reactor is located within an oven, consisting of a stainless steel

shell internally covered with refractory material and filled by electrical resistance. Catalyst loading and uploading is carried out from the upper part of the reactor.

2.3.1.5. Sampling and product collecting

The reaction products exiting from the upper (FBR) or lower (PBR) part of the reactor pass through two particle filters (of 15 and 2 μm) in series to avoid particle dragging into the chromatograph by attrition. Sampling is performed continuously, diluting a sample of the products (approximately 2 ml/min) with the He carrier (30 ml/min) and feeding them together to the Varian CP-490 Micro GC unit through a heated line at 130 °C to avoid condensation.

The remaining product stream is cooled down to 3 °C in a liquid/gas phase separation vessel for the condensation of condensable compounds. The liquid level is controlled by a digital *Toho TTM-005 Series* PID controller and this liquid is collected for its subsequent weighting. Non-condensable gases join the gas stream leaving the Micro GC, pass through a flow meter and are finally sent to vent.

2.3.1.6. Control software and data acquisition

The control of the different elements in the reaction equipment (hot box, thermal treatment unit, catalytic unit, liquid feeding pumps) and the acquisition (every 5 s) and recording of real-time data are carried out by the *Process@* process control software, which enables sending set-point values to the control devices and reading the current values of the process. The security system consists of a computer-independent microprocessor. As the system is fully automated, the software allows the design of a table with several consecutive sessions, including: Start, Reduction, Sweep, Water feeding, Bio-oil feeding, Feeding shutdown, Cooling and System shutdown. In each session, the duration and operating variables can be modified.

2.3.2. Fluid dynamic and operating conditions

The use of a fluidized-bed reactor (FBR) minimises the temperature gradient in the catalytic bed. It also mitigates coke formation on the catalyst, resulting in

slower deactivation. In order to maintain correct fluidization (approaching the ideal plug flow in the gas and perfect mixing in the solids), dead zones and the formation of bubbles (slugs) must be avoided. This requires an appropriate gas flow rate, particle size and solid mass.

The fluid dynamic conditions were studied in previous works [1, 4]. It was determined that a catalyst particle size between 150 and 250 µm is required to avoid internal diffusion limitation. An inert solid with good fluid dynamic properties (SiC) in which to dilute the catalyst is also required to obtain good fluid dynamic properties. SiC with a particle size (~ 75 µm) smaller than the catalyst size was used to facilitate a correct separation of both by sieving. In addition, an inert/catalyst mass ratio > 8 was set to ensure sufficient bed height for fluidization. The fluid dynamic conditions determined are shown in Table 2.9.

Table 2.9. Fluid dynamics conditions.

	No sorbent	With sorbent
Minimum fluidization velocity, cm/s	0.60	0.72
Minimum fluidization flow, cm^3/s	2.3	2.7
Linear velocity/minimum fluidization velocity	~ 7	~ 6
Bed height/bed diameter	2	2

When using different mass of catalyst (and of sorbent in the SESR runs), in order to achieve the established bed height/bed diameter ratio, the mass of the inert solid (SiC) was varied while maintaining the total mass of the catalytic bed (catalyst+(sorbent)+inert) constant (25 g).

Prior to each reaction, the catalyst was activated by reduction with a stream of 5-7 vol.% H_2 diluted in N_2 at a heating ramp of 5-10 °C/min, up to the temperature established by TPR analysis of the fresh catalysts. The operating conditions for the kinetic runs with individual model oxygenates and bio-oil are summarised in Table 2.10.

Table 2.10. Operating conditions for the runs with individual oxygenates and bio-oil.

Steam reforming (SR) of individual oxygenates	
Oxygenate mass flow rate, g/min	0.074
Water flow rate, ml/min	0.062-0.0222
Inert flow rate, ml/min	20-150
Reforming temperature, °C	600 and 700
Steam/Carbon (S/C) molar ratio	3 (6 for levoglucosan)
Catalyst mass, g	0.15 (0.075 for levoglucosan)
Space time, $g_{catalyst}{\cdot}h/g_{oxygenates}$	0.034 (0.080 for levoglucosan)
Time on stream (TOS), h	5
Sorption enhanced steam reforming (SESR) of bio-oil	
Bio-oil flow rate, ml/min	0.06
Water flow rate, ml/min	0.102
Inert flow rate, ml/min	75
Reforming temperature, °C	550, 600, 650, 700
Steam/Carbon (S/C) molar ratio	3.4
Sorbent mass, g	5 and 10
Catalyst mass, g	0.5, 1.0 and 1.25
Sorbent/Catalyst mass ratio (SC_{MR})	0 (conventional SR), 4, 10 and 20
Space time, $g_{catalyst}{\cdot}h/g_{oxygenates}$	0.15, 0.30 and 0.37
Time on stream (TOS), h	5
Combined steam/dry reforming (CSDR) of bio-oil	
Bio-oil flow rate, ml/min	0.06
Water flow rate, ml/min	0.023 and 0.043
CO_2 flow rate, ml/min	26.8 and 53.6
Inert flow rate, ml/min	101-213
Reforming temperature, °C	600, 700, 800
Steam/Carbon (S/C) molar ratio	0.5 (no additional water), 1.2, 1.7
CO_2/Carbon (CO_2/C) molar ratio	0 (conventional SR), 0.6 and 1.1
Catalyst mass, g	0.4 and 0.8
Space time, $g_{catalyst}{\cdot}h/g_{oxygenates}$	0.125 and 0.250
Time on stream (TOS), h	6

2.3.3. Product analysis

The reforming reactions produce products in three phases (gas, liquid and solid), which are analysed separately due to the configuration of the reaction equipment.

Gas products were analysed in-line in a Varian CP-490 Micro GC gas micro-chromatograph provided with three analytical modules (equipped with injector, column and TCD detector): (i) a molecular sieve (MS5) for the quantification of H_2, O_2, N_2, CH_4 and CO; (ii) Porapak Q (PPQ), for differentiating between CH_4, CO_2, light hydrocarbons (C_2-C_4) and water; and (iii) Stabilwax to separate light oxygenated compounds (C_2-C_3) and water (although the analysis in this module has not been used in this Thesis). The MS5 and PPQ modules have a microinjector module with reflux (backflush) with variable injection volume that allows programming of flow rates and flow reversal in each column to avoid the entering of undesired compounds in the modules. The method for this analysis is established as follows: sampling time, 30 s; run time, 300 s and sampling inlet line temperature, 110 °C. The conditions of each module are listed on Table 2.11.

The identification of each chromatographic peak is done based on a previous calibration with patterns of known concentration, both in gas and liquid mixtures. Therefore, a calibration factor for each compound is obtained, which relates the area of each peak with the molar concentration. These factors were calculated taking N_2 as a reference, whose calibration factor is defined as 1. Data acquisition and processing is carried out with the *Soprane II* software.

Table 2.11. Analysis conditions used in the three analytical modules of the Varian CP-490 Micro GC.

Module	**MS5**	**PPQ**	**Stabilwax**
Injector temperature, °C	90	110	110
Column temperature, °C	80	80	80
Injection time, ms	100	50	100
Backflush time, s	26	30	-
Column pressure, psi	20	31	15

Liquid products are separated by condensation and are collected in a vessel at the reactor exit. The identification of compounds in the condensed fraction was carried out in a *Shimadzu GC/MS-QP2010S* unit, based on the procedure previously described in section 2.1.2 for bio-oil analysis.

The yield of ***solid residue*** (pyrolytic lignin, PL) deposited in the thermal unit (unit 1) was quantified with Eq. (2.4) (mass of deposited PL per unit mass of bio-oil fed, on a water-free basis, expressed as a percentage):

$$Y_{PL}=\frac{\text{deposited PL (g)}}{\text{Bio-oil fed (g)}}\cdot 100 \tag{2.4}$$

Its elemental composition was analysed on an *EA Flash 2000* elemental analyser (section 2.1.2).

2.3.4. Calculation procedure of the equilibrium composition

The equilibrium composition of oxygenates and simulated bio-oil reforming can be estimated by minimisation of the total Gibbs energy method (non-stoichiometric approach), which can be calculated as follows [310]:

$$\frac{G}{RT}=\left(\sum_{i=1}^{N} n_i\left[\frac{G_i^{\circ}}{RT}+\ln\left(y_i P\right)\right]\right)_{gas}+\frac{1}{RT}\left(\sum_{i=1}^{N} n_i G_i^{o}\right)_{líquid} \tag{2.5}$$

where G and G_i^0 are the Gibbs energies of the system and of i product at their standard states, respectively; R, T and P are the universal gas constant, temperature and pressure, respectively; y_i is the mole fraction of i product; N is the total number of products; and n_i is the number of moles of i product.

Besides, the elemental mass balance is fulfilled:

$$\sum_{i=1}^{N} n_i \alpha_{ik}=b_k \qquad k=1,...M \tag{2.6}$$

where b_k is the total number of atoms of each k atomic species (C, H or O) in the system; α_{ik} is the number of atoms of k atomic species (C, H or O) contained in each molecule of i product; and M is the total number of atomic species (C, H and O).

The calculations were performed simulating a Gibbs reactor with ProII software, using the SRK (Soave-Redlich-Kwong) thermodynamic model. The validation of the calculation procedure (with ProII software and using the SRK thermodynamic model) was carried out by comparing the results with those obtained with other software (DWSIM) and other thermodynamic models (Peng-Robinson (PR) and UNIFAC) and is included in Table A.1-Table A.3 (section A.1 in Annexes). The results in Table A.1 and Table A.3 show that the differences in the molar flow rates of the products calculated with SRK and PR models are insignificant, so the relative error is less than 0.05 %. Moreover, the percentage relative error in the products molar flow rates calculated with both simulation software (Table I.2) is low, below 3.5 %, and this error is attributable to the differences in the convergence parameters of the Gibbs reactor used by both simulators, less restrictive in DWSIM.

The process flow diagram for oxygenates SR and CSDR of simulated bio-oil are shown in Figure 2.14 and Figure 2.15, respectively, with heat exchangers for heating individual feed stream (oxygenates/bio-oil, water, N_2 and CO_2), a mixer and a Gibbs reactor.

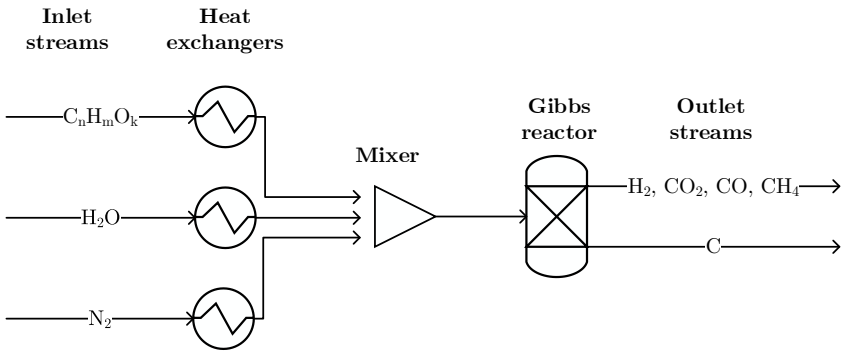

Figure 2.14. Flow diagram considered for the simulated SR process.

The operating conditions studied for oxygenates reforming are: pressure, 1 atm; temperature, 300-1000 °C, with steps of 50 °C, and additional simulations (firstly every 10 °C and then every 2 °C) in the proximity of the maximum H_2 flow rates for the precise location of the optimum temperature; and S/C ratio, 0.5-1-1.5-3-5-7-9-12-16.

The operating conditions studied for the CSDR of simulated bio-oil are: pressure, 1 atm; temperature, 300-900 °C, with steps of 50 °C and additional simulations every 1 °C in the proximity of the maximum syngas (H_2+CO mixture) flow rate and of the targeted H_2/CO ratios (1 and 2) for the accurate location of the required temperature values; S/C ratio, 0.5-3 (with steps of 0.5) and CO_2/C molar ratio, 0 (conventional SR)-5 (with steps of 0.5).

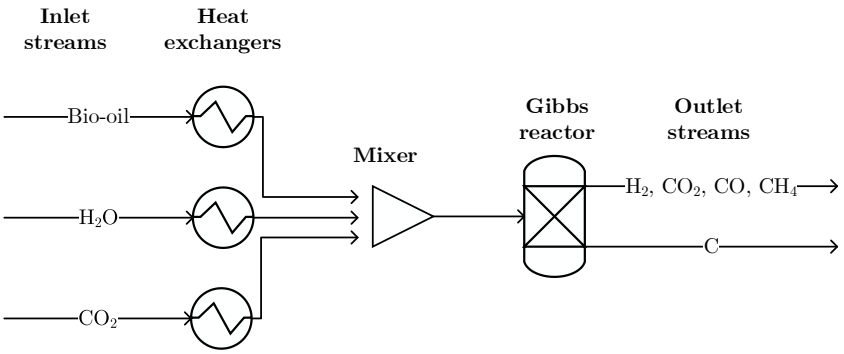

Figure 2.15. Flow diagram considered for the simulated SR (no CO_2 addition) and CSDR processes.

In addition to the oxygenate compounds (Table 2.1 and Table 2.6), the components considered in the reaction medium are H_2O, CO_2 (which is a product and also a reactant of the CSDR process), H_2, CO, CH_4 and carbon (graphite). The presence of light hydrocarbons (C_2-C_3) was not considered since their formation is insignificant. Besides, the consideration of graphite carbon as a representative of coke is an approach required by the software database. However, it is well established in the literature that the structure of coke is much more complex, which includes encapsulating amorphous carbon structures (deposited on or near the metal sites) and structured carbon [255, 311, 312]. A better

prediction of coke formation would require considering different carbon deposits representations, whose thermodynamic properties are not available in conventional databases [46].

2.3.5. Reaction indices

2.3.5.1. Steam reforming (SR) and sorption enhanced steam reforming (SESR)

The conversion of oxygenates in the treated bio-oil (that is, the volatiles oxygenates exiting the Unit 1 for thermal treatment) is expressed as the carbon units converted into gas, as indicated in (Eq. (2.7)), and H_2 yield and yield of carbon products (CO_2, CO, CH_4 and light hydrocarbons (C_aH_b)) are calculated with Eq. (2.8) and Eq.(2.9), respectively:

$$X = \frac{F_{out,\,gas}}{F_{in}} \cdot 100 \tag{2.7}$$

$$Y_{H_2} = \frac{F_{H_2}}{F^{o}_{H_2}} \cdot 100 \tag{2.8}$$

$$Y_i = \frac{F_i}{F_{in}} \cdot 100 \tag{2.9}$$

In these equations, $F_{out,gas}$ is the carbon-based molar flow rate of the carbonaceous gaseous product (CO_2, CO, CH_4 and light C_aH_b) at the reactor outlet and F_{in} is the carbon-based molar flow rate of oxygenates at the reactor inlet (Unit 2). F_{H2} is the H_2 molar flow rate in the product stream and $F^{o}_{H_2}$ is the stoichiometric molar flow rate, which is calculated as $((2n + m/2 - k)/n) \cdot F_{in}$, according to the global stoichiometry for the bio-oil ($C_nH_mO_k$) steam reforming (Eq. (1.13), including the WGS reaction, with a value of 2.17 moles of H_2 per C atom fed). F_i is the carbon-based molar flow rate of the i product (CO_2, CO, CH_4 and C_aH_b) in the effluent (out) stream of the reactor. Coke yield was quantified referring the total amount of coke deposited at the end of the reaction to the total mass of C at the reactor inlet (Unit 2).

2.3.5.2. Combined steam/dry reforming (CSDR)

In order to evaluate the CSDR process, the reaction indices for the quantification of the catalyst performance were the same as those defined in section 2.3.5.1 (for SR and SESR runs), with a difference in the definition of the yield of carbon products (CO, CH_4 and C_aH_b) (Eq.(2.10)), CO_2 yield (Eq.(2.11)) and conversion of oxygenates (Eq. (2.12)). Likewise, new reaction indices were defined: syngas (H_2+CO) yield (Eq. (2.13)), H_2/CO molar ratio (Eq. (2.14)) and conversion of CO_2 (Eq. (2.15)).

$$Y_i = \frac{F_i}{F_{in}} \cdot 100 \tag{2.10}$$

$$Y_{CO_2} = \frac{F_{out,\,CO_2} - F_{in,\,CO_2}}{F_{in}} \cdot 100 \tag{2.11}$$

$$X = \frac{F_{out,\,gas} - F_{in,\,CO_2}}{F_{in}} \cdot 100 \tag{2.12}$$

$$Y_{syngas} = \frac{F_{H_2} + F_{CO}}{F^{o}_{H_2+CO}} \cdot 100 \tag{2.13}$$

$$H_2/CO = \frac{F_{H_2}}{F_{CO}} \tag{2.14}$$

$$X_{CO2} = \frac{F_{in,\,CO_2} - F_{out,\,CO_2}}{F_{in,\,CO_2}} \cdot 100 \tag{2.15}$$

In these equations, F_i is the carbon-based molar flow rate of the i products (CO, CH_4 and C_aH_b) in the effluent (out) stream. $F_{out,CO2}$ and $F_{in,CO2}$ are the molar flow rate of CO_2 in the reactor outlet and inlet, respectively. F_{H2} and F_{CO} are the H_2 and CO molar flow rates in the product stream and $F^{o}_{H_2+CO}$ is the H_2+CO stoichiometric molar flow rate for the SR process, calculated as $((n+(n+m/2-k))/n)\cdot F_{in}$ according to Eq. (1.14), with a value of 2.17 moles of H_2+CO per C atom fed.

Moreover, to highlight the interest of the CSDR process for the mitigation of CO_2 emissions, it is worth defining a reduction of CO_2 emissions index (Eq. (2.16)), which quantifies the relative decrease in CO_2 emission of the CSDR process with respect to the SR process as follows:

$$R_{CO2}=\frac{\left(F_{out,\ CO_2\ (SR)}+F_{in,\ CO_2}\right)-F_{out,\ CO_2\ (CSDR)}}{F_{out,\ CO_2(SR)}+F_{in,\ CO_2}}\cdot 100 \tag{2.16}$$

where $F_{out,\ CO2\ (SR)}$ and $F_{out,\ CO2\ (CSDR)}$ are the molar flow rate of CO_2 in the reactor outlet for the SR and CSDR processes, respectively. This definition takes into account not only the possible lower CO_2 flow rate in the product stream of the CSDR process compared to the SR process, but it also considers the CO_2 flow rate at the reactor inlet in the CSDR process ($F_{in,\ CO2}$), because it would contribute to total CO_2 emissions in the factory if not used in the CSDR reactor.

Chapter 3

ROLE OF INDIVIDUAL OXYGENATES IN THE STEAM REFORMING OF BIO-OIL

This Chapter aims to take a step forward in understanding the ideal conditions for the reforming of raw bio-oil. Firstly, the equilibrium yield of H_2 and by-products, and energy requirements for the steam reforming of different oxygenates in bio-oil (acids, ketones, aldehydes, phenols and saccharides) have been compared for a wide range of conditions (temperature, S/C ratio and N_2 co-feeding) by thermodynamic analysis (using ProII software). A deep analysis of the results allowed the proposal of original correlations to predict the maximum equilibrium H_2 yield from the oxygenate composition (H/C/O) and C/S in the feed, as well as the temperature required to obtain that maximum and the corresponding values of carbon products yield. Secondly, an experimental study of the SR process was carried out with the aim of understanding the influence of individual oxygenate compounds with different functional groups present in bio-oil (acetic acid, acetaldehyde, acetol, ethanol, acetone, catechol, guaiacol and levoglucosan) on the deactivation behaviour and coke deposition upon the Ni/Al_2O_3 catalyst derived from $NiAl_2O_4$ spinel. In this way, the results obtained have allowed stablishing the main responsible for catalyst deactivation during SR of bio-oil, as well as the coke characteristics that mainly affect the deactivation of the catalyst.

The results of this Chapter have been published in *Energy Convers. Manag.* 2021, 239, 114181 and *Fuel.* 2022, 321, 124009.

3.1. THERMODYNAMIC STUDY OF THE EFFECT OF FEED COMPOSITION

In this section, the thermodynamic results (equilibrium product distribution and heat duties) corresponding to the SR of different oxygenate model compounds are analysed. The results of the maximum H_2 yield corresponding to each oxygenate as well as the temperature at which this maximum is reached and the corresponding equilibrium yields of carbon products have been correlated with the composition of the oxygenate and the feed composition, and empirical correlations for their calculation from the H/C/O composition of the oxygenate and the C/S ratio in the feed have been obtained. The incidence of N_2 co-feeding in the SR was also analysed.

3.1.1. Products distribution

In section A.2 of Annexes the effect of temperature on the equilibrium molar flow rates in the SR of each oxygenate is shown (Figure A.1). The effect of S/C molar ratio and temperature on the molar flow rates of H_2, CO_2 and CO for WGS reaction is also shown (Figure A.2), as it helps understanding the results of the SR of the oxygenates, due to the relevant contribution of WGS reaction to the overall mechanism of SR reactions.

As an example of the results of equilibrium composition in the SR of oxygenates, Figure 3.1 and Figure 3.2 show the joint effect of temperature and S/C ratio on the yield of H_2 and carbon by-products, respectively, for guaiacol. The effect of these variables is consistent with well established results in the literature for different oxygenates [313–315] and it is similar to that observed for the rest of oxygenates (section A.2 in Annexes). Thus, the yields of H_2 (Figure 3.1) and CO_2 (Figure 3.2a), main products of reforming, go through a maximum as the temperature increases, because in addition to the advance of the reforming reactions (of oxygenates and CH_4, Eqs. (1.14) and (1.17), respectively), the reverse-WGS reaction (Eq. (1.15)) is favoured at high temperature.

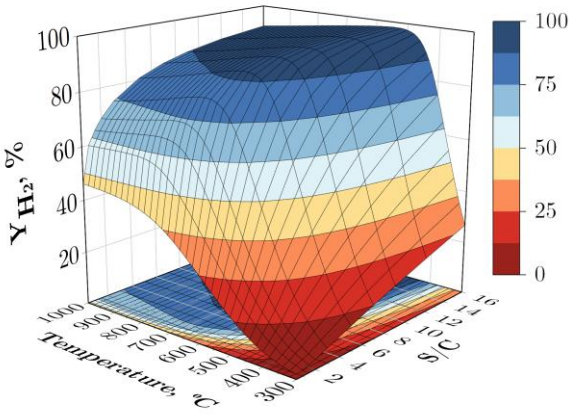

Figure 3.1. Effect of temperature and S/C ratio on the yield of H_2 in the SR of guaiacol.

The yield of CO (Figure 3.2b) increases with temperature and the yield of CH_4 (Figure 3.2c) decreases because its reforming is favoured (Eq. (1.17)). Similarly, S/C ratio noticeably affects the yield of all products, mainly because the excess of water shifts the equilibrium of WGS (Eq. (1.15)) and methane reforming reactions (Eq. (1.17)) and, moreover, oxygenates reforming reactions (Eq. (1.14)) are favoured over decomposition reactions (Eq. (1.16)). Consequently, the yields of H_2 (Figure 3.1) and CO_2 (Figure 3.2a) continuously increase with S/C ratio, the yield of CO decreases (Figure 3.2b) (more noticeably at high temperatures, when there is a higher yield of this product) and the yield of CH_4 also decreases (Figure 3.2c) except for very low temperatures, at which the reforming of CH_4 is thermodynamically disfavoured.

Coke yield, Figure 3.2d, is only significant for very low values of the S/C ratio (lower than 1.5, which is below the stoichiometric S/C ratio for guaiacol, $(S/C)_{st}$ of 1.71). As the S/C ratio increases and above 600 °C, the coke yield drops sharply. This result is a consequence of the extent of the gasification reactions of coke with CO_2 (reverse-Boudouard reaction, Eq. (1.21)) and with H_2O (Eq. (1.22)).

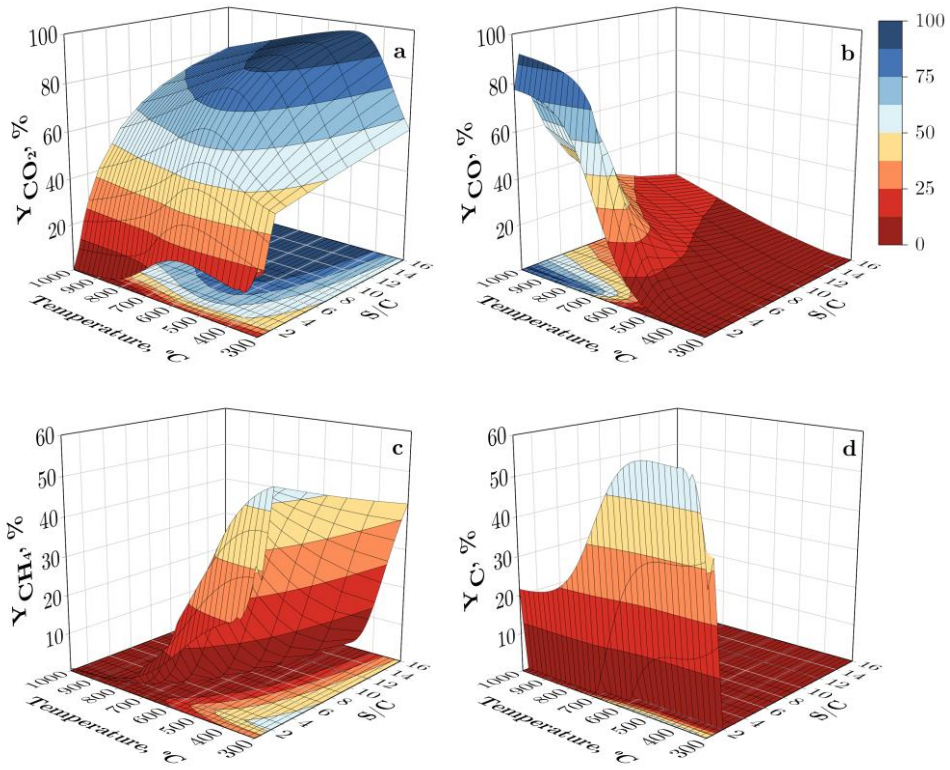

Figure 3.2. Effect of temperature and S/C ratio on the yield of carbon products (CO_2, CO, CH_4 and C (graphite)) in the SR of guaiacol.

To show in a simple way the values of the maximum H_2 yield for the different oxygenates and the temperature and S/C ratio required, Figure 3.3a and Figure 3.3b show the effect of the S/C ratio on the maximum H_2 yield, and Figure 3.3c and Figure 3.3d show the corresponding temperature. The results have been grouped in light oxygenates (Figure 3.3a and Figure 3.3c) and heavy ones (Figure 3.3b and Figure 3.3d). It should be noted that the results are the same for acetic acid, hydroxyacetaldehyde and mannose. Interestingly, the characteristic SR values of these three compounds are also equal, $(S/C)_{st}$ of 1 and H_2^o of 2 (Table 2.2), which indicates that these values determine the results, regardless of the structure and molecular weight of the oxygenate. Comparing the results for the different oxygenates, the differences in the maximum H_2 yields (Figure 3.3a and Figure 3.3b) are small, and decrease with increasing the S/C ratio. The general

trend is that the maximum H_2 yield increases markedly with increasing S/C ratio and that this effect gradually diminishes. Conversely, the temperature at which the maximum H_2 yield is reached (Figure 3.3c and Figure 3.3d) decreases with increasing the S/C ratio, in agreement with Xie et al. [314], this effect also being less noticeable with increasing S/C ratio.

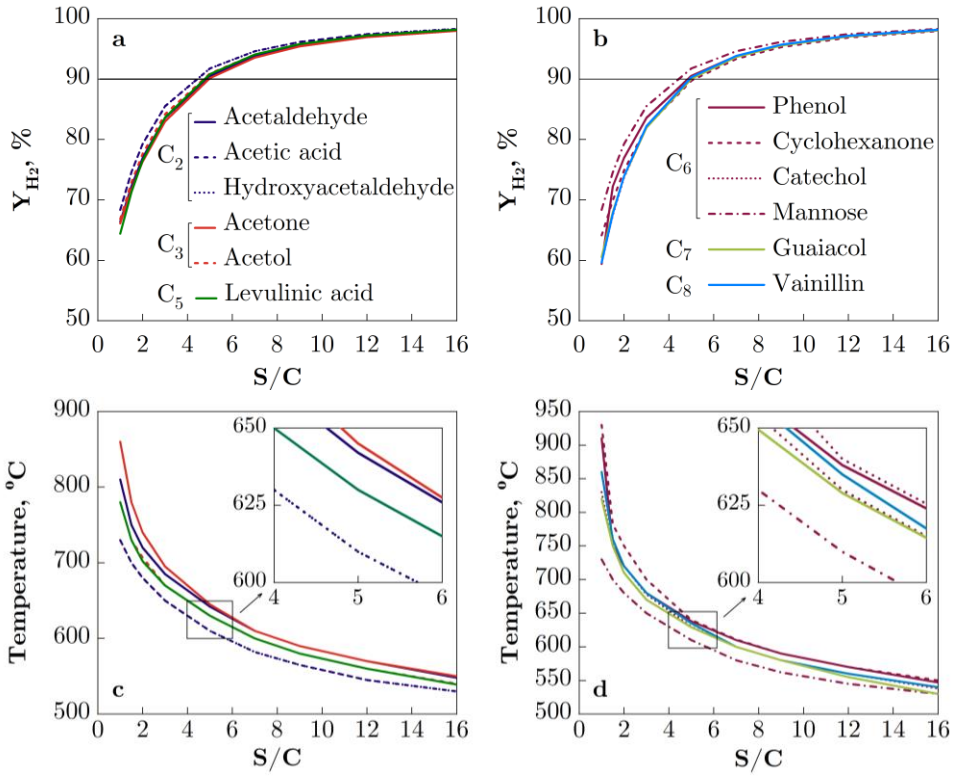

Figure 3.3. Comparison for the different oxygenates of the effect of the S/C ratio on the maximum H_2 yields (a and b) and on the temperature at which these maximums are reached (c and d).

Table 3.1 shows the values of the maximum H_2 yield, the temperature at which these maximums are reached and the corresponding yields of CO_2, CO and CH_4 for the SR of the different oxygenates with S/C ratios of 1.5, 5 and 12. The maximum H_2 yield is in the 74.6–66.8 % range for S/C ratio of 1.5, 91.8–89.7 % for S/C ratio of 5 and 97.4–96.9 % for S/C ratio of 12. The required temperature

is in the range of 700–796 °C, 610–644 °C and 546–572 °C, respectively. Under the conditions of maximum H_2 yield, the CH_4 yields are always very low (generally less than 1 %, the lower the CH_4, the higher the S/C ratio). The differences in CO_2 and CO yields for the different oxygenates are greater, especially for low S/C ratio, with ranges of CO yield between 46.8–77.2 % and of CO_2 yield between 22.0–52.2 %, for S/C ratio of 1.5. These differences are attenuated for a high S/C ratio (range of CO yield of 4.4–7.0 % and CO_2 yield of 92.7–95.4 % for S/C ratio of 12).

Table 3.1. Values of the maximum equilibrium H_2 yield, the temperature at which these maximums are reached and the corresponding yields of CO_2, CO and CH_4, for different values of the S/C ratio in the feed, for the different oxygenated compounds.

	Acetaldehyde	Acetic acid*	Acetone	Acetol	Levulinic acid
$Y_{H2\ max}$, %					
S/C=1.5	72.2	74.6	71.7	72.9	71.3
S/C=5	90.5	91.8	90.2	90.9	90.8
S/C=12	97.1	97.4	96.9	97.2	97.2
T, °C					
S/C=1.5	754	700	776	734	734
S/C=5	634	610	642	626	622
S/C=12	564	546	570	558	556
Y_{CO2}, %					
S/C=1.5	33.4	52.2	26.6	39.9	39.8
S/C=5	78.9	85.2	76.4	80.7	82
S/C=12	93.4	95.4	92.8	94.2	94.5
Y_{CO}, %					
S/C=1.5	65.6	46.8	72.8	59	59.2
S/C=5	20.2	14.2	22.8	18.6	17.3
S/C=12	6.4	4.4	6.9	5.6	5.3
Y_{CH4}, %					
S/C=1.5	0.86	1.02	0.76	0.95	0.91
S/C=5	0.77	0.59	0.82	0.71	0.69
S/C=12	0.30	0.21	0.32	0.27	0.24

* The same results for hydroxyacetaldehyde and mannose

Table 3.1. Continued (heavy compounds).

	Phenol	Cyclohexanone	Catechol	Guaiacol	Vanillin
$Y_{H2\ max}$, %					
S/C=1.5	66.8	69.9	67.5	68	67.7
S/C=5	89.7	89.7	90.2	90	90.3
S/C=12	97.0	96.9	97.1	97.1	97.2
T, °C					
S/C=1.5	780	796	754	764	748
S/C=5	634	644	626	630	624
S/C=12	562	572	556	560	554
Y_{CO2}, %					
S/C=1.5	24.7	22	32.3	29.4	33.8
S/C=5	78.7	75.6	80.6	79.5	81.7
S/C=12	93.9	92.7	94.4	94.1	94.8
Y_{CO}, %					
S/C=1.5	74.6	77.2	66.8	69.7	65.4
S/C=5	20.5	23.5	18.8	19.7	17.5
S/C=12	5.8	7.0	5.4	5.7	4.9
Y_{CH4}, %					
S/C=1.5	0.70	0.64	0.82	0.79	0.85
S/C=5	0.78	0.87	0.71	0.76	0.69
S/C=12	0.27	0.32	0.24	0.26	0.24

Overall, for all the S/C ratios, according to the compromise of the values of the maximum H_2 yield, the required temperature and the yield of by-products, the order of quality of the SR of the oxygenates is:

$$\begin{pmatrix}\text{acetic acid}\\ \text{hydroxyacetaldehyde}\\ \text{mannose}\end{pmatrix} > \begin{pmatrix}\text{levulinic}\\ \text{acid}\\ \text{acetol}\end{pmatrix} > \begin{pmatrix}\text{acetaldehyde}\\ \text{vanillin}\\ \text{catechol}\end{pmatrix} > \begin{pmatrix}\text{phenol}\\ \text{guaiacol}\end{pmatrix} > \begin{pmatrix}\text{acetone}\\ \text{cyclohexanone}\end{pmatrix}$$

According to this order, it is observed that the maximum H_2 yield is higher (and the temperature required to reach it is lower) when the $(S/C)_{st}$ ratio of the oxygenates decreases (Table 2.2). It is also observed in Table 3.1 that the highest

yield of carbon by-products (CO and CH_4) corresponds to acetone and cyclohexanone.

From all these results empirical equations were established, depending on the carbon to steam (C/S) molar ratio in the feed and on the composition of the oxygenate compound (expressed in terms of their H/C, O/C and O/H atomic ratios), to calculate the maximum equilibrium yield of H_2 (Eq. (3.1)) the temperature necessary to reach this maximum (Eq. ((3.2)) and the corresponding values of the yield of the carbon products (Eqs. (3.3)-(3.5)) in the SR of any oxygenated compound. Figure 3.4 shows how well these equations fit the values given in Table 3.1. The calculation steps followed to obtain Eqs. (3.1)-(3.5) have been explained in section A.3 of the Annexes. The interest of these equations, obtained for a high number of oxygenates of different composition and molecular weight, lies in their application for a rapid estimation of the equilibrium results in the reforming of bio-oil based on its composition, determined by elemental analysis.

$$Y_{H_2}=\left(101.2\text{-}59.46\ \left(\frac{C}{S}\right)\right)+\left(-0.429+6.279\left(\frac{C}{S}\right)\right)\cdot\left(\frac{H}{C}+\frac{O}{C}+\frac{O}{H}\right) \tag{3.1}$$

$$T=\left(553.4+387.1\ \left(\frac{C}{S}\right)\right)+\left(-7.252\text{-}100.0\left(\frac{C}{S}\right)\right)\cdot\left(\frac{O}{C}+\frac{O}{H}\right) \tag{3.2}$$

$$Y_{CO_2}=\left(102.3\text{-}130.4\ \left(\frac{C}{S}\right)\right)+\left(-0.848+37.78\left(\frac{C}{S}\right)\right)\cdot\left(\frac{O}{C}+\frac{O}{H}\right) \tag{3.3}$$

$$Y_{CO}=\left(-2.81+130.2\ \left(\frac{C}{S}\right)\right)+\left(1.099\text{-}38.65\left(\frac{C}{S}\right)\right)\cdot\left(\frac{O}{C}+\frac{O}{H}\right) \tag{3.4}$$

$$Y_{CH_4}=\left(-0.24+7.45\ \left(\frac{C}{S}\right)\text{-}9.27\left(\frac{C}{S}\right)^2\right)+\left(0.08\text{-}2.1\left(\frac{C}{S}\right)+3.66\left(\frac{C}{S}\right)^2\right)\cdot\left(\frac{O}{C}+\frac{O}{H}\right) \tag{3.5}$$

It should be noted that these equations apply for C/S molar ratio between 0.08-0.67, (H/C+O/C+O/H) atomic ratio between 1.33-3.5, (O/C+O/H) atomic ratio between 0.25-1.5, and in Eq. (3.2) the temperature is expressed in °C.

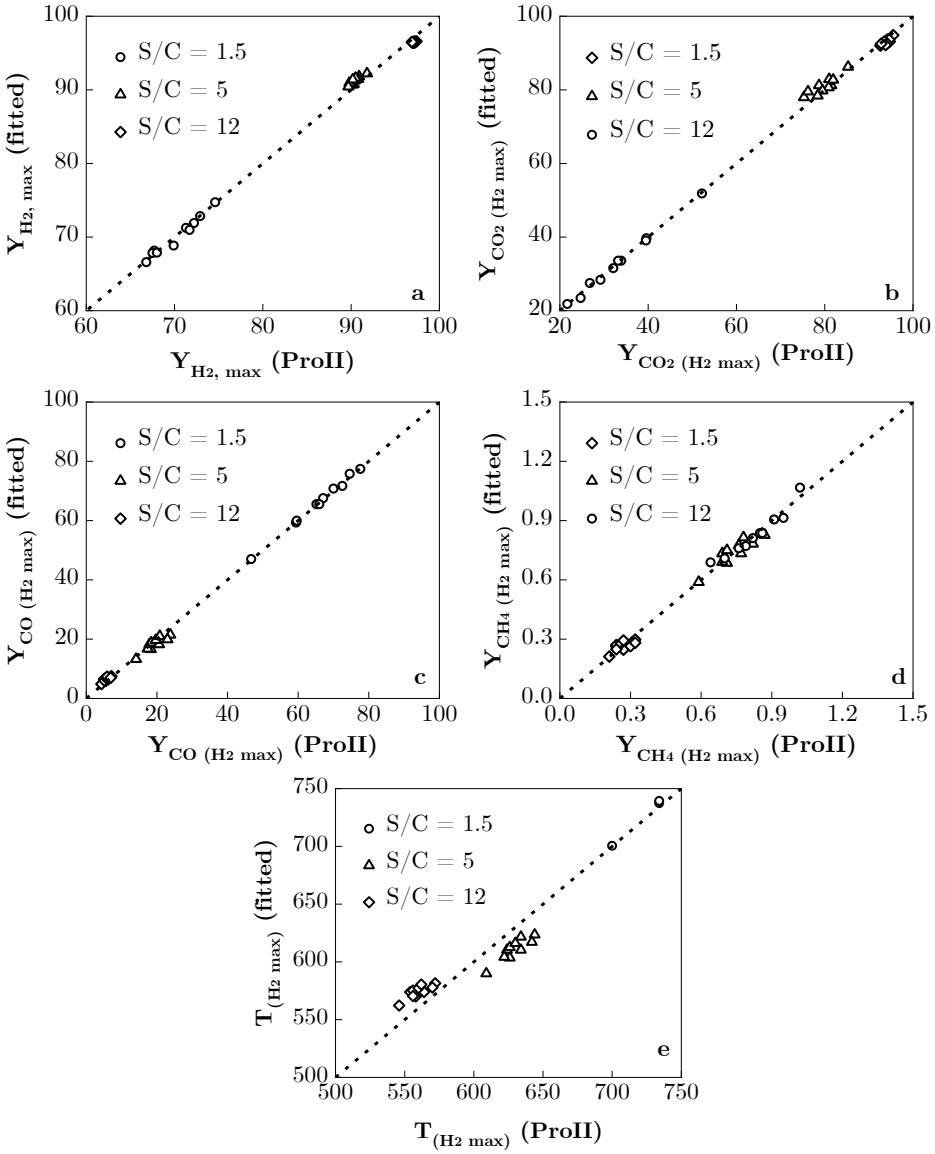

Figure 3.4. Parity plots for the values obtained by minimisation of Gibbs energy (software ProII) and calculated with Eqs. (3.1)-(3.5) of the maximum equilibrium H_2 yield (a) and corresponding yields of CO_2 (b), CO (c), CH_4 (d) and temperature necessary to reach this maximum (e), at different S/C ratios.

Considering the importance of catalyst deactivation for the viability of the reforming process [255, 268], attention has been paid to the formation of coke. As aforementioned, the thermodynamic results of coke formation are only important when the S/C ratio is significantly lower than the stoichiometric value and at low temperature. The results in Figure 3.5 (for S/C ratio of 1.5) correspond to this condition for most oxygenates, except for acetic acid, hydroxyacetaldehyde and mannose, whose coke yield is negligible under the conditions of Figure 3.5. For the rest of compounds, a high coke yield is observed when the temperature decreases below 600-640 °C. The importance of the oxygenate composition in the results is noteworthy, with a greater tendency for coke formation from the higher molecular weight oxygenates in the order: phenol > catechol ≈ guaiacol > vanillin. Among the lower molecular weight oxygenates, acetone is the one with the highest coke formation capacity.

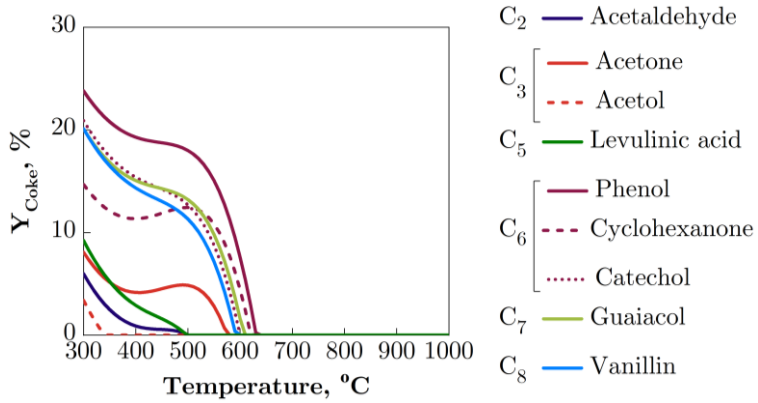

Figure 3.5. Comparison for different oxygenates of the evolution with temperature of the coke yields at S/C ratio of 1.5 (insignificant coke yield for acetic acid, hydroxyacetaldehyde and mannose).

It should be noted that these results are consistent with the experimental deposition of coke in the bio-oil SR, where phenolic components and ketones are attributed a relevant role as coke precursors [255]. Li et al. [311] found that coke deposition is notably higher in sugars reforming than in acetic acid reforming. Furthermore, the nature and composition of coke is different, being structured in nanotubes and with C=C species the one formed in the reforming of acetic acid

and amorphous and with C=O species in the reforming of sugars. Likewise, the results in Figure 3.5 are consistent with the decrease in coke deposition (due to gasification) observed in the reforming of ethanol [268] and bio-oil [255], and in the in-line reforming of biomass pyrolysis oxygenates [316]. Any case, it should be pointed out that under conditions of maximum H_2 yield (with S/C ratios ≥ 5 in order to achieve H_2 yield above 90 %), coke yield will be insignificant for the whole temperature range studied in this work and the catalyst will be stable.

3.1.2. Energy requirement

As an example, Figure 3.6 (corresponding to the SR of guaiacol) shows the effect of temperature and the S/C ratio on the heat of reaction (ΔH_r) (Figure 3.6a) and heat exchangers duty (ΔH_{HE}) (Figure 3.6b). As expected, SR is exothermic at low temperature, due to the predominance of methanation, cracking and Boudouard reactions, and it becomes endothermic with increasing temperature, when the progress of the reforming reactions is greater. ΔH_r increases sigmoidally with increasing temperature (Figure 3.6a), with a different effect of the S/C ratio depending on the temperature. Below 600 °C, as the S/C ratio increases, the heat of reaction increases, and above 600 °C it decreases. Recently, Rodrigues et al. [317] have reported these same trends in the effect of S/C ratio and temperature on the heat of reaction for the SR of a simulated bio-oil (composed of phenol/acetone/acetic acid). This different effect of S/C ratio on the heat of reaction at different temperatures is due to the fact that at low temperature the excess of water favours endothermic reactions, such as oxygenates reforming, whereas at high temperature the reaction favoured by excess of water is the exothermic WGS reaction. Furthermore, the heat exchangers duty increase with temperature and S/C ratio (linearly in the case of the effect of temperature) (Figure 3.6b).

In Figure 3.6 it is observed that the temperature required for the process to be thermoneutral (ΔH_r=0) decreases with increasing S/C ratio. These temperature values are different for the oxygenates studied. Figure 3.7 shows the combinations of temperature and S/C ratio for the thermoneutral regime with each of the

oxygenates studied. The region below each curve corresponds to an exothermic regime and the region above to an endothermic regime. An order from lower to higher temperature can be established for the thermoneutral regime according to the functional groups in the oxygenates, acids < ketones < phenols < aldehydes < saccharides. The higher temperature for hydroxyacetaldehyde with respect to acetaldehyde, for acetol with respect to acetone, or to a lesser extent when comparing the results for phenol and catechol, can be attributed to the additional presence of an -OH group, which significantly enlarges the exothermic regime.

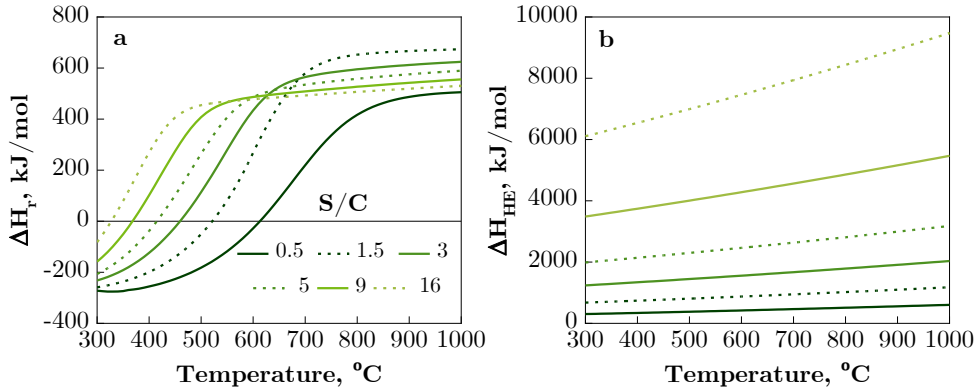

Figure 3.6. Effect of temperature on the heat of reaction (a) and on the heat exchangers duty (b), in the SR of guaiacol for different values of S/C ratio.

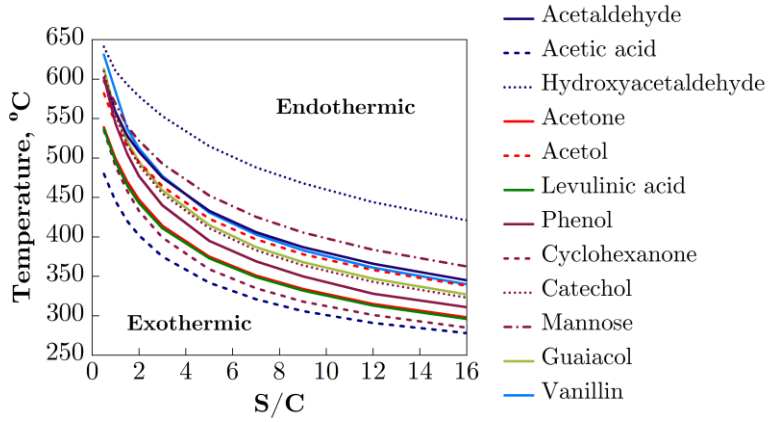

Figure 3.7. Comparison of the conditions of temperature and S/C ratio corresponding to the thermoneutral regime (ΔHr=0) in the SR of different oxygenates.

The aforementioned results show that the conditions (temperature and S/C ratio) that maximise H_2 production clearly correspond to endothermic regime. Figure 3.8 compares the effect of the S/C ratio on the reaction heat (ΔH_r) (Figure 3.8a and Figure 3.8b) and on the heat exchangers duty (ΔH_{HE}) (Figure 3.8c and Figure 3.8d) for the SR of the different oxygenates. The results correspond to the temperatures that maximise the H_2 yield. It is observed that the type of functional group influences the ΔH_r, which increases with increasing number of C atoms in the oxygenate and is lower with the presence of an OH group (compare acetone and acetol, acetaldehyde and hydroxyacetaldehyde, as well as phenol and catechol).

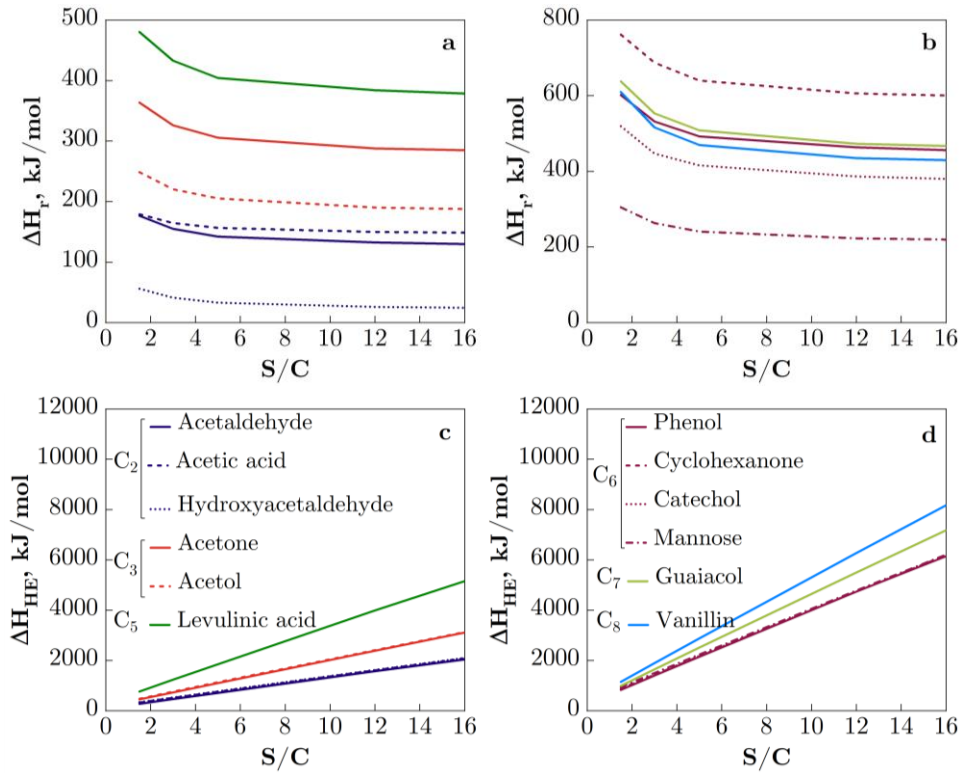

Figure 3.8. Comparison for different oxygenates of the effect of the S/C ratio on the heat of reaction (a, b) and on the heat exchangers duty (c, d). The temperature for each S/C ratio corresponds to the required for reaching maximum H_2 yield.

The value of ΔH_{HE} increases linearly with the number of C atoms as shown in Figure 3.9, but is practically independent of the type of functional groups in the oxygenate, especially for a high S/C ratio, when the duty mainly corresponds to the heating of the water fed. As observed in Figure 3.8a and Figure 3.8b, as the S/C ratio increases the ΔHr decreases asymptotically, being almost constant above S/C ratio of 5, whereas ΔH_{HE} increases linearly.

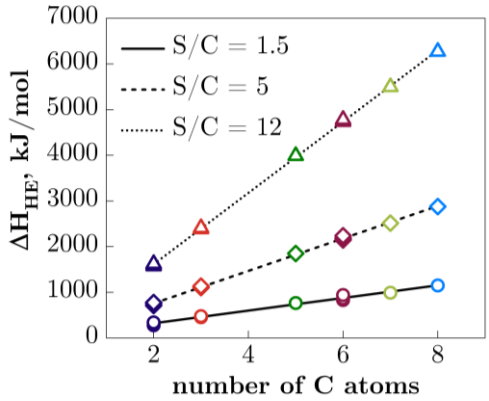

Figure 3.9. Effect of the number of C atoms in the oxygenated compound on the heat exchangers duty, for three different values of the S/C ratio in the feed. The temperature for each S/C ratio corresponds to the required for reaching maximum H_2 yield for each oxygenate.

For the selection of the optimum S/C ratio, the energy requirement should be analysed in terms of the H_2 production. For that purpose, the energy efficiency has been defined as the difference between the energy contained in the H_2 obtained from 1 mole of oxygenate reformed (considering 241.8 kJ/mol_{H2}, [318]) to the total heat duty, and these values have been plotted as a function of S/C ratio (Figure 3.10). As observed, the maximum energy efficiency corresponds to S/C ratio between 1.5 and 2, depending on the oxygenate. According to Eqs. (3.1) and (3.4), at these S/C ratios, the maximum H_2 yields for the different oxygenates, and their corresponding CO yields, were between 66-80 % and 35-77 %, respectively, and the corresponding H_2/CO molar ratios were between 1.9-4.6, which could be suitable for using the product stream as syngas. But if the target is obtaining a high purity H_2 stream, a higher S/C ratio should be used. As shown

in Figure 3.10, for all compounds the energy efficiency is positive (the energy contained in the H_2 formed exceeds the total heat duty required for obtaining it) for S/C ratio values below the range 5-8 (depending on the oxygenated compound). Based on these results, S/C ratio of 5 can be selected as a suitable compromise for the set of oxygenated compounds studied, in order to obtain high H_2 yield (above 90 %) while maintaining a positive value of the difference between the energy contained in the H_2 produced and the total heat duty necessary to produce it. Moreover, with this S/C ratio the deposition of coke is negligible. This result is important to achieve the stability of the catalyst, which determines the viability of this reaction. In these conditions, the ΔH_r is a small fraction (in the 4–23 % range for S/C ratio of 5 and 2–11 % for S/C ratio of 12) of the total energy requirement for SR of the different oxygenates studied.

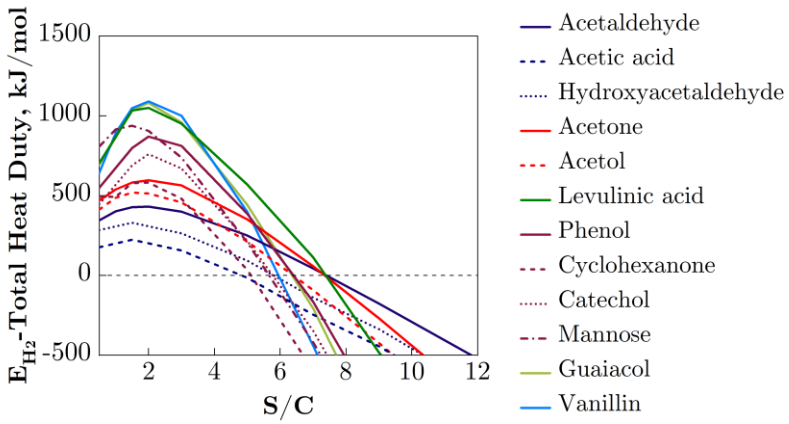

Figure 3.10. Evolution with the S/C molar ratio of the difference between the energy contained in the H_2 formed and total heat duty required to obtain it in the SR of each oxygenated compound.

When the values of the reaction heat in Figure 3.8a and Figure 3.8b are compared with the composition of the corresponding oxygenate, it is observed that, overall, ΔH_r increases with the number of C atoms and also with the number of H atoms, but it decreases with increasing O atoms. Consequently, a linear relationship between the reaction heat and the corresponding values of (C+H-O) can be stablished, as shown in Figure 3.11 for a S/C ratio of 5 as an example (the same

trend is obtained for other S/C ratios). Quite a good linear fitting is obtained for most of the compounds, with the following exceptions. On the one hand, the ΔH_r for mannose is too low, but this could be explained because this compound does not vaporize but decomposes at reforming temperature. On the other, the compounds with –OH functionality lay below the overall general trend, as commented in Figure 3.7.

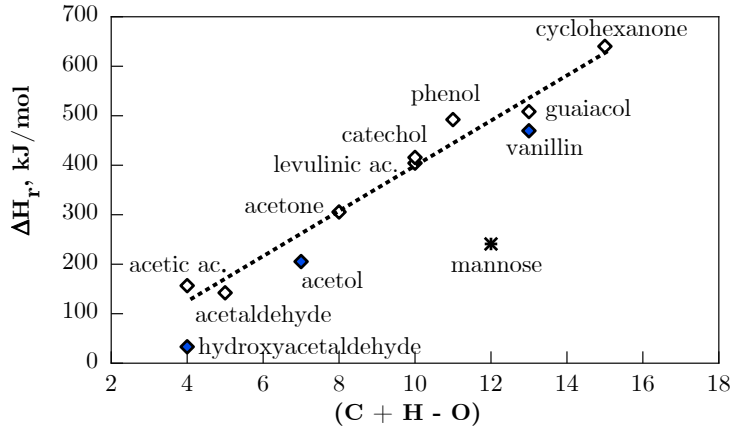

Figure 3.11. Dependence of the reaction heat with the atomic composition of the oxygenated compound.

3.1.3. Dilution of the feed with N_2

The effect of inert gas (N_2) addition upon the product yields and duty requirements has been studied in the SR of hydroxyacetaldehyde and guaiacol, taken as examples. The information obtained is important to evaluate the possibility of performing the OSR with air instead of O_2, and also for the in-line SR of the stream of oxygenates (diluted in N_2) formed in the fast pyrolysis of biomass [319]. The results shown in Figure 3.12 (products yield) correspond to two values of S/C ratio, 1.5 and 5, and at 630 °C. This temperature is adequate to maximise the H_2 yield with a S/C ratio of 5 (Table 3.1).

The changes observed in the equilibrium composition depend on the temperature and the S/C ratio, being greater at low temperature and low S/C ratio. For the S/C ratio of 1.5, the addition of N_2 in the feed leads to a slight increase in the H_2

and CO yields, whereas the CH_4 yield decreases and that of CO_2 remains almost constant. The excess of water in the reaction medium (S/C ratio of 5) attenuates these effects. These results are explained because the presence of inert favours the reactions that take place with an increase in the number of moles, such as the SR of oxygenates and methane. Furthermore, the results are consistent with those of the literature. Thus, in the SR of ethanol Hernández and Kafarov [320] reported that below 550 °C with S/C ratio of 1.5 the H_2 yield even doubled for enough high inert/(steam/ethanol) ratio, but for S/C ratio of 4.5 and above 650 °C, the H_2 yield remained unchanged with increasing inert flow rate in the feed. Similarly, Baamran and Tahir [135] have reported no significant changes in the equilibrium of H_2 yield above 500 °C with high water dilution (95 wt% water) in the SR of phenol.

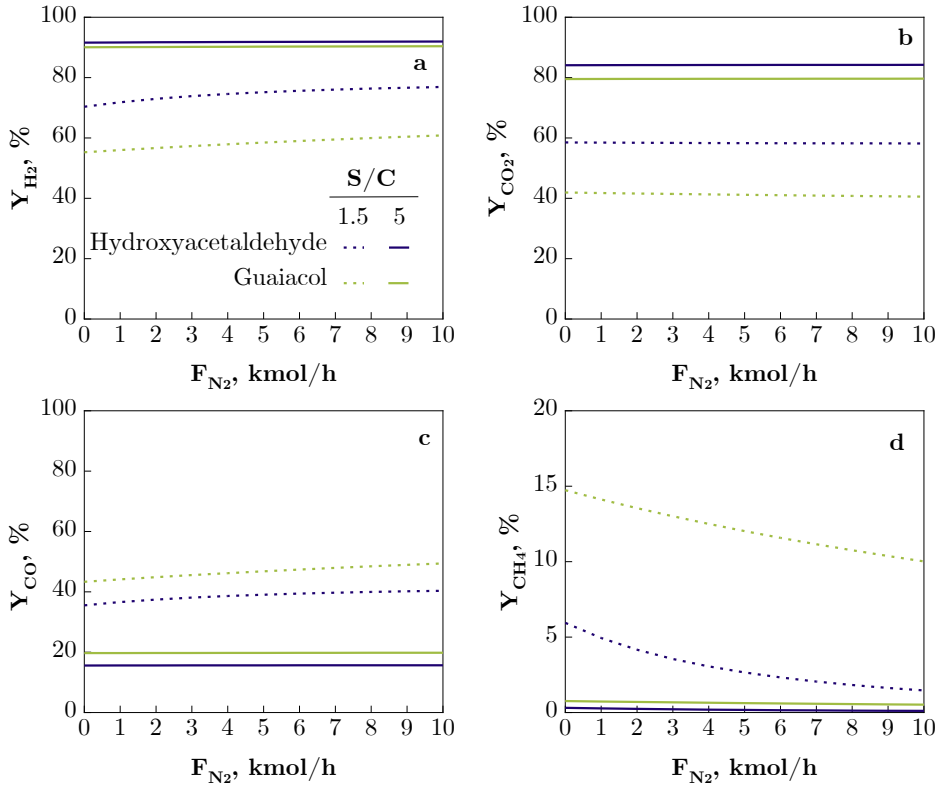

Figure 3.12. Effect of inert (N_2) addition in the feed stream on the yield of H_2 (a), CO_2 (b), CO (c) and CH_4 (d) in the SR of hydroxyacetaldehyde and guaiacol, at 630 °C and S/C ratios of 1.5 and 5.

Similarly to that observed for H_2 yield, the ΔH_r (Figure 3.13a) increases slightly with N_2 addition for a low S/C ratio, with this increase being more clearly observable in the SR of a heavy compound, such as guaiacol. Nevertheless, the increase in the ΔH_r is noticeably attenuated when there is a high water dilution, so that it is hardly observable for S/C ratio of 5. Conversely, ΔH_{HE} values (Figure 3.13b) increase slightly with increasing molar flow rate of N_2 fed, linearly and similarly for both oxygenates, the increase being independent of the S/C ratio.

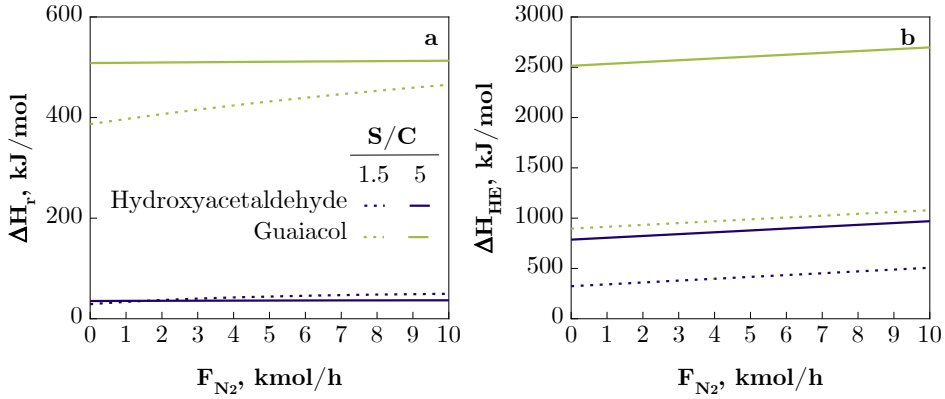

Figure 3.13. Effect of inert (N_2) addition in the feed stream on the reaction heat (a) and heat exchangers duty (b) in the SR of hydroxyacetaldehyde and guaiacol, at 630 °C and S/C ratios of 1.5 and 5.

Taking into account the results of this section, a slightly positive effect of the N_2 feed on the H_2 yield is verified, without a great penalty in the energy requirements of the reaction and in the previous heating of the feed.

3.2. ROLE OF INDIVIDUAL OXYGENATES IN DEACTIVATION BY COKE OF A $NiAl_2O_4$ DERIVED CATALYST

In this section, the influence of oxygenates composition in bio-oil on the deactivation by coke of a Ni/Al_2O_3 catalyst derived from $NiAl_2O_4$ spinel has been approached by studying the SR of a wide range of model oxygenates with different functionalities, including acetic acid, acetone, ethanol, acetaldehyde, acetol, catechol, guaiacol and levoglucosan. The conditions selected for this study

(gathered in Table 2.10), with low values of space time, allow to observe a significant deactivation in a short reaction time.

3.2.1. Effect of feed composition on catalyst performance

In order to assess the catalyst activity, selectivity and stability for the different feeds studied, the evolution with TOS of carbon conversion and yield of H_2 at 600 and 700 °C is shown in Figure 3.14 for each oxygenated compound.

At 600 °C, the initial H_2 yield (fresh catalyst) varies between 42 % (for acetone, Figure 3.14e) and 61 % (for acetaldehyde, Figure 3.14b), with similar values (near 50 %) for the rest of oxygenates, thus evidencing similar reactivity at this temperature. The increase in temperature up to 700 °C enhances the carbon conversion and H_2 yield at zero time on stream in the SR of all oxygenates, with this increase being more significant for acetaldehyde, ethanol and acetol (almost 100 % conversion), and also for acetic acid and catechol (around 93 % conversion). However, it is less noticeable for the guaiacol+ethanol mixture, acetone and levoglucosan, thus evidencing the lower reactivity towards SR reactions at high temperature of the latter oxygenates. The low increase with temperature of the carbon conversion for the guaiacol+ethanol mixture (Figure 3.14g), compared to that obtained with ethanol (Figure 3.14c), gives evidence of a low effect of temperature for guaiacol, whose reactivity for SR reactions is noticeably lower than that of ethanol, acetic acid, acetaldehyde, acetol and catechol. Moreover, the initial H_2 yield in the SR of ethanol at 700 °C (70 %) is lower than that obtained with the other oxygenates (around 80 %), in spite of its high carbon conversion (100 %). This result reveals the higher selectivity of the catalyst for H_2 forming reactions (steam reforming and WGS) in the SR of acetic acid, acetol and acetaldehyde compared to ethanol, whose reforming produces significant CH_4 formation. The high H_2 yield (80 %) obtained in the SR of levoglucosan at 700 °C, in spite of its non-complete carbon conversion, should be attributed to the high S/C ratio used in the SR of this oxygenate (6), that significantly promotes WGS reaction.

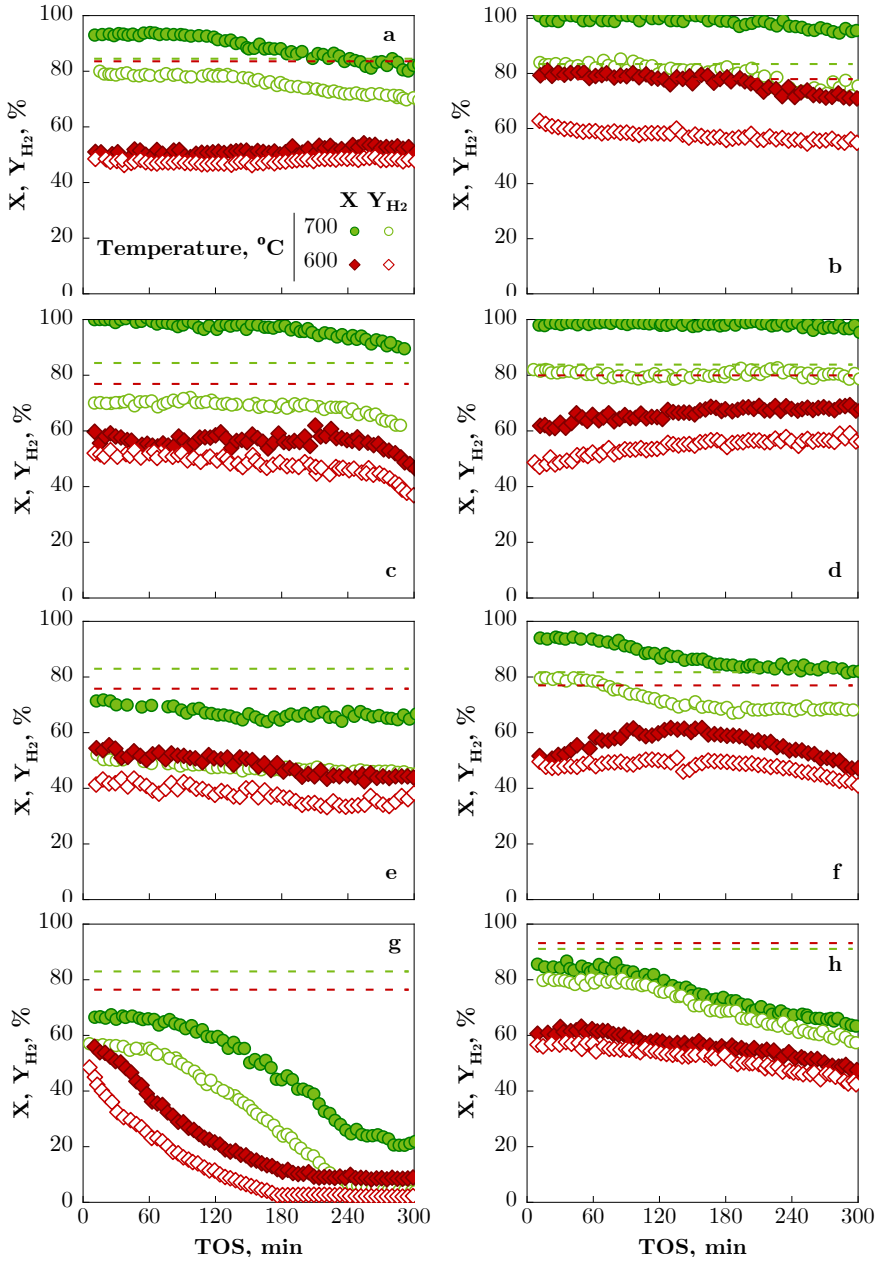

Figure 3.14. Evolution with TOS of carbon conversion and H_2 yield in the SR with Ni/Al_2O_3 catalyst of acetic acid (a), acetaldehyde (b), ethanol (c), acetol (d), acetone (e), catechol (f), guaiacol+ethanol mixture (g), and levoglucosan (h). Dashed lines for thermodynamic values.

Regarding the stability of the catalyst, overall, the conversion and H_2 yield remain constant or even increase (for acetic acid (Figure 3.14a), acetol (Figure 3.14d) and catechol (Figure 3.14f)) at 600 °C and slightly decrease with TOS at 700 °C in the SR of all the studied oxygenates, except for guaiacol+ethanol mixture. The increase in conversion and H_2 yield with TOS can be explained by the formation of a remarkable amount of filamentous coke (as shown later), which leads to an improved Ni dispersion and better accessibility of reactants due to the tip-growth mechanism of carbon filaments [260]. Conversely, in the SR of the guaiacol+ethanol mixture (Figure 3.14g) there is a fast decrease in conversion and H_2 yield at both 600 and 700 °C, until the values corresponding to the thermal reaction routes (in the absence of catalyst) are reached. Therefore, this result evidences a much faster deactivation rate of the catalyst in the SR of this mixture than for the rest of the oxygenates studied.

3.2.2. Characterization of used catalyst samples

In order to identify the causes responsible for the deactivation of Ni/Al_2O_3 catalyst derived from $NiAl_2O_4$ spinel, and to better understand its deactivation behaviour in the SR of the different oxygenates, a thorough characterization of the used catalyst samples has been performed using complementary techniques, including TPO, N_2 adsorption-desorption, XRD, SEM and TEM images and Raman spectroscopy. These techniques have allowed determining the amount, nature, morphology and structure of the coke deposited on the catalyst, as well as the changes in the metal sites and porous structure of the catalyst. It should be noted that Ni oxidation was ruled out as deactivation cause, because previous studies with this catalyst showed that there were no significant reduction peaks in the H_2-TPR profiles of selected catalyst samples used in the SR [96] and OSR [303] of bio-oil, due to the highly reducing environment in the reforming reaction, with a high H_2 content. The results of the rest of characterization techniques are presented in the following sections.

3.2.2.1. Results of TPO analysis

Figure 3.15 and Figure 3.16 show the TPO profiles of the catalyst samples used in the SR of the oxygenates at different temperatures, which provide information on the total content of coke deposited (estimated from the total area under the TPO profiles, shown in Figure 3.17), and also provide qualitative information on the nature and/or location of the coke in the catalyst structure [321].

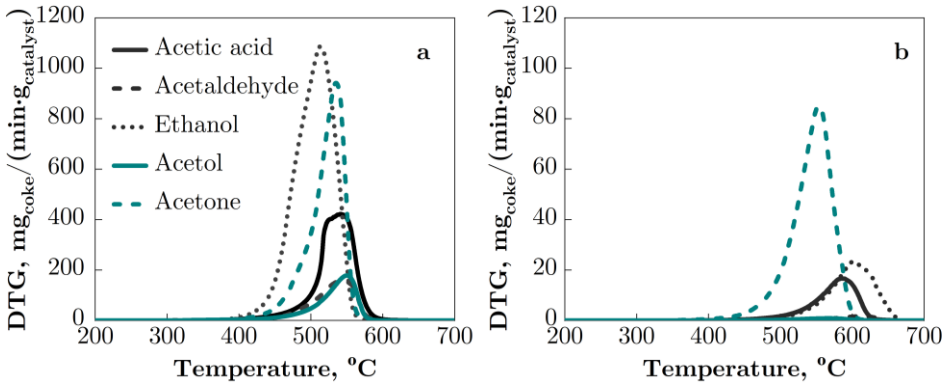

Figure 3.15. TPO profiles of the Ni/Al_2O_3 catalyst used in the SR at 600 °C (a) and 700 °C (b) of the light non-phenolic oxygenates.

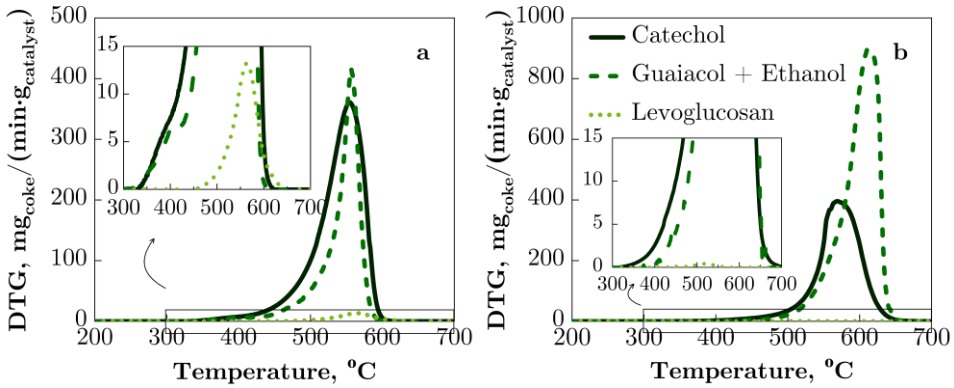

Figure 3.16. TPO profiles of the Ni/Al_2O_3 catalyst used in the SR at 600 °C (a) and 700 °C (b) of the phenolic oxygenates and levoglucosan.

The size and location of combustion peaks in Figure 3.15 and Figure 3.16 evidence differences in the amount and nature of coke deposited with the different

oxygenates and at different temperature. Noticeably, in the TPO profiles there is apparently a unique combustion peak, with maximum in the 500-550 °C range for the SR at 600 °C. This maximum shifts towards higher combustion temperature for the catalyst used in the SR at 700 °C, which suggests that the coke evolves into a more condensed and graphitic-like structure, with lower H/C ratio, and therefore, a higher combustion temperature is required [321]. A shoulder burning at low temperature is also observed in the TPO profiles for the samples used at 600 °C with catechol and guaiacol+ethanol, which is more noticeable for the latter, but is not observed in the SR of the non-phenolic oxygenates (Figure 3.15). This result confirms the previously reported relevant role of phenolic compounds as precursors of the coke burning at low temperature (located near metal sites, causing its partial or total encapsulation), deposited in the SR of bio-oil over this catalyst [94]. Taking into account the similar amount of this coke type deposited for catechol and for the mixture (guaiacol+ethanol), with only 50 wt% of guaiacol, it can be concluded that the latter is more prone to its formation.

The coke content (Figure 3.17) notably decreases with reforming temperature in the SR of non-phenolic compounds, but, conversely, it increases in the SR of phenolic compounds (catechol and guaiacol), which suggests a different mechanism of coke formation and evolution for the two groups of compounds. At 600 °C, the amount of coke follows the order: ethanol > acetone > acetic acid ≈ catechol > guaiacol+ethanol > acetaldehyde ≈ acetol > levoglucosan, whereas at 700 °C the order is guaiacol+ethanol > catechol >> acetone > ethanol > acetic acid > acetaldehyde > acetol > levoglucosan.

Comparing the results of Figure 3.17 with the deactivation results (Figure 3.14), it is noteworthy that there is no direct relationship between the amount of coke and the deactivation rate. This result has also been reported in previous works on oxygenates reforming [142, 145, 255, 260, 267, 268] and is explained by the fact that other characteristics of the coke (morphology, structure and location) have a greater impact on deactivation than its content. In addition, it is observed that with similar TPO profiles in terms of peak position (as in the case of coke

for the SR of guaiacol+ethanol and catechol at 600 °C) the deactivation rate is different (much faster in the SR of guaiacol+ethanol). Consequently, although the TPO profile of the coke provides valuable qualitative information on the level of condensation and heterogeneity of the coke, to understand the deactivation of the catalyst it is necessary to complete the information on the coke with other characterization techniques of the used catalyst, which will be shown in subsequent sections.

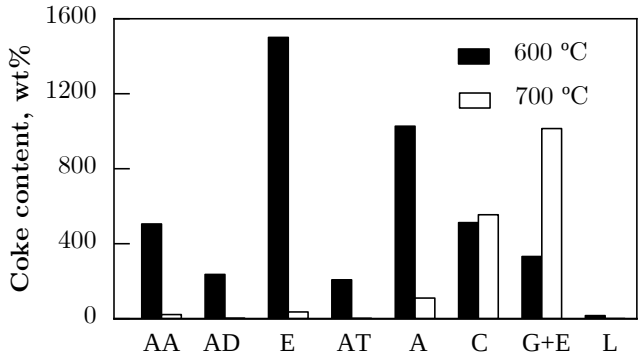

Figure 3.17. Comparison of coke content (wt%) deposited on Ni/Al_2O_3 catalyst in SR of oxygenates at 600 and 700 °C. AA= acetic acid; AD=acetaldehyde; E=ethanol; AT=acetol; A=acetone; C=catechol; (G+E)=guiaiacol+ethanol; L=levoglucosan.

3.2.2.2. Physical properties of used catalysts

The textural properties of fresh-reduced and used catalyst samples (BET surface area, pore volume and average pore diameter) have been determined by means of N_2 adsorption-desorption and are displayed in Table 3.2. The N_2 adsorption-desorption isotherms and BJH pore volume distribution of used Ni/Al_2O_3 catalyst samples are shown in Figure 3.18. All the samples have isotherm of type IV according to the IUPAC classification, which is associated with capillary condensation taking place in mesopores. The isotherm of fresh-reduced catalyst (Figure 2.5a) presents a hysteresis of the type H2, attributed to a difference in mechanism between condensation and evaporation processes occurring in pores with narrow necks and wide bodies (often referred to as 'ink bottle' pores). Conversely, a H3-type hysteresis cycle is observed for most of the isotherms of

catalyst samples used in SR of pure oxygenated compounds, which does not exhibit any limiting adsorption at high P/P_0, and is associated to aggregated of plate-like particles giving rise to slit-shaped pores [300].

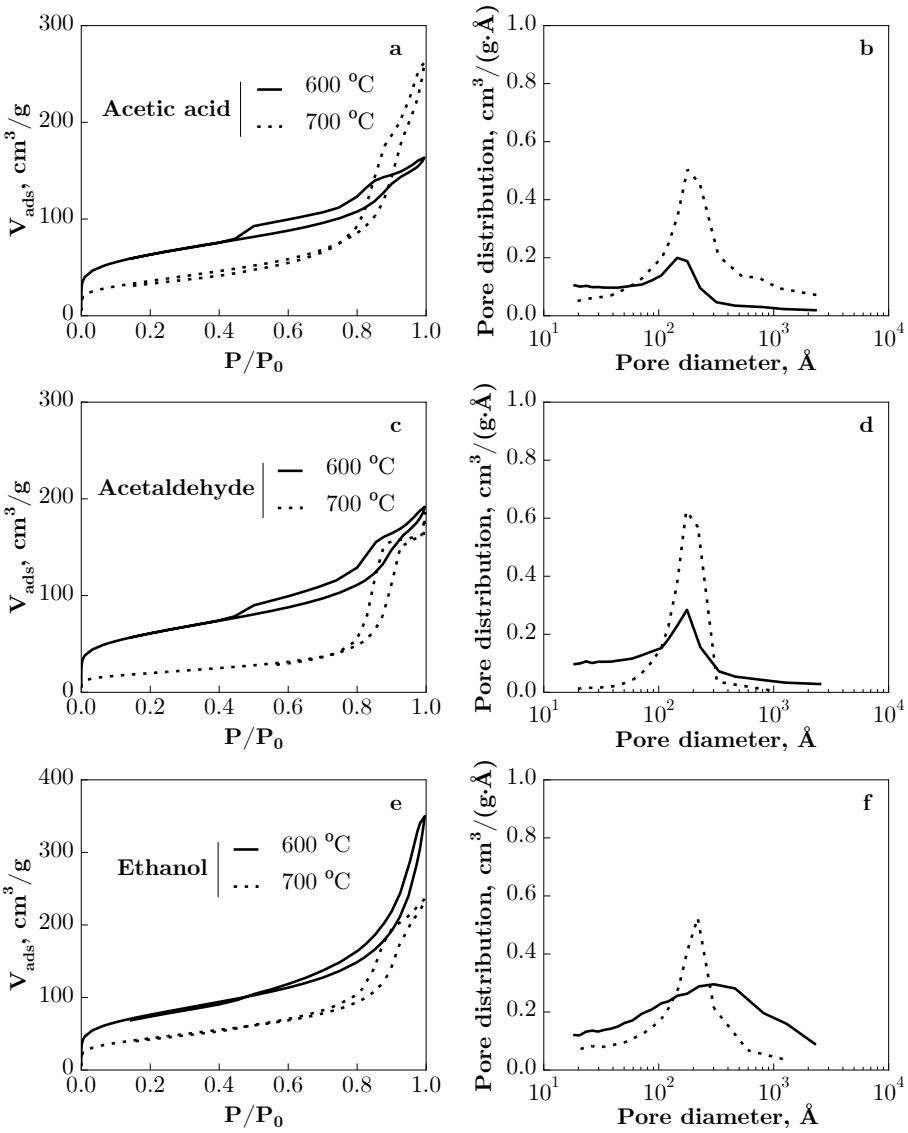

Figure 3.18. N_2 adsorption-desorption isotherms (left graphs) and BJH pore volume distribution (right graphs) of Ni/Al_2O_3 catalyst samples used in the SR of acetic acid (a, b), acetaldehyde (c, d), ethanol (e, f), acetol (g, h), acetone (i, j), catechol (k, l) and guaiacol+ethanol (m, n).

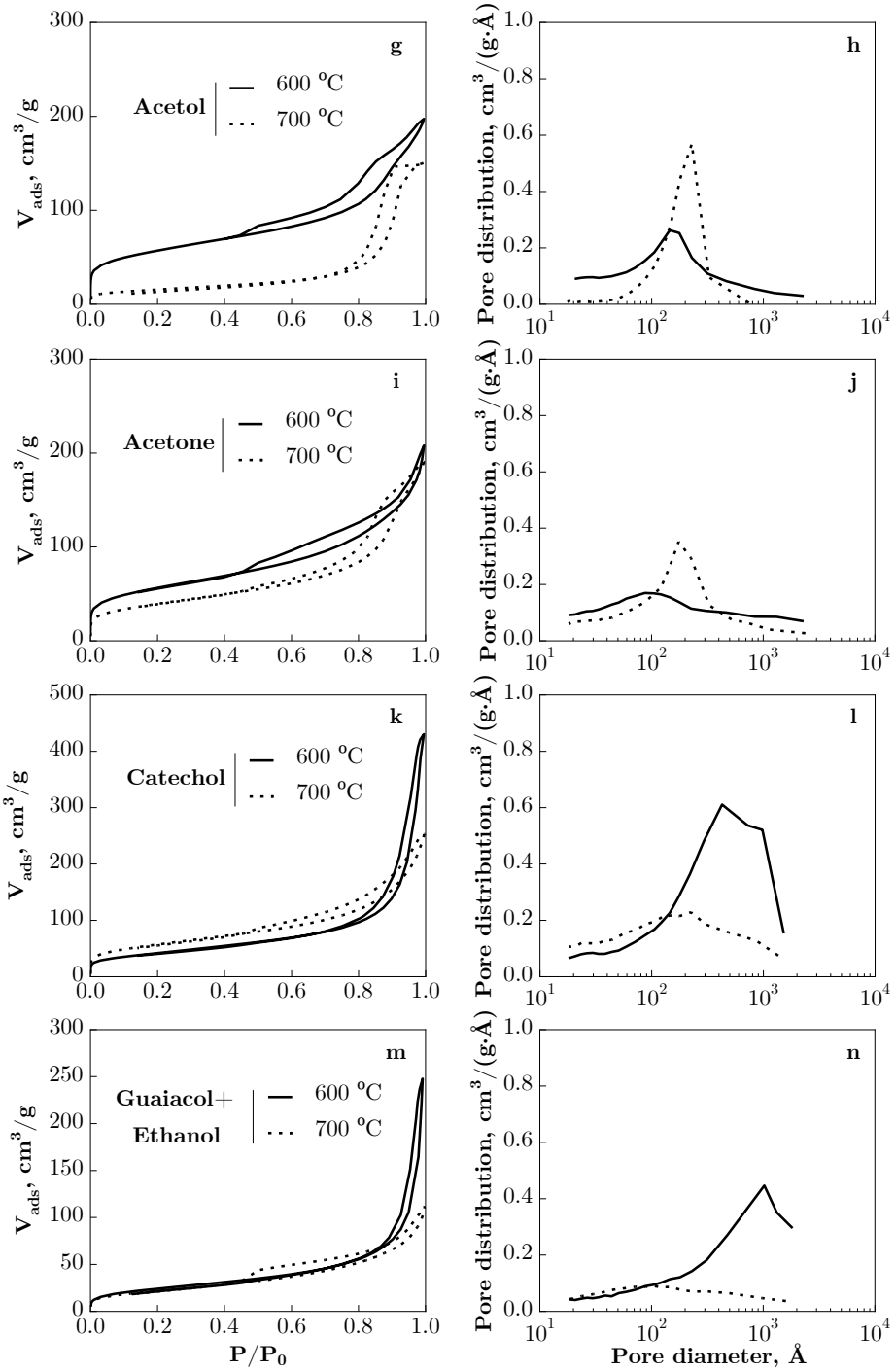

Figure 3.18. Continued.

Overall, the shape of the isotherms in Figure 3.18 for used catalyst samples does not change with SR temperature, but there are significant differences in the values of textural properties (BET surface area, pore volume and average pore diameter, gathered in Table 3.2).

Table 3.2. Physical properties of the catalyst used in the SR of oxygenates and of fresh-reduced catalyst.

Catalyst	**S_{BET}, m^2/g**	**V_{pore}, cm^3/g**	**d_{pore} (BJH), nm**
Fresh-reduced	65.1	0.23	13.1
AA-600	224	0.24	6.8
AA-700	125	0.34	13.4
AD-600	215	0.27	7.8
AD-700	70	0.25	13.9
E-600	266	0.44	11.1
E-700	152	0.34	10.9
AT-600	201	0.28	8.5
AT-700	65	0.23	15.7
A-600	199	0.27	8.7
A-700	139	0.27	10.1
C-600	147	0.46	19
C-700	198	0.33	9.2
G+E-600	85	0.25	19.7
G+E-700	77	0.14	8.7
L-700	64	0.24	15.0

In the region of low partial pressures ($P/P_0 \approx 0$), the volume adsorbed in samples of catalyst used in the SR of aliphatic oxygenates and catechol at 600 °C increases noticeably due to the high BET surface area of these samples (which is more than double that of the fresh-reduced catalyst). This result can be explained by the deposition of porous carbon structures, such as carbon filaments (in agreement with the SEM images shown later, in Figure 3.22 and Figure 3.23), and is

consistent with the high stability observed in the SR at 600 °C of these oxygenates. In the samples of catalyst used at 700 °C and with the lowest values of coke deposition (SR of acetaldehyde, acetol and levoglucosan), the physical properties resemble those of the fresh catalyst. On the other hand, the significantly lower total volume adsorbed at high pressures ($P/P_0 \approx 1$) in the catalyst sample used in the SR of (guaiacol+ethanol) mixture at 700 °C (Figure 3.18m) evidences the partial blockage of the mesopores, thus causing a decrease in BET surface area and pore volume (in spite of a high presence of carbon filaments). This partial blockage of the porous structure would contribute to a rapid deactivation, as observed in the SR at 700 °C of this feed (Figure 3.14g).

3.2.2.3. Metallic and structural properties of used catalysts

The XRD analysis was carried out to analyse the crystalline structure of the catalyst and of the coke, and also to determine the average size after reaction of Ni metal crystals, by means of Debye-Scherrer equation, at $2\theta = 51.8\,^{\circ}$ (Ni^0 (200) plane). Figure 3.19 shows the XRD diffractograms of catalyst samples used in the SR of oxygenates at 600 °C (a) and at 700 °C (b).

In the fresh-reduced catalyst (Figure 2.8a) peaks corresponding to Ni^0 (diffraction angle at 44.6° in (111) plane, 51.8° in (200) plane and 76.3° in (110) plane, PDF 04-010-6148) and Al_2O_3 (37.5°, 45.9° and 66.3°, PDF 04-005-4662) have been identified. The same diffraction peaks are observed in the used catalysts. Therefore, the presence of NiO is not detected, in agreement with the previous assumption of ruling out Ni oxidation as a deactivation cause, which corroborates the high reducing capacity of the reaction medium to keep the active metal in a reduced state.

Moreover, the XRD pattern of most of the used catalyst samples shows the presence of a broad peak at a diffraction angle $2\theta = 26°$, which corresponds to high crystallinity cokes (graphite carbon), a characteristic peak usually identified in catalysts used in the steam reforming of pure oxygenated compounds (or some mixtures), such as ethanol [259], acetone [128] or acetic acid [322]. The intensity of this peak is in a reasonable agreement with carbon amounts (Figure 3.17).

Thus, its intensity is high for all the samples used at 600 °C, except for levoglucosan, and for the samples used at 700 °C with phenolic compounds or acetone in the feed, but it is not observed at this temperature for levoglucosan, acetaldehyde and acetol, due to their low coke content (< 3 %). Nevertheless, there is not a linear relationship between the intensity of this peak and the amount of coke, which is consequence of differences in the crystallinity level of the different coke deposits.

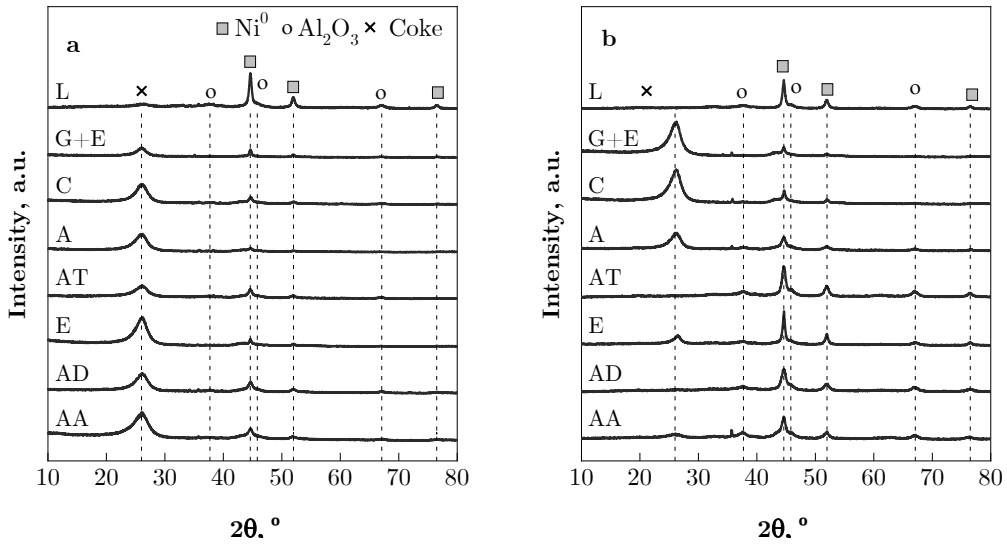

Figure 3.19. XRD patterns of Ni/Al_2O_3 catalyst samples used in the SR of oxygenates at 600 °C (a) and 700 °C (b).

The calculated average Ni^0 particle size for this batch of fresh-reduced catalyst is 13 nm. In the used catalyst samples, the measurement of metal crystal size from XRD diffractograms is hindered when the coke content is high (as it masks the Ni^0 diffraction peaks). Therefore, the calculation is only possible with low-moderate coke contents (below 120 wt%). For the used catalyst samples with low coke content, the Ni^0 crystal size is between 9-12 nm (even lower than for the fresh Ni/Al_2O_3 catalyst), except for the SR of levoglucosan, which slightly increases (17 nm). This moderate sintering of Ni^0 crystals could be responsible for

the moderate deactivation rate observed in the SR of levoglucosan (Figure 3.14h), despite the low coke content deposited in these experiments (Figure 3.17).

3.2.2.4. Morphology and location of coke

Figure 3.20 and Figure 3.21 show BSE-SEM images for the used catalyst in the SR of oxygenates at 600 and 700 °C, respectively. The BSE-SEM images allow determining the presence of some type of elements on the external surface of the particles based on the brightness intensity [255]. In contrast to the high brightness intensity of the fresh-reduced catalyst (Figure 2.11a), indicating the presence of heavy elements (Ni and Al) that constitute the catalyst phases, the particles of the used catalyst samples are generally homogeneous and exhibit a low brightness intensity (dark appearance), which indicates the predominant presence of coke on the external surface of the particles. However, the catalyst used in the SR of levoglucosan at 700 °C (Figure 3.21h) shows a homogeneous high brightness intensity, similar to that of the fresh catalyst, which confirms the very low coke deposition observed in the TPO results. On the other hand, the catalyst used in the SR of acetaldehyde at 700 °C (Figure 3.21b) shows heterogeneous particles, some with high brightness intensity and others with a dark appearance, which is indicative of the heterogeneous coke deposition.

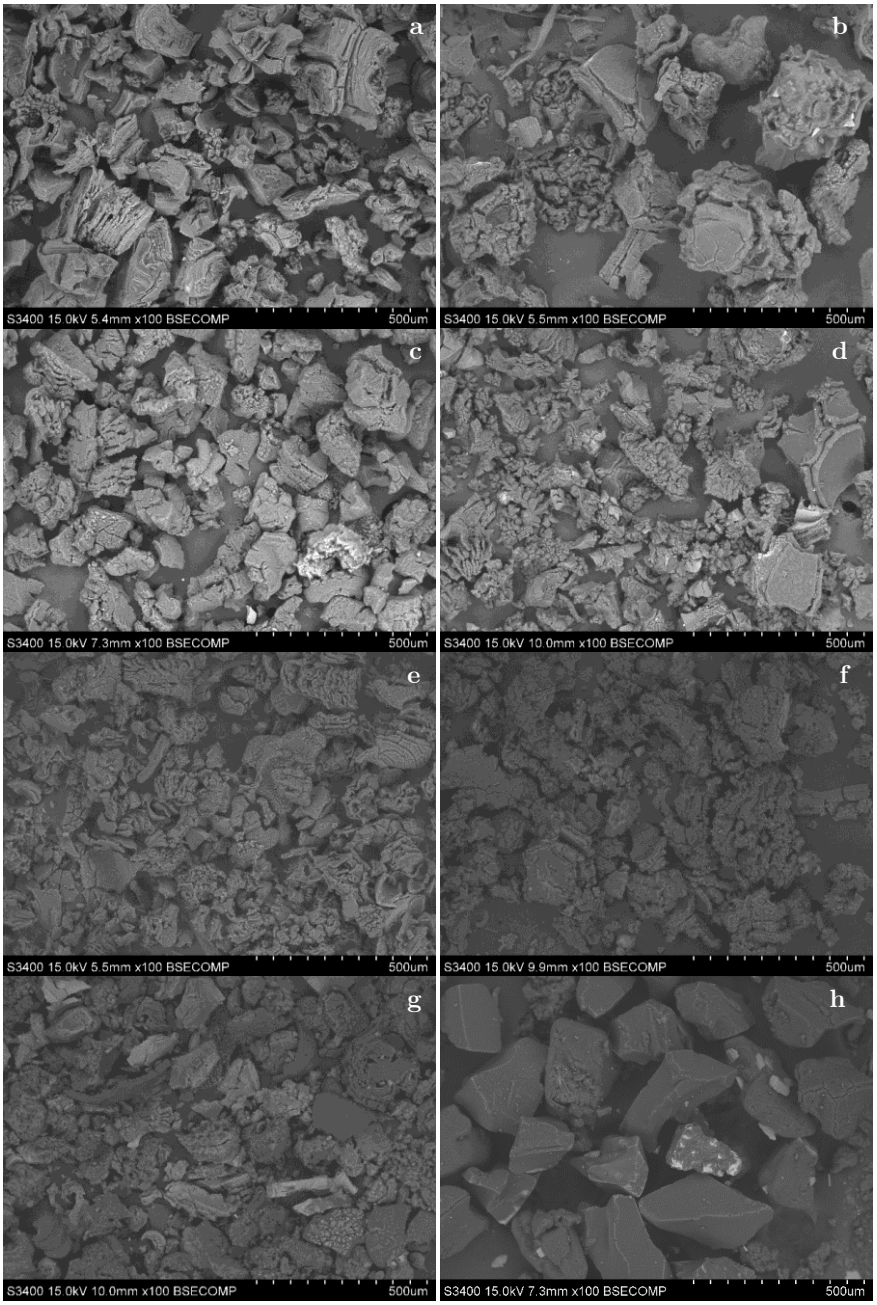

Figure 3.20. BSE-SEM images of Ni/Al_2O_3 catalyst samples used in the SR of acetic acid (a), acetaldehyde (b), ethanol (c), acetol (d), acetone (e), catechol (f), guaiacol+ethanol (g) and levoglucosan (h) at 600 °C.

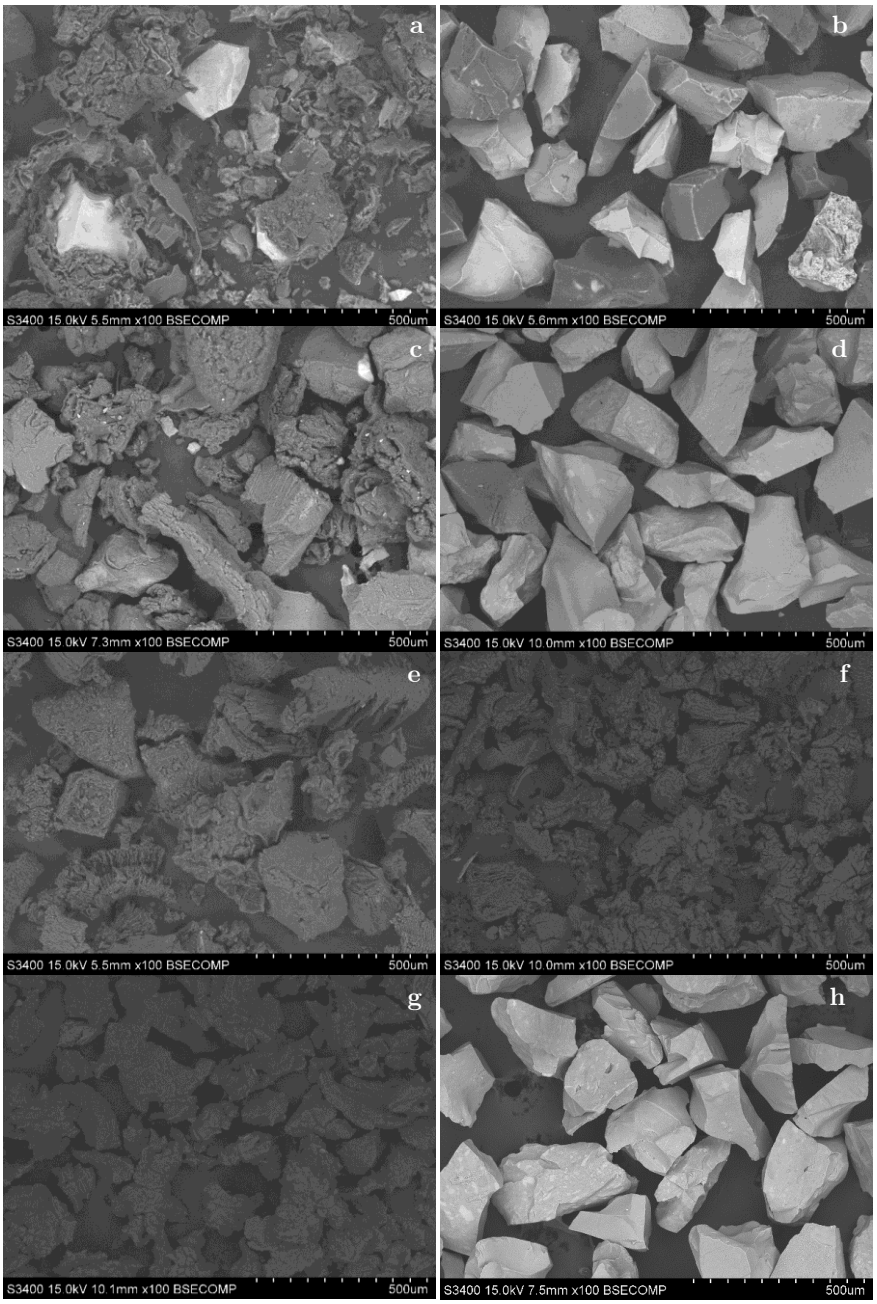

Figure 3.21. BSE-SEM images of Ni/Al_2O_3 catalyst samples used in the SR of acetic acid (a), acetaldehyde (b), ethanol (c), acetol (d), acetone (e), catechol (f), guaiacol+ethanol (g) and levoglucosan (h) at 700 °C.

Additionally, these images also show differences in the particle shapes and textures that can be correlated with the coke content (Figure 3.17). The particle shape of the used catalysts is similar to that of the fresh-reduced catalyst when the coke content is low (< 20 wt%, SR of levoglucosan at 600 °C (Figure 3.20h) and acetaldehyde, acetol and levoglucosan at 700 °C (Figure 3.21b, Figure 3.21d and Figure 3.21h, respectively)), being irregular with a smooth surface and sizes in between 150 and 250 µm (original catalyst particle size). When the coke content is moderately high (between 20-120 wt%, in the SR of acetic acid, ethanol and acetone at 700 °C (Figure 3.21a, Figure 3.21c and Figure 3.21e, respectively)), the particle texture of the used catalyst sample changes to a rough surface keeping the original catalyst particle size. In particular, the catalyst used in the SR of acetic acid at 700 °C (Figure 3.21a) shows bare catalyst particles with fragments of coke shells, evidencing the low mechanical strength of the superficial coke shells. When the coke content is high (> 200 wt%), the particles of the used catalysts (rest of the experiments) have a rough surface and are remarkably smaller than the original catalyst particle size, which may indicate a collapse of the catalyst particles due to the excessive coke growth.

Figure 3.22 and Figure 3.23 show the SE-SEM images of the used catalyst surfaces. In general, at 600 °C (Figure 3.22), the images show the formation of carbon filaments from all the model compounds with different characteristics (heterogeneous in size and texture). In particular, the carbon filaments from SR of ethanol (Figure 3.22c) show a rough surface, indicating the growth/deposition of carbon along the filaments. Additionally, the formation of an amorphous carbon phase is observed in the catalyst used in the SR of guaiacol+ethanol (Figure 3.22g), and in comparison with the catalyst used in the SR of ethanol (Figure 3.22c), this carbon phase is inferred to be formed from guaiacol. At 700 °C (Figure 3.23), the SE-SEM images clearly show the predominant formation of carbon filaments from acetic acid, acetaldehyde, ethanol, acetone and catechol. The aforementioned peculiar feature of the carbon filaments from ethanol is highly noticeable at this temperature (Figure 3.23c), indicating that the growth/deposition of carbon along the filaments is favoured. A second carbon phase in between the filaments is observed in the SR of guaiacol+ethanol (Figure

3.23g), probably due to the formation of pyrolytic carbon from guaiacol (as explained in discussion section) which is more predominant on some regions of the catalyst surface (Figure B.10). On the other hand, the surface of the used catalysts with low coke content (SR of acetol and levoglucosan, Figure 3.23d and Figure 3.23h, respectively) resembles that of the fresh catalyst, which confirms no significant coke deposition.

To study the location of coke on the catalyst surface, Figure 3.24 shows contrasts of BSE-SEM and SE-SEM images for selected used catalyst samples. In the used catalyst with carbon filaments, Ni crystals are often visualized on the tip of the filaments, but not for all the cases. Interestingly, for the catalyst used in the SR of acetic acid at 600 °C (Figure 3.24c), a large filament was captured showing various Ni crystals along it, which indicates that various Ni crystals may be involved in the growth of large filaments. To complement these observations, selected used catalyst samples were also analysed using TEM, and the images (Figure 3.25 and Figure 3.26) evidence the formation of hollow carbon filaments (carbon nanotubes) with thick walls (probably multiwall carbon nanotubes, MWCNT) and the presence of Ni crystals on the tip of or along the filaments with no evidence of sintering. Particularly, the catalysts used in the SR of guaiacol+ethanol at 600 and 700 °C (Figure 3.25) showed two carbon phases (amorphous and filaments). The presence of Ni crystals on the tip of the filaments is an expected observation based on the tip growth mechanism commonly described for the formation of carbon filaments on different Ni catalysts used in the SR of oxygenates [260–262, 323]. It also explains the catalyst stability observed in the experiments for the SR of acetic acid, acetaldehyde, ethanol, acetol, acetone, catechol and levoglucosan (Figure 3.14) in spite of the high content of filaments, because Ni crystals are exposed and accessible for the reactants. However, the rapid catalyst deactivation observed for the SR of guaiacol+ethanol in Figure 3.14g is associated to the formation of a second carbon phase at 600 and 700 °C, which is also observed in the SR of raw bio-oil [96, 266]. This carbon phase is formed from guaiacol and has an amorphous nature at 600 °C and a pyrolytic nature at 700 °C based on the coke combustion characteristics (Figure 3.16a and Figure 3.16b, respectively).

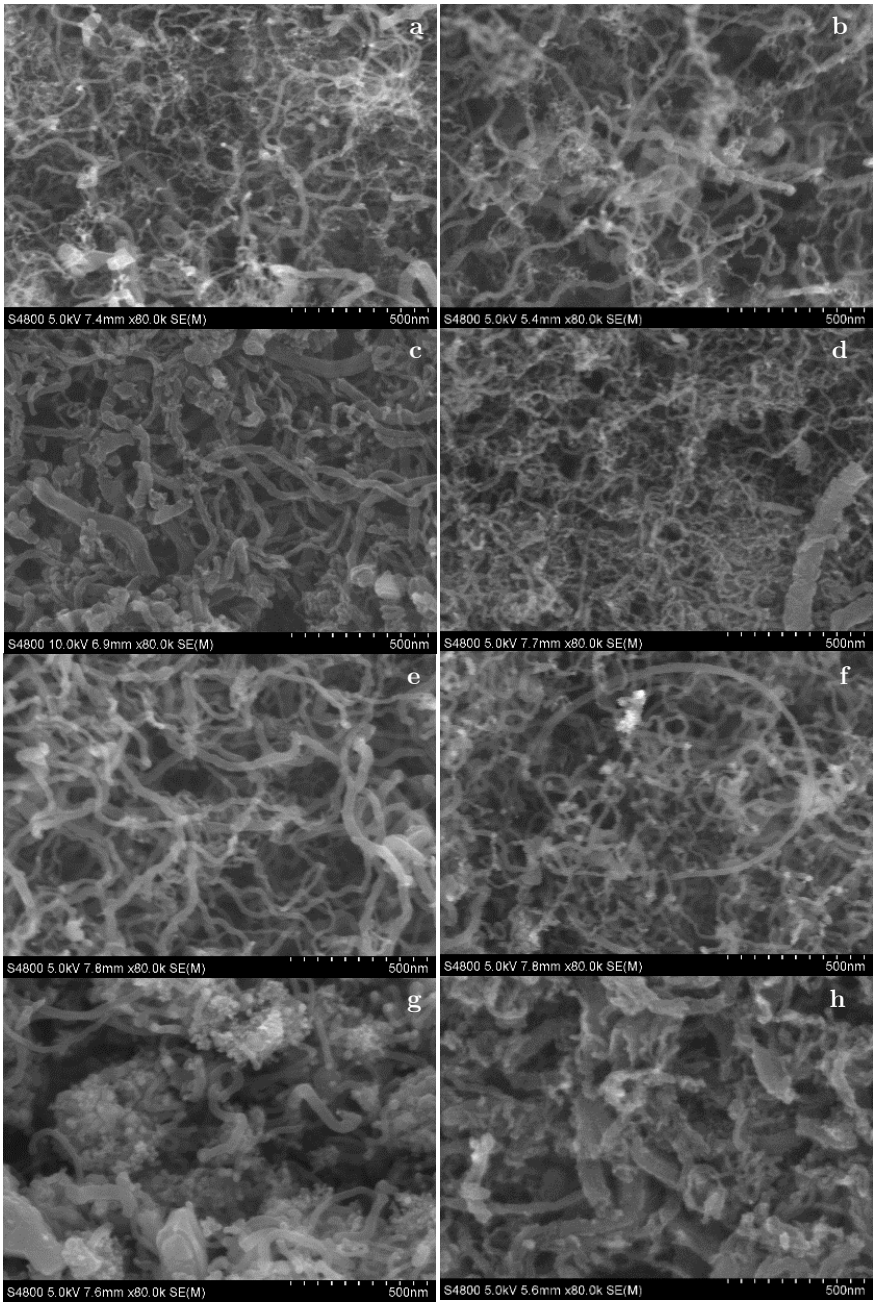

Figure 3.22. SE-SEM images of Ni/Al_2O_3 catalyst samples used in the SR of acetic acid (a), acetaldehyde (b), ethanol (c), acetol (d), acetone (e), catechol (f), guaiacol+ethanol (g) and levoglucosan (h) at 600 °C.

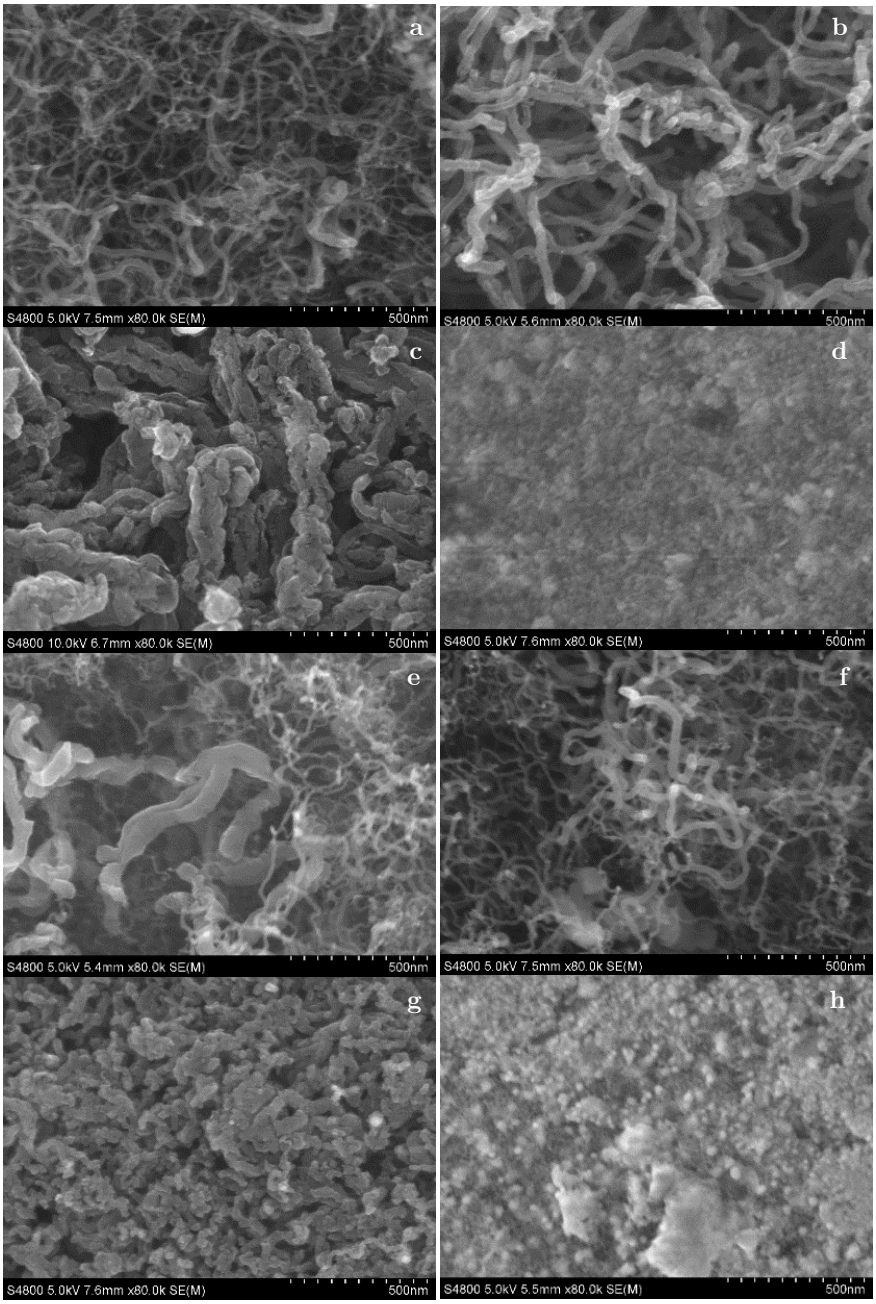

Figure 3.23. SE-SEM images of Ni/Al_2O_3 catalyst samples used in the SR of acetic acid (a), acetaldehyde (b), ethanol (c), acetol (d), acetone (e), catechol (f), guaiacol+ethanol (g) and levoglucosan (h) at 700 °C.

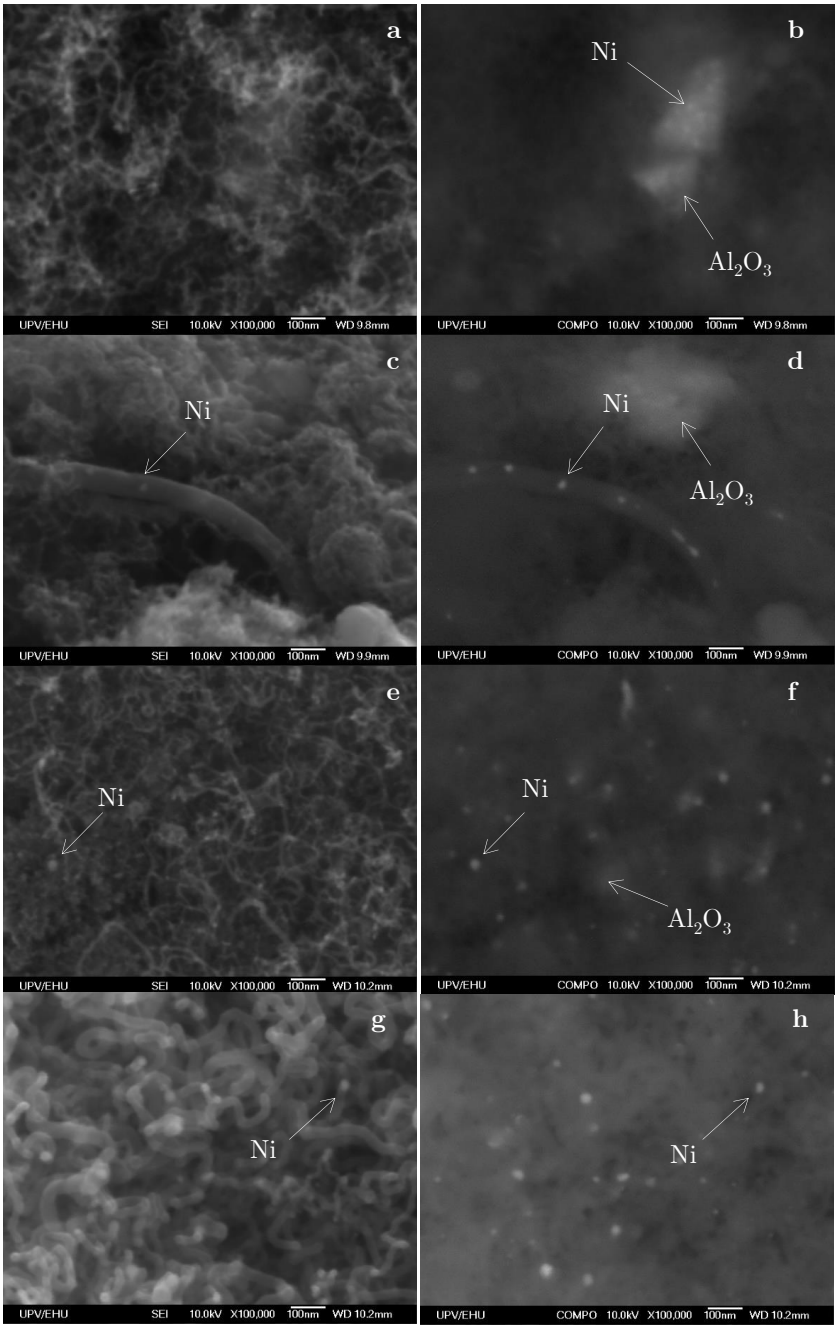

Figure 3.24. SE-SEM (a, c, e, g, i, k) and BSE-SEM (b, d, f, h, j, l) images of Ni/Al_2O_3 catalyst samples used in the SR of acetic acid (a-f) at 600 °C (a-d) and 700 °C (e, f) and guaiacol+ethanol (g-l) at 600 °C (g-j) and 700 °C (k, l).

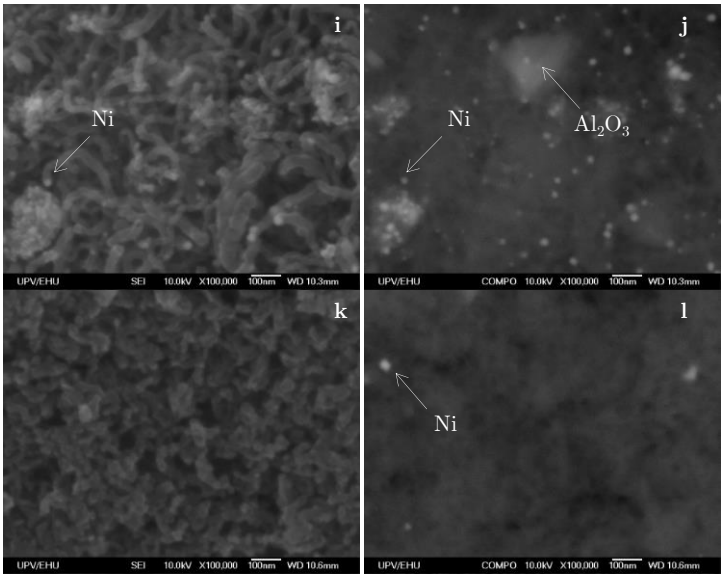

Figure 3.24. Continued.

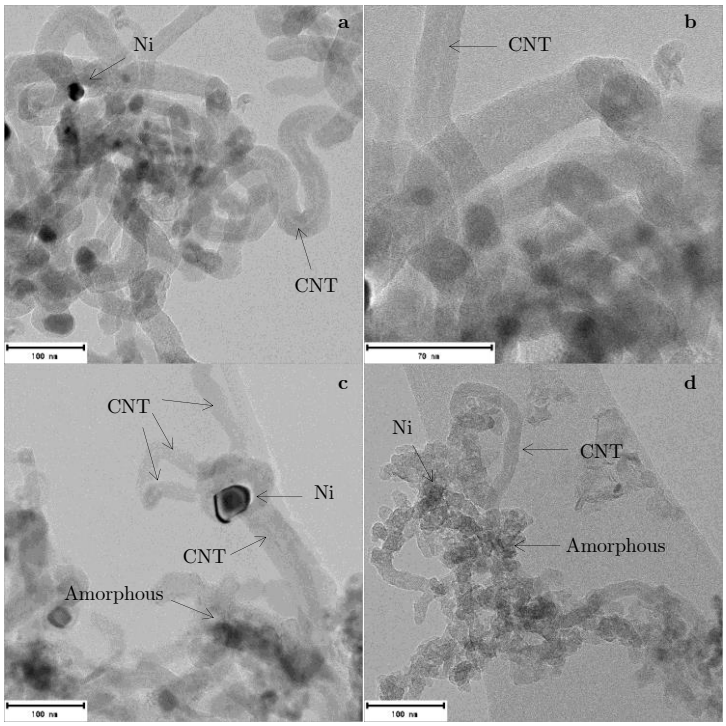

Figure 3.25. TEM images of Ni/Al_2O_3 catalyst samples used in the SR of guaiacol+ethanol at 600 °C (a-c) and 700 °C (d).

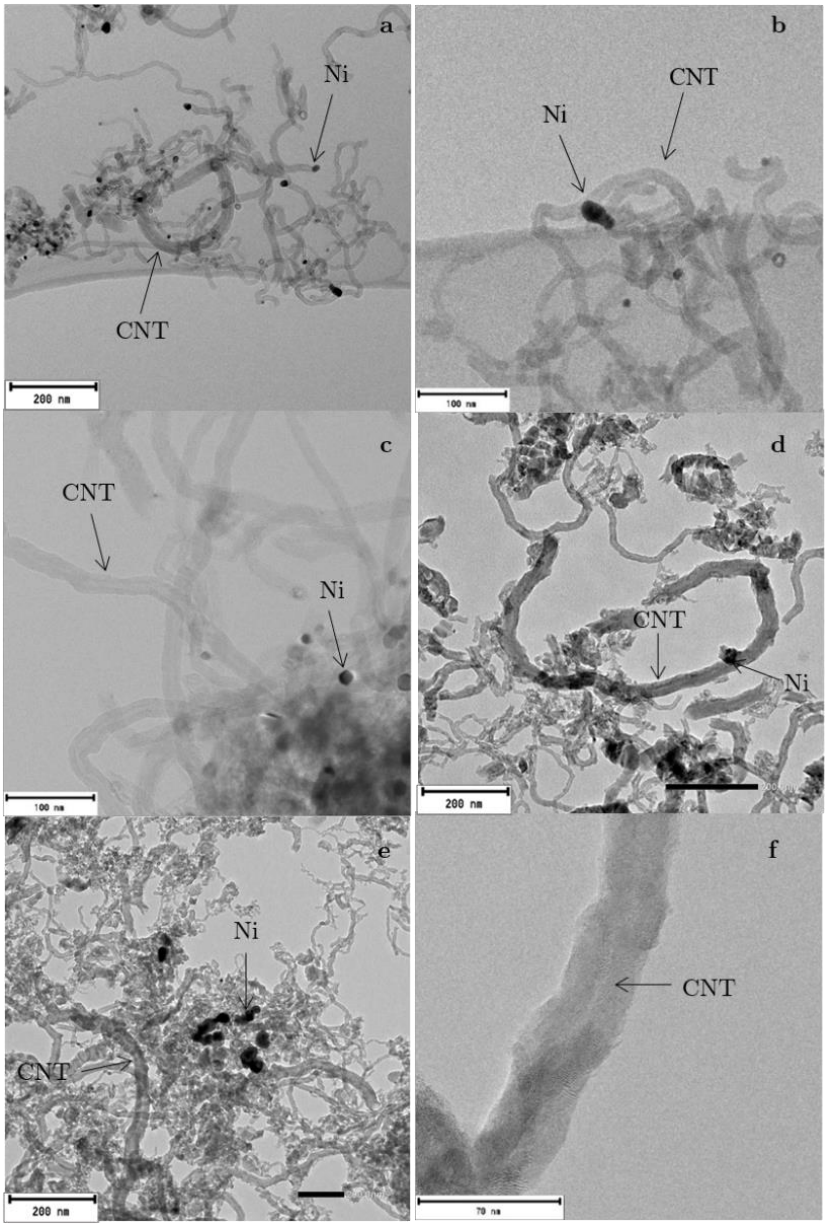

Figure 3.26. TEM images of Ni/Al_2O_3 catalyst samples used in the SR of catechol (a-c) and acetone (d-f) at 600 °C.

3.2.2.5. Structural properties of coke

Figure 3.27 shows the Raman spectra of selected used catalyst samples to further study the structural properties of coke. All the samples show the typical D (corresponding to sp^2 hybridized carbons in aromatic rings, at ~1343 cm^{-1}) and G (corresponding to sp^2 hybridized carbons in aromatic rings and olefins, at ~1589 cm^{-1}) bands as commonly found for various carbon structures, and the corresponding second-order bands in the 2500-3500 cm^{-1} region (Figure B.11) [96, 324, 325]. At 600 °C, the G and D bands have similar features for all the used catalyst samples (SR of ethanol, acetol, guaiacol+ethanol and levoglucosan) with noticeable different intensities for the D band. The intensity ratio between the D and G band (I_D/I_G) determined from deconvolution (procedure described in Annexes and results summarised in Table 3.3) is notoriously higher for the coke formed from the SR of ethanol, and consecutively decreases for the coke corresponding to acetol, levoglucosan and guaiacol+ethanol. At 700 °C, the D and G band features are significantly different. Thus, the coke formed from ethanol has narrow D and G bands, the G band has a shoulder at 1605 cm^{-1} and noticeable higher I_D/I_G ratio. The spectra of the coke formed from levoglucosan present a high noise level, which is coherent with the low coke content determined from the TPO analysis.

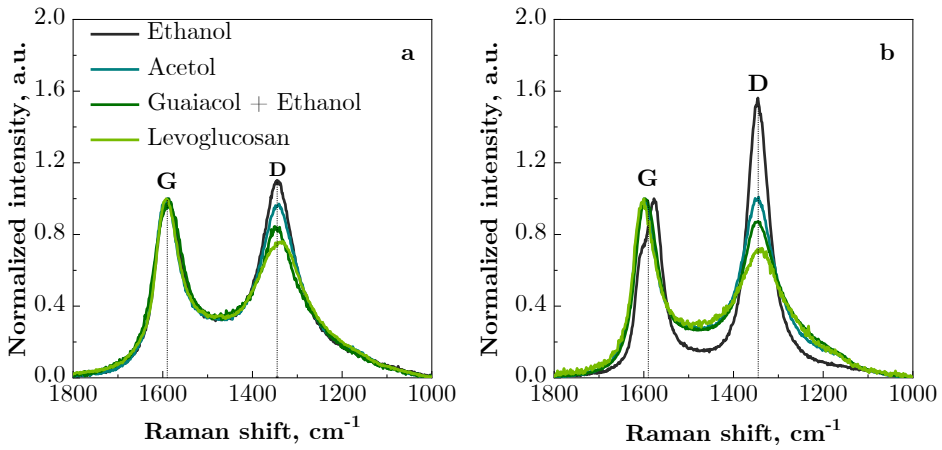

Figure 3.27. Raman spectra of Ni/Al_2O_3 catalyst samples used in the SR of ethanol, acetol, guaiacol+ethanol and levoglucosan at 600 °C (a) and 700 °C (b).

Moreover, the Raman spectra mostly correspond to carbon nanotubes (CNT) with different structural qualities, in coherency with the results of SEM and TEM analyses, which revealed the presence of CNT in the catalyst samples used in the SR of ethanol, acetol, guaiacol+ethanol and levoglucosan at 600 °C and ethanol and guaiacol+ethanol at 700 °C. The spectrum for ethanol at 700 °C is very close to that of MWCNT, exhibiting dominant narrow D and G bands [326–328]. The intensity ratio between the D3 (assigned to amorphous carbon) and G bands (I_{D3}/I_G) (listed in Table 3.3) provides an indicator for measuring the quality of carbon nanotubes [327], indicating that those formed from ethanol at 700 °C would have the highest purity having the lowest I_{D3}/I_G ratio (0.06).

Table 3.3. Raman spectra deconvolution results of the coke deposited on used catalysts.

Catalyst	$FWHM_D$	$FWHM_{D3}$	$FWHM_G$	I_D/I_G	I_{D3}/I_G
E-600	95.0	143	63.0	1.1	0.20
E-700	58.0	65.0	45.0	1.7	0.06
AT-600	110	138	59.0	0.98	0.21
AT-700	95.0	138	53.0	1.0	0.20
G+E-600	96.0	167	75.0	0.71	0.18
G+E-700	97.0	137	56.0	0.81	0.16
L-600	147	142	57.0	0.82	0.21
L-700	138	148	53.0	0.75	0.20

It is also observed that the Raman spectra for the catalyst samples used in the SR of guaiacol+ethanol at 600 and 700 °C is typical of carbon structures with different degree of order [329], which is in agreement with the formation and deposition of a second carbon phase between the filaments. This result is in agreement with the BSE-SEM (Figure 3.21g) and SE-SEM (Figure 3.23g) images discussed above. Based on the I_D/I_G ratio, being higher at 700 °C than at 600 °C, the second carbon phase is predominantly amorphous with ordered domains below 2 nm, but it is more structured at 700 °C, which is consistent with the higher combustion temperature observed in the TPO analysis (Figure 3.16b). This relationship between TPO and Raman spectroscopic analyses has been also

observed for this catalyst sample used in the SR of raw bio-oil [96], evidencing the formation of carbon filaments and amorphous carbon with different degree of order, which indicates an analogy between coke deposition in the SR of guaiacol and raw bio-oil.

3.2.3. Discussion

The deactivation of the catalyst in the SR of oxygenates can be explained by the steps in Figure 3.28, where the nature of the coke is key.

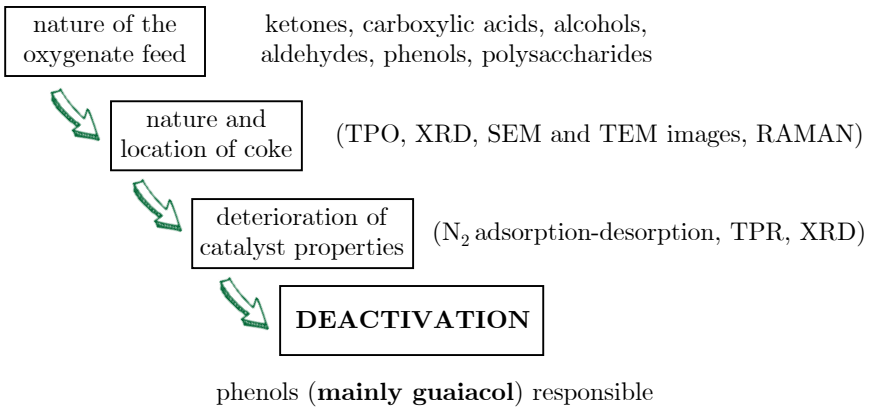

Figure 3.28. Effect of the oxygenate nature on the deactivation of Ni/Al_2O_3 catalyst in the SR of oxygenates.

3.2.3.1. Coke as the main cause of deactivation

The characterization of used catalyst samples (amount and morphology of coke deposits, sections 3.2.2.1, 3.2.2.4 and 3.2.2.5, as well as physical, metallic and textural properties, section 3.2.2.2 and 3.2.2.3) has allowed establishing the deactivation causes of the Ni/Al_2O_3 catalyst derived from $NiAl_2O_4$ spinel in the SR of the different oxygenates. Firstly, Ni oxidation has been ruled out as a deactivation cause, due to the absence of NiO_x diffraction peaks (XRD measurements) in all the used catalyst samples, which is coherent with the highly reducing atmosphere along the SR reactions, and is in agreement with the results reported for the SR of raw bio-oil [96]. Secondly, Ni sintering does not appear to

be a relevant cause of deactivation of this catalyst, since it is not observed a significant increase in the average Ni^0 crystal size, except for SR of levoglucosan, where a slight deactivation is observed (Figure 3.14h). Nevertheless, a similar moderate Ni sintering has been reported in the SR of raw bio-oil at 700 °C with this catalyst [96], which does not explain the rapid deactivation for this reaction. Consequently, the main cause of the rapid deactivation of Ni/Al_2O_3 catalyst in the SR of bio-oil and of the guaiacol+ethanol mixture must be attributed to coke deposition.

3.2.3.2. Relevance of coke nature in deactivation

By relating the results of TPO analysis and SEM images of the used samples (sections 3.2.2.1 and 3.2.2.4) to the deactivation rate of the catalysts, it has become clear that deactivation is directly related to the nature of the coke, in agreement with previous results in literature for different catalysts [142, 145, 255, 260, 267, 268]. Thus, a large amount of filamentous coke is deposited in the SR of most of the pure oxygenates studied (especially at 600 °C), but it does not cause a significant impact on the activity of the catalyst. The increase in S_{BET} (Table 3.2) and the BSE-SEM images (Figure 3.20 and Figure 3.21) for the catalyst samples used in the SR of oxygenates (such as acetic acid, acetaldehyde, ethanol, acetol and acetone) evidences the deposition of a porous and filamentous coke with contents in the catalyst above 20 wt%, which does not hinder the access of reactants to the metal sites in the reaction time studied. However, for a high time on stream, it can create a slight plug on pores or it may grow as clumps of entangled filaments that encapsulate metal particles [255], which can originate a decrease in activity as that observed at high reaction time in the SR of ethanol (Figure 3.14c).

The low values of S_{BET} in the catalyst used in SR of guaiacol+ethanol (only slightly higher than those of the fresh-reduced catalyst) are explained by the formation of both i) filamentous coke that is probably stacked on the surface of the catalyst and causes an increase in BET surface area (with high contribution of ethanol to the formation of this type of coke) and ii) an amorphous carbon

phase between the carbon filaments, probably due to the formation of pyrolytic carbon from guaiacol, which is promoted at high temperature, and that clogs the porous structure and contributes to the rapid deactivation observed for the mixture (guaiacol+ethanol) (Figure 3.14g). This formation of pyrolytic coke by repolymerization of phenols in bio-oil is well established in the literature [164].

According to the literature, the importance of the properties of the catalyst in the nature of the coke should be pointed out. Thus, Zhang et al. [142], observed the prevalent formation of amorphous coke from guaiacol on Ni/Al_2O_3 catalyst, whereas carbon nanotubes are preferentially formed on Ni/SBA-15 catalyst.

3.2.3.3. Role of different oxygenates in deactivation

Due to the filamentous nature of coke, the catalyst stability is high in the SR of non-phenolic oxygenates, (Figure 3.14a-Figure 3.14e), as well as in the SR of catechol (Figure 3.14f) and levoglucosan (Figure 3.14h). Conversely, the catalyst is completely deactivated after 300 min reaction in the SR of the guaiacol+ethanol mixture at both temperatures studied. Taking into account the high stability observed in the SR of ethanol (Figure 3.14c), it can be concluded that guaiacol is the responsible for the rapid catalyst deactivation observed in Figure 3.14g.

The origin of long and heterogeneous carbon filaments in the SR of aliphatic oxygenates (Figure 3.22 and Figure 3.23) can be attributed to the reaction of CO (Boudouard reaction, Eq. (1.21)) and CH_4 decomposition (Eq. (1.20)) [259, 330, 331]. As CH_4 decomposition is favoured above 750 °C, in the conditions of this study the main origin of this coke is probably the exothermic Boudouard reaction, whose extent is favoured at lower temperature. Moreover, in the SR of ethanol at 600 °C with the same catalyst, the contribution to the formation of filamentous coke by the route of dehydration to ethylene over the acid sites of the Al_2O_3 support followed by the ethylene decomposition on the $Ni\text{-}Al_2O_3$ interface has been proved [132]. Also, acetone is an important precursor of filamentous coke [103, 111], which can explain the higher amount of coke deposited in the SR of acetone than in the SR of acetic acid, acetaldehyde or acetol.

The formation of filamentous coke is also significant in the SR of the phenolic compounds, as revealed by SEM images (Figure 3.22f, Figure 3.22g, Figure 3.23f and Figure 3.23g) and the high combustion peak located at high temperature in the TPO profiles (Figure 3.16). But differently to the SR of aliphatic oxygenates, the presence of a small coke fraction burning at low temperature (amorphous and encapsulating coke) is observed in the SR at 600 °C of catechol and more notoriously in the SR of the guaiacol+ethanol mixture (Figure 3.16a). For this latter feed, the formation of this amorphous carbon phase could explain the lower amount of filamentous coke deposited at this temperature (Figure 3.22g) compared to the SR of ethanol (Figure 3.22c). Thus, the formation of encapsulating coke on metal sites hinders the mechanisms of filamentous coke formation, which requires diffusion of C species through Ni metal particles, their precipitation on the base of the Ni crystallite and the formation of a carbon filament growing in size [259, 332].

3.2.3.4. Effect of temperature

The difference in the results of coke amount at 600 and 700 °C can be explained by the effect of temperature on the reactions involved in their formation (mainly Boudouard reaction, Eq. (1.21) and polymerization reactions) and their elimination (gasification reaction, Eq. (1.22)). Thus, the polymerization and gasification reactions are favoured with the increase in temperature, whereas the Boudouard reaction is disfavoured. Consequently, the increase in the reaction rate of gasification and the lower extent of Boudouard reaction explain the sharp reduction of coke amount on the catalyst observed in the SR of aliphatic oxygenates at 700 °C [333]. Nevertheless, in the SR of phenolic oxygenates the coke amount is higher at 700 °C, especially for the guaiacol+ethanol mixture, because guaiacol polymerization (with pyrolytic carbon formation, Figure 3.23g) is favoured to a greater extent than gasification. A similar result was previously reported for other heavy oxygenates like glucose and m-xylene [103, 311].

This effect of temperature on coke formation is very important in the reforming of levoglucosan, where the coke amount is 16.7 wt% at 600 °C and 0.5 wt% at

700 °C. Considering the ease of cracking of this oxygenate [334], it can be understood that the increase in the cracking rate favours the SR of the intermediates to a greater extent than their polymerization, which explains the low coke deposition.

3.2.3.5. Comparison with deactivation in the SR of raw bio-oil

In a previous study of the deactivation of the same $NiAl_2O_4$ spinel derived catalyst in the SR of raw bio-oil [96] was found that the coke is mainly constituted of short and heterogeneous filaments, representing much lower amounts than those formed in this Thesis from aliphatic oxygenates, being remarkable the presence of amorphous and encapsulating coke. Based on the results of the present Thesis, the formation of this coke may be attributed to the high content of guaiacols and catechols and heavier phenolic compounds in raw bio-oil, whose polymerization significantly inhibits the mechanisms of formation of abundant and long carbon filaments on the catalyst surface from aliphatic oxygenates present in bio-oil.

Consequently, the phenolic compounds have a relevant role in the deactivation of $NiAl_2O_4$ derived catalyst during the SR of raw bio-oil. Nevertheless, the decrease in carbon conversion [96] is faster than that observed in the SR of the guaiacol+ethanol mixture (Figure 3.14g), which evidences the significant contribution of other compounds in bio-oil, most probably heavier phenolic compounds, to the deactivation of the catalyst. Moreover, a synergistic effect of the presence of different compounds in bio-oil (with different functionalities) could also contribute to a more rapid deactivation in the SR of bio-oil than in the SR of each pure oxygenated compound.

Chapter 4

SORPTION ENHANCED STEAM REFORMING (SESR) OF RAW BIO-OIL

In this Chapter, the SESR of raw bio-oil is studied from three perspectives. Firstly, the effect of sorbent type (dolomite or CaO/mayenite), catalyst type (Ni/Al_2O_3 obtained by reduction of a $NiAl_2O_4$ spinel or Ni/CeO_2 prepared by wet-impregnation) and sorbent/catalyst mass ratio (0, 4, 10 and 20) is analysed in a packed-bed reactor. Secondly, the behaviour of packed-bed and fluidized-bed reactors with $NiAl_2O_4$ spinel derived catalyst and dolomite as sorbent is compared. Finally, the effect of operating conditions (temperature, space time, sorbent/catalyst mass ratio, time on stream) on the performance of the ($NiAl_2O_4$ spinel derived catalyst)/dolomite system and the reproducibility of operating in reaction-regeneration cycles are studied.

Part of the results in this Chapter have been published in *Chem. Eng. Trans.* 2022, 92, 241-246, *Fuel Process. Technol.* 2023, 247, 107799 and *Chem. Eng. J.* 2023, 458, 141494.

4.1. EFFECT OF SORBENT TYPE, CATALYST SUPPORT AND SORBENT/CATALYST MASS RATIO

In this section, the SESR of raw bio-oil has been studied with two sorbents (dolomite or CaO/mayenite, denoted Ca-M hereafter) and two Ni-based catalysts (Ni/Al_2O_3 obtained by reduction of a $NiAl_2O_4$ spinel or Ni/CeO_2 prepared by wet impregnation) with different sorbent/catalyst mass ratios in order to select the most suitable sorbent/catalyst pair and the optimum amount of sorbent and catalyst for maximising the H_2 yield and catalyst stability. For that purpose, firstly, the effect of the sorbent type has been analysed using Ni/Al_2O_3 catalyst. Secondly, the effect of the type of Ni-based catalyst was analysed comparing the performance of Ni/Al_2O_3 (25 wt% of Ni) and Ni/CeO_2 (10 wt% of Ni) catalysts and using the sorbent selected in the previous task. A packed-bed reactor was used in the following conditions: 600 °C; S/C ratio of 3.4 (~ 2 times the stoichiometric value); time on stream, 5 h and space-time, 0.15 $g_{catalyst}·h/g_{oxygenates}$ in the runs with Ni/Al_2O_3 catalyst. Since the two catalysts have different Ni contents (due to the different configuration (bulk and supported) and the different preparation method, optimised for each them), the runs with Ni/CeO_2 catalyst were carried out with both the same total mass of catalyst as in the Ni/Al_2O_3 runs (0.5 g, corresponding to a space time of 0.15 $g_{catalyst}·h/g_{oxygenates}$) and the same total mass of Ni in the bed (0.125 g Ni, corresponding to a space time of 0.37 $g_{catalyst}·h/g_{oxygenates}$). The sorbent/catalyst mass ratio (SC_{MR}) was 10 and 20 for Ni/Al_2O_3 catalyst and 4, 10 and 20 for Ni/CeO_2 catalyst. The experiment with a SC_{MR} of 4 corresponds to 0.37 $g_{catalyst}·h/g_{oxygenates}$ (1.25 g of catalyst and 5 g of sorbent). The lower SC_{MR} for both catalysts corresponds to the same sorbent/Ni mass ratio of 40.

4.1.1. Conversion and products yields

4.1.1.1. Ni/Al_2O_3 catalyst. Comparison of the sorbent type

In order to analyse the effect of using dolomite or Ca-M as in-situ sorbent in the reforming of raw bio-oil with Ni/Al_2O_3 catalyst, the results obtained in the SESR

runs have been compared with the SR run ($SC_{MR} = 0$) under the same conditions. Figure 4.1 shows the product yield distribution at the beginning of the reaction runs (CO_2 capture or pre-saturation period in the SESR runs). The results in this figure evidence that the presence of a sorbent significantly modifies the product distribution and that both sorbents have different role in the SESR run. Therefore, in the absence of sorbent (SR conditions), at the beginning of the reaction there is almost complete bio-oil conversion and high H_2 and CO_2 yield, close to the thermodynamic equilibrium [313], with a yield of CO approximately of 18 %, yield of CH_4 of ~ 4 % and null formation of C_aH_b.

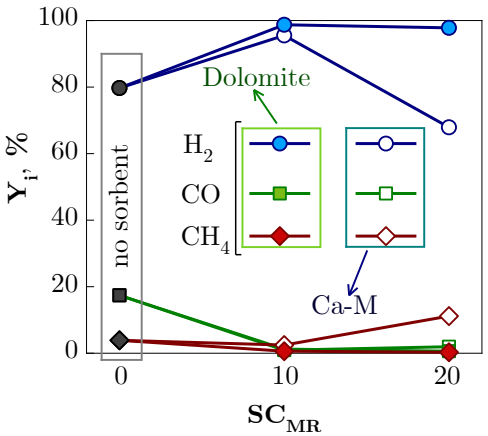

Figure 4.1. Effect of the SC_{MR} ratio in the product yield distribution (H_2, CO and CH_4) in the CO_2 capture period using dolomite or Ca-M as sorbent in the SESR runs with Ni/Al_2O_3 catalyst at 600 °C and space time of 0.15 $g_{catalyst}·h/g_{oxygenates}$. Black markers: SR condition (without sorbent).

The use of a sorbent in-situ in the reaction bed (SESR run), involves an increase in H_2 yield to almost 100 %, and a decrease in CO and CH_4 yield to almost negligible values, since the carbonation reaction (Eq. (1.24)) shifts the equilibrium of WGS (Eq. (1.15)) and methane SR (Eq. (1.17)) reactions. This situation is observed with dolomite as a sorbent at both sorbent/catalyst ratios studied. However, with Ca-M sorbent, the higher sorbent/catalyst mass ratio studied (SC_{MR} of 20) leads to a lower H_2 yield and higher CH_4 yield compared to the SR

run. This result suggests a noticeable promotion of oxygenates decomposition/cracking reactions (Eq. (1.16)) caused by Ca-M sorbent.

The higher activity for the decomposition/cracking reactions of the Ca-M sorbent with respect to dolomite can be seen in Figure 4.2, which shows the conversion and yield of products obtained in the SR run without catalyst or sorbent (thermal run, Figure 4.2a), with dolomite sorbent (Figure 4.2b) and with Ca-M sorbent (Figure 4.2c). As observed, at the beginning of the reaction (CO_2 capture period for both sorbents), the yield of C_aH_b and CH_4 (especially the latter) is higher with Ca-M sorbent (Figure 4.2c) than with dolomite (Figure 4.2b).

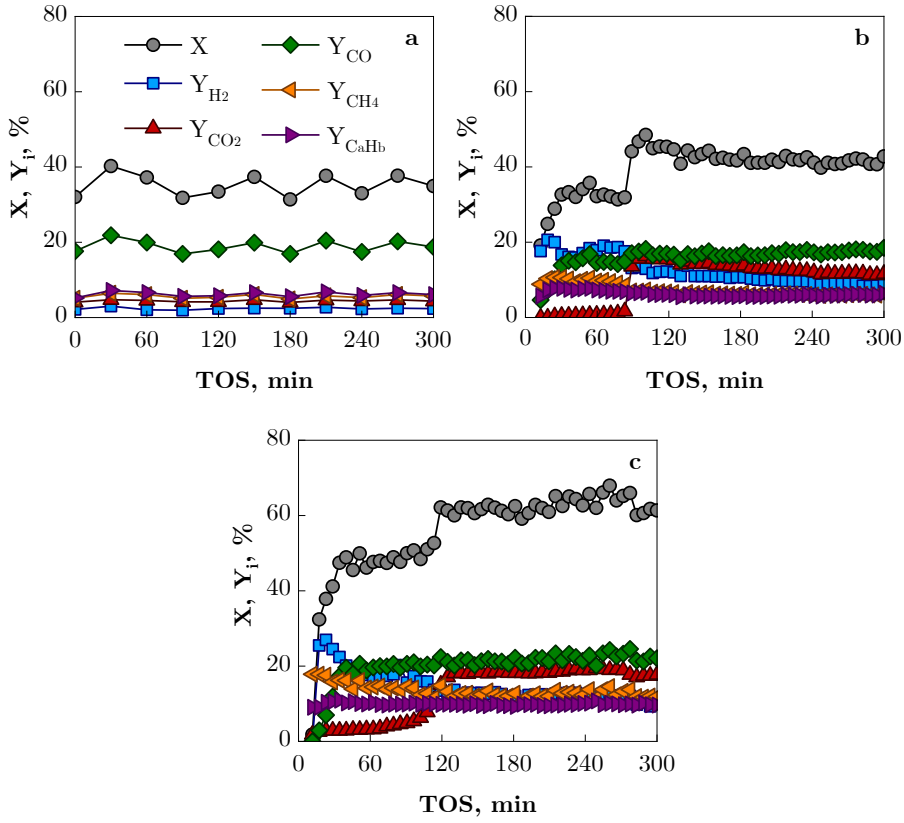

Figure 4.2. Evolution with TOS of the conversion and products yields in a blank experiment (absence of catalyst nor sorbent, thermal effect) (a) and in runs with 5 g of sorbent (dolomite (b) and Ca-M (c)) at 600 °C.

The evolution of conversion and yield of products (H_2, CO_2, CO, CH_4 and C_aH_b) with TOS under the conditions of Figure 4.1 are depicted in Figure 4.3, both in the pre-saturation (insignificant yield of CO_2) and post-saturation periods. The evolution with TOS of the reaction indices in this figure shows that in the SR run (black markers), the conversion and products yield remain almost constant during 2 h, and subsequently, the conversion (Figure 4.3a) and the yields of H_2 and CO_2 (Figure 4.3b and Figure 4.3c, respectively) decrease, the yield of C_aH_b increases (Figure 4.3f) and the yields of CO and CH_4 (Figure 4.3d and Figure 4.3e, respectively) remain almost constant. These evolutions with TOS of products yields give evidence of the deactivation of the catalyst for the reforming and WGS reactions, and are consistent with the reaction mechanism of the SR of bio-oil over Ni catalysts that has been explained elsewhere [96, 335].

In the SESR runs (green and blue markers in Figure 4.3), three regions are observed: pre-breakthrough (CO_2 capture), breakthrough (dolomite saturation) and post-breakthrough. In the capture period, the higher H_2 yield and the lower yields of CO and CH_4 compared to the SR run (black markers) are explained by the shift of the WGS reaction equilibrium by CO_2 capture (Eq. (1.15)) and, as a consequence, the shift of the CH_4 SR reaction equilibrium (Eq. (1.17)). In this period the H_2 yield remains constant for both SC_{MR} studied with dolomite, and for SC_{MR} of 10 with Ca-M sorbent. The duration of the capture-period is slightly longer for the Ca-M sorbent, due to the higher CO_2 capture capacity of this sorbent (around 48 wt%) compared to dolomite (around 41 wt%), in coherence with its higher CaO content (69 wt%) over that of dolomite (61 wt%). The breakthrough period involves the depletion of the carbonation reaction efficiency and therefore, a sudden increase in the yield of CO_2 (Figure 4.3c) and a decrease in the yield of H_2 (Figure 4.3b) is observed. In the post-breakthrough period, after sorbent saturation, CO_2 removal is no longer effective and SR and WGS reactions occur together with other secondary reactions responsible for coke formation. Consequently, during this period the reaction indices evolve with TOS due to the catalyst and sorbent deactivation.

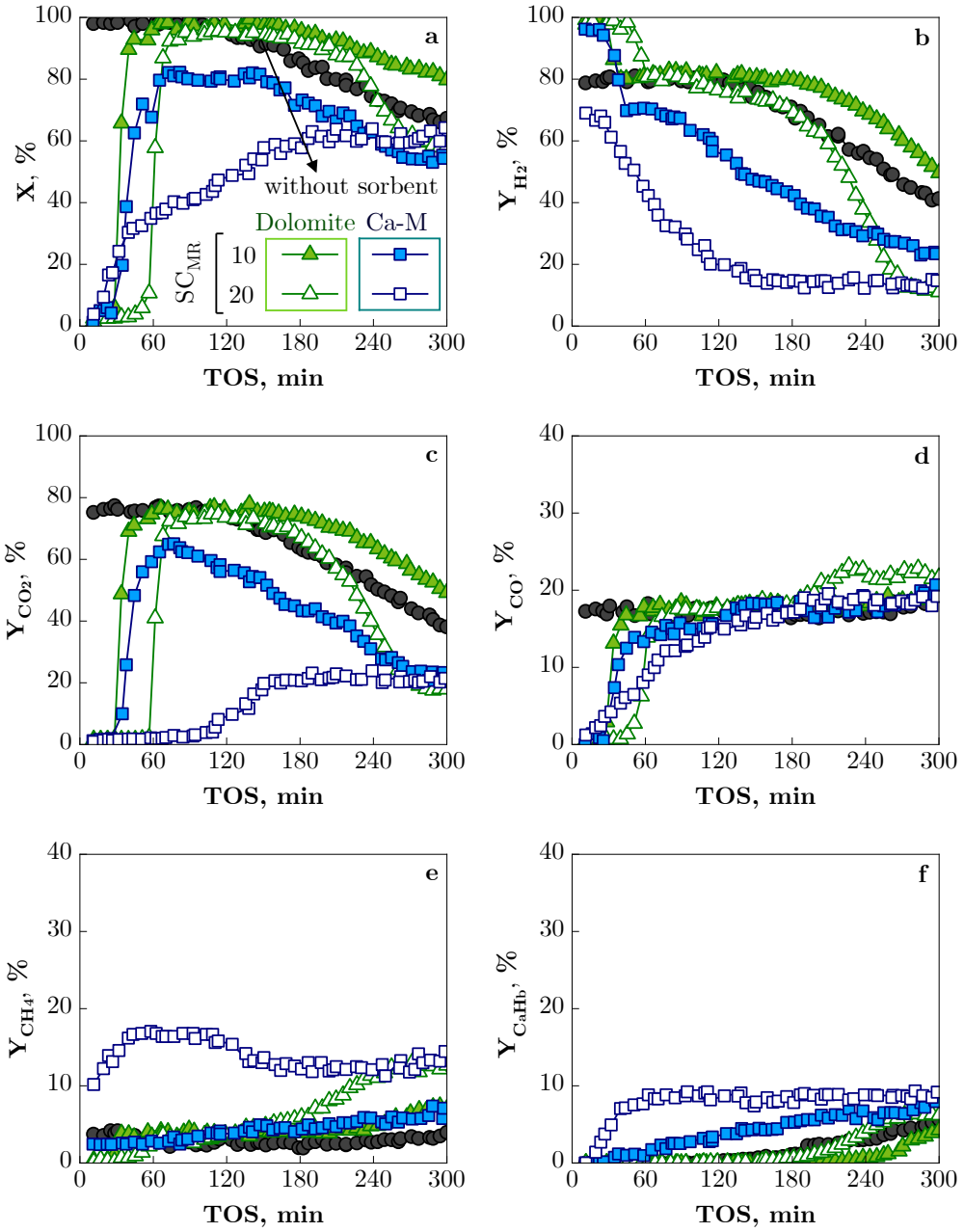

Figure 4.3. Effect of sorbent (dolomite (green triangles) or Ca-M (blue squares)) on the evolution with TOS of conversion (a) and yields of H_2 (b), CO_2 (c), CO (d), CH_4 (e) and C_aH_b (f) in the SESR run with Ni/Al_2O_3 catalyst, for values of SC_{MR} of 10 (full markers) and 20 (empty markers). Space time, 0.15 $g_{catalyst}{\cdot}h/g_{oxygenates}$. Black circles: SR run (without sorbent).

In the post-breakthrough period, conversion and H_2 and CO_2 yields (Figure 4.3a-Figure 4.3c, respectively) show decreasing trend, which is faster with Ca-M and at high sorbent/catalyst mass ratios. Thus, for a Ca-M/catalyst ratio of 20 (with the same mass of catalyst and twice the sorbent amount than with a SC_{MR} of 10) the decrease in H_2 yield is observable even in the CO_2 capture period. The faster deactivation and lower extent of reforming reactions in the SESR run with Ca-M sorbent and SC_{MR} of 20, entail less CO_2 formation than using dolomite as sorbent under the same conditions, which explains the significantly longer duration of the CO_2 capture period for Ca-M sorbent in Figure 4.3. Interestingly, the use of dolomite with a low sorbent/catalyst ratio allows for a more stable operation than in the SR run, but it leads to a faster deactivation for a high sorbent/catalyst ratio.

The aforementioned results evidence that the competition of oxygenates decomposition/cracking reactions over the sorbent with those of reforming and WGS reactions over the catalyst conditions the selection of the sorbent and of the sorbent/catalyst ratio to be used in the SESR run. Thus, dolomite has a superior performance as a CO_2-sorbent in the SESR of raw bio-oil than Ca-M due to its lower activity for decomposition/cracking of oxygenates (Figure 4.2), which allows using a higher SC_{MR} in the catalytic bed (which leads to a longer duration of the complete CO_2 capture period with near 100 % H_2 yield) and with higher stability. Furthermore, it has been verified by carbonation-decarbonation cycles in thermobalance (Figure 4.4) that the dolomite used in this work has a higher stability for CO_2 capture in successive reaction-regeneration cycles than the prepared Ca-M sorbent, indicating a better performance of the former in the cyclic operation in the SESR of bio-oil.

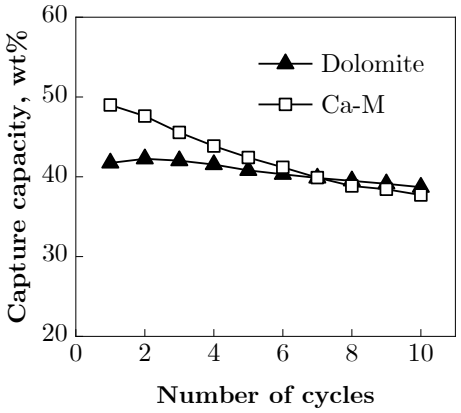

Figure 4.4. Evolution of CO_2 capture capacity of dolomite and Ca-M in successive carbonation-decarbonation cycles in thermobalance.

The values of yield and selectivity of H_2 obtained in this work in the SESR of raw bio-oil with dolomite+Ni/Al_2O_3 system are equal to or surpass results in the literature concerning the SESR of bio-oil or pure oxygenates with different sorbents and catalysts, or with sorbent-catalyst bifunctional materials. Thus, Remiro et al. [204] reported near 99 % H_2 yield in the SESR of aqueous bio-oil with Ni/La_2O_3-αAl_2O_3 catalyst and dolomite as sorbent at 600 °C, S/C ratio of 12 and with a sorbent/catalyst ratio < 6. Xie et al. [203] reported lower H_2 yield and concentration (over 85 % and 90 %, respectively) in the SESR of bio-oil from corn cob (near 44 wt% water content) with Ce-Ni/Co supported on the Al_2O_3 as the catalyst and CaO powder as the sorbent in the 750-800 °C range at S/C ratio of 12. With a Ni/CeO_2-ZrO_2-CaO bifunctional material (15 % Ni and Ce:Zr:Ca of 1.2:1:5), Li et al. [192] reported a maximum H_2 yield of 77.8 % in the SESR of poplar sawdust pyrolysis oil, at 550 °C (with S/C ratio of 4 and LHSV of 0.48 ml/g·h), although its performance was excellent in the SESR of acetic acid under the same conditions, with a purity of H_2 up to 98.5 % and H_2 yield of 83.7 % and acetic acid conversion above 93 %. A lower purity of H_2 (near 70 % at 650 °C and S/C ratio of 3) was reported by Wang et al. [20] in the SESR of phenol with Ni/CaO–$Ca_{12}Al_{14}O_{33}$ catalytic sorbents (with 9 wt% Ni and CaO/$Ca_{12}Al_{14}O_{33}$ ratio of 3), but it improved to 83.2 % for the bimetallic catalyst Ni-Co/CaO–$Ca_{12}Al_{14}O_{33}$. In the SESR of acetic acid, acetone or their blends over a Pd/Ni–Co

hydrotalcite-like material catalyst and dolomite as CO_2 sorbent, Esteban-Diez et al. [196] achieved H_2 purities of 99.2–99.4 % at 575 °C and atmospheric pressure and H_2 yields that were lower in the SESR of the blends (83.3–88.6 %) compared to the individual model compounds (90.2–95.9 %). Moreover, the H_2 yield values were significantly affected by the increase in the WHSV. These lower H_2 yield values, in spite of H_2 selectivity of almost 100 %, could be explained by an incomplete feed conversion and, moreover, it could be presumable due to a high yield of solid carbon (coke deposited over the catalyst), although this aspect was not usually approached in the SESR studies. In a previous section of Chapter 3 (section 3.2), a high deposition of coke deposits in the form of carbon nanotubes, formed by Boudouard reaction, was demonstrated in the SR of acetone and acetic acid over a $NiAl_2O_4$ spinel-derived catalyst at 600 °C, resulting in a significant decrease in the H_2 yield.

4.1.1.2. Ni/CeO_2 catalyst

The SESR runs with Ni/CeO_2 catalyst were carried out with dolomite as sorbent, (selected in section 4.1.1.1) and the results have been compared to those obtained with Ni/Al_2O_3+dolomite. Figure 4.5 shows the yields of products (H_2, CO, CH_4 and C_aH_b) in the pre-saturation period with SC_{MR} of 10 and 20 for a space time of 0.15 $g_{catalyst}{\cdot}h/g_{oxygenates}$ (full coloured markers) and SC_{MR} of 4 for 0.37 $g_{catalyst}{\cdot}h/g_{oxygenates}$ (empty markers). These latter conditions correspond to the same sorbent mass (5 g) and Ni content in the catalytic bed (0.125 g Ni) (equal sorbent/Ni mass ratio) than that used in the run with Ni/Al_2O_3+dolomite and SC_{MR} of 10 (section 4.1.1.1).

The comparison of the results at zero TOS with Ni/Al_2O_3 and Ni/CeO_2 catalysts in the SR conditions (absence of sorbent, black markers in Figure 4.1 and Figure 4.5) shows that the former leads to higher H_2 yield and lower yields of CO and CH_4 than the latter, which suggests a higher promotion of the reforming reactions (of oxygenates and also of CH_4 and C_aH_b) and WGS reaction. The high activity and stability of Ni/Al_2O_3 catalyst derived from $NiAl_2O_4$ spinel for CH_4 reforming is well established in the literature [336]. Also, the high yield of CH_4 with Ni/CeO_2

catalyst could be due to the promotion of methanation reactions, as proposed by Sun et al. [337]. According to these authors, the CO_2 is reduced to CO over oxygen vacancies on CeO_2, and subsequently CO desorbs and diffuses to Ni sites where hydrogenation to CH_4 occurs. The high methanation activity of Ni/CeO_2 catalyst is verified by Hongmanorom et al. [338], who emphasize the ability of Ni dispersed in CeO_2 to facilitate H_2 dissociation and the generation of *H and *HCO intermediates to form CH_4 species.

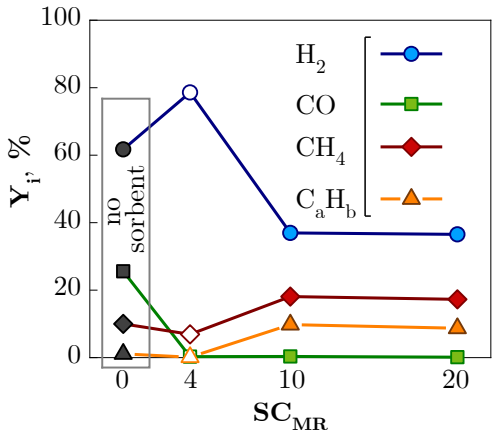

Figure 4.5. Effect of SC_{MR} in the product yield distribution (H_2, CO, CH_4 and C_aH_b) in the CO_2 capture period in the SESR runs with Ni/CeO_2 catalyst using dolomite as sorbent. Space time, 0.15 $g_{catalyst}{\cdot}h/g_{oxygenates}$ (full markers) or 0.37 $g_{catalyst}{\cdot}h/g_{oxygenates}$ (empty markers). Black markers: SR condition (without sorbent).

Moreover, differently to Ni/Al_2O_3 catalyst (Figure 4.1), the use of dolomite with Ni/CeO_2 catalyst for a space time of 0.15 $g_{catalyst}{\cdot}h/g_{oxygenates}$ (full coloured markers in Figure 4.5) does not boost the values of H_2 yield and selectivity during the CO_2 capture period over those corresponding to SR condition (black markers). Thus, the H_2 yield is significantly lower compared to SR run, whereas those of CH_4 and C_aH_b are higher. It should be noted that the difference in H_2 yield compared to SR conditions observed in Figure 4.5 for SC_{MR} of 4 (empty markers) is partially due to the higher space time (0.37 $g_{catalyst}{\cdot}h/g_{oxygenates}$) used in SESR run compared to the SR run (0.15 $g_{catalyst}{\cdot}h/g_{oxygenates}$). The insignificant amount of CO obtained in the CO_2 capture period in the SESR runs is due to aforementioned shift of the

WGS reaction (Eq. (1.15)) caused by the removal of CO_2 from the reaction medium by the carbonation reaction (Eq. (1.24)).

The evolution with TOS of conversion and yield of H_2, CO_2, CO, CH_4 and C_aH_b for SC_{MR} of 4 and 10 are depicted in Figure 4.6 (red-orange markers), together with the results of the SR run (black markers). For a better comparison of the results with both catalysts under comparable SESR conditions, the results of the reaction with Ni/Al_2O_3+dolomite (green markers) are also included in this figure. The evolution with TOS of conversion and products yield in the SESR with Ni/CeO_2+dolomite for SC_{MR} of 20 is depicted in Figure 4.7.

The high catalyst stability observed in the SESR run with SC_{MR} of 4 (orange empty markers in Figure 4.6), should be attributed to the higher value of space time (more than twice) compared to the SR and SESR runs with SC_{MR} of 10. It is well established in the literature [96, 164] that, in bio-oil SR, deactivation is related to the concentration of oxygenates, which is higher with decreasing space time, as a consequence of the lower extent of SR reaction. Under high space time conditions, the H_2 yield (Figure 4.6b) remains constant in the CO_2 capture period and after the saturation of dolomite the yields of H_2 and CO_2 decrease slowly with TOS during the following 2 h on stream and, afterwards a rapid catalyst deactivation occurs, although slower than in the SR run with low space time value. Comparing the results for a SC_{MR} of 10 (red markers in Figure 4.6) with those for a SC_{MR} of 20 (Figure 4.7), a fairly similar performance is observed, although the duration of the capture period is double with twice the sorbent mass (SC_{MR} of 20). Comparing these results with those obtained with Ni/Al_2O_3 catalyst with the equal sorbent and Ni amount in the catalytic bed (green markers in Figure 4.6), it is observed that the H_2 yield in the CO_2 capture period is lower with Ni/CeO_2 and, moreover, once the sorbent is saturated, the stability period is shorter and the subsequent decrease in H_2 yield with TOS is faster than with Ni/Al_2O_3 catalyst.

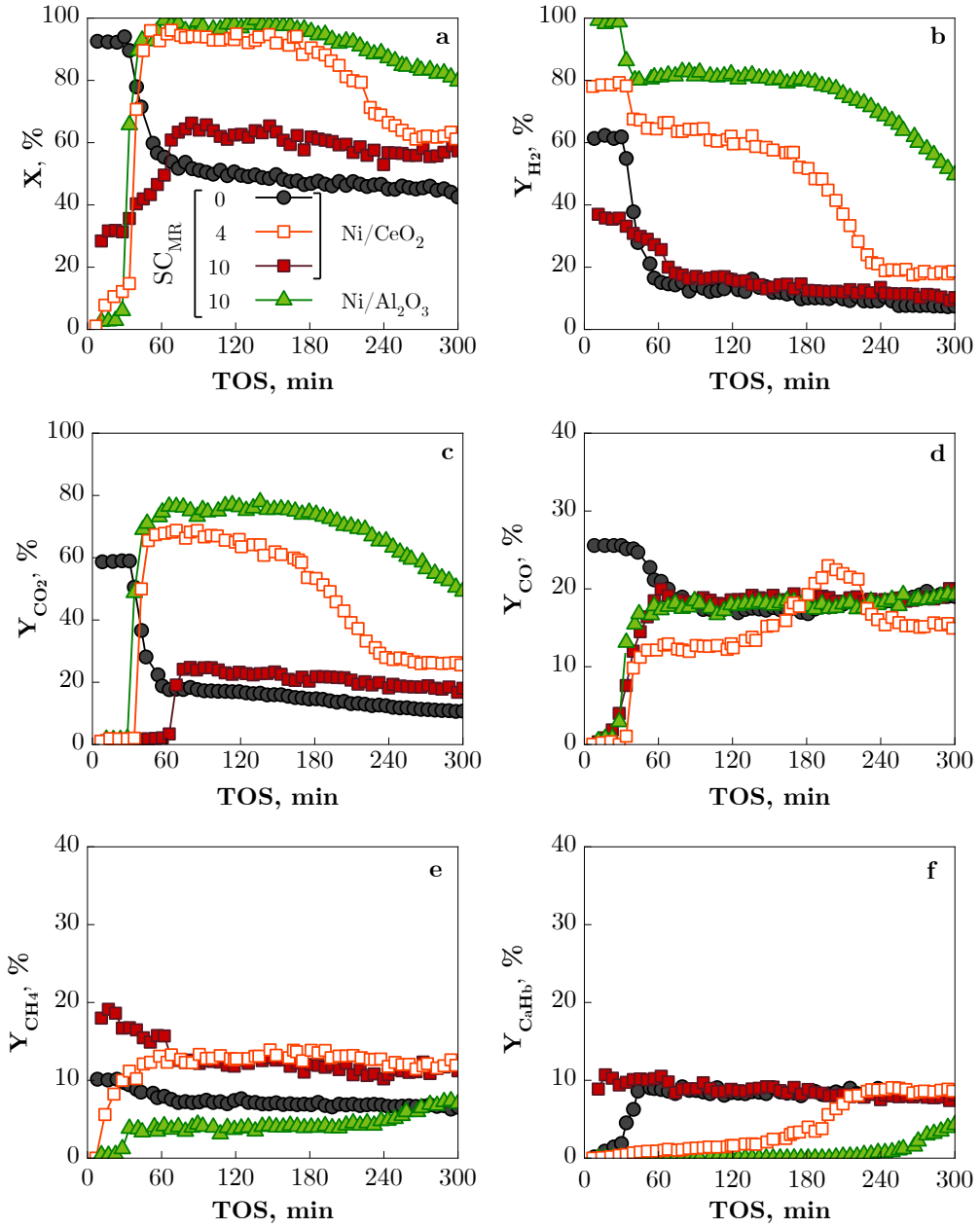

Figure 4.6. Evolution with TOS of conversion (a) and yields of H_2 (b), CO_2 (c), CO (d), CH_4 (e) and C_aH_b (f) in the SR run with Ni/CeO_2 (black markers) and SESR runs using dolomite with Ni/CeO_2 (red-orange markers) or Ni/Al_2O_3 (green markers) catalysts, for SC_{MR} of 4 (empty markers) and 10 (full markers). Space time ($g_{catalyst}$·h/$g_{oxygenates}$), 0.15 (full markers) and 0.37 (empty markers).

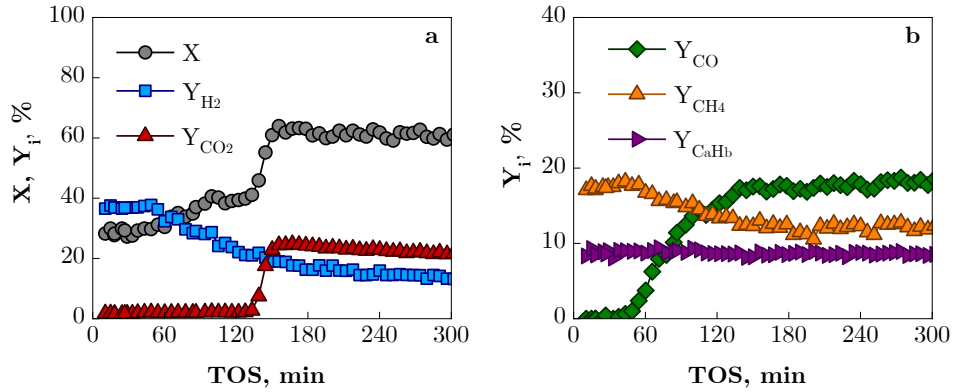

Figure 4.7. Evolution with TOS of conversion and yields of H_2 and CO_2 (a) and of the carbon by-products (CO, CH_4 and C_2-C_3 hydrocarbons (C_aH_b)) in the SESR run with Ni/CeO_2 catalyst using dolomite as sorbent. Sorbent/catalyst mass ratio, 20; space time, 0.15 $g_{catalyst}$ $h/g_{oxygenates}$.

The comparison of the results with Ni/CeO_2 and Ni/Al_2O_3 catalysts shows the superior performance of the latter in both the SR and SESR of bio-oil with dolomite as a sorbent, which is due to its higher activity for reforming reactions (of oxygenates and also of CH_4 and light hydrocarbons (C_aH_b)) and WGS reaction, whereas methanation reaction is more promoted by Ni/CeO_2 catalyst [337]. This better behaviour of Ni/Al_2O_3 catalyst in the SR run is probably due to a stronger metal-support interaction (favoured by the acidity of the Al_2O_3 support), which has a positive effect on its activity for reforming reactions [316, 339, 340]. The higher activity of Ni/Al_2O_3 catalyst for reforming reactions counteracts the catalytic activity of dolomite for decomposition/cracking reaction, allowing a higher H_2 yield (almost 100 %) in the CO_2 capture period than with Ni/CeO_2 catalyst, and with a significantly higher SC_{MR}, which implies a longer duration of the effective CO_2 capture.

4.1.2. Characterization of used catalysts and sorbents

In order to ascertain the causes of the different stability observed in the SR and SESR runs with both catalysts and sorbents, the used samples were characterized by several techniques and compared to those of the fresh-reduced catalysts and calcined sorbents. After each reaction, the three components of the catalytic bed (catalyst/sorbent/inert solid) were separated by sieving, using sieves of different mesh sizes for each catalyst/sorbent combination, depending on the particle size of the three components of the catalytic bed

4.1.2.1. Results of TPO analysis

Coke deposition on the used catalysts was analysed by TPO, which provides information on the total amount of deposited coke (area under the TPO profiles) and the nature and/or location of the coke in the catalyst structure (position of combustion peaks). Figure 4.8 and Figure 4.9 show the TPO profiles and coke content (wt%) on the used Ni/Al_2O_3 and Ni/CeO_2 catalysts, respectively.

The TPO profiles in Figure 4.8a, Figure 4.8b and Figure 4.9a have been deconvoluted into several Gaussian peaks with Matlab (depicted in Figure B.15 and Figure B.16, respectively, in the Annexes). The deconvoluted peaks can be grouped into two combustion domains: coke burning at low temperature (with its maximum below 500 °C, denoted LT-coke) and coke burning at high temperature (HT-coke). According to literature [164, 255, 259–266], the different location of combustion peaks may be attributable to different coke nature and/or location: coke burning at low temperature is amorphous carbon, most frequently deposited on or near metal sites, encapsulating them and causing fast deactivation [255, 260, 264] and coke burning at high temperature, which can be of different nature depending on the feed reformed, both carbon filaments (mostly formed in the reforming of pure oxygenates and that have low impact on deactivation [259–262]) and pyrolytic carbon (formed mostly in the reforming of bio-oil under severe reforming conditions, and with high impact on deactivation [164, 255, 263–266]).

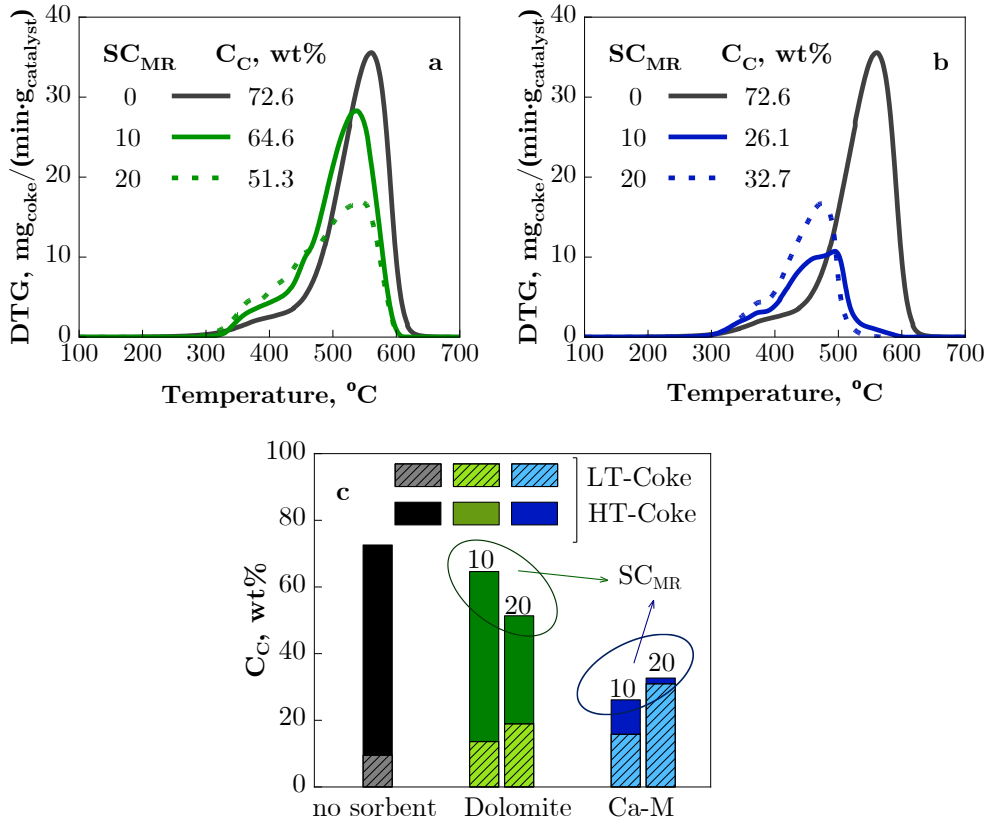

Figure 4.8. TPO profiles (a, b) and coke content (c) deposited on Ni/Al_2O_3 catalyst used in the SR and SESR runs with dolomite (a, green bars) or Ca-M (b, blue bars) as sorbents for different values of SC_{MR}.

The comparison of the TPO profiles and coke content for Ni/Al_2O_3 and Ni/CeO_2 catalysts evidence that the support has a significant impact on coke nature and content. On the one hand, the coke content in Ni/CeO_2 (Figure 4.9b) is significantly lower than in Ni/Al_2O_3 catalyst (both in SR and SESR runs, Figure 4.8c), which could be attributed to the good redox properties of CeO_2 and its capacity for O_2 storage, which promotes the gasification of coke during the reaction [282, 341]. On the other hand, the coke combustion peaks for Ni/CeO_2 catalyst are located at lower temperature than for the coke deposited on Ni/Al_2O_3 catalyst, especially those corresponding to amorphous coke burning at low temperature (LT-coke). The redox property of CeO_2 could have a synergistic

effect on promoting the combustion of amorphous coke towards a lower combustion temperature [282]. The shift of the combustion peaks of the amorphous coke towards a lower temperature allows differentiating in the TPO profiles of Ni/CeO_2 catalyst (Figure 4.9a) several combustion peaks corresponding to LT-coke, denoted LT1 (maximum near 300 °C) and LT2 (those with maximum between 350-500 °C) in Figure 4.9b. In the TPO profiles for Ni/Al_2O_3 catalysts the peaks are very close, so a single peak of LT-coke is apparently observed, although it has one or several shoulders (more noticeable when using Ca-M sorbent or high SC_{MR}) and can be deconvoluted into two or even three combustion peaks (Figure B.15). Interestingly, in the SR run (no sorbent) with Ni/Al_2O_3 catalyst the HT-coke prevails, with its maximum at 560 °C, whereas in the SR with Ni/CeO_2 catalyst there are similar amount of LT-coke and HT-coke.

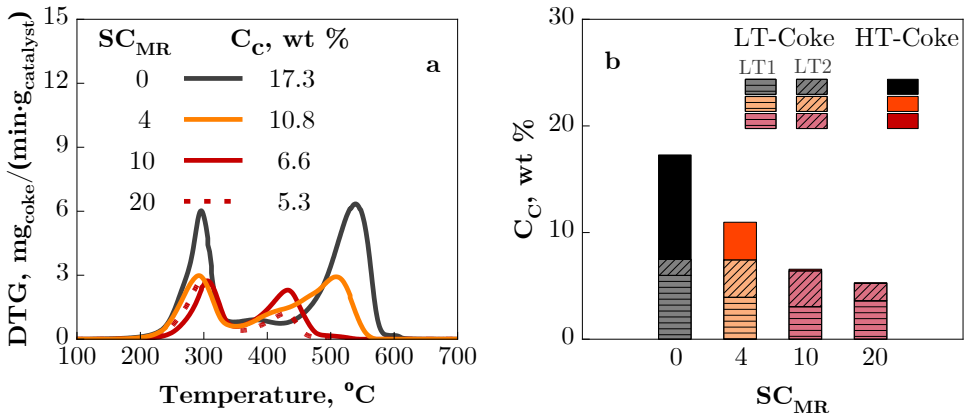

Figure 4.9. TPO profiles (a) and coke content (b) deposited on Ni/CeO_2 catalyst used in the SR and SESR runs with dolomite as sorbent for different values of SC_{MR}.

The results in Figure 4.8 and Figure 4.9 show that for both catalysts, the presence of a sorbent attenuates the total coke content, which decreases overall as the sorbent/catalyst ratio increases, and also noticeably affects the coke nature. Thus, the formation of HT-coke is selectively attenuated (more noticeably for Ni/CeO_2 catalyst and with the Ca-M sorbent in the case of Ni/Al_2O_3 catalyst) and its combustion shifts towards lower combustion temperature. In the SESR run with Ni/Al_2O_3 catalyst (Figure 4.8), LT-coke increases with the presence of a sorbent,

mainly with Ca-M and with increasing SC_{MR}, although with Ni/CeO_2 catalyst this effect of the sorbent is small. This attenuation of the total coke deposition in the SESR runs could be partially explained by the role of the sorbent as an acceptor of part of the coke formed by the decomposition of the heavy oxygenates in the bio-oil (Eq. (1.16)), which contributes to attenuate the deposition of coke by this mechanism on the external surface of the catalyst [265, 266].

4.1.2.2. Structural properties of the used catalysts

The possible sintering of Ni crystals and the crystalline structure of the coke deposits were analysed by XRD. Figure 4.10 shows the XRD diffractograms of Ni/Al_2O_3 catalyst samples used in the SR run and SESR runs with dolomite or Ca-M as sorbents. The average size of Ni^0 crystals of each used sample has been calculated by Debye-Scherrer equation, at $2\theta = 51.8°$ (Ni^0 (200) plane). The average crystal size is 15 nm for this batch of fresh-reduced Ni/Al_2O_3 catalyst and it increases to 17 nm for the catalyst used in the SR run, and to 20 and 19 nm for the samples used in the SESR runs with dolomite or Ca-M as sorbents, respectively. These results give evidence of an insignificant Ni sintering. Therefore, it is not expected that this small increase in Ni particle size will cause a significant impact on catalyst deactivation, whose main cause will be the high coke deposition, as it has been proven for this catalyst in the SR of individual oxygenates (section 3.2), bio-oil [96, 174] and of volatile oxygenates from biomass pyrolysis [342]. Moreover, no NiO peaks are observed in the diffractograms of Ni/Al_2O_3 used catalyst, which corroborates that Ni oxidation is not a deactivation cause. The presence of a broad peak at a diffraction angle of $2\theta = 26°$ is observed in the XRD pattern for the samples used in the SR run and SESR runs with dolomite, which corresponds to crystalline cokes (ordered carbon structures). However, the samples used in the SESR runs using Ca-M as sorbent do not present diffraction peaks related to crystalline carbonaceous structures, indicating that the coke deposited is predominantly amorphous, in agreement with TPO profiles for these samples, which show mainly LT-coke (blue curves in Figure 4.8b). The presence of peaks of SiC ($2\theta = 35.7°$) in the sample used in the SR run

and of $CaCO_3$ ($2\theta = 29.3$ and 35.6°) in the samples used in the SESR runs (mainly with Ca-M sorbent) is due to a non-perfect separation of Ni/Al_2O_3 catalyst from the inert solid (SiC) or the sorbent (dolomite or Ca-M) in the sieving of the catalytic bed which is necessary to obtain the used catalyst samples.

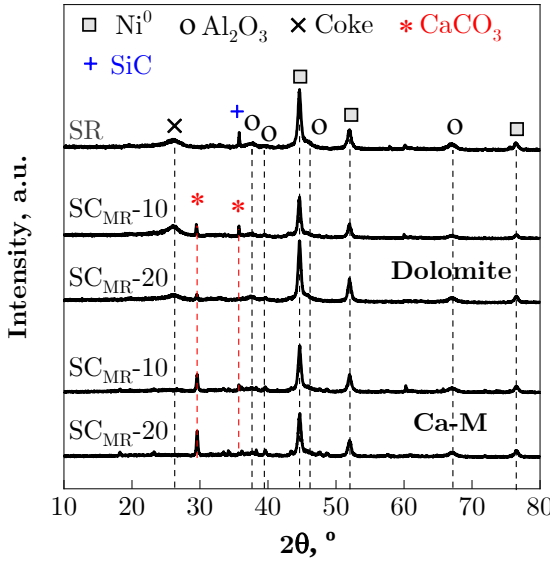

Figure 4.10. XRD patterns of the Ni/Al_2O_3 catalyst samples used in the SR run and SESR runs for different sorbent/catalyst mass ratios with dolomite or Ca-M as sorbent.

The XRD spectra of the Ni/CeO_2 catalyst samples used in SR run and SESR runs with dolomite for different sorbent/catalyst mass ratios are depicted in Figure 4.11. In the used samples, the intensity of the diffraction peaks for CeO_2 decreases noticeably in the samples used in SESR runs with dolomite, and quite noticeable peaks not present in the fresh-reduced catalyst (Figure 2.8b) appear, which correspond to inert solid (SiC, $2\theta = 34.2$, 35.7, 38.2, 41.5, 60.1, 65.7 and 71.8°) (sample used in SR run) and magnesium calcite ($MgCaCO_3$, 23.2, 29.5, 31.4, 36.1, 39.6, 43.0, 48.6, 57.6, 60.9, 64.9 and 73°) (samples used in SESR runs with dolomite). These results are the consequence of the greater difficulty, compared to Ni/Al_2O_3, for separating Ni/CeO_2 catalyst from the inert solid (SiC) and the sorbent (dolomite), due to their similar ranges of particle size. Similar to Ni/Al_2O_3 catalyst used in SESR runs with Ca-M sorbent (Figure 4.10), the

presence of crystalline coke peaks is not observed at $2\theta = 26°$, in agreement with the low (SC_{MR} of 0 and 4) or negligible (SC_{MR} of 10 and 20) content of HT-coke observed in the TPO profiles (Figure 4.9).

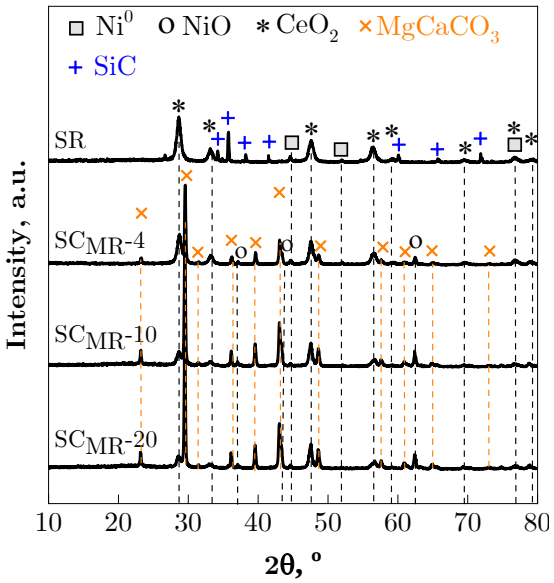

Figure 4.11. XRD patterns of the Ni/CeO_2 catalyst samples used in the SR run and SESR runs for different sorbent/catalyst mass ratios with dolomite as sorbent.

4.1.2.3. Physical properties of catalysts and sorbents

The textural properties (BET surface area, pore volume and average pore diameter) of used catalyst and saturated sorbents were determined by N_2 adsorption-desorption and are displayed in Table 4.1 for catalysts and in Table 4.2 for sorbents. The N_2 adsorption-desorption isotherms and BJH pore volume distribution are shown in Figure B.1 and Figure B.2 (used Ni/Al_2O_3 and Ni/CeO_2 catalysts, respectively) and Figure B.3 and Figure B.4 (saturated sorbents used in the SESR runs with Ni/Al_2O_3 or Ni/CeO_2 catalysts, respectively).

Table 4.1. Physical properties of fresh-reduced Ni/Al_2O_3 and Ni/CeO_2 catalysts and samples used in the SR and SESR runs.

Catalyst	**Sorbent**	**SC_{MR}**	**S_{BET}, m^2/g**	**V_{pore}, cm^3/g**	**d_{pore}, nm**
Fresh Ni/Al_2O_3	-	-	65.1	0.234	13.1
Used Ni/Al_2O_3	-	0	64.2	0.168	12.9
	Dolomite	10*	43.2	0.122	17.4
		20	42.2	0.118	14.1
	Ca-M	10	32.1	0.084	11.8
		20	27.6	0.072	12.5
Fresh Ni/CeO_2	-	-	23.1	0.073	9.3
Used Ni/CeO_2	-	0	6.6	0.017	23.4
	Dolomite	4*	14.4	0.025	14.5
		10	8.4	0.016	15.9
		20	7.1	0.015	17.6

* sorbent/Ni catalyst mass ratio=40

Table 4.2. Physical properties of fresh/calcined and saturated sorbent used in the SESR runs.

Sorbent	**SC_{MR}**	**S_{BET}, m^2/g**	**V_{pore}, cm^3/g**	**d_{pore}, nm**
Fresh dolomite	-	17.5	0.058	13.2
dolomite used with Ni/Al_2O_3	10*	8.0	0.017	16.6
	20	7.3	0.014	16.5
dolomite used with Ni/CeO_2	4*	6.8	0.013	15.0
	10	8.4	0.016	15.9
	20	7.1	0.015	17.6
Fresh Ca-M	-	11.3	0.023	13.9
Ca-M used with Ni/Al_2O_3	10	5.7	0.011	18.3
	20	7.0	0.014	15.8

* sorbent/Ni catalyst mass ratio=40

Overall, the presence and type of sorbent do not affect the shape of the isotherms of the used catalysts, which have a type IV isotherm (Figure B.1 and Figure B.2), with a hysteresis curve of type H3. For the Ni/Al_2O_3 catalyst there is a loss of mesoporosity in the SESR runs (significantly lower total volume adsorbed at high pressures ($P/P_0 \approx 1$), Figure B.1). This is more noticeable with the Ca-M sorbent and with the increase in the sorbent/catalyst ratio, evidencing the partial blockage of the mesopores and thus causing a decrease in BET surface area and pore volume (Table 4.1). For the Ni/CeO_2 catalyst, the decrease in S_{BET} and pore volume in both SR and SESR runs is more noticeable than for used Ni/Al_2O_3 catalyst (Table 4.1), and the average pore diameter increases, due to the decrease in the BET surface area and pore volume. The decrease in catalyst porosity is a consequence of coke deposition, which can cause pore blockage, thus contributing to a more rapid deactivation. However, there is not a direct correlation between the coke content (Figure 4.8c and Figure 4.9b) and the decrease in BET surface area for both catalysts (Table 4.1), and their impact on catalyst deactivation (Figure 4.3, Figure 4.6 and Figure 4.7). This is due to the differences in the porosity of the supports (significantly lower for CeO_2) and in the characteristics and location of the coke, which are analysed in the next section.

All the saturated sorbent samples (Figure B.3 (SESR runs with Ni/Al_3O_3) and Figure B.4 (SESR runs with Ni/CeO_2)) present an isotherm type IV characteristic of mesoporous materials, with lower BET surface area and pore volume than the fresh/calcined samples (Table 4.2), thus revealing partial blockage of the mesoporous structure due to the formation of calcium carbonate by CO_2 capture [343]. The BET surface area (17.5 m^2/g) and pore volume (0.058 cm^3/g) for calcined dolomite sample are higher than those of fresh Ca-M (11.3 m^2/g and 0.023 cm^3/g, respectively), whereas their values are similar for saturated/used sorbents (in the range of 5.7-8.4 m^2/g and 0.011-0.017 cm^3/g for BET surface area and pore volume, respectively). The lower relative porosity loss of the used Ca-M sorbent can be attributed to the presence of mayenite. It has been proven that its presence attenuates the progressive sintering that the CaO sorbent undergoes in successive carbonation-calcination cycles [186, 344]. The slight increase in the

average pore diameter in the saturated sorbent samples suggests a selective loss of the narrower pores.

4.1.2.4. Morphology and location of coke

The morphology and location of coke deposited on the catalyst particle surface was assessed using SEM analysis. A backscattered electron (BSE) detector was used to analyse the relative presence of components on the catalyst particle surface, according to the brightness levels: the lightest level indicates the presence of heavy components such Ni, Al and Ce, whereas the darkest level indicates light components such as C. Figure 4.12 shows the BSE-SEM images of Ni/Al_2O_3 catalyst used in the bio-oil SR or SESR with dolomite as sorbent. When compared with the fresh catalyst (Figure 2.11a), it is evident that there is carbon (coke) deposited on the external surface of the catalyst particles used in the SR run (Figure 4.12a) or SESR runs (Figure 4.12b), as indicated by the different brightness levels. Almost all the particles in the sample used in the SR run are homogeneously dark (Figure 4.12a), which evidences that the carbon deposition on the particle surface is more severe than in those used in the SESR runs. On the other hand, the use of a sorbent (Figure 4.12b) results in a heterogeneous carbon deposition on the external surface of the catalyst particles, distinguishing different particle types: bright particles with a smooth surface (A), slight bright particles with a rough surface (B, which are dominant with dolomite) and dark particles (C, high carbon deposition on the surface). The lower deposition of external coke is in line with the above mentioned TPO results and the decrease of HT-coke due to the role of the sorbent to partially retain this coke formed by decomposition of the heavy oxygenates in the bio-oil.

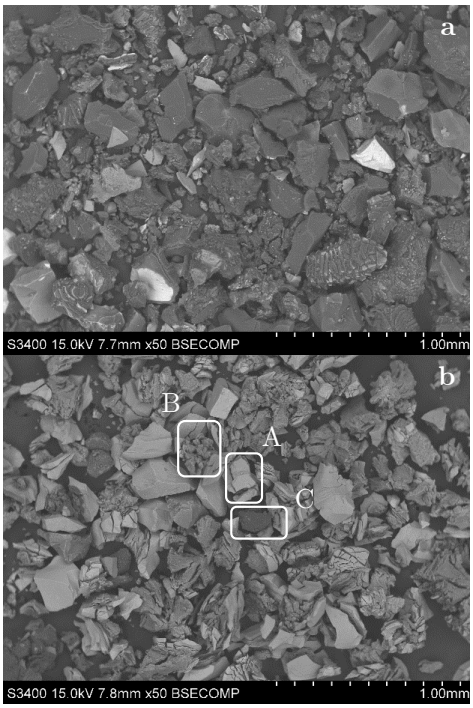

Figure 4.12. BSE-SEM images of Ni/Al_2O_3 catalyst used in the SR run (a) and in the SESR run with dolomite (b) as sorbent, with sorbent/catalyst mass ratio of 20.

To study the coke morphology in more detail, SEM images were taken using a secondary electron detector (SE-SEM) enabling to zoom on the catalyst surface. Figure 4.13 shows the most representative SE-SEM images for Ni/Al_2O_3 catalyst used in SR run and SESR runs with each of the two sorbents. The surface of the Ni/Al_2O_3 catalyst particles used in the SR run (Figure 4.13a) are greatly homogeneous with a rough surface constituted of carbon spheres and filaments. Nevertheless, the surface of the catalyst particles used in the SESR runs with high SC_{MR} (Figure 4.13 b-e) is heterogeneous as previously seen using the BSE detector (Figure 4.12b). The coke morphology is different compared to that observed in the SR, because the formation of filamentous coke is incipient with dolomite as a sorbent (Figure 4.13b) and negligible with Ca-M sorbent (Figure 4.13d), and the coke is deposited as an amorphous mass of carbon with both sorbents (Figure 4.13c and Figure 4.13e).

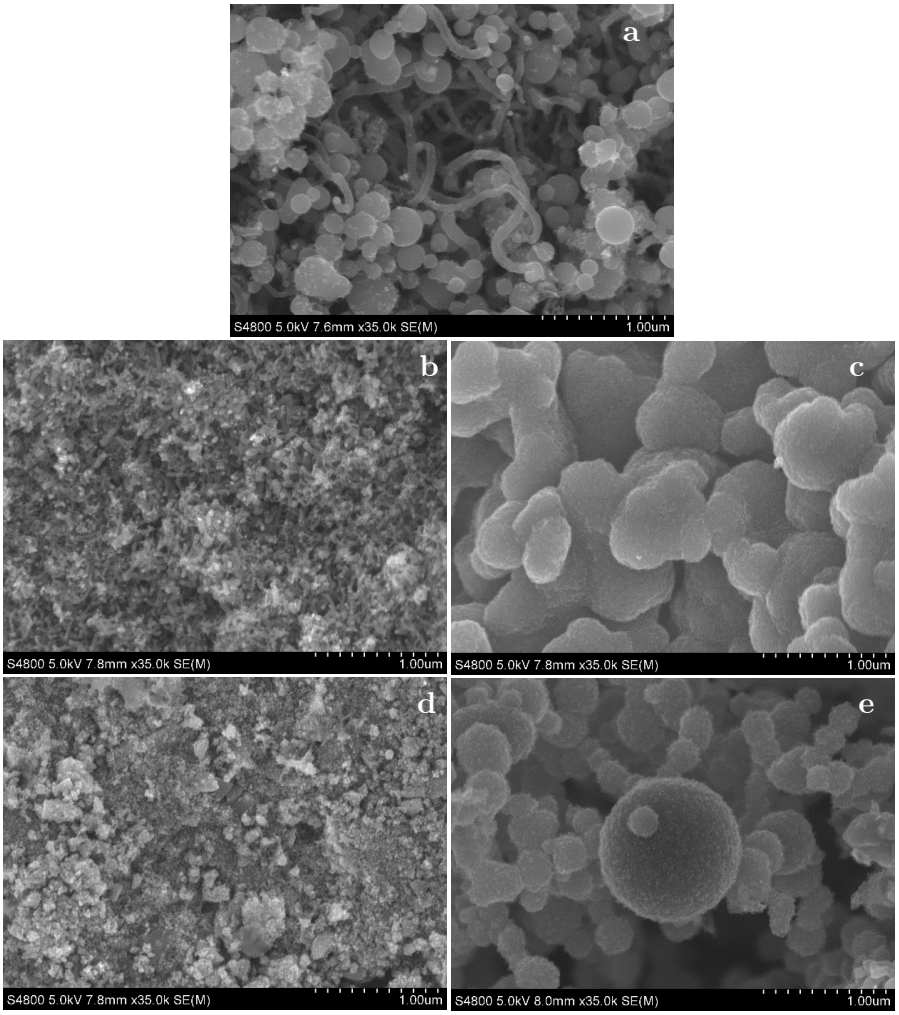

Figure 4.13. SE-SEM images of Ni/Al_2O_3 catalyst used in the SR run (a) and SESR runs with dolomite (b-c) or Ca-M (d-e) as sorbents, with sorbent/catalyst mass ratio of 20.

Figure 4.14 shows SEM images using a secondary electron detector (SE-SEM) of the Ni/CeO_2 catalyst used in the bio-oil SR run or SESR runs with dolomite as sorbent and different dolomite/catalyst ratios. The particles of the sample used in the SR run have some presence of very short carbon filaments on the external surface (Figure 4.14a). Amorphous carbons are all over the external surface of the catalyst used in the SESR run with a dolomite/catalyst ratio of 20 (Figure

4.14b), and a mix of amorphous carbon and some carbon filaments are observed in the sample used with a SC_{MR} of 4 (Figure 4.14c). The mass of amorphous carbon observed on this catalyst seems to be smaller than that observed in the SESR runs with dolomite or Ca-M on the Ni/Al_2O_3 catalyst, being coherent with the lower coke content for this catalyst (Figure 4.9) than for Ni/Al_2O_3 catalyst (Figure 4.8).

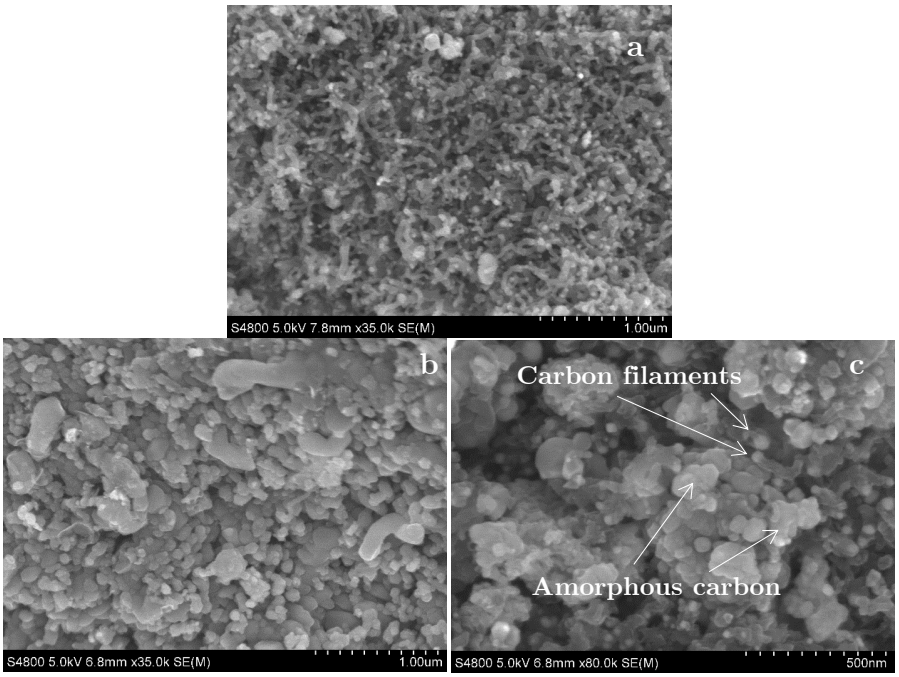

Figure 4.14. SE-SEM images of Ni/CeO_2 catalyst used in the SR run (a) and in the SESR runs with dolomite/catalyst ratio of 20 (b) and 4 (c).

4.1.2.5. Relationship of the deactivation behaviour of the catalyst with the coke deposition

The deactivation of the Ni/Al_2O_3 catalyst in the SESR of raw bio-oil is significantly affected by the presence of a CO_2 sorbent, as it involves a change in the nature and amount of the coke deposited in the catalyst due to the activity of the sorbent for the oxygenates decomposition/cracking reactions, which is different for dolomite and Ca-M. In the reforming without sorbent (SR

conditions) there is a prevailing formation of ordered carbon (filaments and spheres) on the external surface of the Ni/Al_2O_3 catalyst particles (Figure 4.10 (upper curve) and Figure 4.13a), that burns at high temperature (HT-coke, Figure 4.8), and the formation of amorphous carbon burning at low temperature (LT-coke) is low. Amorphous carbon may be formed from oxygenates decomposition or polymerization, whereas more ordered structures (carbon filaments and spheres) may be formed from the CO disproportionation reaction (Eq. (1.21)). This coke deposition causes a reduction of about 28 % of the pore volume without affecting the BET surface area with respect to the fresh-reduced catalyst (Table 4.1), meaning that part of the pores are blocked while the carbon filaments contribute to keep a high surface area. In the SESR runs with dolomite or Ca-M as sorbents the formation of ordered carbon structures is attenuated (Figure 4.10) and the external surface of many particles remains bare (without any carbon deposit, Figure 4.12b), these effects being more noticeably with the Ca-M sorbent and increasing SC_{MR}. Conversely, the presence of a sorbent promotes the formation of amorphous carbon burning below 500 °C (LT-coke in Figure 4.8). It is noted that the amorphous carbon encapsulates Ni sites (most probably corresponds to the shoulder peak appearing at the lower combustion temperature in Figure 4.8a and Figure 4.8b) and also partially covers the catalyst external surface (visible in Figure 4.13c and Figure 4.13e), which most probably corresponds to the combustion peak with the maximum around 470 °C in Figure 4.8a and Figure 4.8b. This coke is the plausible explanation for the decrease in the surface area and pore volume for the Ni/Al_2O_3 catalyst used in the SESR runs (Table 4.1), that is more pronounced with Ca-M sorbent and with higher SC_{MR}. The attenuation of HT-coke in the SESR runs may be explained by: 1) the absence of CO during the capture period (Figure 4.3d) due to the shift of WGS reaction towards H_2 and CO_2 caused by CaO carbonation, that disfavours CO disproportionation reaction during this period, and 2) the increase in the formation of amorphous carbon (favoured by the contribution of the sorbent to oxygenates decomposition reactions) that hinders the development of carbon filaments (section 3.2).

The comparison of the results of coke deposition over Ni/Al_2O_3 catalyst with the evolution of products yield along the reaction (Figure 4.3) confirms the well-known fact that the total amount of coke has lower impact on catalyst stability than its nature [255, 260, 264]. Amorphous LT-coke (mostly the fraction burning at the lower temperature) has a higher impact on catalyst deactivation than HT-coke (especially that of filamentous nature, observed in the SR run (Figure 4.13a)). Thus, the higher activity for decomposition/cracking reactions (Eq. (1.16)) of Ca-M compared to dolomite explains the faster catalyst deactivation observed when using the Ca-M sorbent and with increasing sorbent/catalyst ratios, as it leads to a higher amorphous coke formation, in agreement with TPO profiles in Figure 4.8a and Figure 4.8b.

Likewise, in spite of the lower amount of coke deposited over Ni/CeO_2 catalyst than Ni/Al_2O_3 catalyst (Figure 4.8 and Figure 4.9), the faster deactivation of the former is noteworthy both in the SR and SESR runs (Figure 4.3 and Figure 4.6). This result can be explained by the different nature and location of the coke deposited on both catalysts and by their different porous structure and location of Ni crystals on the support. The SR of raw bio-oil over Ni/CeO_2 catalyst forms some short carbon filaments visible on the external surface of the catalyst particles (Figure 4.14a), that presumably burns above 500 °C (Figure 4.9), but there is a high formation of amorphous and encapsulating coke over the catalyst surface (LT1 and LT2 coke) that greatly reduces the pore volume by 78 % and the surface area by 71 % with respect to the fresh-reduced catalyst (Table 4.1), evidencing a severe pore blockage that, jointly with the encapsulation of metal sites, causes a more rapid deactivation than in the SR with Ni/Al_2O_3 catalyst.

4.2. COMPARISON OF SR AND SESR IN PACKED AND FLUIDIZED-BED REACTORS

The choice of appropriate reactors and reforming strategies is key to make progresses on scaling up H_2 production processes from raw bio-oil. Therefore, this section compares the performance (conversion, product yields and deactivation) of packed-bed and fluidized-bed reactors (PBR and FBR, respectively) for the H_2

production from raw bio-oil by SR and SESR, using the best catalyst selected in previous section (Ni/Al_2O_3 obtained by reduction of a $NiAl_2O_4$ spinel) and with the most suitable sorbent (dolomite) to capture CO_2 in the SESR runs. The experiments were carried out at 600 °C; S/C ratio, 3.4; space time, 0.15 $g_{catalyst}{\cdot}h/g_{oxygenates}$; time on stream, 5 h; dolomite/catalyst ratio, 10 (SESR runs).

4.2.1. Performance of the packed and fluidized-bed reactors

The influence of using a PBR or FBR on the behaviour of Ni/Al_2O_3 catalyst derived from $NiAl_2O_4$ spinel in the reforming of bio-oil both under SR conditions (without sorbent) or under SESR conditions (with dolomite) is compared in this section.

4.2.1.1. Steam reforming

Figure 4.15 shows the evolution with TOS of the conversion and product yields obtained in the PBR (full markers) and FBR (empty markers) in the absence of CO_2 sorbent in the conventional SR. The comparison of the results in both reactors show a higher initial stability in the PBR, in which the conversion and H_2 and CO_2 yields remain almost constant along 120 min (Figure 4.15a), and are close to the thermodynamic equilibrium. Thus, according to prior studies [313], at 600 °C and S/C ratio of 3.4 (this being the S/C ratio resulting in the treated bio-oil, once subtracted the PL deposited in Unit 1 during the thermal treatment) in the thermodynamic equilibrium the oxygenates conversion is complete and the yields of H_2 and CO_2 are 82.3 % and 73.4 %, respectively. Nevertheless, subsequently they rapidly decrease due to catalyst deactivation for the WGS (Eq. (1.15)) and reforming (Eq. (1.14)) reactions. The increase of light hydrocarbons (C_aH_b) yield after 120 min in Figure 4.15b can be explained because the extent of its forming reaction (oxygenates decomposition/cracking reaction, Eq. (1.16)) is favoured by the increase of oxygenates concentration as the catalyst is deactivated, and by the deactivation of their reforming reaction (Eq. (1.18)). Interestingly, the yields of CO and CH_4 (intermediate compounds in the overall reaction scheme, Eqs. (1.13)-(1.22)) remain almost constant with TOS, which

suggests that their forming and disappearing reactions are similarly affected by the catalyst deactivation [96].

In the FBR (empty markers in Figure 4.15) there are lower initial values of conversion and H_2 and CO_2 yields (Figure 4.15a) and higher CH_4 yield (Figure 4.15b) than in the PBR due to the less effective gas-solid contact. Moreover, an initial steady period of complete carbon conversion in the reforming reactions is not observed in the FBR, so that the carbon conversion and the yields of H_2 and CO_2 decrease from the beginning of the reaction. Therefore, H_2 yield is initially lower and decreases more rapidly at the beginning of the reaction in the FBR (probably due to the higher concentration of unreacted oxygenates, which are the main precursors of coke by decomposition/cracking) [164]. However, the deactivation rate is slower in the FBR than in the PBR with increasing TOS, and a similar H_2 yield is achieved after 300 min TOS, around 41 %. The hydrocarbons yield remains nearly null in FBR (Figure 4.15b), which evidences a slow deactivation of their reforming reaction (Eq. (1.18)), whereas CO yield slightly increases, evidencing that catalyst deactivation also affects the WGS reaction (Eq. (1.15)) [96, 303]. This lower deactivation in the FBR is in agreement with the results in the literature on biogas reforming [155], pure oxygenates [156], aqueous fraction of bio-oil [151, 157, 158] and raw bio-oil [148].

These different deactivation trends in both reactors is consequence of the complexity of the coke formation mechanism, as explained in section 4.2.2, which depends on the evolution with TOS of the extent of its formation reactions (Eqs. (1.16), (1.20) and (1.21)) and its removal by gasification (Eq. (1.22)). Moreover, as established in the literature [255, 321, 342], the nature of the coke formed at different reaction steps (Eqs. (1.16), (1.20) and (1.21)) is different and has a different impact on catalyst deactivation. The gas-solid contact regime, which is different in both reactors, and the movement of the catalyst particles in the fluidized reactor will have an impact on the extent of these coke formation reactions.

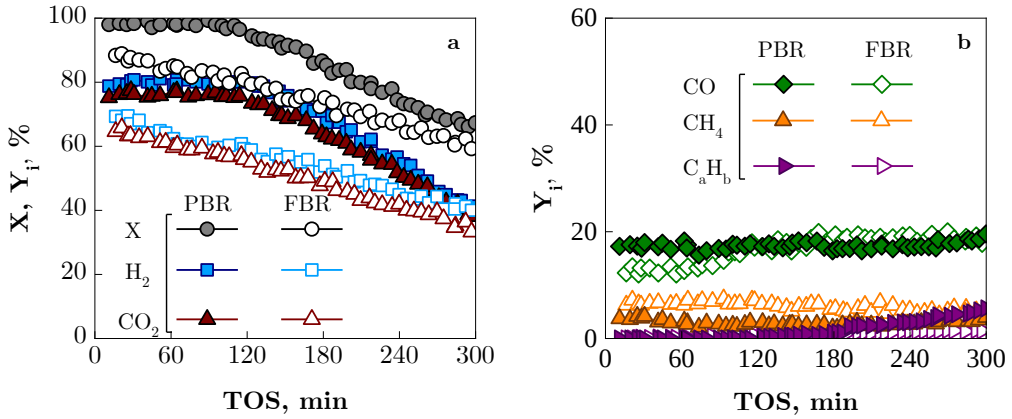

Figure 4.15. Evolution with TOS of conversion and H_2 and CO_2 yields (a) and CO, CH_4 and light hydrocarbons (C_aH_b) yields (b) in the SR runs with Ni/Al_2O_3 catalyst in PBR (full markers) and FBR (empty markers) at 600 °C, S/C ratio of 3.4 and space time of 0.15 $g_{catalyst}$ $h/g_{oxygenates}$.

4.2.1.2. Sorption enhanced steam reforming

Figure 4.16 compares the performance along TOS of the PBR and FBR in the SESR runs. In the initial CO_2 capture period, whose duration is almost 30 min in both reactors, the H_2 yield is almost 100 % in PBR run and 92 % in FBR (Figure 4.16a). In this period, complete oxygenate conversion is achieved in PBR and, therefore, the conversion to gas defined by Eq. (2.7) is near zero because the yields of CO, CH_4 and hydrocarbons are almost null in this period (Figure 4.16b).

After the saturation of dolomite, in the PBR (full makers) the conversion is almost complete up to 160 min TOS, with high H_2 and CO_2 yields (80 % and 70 %, respectively). In this period the CO yield is around 17 % and CH_4 yield is low (3-4 %). Moreover, hydrocarbons formation (C_aH_b) (Figure 4.16b) is null, and the duration of the stable period is even longer than in the SR run (Figure 4.15a). Subsequently, the conversion and yields of H_2 and CO_2 sharply decrease, which evidences a rapid catalyst deactivation for the reforming of oxygenates and of CH_4 and C_aH_b, whose yields increase after 180-240 min TOS. CO yield keeps quite constant, which points to a similar deactivation rate of the reactions of CO formation and conversion. In the FBR (empty markers in Figure 4.16), the yields

of H_2 and CO_2 after dolomite saturation are lower than in the PBR, coherently with the results obtained in the SR runs (Figure 4.15). Interestingly, a short stable period (around 40 min) with almost constant yields is observed, that could be attributed to the activity of dolomite, so that the reactor operates initially which excess of active sites for oxygenates conversion (thus partially overcoming the less effective gas-solid contact in the fluidized-bed). Nevertheless, the decrease in conversion and in the yields of H_2 and CO_2 in the FBR (Figure 4.16a) is faster in the presence of dolomite than in the SR run without dolomite (Figure 4.15a).

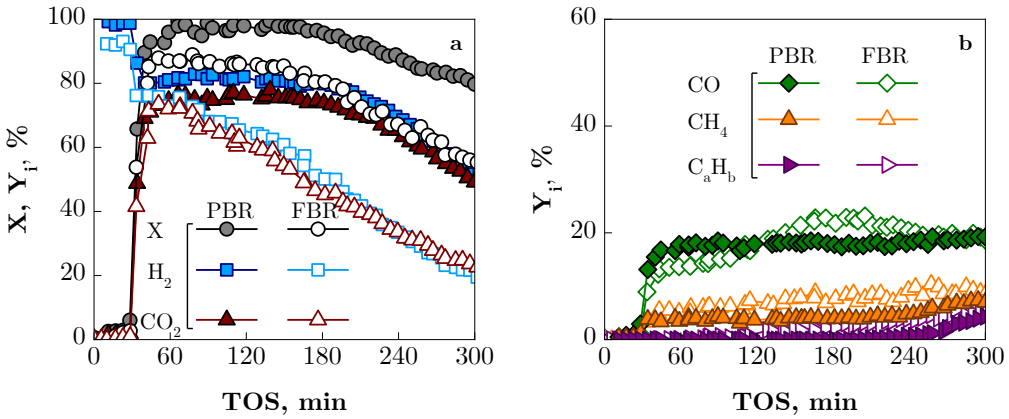

Figure 4.16. Evolution with TOS of conversion and H_2 and CO_2 yields (a) and CO, CH_4 and hydrocarbons (C_aH_b) yields (b) in the SESR runs with Ni/Al_2O_3 catalyst and dolomite as sorbent in PBR (full markers) and FBR (empty markers) at 600 °C, S/C ratio of 3.4; space time of 0.15 $g_{catalyst}$ h/$g_{oxygenates}$ and dolomite/catalyst mass ratio of 10.

In view of the aforementioned results, in the CO_2 sorption period, the presence of dolomite significantly modifies the product distribution in both beds, allowing obtaining almost pure H_2. In the post-saturation period, the presence of dolomite seems to have two opposite effects on the catalyst deactivation in both fluid dynamic regimes. On the one hand, it enlarges the duration of the pseudo-stable period compared to the SR runs without dolomite, which could be explained by the dolomite activity for the conversion of oxygenates by reforming (Eq. (1.14)), interconversion (Eq. (1.19)) and decomposition/cracking (Eq. (1.16)) reactions [265]. On the other hand, the presence of dolomite originates a faster deactivation

of the catalyst, so that after the pseudo-stable period there is a more rapid decrease in the carbon conversion and yields of H_2 and CO_2 than in the SR run without dolomite. This fact suggests that the presence of dolomite has a negative impact on deactivation, which is greater than its positive role of acting as a catalyst guard, retaining on its surface a fraction of the coke (in particular that related to lignin derived oxygenates and predominantly deposited on the external surface of the dolomite and catalyst particles) [266].

The comparison of the results in the PBR and FBR for the SR and SESR of raw bio-oil shows the importance of the fluid dynamic regime of the reactor on the conversion of oxygenates, product yields and their evolution with TOS. The less effective gas-catalyst contact occurring in the FBR explains the lower initial carbon conversion and yields of H_2 and CO_2, as reported in the literature in the SR of different feeds [148, 151, 158, 161–163]. As a consequence, coke deposition is favoured due to the higher concentration of oxygenates (coke precursors by decomposition/cracking reactions, Eq. (1.16)), although this effect will be partially mitigated by the "catalyst rejuvenation", due to the movement of the particles that favours their contact with the gas stream, promoting gasification and attenuation of coke evolution. This phenomenon, with notable incidence at high temperatures in the reforming of different feeds [148, 151, 155–158], will have a lower effect at 600 °C (temperature required for CO_2 sorption, but insufficient to promote the efficient gasification of the coke).

4.2.2. Characterization of used catalyst and coke

This section shows the results of the characterization of the used catalyst samples and of deposited coke in order to better understand the effect of the fluid dynamic regime of the reactor and the role of using dolomite as a CO_2 sorbent in the possible causes of deactivation. These causes include: i) deposition of coke on the catalyst surface (amount and characteristics of coke deposits), ii) changes in Ni oxidation state and crystal size, and iii) aging and clogging of the support.

It should be noted that after each reaction, the solids composing the catalytic bed were separated by sieving, to avoid masking the characterization of the used

catalyst by the presence of the other solids (inert in the SR runs or inert/sorbent in the SESR runs). The particle size selected for each solid (SiC, ~ 75 µm; dolomite 90-125 µm; catalysts 150-250 µm) facilitates this separation. Thus, only traces of inert or dolomite might remain in the used catalyst after sieving.

4.2.2.1. Structural properties

Figure 4.17 shows the XRD patterns of catalyst samples used in the SR and SESR runs with PBR or FBR. Notice that the XRD patterns of the samples used in PBR under these conditions correspond to the two upper XRD patterns in Figure 4.10, previously commented, which have also been included in Figure 4.17 for a clearer comparison of the results in both reactors. Similarly to what was observed in PBR, no NiO peaks are detected in the samples used in FBR and the average Ni^0 particle size, calculated using Debye-Scherrer equation at $2\theta = 51.8°$, is similar for the fresh-reduced (15 nm) and catalyst samples used in FBR (16-17 nm), which also allows excluding Ni oxidation and Ni sintering as deactivation causes in FBR. Consequently, this must be attributed to coke deposition. The presence of a broad peak at a diffraction angle of $2\theta = 26°$ for the catalyst used in PBR in SR conditions suggests the presence of a high crystallinity coke (graphitic carbon), which is less observable for that used in FBR. Moreover, the use of dolomite increases the intensity of this diffraction peak in both reactors, which indicates the presence of more crystalline carbon structures.

The deposition of different types of coke (inside and outside the particles) causes the deterioration of the catalyst properties, leading to a partial blocking of the pores of the Al_2O_3 support, which together with the encapsulation of the Ni sites by amorphous coke are the causes of catalyst deactivation [174, 307]. To evaluate the deterioration of the porous structure of the catalyst, N_2 adsorption-desorption isotherms have been obtained for used catalyst samples (Figure B.1a and Figure B.1b for PBR (SR and SESR (SC_{MR} of 10) runs) and Figure B.5 for FBR (SR and SESR runs)), from which the textural properties (BET surface area, pore volume and average pore diameter) have been calculated. For the SR runs, there is an increase in BET surface area for the catalyst used in FBR (72.8 m^2/g)

compared to that of the fresh-reduced catalyst (65.1 m^2/g). Nevertheless, the BET surface area of the catalyst used in the PBR (64.2 m^2/g) is slightly lower than that of the fresh-reduced catalyst. This result evidences a different morphology of coke formed in the PBR than in the FBR. Conversely, the pore volume of the catalyst used in FBR decreases (values of 0.18 cm^3/g compared to 0.24 cm^3/g for fresh catalyst), which suggests a partial blockage of the mesoporous structure of Al_2O_3 support according to the deposition of low porosity coke (amorphous carbon). This decrease in BET surface area and pore volume is more noticeable in the PBR (see the three first rows in Table 4.1). The slight increase in BET surface area for the catalyst used in the SESR run in the FBR (69.6 m^2/g) compared to the fresh catalyst (65.1 m^2/g) could be explained by additional porosity created by some filamentous coke deposited on this sample, which partially counteracts the decrease in BET surface area due to amorphous coke.

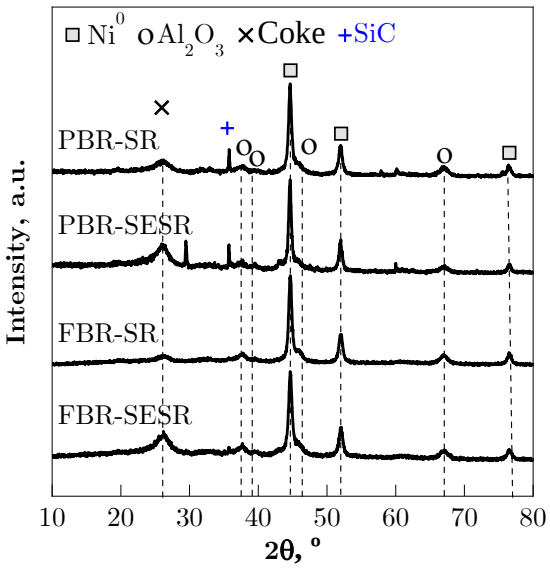

Figure 4.17. XRD patterns of Ni/Al_2O_3 catalyst samples used with a PBR or FBR in the SR and SESR runs.

4.2.2.2. Morphology and location of coke

The BSE-SEM detector was used to distinguish between different elements on the external surface of the catalyst particles based on the brightness intensity, and SE-SEM images of the catalyst particles zoomed in on the catalyst surface were taken in order to determine the coke morphology in more detail.

Figure 4.18 and Figure 4.19 compare BSE-SEM images of the catalyst particles used in the SR and SESR runs, respectively, with the two different reactors. Differently from the fresh catalyst (Figure 2.11a), all the used samples exhibit a low brightness intensity (dark appearance), which is indicative of carbon deposition on the external surface of the particle. Based on the brightness intensity, in the absence of dolomite (SR runs) carbon deposition is more severe on the catalyst used in a PBR (Figure 4.18a) than on that used in the FBR (Figure 4.18b). The latter shows a homogeneous higher brightness level, which evidences less coke deposition on the external surface of the particle.

Nonetheless, the use of dolomite (Figure 4.19) results in a heterogeneous coke deposition, showing differences in the particle shapes and textures for both reactors. In the PBR (Figure 4.19a), the agglomeration of catalyst particles embedded in coke agglomerates can be seen, whereas the particles used in the FBR are separated, with the presence of abundant carbonaceous material on their surface (Figure 4.19b).

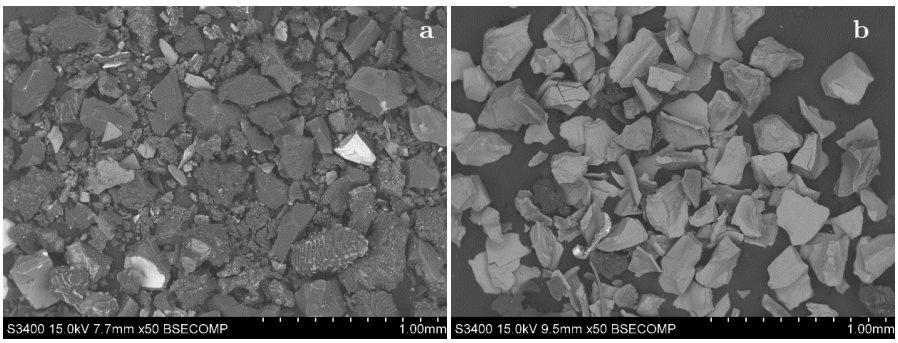

Figure 4.18. BSE-SEM images of the catalyst used in the SR runs in PBR (a) and FBR (b).

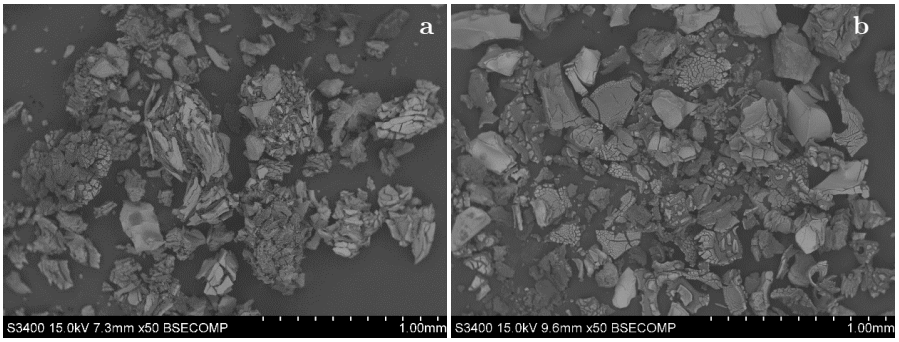

Figure 4.19. BSE-SEM images of the catalyst used in the SESR runs in PBR (a) and FBR (b).

The SE-SEM images of catalyst particles used in the two different reactors are shown in Figure 4.20 (used in SR runs) and Figure 4.21 (used in SESR runs). In some particles of the sample used in the SR run in FBR (those with dark rough surface in Figure 4.18b) the presence of mostly thin, loose and short carbon filaments is observed (Figure 4.20b). Nevertheless, most of the catalyst particles used in FBR (slight bright smooth particles in Figure 4.18b) show a porous surface resembling that of the fresh-reduced catalyst (Figure 4.22), evidencing a low carbon deposition on their external surface. In the catalyst used in PBR (Figure 4.20a) some carbon filaments are also observed, which are more heterogeneous than those formed in the fluidized-bed, and interestingly, abundant carbon spheres are formed. In the catalyst used in the SESR run in PBR (Figure 4.21a), the presence of carbon spheres is negligible, and the presence of carbon filaments predominates, as in the catalyst used in the FBR (Figure 4.21b). This higher amount of carbon filaments deposited on the catalysts samples used in the SESR runs compared to SR runs is coherent with the observation of more crystalline coke structures in the XRD diffractograms of these samples (Figure 4.17).

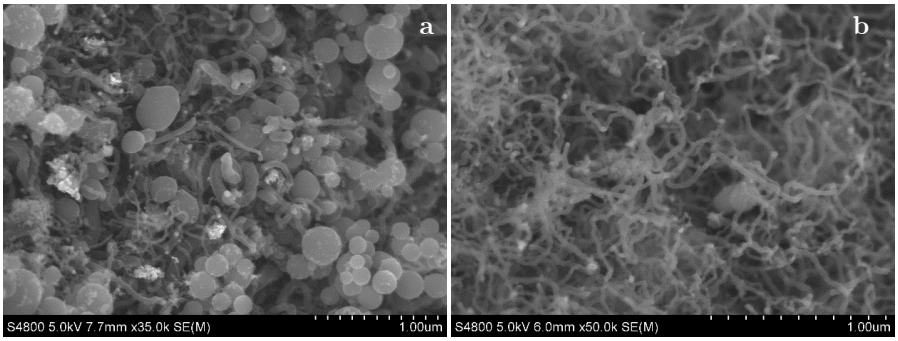

Figure 4.20. SE-SEM images of the catalyst used in the SR runs in PBR (a) and FBR (b).

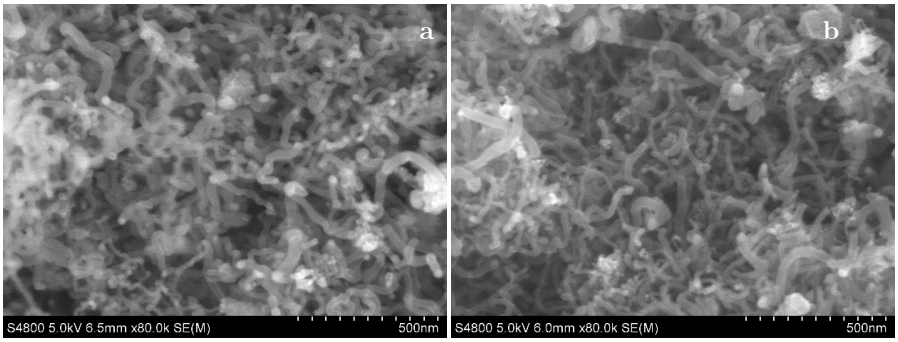

Figure 4.21. SE-SEM images of the catalyst used in the SESR runs in PBR (a) and FBR (b).

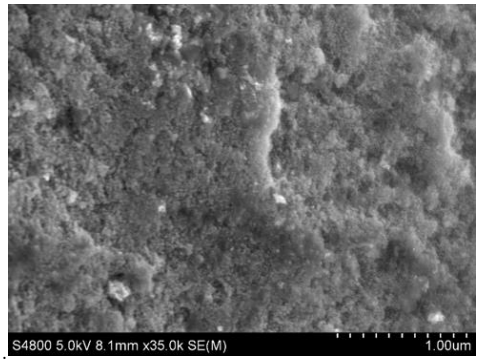

Figure 4.22. SE-SEM image of the slight bright particles of the catalyst used in the SR run in the FBR.

4.2.2.3. Amount and types of coke

The amount of coke deposited on the catalyst and on dolomite and its nature and/or location in the particle have been determined by TPO analysis of the used materials. Figure 4.23 shows the TPO profiles of the catalyst used in the SR (Figure 4.23a) and SESR (Figure 4.23b) runs with both reactor configurations (PBR and FBR). In terms of total coke contents (Table 4.3), a lower amount is observed in the catalyst used in FBR compared to the one used in PBR. Therefore, in the SR run this difference is considerable and the contents are 73 wt% and 17 wt% for PBR and FBR, respectively. This difference, smaller in the SESR runs, is in agreement with the higher pore blockage and decrease of the BET surface area in the PBR, commented in section 4.2.2.1. This result is coherent with the established effect of particle movement in the FBR on attenuating coke formation in the reforming of different feeds [151, 155–158].

The comparison of the average coke yields on the catalyst after 300 min TOS (Figure 4.24) shows that it decreases with the presence of dolomite in the PBR, but conversely increases in the FBR. The coke yield deposited on dolomite in the SESR runs (3.7 % and 2.9 % in PBR and FBR, respectively, Figure 4.24) highlights the coke-forming capacity of dolomite, and suggest that the vigorous contact between catalyst and dolomite in the FBR (with dolomite/catalyst ratio of 10) favours the mechanisms of coke formation on the catalyst. This coke-forming capacity of dolomite has been demonstrated in previous works [265, 266] in which dolomite has been used as a guard-bed prior to the reforming reactor due to its capacity for the pre-reforming of oxygenates from the bio-oil, so that it modifies the composition of the oxygenates and enables the extent of the reforming in the subsequent reforming step.

In all the TPO profiles in Figure 4.23 two combustion domains are identified, as previously observed in Figure 4.8a for this catalyst/sorbent system, which is attributable to different coke nature: a fraction burning at low temperature (LT-coke) and a fraction burning at high temperature (HT-coke). These TPO profiles are in line with the XRD diffractograms in Figure 4.17, showing low peak intensity at θ=26° (corresponding to coke crystalline structures) in the sample

used in the SR run in FBR (whose HT-coke fraction is minority). Furthermore, the comparison of the results of coke morphology (section 4.2.2.2) with those of coke content and combustion characteristics (Figure 4.23) evidences that there is a direct correlation between HT-coke fraction and the coke that is clearly visible on the catalyst external surface. Thus, most of the used catalyst particles in the SR run in FBR (with minority formation of HT-coke, Figure 4.23a), are bright (Figure 4.18b).

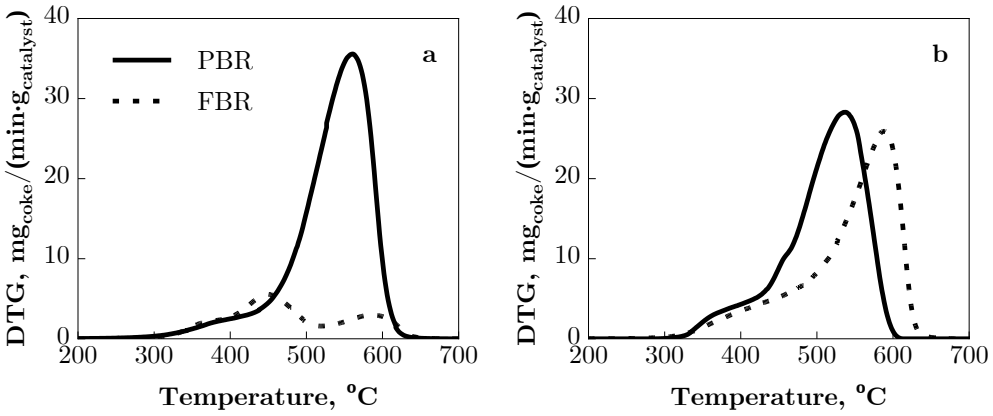

Figure 4.23. TPO profiles for the catalyst used in the SR (a) and SESR (b) runs in PBR (solid lines) or FBR (dashed lines).

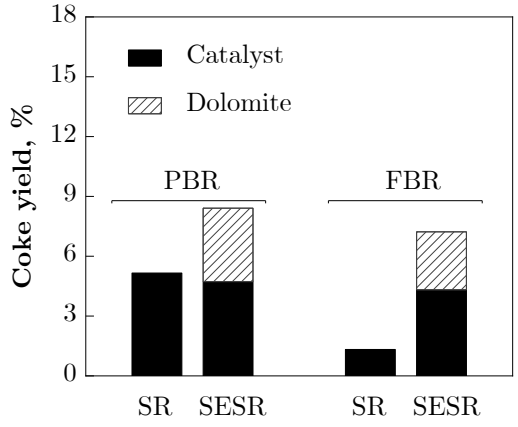

Figure 4.24. Comparison of coke SR yields on catalyst and sorbent in SR and SESR runs with both reactor types.

The TPO profiles in Figure 4.23 were deconvoluted into several combustion peaks, and those with the maximum of the peak located below 500 °C were assigned to LT-coke, while those with maximum of combustion peak above 500 °C were assigned to HT-coke. The results of the deconvolution of the TPO profiles of the catalyst used in the SR run in PBR (Table 4.3), evidence that HT-coke is the prevailing coke fraction in this sample (89.2 % of the total coke), whose combustion peak has a maximum at 560 °C (Figure 4.23a). When dolomite is used in the PBR (SESR runs), HT-coke formation decreases and its combustion peak shifts towards lower combustion temperature (538 °C), whereas the growth of the LT-coke fraction is promoted (Figure 4.23b). As a result, the HT-fraction is 76.7 % of the total coke.

Table 4.3. Total coke and coke fractions content (wt%), and fraction of LT-coke deposited on the catalyst for SR and SESR runs with both reactor types.

Reactor type	**Run**	**Coke content, wt%**			**LT-coke fraction**
		LT-coke	HT-coke	Total	
PBR	SR	7.9	64.7	72.6	10.8
	SESR	15.0	49.6	64.6	23.3
FBR	SR	12.2	5.0	17.2	70.7
	SESR	13.6	43.9	57.5	23.7

The relative content of coke fractions in the catalyst used in SR run with FBR (dashed lines in Figure 4.23a) differs significantly from that used in the PBR (solid lines). Thus, in the FBR the formation of HT-coke (5.0 wt%, Table 4.3) is noticeably attenuated compared to the PBR (64.7 wt%) and it burns at higher temperature (maximum at 587 °C), which suggests that it is more structured coke. This may be a consequence of the favoured gasification of HT-coke in the FBR, that noticeable reduces its amount, but leaves a carbon structure that is more condensed/developed. Nevertheless, the content of LT-coke (12.2 wt%) is slightly higher than in the PBR (7.9 wt%), most probably due to the lower conversion and, consequently, higher concentration of oxygenates, which are precursors of the amorphous LT-coke formation by decomposition/cracking

reaction (Eq.(1.16)). Conversely, in the presence of dolomite (SESR runs, Figure 4.23b), the formation of HT-coke is predominant (43.9 wt%, 76.3 % of the total coke) over LT-coke (content of 13.6 wt%).

The different evolution observed in the formation of both coke fractions due to the presence of dolomite seems to indicate a change in the mechanism of coke formation, and this variation is affected differently by the fluid dynamic regime in the reactor. The possible cause of this change may be the role of dolomite as a catalyst for the interconversion reactions of the oxygenates in the bio-oil [265]. Consequently, changes in the composition of the oxygenates will have a major impact on coke formation and nature, as has been demonstrated in section 3.2. In the FBR, a synergy between the mechanisms of coke formation on both solids cannot be ruled out, so that the deposition of amorphous coke on dolomite (exclusive because no HT-coke is formed, as shown in Figure 4.25) favours the development of the mechanism of coke formation and evolution on the catalyst, due to the vigorous contact between the catalyst and dolomite particles in this reactor.

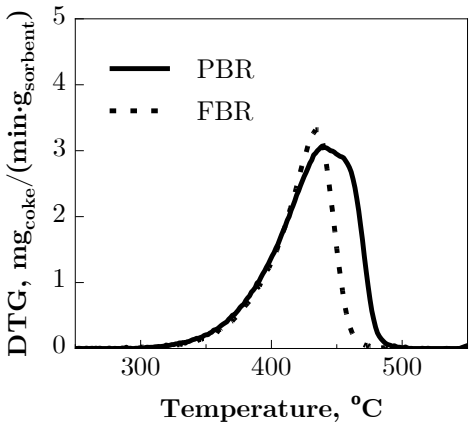

Figure 4.25. TPO profiles for the dolomite used in the SESR runs in a PBR (solid lines) or FBR (dashed lines).

Another plausible explanation is the water adsorption capacity of saturated dolomite ($CaCO_3$+MgO), considering that $CaCO_3$ is able to adsorb water at high

temperatures [345]. Although the water adsorption capacity of the saturated dolomite (0.017 and 0.010 mmol/g at 150 °C and 400 °C, respectively) is lower than that of the catalyst (0.096 and 0.031 mmol/g at 150 °C and 400 °C, respectively), the presence of a large amount of dolomite in the catalytic bed (dolomite/catalyst ratio of 10) may cause a water adsorption competition with the catalyst, which negatively affects the coke gasification.

4.2.2.4. Structure of coke

Figure 4.26 shows the Raman spectra of the used catalyst samples. All the samples show the typical G (1589 cm^{-1}) and D (1343 cm^{-1}) bands attributable to different carbon structures, and other minor bands are also inferred at around 1200 cm^{-1} (associated to C-H vibrations) and 1500 cm^{-1} (associated to amorphous carbon and denoted as D3). The spectra were deconvoluted into these four bands in order to have a better interpretation based on the D and G band widths and intensity ratios between G and D or D3 (summarised results in Table 4.4 and Figure B.13).

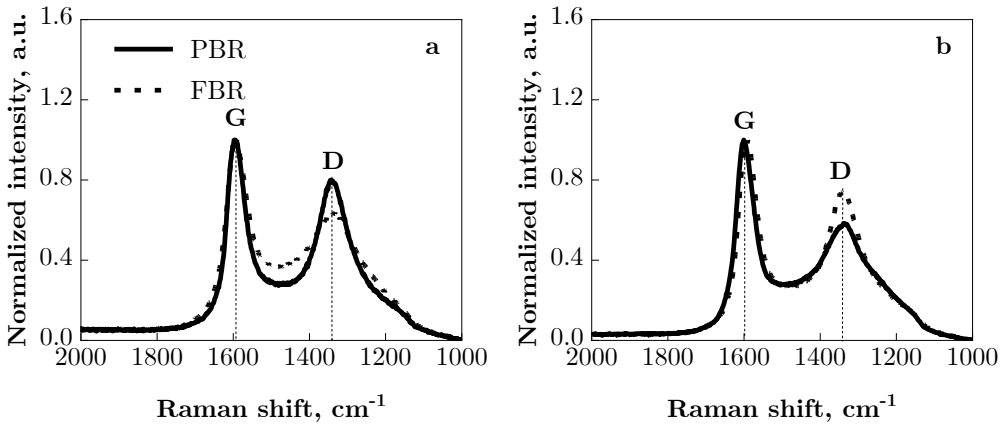

Figure 4.26. Raman spectra of the catalyst used in the SR (a) and SESR (b) runs in PBR (solid lines) or FBR (dashed lines).

Table 4.4. Results of Raman spectra deconvolutions for the used catalysts.

Run	Reactor type	D width	G width	A_D/A_G[1]	I_D/I_G[2]	A_{D3}/A_G[1]	I_{D3}/I_G[2]
SR	PBR	108	52.7	1.62	0.788	0.420	0.153
	FBR	152	62.3	1.54	0.628	0.599	0.210
SESR	PBR	142	52.9	1.50	0.558	0.450	0.152
	FBR	112	53.9	1.49	0.718	0.392	0.145

[1] Calculated from the deconvoluted band areas.
[2] Calculated from the deconvoluted band height.

The deconvolution results can be interpreted under these premises:

- Smaller D and G band widths are related to more ordered and/or more homogeneous structures [346].
- The D/G band ratio is related to the degree of order or "graphitization" of the carbon structure, but the interpretation depends on the nature of the carbon structures. As observed by SEM images, the coke is composed of amorphous carbon and carbon nanostructures (filaments and spheres). These carbon nanostructures typically have more intense D bands [327, 347, 348], and therefore a higher D/G intensity or area ratio would indicate the presence of these structures (together with the observation of smaller D and G band widths).
- The D3/G ratio gives a direct indicator of the relative content of amorphous carbon [327], and so as the D3 band increases, the sample would have more amorphous carbon structures (together with the increase in the D band width).

Based on these premises and the deconvolution results, the coke formed in the SR in the PBR has a more ordered structure (higher D/G ratio and lower D band width) with less relative content of amorphous carbon structures (lower D3/G ratio) than that formed in the FBR. Contrariwise, the coke formed in the SESR in the FBR has a more ordered structure (higher D/G ratio and lower D band width) than that formed in the PBR, while the relative content of amorphous carbon structures is slightly lower. In any case, the coke formed in the SESR in

both reactors has lower D3/G ratios than that formed in the SR in the FBR and smaller D band widths, which indicates that the coke formed in the SESR is more structured than that formed in the SR in the FBR. These observations are consistent with the SEM and TPO results that evidence a high presence of carbon filaments and spheres in the coke formed in the SR in the PBR, whereas that formed in the FBR is mostly amorphous carbon with low presence of carbon filaments. Similarly, the coke formed in the SESR in both reactors is mostly composed of carbon filaments, and these results confirm that the carbon filaments formed in the FBR are more structured than those formed in the PBR. Interestingly, the D3/G ratio calculated from the deconvolutions are linearly correlated with the combustion temperature corresponding to the maximum TPO peak (Figure 4.27). This confirms that the combustion behaviour is mostly related to the carbon structure nature.

The coke deposited on the sorbent was also analysed by Raman spectroscopy (Figure B.14 and Table 4.5) and the results indicate that this coke is composed of amorphous carbon (large D and G band widths and high D3/G ratios). This is also confirmed by the low temperature combustion determined by TPO analysis (Figure 4.25), which is consistent with that of amorphous carbon structures.

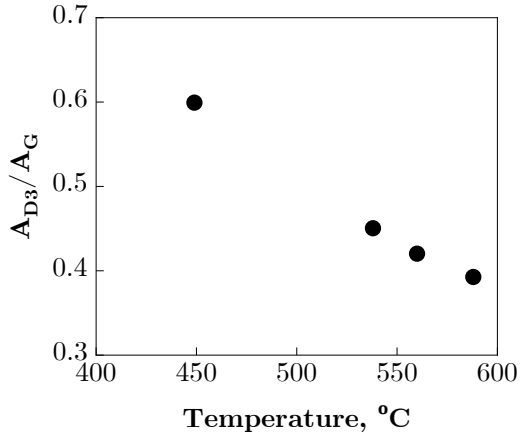

Figure 4.27. Linear correlation between the A_{D3}/A_G ratio and the combustion temperature corresponding to the maximum TPO peak.

Table 4.5. Results of Raman spectra deconvolutions for the used dolomite.

Reactor type	D width	G width	A_D/A_G[1]	I_D/I_G[2]	A_{D3}/A_G[1]	I_{D3}/I_G[2]
PBR	166	60.7	1.69	0.619	0.566	0.212
FBR	143	58.0	1.30	0.529	0.607	0.197

[1] Calculated from the deconvoluted band areas.
[2] Calculated from the deconvoluted band height.

4.2.3. Discussion

The results show that the fluid dynamic regime in the reactor significantly affects oxygenates conversion, products yields and catalyst stability in the SR and SESR of raw bio-oil. Presumably, the bubbling and slugging phenomena can occur in the fluidized regime, causing a fraction of the gas feed to bypass the catalyst particles and remain unreacted, which decreases the conversion and products yields. Likewise, both the fluid dynamic regime in the reactor and the reforming strategy (SR or SESR) greatly affects coke deposition (quantity and nature), which is related to catalyst stability. This section mainly discusses this latter complex effect on the coke formation and incidence on the catalyst deactivation.

In general, coke is deposited on the external and internal surface of the Ni/Al_2O_3 catalyst particles. The internal coke is related to amorphous carbon (LT-coke) formed from oxygenates decomposition/cracking reaction whereas the external coke is related to developed carbon structures of carbon filaments and spheres (HT-coke) mostly formed from CH_4/hydrocarbons decomposition and Boudouard reactions.

In the SR runs, coke is deposited on both the external and internal surfaces of the catalyst particles in the PBR, whereas coke is preferentially deposited on the internal surface of the catalyst particles in the FBR. This difference on the preferential location of coke in the catalyst particles may be due to a phenomenon of catalyst "rejuvenation" in the FBR, which consists of favouring the coke gasification on the external surface because the particles are constantly moving in the bed, being in contact with a gaseous stream that favours its partial

gasification and/or hinders the development of carbon filaments. Likewise, the external coke formed in the PBR is composed of carbon filaments and spheres, whereas that formed in the FBR is composed of solely carbon filaments. The formation of carbon spheres may be due to the favoured development of these carbon structures in a static bed, whereas the moving particles in the FBR partially stop this development together with the occurrence of the "rejuvenation" phenomenon. The results confirm that the use of a FBR is adequate to stop the formation of HT-coke at the temperature of this study (600 °C), which is suitable for maximising CO_2 capture in the SESR run [207].

In the SESR runs, the presence of dolomite has different effects on the coke deposition according to the reactor type. In the PBR, dolomite presumably acts as a guard catalyst as the yield of coke on the catalyst decreases. Dolomite is able to catalyse the oxygenates decomposition/cracking reaction [265, 266], thus competing with the Ni catalyst, and then part of the carbon fed remains as amorphous carbon (LT-coke) on the dolomite. Likewise, dolomite contribute to prevent the formation of carbon spheres in the duration of the reaction run tested in this work, which contributes to prolong the period of pseudo-stable activity in comparison with the SR process. This may be due to the fact that this HT-coke mainly comes from the by-products (negligible at the beginning of the reaction run because the CO_2 capture shifts the reactions equilibria towards the formation of H_2 and CO_2), which slows down the development of carbon structures. In the FBR, the presence of dolomite seems to favour the formation of carbon filaments (HT-coke) in comparison with the SR process, apparently lessening the effect of dolomite as a guard catalyst that occurs in the PBR. This effect of dolomite in the FBR may be due to two phenomena: i) dolomite favours the formation of carbon filaments from CH_4, hydrocarbons and CO originated from oxygenates decomposition/cracking reaction in the presence of dolomite, and the vigorous contact between dolomite and all catalyst particles in the FBR accelerates the mechanism of formation of these filaments upon the catalyst; ii) moreover, dolomite, especially when saturated, competes for the water adsorption preventing the "rejuvenation" effect expected in the FBR.

The correlation between the coke nature/quantification and the catalyst deactivation is unclear for all the scenarios studied in this work. Presumably, the formation of LT-coke (amorphous carbon) may contribute to block the Ni sites in the internal surface of the catalyst particles in the SR of bio-oil in the FBR, which causes a slow deactivation, while a major part of the Ni sites in the external surface remains available for the reaction. However, the faster catalyst deactivation in the PBR may be related to the formation of carbon spheres (HT-coke) because these structures may encapsulate Ni sites [349] and their volume may block the access to the pores. Although carbon filaments (also part of the HT-coke) are commonly regarded as non-deactivated coke species because they typically follow a tip-growth mechanism, a base-growth mechanism is also likely to take place that can cause catalyst deactivation [349]. Thus, it is probably that the formation mechanism of carbon filaments has changed to a base-growth mechanism in the SESR process, in which Ni sites remain attached to the support and the filaments grow from them causing an encapsulation. Thus, the HT-coke composed of carbon filaments or spheres may cause catalyst deactivation depending on the growth mechanism.

4.3. EFFECT OF CONDITIONS AND CYCLIC OPERATION WITH $NiAl_2O_4$/DOLOMITE SYSTEM

This section deepens into the performance of the catalyst prepared by reduction of a $NiAl_2O_4$ spinel together with dolomite as a CO_2 sorbent in the SESR of raw bio-oil in a FBR. On the one hand, the effect of different operating variables (reaction temperature, dolomite/catalyst mass ratio and space time) is analysed (sections 4.3.1 and 4.3.2). On the other hand, the performance of the system operating in reaction-regeneration cycles has been analysed (sections 4.3.3 and 4.3.4), due to the ongoing challenge of establishing suitable reaction conditions for stable cyclic operations in the SESR of bio-oil.

4.3.1. Behaviour under different conditions

The effect of operating conditions on the reaction indices in the SESR of bio-oil both in the CO_2 capture period (time on stream, 50 min) and after dolomite saturation (time on stream, 300 min) are presented in this section, in order to analyse the activity and stability of the $NiAl_2O_4$/dolomite system. The focus is mainly on the effect of temperature, but the effect of sorbent/catalyst mass ratio and space time are also addressed, considering the relationship between the influences of these variables.

Figure 4.28 compares values of product distribution results in the CO_2 capture period of the SESR runs (for values of sorbent/catalyst mass ratio of 10 and 20) and at zero time in the SR runs (sorbent/catalyst mass ratio of 0) at different temperatures in the 550-700 °C range, with S/C ratio of 3.4 and space time of 0.15 $g_{catalyst}{\cdot}h/g_{oxygenates}$, whereas Figure 4.29, Figure 4.30 and Figure 4.31 show the evolution with TOS of conversion and product yields for the different temperatures in the SR run and in the SESR runs with sorbent/catalyst mass ratio of 10 and 20, respectively. A low space time (0.15 $g_{catalyst}{\cdot}h/g_{oxygenates}$) was used to better appreciate the effect of temperature on the catalyst stability in the post-saturation period in these three latter figures.

In Figure 4.28, the values of SESR runs are average values over the CO_2 capture period, whereas, as previously mentioned, the values of SR run (with a noticeable deactivation, as shown in Figure 4.29) correspond to zero time on stream. Light hydrocarbons (C_aH_b) yield is not shown because it is not significant for all the reaction conditions studied. In the SR runs (solid lines in Figure 4.28), increasing the temperature increases the H_2 yield (from 58 % at 550 °C to 81 % at 700 °C), as the reforming of oxygenates and CH_4 is favoured. Consequently, the yield of CH_4 is negligible at 700 °C. The CO yield increases with increasing temperature as a consequence of favouring the reverse-WGS reaction.

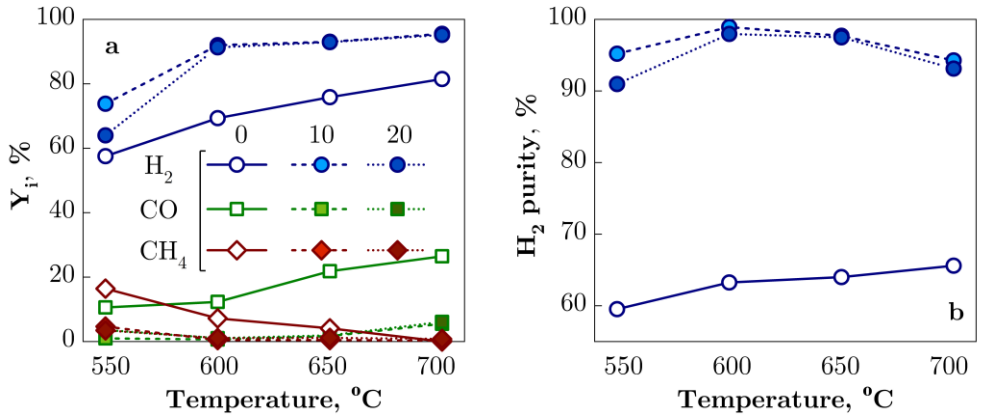

Figure 4.28. Effect of temperature on product yield distribution (H_2, CO and CH_4) (a) and H_2 purity (b) in the CO_2 capture period for different sorbent/catalyst mass ratio (0 (SR), 10 and 20). Space time, 0.15 $g_{catalyst}$·h/$g_{oxygenates}$; S/C ratio, 3.4.

In the SESR runs (dashed and dotted lines in Figure 4.28), the temperature also affects the CO_2 adsorption equilibrium, which becomes unfavourable as the reaction temperature increases. In the studied range, the increase in temperature favours the formation of H_2, whose yield increases from 74 % to 92 % between 550 and 600 °C for a sorbent/catalyst mass ratio of 10 (Figure 4.28a). It is noteworthy that at 600 °C the reforming of CH_4 is almost complete with a yield of less than 1 %. Above this temperature, the yield of H_2 increases only slightly, despite the increase in oxygenate conversion (Figure 4.29a). This result is explained by the fact that the CO_2 capture by dolomite is unfavourable above 600 °C [207]. Thus, at 650 and 700 °C, the capture capacity of the sorbent decreases slightly, as observed in the pre-breakthrough period in Figure 4.30c and Figure 4.31c. The yield of CH_4 remains almost null in the CO_2 capture period above 600 °C, despite the promotion of its formation by cracking/decomposition reaction of oxygenates (Eq. (1.16)) by dolomite, which is explained by the high activity of the Ni/Al_2O_3 catalyst for its SR at these temperatures [96]. Nevertheless, the CO yield (which is less than 1 % at 600 °C) increases slightly to 6 % at 700 °C with a sorbent/catalyst mass ratio of 10 due to the promotion of the reverse-WGS reaction with increasing temperature, which leads to a decrease in H_2 purity at high temperatures (Figure 4.28b).

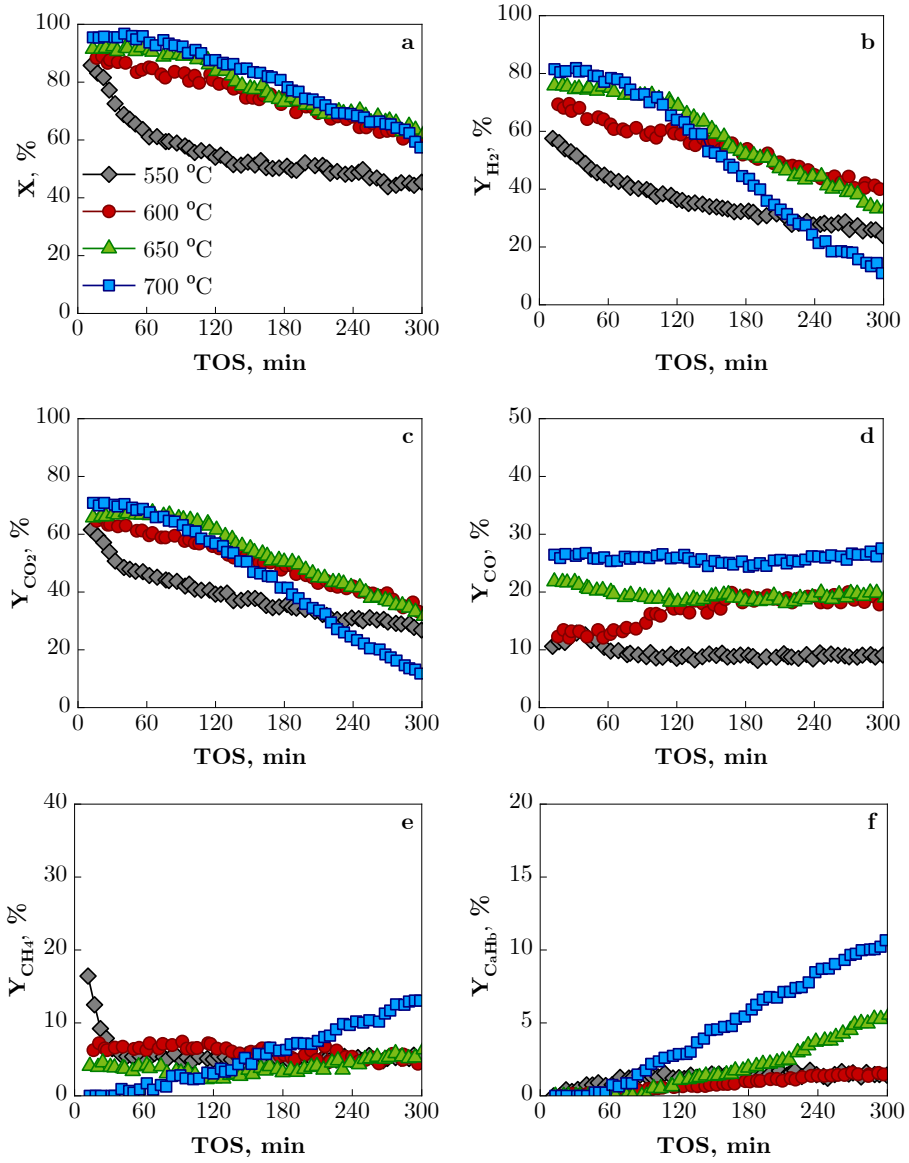

Figure 4.29. Effect of temperature on the evolution with TOS of conversion (a) and yields of H_2 (b), CO_2 (c), CO (d), CH_4 (e) and C_aH_b (f) in the SR run. Space time, 0.15 $g_{catalyst}{\cdot}h/g_{oxygenates}$; S/C ratio, 3.4.

For a sorbent/catalyst mass ratio of 20 (dotted lines in Figure 4.28), the product yields in the CO_2 capture period are almost equal to those obtained for a sorbent/catalyst mass ratio of 10, except at 550 °C. At this low temperature, the H_2 yield for a sorbent/catalyst mass ratio of 20 is only 64 % (slightly higher than that obtained in the SR run), which can be attributed to the significant deactivation of the catalyst along the CO_2 capture period in the SESR run with high dolomite loading, as observed in Figure 4.31. This catalyst deactivation is due to the activity of the dolomite for decomposition/cracking of oxygenates [297], favoured by the low extent of the SR reactions at this low temperature for this low space time.

In Figure 4.30 and Figure 4.31 the three aforementioned periods for the SESR reactions are observed: pre-breakthrough (with CO_2 capture), breakthrough (dolomite saturation) and post-breakthrough. In the conditions of Figure 4.30 (dolomite/catalyst mass ratio of 10), the duration of the pre-breakthrough period is around 30 min above 600 °C and it has slightly longer duration at 550 °C (Figure 4.30c). The duration of this period is doubled when twice the sorbent/catalyst ratio is used (Figure 4.31).

The evolution of the product distribution with TOS corresponding to the post-breakthrough period (after CO_2 capture) in Figure 4.30 and Figure 4.31 is a consequence of catalyst deactivation and in order to explain the effect of temperature on these trends it is necessary to take into account the different residual activity of the catalyst at the beginning of this period. Moreover, the relationship between the effects of temperature and oxygenate concentration (as coke precursors) on deactivation [164, 266], and the role of dolomite in activating coke formation should be considered [204]. Thus, as mentioned above, at low temperature (550 °C) the catalyst has undergone significant deactivation during the CO_2 capture period because the space time was low to convert all the oxygenates, which explains the subsequent slow decrease in conversion (Figure 4.30a) and yields of H_2 (Figure 4.30b) and CO_2 (Figure 4.30c), and the slow increase in CO yield (Figure 4.30d). These trends indicate that the catalyst/sorbent system has reached a quasi-steady state at this temperature.

Conversely, above 600 °C, the catalyst/sorbent system has a higher remaining activity after the CO_2 capture period and its deactivation is slightly more pronounced with increasing temperature, as observed by the faster decrease in H_2 yield with TOS (Figure 4.30b). This decrease is explained by the attenuation of the SR and WGS reactions, with a consequent increase in the yields of CO (Figure 4.30d), CH_4 (Figure 4.30e) and light hydrocarbons (C_aH_b) (Figure 4.30f). The increase in the extent of decomposition/cracking reactions of oxygenates over dolomite (Eq. (1.16)) with increasing temperature contributes to the increase in the yield of carbonaceous products [266], which explains why the decrease in oxygenate conversion over time (Figure 4.30a) is less pronounced than the decrease in H_2 yield (Figure 4.30b) at high temperature.

When comparing the results of Figure 4.30 (corresponding to SESR with a sorbent/catalyst mass ratio of 10), Figure 4.29 (SR) and Figure 4.31 (SESR with a sorbent/catalyst mass ratio of 20), it is observed that the effect of temperature on catalyst stability is dependent on the presence and content of dolomite. Thus, at low temperatures (550-600 °C), the presence and content of dolomite has a negative effect, leading to catalyst deactivation. At 650 °C, the presence and content of dolomite prolongs the stability period of the catalyst, but after this period, the deactivation is faster than in the SR process, with a rapid decrease in the reaction indices. This deactivation rate is faster for the higher dolomite content (Figure 4.31). Consequently, the H_2 yield after 300 min on stream at this temperature is 33 %, 20 % and 17 % for SR (Figure 4.29b), sorbent/catalyst mass ratio of 10 (Figure 4.30b) and 20 (Figure 4.31b), respectively. On the contrary, at 700 °C, the moderate presence of dolomite (sorbent/catalyst mass ratio of 10) has a positive effect, with the reaction indices decreasing more slowly with TOS than in the SR run (Figure 4.29). This result is explained by the activity of dolomite for SR reactions at this temperature, and also because dolomite deactivates more slowly than the catalyst [265]. However, for a sorbent/catalyst mass ratio of 20, the excess of dolomite favours higher coke formation by decomposition/cracking of oxygenates (Eq. (1.16)), with a consequent increase in the catalyst deactivation rate.

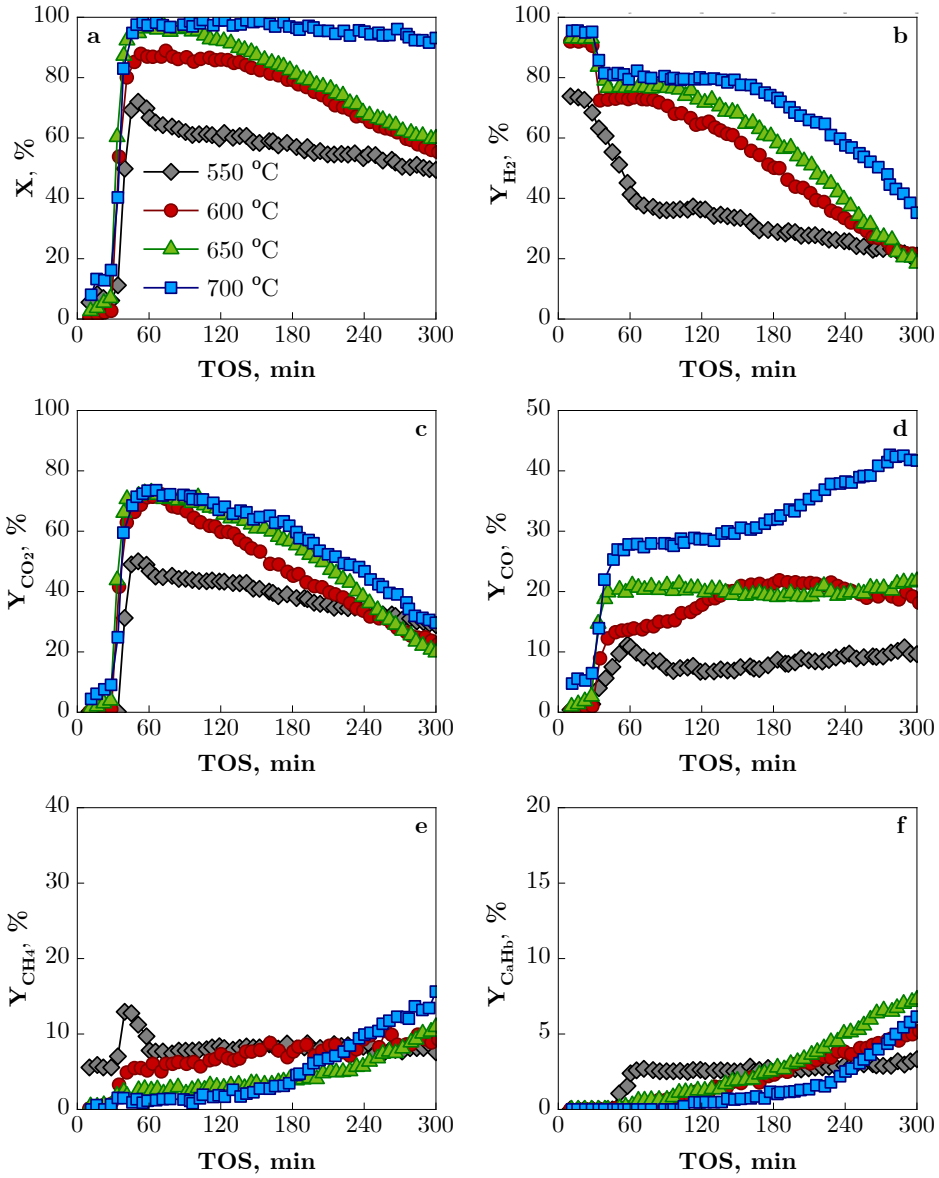

Figure 4.30. Effect of temperature on the evolution with TOS of conversion (a) and yields of H_2 (b), CO_2 (c), CO (d), CH_4 (e) and C_aH_b (f) in the SESR run. Space time, 0.15 $g_{catalyst}$·h/$g_{oxygenates}$; sorbent/catalyst mass ratio, 10; S/C ratio, 3.4.

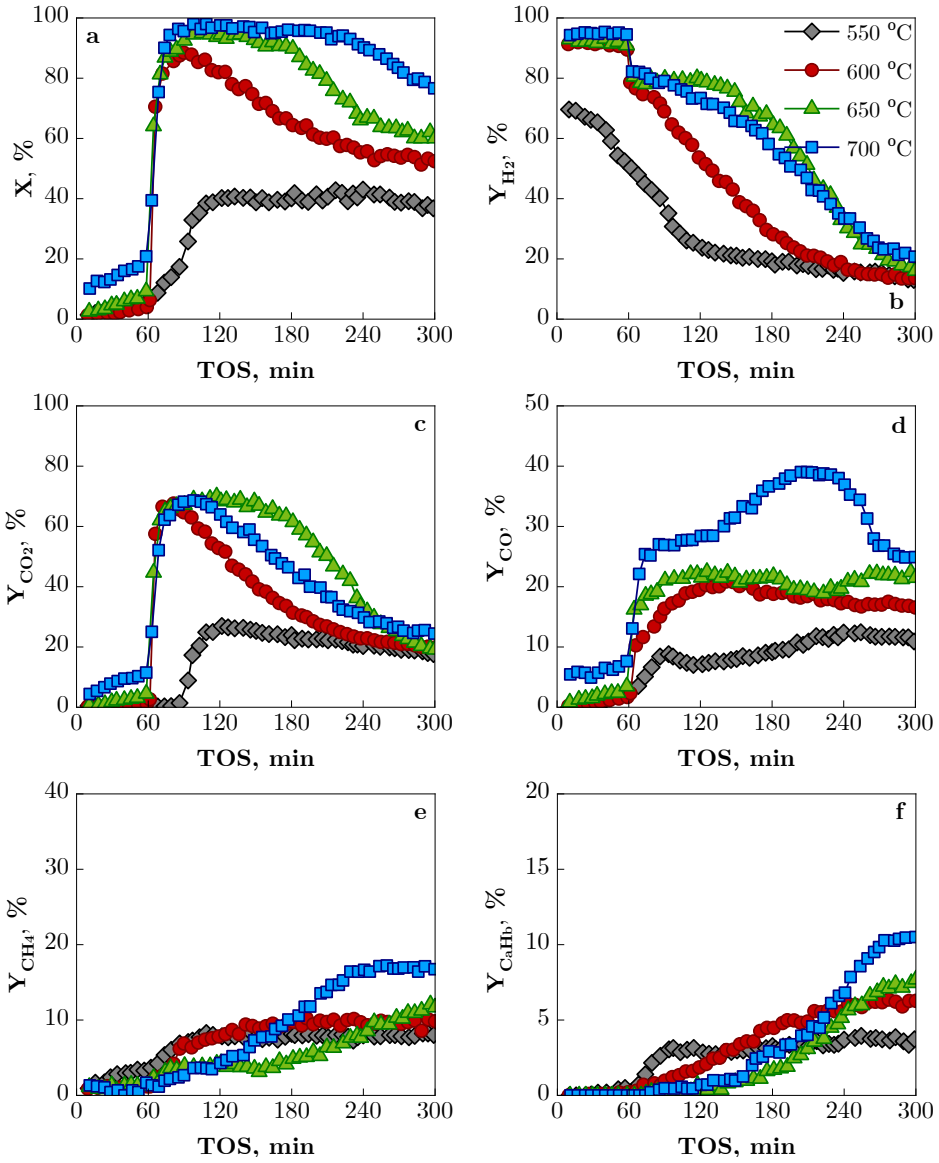

Figure 4.31. Effect of temperature on the evolution with TOS of conversion (a) and yields of H_2 (b), CO_2 (c), CO (d), CH_4 (e) and C_aH_b (f) in the SESR run. Space time, 0.15 $g_{catalyst}$·h/$g_{oxygenates}$; sorbent/catalyst mass ratio, 20; S/C ratio, 3.4.

According to the above results, the best compromise between the reaction temperature and the value of the sorbent/catalyst mass ratio, in order to maximise the yield and purity of H_2, and the stability of the process, corresponds to intermediate values of both variables: 600-650 °C and a sorbent/catalyst mass ratio of 10. At lower temperatures, the rate of the reforming reactions is limited, favouring decomposition/cracking reactions of oxygenates, with higher formation of coke, which deactivates the catalyst, and CH_4 as a by-product. At temperatures above 650 °C, the high H_2 yield is offset by its dilution with CO_2 and CO, due to the lower adsorption capacity of dolomite and the formation of CO favoured by the reverse-WGS reaction. The use of a high sorbent/catalyst mass ratio (of 20 in this study) increases the CO_2 capture time, but has the disadvantage of a lower stability of the Ni catalyst, since it favours the formation of coke by decomposition of oxygenates activated by the dolomite.

In addition to the variables studied above (reaction temperature and sorbent/catalyst mass ratio), the effect of space time was also studied, because the amount of available active catalyst sites affects the extent of reforming and WGS reactions, and consequently the distribution of products and catalyst deactivation. In bio-oil SR, catalyst stability is known to improve with increasing space time values due to the lower concentration of oxygenates in the reaction medium as a result of the higher extent of oxygenate reforming reactions [164, 171]. Figure 4.32 shows the evolution of the reaction indices with time on stream for a high space time of 0.30 $g_{catalyst}{\cdot}h/g_{oxygenates}$ (twice that of Figure 4.30). The results correspond to 600 °C and a sorbent/catalyst mass ratio of 10 (the best conditions previously determined). Comparing the results in Figure 4.32 with the corresponding results in Figure 4.30 at the same temperature, the duration of the CO_2 capture period is now longer (about 50 min compared to 30 min in Figure 4.30) due to the higher content of dolomite in the bed (10 g, compared to 5 g in Figure 4.30). It should be noted that this dolomite content is the same as that used in the runs with a sorbent/catalyst mass ratio of 20 (Figure 4.31), but now with twice the amount of catalyst.

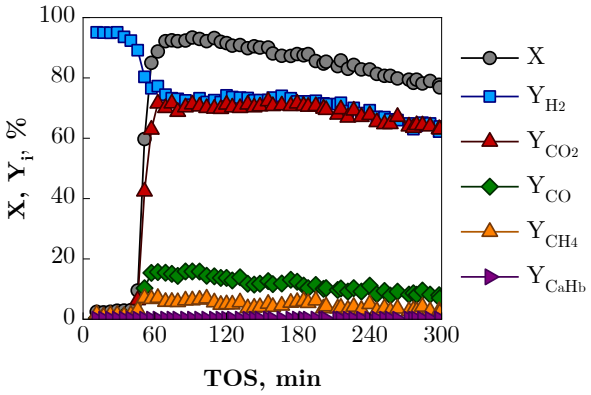

Figure 4.32. Evolution with TOS of carbon conversion and product yields. Temperature, 600 °C; space time, 0.30 $g_{catalyst}$·h/$g_{oxygenates}$; sorbent/catalyst mass ratio, 10; S/C, 3.4.

Comparing the product yields results in the CO_2 capture period in Figure 4.32 and the red curves in Figure 4.30 (those corresponding to 600 °C with half the space time as in Figure 4.32), a significant improvement in H_2 yield and purity is observed with increasing space time, with values of 95 % and almost 100 %, respectively, in Figure 4.32. The combined effect of the increase of the CO_2 capture capacity by increasing the amount of dolomite and of the extent of reforming and WGS reactions by increasing the amount of catalyst contributes to this result. Furthermore, after the CO_2 capture period, it is observed that the stability of the catalyst has increased with increasing space time value. As a result, the H_2 yield remains high (around 72 %) after 5 h of operation.

4.3.2. Characterization of the catalyst and sorbent used under different conditions

The results in section 4.3.1 evidence that the stability of the catalyst depends on the operating conditions. In order to identify the causes responsible for the deactivation and its dynamics during the CO_2 capture periods in Figure 4.30, samples of the catalyst used after 50 min on stream (end of the CO_2 capture period) and after 300 min on stream (end of the runs in Figure 4.30, corresponding to the post-capture period) were analysed using different techniques (TPO, XRD, N_2 adsorption-desorption and SEM). After each reaction, the three components

of the catalytic bed (catalyst/sorbent/inert solid) were separated by sieving, in order to characterize the used catalyst separated from the sorbent and inter solid.

4.3.2.1. Coke deposition

Figure 4.33 shows the TPO profiles and the corresponding coke content (wt%) for the catalyst used at different temperatures. It should be noted that the scale of the two graphs is different. Graph (a) corresponds to the runs performed up to the breakthrough regime with CO_2 capture (50 min on stream), whereas graph (b) corresponds to the catalyst used in the 300 min duration runs (corresponding to the reactions in Figure 4.30). For comparison, the TPO profiles for the catalysts used in the SR runs (without sorbent) are plotted in Figure 4.34. The aforementioned two combustion domains corresponding to coke burning below 500 °C or above 500 °C are observed in Figure 4.33, but with notable differences for the different temperatures, revealing a remarkable effect of the reforming temperature on the coke content and nature in the two groups of runs. For the catalysts used only in the CO_2 capture period (Figure 4.33a), the coke burning below 500 °C (presumably amorphous coke and deposited on the Ni sites) is the only coke fraction at a reforming temperature of 550 °C. As the reaction temperature increases, the total coke content decreases, and so does this amorphous coke fraction, while a fraction burning above 500 °C appears at 600 °C and becomes the predominant fraction above 650 °C. These trends indicate that the deposition of coke is attenuated, but the deposited coke is more refractory as the reforming temperature increases.

Comparison of the TPO profiles in Figure 4.33a and Figure 4.33b shows that at a reforming temperature of 550 °C the nature of the deposited coke is similar, although the coke content increases for the higher TOS (Figure 4.33b). Therefore, at a reforming temperature of 550 °C, there is a rapid deposition of amorphous coke during the CO_2 capture period, which is deposited on the metal sites, its main origin being the decomposition/cracking of oxygenates (Eq. (1.16)), as mentioned in sections 4.1.2.1 and 4.2.2.3. The deposition of the same type of amorphous coke continues for the rest of the reaction at 550 °C (Figure 4.33b),

although more slowly than during the CO_2 capture period. Moreover, it is noteworthy that the content of amorphous coke in Figure 4.33a decreases with increasing temperature, as its gasification is promoted (Eq. (1.22)), whereas the formation of coke burning above 500 °C is favoured, which is related to a more structured coke: filamentous coke, formed by CH_4 decomposition (Eq. (1.20)) and Boudouard reaction (Eq. (1.21)) [255, 259]; or pyrolytic coke, formed by decomposition/cracking of oxygenates (Eq. (1.16))[303].

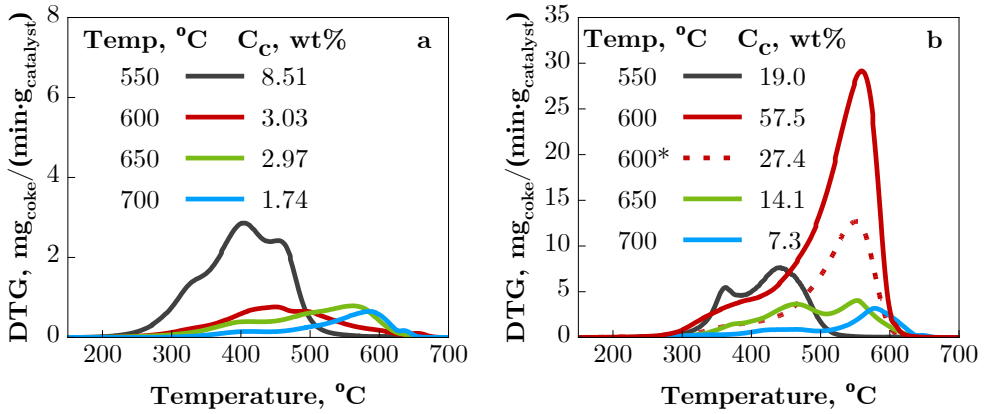

Figure 4.33. TPO profiles and coke content (wt%) for the catalyst used at different temperatures in the CO_2 capture period (50 min on stream) (a) and after 300 min on stream (b). Space time, 0.15 $g_{catalyst}$·h/$g_{oxygenates}$ (* 0.30 $g_{catalyst}$·h/$g_{oxygenates}$ for dashed red line in graph b); sorbent/catalyst mass ratio, 10; S/C, 3.4.

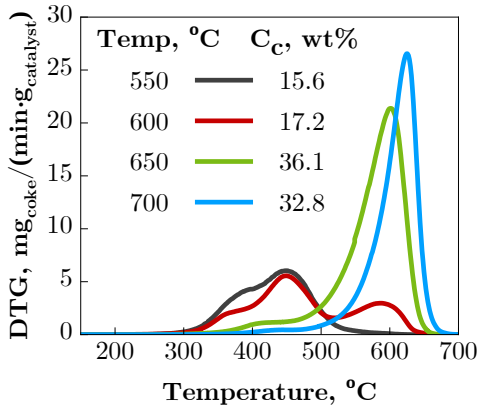

Figure 4.34. TPO profiles and coke content (wt%) for the catalyst used at different temperatures in the SR run. Space time, 0.15 $g_{catalyst}$·h/$g_{oxygenates}$; S/C, 3.4; TOS, 5 h.

The TPO profile for the reforming temperature of 600 °C in the period after CO_2 capture (Figure 4.33b) and the difference of this profile with the one in Figure 4.34, corresponding to the SR (without dolomite) of the bio-oil, reveals a remarkable role of dolomite in the coke deposition at this reforming temperature. In the previous section (section 4.2), this higher deposition of filamentous coke is explained by the synergy of the coke formation mechanism on the catalyst and the dolomite. This synergy is facilitated by the good contact between the two solids in the fluidized-bed reactor, which increases the formation of filamentous coke structures. However, this role of dolomite in coke deposition is not relevant at 650 and 700 °C and the TPO profile shows a similar trend in the different reaction periods (compare green and blue curves in Figure 4.33a and Figure 4.33b). At these temperatures the coke formation mechanisms are limited by gasification, and furthermore, the formation of filamentous coke by Boudouard reaction is disfavoured with increasing temperature. The attenuation of coke deposition above 650 °C is particularly important after the CO_2 capture period, where the formation of structured coke on the catalyst is notably decreased (Figure 4.33b). However, this coke fraction is present in the majority of the SR runs of bio-oil at high temperature (as observed in Figure 4.34). The explanation for the low deposition of structured coke in the SESR runs at high temperature is the contribution of dolomite to the reforming of oxygenates from bio-oil [265], which is evidenced when comparing the results in Figure 4.30a (SESR) and Figure 4.29a (SR). Besides, the activity of dolomite for tar gasification is well established [350, 351], so it is likely to be active in the gasification of coke evolution intermediates. These results in Figure 4.33b and Figure 4.34 (blue curves corresponding to 700 °C) are coherent with the higher stability in the SESR runs compared to the SR runs (compare blue markers in Figure 4.30 and Figure 4.29, respectively). The attenuation of coke deposition on Ni-based catalysts above 700 °C and S/C ratio above 2 has been observed in the literature in the SR of biomass gasification gas [352].

The results of the nature of the coke (amorphous or filamentous) obtained from the TPO analysis were corroborated by SEM images of the catalyst used at selected operating conditions, as shown in Figure 4.35. Thus, in the SEM images

of the catalyst particles used at 600 °C and with a sorbent/catalyst mass ratio of 10 (Figure 4.35c and Figure 4.35d), a high presence of carbon filaments is observed. Conversely, there are no carbon filaments in the catalyst used at 550 °C with a sorbent/catalyst mass ratio of 10 (Figure 4.35a and Figure 4.35b) and the presence of carbon filaments is clearly a minority in the catalyst particles used at 700 °C with a sorbent/catalyst mass ratio of 20 (Figure 4.35e and Figure 4.35f).

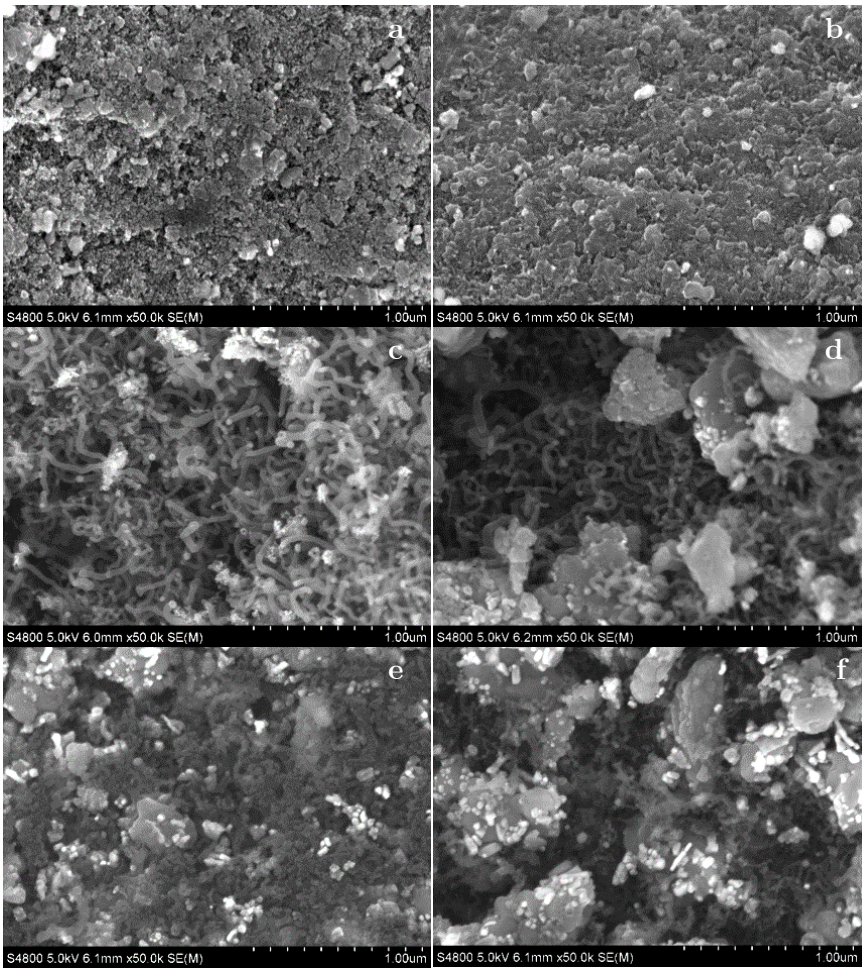

Figure 4.35. SE-SEM images of the catalyst used in the SESR runs with dolomite/catalyst mass ratio of 10 at 500 °C (a,b) and 600 °C (c,d), and with dolomite/catalyst mass ratio of 20 at 700 °C (e,f). Space time, 0.15 $g_{catalyst}{\cdot}h/g_{oxygenates}$; S/C ratio, 3.4; TOS, 5 h.

Regarding the effect of space time on coke deposition, the comparison of the TPO profiles for two space time values at 600 °C (continuous and dashed red lines in Figure 4.33b) confirms the well-known fact that coke deposition in bio-oil reforming is significantly attenuated with decreasing oxygenate concentration (precursors of amorphous coke) [96, 168, 171]. In this case, both amorphous coke and filamentous coke formation are notably attenuated by doubling the space time, as the higher amount of catalyst promotes the reforming of oxygenates, CH_4 and light hydrocarbons.

4.3.2.2. Deterioration of the used catalyst properties

In order to assess the sintering of Ni crystals and the crystalline state of the coke deposits, Figure 4.36 shows the XRD patterns of the catalyst samples used at different temperatures under the conditions of Figure 4.30 and Figure 4.31 (sorbent/catalyst mass ratio of 10 and 20, respectively). Peaks corresponding to Ni^0 and Al_2O_3 crystals are identified, but the presence of NiO is not detected, confirming the high reducing capacity of the reaction medium to maintain the active metal in a reduced state at the different temperatures. The average size of the Ni crystals of the used catalyst samples (Table 4.6) was calculated from the diffraction peak at $2\theta = 51.8°$ using the Debye-Scherrer equation. The estimated value increases slightly in the range of 15–20 nm for the used catalysts compared to the fresh-reduced catalyst (15 nm), indicating no significant sintering phenomenon of the Ni crystals. Consequently, as observed at 600 °C in sections 4.1.2.2 and 4.2.2.1, Ni sintering is not a deactivation cause for this catalyst under SESR conditions over the whole 550-700 °C range, as previously observed under SR conditions [96].

The presence of a broad peak at a diffraction angle of $2\theta = 26°$, corresponding to high crystallinity coke (graphitic carbon), is observed in the catalyst samples used at 600 °C (more pronounced at the lowest space time). This result is coherent with the TPO profiles in Figure 4.33b and the SEM images in Figure 4.35c and Figure 4.35d, and corroborates the structured nature of the main combustion peak in the coke deposited at 600 °C, whose amount decreases significantly with

increasing space time. The absence of the diffraction peak at the angle of 26° in the coke deposited at 550 °C corroborates its amorphous nature. For the catalysts used in the SESR above 650 °C, although some structured coke is deposited according to the TPO profiles (Figure 4.33b), its small amount does not allow it to be detected in the corresponding XRD patterns in Figure 4.36.

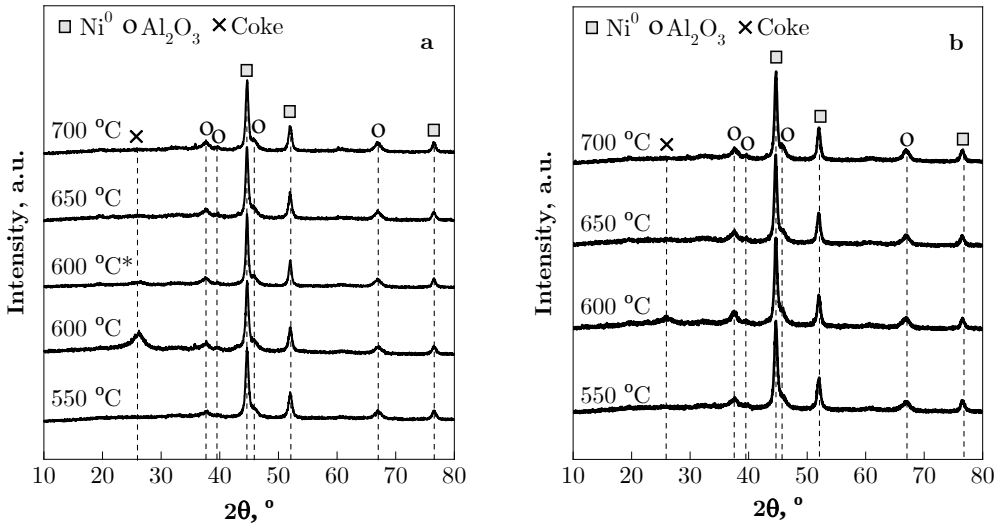

Figure 4.36. XRD patterns of Ni/Al_2O_3 catalyst samples used in the SESR runs at different temperatures. Space time, 0.15 $g_{catalyst}·h/g_{oxygenates}$ (* 0.30 $g_{catalyst}·h/g_{oxygenates}$); S/C ratio, 3.4; TOS, 5h; sorbent/catalyst mass ratio of 10 (a) and 20 (b).

To assess the deterioration of the porous structure of the catalyst, and its contribution to deactivation, N_2 adsorption-desorption isotherms have been obtained for used catalyst samples (Figure B.6 in Annexes), from which the physical properties (BET surface area, pore volume and average pore diameter) have been determined (Table 4.6). All the samples in Figure B.6 show a type IV isotherm, characteristic of mesoporous materials. Similarly to the fresh-reduced catalyst (Figure 2.5a), the samples used at the lower temperature (Figure B.6a) present a hysteresis of the type H2, which is attributed to a difference in mechanism between condensation and evaporation processes occurring in pores with narrow neck and wide bodies. Conversely, a H3-type hysteresis cycle is observed in the isotherms of the catalysts used above 600 °C (Figure B.6c,e,g),

which shows no limiting adsorption at high P/P_0, and is associated to aggregated plate-like particles giving rise to slit-shaped pores [300]. Overall, there is an evolution of mesoporosity with a slight progressive decrease from the highest temperature to 550 °C. For most of the used samples, the total volume adsorbed at high pressures ($P/P_0 \approx 1$) is lower than that of the fresh-reduced sample, demonstrating the partial blockage of the mesopores, which is more pronounced at the lowest reforming temperature and is therefore coherent with a more rapid deactivation (Figure 4.30).

Table 4.6. Physical-chemical properties (average Ni^0 crystal size (d_{Ni}), BET surface area (S_{BET}), pore volume (V_{pore}) and average pore diameter (d_{pore}) of fresh Ni/Al_2O_3 catalyst and samples used in the SESR of raw bio-oil at different temperatures and sorbent/catalyst mass ratio. Space time, 0.15 $g_{catalyst}·h/g_{oxygenates}$; S/C ratio, 3.4.

Sample	**Temperature, °C**	**d_{Ni}, nm**	**S_{BET}, m^2/g**	**V_{pore}, cm^3/g**	**d_{pore}, nm**
Fresh Ni/Al_2O_3	-	15	65.1	0.24	13.1
Used (sorbent/catalyst mass ratio = 10)	550	15	62.3	0.11	7.1
	600	16	69.9	0.18	13.4
	600*	20	79.6	0.25	13.4
	650	16	60.6	0.20	14.4
	700	16	65.0	0.26	15.4
Used (sorbent/catalyst mass ratio = 20)	550	16	58.9	0.13	8.3
	600	16	52.1	0.13	10.8
	650	16	55.5	0.16	12.0
	700	17	57.9	0.21	13.1

* Space time, 0.30 $g_{catalyst}·h/g_{oxygenates}$

For all the reforming temperatures studied, the BET surface area of the used catalyst decreases with increasing dolomite presence, evidencing a partial blockage of the mesoporous structure of the catalysts, which is promoted at higher

sorbent loadings, probably due to the high deposition of a low porosity coke. On the other hand, the increase in BET surface area observed for the used samples at 600 °C (more pronounced at high space time) compared to the fresh-reduced catalyst evidences that there is an additional porosity created by the filamentous coke deposited on these samples. Overall, the average pore diameter and pore volume decrease compared to the fresh-reduced sample (more noticeable at low temperatures, 550 and 600 °C), probably due to the blockage of part of the porous surface. To sum up, the different BET surface area values (higher or lower than those of the fresh-reduced catalyst, depending on the reaction conditions) indicate the formation of both: i) filamentous coke (at 600 °C), which is probably stacked on the surface of the catalyst, causing an increase in the BET surface area, and ii) coke clogging the porous structure, causing a decrease in the BET surface area.

4.3.3. Behaviour in the cyclic operation with joint regeneration of the catalyst and sorbent

The scale-up of the SESR of bio-oil requires the operation in reaction-regeneration cycles, recovering the CO_2 capture capacity of the sorbent (by decarbonation) and reactivating the catalyst (by coke combustion). The challenge is to perform these operations simultaneously and in the same unit, avoiding the technological difficulties of separating and treating the two materials. The $NiAl_2O_4$ spinel-derived catalyst is particularly attractive for this purpose because the spinel is completely reconstructed by coke combustion at high temperature (850 °C, which is necessary for the efficient decarbonation of dolomite) and the subsequent reduction of the reconstructed $NiAl_2O_4$ spinel at 850 °C achieves a good dispersion of Ni crystals on the Al_2O_3 support, recovering the activity of the fresh Ni/Al_2O_3 without the sintering problems of supported Ni catalysts prepared by impregnation [149, 282]. Dang et al. [353] highlighted the regenerability of Ni/Al_2O_3 derived from $NiAl_2O_4$ spinel in the dry reforming of CH_4, explaining the reversible phase change of this catalyst (between $NiAl_2O_4$ and Ni/Al_2O_3) in successive oxidation (coke combustion)/reduction treatments. These authors propose a strategy of surface spatial confinement in γ-Al_2O_3 layers to mitigate the sintering by migration of Ni under high temperature regeneration conditions

(required for high amounts of coke). Also, Du et al. [354] proposed a feasible strategy to regenerate a Ni/Al_2O_3 catalyst deactivated by coke and Ni sintering in the CO methanation reaction by a solid-phase reaction between NiO and Al_2O_3 to form $NiAl_2O_4$ spinel followed by its controlled reduction, as it burns the deposited carbon and redisperses the Ni nanoparticles well.

In this Thesis, the efficiency of the joint reactivation of Ni/Al_2O_3 catalyst derived from $NiAl_2O_4$ spinel and dolomite as sorbent has been studied running 7 reaction-regeneration cycles. The conditions in the reaction step (established by the results in section 4.3.1) are 600 °C, space time of 0.30 $g_{catalyst}{\cdot}h/g_{oxygenates}$ (corresponding to 1 g of catalyst), sorbent/catalyst mass ratio of 10, S/C molar ratio of 3.4 and TOS of 120 min. These conditions allow to operate with a sufficiently high CO_2 capture time (around 60 min), with the appropriate sorbent/catalyst mass ratio of 10. The regeneration step consisted of coke combustion and CO_2 removal in an external oven at 850 °C for 4 h in air atmosphere (enough time for the complete removal of the coke deposits and CO_2). After each regeneration step, the catalyst+sorbent were subjected to a reduction step (at 850 °C for 4 h in H_2-N_2 (7 vol.% H_2)) in order to obtain the active Ni^0 particles. The catalyst samples obtained at the end of some of the reaction steps were characterized using different techniques (section 2.2.2) in order to know the evolution of their properties in the successive cycles.

Figure 4.37 shows the evolution with time on stream of the reaction indices in the 1st reaction step (fresh material) (graph a) and in the 7th reaction step (graph b) and Figure 4.38 shows the evolution of the H_2 yield in the CO_2 capture period in the successive reaction steps. When comparing the 1st and 7th reaction steps, a rather similar performance of the catalysts/sorbent bed is observed, indicating a good overall recovery in the regeneration step of both, the catalyst activity and the CO_2 sorption capacity of the dolomite. Nevertheless, the H_2 yield in the 7th reaction step is slightly lower than that obtained with the fresh catalyst in the 1st reaction, and a small CH_4 yield is observed in the CO_2 capture period. As observed in Figure 4.38, this slight decrease in H_2 yield in the CO_2 capture period occurs in the 2nd and 3rd reaction steps (after the first and the second regeneration,

respectively), but the catalyst/sorbent bed reaches a stable performance from the 3rd reaction step onwards.

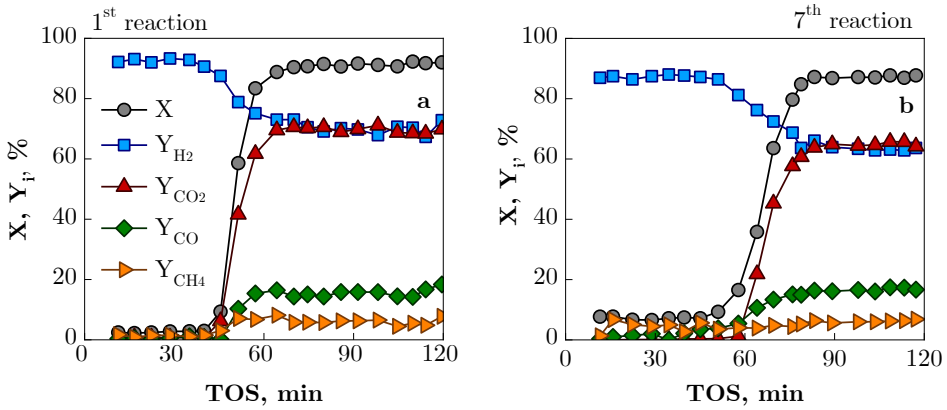

Figure 4.37. Evolution with TOS of carbon conversion and product yields in the 1st (a) and 7th (b) reaction steps (with intermediate regenerations). Reaction conditions: 600 °C; space time, 0.30 $g_{catalyst}$·h/$g_{oxygenates}$; sorbent/catalyst mass ratio, 10; S/C ratio, 3.4. Regeneration conditions: calcination with air in an external oven at 850 °C for 4 h.

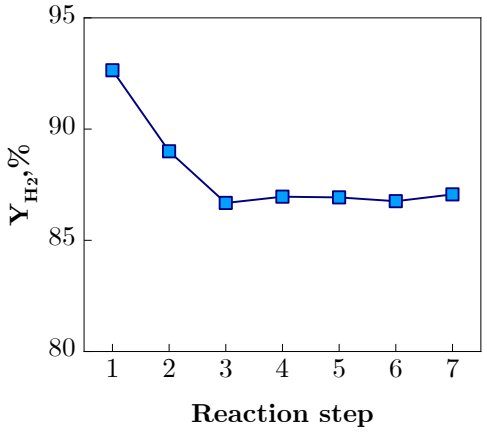

Figure 4.38. Evolution of H_2 yield in the CO_2 capture period in successive reaction steps (with intermediate regenerations). Reaction and regeneration conditions of Figure 4.37.

The possible causes of the decrease in H_2 yield during the CO_2 capture period observed in the first two cycles are the incomplete recovery of the CO_2 sorption capacity of the sorbent and/or of the activity for the reforming and WGS reactions of the catalyst. It is interesting to note that in Figure 4.37 the duration

of the capture period in the 7th reaction step is even slightly longer than in the 1st step, suggesting that the dolomite has fully recovered its CO_2 capture capacity. In order to better identify the material that does not recover its activity, Figure 4.39 shows the evolution of the CO_2 yield over time in different reaction steps (1st, 2nd, 3rd and 7th). It can be observed that the duration of the CO_2 capture period is shorter in the first cycles and remains constant and longer after the third cycle. Consequently, the decrease in H_2 yield during the CO_2 capture period in the first cycles (Figure 4.38) can be attributed to the irreversible deactivation of the catalyst. Thus, lower activity for the reforming and WGS reactions results in lower net CO_2 formation, which may explain the slight increase in the CO_2 capture period duration observed in Figure 4.39 from the third cycle onwards. The lower catalyst activity also explains why complete reforming of CH_4 is not achieved during the CO_2 capture period in the last reaction steps (Figure 4.37b). Moreover, the results in Figure 4.39 evidence that subjecting the dolomite jointly with the catalyst to the successive reduction steps, prior to each reaction, does not have a negative impact on the performance of the dolomite.

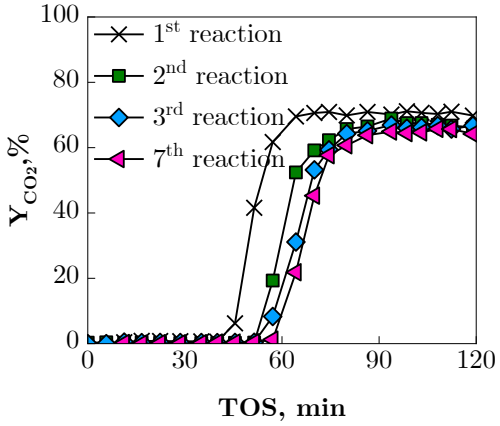

Figure 4.39. CO_2 yield with TOS in successive reaction steps (with intermediate regenerations). Reaction and regeneration conditions of Figure 4.37.

In view of the above results, the behaviour of the system composed of Ni/Al_2O_3 catalyst derived from $NiAl_2O_4$ spinel and dolomite in the SESR of bio-oil in successive reaction-regeneration cycles is quite satisfactory, as it allows a reproducible performance from the 3rd reaction cycle onwards. The slight loss of catalyst activity observed between the first two reaction-regeneration cycles suggests a deterioration of the catalyst properties (as shown in the next sections), but the catalyst reaches an apparent stabilization (constant activity) after two reaction-regeneration cycles.

4.3.4. Characterization of the catalyst used in the cyclic operation

The catalyst used in some reaction steps and also the catalyst regenerated after the 7th reaction were characterized by several techniques (TPO, TPR, XPS and XRD) in order to analyse the possible changes in the physical-chemical properties of the catalyst along the cyclic operation and to correlate them with the kinetic performance observed in section 4.3.3.

4.3.4.1. Coke deposition

Figure 4.40 depicts the TPO profiles of the catalyst samples used after the 1st and 7th reaction steps. For both samples there is a major combustion peak burning above 500 °C that corresponds to structured coke, with a low amount of amorphous coke burning below 500 °C. The coke content decreases in the successive reaction steps (from 17.2 wt% in the first reaction to 12.8 wt% in the seventh reaction), especially the structured coke, whereas the amorphous carbon remains fairly constant. The difference in coke deposition in Figure 4.40 is consistent with the slightly lower catalyst activity observed after the first two reaction-regeneration cycles (Figure 4.38).

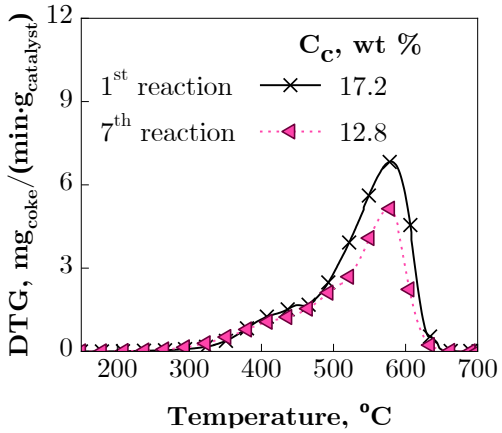

Figure 4.40. Comparison of the TPO profiles and coke content (wt%) deposited on Ni/Al_2O_3 catalyst samples used in the 1st and 7th reaction steps.

4.3.4.2. Deterioration of the catalyst properties

Figure 4.41 shows the TPR profiles of the fresh catalyst and the catalyst regenerated after the 7th reaction step. Both samples require a high temperature for the complete reduction of all the Ni species, consistent with the predominant presence of the $NiAl_2O_4$ spinel structure in the fresh and the regenerated catalysts.

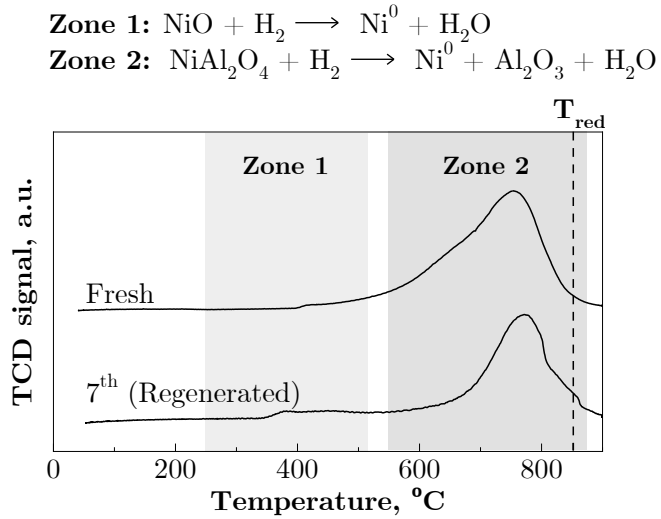

Figure 4.41. TPR profiles of fresh catalyst and regenerated after the 7th reaction step.

The TPR profile of the fresh catalyst shows a broad and asymmetric reduction peak between 500 and 900 °C, with its maximum at 750 °C. The regenerated catalyst has a similar TPR profile to the fresh catalyst, but shows a more symmetrical and slightly less wide reduction peak, which suggests that the reconstructed $NiAl_2O_4$ spinel is more homogeneous. Besides, the maximum is shifted to a higher reduction temperature (peak at 775 °C), that is, a higher temperature is required for the complete reduction of the reconstructed Ni spinel structure in the regenerated catalyst. Moreover, a small content of NiO species is also observed in the 300-500 °C range of this sample, which means that the spinel is not fully restored after successive reaction-regeneration steps.

The Ni content of the regenerated catalyst after the 7^{th} reaction step was quantified by H_2-TPR treatment carried out in a thermobalance (up to 1000 °C to ensure the complete reduction of Ni) by determining the mass loss associated with the H_2O formed. The calculated Ni content (29.1 wt%) is practically the same as that determined for the fresh catalyst (30.7 wt%), showing that there is no significant loss of Ni in the successive reaction-regeneration cycles. XPS analysis (Table 4.7) was also used to quantify the changes in surface Ni content on the fresh and reconstructed spinel after reaction-regeneration cycles. It is noteworthy that the surface Ni content of the fresh spinel is slightly lower than its average Ni content, indicating that the Ni crystals will not be completely uniformly distributed on the catalyst particle after the spinel reduction, with the internal Ni content being slightly higher than that on the surface of the particle. Moreover, the external Ni content decreases slightly after the first two reaction-regeneration cycles and then remains almost constant in the subsequent reaction steps. This result suggests that there is a slight redistribution of Ni towards the interior of the catalyst particle after the first two reaction-regeneration cycles, but a stable and fully reproducible redispersion of the Ni crystals is achieved in the subsequent cycles. It should be noted that this trend towards a stabilization operating in reaction-regeneration cycles has also been observed in a commercial Ni supported on Ca-Al_2O_3 catalyst used in the in-line SR of pyrolysis volatiles from biomass [355] and high-density polyethylene (HDPE) [356]. However, the remaining activity in the pseudo-stable state is higher in the catalyst used in this

Thesis, which is explained by the aforementioned regeneration capacity of the $NiAl_2O_4$ spinel.

Table 4.7. Surface Ni content evolution on the fresh and reconstructed spinel after successive reaction-regeneration cycles determined by XPS analysis.

Cycle	Ni, wt%
Fresh $NiAl_2O_4$	22.8
1st reaction-regeneration	20.8
3rd reaction-regeneration	17.9
7th reaction-regeneration	18.6

The XRD diffractograms of the used catalyst samples after the 1st and 7th reaction steps are plotted in Figure 4.42. Similar to the samples used at 600 °C in 300 min runs (Figure 4.36), the species identified in the XRD pattern of the catalyst used after the 1st reaction step are Ni^0, Al_2O_3 and some crystalline coke. The decrease in the intensity of the crystalline coke in the XRD diffractograms of the catalyst used in the 7th reaction compared to that of the 1st reaction is consistent with the decrease in the fraction of HT-coke (structured coke) in Figure 4.40. However, the XRD pattern of the sample corresponding to the 7th reaction step shows that some $NiAl_2O_4$ spinel species still remain in the used sample. This result evidences that the spinel structure (reconstructed in the regeneration step, as shown in Figure 4.42) is not completely reduced at the reduction temperature used in the reaction-regeneration cycles (850 °C). However, after reduction of the regenerated catalyst at 900 °C (externally, in a Micromeritics AutoChem II 2920 apparatus), the only species observed are Ni^0 and Al_2O_3, as in the fresh-reduced (at 850 °C) catalyst (Figure 2.8a). This result is in agreement with the TPR results (Figure 4.41) and shows that a higher reduction temperature (> 850 °C) is required for

the complete reduction of the $NiAl_2O_4$ spinel after the joint regeneration of the catalyst/sorbent bed. It should be noted that the Ni^0 crystal size (calculated by the Debye-Scherrer equation from the diffraction peak at $2\theta = 51.8°$) for the catalyst used in the 7th reaction step (14 nm) is even slightly smaller than for the fresh-reduced catalyst (15 nm), confirming that there is no sintering of the Ni^0 crystals under the conditions studied.

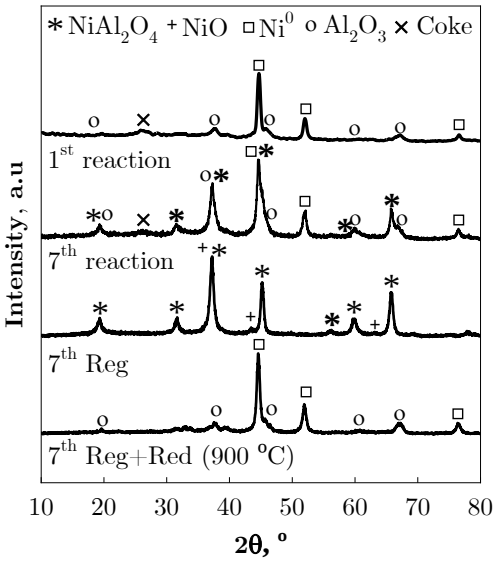

Figure 4.42. XRD pattern of Ni/Al_2O_3 catalyst samples used in the 1st and 7th reaction steps, the catalyst regenerated after the 7th step and after its subsequent reduction at 900 °C.

Therefore, the $NiAl_2O_4$ spinel-derived catalyst and dolomite are suitable for its use in bio-oil SESR, since the catalyst/sorbent bed can be jointly regenerated together at elevated temperature to recover both catalytic activity and CO_2 capture capacity.

Chapter 5

COMBINED STEAM/DRY REFORMING (CSDR) OF RAW BIO-OIL

This Chapter approaches the combined reforming (with steam and CO_2) of raw bio-oil as an efficient route to attain the combined objectives of CO_2 valorization and sustainable production of syngas from biomass with a suitable H_2/CO ratio for the synthesis of chemicals and fuels. Firstly, a thermodynamic analysis of a simulated bio-oil (mixture of individual oxygenated compounds present in a real bio-oil) is performed for different reaction temperatures and feed compositions (S/C and CO_2/C molar ratios). From these results, the range of operating conditions that maximise the syngas yield and those required to produce a syngas with a target H_2/CO ratio have been delimited. The energy requirements of the process for the different configurations have also been calculated. Secondly, an experimental study of the CSDR of a raw bio-oil with a Ni/Al_2O_3 catalyst derived from $NiAl_2O_4$ spinel has been carried out, focusing on the effect of operating conditions (temperature, CO_2/C ratio, S/C ratio and space time) on the conversion of both oxygenates in bio-oil and CO_2, on syngas yield and composition, and catalyst stability.

Part of the results in this Chapter have been published in *Chem. Eng. Trans.* 2023, 99, 355-360 and *J. CO2 Util.* 2023, 72, 102503.

5.1. THERMODYNAMIC STUDY OF THE CSDR OF A SIMULATED BIO-OIL

In this section, the thermodynamic analysis of the CSDR of a simulated bio-oil has been performed at different values of temperature and feed composition (molar ratios of CO_2/C and S/C, referred to C in the bio-oil at the reactor inlet). The simulated bio-oil is composed of 6 typical compounds (acetic acid, hydroxyacetone, 2-methoxyphenol, furfural, ethanol and acetone), which are representative of the majority families of oxygenates in the composition of raw bio-oils (comprising both aqueous and organic fractions). Emphasis has been placed on the capacity of the CSDR of bio-oil for CO_2 valorization and, with this goal in mind, special attention has been paid to delimiting the conditions that allow positive values of CO_2 conversion and/or reduction of CO_2 emissions compared to the conventional SR process (without CO_2 addition). Besides, the operating conditions that maximise the yield of syngas (mixture of H_2+CO) and those required to produce a syngas with a H_2/CO ratio of 1 and 2 have been identified. The energy requirements of the unit have also been considered for all the proposed configurations, as the viability of the process for the industrial implementation requires the production of syngas with a reasonable energy requirement.

5.1.1. Effect of operating conditions on products yields and CO_2 conversion

Figure 5.1 shows the joint effect of temperature and CO_2/C ratio on the yield of H_2 and carbon by-products (graphs a-e), syngas yield (graph f), H_2/CO ratio (graph g) and CO_2 conversion (graph h), at a fixed S/C ratio of 0.5 taken as an example, which is close to the stoichiometric value for a real bio-oil. To appreciate better the effect of the CO_2/C ratio on these reaction indices, Figure A.10 (Annexes) shows their evolution as a function of the CO_2/C ratio, with the temperature as a parameter. Moreover, the joint evolution with temperature of the equilibrium flow rates of products for different feed compositions is depicted in Figure A.11. This type of plot is commonly used in thermodynamic studies of

reforming processes [357, 358], and is useful for understanding the trends in the reaction indices shown in Figure 5.1. From these values of equilibrium products flow rate, the equilibrium constants of the main reactions involved in the process have been evaluated for the whole range of temperatures studied. The results (depicted in Figure A.12) are in total agreement with those previously reported by Caravella et al. [359].

At low temperature, the main products are CH_4 and coke with small yields of H_2, CO_2 and CO, which indicates that strongly endothermic steam reforming reactions hardly occur in these conditions and there is a higher extent of oxygenates cracking and coke formation reactions. As the temperature increases, the yields of H_2 and CO_2 increase until reaching a maximum that is more remarkable and shifts towards lower temperatures with increasing CO_2/C ratio, being located at 600 °C (H_2 yield, Figure 5.1a) and 400 °C (CO_2 yield, Figure 5.1b) for a CO_2/C ratio of 5. Above 400 °C, the yield of CO increases continuously with temperature (more noticeably between 500-700 °C, Figure 5.1c), whereas the CH_4 yield (Figure 5.1d), conversely to CO, decreases with temperature, being insignificant above 800 °C for CO_2/C ratio above 0.5. This effect of temperature on the equilibrium yields of the different products is a consequence of the different impact that this variable has on the equilibrium constants of the reactions involved in the process, mainly on Boudouard reaction (Eq. (1.21)), WGS (Eq. (1.15)) and methane dry reforming (MDR) (Eq. (1.26)). Thus, as observed in Figure A.12, below 500 °C the equilibrium constant for the Boudouard reaction is several orders of magnitude higher than those of the rest of the reactions involved in the process. These values explain that, apart from CO_2 (which is fed to the Gibbs reactor with the oxygenated compounds), coke is by far the major carbon containing compound in the equilibrium at temperatures below 500 °C, as shown in Figure A.11a-Figure A.11c. Nevertheless, the equilibrium constant of the Boudouard reaction decreases more than two orders of magnitude when temperature increases from 500 to 700 °C range (red curve in Figure A.12), whereas the equilibrium constant of the MDR increases three orders of magnitude and the reverse-WGS also increases slightly. These changes in the equilibrium constants explain the rapid decrease in the 500-700 °C range of the yield of CO_2

and coke (Figure 5.1b and Figure 5.1e, respectively), or their equilibrium flow rates (Figure A.11a-Figure A.11c.), together with the parallel rapid increase in CO yield (Figure 5.1c) or its equilibrium flow rate (Figure A.11a-Figure A.11c.). Above 750 °C and in the absence of coke or CH_4, the reaction governing the composition of the products is the reverse-WGS, whose equilibrium constant increases slightly with temperature (blue curve in Figure A.12), which explains the slight decrease in the yields of H_2 and CO_2 at high temperatures.

Regarding the effect of CO_2/C ratio, at high temperatures the coke yield noticeably decreases with increasing CO_2/C ratio (Figure 5.1e), which is the expected result according to Le Châtelier's principle [360], because the addition of the product CO_2 promotes the reverse-Boudouard reaction. Nevertheless, at low temperature the coke formation is promoted with the increase in CO_2/C ratio (Figure 5.1e and blue curve in Figure A.10e). This unexpected result can be explained by the noticeable higher value of the equilibrium constant of the Boudouard reaction at these temperatures over the reverse-WGS and MDR reactions (Figure A.12). Thus, although the increase in CO_2/C ratio promotes the formation of CO through MDR and reverse-WGS reactions, all the CO formed is rapidly converted by Boudouard reaction, which explains the increase in coke yield. The H_2 yield does not change with the CO_2 addition below 600 °C (Figure 5.1a and blue and red curves in Figure A.10a), because the decrease in H_2 yield caused by the promotion of the reverse-WGS reaction due to Le Châtelier's principle is well balanced by the increase due to the promotion of MDR reaction. However, at higher temperatures (where the amount of CH_4 is insignificant (green lines in Figure A.11) due to the high value of the equilibrium constant of MDR, Figure A.12), the H_2 yield decreases continuously with the increase of the CO_2/C ratio (Figure A.10a), which can be explained by the promotion of the reverse-WGS reaction by Le Châtelier's principle. Moreover, the increase in CO_2/C ratio leads to a rapid decrease in the yield of CH_4 (Figure 5.1d and Figure A.10d) due to the promotion of MDR reaction, and also leads to a decrease in the yield of CO_2 (Figure 5.1b and Figure A.10b), in this case by the promotion of both the reverse-Boudouard and the reverse-WGS reactions. Accordingly, the yield of CO increases continuously with the CO_2/C ratio (Figure 5.1c), although the increase

is very small below 500 °C (blue curve in Figure A.10c), due to the previously mentioned prevailing role of Boudouard reaction at low temperatures.

Focusing on the syngas production goal, although the yield of H_2 decreases at high temperature and by increasing the CO_2/C ratio, the syngas yield (Figure 5.1f) continuously increases with both variables, reaching values of 100 % (at lower temperature with increasing CO_2/C ratio). Furthermore, in Figure 5.1g it is observed that the increase of the two variables has a negative effect on the H_2/CO ratio of syngas. For any temperature, the H_2/CO ratio decreases continuously with increasing CO_2/C ratio, with a potential trend (Figure A.10g). Below 600-700 °C (depending on the CO_2/C ratio) the H_2/CO ratio decreases very rapidly with increasing temperature, but remains almost constant at higher temperatures. These trends of the H_2/CO ratio can be explained by Le Châtelier's principle and by the effect of temperature of the equilibrium constants. Thus, the increase in CO_2/C ratio and in temperature promotes the reverse-WGS and reverse-Boudouard reactions, leading to the conversion of CO_2 and H_2 into H_2O and CO, and the conversion of CO_2 and coke into CO, respectively. The increasing CO and decreasing H_2 determine the decrease in H_2/CO ratio. This result determines the use of the syngas produced as raw material in different catalytic processes. Thus, in the methanol and Fischer-Tropsch synthesis, the desired H_2/CO ratio is 2, whereas in other processes such as direct DME synthesis, acetic acid or ethanol formation and oxo-synthesis, the stoichiometric requirement of H_2 is lower and a H_2/CO ratio of 1 is suitable [243–247]. Nevertheless, when syngas is directly used as fuel for power generation (in gas turbines, internal combustion engines or fuel cells) a H_2 rich gas (H_2/CO ratio $\geq$ 50) is required [248]. The results in Figure 5.1g indicate that achieving interesting values of the H_2/CO ratio requires limiting the values of the temperature.

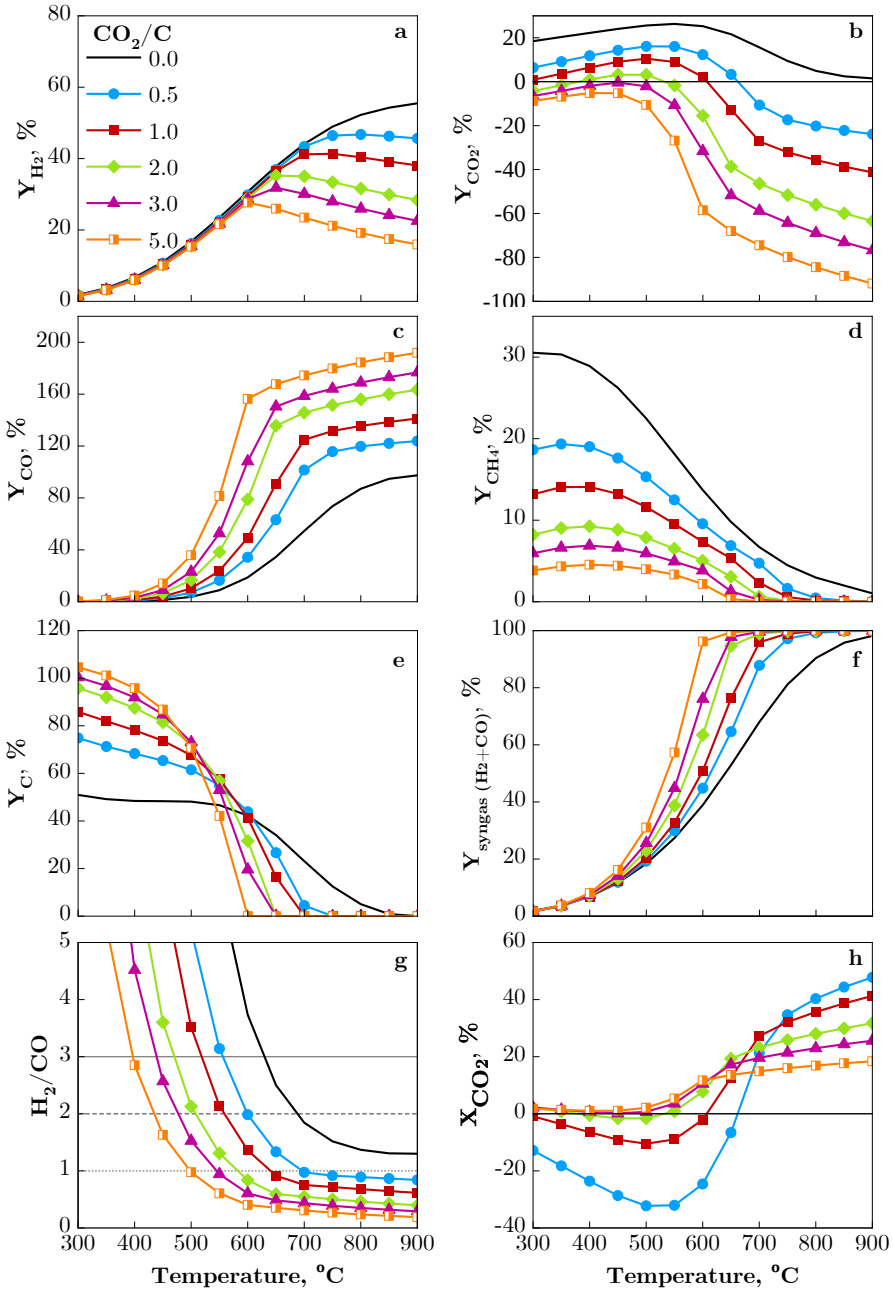

Figure 5.1. Effect of temperature and CO_2/C ratio on products yields (a-e), syngas yield (f), H_2/CO ratio (g) and CO_2 conversion (h), for S/C ratio of 0.5.

Regarding CO_2 yield, a lower CO_2 yield evidences its higher conversion. From the perspective of controlling CO_2 emissions, it is relevant that the yield of CO_2 (Figure 5.1b) reaches negative values as the temperature increases and mainly by increasing the CO_2 addition, indicating the important role it plays as a reactant in the overall reaction scheme under CSDR conditions. In Figure 5.1h positive CO_2 conversions can be observed especially at high temperature. Thus, CO_2 conversions between 15-48 % are obtained above 700 °C at any CO_2/C ratio, with the highest value at 900 °C and CO_2/C ratio of 0.5. These CO_2 conversion values are similar to those reached in the catalytic processes with higher technological development for the valorization of CO_2, such as the synthesis of methanol and DME from syngas with CO_2 co-feeding [361].

Figure 5.2 depicts the evolution of the reaction indices with temperature for different values of S/C ratio, at a fixed CO_2/C ratio of 1.5 taken as an example. To appreciate better the effect of the S/C ratio on these reaction indices, Figure A.13 shows their evolution as a function of the S/C ratio, with the temperature as a parameter. The trends with temperature of all the results in Figure 5.2 are qualitatively the same as those shown in Figure 5.1 (corresponding to S/C ratio of 0.5), and therefore the next comments will be focus on the effect of S/C ratio, which can be mostly explained by Le Châtelier's principle. Thus, the addition of H_2O promotes the SR reactions for oxygenates (Eq. (1.14)) and CH_4 (Eq. (1.17)) and shifts the equilibrium of WGS reaction (Eq. (1.15)). Consequently, the yields of H_2 and CO_2 increase with S/C ratio (as observed in Figure 5.2a and Figure A.13a for H_2 and in Figure 5.2b and Figure A.13b for CO_2), whereas the yield of CO decreases, with a noticeable effect above 550 °C (Figure 5.2c and Figure A.13c). The yield of CH_4 (Figure 5.2d and Figure A.13d) also decreases with increasing S/C ratio in the 550-700 °C range, but below 500 °C it increases with S/C ratio due the thermodynamically favoured methanation reaction (reverse of SR of CH_4, Eq (1.17)). The yield of coke (Figure 5.2e and Figure A.13e) decreases significantly with the increase in S/C ratio, which is consequence of the promoted gasification of coke with H_2O (Eq. (1.22)) and with CO_2 (reverse of Boudouard reaction, Eq. (1.21)). Additionally, the temperature required for null formation of coke and of CH_4 decreases with the increase in S/C ratio.

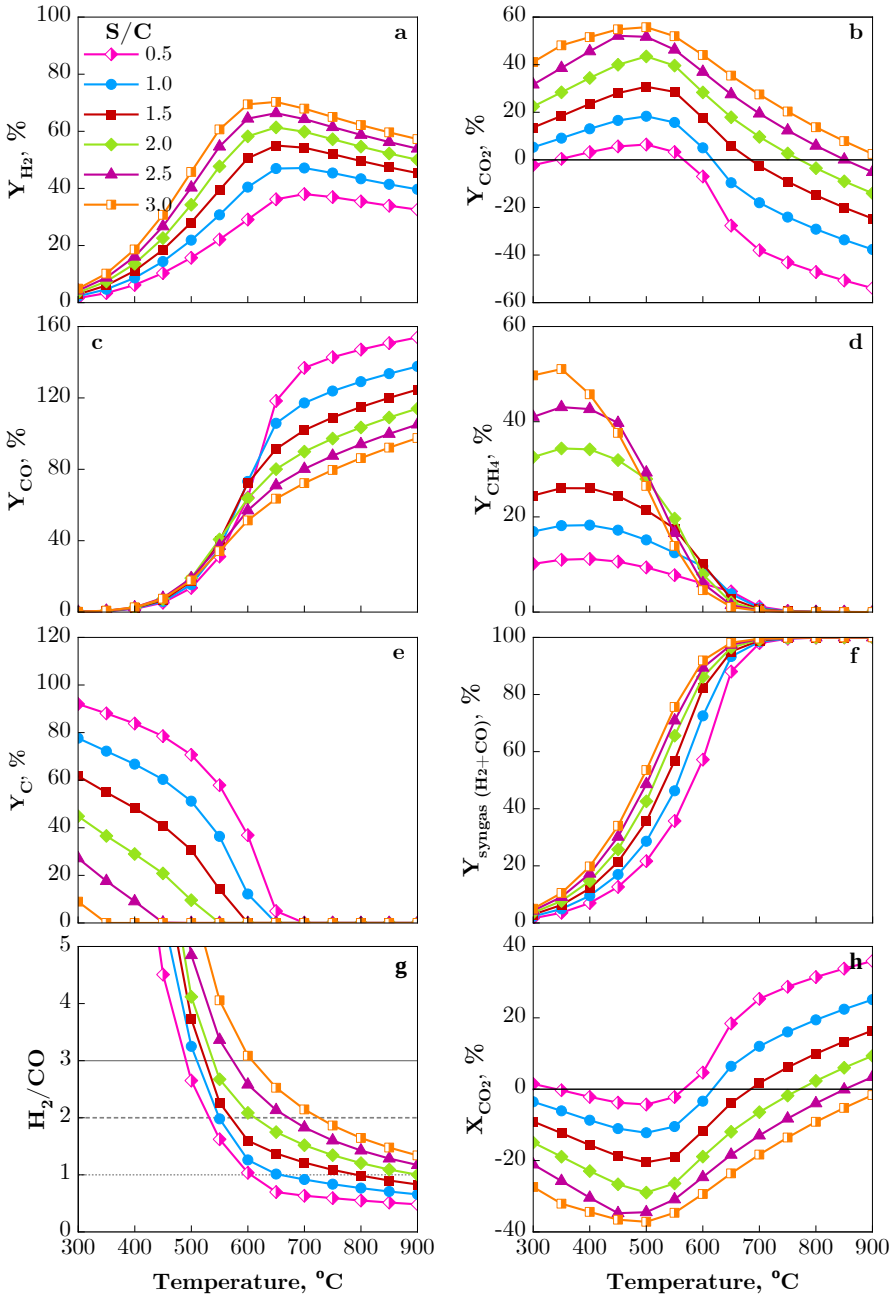

Figure 5.2. Effect of temperature and S/C ratio on products yields (a-e), syngas yield (f), H_2/CO ratio (g) and CO_2 conversion (h), for CO_2/C ratio of 1.5.

In Figure 5.2f it is observed that the syngas yield is 100 % above 700 °C for any S/C ratio. The H_2/CO ratio of syngas (Figure 5.2g) increases with the S/C ratio (almost linearly, as shown in Figure A.13g), but decreases rapidly with increasing temperature (an exponential increase with the inverse of temperature has been found for each S/C ratio, as shown in Figure A.14). Interestingly, under the conditions of Figure 5.2, it is feasible to produce a syngas with a H_2/CO ratio in the 1-2 range, suitable for the applications previously mentioned, while achieving positive CO_2 conversion.

With the temperature increasing, the reverse of WGS reaction (Eq. (1.15)) is promoted, which provokes a decrease in CO_2 yield (Figure 5.2b), attaining negative values for low S/C ratios, which means that the CO_2 fed is being converted. Therefore, at high temperatures, positive CO_2 conversions are achieved when operating with low S/C ratios (< 2.5) (Figure 5.2h). It should be noted that, in this situation, the CSDR process achieves the CO_2 valorization objective by producing syngas with an interesting H_2/CO ratio. Thus, a H_2/CO ratio of 1 with a CO_2 conversion close to 10 % is obtained at 700 °C, 800 °C and 900 °C with S/C ratios of 1.15, 1.5 and 2.0, respectively.

Considering the current interest in low environmental impact technologies, it is relevant to analyse the reduction of CO_2 emissions (R_{CO2}) in the CSDR process compared to the conventional SR unit. The results are plotted in Figure 5.3. In spite of the negative CO_2 conversion in some conditions at low temperature, there is a reduction of CO_2 emissions in the CSDR respect to SR process in the whole range of conditions studied. R_{CO2} increases with the increase in temperature above 550 °C. The qualitative evolution with temperature of the values of R_{CO2} in Figure 5.3 is opposite to the evolution of CO_2 yield (Figure 5.1b and Figure 5.2b). Thus, at low temperatures, R_{CO2} decreases slightly with temperature until a minimum is reached (in the 400-500 °C range, depending on the feed composition), and then it increases sharply in the 500-700 °C range due to the sharp decrease in the equilibrium constant of the Boudouard reaction (Eq. (1.21)), which leads to a sharp decrease in the yield of CO_2. Subsequently, R_{CO2} increases slightly for temperatures above 700 °C due to the slight increase with temperature in the

equilibrium constant of the reverse-WGS reaction (reverse of Eq. (1.15)) (Figure A.12), which involves a further slight decrease in the yield of CO_2. These trends of R_{CO2} values are similar to those observed for CO_2 conversion in Figure 5.1h and Figure 5.2h, for different values of CO_2/C ratio and S/C ratio, respectively, evidencing a relationship between both reaction indices. This relationship is more clearly visualized in Figure A.15, which shows the change in R_{CO2} as a function of X_{CO2} conversion for the range of positive conversions. As observed in this figure, the reduction of CO_2 emissions increases almost linearly with the CO_2 conversion, with this relationship being highly dependent on the CO_2/C ratio (the higher the CO_2/C ratio, the lower the reduction of CO_2 emissions, as shown in Figure A.15a), but with little dependence on the S/C ratio (Figure A.15b).

Regarding the effect of feed composition on the values of R_{CO2}, it is observed in Figure 5.3 that the effect of the CO_2/C ratio (Figure 5.3a) is more important than the effect of the S/C ratio (Figure 5.3b), but it should be noted that this difference could be attributed to the definition of this reaction index, that includes the flow rate of CO_2 fed to the reactor. The increase in both ratios leads to a lower value of R_{CO2}, coherently with the decrease in X_{CO2}, indicating that the difference between the emissions of the CSDR and SR processes decreases with the increase in both CO_2/C and S/C ratios.

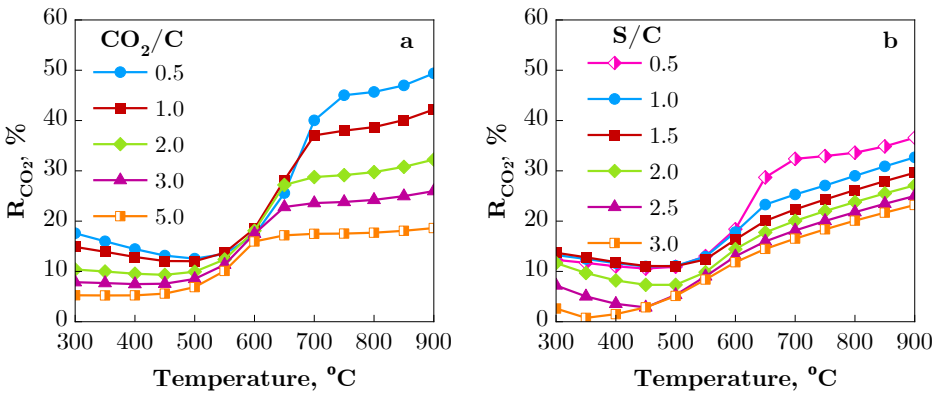

Figure 5.3. Effect of temperature on the reduction of CO_2 emissions in the CSDR of bio-oil compared to the conventional SR (R_{CO2}) for different CO_2/C ratios (a, with S/C ratio of 0.5) and different S/C ratios (b, with CO_2/C ratio of 1.5).

5.1.2. Effect of operating conditions on energy requirements

Figure 5.4 shows the effect of temperature on the reaction heat (ΔH_r) (graphs a and b) and heat exchangers duty (ΔH_{HE}) (graphs c and d) for different CO_2/C ratios with S/C ratio of 0.5 (graphs a and c) and different S/C ratios with CO_2/C ratio of 1.5 (graphs b and d). As expected, at low temperature (below 450-550 °C, depending on the feed composition) the process is exothermic for all the feed compositions (Figure 5.4a-b), due to the predominance of methanation, cracking and Boudouard reactions, and becomes endothermic with increasing temperature (predominance of dry/steam reforming reactions). The curves for ΔH_r (Figure 5.4a-b) show a sigmoidal behaviour with increasing temperature, so that their values hardly vary with temperature above 700 °C for any CO_2/C or S/C ratio. Above 450 °C, the values of ΔH_r increases along with the CO_2/C ratio (Figure 5.4a), more notably in the 550-650 °C range, because at high temperatures the promoted reactions by the excess of CO_2 are the DR of oxygenates (Eq. (1.25)) and methane (Eq. (1.26)), and the reverse of both WGS and Boudouard reactions (Eqs. (1.15) and (1.21), respectively). The effect of the S/C ratio on the ΔH_r varies with temperature (Figure 5.4b). Below 650 °C, ΔH_r increases with the S/C ratio, but the opposite occurs above 650 °C. This opposite effect of the S/C ratio is because at low temperatures the excess of water preferably favours endothermic reactions of SR, whereas at high temperatures the reaction promoted is the exothermic WGS reaction [317]. Besides, the heat exchangers duty increases with temperature (linearly) and with the CO_2/C or S/C ratios (Figure 5.4c and Figure 5.4d, respectively).

Figure 5.4a-b show that the temperature required to get a thermoneutral CSDR process (with $\Delta H_r = 0$) decreases with increasing both CO_2/C and S/C ratios. The thermoneutrality condition is important for the viability of the process and has been studied in detail. Figure 5.5 presents the combination of temperature and CO_2/C (graph a) or S/C (graph b) ratios for the thermoneutral regime. The zone above this curve corresponds to an endothermic regime, whereas the area below, to an exothermic regime.

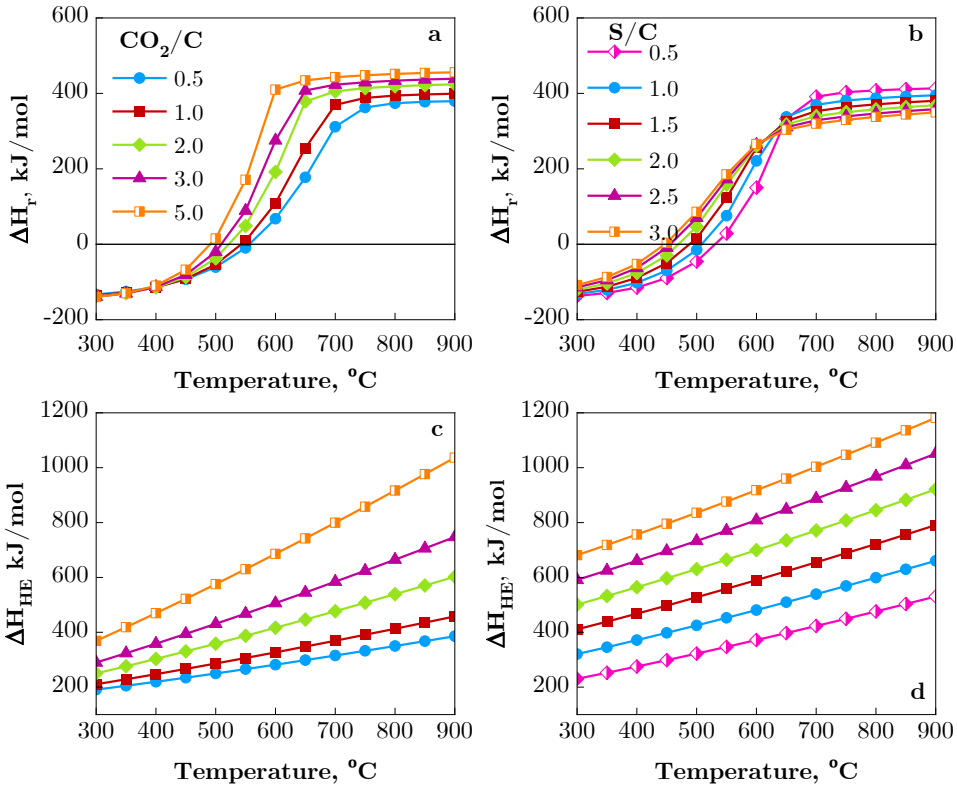

Figure 5.4. Effect of temperature on the reaction heat (ΔH_r) (a and b) and on the heat exchangers duty (ΔH_{HE}) (c and d) for different CO_2/C ratios (a and c, with S/C ratio of 0.5) and for different S/C ratios (b and d, with CO_2/C ratio of 1.5).

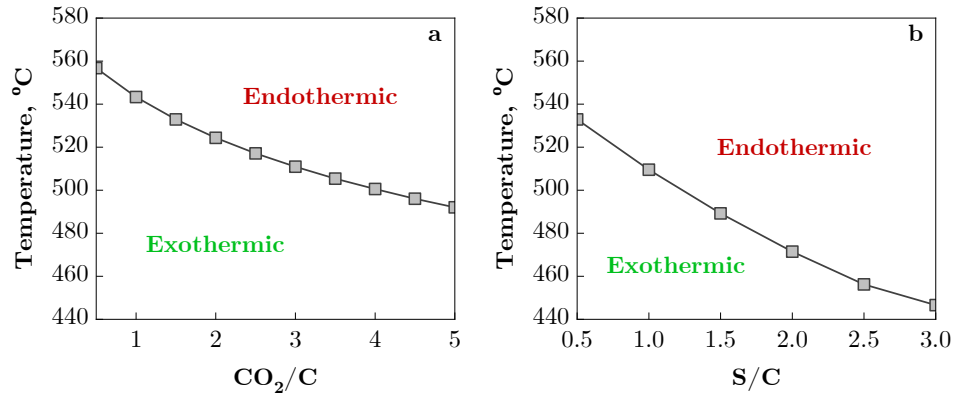

Figure 5.5. Values of temperature and CO_2/C ratio (a, with S/C ratio of 0.5) or S/C ratio (b, with CO_2/C ratio of 1.5) corresponding to the thermoneutral regime (ΔH_r=0).

5.1.3. Operating conditions for maximising syngas production

Figure 5.6a shows the reaction temperature required to achieve the maximum syngas yield (almost 100 %) for different feed compositions (combinations of CO_2/C and S/C ratios). The corresponding values of H_2/CO ratio, CO_2 conversion and reduction of CO_2 emissions are depicted in Figure 5.6b, c and d, respectively. These results are useful to establish suitable operating conditions for a balance between syngas yield, H_2/CO ratio and CO_2 conversion.

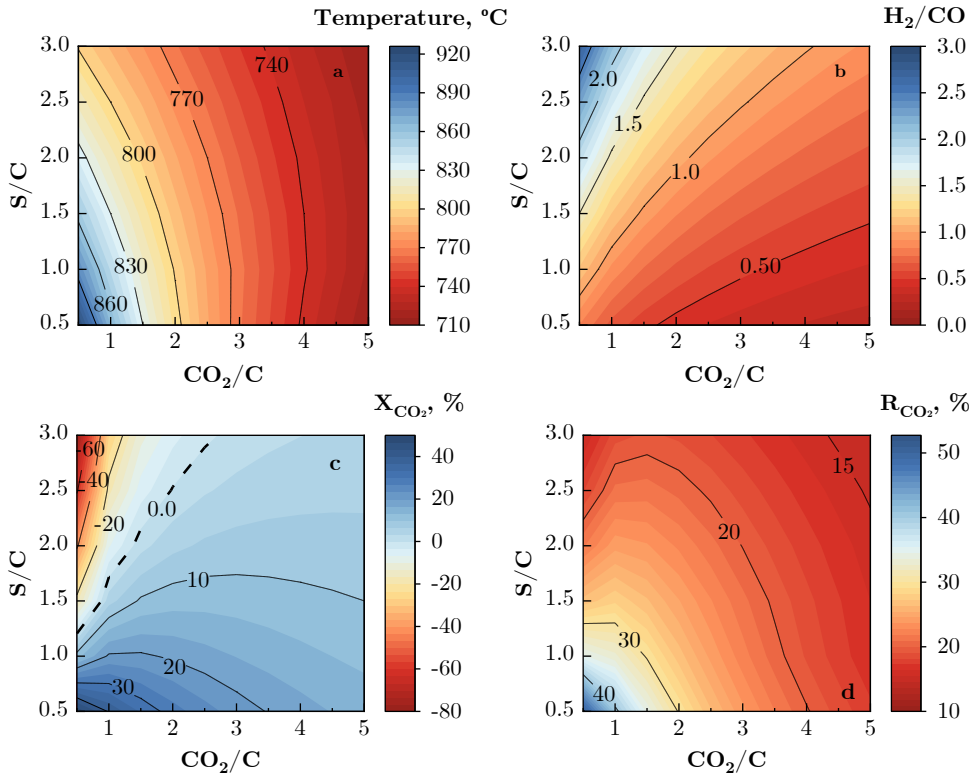

Figure 5.6. Temperature required for maximising syngas yield for different values of CO_2/C and S/C ratios in the feed (a) and corresponding values of H_2/CO ratio in syngas (b), CO_2 conversion (c) and reduction of CO_2 emissions (d).

The increase in both CO_2/C and S/C ratios decreases the temperature needed to achieve the maximum syngas yield (Figure 5.6a), although for $CO_2/C \geq 4$ the effect of S/C ratio on the required temperature is very small. The H_2/CO ratio (Figure 5.6b) decreases by increasing CO_2 addition, as it promotes the reverse of

WGS reaction (Eq. (1.15)), thus increasing CO yield and decreasing H_2 yield. Conversely, an increase in S/C ratio favours the extent of WGS and SR reactions (Eqs. (1.14) and (1.17), respectively) and results in a syngas with a higher H_2/CO ratio. As for CO_2 conversion (Figure 5.6c), a wide range of operating conditions enable to obtain positive values, which involves the valorization of the CO_2 inlet stream. As observed, low CO_2/C and S/C ratios allow attaining high positive CO_2 conversions (in the 30-49 % range), but these conditions require a high reaction temperature (above 860 °C, Figure 5.6a), and lead to low H_2/CO ratio (< 1, Figure 5.6b), which is of low interest for the synthesis of fuels and chemicals.

Table 5.1 shows the set of operating condition thresholds for which positive CO_2 conversion is obtained (feed compositions corresponding to the right of the dashed line in Figure 5.6c). As observed, the higher the CO_2/C ratio, the higher the S/C ratio needed to achieve positive CO_2 conversion. Interestingly, a constant H_2/CO ratio (1.3) is obtained with these threshold combinations of CO_2/C and S/C ratios that lead to positive CO_2 conversion, because both ratios have an opposite effect on H_2/CO ratio (see Figure 5.1g and Figure 5.2g). It should be highlighted that a reduction of CO_2 emissions compared to the SR process (R_{CO2}) is feasible in any condition (CO_2/C or S/C ratio), attaining positive values of R_{CO2} from 14 % to 51 % under conditions of maximum syngas yield (Figure 5.6d). The increase in the CO_2/C ratio leads to a lower value of R_{CO2}, because an over-addition of CO_2 hinders its complete conversion. Likewise, the increase in the S/C ratio also has a negative effect on the R_{CO2}, because it promotes SR and WGS reactions, giving more CO_2 as a product.

Concerning the energy requirement for maximising syngas yield, Figure 5.7 shows the effect of CO_2/C and S/C ratios on the reaction heat (ΔH_r, Figure 5.7a) and on the heat exchangers duty (ΔH_{HE}, Figure 5.7b). These results correspond to the reforming temperature that maximise the syngas yield for each combination of CO_2/C and S/C ratios (Figure 5.6a). As observed in Figure 5.7a, ΔH_r increases by increasing CO_2/C ratio but decreases almost linearly with increasing S/C ratio. As mentioned above, the decrease of ΔH_r with increasing S/C ratio is due to the promotion of the exothermic WGS reaction. Nonetheless, DR reactions and the

reverse of both Boudouard and WGS reactions (endothermic reactions) are favoured with CO_2 addition, which explains the higher ΔH_r operating under these conditions. Interestingly, the ΔH_r is almost the same (near 355 kJ/mol) for all the feed compositions that lead to null CO_2 conversion (Table 5.1). On the other hand, the value of ΔH_{HE} increases linearly with both S/C and CO_2/C ratios (Figure 5.7b), because more energy is required to heat each stream when there is a higher water or CO_2 supply.

Table 5.1. Threshold values of S/C ratio and temperature required to attain > 99.9 % syngas yield with positive CO_2 conversion for different CO_2/C ratios and corresponding values of H_2/CO ratio in the syngas, reduction of CO_2 emissions compared to the SR process, reaction heat and heat exchangers duty.

	CO_2/C				
	0.5	1.0	1.5	2.0	2.5
maximum S/C	1.2	1.7	2.1	2.5	2.9
minimum T, °C	878.2	825.7	794.8	773.6	758.4
H_2/CO	1.3	1.3	1.3	1.3	1.3
R_{CO2}, %	35.2	28.0	23.5	20.5	18.4
ΔH_r, kJ/mol	355.5	357.4	356.1	354.0	351.7
ΔH_{HE}, kJ/mol	552.5	721.5	874.6	1014.4	1145.6

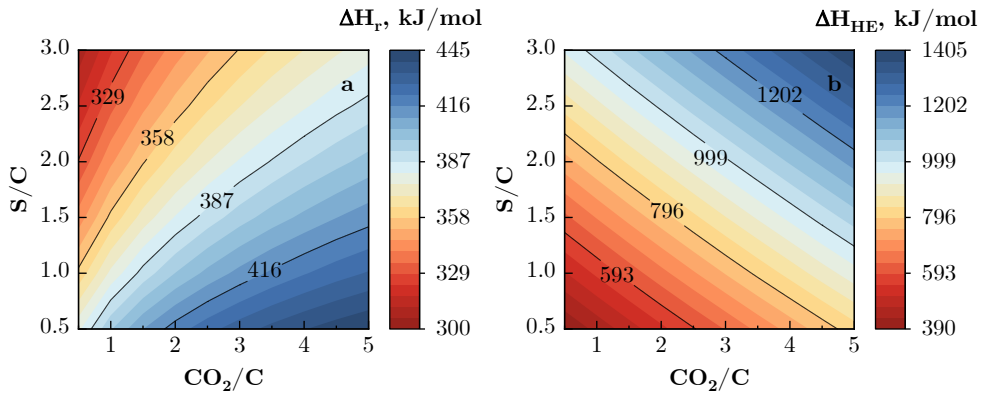

Figure 5.7. Reaction heat (a) and heat exchangers duty (b) at the temperature required for reaching maximum syngas (Figure 5.6a), for different values of CO_2/C and S/C ratios in the feed.

5.1.4. Operating conditions for obtaining H_2/CO ratios of 1 and 2 in the syngas

As aforementioned, a challenge in the CSDR of bio-oil is to achieve a syngas with a H_2/CO ratio suitable for use in different applications, in particular as raw material in catalytic processes for the production of fuels and chemicals [216–218]. Considering the effect of the reaction conditions on the H_2/CO ratio, indirectly analysed in the previous sections, this section has been oriented to propose the reaction conditions (temperature, CO_2/C ratio and S/C ratio) required to attain target H_2/CO ratios of 1 and 2. Also, the corresponding values of syngas yield, CO_2 conversion and reduction of CO_2 emissions have been calculated. The results are depicted in Figure 5.8 (for a H_2/CO ratio of 1) and Figure 5.9 (for a H_2/CO ratio of 2). It is remarkable that without the addition of CO_2 at the inlet system (SR operation) the minimum H_2/CO ratio is 1.3 (see Figure 5.1g).

In Figure 5.8a it is observed that the temperature required to reach a H_2/CO ratio of 1 decreases with CO_2/C ratio but increases with S/C ratio. Thus, for a CO_2/C ratio of 0.5 the required temperature varies in the 695-2055 °C range (excessive from an application point of view), whereas for a CO_2/C ratio of 5 it varies in the 497-683 °C range. Moreover, it is relevant to focus on the syngas yield obtained for the different feed compositions for this H_2/CO ratio (Figure 5.8b). The increase in CO_2/C ratio significantly decreases the syngas yield, as it promotes the reverse of WGS reaction (Eq. (1.15)). Thus, for S/C ratios in the 0.5-1 range, the syngas yield decreases from 45-100 % range at CO_2/C ratio of 0.5 to 13-51 % range at CO_2/C ratio of 5 (orange colour area in Figure 5.8b). On the contrary, the increase of S/C ratio increases the yield of syngas, as it favours the SR reactions (Eqs. (1.14) and (1.17)). Moreover, with a high S/C ratio the temperature required to achieve the target H_2/CO ratio of 1 is high (Figure 5.8a), which also favours the SR reactions. As a consequence of these effects, the higher the CO_2/C ratio, the higher the S/C ratio needed to attain a syngas yield above 99 %, as gathered in Table 5.2. Thus, for CO_2/C ratios of 1, 3 and 5, S/C ratios above 1.0, 1.9 and 2.5, respectively, are required. It is interesting to note, because of its impact on catalyst deactivation (important for the viability of the CSDR

bio-oil process), that the conditions leading to low syngas yield boost the coke yield (Figure A.16a), which reaches values in the 20-72 % range for CO_2/C ratio above 3 and S/C ratio below 1. Nevertheless, null coke yields are obtained with S/C ratio above 1.5 and CO_2/C ratio below 4. Likewise, it is interesting to analyse the CH_4 yield results (Figure A.16b). Thus, CH_4 yields of 8-9 % are obtained with high values of CO_2/C ratios and S/C ratios around 1-1.5 or low S/C ratios (between 0.5-1) and CO_2/C ratios around 2-3 due to the low temperature required to reach the target H_2/CO ratio of 1 for these feed compositions (Figure 5.8a), which does not favour its reforming. Nevertheless, as the S/C ratio increases (higher temperature required), CH_4 yield drops to almost zero.

Interestingly, the conversion of CO_2 is positive, between 1-29 % under all the conditions providing H_2/CO ratio of 1 (Figure 5.8c), and in the 2.7–26.2 % range for the conditions leading to maximum syngas yield (Table 5.2), which evidences a successful outcome in view of the bio-oil CSDR process's contribution to valorize CO_2 coming from any other stream/unit in the factory. The CO_2 conversion decreases noticeably with increasing CO_2/C ratio, but increases slightly with increasing S/C ratio. It is important to note, however, that operating at low CO_2/C ratios and high S/C ratios involves operating at too high temperatures (typically above 1300 °C, Figure 5.8a) that are outside the operating range of the reforming units. The reduction of CO_2 emissions of the CSDR process with respect to the SR process (Figure 5.8d) follows a similar tendency to the CO_2 conversion for the different CO_2/C and S/C ratios. Thus, positive reductions in the 7-47 % range are achieved for the whole range of feed compositions studied, and in the 13-42 % range for the S/C and CO_2/C combinations that provide the maximum syngas yield (Table 5.2).

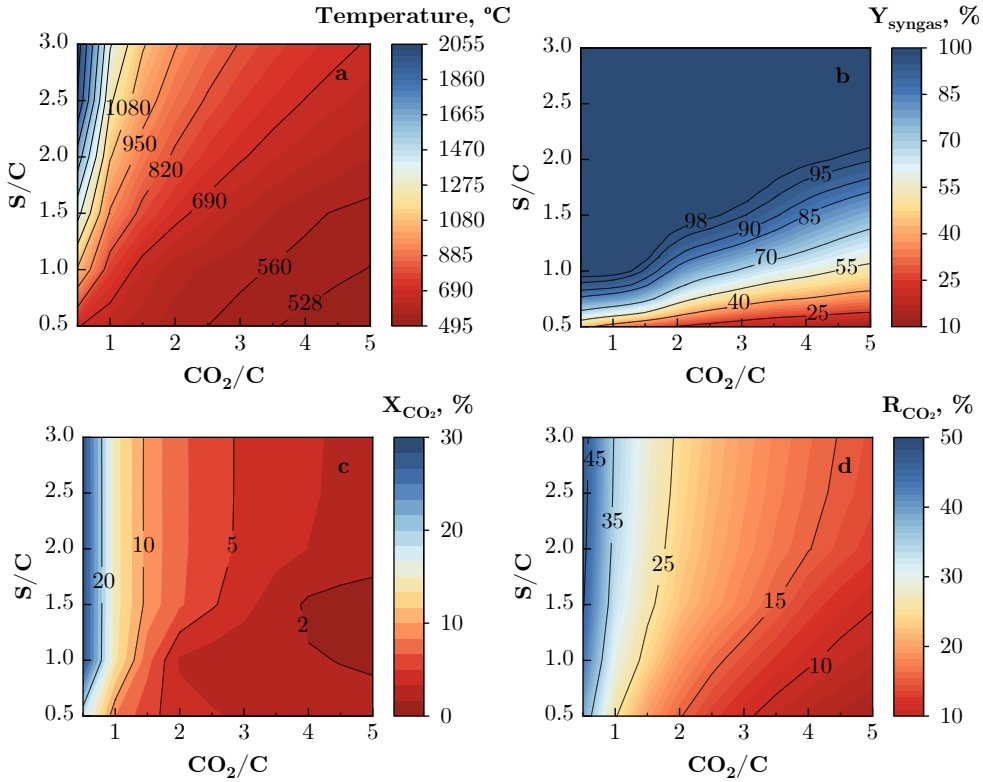

Figure 5.8. Temperature required to obtain a syngas with a H_2/CO ratio of 1 for different values of CO_2/C and S/C ratios in the feed (a) and corresponding values of syngas yield (b), CO_2 conversion (c) and reduction of CO_2 emissions (d).

Table 5.2. Threshold values of S/C ratio and temperature required to attain > 99 % syngas yield with a H_2/CO ratio of 1 for different CO_2/C ratios and corresponding values of CO_2 conversion, reduction of CO_2 emissions compared to the SR process, reaction heat and heat exchangers duty.

	CO_2/C					
	0.5	1.0	2.0	3.0	4.0	5.0
minimum S/C	0.9	1.0	1.5	1.9	2.2	2.5
minimum T, °C	993	765	710	685	657	637
X_{CO2}, %	26.2	13.8	6.8	4.5	3.4	2.7
R_{CO2}, %	42.1	29.3	21.9	18.1	15.4	13.4
ΔH_r, kJ/mol	351.6	365.6	366.3	366.7	366.8	366.9
ΔH_{HE}, kJ/mol	534.9	586.4	712.8	899.8	1037.3	1167.0

In order to attain a syngas with a H_2/CO ratio of 2 in the CSDR of bio-oil, the reaction conditions shown in Figure 5.9 are required. Figure 5.9a shows the effect of the CO_2/C and S/C ratios on the temperature required and Figure 5.9b-Figure 5.9d show the corresponding values of syngas yield, CO_2 conversion and reduction of CO_2 emissions, respectively. Overall, the trends with the S/C and CO_2/C ratios of the required temperature and of the rest of reaction indices are qualitatively similar to those aforementioned for a H_2/CO ratio of 1 (Figure 5.8), that is, the syngas yield decreases as the CO_2/C ratio increases and the S/C ratio decreases. For all the feed compositions, the temperature required to achieve a H_2/CO ratio of 2 (Figure 5.9a) is lower than that needed to achieve the ratio of 1 (Figure 5.8a). Interestingly, for the target H_2/CO ratio of 2, the ranges of CO_2/C and S/C ratios that allow attaining the maximum syngas yield (Table 5.3) are narrower than those needed for a H_2/CO ratio of 1 (Table 5.2). Thus, for a H_2/CO ratio of 2 a syngas yield above 98 % is reached with a CO_2/C ratio in the 0.5-2.5 range and a S/C ratio in the 1.8-3 range, and the required temperature for such feed compositions varies in the 749-631 °C range (Table 5.3). This temperature range is interesting from the point of view of the design and operability of the process on a larger scale. For the H_2/CO ratio of 1, the range of S/C ratios for reaching maximum syngas yield is wider (Figure 5.8b), so that above 99 % can be attained at a reasonable temperature with suitable combinations of S/C and CO_2/C ratios (Table 5.2).

Concerning CO_2 conversion (Figure 5.9c), differently from that observed for H_2/CO ratio of 1 (Figure 5.8c), positive values are attained with a narrow range of the feed compositions. The results improve with increasing CO_2/C ratio, whereas the S/C ratio negatively affects the CO_2 conversion, as it promotes SR and WGS reactions instead of DR reactions. Thus, positive CO_2 conversions are achieved (between 0.20 and 1 %) with CO_2/C ratios in the 3-5 range and S/C ratio of 0.5. However, these conditions require operating at low temperature (430-470 °C), which unfortunately leads to too low syngas yields (13-19 %, Figure 5.9b).

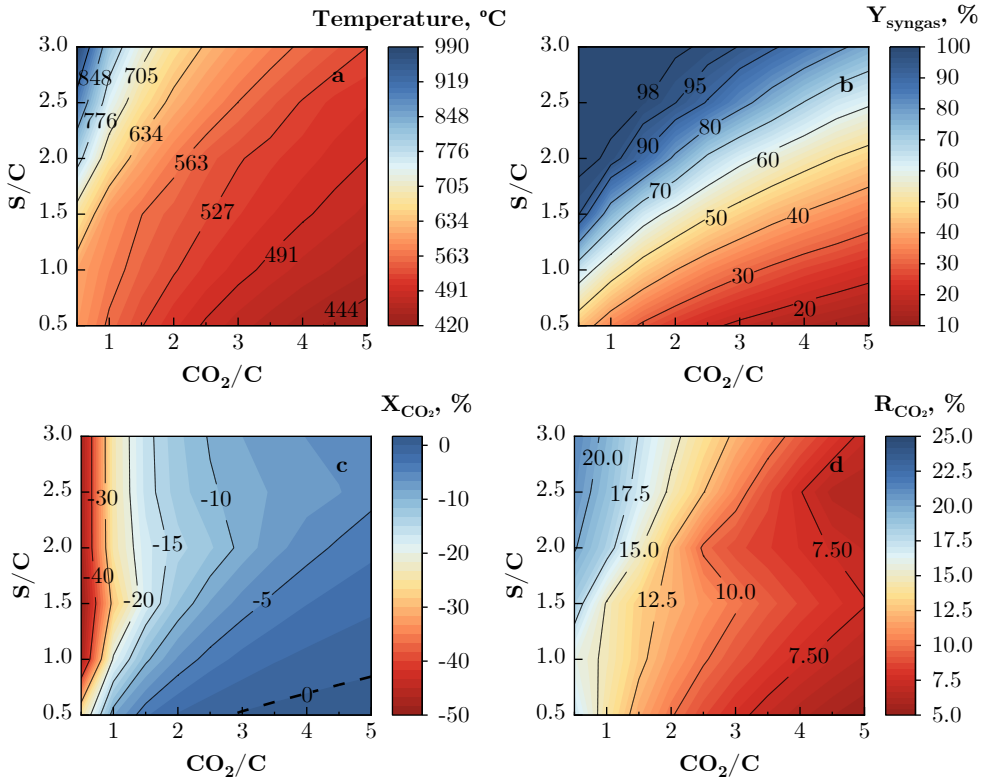

Figure 5.9. Temperature required to obtain a syngas with a H_2/CO ratio of 2 for different values of CO_2/C and S/C ratios in the feed (a) and corresponding values of syngas yield (b), CO_2 conversion (c) and reduction of CO_2 emissions (d).

As observed in Figure 5.9d, the CO_2/C ratio has a significant effect on the reduction of CO_2 emissions, so that R_{CO2} increases significantly as the CO_2/C ratio decreases. The S/C ratio has a lower effect, although a slight higher R_{CO2} value is observed for high S/C ratios. The values of R_{CO2} obtained when achieving a H_2/CO ratio of 2 in the syngas vary in the 5-22 % range for the whole range of CO_2/C and S/C ratios studied (Figure 5.9d) and in the 14-19 % range for the conditions needed to achieve a syngas yield > 98 % (Table 5.3).

In Figure A.17a it is observed that the coke yield for a H_2/CO ratio of 2 is higher than that obtained for the target H_2/CO ratio of 1 (Figure A.16a), with values in the 57-91 % range for conditions corresponding to a low syngas yield (S/C ratio below 1 and CO_2/C ratio above 3). Low CO_2/C ratios (in the 0.5-2.5 range) and

high S/C ratios (in the 2-3 range) are required to obtain null coke yields. Regarding CH_4 yield (Figure A.17b), it decreases with the increase in the CO_2/C ratio at low S/C ratios (0.5 and 1), because these conditions promote its DR reaction, but conversely, it increases with CO_2/C ratio for high S/C ratios (in the 2-3 range). Moreover, the CH_4 yield goes through a maximum (in the 16-18 % range) with S/C ratio, whose position is located at a higher CO_2/C ratio with increasing S/C ratio, and it drops to almost 0 when operating with S/C ratio above 2.5 and CO_2/C ratio below 1.5.

Table 5.3. Threshold values of S/C ratio and temperature required to attain > 98 % syngas yield with a H_2/CO ratio of 2 for different CO_2/C ratios and corresponding values of CO_2 conversion, reduction of CO_2 emissions compared to the SR process, reaction heat and heat exchangers duty.

	CO_2/C				
	0.5	1.0	1.5	2.0	2.5
minimum S/C	1.8	2.1	2.5	2.9	3.0
minimum T, °C	748.7	687.7	666.1	654.6	631.1
X_{CO2}, %	-48.5	-24.3	-16.2	-12.2	-9.7
R_{CO2}, %	19.4	18.4	16.8	15.3	13.9
ΔH_r, kJ/mol	316.9	316.8	316.7	316.5	316.4
ΔH_{HE}, kJ/mol	643.8	733.6	853.1	982.5	1044.8

Figure 5.10 shows the effect of S/C and CO_2/C ratios on the reaction heat (ΔH_r, graphs a and b, respectively) and heat exchangers duty (ΔH_{HE}, graphs c and d, respectively) of the CSDR of raw bio-oil for target H_2/CO ratios of 1 (a and c,) and 2 (b and d). The results in Figure 5.10a show that all CO_2/C and S/C ratios that provide a H_2/CO ratio of 1 clearly correspond to an endothermic regime ($\Delta H_r > 0$). For CO_2/C ratios in the 0.5-2 range, the ΔH_r goes through a slight maximum with S/C ratio, but for higher CO_2/C ratios it increases continuously with S/C ratio. Interestingly, for CO_2/C ratio > 2.5 and S/C ratio > 2, ΔH_r is almost constant, around 370 kJ/mol. Besides, the ΔH_{HE} (Figure 5.10c) increases noticeably with S/C ratio. Nevertheless, ΔH_{HE} goes through a slight minimum

with CO_2/C ratio, which is more remarkable for high S/C ratios. Overall, for CO_2/C ratios above 2, the ΔH_{HE} increases slightly with CO_2/C ratio.

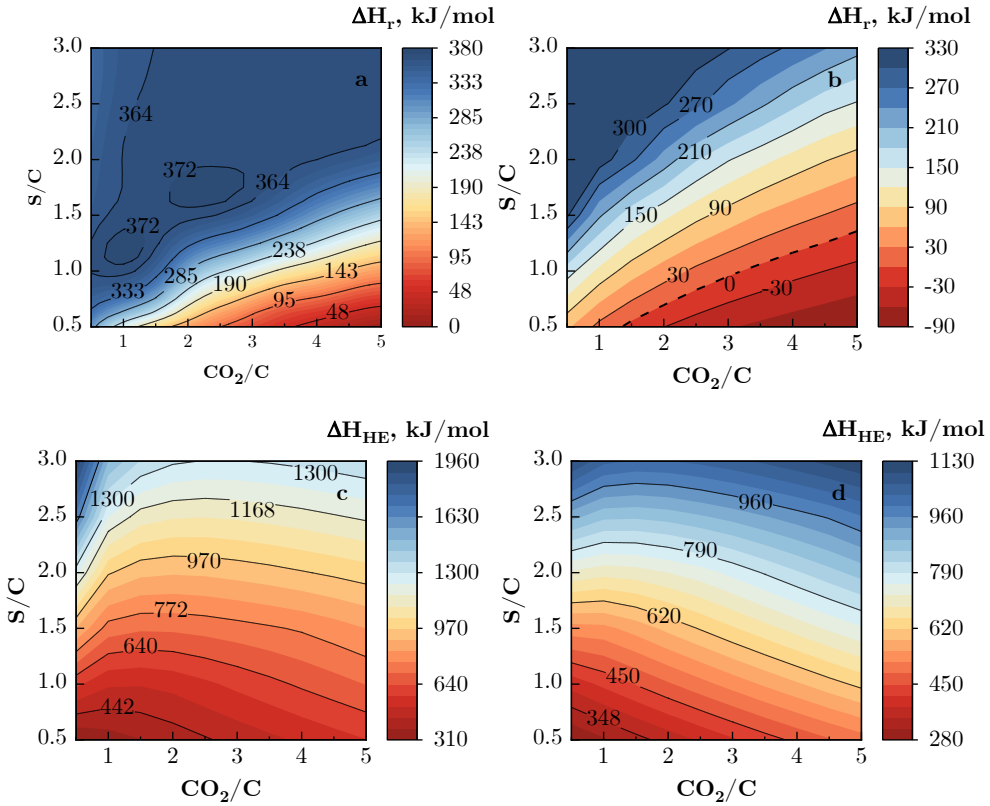

Figure 5.10. Reaction heat (a) and heat exchangers duty (b) at the temperature required for reaching a syngas with a H_2/CO ratio of 1 (a and c) and 2 (b and d), for different values of CO_2/C and S/C ratios in the feed.

The energy requirement shows somehow a different trend when the target H_2/CO ratio is different. The overall energy requirement is lower for the H_2/CO ratio of 2 (Figure 5.10b and Figure 5.10d) than for the ratio of 1 (Figure 5.10a and Figure 5.10c), because the temperatures required are lower (compare Figure 5.8a (H_2/CO ratio of 1) and Figure 5.9a (H_2/CO ratio of 2)). Differently to that observed for the ratio of 1, where the regime is always endothermic (Figure 5.10a), the results in Figure 5.10b indicate that there are feed compositions that allow an exothermic regime. Specifically, these conditions correspond to CO_2/C ratios above 1.5 and

low S/C ratios (0.5-1). The increase in the CO_2/C ratio decreases the ΔH_r. On the contrary, as the S/C ratio increases, the ΔH_r increases. For high S/C ratios (from 2 to 3) and low CO_2/C ratios (up to about 1.5), the ΔH_r remains constant at around 325 kJ/mol. The ΔH_{HE} (Figure 5.10d) increases quite linearly with increasing S/C ratio. For S/C ratios from 0.5 to 1.5, an increase in the CO_2/C ratio continuously increases the ΔH_{HE}. However, for S/C ratios above 1.5, there is a slight minimum in the ΔH_{HE} for low CO_2/C ratios.

5.2. EFFECT OF REACTION CONDITIONS WITH $NiAl_2O_4$ DERIVED CATALYST

In this section the combined steam and CO_2 reforming (CSDR) of raw bio-oil with Ni/Al_2O_3 catalyst derived from $NiAl_2O_4$ spinel has been studied. The reactions were carried out in a fluidized-bed reactor at operating conditions selected from the previous section, looking for obtaining a high production of syngas with adequate composition (H_2/CO ratio) for the synthesis of value-added chemicals and fuels, while attaining positive CO_2 conversion and high reduction of CO_2 emissions: temperature between 600-800 °C; CO_2/C molar ratio between 0 (conventional SR)-1.1; S/C molar ratio between 0.5 (corresponding to the water contained in the bio-oil feed)-1.7; space time of 0.125 and 0.250 $g_{catalyst}{\cdot}h/g_{oxygenates}$ and time on stream, 6 h.

5.2.1. Effect of operating conditions on conversion and products yields

This section presents the results for the effect of reaction temperature and feed compositions (CO_2/C molar ratio and S/C molar ratio) on the behaviour of Ni/Al_2O_3 catalyst in the SR (no CO_2 in the feed) and CSDR of raw bio-oil.

5.2.1.1. Effect of temperature

Figure 5.11 shows the evolution with TOS of conversion of oxygenates at three temperatures (600, 700 and 800 °C) for a CO_2/C molar ratio of 1.1, with low values of S/C ratio (of 0.5, corresponding to the water contained in the bio-oil feed) and space time (0.125 $g_{catalyst}{\cdot}h/g_{oxygenates}$) in Figure 5.11a, and high values

of S/C ratio and space time (1.7 and 0.250 $g_{catalyst}·h/g_{oxygenates}$, respectively) in Figure 5.11b.

Overall, the conversion of oxygenates at zero time increases with temperature, with this effect being much more noticeable for the most unfavourable conditions (low S/C ratio and low space time, Figure 5.11a, which are further from equilibrium conditions). In addition, the stability of the catalyst is significantly higher as the reaction temperature increases, with the deactivation being more severe under the conditions of Figure 5.11a. The attenuation of the deactivation at high S/C ratio and space time conditions (Figure 5.11b) is mainly a consequence of the increase in space time, since, as will be shown later (section 5.2.1.3), the small increase in S/C ratio (from 0.5 to 1.7) has no relevant effect on the catalyst deactivation.

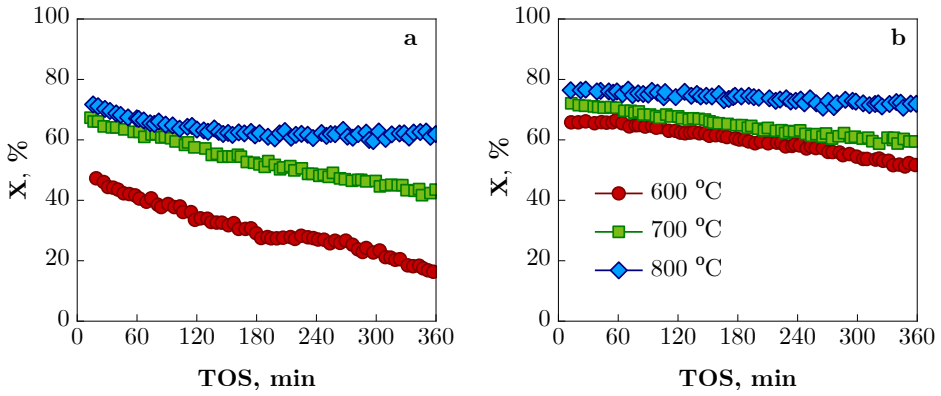

Figure 5.11. Effect of temperature on the conversion of oxygenates in the CSDR runs for a CO_2/C ratio of 1.1 with S/C ratio of 0.5 and space time of 0.125 $g_{catalyst}·h/g_{oxygenates}$ (a) and S/C ratio of 1.7 and space time of 0.250 $g_{catalyst}·h/g_{oxygenates}$ (b).

Figure 5.12 depicts the effect of temperature on the evolution with TOS of the yields of H_2 and main carbon by-products (CO, CO_2) for the same conditions as in Figure 5.11. The results for the minor carbon by-products (CH_4 and light hydrocarbons C_aH_b (mainly ethylene)) are shown in Figure C.1.

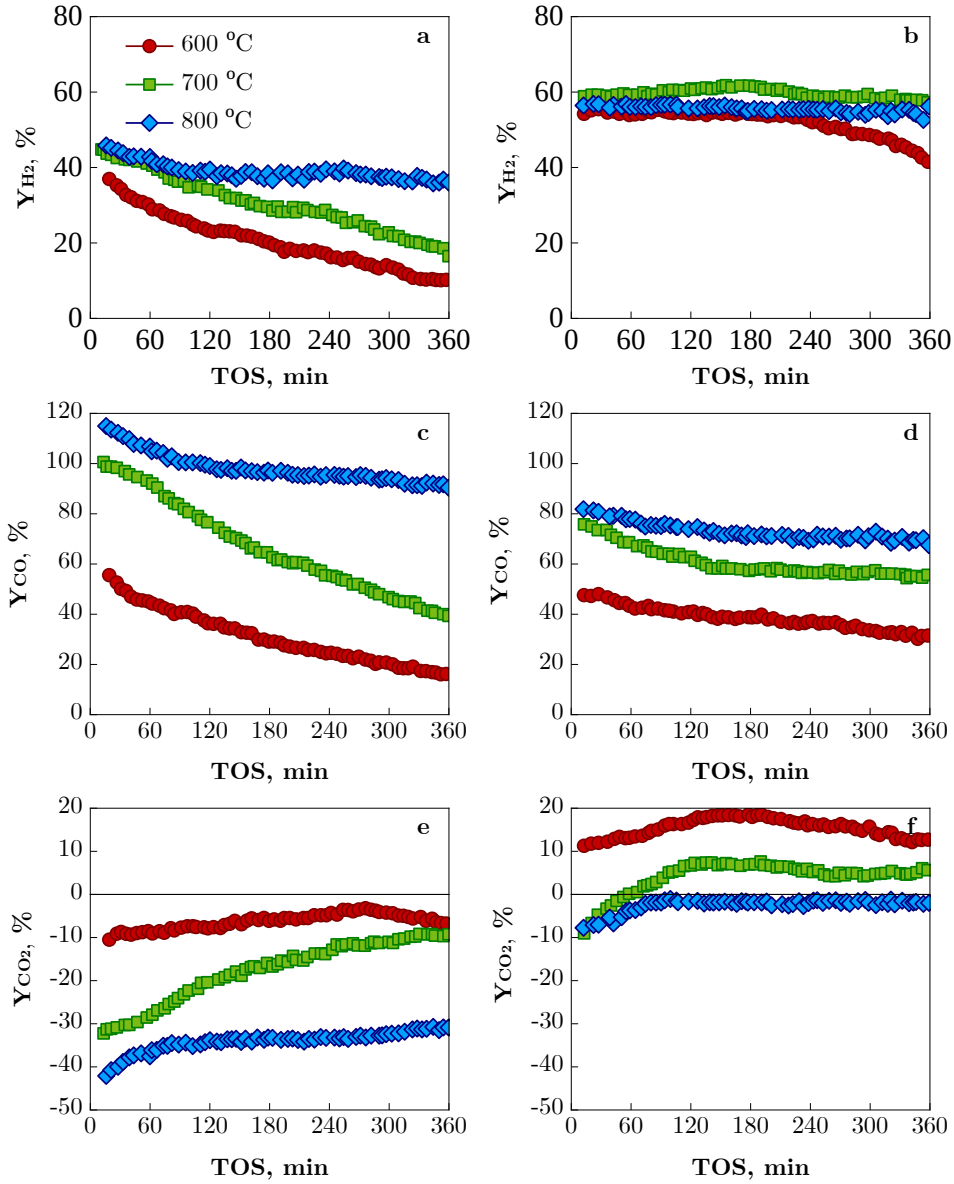

Figure 5.12. Effect of temperature on the evolution with TOS of the yield of H_2 (a, b), CO (c, d) and CO_2 (e, f) in the CSDR runs for a CO_2/C ratio of 1.1 with S/C ratio of 0.5 and space time of 0.125 $g_{catalyst}$·h/$g_{oxygenates}$ (left graphs) and S/C ratio of 1.7 and space time of 0.250 $g_{catalyst}$·h/$g_{oxygenates}$ (right graphs).

The initial yields of H_2 and CO increase with reaction temperature, most notably from 600 to 700 °C. Above 700 °C, the trend slows down, especially for H_2, whose yield actually reaches a maximum at 700 °C under conditions of high S/C ratio and space time (Figure 5.12b). This increase in H_2 and CO yields can be attributed to a higher extent of oxygenates SR (Eq. (1.14)), CH_4 SR (Eq. (1.17)) and CH_4 DR (Eq. (1.26)), which are favoured by increasing temperature. Moreover, the increase of CO with temperature is also explained by the promotion of the reverse of both WGS and Boudouard reactions. The promotion of the reverse-WGS with temperature also explains the maximum in H_2 yield obtained at 700 °C under conditions of high oxygenates conversion (Figure 5.11b). The decrease in the yields of H_2 and CO with TOS, with similar trend to that observed for oxygenates conversion (Figure 5.11), is slower at higher temperatures.

From the perspective of maximising the conversion of CO_2 or controlling its emission, it is relevant that the yield of CO_2 reaches negative values (Figure 5.12e-f), which indicates its conversion. As mentioned above, with increasing temperature, the reverse-WGS and CH_4 DR reactions are promoted, resulting in a decrease of the CO_2 yield, being negative for low S/C ratio at any temperature (Figure 5.12e), which means that the CO_2 is being effectively converted. With a high S/C ratio (S/C ratio of 1.7, Figure 5.12f), negative values of CO_2 yield are obtained at 800 °C and at the beginning of the reaction at 700 °C. Contrary to the yield of H_2 and CO, the yield of CO_2 increases over TOS or passes through a maximum, which is explained by the catalyst deactivation for the CO_2 conversion reactions (DR of CH_4 and reverse-WGS).

Conversely to aforementioned results for CO, the CH_4 yield at zero time on stream decreases with temperature, being null at 800 °C (Figure C.1a-b), which is explained because of the lower concentration of oxygenates (reactants in the formation of these by-product Eq. (1.16)) due to the higher extent of their reforming reactions at this temperature. Moreover, the SR and DR of CH_4 are promoted at high temperature. The CH_4 yield remains null along the reaction at 800 °C, but increases with TOS at 700 °C under unfavourable conditions (low S/C ratio and space time values, Figure C.1a) due to catalyst deactivation for

both oxygenate and CH_4 reforming reactions. The decrease in CH_4 yield observed at the lower temperature for both space time values studied could be explained because the catalyst deactivation affects the methanation reaction (reverse of SR of CH_4), which is favoured at low temperatures. At zero time on stream (fresh catalyst), the yield of C_aH_b is zero and remains null during the reactions at high S/C ratio and high space time (Figure C.1d), except for a small increase at the end of the reaction at 600 and 700 °C, at which the deactivation of the catalyst is more noticeable. Nonetheless, at low S/C and low space time, the reforming of light hydrocarbons is affected by catalyst deactivation at temperatures below 800 °C, and its yield increases steadily over TOS (Figure C.1c), reaching after 360 min higher values as the temperature increases, of 3-6 % in the 600-700 °C range.

The syngas yield, H_2/CO ratio, CO_2 conversion and reduction of CO_2 emissions were evaluated according to Eqs. (2.13), (2.14), (2.15) and (2.16), respectively. Figure 5.13 shows the values of these reaction indices corresponding to time on stream values of 0 (fresh catalyst) and 360 min, for the same reaction conditions as in Figure 5.11 and Figure 5.12. The syngas yield (Figure 5.13a-b) increases continuously with temperature due to the increase in the yields of H_2 (Figure 5.12a-b) and especially of CO (Figure 5.12c-d). Nevertheless, after 360 min, the syngas yield decreases for all conditions studied, with the decrease being less noticeable at 800 °C and high values of S/C ratio and space time (Figure 5.13b), indicating a slower deactivation of the catalyst under these conditions. Moreover, the decrease in syngas yield at high reaction time is more significant at lower temperatures, so that the upward trend of the syngas with temperature is more noticeable for the used catalyst under these conditions. Conversely, the increase in the reaction temperature involves a decrease in the H_2/CO ratio of the syngas (Figure 5.13c-d) due to the promotion of the reverse-WGS reaction. The initial-final values of the H_2/CO ratio at 600, 700 and 800 °C are 1.40-1.30, 0.90-1.00 and 0.90-0.92, respectively, at low S/C ratio and space time values (Figure 5.13c), and 2.50-2.90, 1.70-2.30 and 1.60-1.70, respectively, at high S/C ratio and space time values (Figure 5.13d). The significant increase of the H_2/CO ratio with TOS observed at high S/C ratio and high space time can be explained by the selective deactivation of the reverse-WGS reaction.

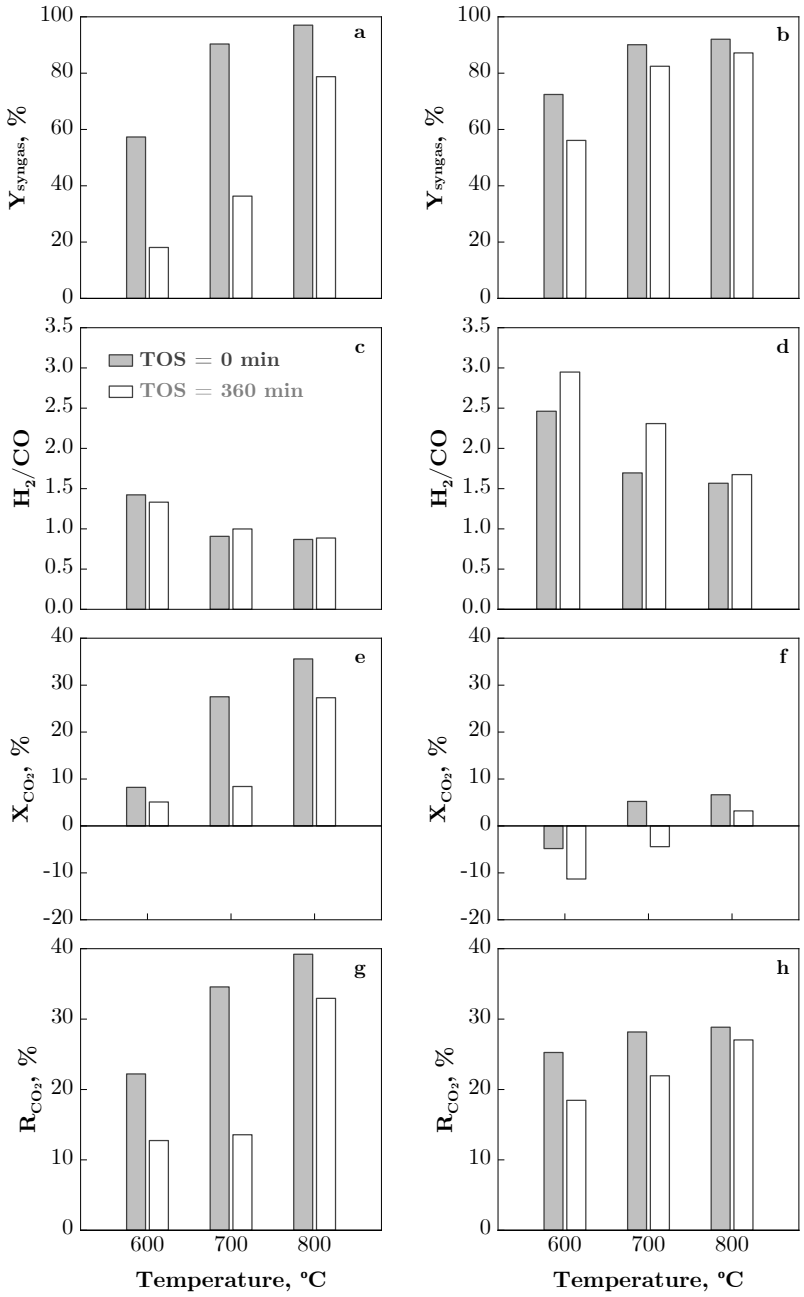

Figure 5.13. Effect of temperature on the initial (TOS=0 min) and final (TOS=360 min) values of syngas yield (a, b), H_2/CO ratio (c, d), CO_2 conversion (e, f) and reduction of CO_2 emissions (g, h) in the CSDR runs with CO_2/C ratio of 1.1. Left graphs: S/C ratio of 0.5 and space time of 0.125 $g_{catalyst} \cdot h/g_{oxygenates}$. Right graphs: S/C ratio of 1.7 and space time of 0.250 $g_{catalyst} \cdot h/g_{oxygenates}$.

The effect of temperature on CO_2 conversion is similar to that observed for syngas yield. For low values of S/C ratio and space time (Figure 5.13e), positive CO_2 conversions are observed, in the 8-36 % range at zero time on stream and 5-27 % range at 360 min on stream, meaning that the CO_2 is fully converted along the reaction under these conditions. However, at high S/C ratio and high space time (Figure 5.13f), the CO_2 conversion is only positive at high temperature, in the 7-3 % range at 800 °C or at zero time on stream at 700 °C.

Despite the negative CO_2 conversion under some conditions (high S/C ratio and space time value at low temperature, Figure 5.13f), R_{CO2} index is positive under all conditions (Figure 5.13g-h). The R_{CO2} index increases with temperature, and more significantly with low S/C ratio and space time values (Figure 5.13g), with values at zero TOS in the 22-39 % range. The R_{CO2} index decreases at 360 min on stream due to the deactivation of the CO_2 converting reactions (DR of CH_4 and reverse-WGS), this effect being more noticeable at low S/C ratio and space time, and mainly at 700 °C (Figure 5.13g).

5.2.1.2. Effect of CO_2/C ratio

The effect of CO_2/C ratio was assessed by varying the CO_2 and N_2 flow rates while keeping the bio-oil flow rate and the rest of the experimental conditions (temperature, S/C ratio and space time) constant. Figure 5.14 shows the evolution with TOS of the conversion of oxygenates at 700 °C with low S/C-space time conditions (0.5 and 0.125 $g_{catalyst}{\cdot}h/g_{oxygenates}$) (Figure 5.14a) and high S/C-space time conditions (1.7 and 0.250 $g_{catalyst}{\cdot}h/g_{oxygenates}$) (Figure 5.14b) for three values of CO_2/C ratio (0 (conventional SR), 0.6 and 1.1). Although the results in section 5.2.1.1 have shown that a higher temperature favours the SR-DR reactions and catalyst stability, the temperature selected for this study has been 700 °C in order to assess the effect of feed composition on catalyst deactivation.

The results in Figure 5.14 show a lower conversion in the CSDR reaction runs compared to the conventional SR (CO_2/C ratio of 0), with the conversion at zero TOS being lower as the CO_2/C ratio increases, regardless of the operating conditions. This could be explained by a competitive adsorption between the

oxygenated compounds and the co-fed CO_2 on the available active sites of the catalyst. This decrease in oxygenates conversion could also be partially due to the peculiar definition of this reaction index, Eq. (2.12), where the co-fed CO_2 is removed from the numerator in order not to overestimate the CO_2 formation by the global SR reaction of bio-oil (Eq. (1.13)). In any case, the fact that the oxygenates conversion does not increase significantly when CO_2 is co-fed with bio-oil suggests that the DR of oxygenates (Eq. (1.25)) does not have a relevant contribution to oxygenates conversion. Consequently, the role of the CO_2 co-fed in the CSDR of bio-oil on the product distribution must be explained mainly by its promotion of the reverse-WGS reaction (Eq. (1.15)) and its contribution to the CH_4 dry reforming (Eq. (1.26)). Increasing the CO_2/C ratio slightly attenuates deactivation when operating at low space time value (Figure 5.14a), but this effect is not noticeable at high space time value (Figure 5.14b), when deactivation is slow even under SR conditions.

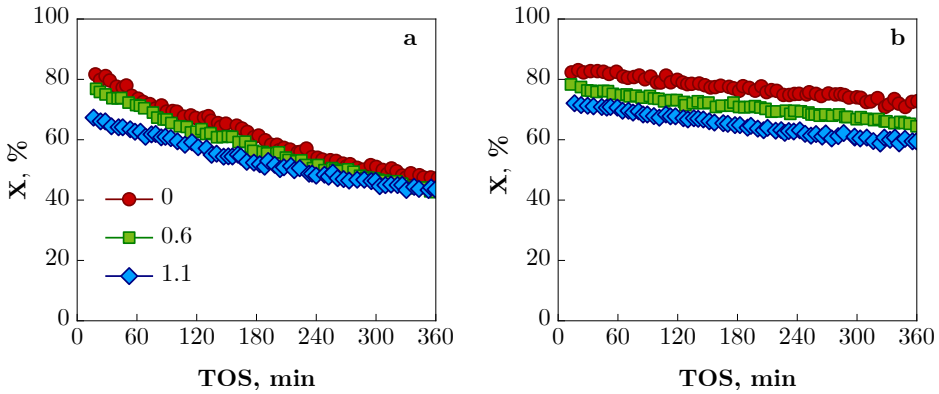

Figure 5.14. Effect of CO_2/C ratio on the conversion of oxygenates in the CSDR runs at 700 °C with S/C ratio of 0.5 and space time of 0.125 $g_{catalyst}{\cdot}h/g_{oxygenates}$ (a) and S/C ratio of 1.7 and space time of 0.250 $g_{catalyst}{\cdot}h/g_{oxygenates}$ (b).

Figure 5.15 depicts the effect of CO_2/C ratio on the evolution with TOS of the yields of H_2, CO and CO_2 at 700 °C for the same values of S/C ratio and space time indicated in Figure 5.14, whereas the results of the carbon by-products (CH_4 and C_aH_b) are plotted in Figure C.2. The results show a decrease in the initial value of H_2 yield with increasing CO_2/C ratio, which can be explained by the

decrease in oxygenates conversion (Figure 5.14) and the promotion of the reverse-WGS reaction. It is also observed a significant decrease in H_2 and CO yields with TOS under the most severe operating conditions (Figure 5.15a and Figure 5.15c, corresponding to low S/C ratio and space time values), evidencing a progressive and significant catalyst deactivation. Interestingly, however, an increase in the CO_2/C ratio attenuates this deactivation. Thus, in the SR process (CO_2/C ratio of 0), the decrease in H_2 yield over 360 min TOS is 81 % for low S/C ratio-space time conditions (red curve in Figure 5.15a). With a small CO_2 addition (CO_2/C ratio of 0.6) the decrease in the H_2 yield is 79 % (green curve in Figure 5.15a) and a further addition of CO_2 (CO_2/C ratio of 1.1) significantly reduces the decrease of H_2 over TOS to 57 % (blue curve in Figure 5.15a).

The initial CO yield (Figure 5.15c-d) is significantly influenced by the CO_2 co-fed. A low CO_2 addition leads to a higher CO yield (87 % for a low S/C-space time and 66 % for a high S/C-space time) compared to the conventional SR (66 % and 45 %, respectively) and it increases considerably with further CO_2 addition (CO_2/C of 1.1), to 101 % and 75 %, respectively. This result is mainly explained by the fact that the reverse-WGS and reverse-Boudouard reactions and the DR of CH_4 are favoured by increasing the addition of CO_2. As for the CO_2 yield (Figure 5.15e and Figure 5.15f), it decreases with the increase in the amount of CO_2 co-fed due to the promotion of reverse-WGS and DR of CH_4 reactions. Under the operating conditions studied in this section, negative values are obtained at low S/C ratio (Figure 5.15e), where CO_2 is effectively converted. When operating with a high S/C-space time conditions (Figure 5.15f), negative values of CO_2 yield are obtained only at high CO_2/C ratio and during the first 50 min on stream.

The initial CH_4 yield (Figure C.2a-b in Annexes) decreases with increasing CO_2/C ratio, confirming that the DR of CH_4 (Eq. (1.26)) is favoured. At high S/C ratio-space time conditions (Figure C.2b), CH_4 is less than 2 % in the SR process and less than 1 % in the CSDR. The initial yield of C_aH_b (Figure C.2c-d) is insignificant for all reaction conditions and remains null over time for the high S/C ratio-space time conditions. Nonetheless, both CH_4 and C_aH_b yields increase after 60 min on stream at low S/C ratio-space time values (Figure C.2a and

Figure C.2c), which is a consequence of the significant deactivation of the catalyst for their reforming reactions under these more severe conditions.

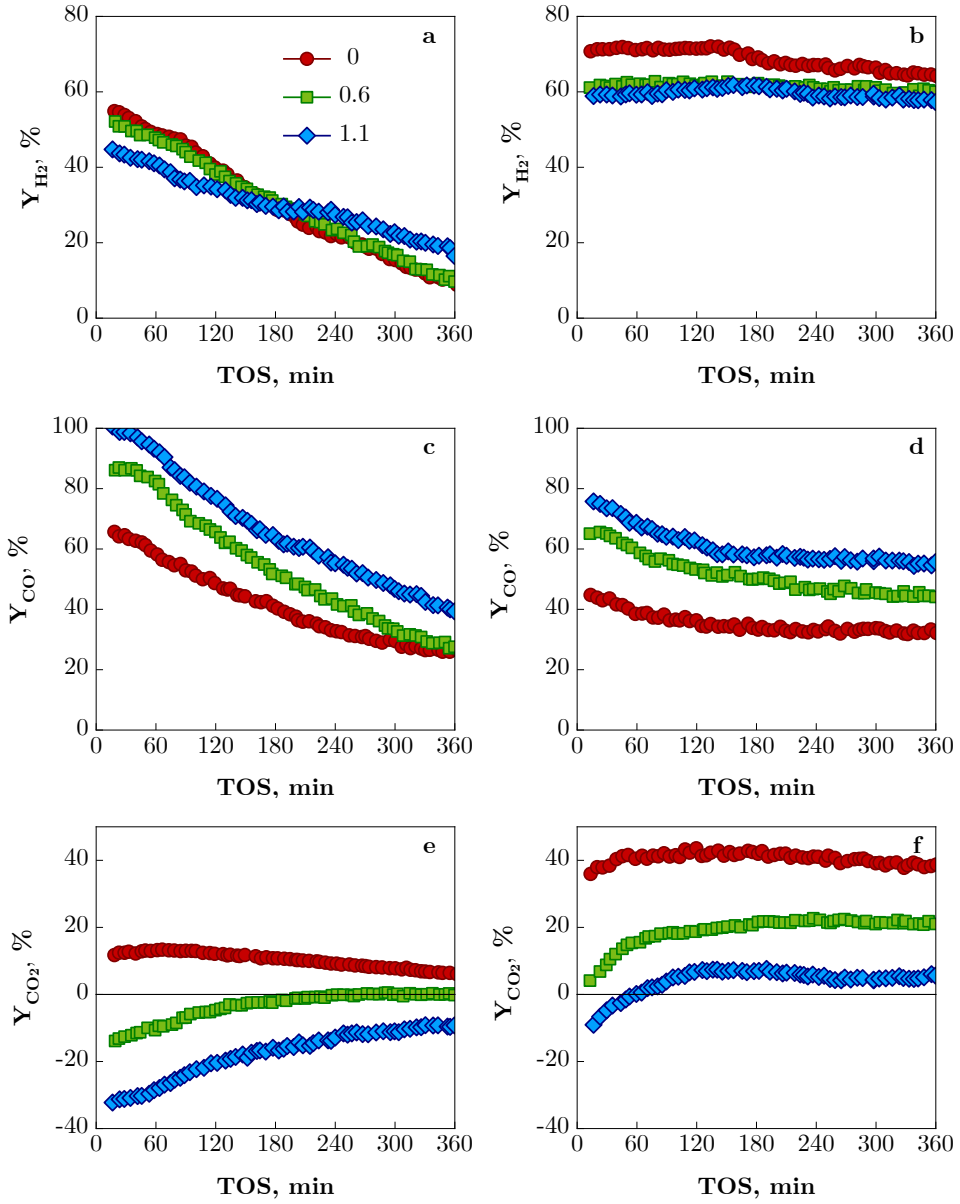

Figure 5.15. Effect of CO_2/C ratio on the evolution with TOS of product yields: H_2 (a, b), CO (c, d) and CO_2 (e, f) in the CSDR runs at 700 °C with S/C ratio of 0.5 and space time of 0.125 $g_{catalyst}$·h/$g_{oxygenates}$ (left graphs) and S/C ratio of 1.7 and space time of 0.250 $g_{catalyst}$·h/$g_{oxygenates}$ (right graphs).

Figure 5.16 shows the initial values corresponding to zero and 360 min on stream of syngas yield (a, b), H_2/CO ratio (c, d), CO_2 conversion (e, f) and reduction of CO_2 emissions (g, h) under the operating conditions of Figure 5.14 and Figure 5.15. Except for the H_2/CO ratio, the other reaction indices decrease over time, evidencing catalyst deactivation, which is more remarkable at low S/C ratio-space time values. Although the initial yield of H_2 decreases with increasing CO_2/C ratio (from 55 to 45 % at low S/C ratio-space time (Figure 5.15a) and from 71 to 59 % at high S/C ratio-space time (Figure 5.15b)), the initial syngas yield increases with the addition of CO_2 (from 57 % to 90.3 % at low S/C ratio-space time conditions (Figure 5.16a) and from 88.9 % to 90.1 at high S/C ratio-space time (Figure 5.16)). This result is consequence of the significant increase in CO yield (Figure 5.15c-d) with the CO_2/C ratio. Moreover, as expected, the syngas yield after 360 min is significantly lower than at zero time on stream due to catalyst deactivation, which is more noticeable under low S/C ratio-space time conditions (Figure 5.16a).

Differently to the syngas yield, the co-feeding of CO_2 leads to a significant decrease in the H_2/CO ratio compared to the SR runs. Thus, under low S/C ratio-space time conditions (Figure 5.16c), the H_2/CO ratio decreases from 1.8 (SR run) to 1.2 and 0.9 with CO_2/C ratios of 0.6 and 1.1, respectively. Under high S/C ratio-space time conditions (Figure 5.16d), the H_2/CO ratio decreases from 3.6 (SR run) to 1.9 and 1.7 with CO_2/C ratios of 0.6 and 1.1, respectively. As commented in section 5.1.1, this reduction in H_2/CO ratio is explained because methane DR and the reverse of both WGS and Boudouard reactions are promoted by the co-feeding of CO_2. The H_2/CO ratio changes with TOS, indicating a different effect of catalyst deactivation on the H_2- or CO- producing reactions. A selective deactivation of the reverse-WGS reaction over other routes of the reaction scheme could also explain the increase in the H_2/CO ratio after 360 min observed under conditions of high S/C ratio and space time for any CO_2/C ratio (Figure 5.16d).

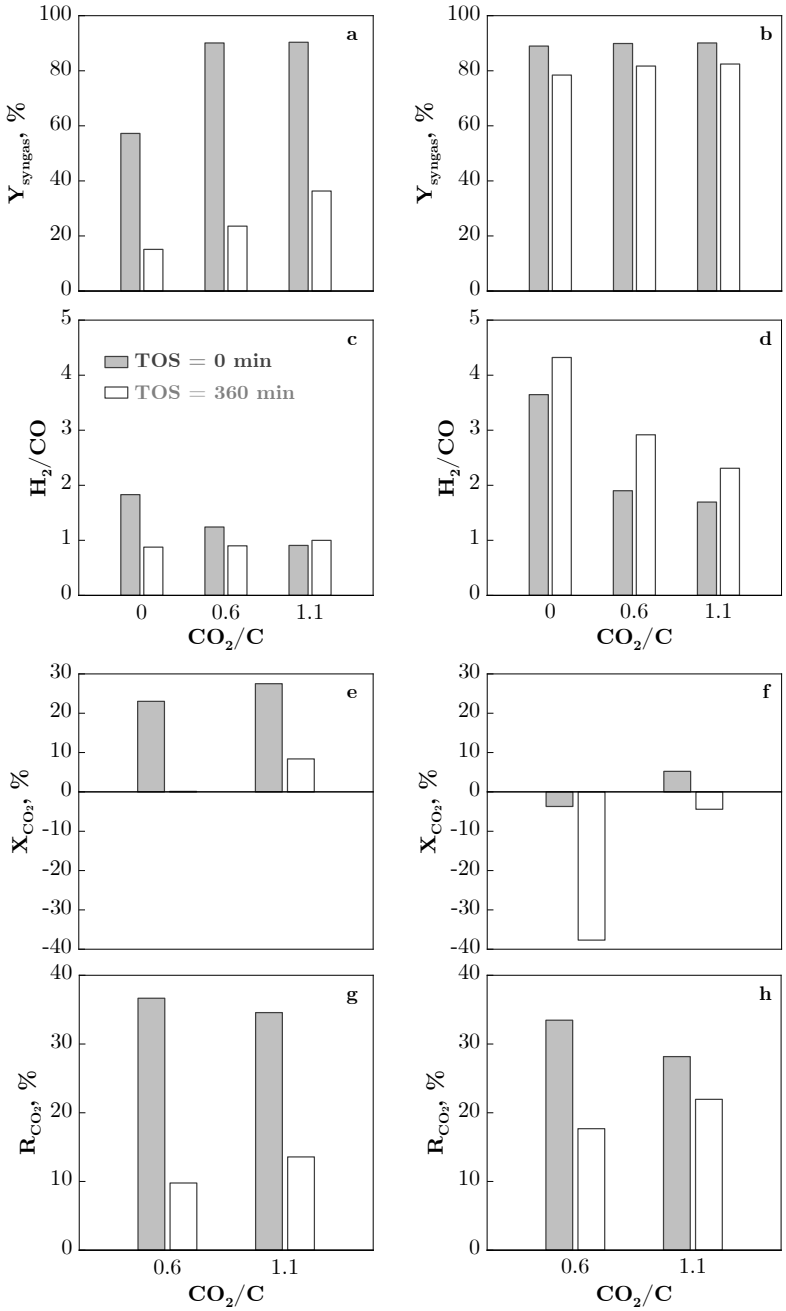

Figure 5.16. Effect of CO_2/C ratio on the initial (TOS=0 min) and final (TOS=360 min) values of syngas yield (a, b), H_2/CO ratio (c, d), CO_2 conversion (e, f) and reduction of CO_2 emissions (g, h) in the CSDR runs at 700 °C. Left graphs: S/C ratio of 0.5 and space time of 0.125 $g_{catalyst}$·h/$g_{oxygenates}$. Right graphs: S/C ratio of 1.7 and space time of 0.250 $g_{catalyst}$·h/$g_{oxygenates}$.

Regarding CO_2 conversion, at low S/C ratio-space time conditions (Figure 5.16e), positive values (in the 23-28 % range at zero TOS) are attained for both CO_2/C ratios and, interestingly, with a greater stability for the highest CO_2/C ratio. It should be emphasized that a reduction of CO_2 emissions compared to the SR process is possible in all conditions. The lower CO_2/C ratio (0.6) leads to a higher initial value of reduction of CO_2 emissions compared to the SR run (37 % and 33 % at low and high S/C ratio-space time conditions, respectively), but it decreases steadily due to the faster deactivation (10 and 18 %, respectively, for 360 min on stream). However, at CO_2/C ratio of 1.1 the effect of catalyst deactivation is less pronounced and the initial values of reduction of CO_2 emissions of 35 % (Figure 5.16g) and 28 % (Figure 5.16h) decreases to 14 % and 22 %, respectively, after 360 min on stream.

5.2.1.3. Effect of S/C ratio

The effect of S/C ratio was studied by adjusting the water and nitrogen flow rates while keeping the bio-oil flow rate constant. Figure 5.17 shows the evolution with TOS of the conversion of oxygenates at 700 °C for different values of S/C ratio (0.5 and 1.7) with a CO_2/C ratio of 0.6 and low space time conditions (0.125 $g_{catalyst}{\cdot}h/g_{oxygenates}$) (Figure 5.17a) and a CO_2/C ratio of 1.1 and high space time conditions (0.250 $g_{catalyst}{\cdot}h/g_{oxygenates}$) (Figure 5.17b). Higher values of the S/C ratio have not been studied because previous thermodynamic studies (section 5.1) have reported that they lead to negative CO_2 conversions and, therefore, to a lower reduction of CO_2 emissions with respect to the SR process. The results in Figure 5.17 show that varying the S/C ratio in the range 0.5-1.7 does not affect the initial conversion and has no significant effect on deactivation, although deactivation appears to be slightly slower at S/C ratio of 1.7.

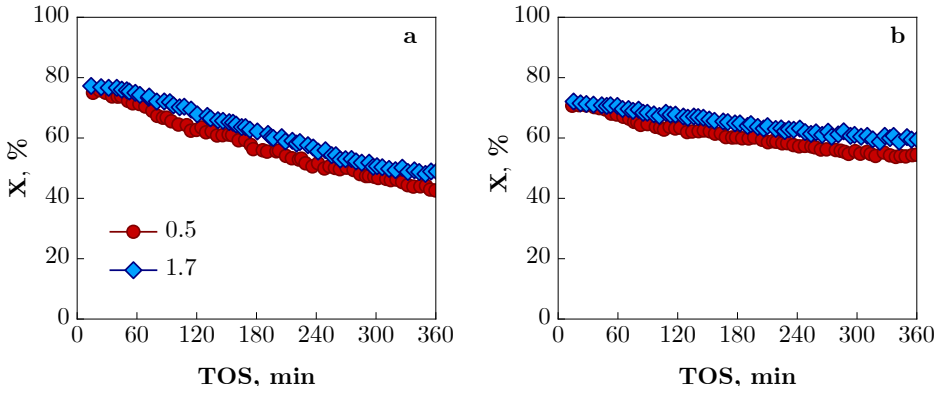

Figure 5.17. Effect of S/C ratio on the conversion of oxygenates in the CSDR runs at 700 °C with CO_2/C ratio of 0.6 and space time of 0.125 $g_{catalyst}$·h/$g_{oxygenates}$ (a) and CO_2/C ratio of 1.1 and space time of 0.250 $g_{catalyst}$·h/$g_{oxygenates}$ (b).

Figure 5.18 depicts the evolution with TOS of the yields of H_2, CO and CO_2 at 700 °C and space time of 0.250 $g_{catalyst}$·h/$g_{oxygenates}$ for different values of S/C ratio (0.5 (corresponding to the water contained in the bio-oil feed), 1.2 and 1.7) at a fixed CO_2/C ratio of 0.6 (left graphs) and 1.1 (right graphs) and the results of the yields of by-products (CH_4 and C_aH_b) under the same conditions are plotted in Figure C.3 of Annexes. The yields of H_2 (Figure 5.18a-b) and CO_2 (Figure 5.18e-f) increase with the S/C ratio, whereas the yield of CO decreases (Figure 5.18c-d), because a high S/C ratio promotes the SR reactions of oxygenates and CH_4 and shifts the equilibrium of the WGS reaction. The initial yield of CH_4 (Figure C.3a-b) also decreases with increasing S/C ratio, being insignificant at high CO_2/C ratio (Figure C.3b), and the initial yield of C_aH_b is insignificant for this high space time value under all the feed compositions studied (Figure C.3c-d). Under the conditions of Figure 5.18 (with high space time and therefore high oxygenates conversion), the increase in the S/C ratio in the 0.5-1.7 range does not have a relevant impact on catalyst deactivation, but a slightly slower decrease in the yields of H_2 and CO is observed at the highest S/C ratio studied.

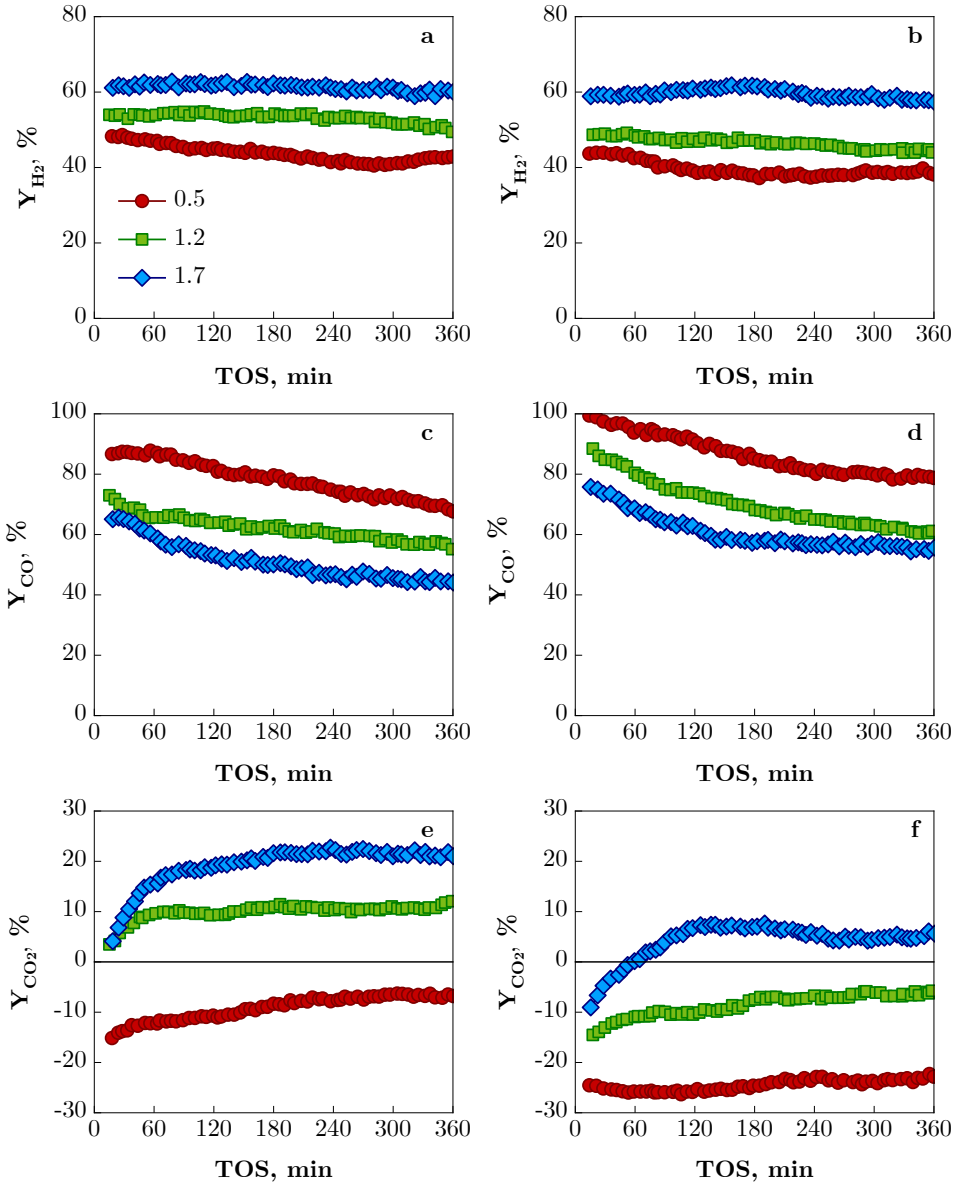

Figure 5.18. Effect of S/C ratio on the evolution with TOS of product yields: H_2 (a, b), CO (c, d) and CO_2 (e, f) in the CSDR runs at 700 °C and space time of 0.250 $g_{catalyst}{\cdot}h/g_{oxygenates}$ with CO_2/C ratio of 0.6 (left graphs) and 1.1 (right graphs).

Figure 5.19 shows the values corresponding to zero and 360 min on stream of syngas yield, H_2/CO ratio, CO_2 conversion and reduction of CO_2 emissions under

the conditions of Figure 5.18. Due to the opposite effect of H_2O addition on the yields of H_2 (which increases) and CO (which decreases), the syngas yield is not significantly affected by the S/C ratio (Figure 5.19a-b), but the H_2/CO ratio of syngas increases noticeably with the S/C ratio (Figure 5.19c-d). For a given S/C, the increase in the H_2/CO ratio over time is most probably due to the selective deactivation of the reverse-WGS reaction, as previously commented for the effect of temperature and CO_2/C ratio. The increase of S/C ratio has a negative effect on the CO_2 conversion (Figure 5.19e and Figure 5.19f) because the CO_2 yield increases (Figure 5.18e-f) due to the promotion of SR and WGS reactions, attaining negative CO_2 conversions in some of the conditions studied (Figure 5.19e). Consequently, it is convenient to work with low S/C ratios to ensure the positive conversion of CO_2: S/C <1.2 for a CO_2/C of 0.6 (CO_2 conversion between 24-12 % at a S/C of 0.5, Figure 5.19e) and S/C < 1.7 for a CO_2/C of 1.1 (CO_2 conversion at zero TOS between 22-5 % in the S/C range of 0.5-1.7, Figure 5.19f). These results matches well with the results of section 5.1.3 (Table 5.1), which show that the higher the S/C ratio, the higher the CO_2/C ratio required to reach positive CO_2 conversion. The reduction of CO_2 emissions also decreases as the S/C ratio increases. The lower CO_2/C ratio (Figure 5.19g) leads to a higher initial values of reduction of CO_2 emissions (from 37.8 % (low S/C) to 33.5 % (high S/C)), whereas with a CO_2/C of 1.1 (Figure 5.19h) the reduction of CO_2 emissions is lower, varying from 32 % (low S/C) to 28 % (high S/C). However, the stability over time on stream of the results is higher for the highest CO_2/C ratio.

The effect of S/C ratio (0.5 and 1.7) at 700 °C and low space time (0.125 $g_{catalyst} \cdot h/g_{oxygenates}$) with a fixed CO_2/C ratio of 0.6 and 1.1 was also studied and the results are shown in Figure 5.20 and Figure C.4 in Annexes (conversion and products yield) and Figure 5.21 (syngas yield and composition, CO_2 conversion and reduction of CO_2 emissions). In these figures, the same effect of the S/C ratio on the initial values of the reaction indices mentioned above for the high space-time conditions (Figure 5.18 and Figure 5.19) is observed, but there is a higher change over TOS of all reaction indices. This result demonstrates that the space time has a much more relevant effect on catalyst deactivation than the S/C or CO_2/C ratios.

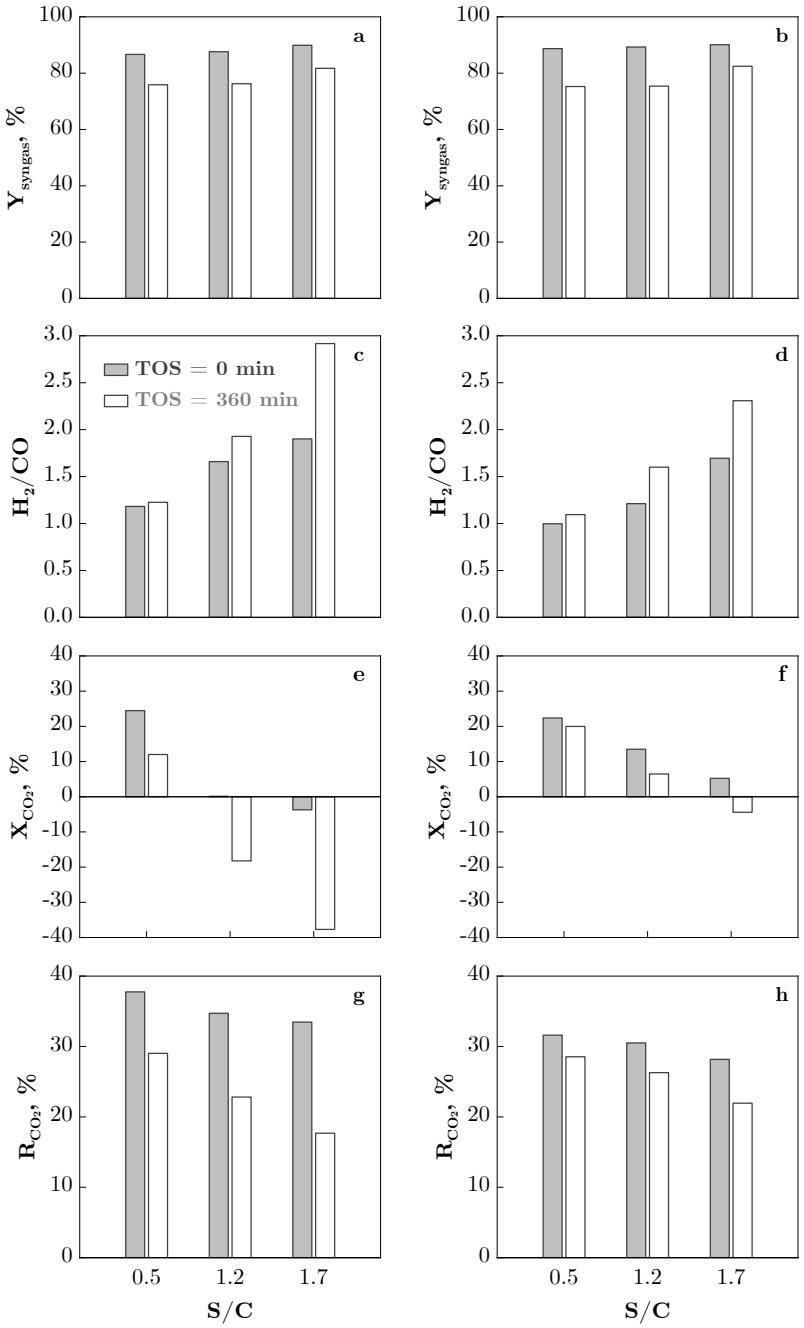

Figure 5.19. Effect of S/C ratio on the initial (TOS=0 min) and final (TOS=360 min) values of syngas yield (a, b), H_2/CO ratio (c, d), CO_2 conversion (e, f) and reduction of CO_2 emissions (g, h) in the CSDR runs at 700 °C and space time of 0.250 $g_{catalyst} \cdot h/g_{oxygenates}$. Left graphs: CO_2/C ratio of 0.6; Right graphs: CO_2/C ratio of 1.1.

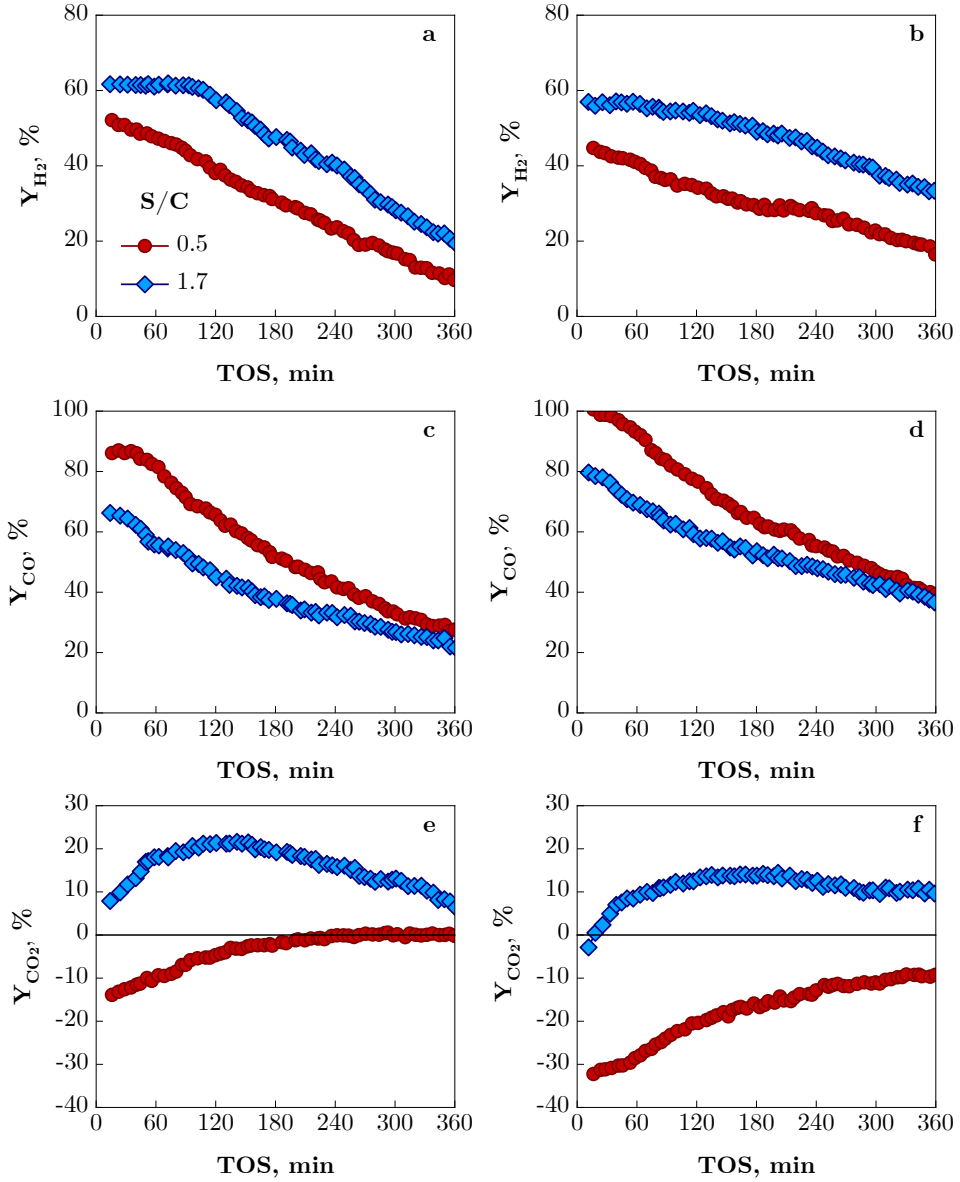

Figure 5.20. Effect of S/C ratio on the evolution with TOS of product yields: H_2 (a, b), CO, (c, d) and CO_2 (e, f) in the CSDR runs at 700 °C and space time of 0.125 $g_{catalyst}$·h/$g_{oxygenates}$ with CO_2/C ratio of 0.6 (left graphs) and 1.1 (right graphs).

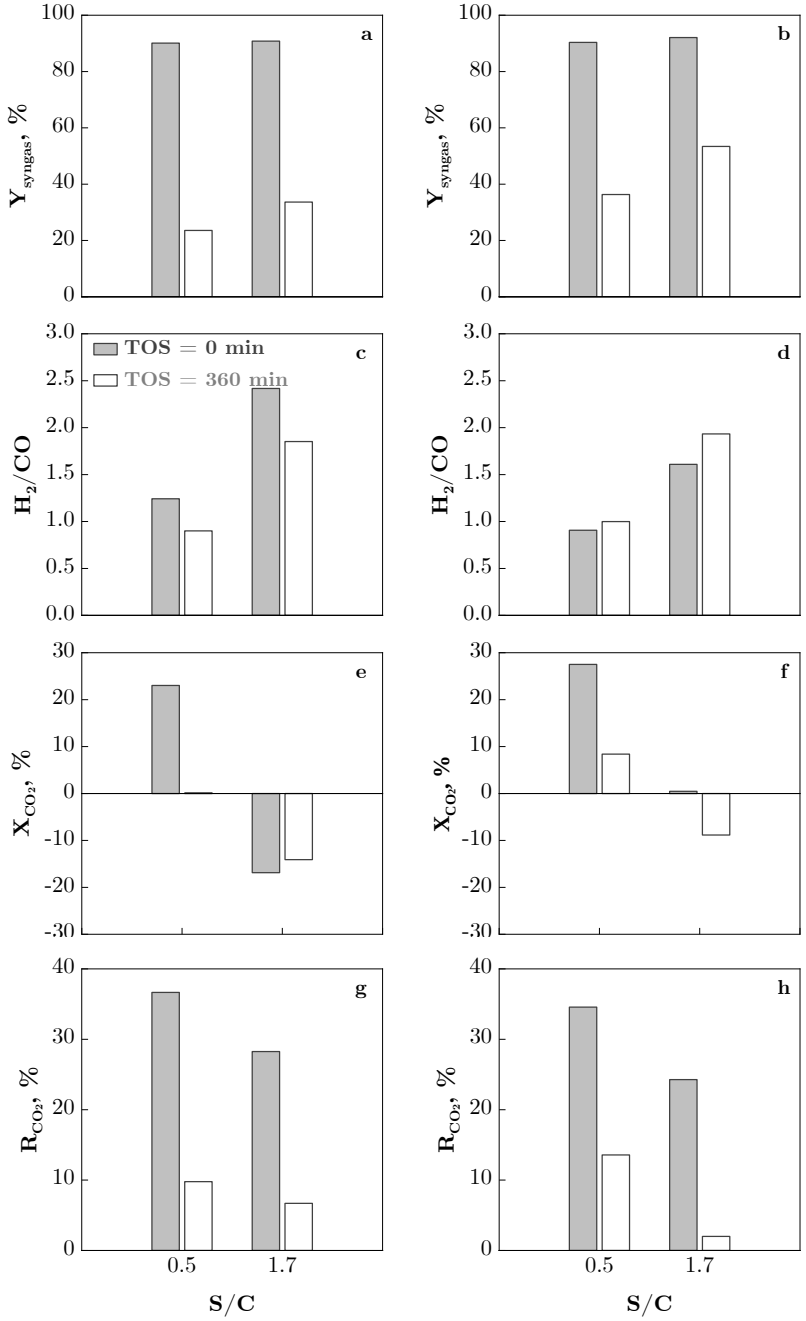

Figure 5.21. Effect of S/C ratio on the initial (TOS=0 min) and final (TOS=360 min) values of syngas yield (a, b), H_2/CO ratio (c, d), CO_2 conversion (e-f) and reduction of CO_2 emissions (g-h) in the CSDR runs at 700 °C and space time of 0.125 $g_{catalyst}$·h/$g_{oxygenates}$. Left graphs: CO_2/C ratio of 0.6; Right graphs: CO_2/C ratio of 1.1.

It is interesting to note that the composition of the syngas (H_2/CO ratio) obtained can be easily adjusted by controlling the operating conditions, and it is feasible to produce a syngas with a H_2/CO ratio in the range of 1-2, suitable for certain applications. In the methanol and Fischer-Tropsch synthesis, the desired H_2/CO ratio is 2, whereas in other processes such as direct DME synthesis, acetic acid or ethanol formation and oxo-synthesis, the stoichiometric requirement of H_2 is lower and a H_2/CO ratio of 1 is suitable [243–247]. Results in previous sections have shown that the H_2/CO ratio decreases with increasing temperature (Figure 5.13c-d) and CO_2/C ratio (Figure 5.16c-d) and with decreasing S/C ratio (Figure 5.19c-d and Figure 5.21c-d). Values of H_2/CO ratio between 1 and 2 are easily attained when operating in the 700-800 °C range, with a CO_2/C ratio in the 0.6-1.1 range and a S/C ratio below 1.7. Furthermore, in this temperature range and with low S/C ratio and high CO_2/C ratio, CO_2 conversion and reduction of CO_2 emissions are maximised

5.2.2. Characterization of used catalyst and coke

This section shows the results of the characterization of the used catalyst samples with different techniques (XRD, TPO, N_2 adsorption-desorption and SEM), in order to ascertain the effect of operating conditions on the deposition of coke on the catalyst surface, changes in Ni oxidation and crystal size, and aging and clogging of the support. It is worth noting that after each reaction, the solids composing the catalytic bed (catalyst+inert (SiC)) were separated by sieving, to avoid masking the characterization of the used catalyst. The particle size selected for each solid (SiC, ~ 75 µm; catalysts 150-250 µm) facilitates this separation. Thus, only traces of inert might remain in the used catalyst after sieving.

5.2.2.1. Structural properties

Figure 5.22 and Figure 5.23 show the XRD patterns of the catalyst samples used in the CSDR runs at different temperatures (Figure 5.22) and different CO_2/C and S/C molar ratios (Figure 5.23).

As in the fresh-reduced catalyst (Figure 2.8a), the presence of Ni^0 and Al_2O_3 species is observed in all used samples, but there are no NiO peaks, confirming that there is no Ni oxidation, due to the highly reducing environment in the CSDR runs, as previously observed in Chapters 3 and 4 under SR and SESR conditions with this catalyst.

The average size of Ni^0 crystals, calculated using Debye-Scherrer equation at $2\theta = 51.8°$, is gathered in Table 5.4 for the effect of temperature and in Table 5.5 for the effect of CO_2/C and S/C molar ratios. As previously observed under SESR conditions (Table 4.6), there is no evidence of a noticeable degree of Ni sintering, as the average crystal size of the used catalyst samples increases very slightly (in the range of 13-18 nm (at different temperatures) and 14-21 nm (at different CO_2/C and S/C ratios) compared to the fresh-reduced catalyst (15 nm). Consequently, under CSDR conditions, coke deposition is also the main cause of deactivation.

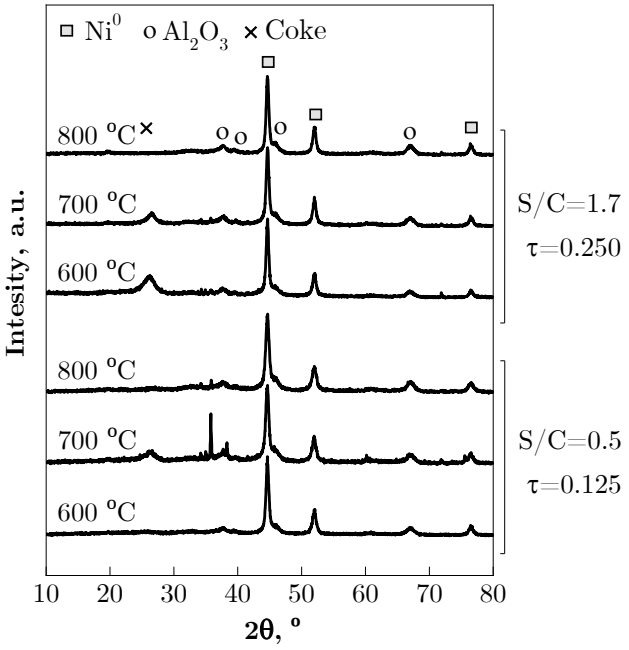

Figure 5.22. XRD patterns of Ni/Al_2O_3 catalyst samples used in the CSDR runs at different temperatures for a CO_2/C ratio of 1.1 with different values of S/C ratio and space time (τ, $g_{catalyst} \cdot h/g_{oxygenates}$).

The presence of a broad peak at a diffraction angle of $2\theta = 26°$ for the catalyst used in the CSDR at 600 °C with high S/C ratio-space time (Figure 5.22) and at 700 °C whatever the space time, CO_2/C and S/C molar ratio conditions (Figure 5.22 and Figure 5.23) suggests the presence of a high crystallinity coke (graphitic carbon). Consequently, these results demonstrate that coke crystallinity is influenced by the reaction conditions.

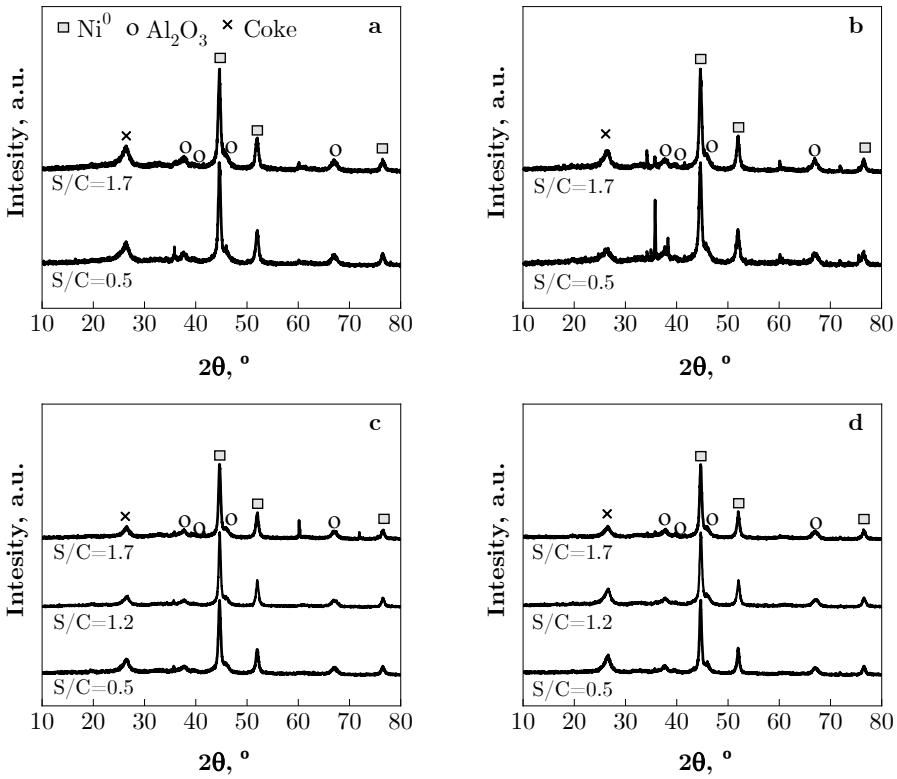

Figure 5.23. XRD patterns of Ni/Al_2O_3 catalyst samples used in the CSDR runs at different S/C ratios at 700 °C with CO_2/C ratio of 0.6 (left graphs) or 1.1 (right graphs) and space time of 0.125 $g_{catalyst}{\cdot}h/g_{oxygenates}$ (upper graphs) or 0.250 $g_{catalyst}{\cdot}h/g_{oxygenates}$ (lower graphs).

Table 5.4. Average Ni^0 crystal size (d_{Ni}) of Ni/Al_2O_3 catalyst samples used in the CSDR runs at 600, 700 and 800 °C for a CO_2/C ratio of 1.1, under low S/C ratio-space time or high S/C ratio-space time conditions.

Temperature, °C	**S/C**	**Space time, $g_{catalyst}$·h/$g_{oxygenates}$**	**d_{Ni}, nm**
600	0.5	0.125	15
700			14
800			13
600	1.7	0.250	18
700			18
800			18

Table 5.5. Average Ni^0 crystal size (d_{Ni}) of Ni/Al_2O_3 catalyst samples used in the CSDR runs at 700 °C for two values of space time and with different combinations of CO_2/C and S/C ratios.

Space time, $g_{catalyst}$·h/$g_{oxygenates}$	**S/C**	**CO_2/C**	**d_{Ni}, nm**
0.125	0.5	0.6	15
		1.1	14
	1.7	0.6	15
		1.1	15
0.250	0.5	0.6	17
		1.1	21
	1.2	0.6	18
		1.1	17
	1.7	0.6	18
		1.1	18

5.2.2.2. Amount and nature of coke

The nature and/or location of the coke deposited on the catalyst particles (combustion peak position) was determined by TPO analysis of the used samples. Figure 5.24 shows the TPO profiles of the used catalyst samples at different reaction temperatures (600, 700 and 800 °C) for a given feed composition and at low and high space time values. As can be seen in Figure 5.24a, the coke formed at 600 °C with a low S/C ratio-space time is predominantly LT-coke, whose combustion peak has a maximum at 449 °C. In contrast, the coke on the catalysts used at 700 and 800 °C is mostly HT-coke (with a maximum at 603 and 610 °C, respectively). Therefore, the increase in temperature from 600 to 800 °C noticeably attenuates the formation of the amorphous coke (first combustion peak). Interestingly, at 600 °C under high S/C ratio-space time conditions (red line in Figure 5.24b), there is a predominant formation of structured carbon on the external surface of the catalyst particles. Thus, the presence of HT-coke (with maximum of combustion peak at 552 °C) is predominant with some presence of LT-coke (442 °C), which is in sharp contrast to the predominant presence of LT-coke observed at 600 °C under low S/C ratio-space time conditions (red line in Figure 5.24a). This result corroborates the relevant role of water (S/C ratio of 1.7) and high space time conditions in favouring the formation of CO by reforming and, as a consequence, also the subsequent Boudouard reaction, thus increasing the formation of filamentous carbon. Likewise, HT-coke prevails at 700 °C and also at 800 °C, although coke formation is insignificant at 800 °C with high S/C ratio-space time conditions (Figure 5.24b) due to the favoured coke gasification at high temperature and with a higher H_2O concentration. [132, 259]. Moreover, the increase in temperature favours the reverse-Boudouard reaction (coke gasification) as shown in section 5.1.1 and Figure A.12.

These TPO profiles in Figure 5.24 are consistent with the XRD diffractograms in Figure 5.22, which show a high intensity peak at θ=26° (corresponding to coke crystalline structures) at 600 °C and high S/C ratio-space time, and at 700 °C for both S/C ratio-space time conditions. The analysis of the TPO profiles shows that the carbon formed becomes more refractory with increasing temperature, as

it shifts towards higher combustion temperatures. However, it should be noted that at 800 °C the deposition of coke is almost insignificant, especially at high S/C ratio-space time conditions, as observed in Figure 5.25, which shows the coke content (wt%) determined from the area under the TPO curves in Figure 5.24. The results in this figure show that an increase in the temperature leads to a significantly lower total coke content.

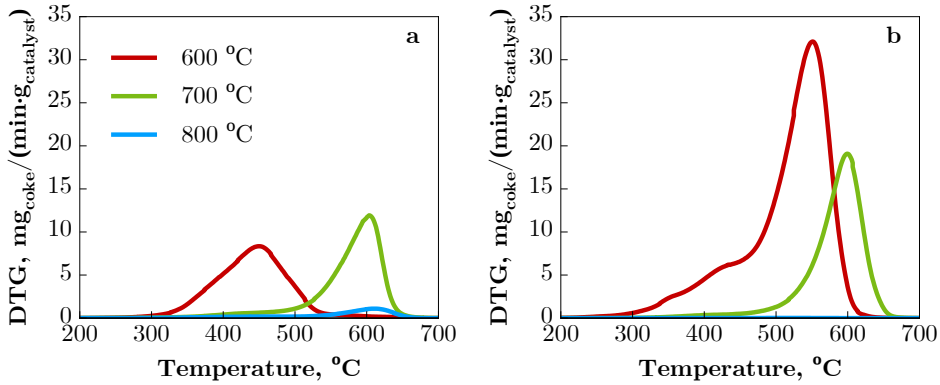

Figure 5.24. Effect of temperature on the TPO profiles of Ni/Al_2O_3 catalyst used in the CSDR runs for a CO_2/C ratio of 1.1 with S/C ratio of 0.5 and space time of 0.125 $g_{catalyst}·h/g_{oxygenates}$ (a) and with S/C ratio of 1.7 and space time of 0.250 $g_{catalyst}·h/g_{oxygenates}$ (b).

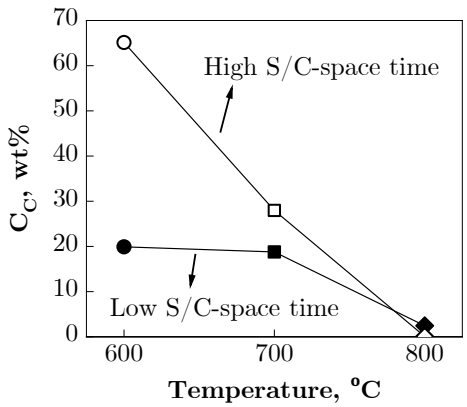

Figure 5.25. Effect of temperature on the coke content (wt%) deposited on Ni/Al_2O_3 catalyst used in the CSDR runs for a CO_2/C ratio of 1.1 with S/C ratio of 0.5 and space time of 0.125 $g_{catalyst}·h/g_{oxygenates}$ (full markers) and with S/C ratio of 1.7 and space time of 0.250 $g_{catalyst}·h/g_{oxygenates}$ (empty markers).

Figure 5.26 shows the effect of S/C ratio on the TPO profiles at 700 °C for different values of CO_2/C ratio and space time. Overall, all the TPO profiles show that HT-coke (that with the maximum of the combustion peak above 500 °C) is the prevailing coke fraction, with the maximum around 603-612 °C (for low space time, Figure 5.26a-b) and 600-609 °C (for high space time, Figure 5.26c-d), that is, the peak maximum shifts slightly towards lower temperatures (5-10 °C) with increasing space time, suggesting that the coke is less structured.

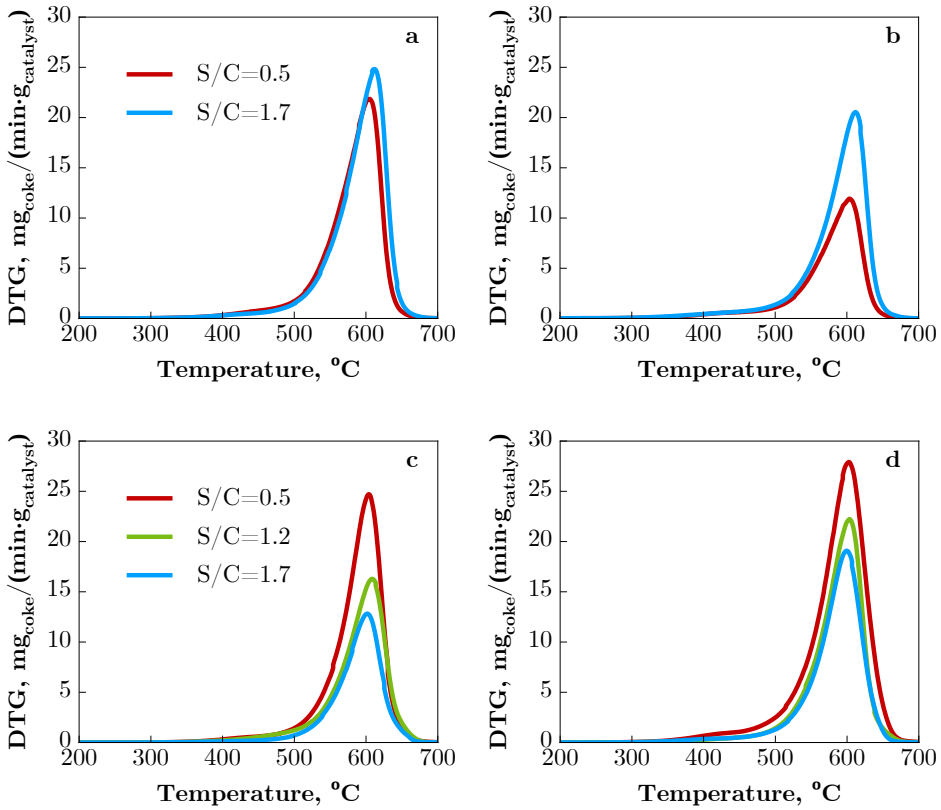

Figure 5.26. Effect of S/C ratio on the TPO profiles of Ni/Al_2O_3 catalyst used in the CSDR runs at 700 °C for different values of CO_2/C ratio (0.6 (a and c) and 1.1 (b and d)) and different space time values (0.125 $g_{catalyst}$·h/$g_{oxygenates}$ (a and b) and 0.250 $g_{catalyst}$·h/$g_{oxygenates}$ (c and d)).

Additionally, Figure 5.27 displays the results of coke content on the used catalysts determined from the TPO profiles of Figure 5.26. As observed in Figure 5.27a, at

low space time conditions, the total coke content decreases with increasing CO_2/C ratio, which is an expected result because the increase in CO_2 content attenuates coke formation by promoting the reverse-Boudouard reaction. Conversely, under high space time conditions (Figure 5.27b), the total coke deposited increases with increasing CO_2/C ratio, which at a first sight is an unexpected result. This result could be explained by the relevant role of CO_2 in promoting the reverse-WGS reaction (whose extent is high under high space time conditions), thus increasing the concentration of CO (precursor of HT-coke by Boudouard reaction).

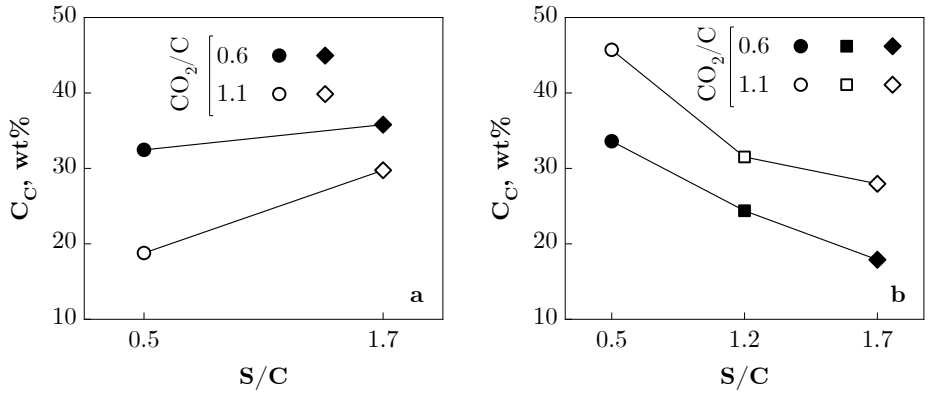

Figure 5.27. Effect of S/C and CO_2/C ratios on the coke content (wt%) deposited on Ni/Al_2O_3 catalyst used in the CSDR runs at 700 °C with a space time of 0.125 $g_{catalyst}{\cdot}h/g_{oxygenates}$ (a) and 0.250 $g_{catalyst}{\cdot}h/g_{oxygenates}$ (b).

Considering the effect of S/C molar ratio on coke deposition, also shown in Figure 5.27, under low space time conditions (Figure 5.27a), the increase in S/C ratio increases the amount of coke, which could be explained because the increase in H_2O concentration attenuates the conversion of oxygenates and thus, increases the coke deposition due to the decomposition/cracking of oxygenates. In contrast, for high space time conditions (Figure 5.27b), the total coke content decreases with increasing S/C ratio, indicating that the increase in H_2O concentration promotes the carbon gasification reaction, besides decreasing the concentration of oxygenates in the bio-oil. The higher H_2O concentration also contributes to a lower concentration of CO (as it shifts the equilibrium of the WGS reaction to the right) and thus to a lower HT-coke formation by Boudouard reaction.

Therefore, these results suggest differences in the mechanism of coke formation, which is significantly affected by the S/C and CO_2/C molar ratios at different space time studied, although the TPO profiles of the resulting carbon deposits in Figure 5.26 do not change significantly.

5.2.2.3. Physical properties

In order to evaluate the deterioration of the porous structure of the catalyst, N_2 adsorption-desorption isotherms (Figure B.7-Figure B.9) were obtained for used catalyst samples. All samples exhibit an isotherm type IV with H2-type hysteresis cycle for the catalyst samples used at low space time, whereas a H3-type hysteresis cycle is noticed for the catalysts used at high space time, which does not show any limiting adsorption at high pressure ($P/P_0 \approx 1$).

When comparing the results of the textural properties for the used catalyst samples in Table 5.6 with those corresponding to the fresh-reduced catalyst (Table 2.7), it can be observed that for low space time conditions (Figure B.7 (solid lines) and Figure B.8), there is a loss of mesoporosity (significantly lower total volume adsorbed at high pressure ($P/P_0 \approx 1$), evidencing a partial blockage of the mesopores by the coke deposited, which causes a decrease in BET surface area, pore volume and average pore diameter, except at 800 °C. This decrease in catalyst porosity contributes to a more rapid deactivation. The effect of reaction temperature on BET surface area, pore volume and average pore diameter of the used catalyst samples is remarkable (Table 5.6). However, the S/C and CO_2/C ratios have a lower effect on the textural properties (Table 5.7). Under low space time conditions, the BET surface area and pore volume of the used catalyst samples are higher with increasing the S/C ratio, while for the highest space time the BET surface area is lower with increasing the S/C ratio. Besides, the higher CO_2/C ratio slightly increases the BET surface area (Table 5.7). However, there is no clear trend for pore volume and average pore diameter.

Table 5.6. Effect of temperature on the physical properties of Ni/Al_2O_3 catalyst samples used in the CSDR runs for a CO_2/C ratio of 1.1 and different values of S/C ratio and space time.

Temperature, °C	**S/C**	**Space time, $g_{catalyst}·h/g_{oxygenates}$**	**S_{BET}, m^2/g**	**V_{pore}, cm^3/g**	**d_{pore}, nm**
600	0.5	0.125	36.0	0.055	6.1
700			43.2	0.141	12.1
800			64.7	0.195	10.9
600	1.7	0.250	80.6	0.211	15.7
700			97.2	0.282	13.4
800			55.6	0.271	19.5

Table 5.7. Effect of space time and feed composition on the physical properties of Ni/Al_2O_3 catalyst samples used in the CSDR of raw bio-oil at 700 °C.

Space time, $g_{catalyst}·h/g_{oxygenates}$	**S/C**	**CO_2/C**	**S_{BET}, m^2/g**	**V_{pore}, cm^3/g**	**d_{pore}, nm**
0.125	0.5	0.6	59.4	0.160	10.3
		1.1	43.2	0.141	12.1
	1.7	0.6	63.9	0.172	10.4
		1.1	69.3	0.179	10.0
0.250	0.5	0.6	94.0	0.200	9.1
		1.1	123.0	0.304	12.3
	1.2	0.6	88.5	0.206	10.1
		1.1	94.5	0.206	9.6
	1.7	0.6	85.1	0.201	10.3
		1.1	97.2	0.282	13.4

These results indicate the relevant impact of the amount and morphology of coke on the physical properties of the used catalysts and the relevance of the reaction conditions (mainly space time and temperature) on these properties. Thus, there is some direct correlation between the amount of coke deposited and the BET surface area of the used catalyst samples at different S/C and CO_2/C ratios. As can be seen in Figure 5.28, the higher the amount of coke deposited, the higher the BET surface area. These results suggest that even at low space time conditions there are some porous structures in the coke deposits which could contribute to an overall high BET surface area (similar to the fresh-reduced catalyst), although they also cause some pore blockage that deactivates the catalyst. Moreover, the increase in BET surface area for the used catalysts compared to that of the fresh-reduced catalyst (65.1 m^2/g) suggests the presence of a porous carbon structure, as that corresponding to filamentous carbon (in agreement with the SEM images shown later), and associated to the HT-coke in the TPO profiles, which is consistent with the high stability observed in the CSDR runs at high space time conditions.

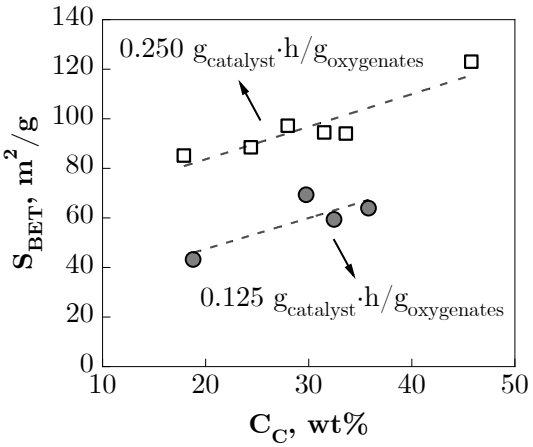

Figure 5.28. Correlation between coke content and BET surface area of Ni/Al_2O_3 catalyst samples used under the operating conditions of Figure 5.26 and Figure 5.27.

5.2.2.4. Morphology and location of coke

Figure 5.29 and Figure 5.30 show SEM images with a backscattered electron (BSE) detector of the catalyst samples used in the CSDR runs at different temperatures and different S/C molar ratios, respectively.

The presence of semi-bright particles in the catalyst samples used in the CSDR run at 600 °C with low S/C ratio and space time (Figure 5.29a) indicates poor coke deposition on the external surface. The lower deposition of external coke is consistent with the TPO results (absence of HT-coke) (Figure 5.24a). In contrast, almost all the particles in the samples used in the CSDR runs at 600 °C with high S/C ratio-space time conditions (Figure 5.29b) and at 700 °C regardless of operating conditions (Figure 5.30) are uniformly dark, which indicates carbon deposition on the external surface of the particles. It should be pointed out that when the coke content is high (65 wt% at 600 °C with high S/C ratio-space time conditions, Figure 5.25), the used catalyst particles have a rough surface (Figure 5.29b), which may indicate a collapse of the catalyst particles due to the excessive coke growth.

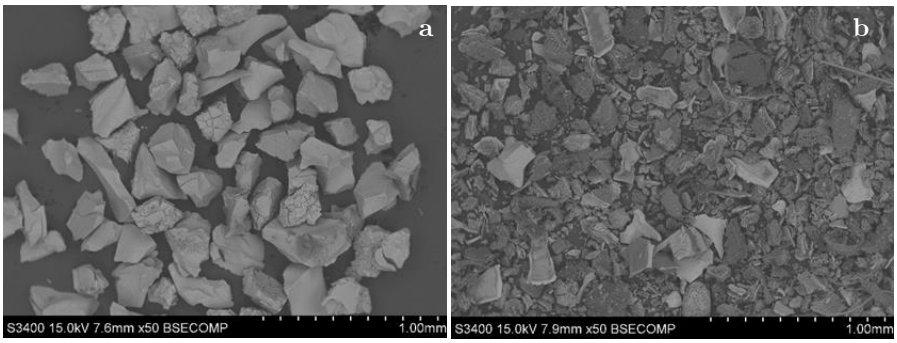

Figure 5.29. BSE-SEM images of Ni/Al_2O_3 catalyst used in the CSDR runs at 600 °C, CO_2/C ratio of 1.1 with S/C ratio of 0.5 and space time of 0.125 $g_{catalyst}{\cdot}h/g_{oxygenates}$ (a) and S/C ratio of 1.7 and space time of 0.250 $g_{catalyst}{\cdot}h/g_{oxygenates}$ (b).

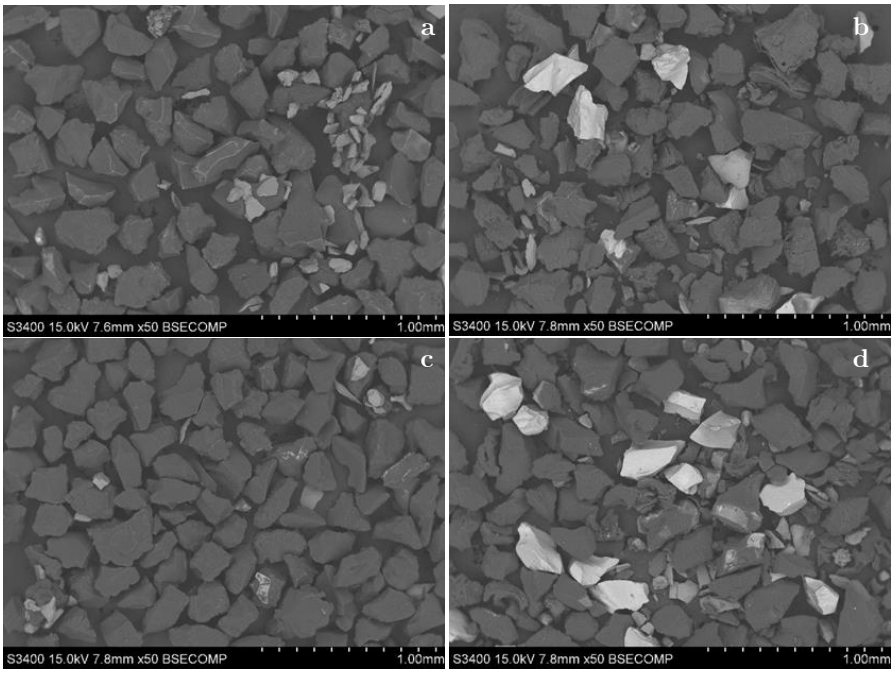

Figure 5.30. BSE-SEM images of Ni/Al_2O_3 catalyst used in the CSDR runs at 700 °C, CO_2/C ratio of 1.1 and S/C ratio of 0.5 (a, b) or S/C ratio of 1.7 (c, d) with space time of 0.125 $g_{catalyst}{\cdot}h/g_{oxygenates}$ (a, c) or space time of 0.250 $g_{catalyst}{\cdot}h/g_{oxygenates}$ (b, d).

The coke morphology is studied in more detail with SEM images using a secondary electron detector (SE-SEM), which enables zooming to the catalyst surface. The surface of the used catalyst at 600 °C with low S/C ratio-space time conditions (Figure 5.31a) shows a porous surface similar to that of the fresh-reduced catalyst (Figure 2.10a), evidencing a low carbon deposition on the external surface. Thus, the coke formed may be composed of amorphous mass of carbon, in line with the TPO results (Figure 5.24a). However, in the catalyst particles used in the CSDR run at 600°C but with a high S/C ratio-space time (Figure 5.31b), the external surface is covered with carbon filaments that are well defined and heterogeneous in size, with remarkably large diameters. In the run at 700 °C with low space time and for both S/C ratios studied (Figure 5.32a and Figure 5.32c), the surface of the catalyst particles shows compacted carbon filaments and a second carbon phase between the filaments, which may consist of a structured carbon, whose formation is promoted at high reaction temperature

(700 °C) and which clogs the porous structure, contributing to a rapid catalyst deactivation (graphs in Figure 5.20) [255]. This formation of structured coke by repolymerization of phenolic compounds in bio-oil is well established in the literature [164]. Its presence agglomerates the carbon filaments and increases the coke combustion temperature, as verified by the TPO measurement (603-612 °C at low space time and around 600-609 °C at high space time) (Figure 5.26). This second phase, with a graphite-like structure, also observed in the SR of bio-oil (CO_2/C ratio of 0) with this catalyst [96], explains the slight crystallinity observed in the XRD patterns for the catalysts used at 700 °C (Figure 5.23b).

In contrast, the catalyst used at high space time (Figure 5.32b and Figure 5.32d) has, in addition to compacted carbon structures, particles with a different coke morphology. Thus, heterogeneous carbon filaments are observed at the lowest S/C ratio tested (Figure 5.32b), whereas at a S/C ratio of 1.7 the particles have a tangle of small carbon filaments alongside the compacted carbon structures (Figure 5.32d). These carbon filaments are responsible for the increase in BET surface area (Table 5.7). Therefore, these catalyst particles covered with filamentous coke can remain active (Figure 5.11b, Figure 5.12b, Figure 5.12d, Figure 5.12f, Figure 5.17b, Figure 5.18b, Figure 5.18d, Figure 5.18f) because the presence of these small carbon filaments does not block access to the active sites of the catalyst [132].

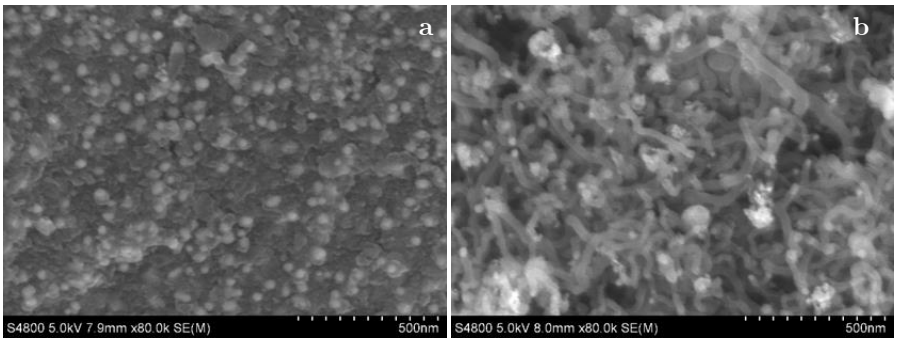

Figure 5.31. SE-SEM images of Ni/Al_2O_3 catalyst used in the CSDR runs at 600 °C, CO_2/C ratio of 1.1 with S/C ratio of 0.5 and space time of 0.125 $g_{catalyst}·h/g_{oxygenates}$ (a) and S/C ratio of 1.7 and space time of 0.250 $g_{catalyst}·h/g_{oxygenates}$ (b).

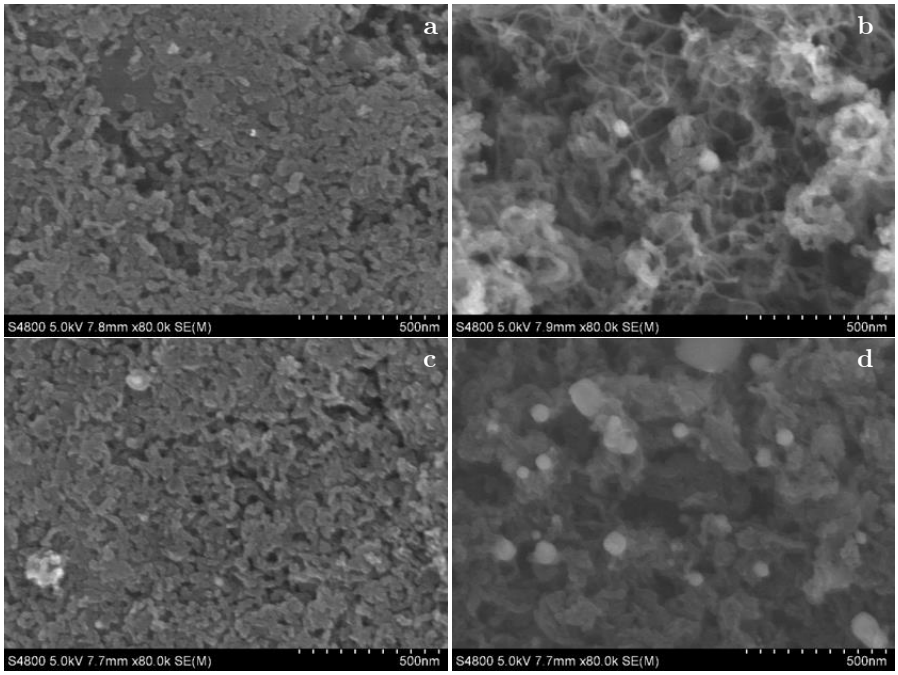

Figure 5.32. SE-SEM images of Ni/Al_2O_3 catalyst used in the CSDR runs at 700 °C, CO_2/C ratio of 1.1 and S/C ratio of 0.5 (a, b) or S/C ratio of 1.7 (c, d) with space time of 0.125 $g_{catalyst}{\cdot}h/g_{oxygenates}$ (a, c) or 0.250 $g_{catalyst}{\cdot}h/g_{oxygenates}$ (b, d).

Chapter 6

CONCLUSIONS

.

On the role of individual oxygenated compounds in the SR of bio-oil.

1. Thermodynamic study

The equilibrium yields of products in the SR of all the oxygenated compounds studied follow the same trend with the increase in temperature: the yield of H_2 and CO_2 pass through a maximum, which is more pronounced at high S/C ratios, especially for CO_2, the yield of CO increases and the yield of CH_4 decreases. The yields of H_2 and CO_2 increase with the S/C ratio, whereas those of CO and CH_4 decrease due to the promotion of WGS and SR reactions, with these trends being attenuated at high S/C ratios.

S/C ratio of 5 and 610–644 °C temperature range are the most suitable conditions for attaining high equilibrium H_2 yields (90-92 %), without excessive penalty in energy requirements in the SR of all oxygenates. The maximum H_2 yield follows an order opposite to the stoichiometric S/C ratio of each oxygenate, in the order acetic acid, hydroxyacetaldehyde, mannose > levulinic acid, acetol > acetaldehyde, vanillin, catechol > phenol, guaiacol > acetone, cyclohexanone, and is obtained at a lower temperature as this ratio decreases.

The inert addition slightly increases H_2 yield and decreases coke formation at S/C ratio of 1.5, but this effect is not significant for S/C ratios above 5.

The coke yield is significant at low temperatures (< 600 °C) and low S/C ratios (below the stoichiometric value). The heavier oxygenates have a greater tendency for coke formation, in the order phenol > catechol ≈ guaiacol > vanillin. Among the light oxygenates (C_1-C_3), acetone has the highest coke formation capacity.

The following original correlations are proposed to predict the maximum yield of H_2, the temperature required to attain it and the corresponding yields of by-products in the SR of oxygenates from the values of the C/S ratio in the feed and the oxygenate composition (expressed as H/C, O/C and O/H ratios):

$$Y_{H_2}=\left(101.2\text{-}59.46\ \left(\frac{C}{S}\right)\right)+\left(\text{-}0.429+6.279\left(\frac{C}{S}\right)\right)\cdot\left(\frac{H}{C}+\frac{O}{C}+\frac{O}{H}\right)$$

$$T=\left(553.4+387.1\ \left(\frac{C}{S}\right)\right)+\left(\text{-}7.252\text{-}100.0\left(\frac{C}{S}\right)\right)\cdot\left(\frac{O}{C}+\frac{O}{H}\right)$$

$$Y_{CO_2}=\left(102.3\text{-}130.4\ \left(\frac{C}{S}\right)\right)+\left(\text{-}0.848+37.78\left(\frac{C}{S}\right)\right)\cdot\left(\frac{O}{C}+\frac{O}{H}\right)$$

$$Y_{CO}=\left(\text{-}2.81+130.2\ \left(\frac{C}{S}\right)\right)+\left(1.099\text{-}38.65\left(\frac{C}{S}\right)\right)\cdot\left(\frac{O}{C}+\frac{O}{H}\right)$$

$$Y_{CH_4}=\left(\text{-}0.24+7.45\ \left(\frac{C}{S}\right)\text{-}9.27\left(\frac{C}{S}\right)^2\right)+\left(0.08\text{-}2.1\left(\frac{C}{S}\right)+3.66\left(\frac{C}{S}\right)^2\right)\cdot\left(\frac{O}{C}+\frac{O}{H}\right)$$

2. Role in the deactivation by coke of the $NiAl_2O_4$ spinel derived catalyst

In the 600-700 °C temperature range, catalyst stability is mainly affected by coke deposition, whose effect on the deactivation rate depends greatly on the nature of the reactant oxygenate, as it influences the nature of the coke and its deactivation capacity.

The most rapid deactivation occurs in the SR of guaiacol, caused by the deposition of pyrolytic and amorphous coke, which blocks the Ni sites and whose formation inhibits that of filamentous carbon. The formation of filamentous coke in the SR of aliphatic oxygenates (especially for ethanol and acetone at 600 °C) by the Boudouard reaction causes only a slight deactivation, because this coke does not contribute to block the porous structure.

The increase in temperature from 600 to 700 °C favours the extent of encapsulating coke formation reactions by polymerization and attenuates the formation of filamentous coke. However, the effect on deactivation is moderate, because the rates of SR and encapsulating coke gasification reactions also increase.

In the SR of raw bio-oil, a synergy between the coke formation mechanisms of the different oxygenates is expected, but the formation of encapsulating coke from phenolic oxygenates is preferential and inhibits the formation of filamentous coke from aliphatic oxygenates. Therefore, guaiacol is a suitable model oxygenated compound for testing the stability of new catalysts and for adjusting the reaction conditions in order to minimise the formation of the deactivating coke.

On the sorption enhanced steam reforming (SESR) of raw bio-oil over Ni-based catalysts.

1- Effect of sorbent type, catalyst support and sorbent/catalyst mass ratio

A suitable sorbent/catalyst mass ratio is required for each sorbent+catalyst pair, because the sorbent not only contributes to CO_2 capture (which shifts reforming and WGS reactions towards H_2 formation), but it is also active for oxygenates decomposition/cracking reaction, which competes with the catalyst activity for reforming reactions, thus affecting the yield of products in the capture period and the morphology and location of the coke, which in turn affects the catalyst stability.

Dolomite is a more suitable sorbent due to its lower activity for decomposition/cracking of oxygenates, that allows i) attaining a higher H_2 yield and purity in the capture period; ii) using a higher sorbent/catalyst mass ratio in the catalytic bed, thus with longer duration of the capture period; and iii) higher catalyst stability due to a lower amorphous and encapsulating coke deposition compared to CaO/mayenite.

The Ni/Al_2O_3 catalyst has superior performance compared to Ni/CeO_2 catalyst due to the higher promotion of oxygenates reforming reaction of the former, which counteracts the decomposition/cracking reaction over the sorbent and allows attaining higher H_2 yield and using higher sorbent/catalyst ratios with higher stability.

The dolomite+(Ni/Al_2O_3 derived from $NiAl_2O_4$ spinel) system is the best choice for the SESR of raw bio-oil. At 600 °C, S/C ratio of 3.4 and space time of 0.15 $g_{catalyst}{\cdot}h/g_{oxygenates}$, a dolomite/($NiAl_2O_4$) mass ratio of 10 allows to reach almost 100 % of H_2 yield and selectivity during the effective CO_2 capture period (about 30 min) and to improve the catalyst stability with respect to the SR when operating in a packed-bed reactor.

2- Comparison of packed and fluidized-bed reactors

The performance of FBR at zero TOS is slightly inferior than that of PBR for both SR and SESR processes, due to the less efficient contact between the gas fluid and catalyst particles (bubbling or slugging phenomena), causing a decrease in the oxygenates conversion and coke formation. The initial oxygenates conversion is almost complete in PBR and of 88 % in FBR, with H_2 yields of 80 % and 69 % for the SR process, and of 99 % and 92 % during the CO_2 capture period of the SESR runs in the PBR and FBR, respectively.

In the SR runs, catalyst deactivation is slower in the FBR due to the rejuvenation of the catalyst surface by the moving particles, which favours external coke gasification and attenuates the growth of carbon filaments on the external surface (amorphous carbon formation in the internal porous structure is unaffected). This phenomenon does not occur in PBR, which leads to more developed coke structures on the catalyst surface, such as carbon filaments and spheres (the latter are responsible for catalyst deactivation, as they can encapsulate Ni sites and block the access to mesopores).

In both reactors, the presence of dolomite prolongs the period of stable performance due to the contribution of dolomite activity to reforming reactions, although the subsequent deactivation is slightly faster compared to the SR process, more noticeably in the FBR.

The effect of dolomite on the amount and nature of coke depends on the reactor type. In PBR, dolomite acts mainly as a guard catalyst, slightly decreasing the total coke content on the catalyst and changing the coke nature

to a combination of amorphous and filamentous carbons (no carbon spheres). In FBR, the presence of dolomite favours the formation of carbon filaments, possibly due to the vigorous contact between dolomite and catalyst particles to favour the coke formation mechanisms, as dolomite favours the decomposition/cracking reaction of oxygenates, forming filamentous coke precursors (CH_4 and hydrocarbons), and competes to adsorb water, preventing coke gasification on the catalyst.

3- Effect of conditions and cyclic operation with Ni/Al_2O_3 catalyst+dolomite

The highest H_2 yield (~ 92 %) and purity (~ 99 %) in the capture period are obtained in the 600-650 °C range and with a dolomite/catalyst mass ratio of 10 due to the synergy between catalyst and sorbent activity. The catalyst exhibits high stability at 600 °C due to the low content and filamentous nature of the coke deposited, whose deposition is attenuated by the gasification (favoured by the increase in temperature) and by the activity of the dolomite under these conditions for the reforming of oxygenates from bio-oil.

The catalyst/sorbent system studied is interesting for the scale-up of bio-oil SESR, due to its good performance in reaction-regeneration cycles. The joint regeneration of the two materials is possible (at 850 °C in air for 4 h), although the catalyst undergoes a partial irreversible deactivation in the first two cycles, after which it reaches a pseudo-stable state with reproducible performance in the subsequent cycles. The causes of the slight irreversible deactivation in the first two cycles (a lower formation of Ni^0 crystals and their redistribution towards the inside of the Al_2O_3 support) are minimised with the reduction of the catalyst at 900 °C.

On the combined steam/dry reforming (CSDR) of raw bio-oil.

1. Thermodynamic study

The results of the thermodynamic study have shown good prospects for the development of bio-oil CSDR technology, combining the objectives of CO_2 and

a biomass derivative (bio-oil) valorization and sustainable production of a syngas with the appropriate composition for its use as raw material in the production of fuels and chemicals.

Above 700 °C, syngas yield > 99 % of the stoichiometric value is achieved for any feed composition, with positive CO_2 conversion when suitable combinations of S/C and CO_2/C ratios are used (the higher the S/C ratio, the higher the CO_2/C ratio required). However, the H_2/CO ratio of the syngas decreases exponentially with increasing temperature, being less than 3 at the conditions that maximise the syngas yield.

At 900 °C with S/CO_2/C ratio of 0.5/0.5/1, almost 100 % of syngas yield is attained with the maximum CO_2 conversion (48 %) and reduction of CO_2 emissions compared to the SR unit (49 %) and with the lowest energy requirement (heat exchanger duty of 390 kJ/mol and reaction heat of 385 kJ/mol), but with a H_2/CO ratio (0.84) of little interest for the production of fuels and chemicals. Obtaining a higher H_2/CO ratio while maintaining maximum syngas yield, requires increasing the S/C ratio, which involves a lower CO_2 conversion and higher heat exchangers duty.

H_2/CO ratio of 1 can be achieved with syngas yield > 99 % and positive CO_2 conversion (in the range of 26-3 %) over a wide range of feed compositions (CO_2/C ratio in the 0.5-5 range and S/C ratio in the 1-2.5 range). However, the range of conditions that maximise the syngas yield (> 98 %) with a target H_2/CO ratio of 2 is narrower (CO_2/C ratio in the 0.5-2.5 range and S/C ratio in the 1.8-3 range) and leads to negative CO_2 conversion (between -48.5 % and -9.7 %) and, therefore, to lower reduction of CO_2 emissions with respect to the SR process (between 19.4 % and 13.9 %) than with a target H_2/CO ratio of 1 (between 13.4 % and 42.1 %).

2. *Effect of operating conditions for $NiAl_2O_4$ spinel-derived catalyst*

The increase in temperature in the 600-800 °C range (mostly between 600-700 °C) leads to a significant increase in oxygenates and CO_2 conversion.

Consequently, the syngas yield and the reduction of CO_2 emissions also increase, but the H_2/CO ratio decreases, reaching values below 1 at 800 °C when operating with a low S/C ratio (0.5) and a high CO_2/C ratio (1.1). The increase of the CO_2/C ratio from 0.6 to 1.1 does not affect the syngas yield (due to its opposite effect on the yields of H_2 and CO), but decreases the H_2/CO ratio of the syngas. The increase of the S/C ratio from 0.5 to 1.7 has practically no effect on the conversion of oxygenates and the syngas yield, but it has an important effect both on the conversion of CO_2 (which decreases notably) and on the composition of the syngas, whose H_2/CO ratio increases significantly.

The main cause of catalyst deactivation is the deposition of coke, whose amount and nature depend on the operating conditions, in particular temperature and space time, due to their incidence on oxygenates concentration (precursors of the amorphous coke that blocks the Ni sites). The coke deposition and the deactivation rate are strongly attenuated with a space time of 0.250 $g_{catalyst} \cdot h/g_{oxygenates}$, which facilitates the formation of filamentous coke, and at 800 °C, which promotes coke gasification. This stability of the catalyst is also improved by increasing the CO_2/C ratio, and is little dependent on the S/C ratio, obtaining for the conditions of 800 °C, CO_2/C ratio of 1.1, S/C ratio of 1.7 and space time of 0.250 $g_{catalyst} \cdot h/g_{oxygenates}$ a syngas yield of about 90 %, with a H_2/CO ratio of 1.6, conversion of oxygenates of 80 % and of CO_2 of 7 %, and a reduction of CO_2 emissions with respect to the SR process of 28 %. The conversion of CO_2 can be significantly increased ($> 23\%$) by decreasing the S/C ratio to 0.5, although at the expense of a reduction in the H_2/CO ratio (< 1) of the syngas produced.

NOMENCLATURE

A_D, A_{D3}, A_G	Area of the D (or D3) and G bands determined from deconvolution of Raman spectra
b_k	Total number of atoms of each k atomic species (C, H, O)
C_C	Coke content, wt%
Ca-M	CaO/mayenite
CO_2/C	CO_2-to-carbon molar ratio
d_p, d_{Ni}	Particle size or average Ni crystal size, nm
d_{pore}	Pore diameter, nm
E_B	Binding energy of the sample electrons, eV
E_k	Kinetic energy of the emitted electrons, eV
F_{H2}	H_2 molar flow rate in the product stream, mol/min
$F^0_{H_2}$	H_2 stoichiometric molar flow rate according to the global stoichiometry for the bio-oil SR (Eq. (1.13)), mol/min
$F^0_{H_2+CO}$	H_2+CO stoichiometric molar flow rate for the SR process, according to Eq. (1.14), mol/min
F_i	Carbon-based molar flow rate of the i product (CO_2, CO, CH_4 and light hydrocarbons (C_aH_b)) in the effluent (out) stream of the reactor, mol C/min
F_{in}	Carbon-based molar flow rate of the oxygenates at the reactor inlet, mol C/min

$F_{in,\ CO2}$, $F_{out,\ CO2}$	CO_2 molar flow rate at the reactor inlet and outlet, respectively, mol/min
$F_{out,\ gas}$	Carbon-based molar flow rates of the carbonaceous gaseous product (CO_2, CO, CH_4 and light hydrocarbons (C_aH_b)) at the reactor outlet, mol C/min
G, G_i^0	Gibbs energy of the system and of i product at standard state, kJ/mol
G_{C1}HSV	Methane-equivalent gas hourly space velocity, h^{-1}
GHSV	Gas hourly space velocity, h^{-1}
HHV	Higher heating value, MJ/kg
hυ	Energy of the incident photon, eV
I_D, I_{D3}, I_G	Intensity of the D (or D3) and G bands determined from deconvolution of Raman spectra
K	Shape factor for Debye-Scherrer equation (common value: 0.9)
LHSV	Liquid hourly space velocity, h^{-1}
M	Total number of atomic species (C, H, O)
m/z	Mass to charge ratio
N	Total number of products
n_i	Number of moles of i product
P	Pressure, atm
P/P_0	Relative pressure
R	Universal gas constant, $8.314 \cdot 10^3$ kJ/mol·K
S/C	Steam-to-carbon molar ratio

$(S/C)_{st}$,	Stoichiometric steam-to-carbon molar ratio
S_{BET}	BET surface area, m^2/g
T	Temperature, °C
TOS	Time on stream, h or min
R_{CO2}	Reduction of CO_2 emissions, %
u	Linear gas velocity, cm/s
u_{mf}	Minimum fluidization velocity, cm/s
V_{ads}	Adsorbed volume of N_2, cm^3/g
V_{pore}	Pore volume, cm^3/g
WHSV	Weight hourly space velocity, h^{-1}
X	Conversion of oxygenates, %
X_{CO2}	Conversion of CO_2, %
y_i	Mol fraction of i product
Y_i	Yield of products, %

Greek letters

ΔH	Enthalpy, kJ/mol
ΔH_r	Reaction heat, kJ/mol
ΔH_{HE}	Heat exchanger duty, kJ/mol
β	Width at half height of the diffraction peak, rad
λ	Radiation wavelength, Å

α_{ik}	Number of atoms of k atomic species (C, H, O) contained in each molecule of i product
τ	Average crystallite size, nm
ϑ	Angle of the peak, °

Abbreviations and acronyms

AE	Alkaline electrolysis
ASTM	American Society for Testing and Materials
ATR	Autothermal reforming
BET	Brunauer-Emmett-Teller
BJH	Barrett-Joyner-Halenda
BRM	Bi-reforming of methane
BSE-SEM	Backscatter electron-Scanning electron microscopy
CCS	Carbon Capture and Storage
CCUS	Carbon Capture, Usage and Storage
C_aH_b	Light hydrocarbons (C_2-C_3)
CLR	Chemical looping reforming
CNT	Carbon nanotubes
CPOX	Catalytic partial oxidation
CSDR	Combined steam/dry reforming
DME	Dimethyl ether
DR	Dry reforming

DTG	Derivative thermogravimetric
FBR	Fluidized-bed reactor
GC	Gas chromatography
GHG	Greenhouse Gas
HDO	Hydrodeoxygenation
HT-Coke	High temperature coke (combustion peak burns at $>$ 500 °C)
HTE	High temperature electrolyser
IPHE	International Partnership for Hydrogen and Fuel Cells in the Economy
IPCC	Intergovernmental Panel on Climate Change
IUPAC	International Union of Pure and Applied Chemistry
LT-Coke	Low temperature coke (combustion peak burns at $<$ 500 °C)
LT1, LT2	Low temperature coke (LT-Coke) with a maximum combustion peak near 300 °C (LT1) and between 350-500 °C (LT2)
LTE	Low temperature electrolyser
MDR	Methane dry reforming
MS	Mass spectrometry
MSR	Methane steam reforming
MWCNT	Multiwall carbon nanotubes
NIST	National Institute of Standards and Technology

OC	Oxidative coupling
OD	Oxidative dehydrogenation
OSR	Oxidative steam reforming
PBR	Packed-bed reactor
PDF	Powder Diffraction File
PEM	Proton exchange membrane
PL	Pyrolytic lignin
PNS	Purple non-sulphur
POX	Partial oxidation
PR	Peng-Robinson
SEM	Scanning electron microscopy
SE-SEM	Secondary electron-Scanning electron microscopy
SiC	Silicon carbide
SOE	Solid-oxide electrolysis
SE-CLSR	Sorption enhanced chemical looping steam reforming
SESR	Sorption enhanced steam reforming
SR	Steam reforming
SRK	Soave-Redlich-Kwong
TCD	Thermal conductivity detector
TEM	Transmission electronic microscopy
TG	Thermogravimetric
TPO	Temperature programmed oxidation

TPOX	Thermal partial oxidation
TPR	Temperature programmed reduction
UNIFAC	Universal quasichemical Functional group Activity Coefficients
UNFCCC	United Nations Framework Convention on Climate Change
WGS	Water-gas-shift
XPS	X-ray photoelectron spectroscopy
XRD	X-ray diffraction
XRF	X-ray fluorescence

REFERENCES

[1] Vicente, J., Catalizadores y condiciones de proceso para la producción de hidrógeno mediante reformado con vapor de dimetil éter y de etanol, Doctoral Thesis, University of the Basque Country, 2012.

[2] Oar-Arteta, L., Catalyst development and kinetic modelling for the steam reforming of dimethyl ether, Doctoral Thesis, University of the Basque Country, 2014.

[3] Montero, C. del R., Condiciones de proceso y modelado cinético del reformado con vapor de etanol sobre catalizador Ni/La_2O_3-αAl_2O_3, Doctoral Thesis, University of the Basque Country, 2015.

[4] Remiro, A., Producción de hidrógeno mediante reformado con vapor de bio-oil. Integración en el proceso de las etapas térmica, catalítica y de captura de CO_2, Doctoral Thesis, University of the Basque Country, 2012.

[5] Aramburu, B., Reformado con vapor de bio-oil: condiciones para el proceso en dos etapas y modelo cinético, Doctoral Thesis, University of the Basque Country, 2016.

[6] Arandia, A., Catalysts and conditions in the oxidative steam reforming of bio-oil for stable H_2 production, Doctoral Thesis, University of the Basque Country, 2018.

[7] Ochoa, A., Catalyst deactivation in the steam reforming of streams derived from plastics and biomass, Doctoral Thesis, University of the Basque Country, 2018.

[8] García, N., Estrategias para mejorar la estabilidad de un catalizador de $NiAl_2O_4$ en la producción de H_2 mediante reformado con vapor del bio-oil, Doctoral Thesis, University of the Basque Country, 2021.

[9] Zhao, Q., Yu, P., Mahendran, R., Huang, W., Gao, Y., Yang, Z., et al., Global climate change and human health: Pathways and possible solutions. *Eco-Environment Heal.* 2022, *1*, 53–62.

[10] Rocha, J., Oliveira, S., Viana, C.M., Ribeiro, A.I., Climate change and its impacts on health, environment and economy, in: *One Health: Integrated Approach to 21st Century Challenges to Health*, Academic Press, 2022, pp. 253–279.

[11] World Greenhouse Gas Emissions: 2019 | World Resources Institute, 2019.

[12] CO_2 emissions from energy combustion and industrial processes, 1900-2021 – Charts – Data & Statistics - IEA, 2022.

[13] Hoang, A.T., Sandro Nižetić, Olcer, A.I., Ong, H.C., Chen, W.H., Chong, C.T., et al., Impacts of COVID-19 pandemic on the global energy system and the shift progress to renewable energy: Opportunities, challenges, and policy implications. *Energy Policy* 2021, *154*, 112322.

[14] Dawn, S., Shree Das, S., Gope, S., Dey, B., García Márquez, F.P., Global power and energy scenario during COVID-19 pandemic: Lessons from lockdown. *Int. J. Electr. Power Energy Syst.* 2022, *137*, 107757.

[15] Global Energy Review: CO_2 Emissions in 2021 – Analysis - IEA, 2022.

[16] Puntoon, W., Tarkhamtham, P., Tansuchat, R., The impacts of economic growth, industrial production, and energy consumption on CO_2 emissions: A case study of leading CO_2 emitting countries. *Energy Reports* 2022, *8*, 414–419.

[17] Greenhouse Gas Emissions from Energy Data Explorer – Data Tools - IEA, 2023.

[18] Goswami, R.K., Mehariya, S., Karthikeyan, O.P., Gupta, V.K., Verma, P., Multifaceted application of microalgal biomass integrated with carbon dioxide reduction and wastewater remediation: A flexible concept for sustainable environment. *J. Clean. Prod.* 2022, *339*, 130654.

[19] Net Zero Emissions – Topics - IEA, 2021.

[20] Climate Change 2022: Mitigation of Climate Change, 2022.

[21] Zhou, X.Y., Lu, G., Xu, Z., Yan, X., Khu, S.T., Yang, J., et al., Influence of Russia-Ukraine war on the global energy and food security. *Resour. Conserv. Recycl.* 2023, *188*, 106657.

[22] Kuzemko, C., Blondeel, M., Dupont, C., Brisbois, M.C., Russia's war on Ukraine, European energy policy responses & implications for sustainable transformations. *Energy Res. Soc. Sci.* 2022, *93*, 102842.

[23] Sharma, R., Kodamana, H., Ramteke, M., Multi-objective dynamic optimization of hybrid renewable energy systems. *Chem. Eng. Process. - Process Intensif.* 2022, *170*, 108663.

[24] Abdin, Z., Zafaranloo, A., Rafiee, A., Mérida, W., Lipiński, W., Khalilpour, K.R., Hydrogen as an energy vector. *Renew. Sustain. Energy Rev.* 2020, *120*, 109620.

[25] Lopes, J.V.M., Bresciani, A.E., Carvalho, K.M., Kulay, L.A., Alves, R.M.B., Multi-criteria decision approach to select carbon dioxide and hydrogen sources as potential raw materials for the production of chemicals. *Renew. Sustain. Energy Rev.* 2021, *151*, 111542.

[26] Soltani, A.K., Kandidayeni, M., Boulon, L., St-Pierre, D.L., Modular energy systems in vehicular applications. *Energy Procedia* 2019, *162*, 14–23.

[27] Juangsa, F.B., Cezeliano, A.S., Darmanto, P.S., Aziz, M., Thermodynamic analysis of hydrogen utilization as alternative fuel in cement production. *South African J. Chem. Eng.* 2022, *42*, 23–31.

[28] Al-Enazi, A., Okonkwo, E.C., Bicer, Y., Al-Ansari, T., A review of cleaner alternative fuels for maritime transportation. *Energy Reports* 2021, *7*, 1962–1985.

[29] Dutta, S., A review on production, storage of hydrogen and its utilization as an energy resource. *J. Ind. Eng. Chem.* 2014, *20*, 1148–1156.

[30] Shafiei, E., Davidsdottir, B., Leaver, J., Stefansson, H., Asgeirsson, E.I., Energy, economic, and mitigation cost implications of transition toward a carbon-neutral transport sector: A simulation-based comparison between hydrogen and electricity. *J. Clean. Prod.* 2017, *141*, 237–247.

[31] Ajanovic, A., Sayer, M., Haas, R., The economics and the environmental benignity of different colors of hydrogen. *Int. J. Hydrogen Energy* 2022, *47*, 24136–24154.

[32] Abe, J.O., Popoola, A.P.I., Ajenifuja, E., Popoola, O.M., Hydrogen energy, economy and storage: Review and recommendation. *Int. J. Hydrogen Energy* 2019, *44*, 15072–15086.

[33] Cho, H.H., Strezov, V., Evans, T.J., A review on global warming potential, challenges and opportunities of renewable hydrogen production technologies. *Sustain. Mater. Technol.* 2023, *35*, e00567.

[34] Global Hydrogen Review 2022 – Analysis - IEA, 2022.

[35] Sdanghi, G., Maranzana, G., Celzard, A., Fierro, V., Towards non-mechanical hybrid hydrogen compression for decentralized hydrogen facilities. *Energies* 2020, *13*, 3145.

[36] Lepage, T., Kammoun, M., Schmetz, Q., Richel, A., Biomass-to-hydrogen: A review of main routes production, processes evaluation and techno-economical assessment. *Biomass and Bioenergy* 2021, *144*, 105920.

[37] Nazir, H., Louis, C., Jose, S., Prakash, J., Muthuswamy, N., Buan, M.E.M., et al., Is the H_2 economy realizable in the foreseeable future? Part I: H_2 production methods. *Int. J. Hydrogen Energy* 2020, *45*, 13777–13788.

[38] Global hydrogen demand by sector in the Net Zero Scenario, 2019-2030 – Charts – Data & Statistics - IEA, 2022.

[39] Dawood, F., Anda, M., Shafiullah, G.M., Hydrogen production for energy: An overview. *Int. J. Hydrogen Energy* 2020, *45*, 3847–3869.

[40] Moliner, R., Lázaro, M.J., Suelves, I., Analysis of the strategies for bridging the gap towards the Hydrogen Economy. *Int. J. Hydrogen Energy* 2016, *41*, 19500–19508.

[41] The Future of Hydrogen – Analysis - IEA, 2019.

[42] Huang, J., Balcombe, P., Feng, Z., Technical and economic analysis of different colours of producing hydrogen in China. *Fuel* 2023, *337*, 127227.

[43] Osman, A.I., Mehta, N., Elgarahy, A.M., Hefny, M., Al-Hinai, A., Al-Muhtaseb, A.H., et al., Hydrogen production, storage, utilisation and environmental impacts: a review. *Environ. Chem. Lett. 2021 201* 2021, *20*, 153–188.

[44] Newborough, M., Cooley, G., Developments in the global hydrogen market: The spectrum of hydrogen colours. *Fuel Cells Bull.* 2020, 16–22.

[45] Nikolaidis, P., Poullikkas, A., A comparative overview of hydrogen production processes. *Renew. Sustain. Energy Rev.* 2017, *67*, 597–611.

[46] Abdalla, A.M., Hossain, S., Nisfindy, O.B., Azad, A.T., Dawood, M., Azad, A.K., Hydrogen production, storage, transportation and key challenges with applications: A review. *Energy Convers. Manag.* 2018, *165*, 602–627.

[47] Liu, X., Chi, J., Dong, B., Sun, Y., Recent progress in decoupled H_2 and O_2 production from electrolytic water splitting. *ChemElectroChem* 2019, *6*, 2157–2166.

[48] Chisholm, G., Zhao, T., Cronin, L., Hydrogen from water electrolysis, in: *Storing Energy*, Elsevier, 2022, pp. 559–591.

[49] David, M., Ocampo-Martínez, C., Sánchez-Peña, R., Advances in alkaline water electrolyzers: A review. *J. Energy Storage* 2019, *23*, 392–403.

[50] Zhou, J., Ji, W., Cao, X., He, W., Fan, J., Yuan, Y., A current perspective on the renewable energy hydrogen production process. *J. Therm. Sci.* 2023, *32*, 542–596.

[51] Martinez-Burgos, W.J., de Souza Candeo, E., Pedroni Medeiros, A.B., Cesar de Carvalho, J., Oliveira de Andrade Tanobe, V., Soccol, C.R., et al., Hydrogen: Current advances and patented technologies of its renewable production. *J. Clean. Prod.* 2021, *286*, 124970.

[52] Dehghanimadvar, M., Shirmohammadi, R., Sadeghzadeh, M., Aslani, A., Ghasempour, R., Hydrogen production technologies: Attractiveness and future perspective. *Int. J. Energy Res.* 2020, *44*, 8233–8254.

[53] Xu, X., Zhou, Q., Yu, D., The future of hydrogen energy: Bio-hydrogen production technology. *Int. J. Hydrogen Energy* 2022, *47*, 33677–33698.

[54] Baykara, S.Z., Experimental solar water thermolysis. *Int. J. Hydrogen Energy* 2004, *29*, 1459–1469.

[55] Funk, J.E., Thermochemical hydrogen production: Past and present. *Int. J. Hydrogen Energy* 2001, *26*, 185–190.

[56] Acar, C., Dincer, I., 3.1 Hydrogen Production, in: *Comprehensive Energy Systems*, Elsevier, 2018, pp. 1–40.

[57] Wajda, T., Gabriel, K., Thermolysis reactor scale-up for pilot scale CuCl hybrid hydrogen production. *Int. J. Hydrogen Energy* 2019, *44*, 9779–9790.

[58] Thomas, D., Baveja, N.A., Shenoy, K.T., Joshi, J.B., Mechanistic and kinetic study of thermolysis reaction with hydrolysis step products in Cu–Cl thermochemical cycle. *Int. J. Hydrogen Energy* 2021, *46*, 12672–12681.

[59] Balaman, Ş.Y., Introduction to biomass—Resources, production, harvesting, collection, and storage, in: *Decision-Making for Biomass-Based Production Chains*, Acedmic Press, 2019, pp. 1–23.

[60] Wang, C., Zhang, X., Liu, Q., Zhang, Q., Chen, L., Ma, L., A review of conversion of lignocellulose biomass to liquid transport fuels by integrated refining strategies. *Fuel Process. Technol.* 2020, *208*, 106485.

[61] Hoang, A.T., Ong, H.C., Fattah, I.M.R., Chong, C.T., Cheng, C.K., Sakthivel, R., et al., Progress on the lignocellulosic biomass pyrolysis for biofuel production toward environmental sustainability. *Fuel Process. Technol.* 2021, *223*, 106997.

[62] Kumar, R., Kumar, A., Pal, A., An overview of conventional and non-conventional hydrogen production methods. *Mater. Today Proc.* 2021, *46*, 5353–5359.

[63] Kapdan, I.K., Kargi, F., Bio-hydrogen production from waste materials. *Enzyme Microb. Technol.* 2006, *38*, 569–582.

[64] Bundhoo, Z.M.A., Coupling dark fermentation with biochemical or bioelectrochemical systems for enhanced bio-energy production: A review. *Int. J. Hydrogen Energy* 2017, *42*, 26667–26686.

[65] Kumar, G., Shobana, S., Nagarajan, D., Lee, D.J., Lee, K.S., Lin, C.Y., et al., Biomass based hydrogen production by dark fermentation — recent trends and opportunities for greener processes. *Curr. Opin. Biotechnol.* 2018, *50*, 136–145.

[66] Łukajtis, R., Hołowacz, I., Kucharska, K., Glinka, M., Rybarczyk, P., Przyjazny, A., et al., Hydrogen production from biomass using dark fermentation. *Renew. Sustain. Energy Rev.* 2018, *91*, 665–694.

[67] Balat, H., Kirtay, E., Hydrogen from biomass – Present scenario and future prospects. *Int. J. Hydrogen Energy* 2010, *35*, 7416–7426.

[68] Akhlaghi, N., Najafpour-Darzi, G., A comprehensive review on biological hydrogen production. *Int. J. Hydrogen Energy* 2020, *45*, 22492–22512.

[69] Arregi, A., Amutio, M., Lopez, G., Bilbao, J., Olazar, M., Evaluation of thermochemical routes for hydrogen production from biomass: A review. *Energy Convers. Manag.* 2018, *165*, 696–719.

[70] Tezer, Ö., Karabağ, N., Öngen, A., Çolpan, C.Ö., Ayol, A., Biomass gasification for sustainable energy production: A review. *Int. J. Hydrogen Energy* 2022, *47*, 15419–15433.

[71] Foong, S.Y., Chan, Y.H., Cheah, W.Y., Kamaludin, N.H., Tengku Ibrahim, T.N.B., Sonne, C., et al., Progress in waste valorization using advanced pyrolysis techniques for hydrogen and gaseous fuel production. *Bioresour. Technol.* 2021, *320*, 124299.

[72] Pandey, B., Prajapati, Y.K., Sheth, P.N., Recent progress in thermochemical techniques to produce hydrogen gas from biomass: A state of the art review. *Int. J. Hydrogen Energy* 2019, *44*, 25384–25415.

[73] Balat, M., Balat, M., Kirtay, E., Balat, H., Main routes for the thermo-conversion of biomass into fuels and chemicals. Part 1: Pyrolysis systems. *Energy Convers. Manag.* 2009, *50*, 3147–3157.

[74] Vuppaladadiyam, A.K., Vuppaladadiyam, S.S.V., Awasthi, A., Sahoo, A., Rehman, S., Pant, K.K., et al., Biomass pyrolysis: A review on recent advancements and green hydrogen production. *Bioresour. Technol.* 2022, *364*, 128087.

[75] Amutio, M., Lopez, G., Artetxe, M., Elordi, G., Olazar, M., Bilbao, J., Influence of temperature on biomass pyrolysis in a conical spouted bed reactor. *Resour. Conserv. Recycl.* 2012, *59*, 23–31.

[76] Gollakota, A.R.K., Reddy, M., Subramanyam, M.D., Kishore, N., A review on the upgradation techniques of pyrolysis oil. *Renew. Sustain. Energy Rev.* 2016, *58*, 1543–1568.

[77] Zhao, Z., Situmorang, Y.A., An, P., Chaihad, N., Wang, J., Hao, X., et al., Hydrogen production from catalytic steam reforming of bio-oils: A critical review. *Chem. Eng. Technol.* 2020, *43*, 625–640.

[78] Mortensen, P.M., Grunwaldt, J.D., Jensen, P.A., Knudsen, K.G., Jensen, A.D., A review of catalytic upgrading of bio-oil to engine fuels. *Appl. Catal. A Gen.* 2011, *407*, 1–19.

[79] Pafili, A., Charisiou, N.D., Douvartzides, S.L., Siakavelas, G.I., Wang, W., Liu, G., et al., Recent progress in the steam reforming of bio-oil for hydrogen production: A review of operating parameters, catalytic systems and technological innovations. *Catalysts* 2021, *11*, 1526.

[80] Valle, B., Remiro, A., García-Gómez, N., Gayubo, A.G., Bilbao, J., Recent research progress on bio-oil conversion into bio-fuels and raw chemicals: a review. *J. Chem. Technol. Biotechnol.* 2019, *94*, 670–689.

[81] Stedile, T., Ender, L., Meier, H.F., Simionatto, E.L., Wiggers, V.R., Comparison between physical properties and chemical composition of bio-oils derived from lignocellulose and triglyceride sources. *Renew. Sustain. Energy Rev.* 2015, *50*, 92–108.

[82] Pinheiro Pires, A.P., Arauzo, J., Fonts, I., Domine, M.E., Fernández Arroyo, A., Garcia-Perez, M.E., et al., Challenges and opportunities for bio-oil refining: A review. *Energy and Fuels* 2019, *33*, 4683–4720.

[83] Zhang, Q., Chang, J., Wang, T., Xu, Y., Review of biomass pyrolysis oil properties and upgrading research. *Energy Convers. Manag.* 2007, *48*, 87–92.

[84] Lu, Q., Li, W.Z., Zhu, X.F., Overview of fuel properties of biomass fast pyrolysis oils. *Energy Convers. Manag.* 2009, *50*, 1376–1383.

[85] Diebold, J.P., Czernik, S., Additives to lower and stabilize the viscosity of pyrolysis oils during storage. *Energy and Fuels* 1997, *11*, 1081–1091.

[86] Gholizadeh, M., Hu, X., Liu, Q., A mini review of the specialties of the bio-oils produced from pyrolysis of 20 different biomasses. *Renew. Sustain. Energy Rev.* 2019, *114*, 109313.

[87] Bridgwater, A. V., Review of fast pyrolysis of biomass and product upgrading. *Biomass and Bioenergy* 2012, *38*, 68–94.

[88] Samec, N., Kegl, B., Dibble, R.W., Numerical and experimental study of water/oil emulsified fuel combustion in a diesel engine. *Fuel* 2002, *81*, 2035–2044.

[89] Elliott, D.C., Hart, T.R., Neuenschwander, G.G., Rotness, L.J., Olarte, M. V., Zacher, A.H., et al., Catalytic hydroprocessing of fast pyrolysis bio-oil from pine sawdust. *Energy and Fuels* 2012, *26*, 3891–3896.

[90] Chaihad, N., Karnjanakom, S., Kurnia, I., Yoshida, A., Abudula, A., Reubroycharoen, P., et al., Catalytic upgrading of bio-oils over high alumina zeolites. *Renew. Energy* 2019, *136*, 1304–1310.

[91] Baloch, H.A., Nizamuddin, S., Siddiqui, M.T.H., Riaz, S., Jatoi, A.S., Dumbre, D.K., et al., Recent advances in production and upgrading of bio-oil from biomass: A critical overview. *J. Environ. Chem. Eng.* 2018, *6*, 5101–5118.

[92] Gunawan, R., Li, X., Larcher, A., Hu, X., Mourant, D., Chaiwat, W., et al., Hydrolysis and glycosidation of sugars during the esterification of fast pyrolysis bio-oil. *Fuel* 2012, *95*, 146–151.

[93] Khosravanipour Mostafazadeh, A., Solomatnikova, O., Drogui, P., Tyagi, R.D., A review of recent research and developments in fast pyrolysis and bio-oil upgrading. *Biomass Convers. Biorefinery* 2018, *8*, 739–773.

[94] Valle, B., García-Gómez, N., Arandia, A., Remiro, A., Bilbao, J., Gayubo, A.G., Effect of phenols extraction on the behavior of Ni-spinel derived catalyst for raw bio-oil steam reforming. *Int. J. Hydrogen Energy* 2019, *44*, 12593–12603.

[95] Trane, R., Dahl, S., Skjøth-Rasmussen, M.S., Jensen, A.D., Catalytic steam reforming of bio-oil. *Int. J. Hydrogen Energy* 2012, *37*, 6447–6472.

[96] García-Gómez, N., Valecillos, J., Remiro, A., Valle, B., Bilbao, J., Gayubo, A.G., Effect of reaction conditions on the deactivation by coke of a $NiAl_2O_4$ spinel derived catalyst in the steam reforming of bio-oil. *Appl. Catal. B Environ.* 2021, *297*, 120445.

[97] Kumar, A., Chakraborty, J.P., Singh, R., Bio-oil: the future of hydrogen generation. *Biofuels* 2017, *8*, 663–674.

[98] Montero, C., Remiro, A., Benito, P.L., Bilbao, J., Gayubo, A.G., Optimum operating conditions in ethanol steam reforming over a Ni/La_2O_3-αAl_2O_3 catalyst in a fluidized bed reactor. *Fuel Process. Technol.* 2018, *169*, 207–216.

[99] Di Michele, A., Dell'Angelo, A., Tripodi, A., Bahadori, E., Sànchez, F., Motta, D., et al., Steam reforming of ethanol over $Ni/MgAl_2O_4$ catalysts. *Int. J. Hydrogen Energy* 2019, *44*, 952–964.

[100] Szijjártó, G.P., Pászti, Z., Sajó, I., Erdohelyi, A., Radnóczi, G., Tompos, A., Nature of the active sites in $Ni/MgAl_2O_4$-based catalysts designed for steam reforming of ethanol. *J. Catal.* 2013, *305*, 290–306.

[101] Tanksale, A., Beltramini, J.N., Lu, G.Q.M., A review of catalytic hydrogen production processes from biomass. *Renew. Sustain. Energy Rev.* 2010, *14*, 166–182.

[102] Takanabe, K., Aika, K. ichi, Seshan, K., Lefferts, L., Catalyst deactivation during steam reforming of acetic acid over Pt/ZrO_2. *Chem. Eng. J.* 2006, *120*, 133–137.

[103] Hu, X., Lu, G., Investigation of the steam reforming of a series of model compounds derived from bio-oil for hydrogen production. *Appl. Catal. B Environ.* 2009, *88*, 376–385.

[104] Hu, X., Lu, G., Inhibition of methane formation in steam reforming reactions through modification of Ni catalyst and the reactants. *Green Chem.* 2009, *11*, 724–732.

[105] Medrano, J.A., Oliva, M., Ruiz, J., García, L., Arauzo, J., Catalytic steam reforming of model compounds of biomass pyrolysis liquids in fluidized bed reactor with modified Ni/Al catalysts. *J. Anal. Appl. Pyrolysis* 2009, *85*, 214–225.

[106] Hu, X., Lu, G., Comparative study of alumina-supported transition metal catalysts for hydrogen generation by steam reforming of acetic acid. *Appl. Catal. B Environ.* 2010, *99*, 289–297.

[107] Vagia, E.C., Lemonidou, A.A., Investigations on the properties of ceria-zirconia-supported Ni and Rh catalysts and their performance in acetic acid steam reforming. *J. Catal.* 2010, *269*, 388–396.

[108] An, L., Dong, C., Yang, Y., Zhang, J., He, L., The influence of Ni loading on coke formation in steam reforming of acetic acid. *Renew. Energy* 2011, *36*, 930–935.

[109] Thaicharoensutcharittham, S., Meeyoo, V., Kitiyanan, B., Rangsunvigit, P., Rirksomboon, T., Hydrogen production by steam reforming of acetic acid over Ni-based catalysts. *Catal. Today* 2011, *164*, 257–261.

[110] Bimbela, F., Chen, D., Ruiz, J., García, L., Arauzo, J., Ni/Al coprecipitated catalysts modified with magnesium and copper for the catalytic steam reforming of model compounds from biomass pyrolysis liquids. *Appl. Catal. B Environ.* 2012, *119–120*, 1–12.

[111] Hu, X., Zhang, L., Lu, G., Pruning of the surface species on Ni/Al_2O_3 catalyst to selective production of hydrogen via acetone and acetic acid steam reforming. *Appl. Catal. A Gen.* 2012, *427–428*, 49–57.

[112] Li, Z., Hu, X., Zhang, L., Liu, S., Lu, G., Steam reforming of acetic acid over Ni/ZrO_2 catalysts: Effects of nickel loading and particle size on product distribution and coke formation. *Appl. Catal. A Gen.* 2012, *417–418*, 281–289.

[113] Medrano, J.A., Oliva, M., Ruiz, J., García, L., Arauzo, J., Catalytic steam reforming of butanol in a fluidized bed and comparison with other oxygenated compounds. *Fuel Process. Technol.* 2014, *124*, 123–133.

[114] Nogueira, F.G.E., Assaf, P.G.M., Carvalho, H.W.P., Assaf, E.M., Catalytic steam reforming of acetic acid as a model compound of bio-oil. *Appl. Catal. B Environ.* 2014, *160–161*, 188–199.

[115] Wang, S., Cai, Q., Zhang, F., Li, X., Zhang, L., Luo, Z., Hydrogen production via catalytic reforming of the bio-oil model compounds: Acetic acid, phenol and hydroxyacetone. *Int. J. Hydrogen Energy* 2014, *39*, 18675–18687.

[116] Hoang, T.M.C., Geerdink, B., Sturm, J.M., Lefferts, L., Seshan, K., Steam reforming of acetic acid - A major component in the volatiles formed during gasification of humin. *Appl. Catal. B Environ.* 2015, *163*, 74–82.

[117] Resende, K.A., Ávila-Neto, C.N., Rabelo-Neto, R.C., Noronha, F.B., Hori, C.E., Hydrogen production by reforming of acetic acid using La–Ni type perovskites partially substituted with Sm and Pr. *Catal. Today* 2015, *242*, 71–79.

[118] Hu, X., Dong, D., Shao, X., Zhang, L., Lu, G., Steam reforming of acetic acid over cobalt catalysts: Effects of Zr, Mg and K addition. *Int. J. Hydrogen Energy* 2017, *42*, 4793–4803.

[119] Zhang, Z., Hu, X., Li, J., Gao, G., Dong, D., Westerhof, R., et al., Steam reforming of acetic acid over Ni/Al_2O_3 catalysts: Correlation of nickel loading with properties and catalytic behaviors of the catalysts. *Fuel* 2018, *217*, 389–403.

[120] Li, J., Mei, X., Zhang, L., Yu, Z., Liu, Q., Wei, T., et al., A comparative study of catalytic behaviors of Mn, Fe, Co, Ni, Cu and Zn–Based catalysts in steam reforming of methanol, acetic acid and acetone. *Int. J. Hydrogen Energy* 2020, *45*, 3815–3832.

[121] Bkangmo Kontchouo, F.M., Shao, Y., Zhang, S., Gholizadeh, M., Hu, X., Steam reforming of ethanol, acetaldehyde, acetone and acetic acid: Understanding the reaction intermediates and nature of coke. *Chem. Eng. Sci.* 2023, *265*, 118257.

[122] Matas Güell, B., Babich, I., Nichols, K.P., Gardeniers, J.G.E., Lefferts, L., Seshan, K., Design of a stable steam reforming catalyst—A promising route to sustainable hydrogen from biomass oxygenates. *Appl. Catal. B Environ.* 2009, *90*, 38–44.

[123] Zheng, X.X., Yan, C.F., Hu, R.R., Li, J., Hai, H., Luo, W.M., et al., Hydrogen from acetic acid as the model compound of biomass fast-pyralysis oil over Ni catalyst supported on ceria–zirconia. *Int. J. Hydrogen Energy* 2012, *37*, 12987–12993.

[124] Hu, X., Lu, G., Investigation of the effects of molecular structure on oxygenated hydrocarbon steam re-forming. *Energy and Fuels* 2009, *23*, 926–933.

[125] Navarro, R.M., Guil-Lopez, R., Ismail, A.A., Al-Sayari, S.A., Fierro, J.L.G., Ni- and PtNi-catalysts supported on Al_2O_3 for acetone steam reforming: Effect of the modification of support with Ce, la and Mg. *Catal. Today* 2015, *242*, 60–70.

[126] Elias, K.F.M., Bednarczuk, L., Assaf, E.M., Ramírez de la Piscina, P., Homs, N., Study of Ni/CeO_2–ZnO catalysts in the production of H_2 from acetone steam reforming. *Int. J. Hydrogen Energy* 2019, *44*, 12628–12635.

[127] Basu, S., Pradhan, N.C., Steam reforming of acetone over NiCoMgAl mixed oxide catalysts obtained from hydrotalcite precursors. *Int. J. Hydrogen Energy* 2020, *45*, 18133–18143.

[128] Guil-Lopez, R., Navarro, R.M., Ismail, A.A., Al-Sayari, S.A., Fierro, J.L.G., Influence of Ni environment on the reactivity of Ni-Mg-Al catalysts for the acetone steam reforming reaction. *Int. J. Hydrogen Energy* 2015, *40*, 5289–5296.

[129] Bimbela, F., Oliva, M., Ruiz, J., García, L., Arauzo, J., Catalytic steam reforming of model compounds of biomass pyrolysis liquids in fixed bed: Acetol and n-butanol. *J. Anal. Appl. Pyrolysis* 2009, *85*, 204–213.

[130] Nichele, V., Signoretto, M., Pinna, F., Menegazzo, F., Rossetti, I., Cruciani, G., et al., Ni/ZrO_2 catalysts in ethanol steam reforming: Inhibition of coke formation by CaO-doping. *Appl. Catal. B Environ.* 2014, *150–151*, 12–20.

[131] Vicente, J., Montero, C., Ereña, J., Azkoiti, M.J., Bilbao, J., Gayubo, A.G., Coke deactivation of Ni and Co catalysts in ethanol steam reforming at mild temperatures in a fluidized bed reactor. *Int. J. Hydrogen Energy* 2014, *39*, 12586–12596.

[132] Valecillos, J., Iglesias-Vázquez, S., Landa, L., Remiro, A., Bilbao, J., Gayubo, A.G., Insights into the reaction routes for H_2 formation in the ethanol steam reforming on a catalyst derived from $NiAl_2O_4$ spinel. *Energy and Fuels* 2021, *35*, 17197–17211.

[133] Matas Güell, B., Babich, I. V., Lefferts, L., Seshan, K., Steam reforming of phenol over Ni-based catalysts – A comparative study. *Appl. Catal. B Environ.* 2011, *106*, 280–286.

[134] Nabgan, W., Tuan Abdullah, T.A., Mat, R., Nabgan, B., Gambo, Y., Triwahyono, S., Influence of Ni to Co ratio supported on ZrO_2 catalysts in phenol steam reforming for hydrogen production. *Int. J. Hydrogen Energy* 2016, *41*, 22922–22931.

[135] Saeed Baamran, K., Tahir, M., Thermodynamic investigation and experimental analysis on phenol steam reforming towards enhanced H_2 production over structured $Ni/ZnTiO_3$ nanocatalyst. *Energy Convers. Manag.* 2019, *180*, 796–810.

[136] Mondal, T., Pant, K.K., Dalai, A.K., Oxidative and non-oxidative steam reforming of crude bio-ethanol for hydrogen production over Rh promoted Ni/CeO_2-ZrO_2 catalyst. *Appl. Catal. A Gen.* 2015, *499*, 19–31.

[137] Han, X., Wang, Y., Zhang, Y., Yu, Y., He, H., Hydrogen production from oxidative steam reforming of ethanol over Ir catalysts supported on Ce–La solid solution. *Int. J. Hydrogen Energy* 2017, *42*, 11177–11186.

[138] Garcia-Garcia, I., Acha, E., Bizkarra, K., Martinez De Ilarduya, J., Requies, J., Cambra, J.F., Hydrogen production by steam reforming of m-cresol, a bio-oil model compound, using catalysts supported on conventional and unconventional supports. *Int. J. Hydrogen Energy* 2015, *40*, 14445–14455.

[139] Mei, Y., Wu, C., Liu, R., Hydrogen production from steam reforming of bio-oil model compound and byproducts elimination. *Int. J. Hydrogen Energy* 2016, *41*, 9145–9152.

[140] Artetxe, M., Alvarez, J., Nahil, M.A., Olazar, M., Williams, P.T., Steam reforming of different biomass tar model compounds over Ni/Al_2O_3 catalysts. *Energy Convers. Manag.* 2017, *136*, 119–126.

[141] Fu, P., Zhang, A., Luo, S., Yi, W., Zhang, Y., Comparative study on the catalytic steam reforming of biomass pyrolysis oil and its derivatives for hydrogen production. *RSC Adv.* 2020, *10*, 12721–12729.

[142] Zhang, Z., Hu, X., Zhang, L., Yang, Y., Li, Q., Fan, H., et al., Steam reforming of guaiacol over Ni/Al_2O_3 and Ni/SBA-15: Impacts of support on catalytic behaviors of nickel and properties of coke. *Fuel Process. Technol.* 2019, *191*, 138–151.

[143] Zhang, Z., Zhang, X., Zhang, L., Wang, Y., Li, X., Zhang, S., et al., Steam reforming of guaiacol over Ni/SiO_2 catalyst modified with basic oxides: Impacts of alkalinity on properties of coke. *Energy Convers. Manag.* 2020, *205*, 112301.

[144] Zhang, L., Yu, Z., Li, J., Zhang, S., Hu, S., Xiang, J., et al., Steam reforming of typical small organics derived from bio-oil: Correlation of their reaction behaviors with molecular structures. *Fuel* 2020, *259*.

[145] Zhang, Z., Sun, Y., Wang, Y., Sun, K., Gao, Z., Xu, Q., et al., Steam reforming of acetic acid and guaiacol over Ni/Attapulgite catalyst: Tailoring pore structure of the catalyst with KOH activation for enhancing the resistivity towards coking. *Mol. Catal.* 2020, *493*.

[146] Wu, C., Liu, R., Sustainable hydrogen production from steam reforming of bio-oil model compound based on carbon deposition/elimination. *Int. J. Hydrogen Energy* 2011, *36*, 2860–2868.

[147] Wang, Z., Pan, Y., Dong, T., Zhu, X., Kan, T., Yuan, L., et al., Production of hydrogen from catalytic steam reforming of bio-oil using $C12A7O^-$-based catalysts. *Appl. Catal. A Gen.* 2007, *320*, 24–34.

[148] Lan, P., Xu, Q., Zhou, M., Lan, L., Zhang, S., Yan, Y., Catalytic steam reforming of fast pyrolysis bio-oil in fixed bed and fluidized bed reactors. *Chem. Eng. Technol.* 2010, *33*, 2021–2028.

[149] Remiro, A., Arandia, A., Oar-Arteta, L., Bilbao, J., Gayubo, A.G., Regeneration of $NiAl_2O_4$ spinel type catalysts used in the reforming of raw bio-oil. *Appl. Catal. B Environ.* 2018, *237*, 353–365.

[150] Czernik, S., French, R., Feik, C., Chornet, E., Hydrogen by catalytic steam reforming of liquid byproducts from biomass thermoconversion processes. *Ind. Eng. Chem. Res.* 2002, *41*, 4209–4215.

[151] Remón, J., Medrano, J.A., Bimbela, F., García, L., Arauzo, J., Ni/Al–Mg–O solids modified with Co or Cu for the catalytic steam reforming of bio-oil. *Appl. Catal. B Environ.* 2013, *132–133*, 433–444.

[152] Fu, P., Yi, W., Li, Z., Bai, X., Zhang, A., Li, Y., et al., Investigation on hydrogen production by catalytic steam reforming of maize stalk fast pyrolysis bio-oil. *Int. J. Hydrogen Energy* 2014, *39*, 13962–13971.

[153] Abbasi, M., Farniaei, M., Abbasi, S., Enhancement of hydrogen production by fluidization in industrial-scale steam reformers. *Theor. Found. Chem. Eng.* 2018, *52*, 416–428.

[154] Papalas, T., Antzaras, A.N., Lemonidou, A.A., Intensified steam methane reforming coupled with Ca-Ni looping in a dual fluidized bed reactor system: A conceptual design. *Chem. Eng. J.* 2020, *382*, 122993.

[155] Effendi, A., Zhang, Z.G., Hellgardt, K., Honda, K., Yoshida, T., Steam reforming of a clean model biogas over Ni/Al_2O_3 in fluidized- and fixed-bed reactors. *Catal. Today* 2002, *77*, 181–189.

[156] Kumar, A., Singh, R., Sinha, A.S.K., Catalyst modification strategies to enhance the catalyst activity and stability during steam reforming of acetic acid for hydrogen production. *Int. J. Hydrogen Energy* 2019, *44*, 12983–13010.

[157] Kechagiopoulos, P.N., Voutetakis, S.S., Lemonidou, A.A., Vasalos, I.A., Hydrogen production via reforming of the aqueous phase of bio-oil over Ni/olivine catalysts in a spouted bed reactor. *Ind. Eng. Chem. Res.* 2009, *48*, 1400–1408.

[158] Remón, J., Broust, F., Valette, J., Chhiti, Y., Alava, I., Fernandez-Akarregi, A.R., et al., Production of a hydrogen-rich gas from fast pyrolysis bio-oils: Comparison between homogeneous and catalytic steam reforming routes. *Int. J. Hydrogen Energy* 2014, *39*, 171–182.

[159] Palma, V., Ruocco, C., Meloni, E., Ricca, A., Oxidative reforming of ethanol over CeO_2-SiO_2 based catalysts in a fluidized bed reactor. *Chem. Eng. Process. - Process Intensif.* 2018, *124*, 319–327.

[160] Kunii, D., Levenspiel, O., Bubbling bed model for kinetic processes in fluidized beds: Gas-solid mass and heat transfer and catalytic reactions. *Ind. Eng. Chem. Process Des. Dev.* 1968, *7*, 481–492.

[161] Rusten, H.K., Ochoa-Fernández, E., Lindborg, H., Chen, D., Jakobsen, H.A., Hydrogen production by sorption-enhanced steam methane reforming using lithium oxides as CO_2-acceptor. *Ind. Eng. Chem. Res.* 2007, *46*, 8729–8737.

[162] Shi, Y., Du, X., Yang, L., Sun, Y., Yang, Y., Experiments on hydrogen production from methanol steam reforming in fluidized bed reactor. *Int. J. Hydrogen Energy* 2013, *38*, 13974–13981.

[163] Fernandez, E., Amutio, M., Artetxe, M., Arregi, A., Santamaria, L., Lopez, G., et al., Assessment of product yields and catalyst deactivation in fixed and fluidized bed reactors in the steam reforming of biomass pyrolysis volatiles. *Process Saf. Environ. Prot.* 2021, *145*, 52–62.

[164] Ochoa, A., Aramburu, B., Valle, B., Resasco, D.E., Bilbao, J., Gayubo, A.G., et al., Role of oxygenates and effect of operating conditions in the deactivation of a Ni supported catalyst during the steam reforming of bio-oil. *Green Chem.* 2017, *19*, 4315–4333.

[165] Setiabudi, H.D., Aziz, M.A.A., Abdullah, S., Teh, L.P., Jusoh, R., Hydrogen production from catalytic steam reforming of biomass pyrolysis oil or bio-oil derivatives: A review. *Int. J. Hydrogen Energy* 2020, *45*, 18376–18397.

[166] Adeniyi, A.G., Otoikhian, K.S., Ighalo, J.O., Steam reforming of biomass pyrolysis oil: A review. *Int. J. Chem. React. Eng.* 2019, *17*.

[167] Remiro, A., Valle, B., Aguayo, A.T., Bilbao, J., Gayubo, A.G., Steam reforming of raw bio-oil in a fluidized bed reactor with prior separation of pyrolytic lignin. *Energy and Fuels* 2013, *27*, 7549–7559.

[168] Remiro, A., Valle, B., Aguayo, A.T., Bilbao, J., Gayubo, A.G., Operating conditions for attenuating Ni/La_2O_3–αAl_2O_3 catalyst deactivation in the steam reforming of bio-oil aqueous fraction. *Fuel Process. Technol.* 2013, *115*, 222–232.

[169] Bimbela, F., Ábrego, J., Puerta, R., García, L., Arauzo, J., Catalytic steam reforming of the aqueous fraction of bio-oil using Ni-Ce/Mg-Al catalysts. *Appl. Catal. B Environ.* 2017, *209*, 346–357.

[170] Valle, B., Aramburu, B., Olazar, M., Bilbao, J., Gayubo, A.G., Steam reforming of raw bio-oil over Ni/La_2O_3-αAl_2O_3: Influence of temperature on product yields and catalyst deactivation. *Fuel* 2018, *216*, 463–474.

[171] Valle, B., Aramburu, B., Benito, P.L., Bilbao, J., Gayubo, A.G., Biomass to hydrogen-rich gas via steam reforming of raw bio-oil over Ni/La_2O_3-αAl_2O_3 catalyst: Effect of space-time and steam-to-carbon ratio. *Fuel* 2018, *216*, 445–455.

[172] Bizkarra, K., Bermudez, J.M., Arcelus-Arrillaga, P., Barrio, V.L., Cambra, J.F., Millan, M., Nickel based monometallic and bimetallic catalysts for synthetic and real bio-oil steam reforming. *Int. J. Hydrogen Energy* 2018, *43*, 11706–11718.

[173] Remiro, A., Ochoa, A., Arandia, A., Castaño, P., Bilbao, J., Gayubo, A.G., On the dynamics and reversibility of the deactivation of a Rh/CeO_2ZrO_2 catalyst in raw bio-oil steam reforming. *Int. J. Hydrogen Energy* 2019, *44*, 2620–2632.

[174] García-Gómez, N., Valecillos, J., Valle, B., Remiro, A., Bilbao, J., Gayubo, A.G., Combined effect of bio-oil composition and temperature on the stability of Ni spinel derived catalyst for hydrogen production by steam reforming. *Fuel* 2022, *326*, 124966.

[175] Capa, A., García, R., Chen, D., Rubiera, F., Pevida, C., Gil, M. V., On the effect of biogas composition on the H_2 production by sorption enhanced steam reforming (SESR). *Renew. Energy* 2020, *160*, 575–583.

[176] Masoudi Soltani, S., Lahiri, A., Bahzad, H., Clough, P., Gorbounov, M., Yan, Y., Sorption-enhanced steam methane reforming for combined CO_2 capture and hydrogen production: A state-of-the-art review. *Carbon Capture Sci. Technol.* 2021, *1*, 100003.

[177] Teixeira, P., Bacariza, C., Correia, P., Pinheiro, C.I.C., Cabrita, I., Hydrogen production with in situ CO_2 capture at high and medium temperatures using solid sorbents. *Energies* 2022, *15*, 4039.

[178] Ng, K.S., Zhang, N., Sadhukhan, J., Techno-economic analysis of polygeneration systems with carbon capture and storage and CO_2 reuse. *Chem. Eng. J.* 2013, *219*, 96–108.

[179] Shokrollahi Yancheshmeh, M., Radfarnia, H.R., Iliuta, M.C., High temperature CO_2 sorbents and their application for hydrogen production by sorption enhanced steam reforming process. *Chem. Eng. J.* 2016, *283*, 420–444.

[180] Salaudeen, S.A., Acharya, B., Dutta, A., CaO-based CO_2 sorbents: A review on screening, enhancement, cyclic stability, regeneration and kinetics modelling. *J. CO_2 Util.* 2018, *23*, 179–199.

[181] Scaltsoyiannes, A., Antzaras, A., Koilaridis, G., Lemonidou, A., Towards a generalized carbonation kinetic model for CaO-based materials using a modified random pore model. *Chem. Eng. J.* 2021, *407*, 127207.

[182] Phromprasit, J., Powell, J., Wongsakulphasatch, S., Kiatkittipong, W., Bumroongsakulsawat, P., Assabumrungrat, S., Activity and stability performance of multifunctional catalyst (Ni/CaO and Ni/$Ca_{12}Al_{14}O_{33}$-CaO) for bio-hydrogen production from sorption enhanced biogas steam reforming. *Int. J. Hydrogen Energy* 2016, *41*, 7318–7331.

[183] Di Giuliano, A., Gallucci, K., Foscolo, P.U., Courson, C., Effect of Ni precursor salts on Ni-mayenite catalysts for steam methane reforming and on Ni-CaO-mayenite materials for sorption enhanced steam methane reforming. *Int. J. Hydrogen Energy* 2019, *44*, 6461–6480.

[184] Sun, H., Wu, C., Shen, B., Zhang, X., Zhang, Y., Huang, J., Progress in the development and application of CaO-based adsorbents for CO_2 capture—a review. *Mater. Today Sustain.* 2018, *1–2*, 1–27.

[185] Wang, X., He, Y., Xu, T., Xiao, B., Liu, S., Hu, Z., et al., CO_2 sorption-enhanced steam reforming of phenol using Ni–M/CaO–$Ca_{12}Al_{14}O_{33}$ (M = Cu, Co, and Ce) as catalytic sorbents. *Chem. Eng. J.* 2020, *393*, 124769.

[186] Li, Z.-S., Cai, N.-S., Huang, Y.-Y., Han, H.-J., Synthesis, experimental studies, and analysis of a new calcium-based carbon dioxide absorbent. *Energy Fuels* 2005, *19*, 1447–1452.

[187] Antzaras, A.N., Lemonidou, A.A., Recent advances on materials and processes for intensified production of blue hydrogen. *Renew. Sustain. Energy Rev.* 2022, *155*, 111917.

[188] Antzaras, A.N., Heracleous, E., Lemonidou, A.A., Hybrid catalytic materials with CO_2 capture and oxygen transfer functionalities for high–purity H_2 production. *Catal. Today* 2021, *369*, 2–11.

[189] Dou, B., Zhang, H., Cui, G., Wang, Z., Jiang, B., Wang, K., et al., Hydrogen production by sorption-enhanced chemical looping steam reforming of ethanol in an alternating fixed-bed reactor: Sorbent to catalyst ratio dependencies. *Energy Convers. Manag.* 2018, *155*, 243–252.

[190] Zeng, P., Dou, B., Zhang, H., Wu, K., Zhao, L., Luo, C., et al., Chemical looping steam reforming of ethanol without and with in-situ CO_2 capture. *Int. J. Hydrogen Energy* 2022, *47*, 6552–6568.

[191] Dou, B., Wu, K., Zhang, H., Chen, B., Chen, H., Xu, Y., Sorption-enhanced chemical looping steam reforming of glycerol with CO_2 in-situ capture and utilization. *Chem. Eng. J.* 2023, *452*, 139703.

[192] Li, D., Xue, H., Hu, R., Effect of Ce/Ca ratio in Ni/CeO_2-ZrO_2-CaO catalysts on high-purity hydrogen production by sorption-enhanced steam reforming of acetic acid and bio-oil. *Ind. Eng. Chem. Res.* 2020, *59*, 1446–1456.

[193] Dang, C., Wu, S., Yang, G., Cao, Y., Wang, H., Peng, F., et al., Hydrogen production from sorption-enhanced steam reforming of phenol over a Ni-Ca-Al-O bifunctional catalyst. *ACS Sustain. Chem. Eng.* 2020, *8*, 7111–7120.

[194] Omoniyi, O.A., Dupont, V., Optimised cycling stability of sorption enhanced chemical looping steam reforming of acetic acid in a packed bed reactor. *Appl. Catal. B Environ.* 2019, *242*, 397–409.

[195] Rodríguez, S., Capa, A., García, R., Chen, D., Rubiera, F., Pevida, C., et al., Blends of bio-oil/biogas model compounds for high-purity H_2 production by sorption enhanced steam reforming (SESR): Experimental study and energy analysis. *Chem. Eng. J.* 2022, *432*, 134396.

[196] Esteban-Díez, G., Gil, M. V., Pevida, C., Chen, D., Rubiera, F., Effect of operating conditions on the sorption enhanced steam reforming of blends of acetic acid and acetone as bio-oil model compounds. *Appl. Energy* 2016, *177*, 579–590.

[197] Rahmanzadeh, L., Taghizadeh, M., Sorption-enhanced ethanol steam reforming on Ce-Ni/MCM-41 with simultaneous CO_2 adsorption over Na- and Zr- promoted CaO based sorbent. *Int. J. Hydrogen Energy* 2019, *44*, 21238–21250.

[198] Dang, C., Yu, H., Wang, H., Peng, F., Yang, Y., A bi-functional Co–CaO–$Ca_{12}Al_{14}O_{33}$ catalyst for sorption-enhanced steam reforming of glycerol to high-purity hydrogen. *Chem. Eng. J.* 2016, *286*, 329–338.

[199] Zhang, Q., Jiang, B., Li, L., Liu, K., He, N., Ma, J., et al., Multifunctional Ni-based oxygen carrier for H_2 production by sorption enhanced chemical looping reforming of ethanol. *Fuel Process. Technol.* 2021, *221*, 106953.

[200] Acha, E., Chen, D., Cambra, J.F., Comparison of novel olivine supported catalysts for high purity hydrogen production by CO_2 sorption enhanced steam reforming. *J. CO_2 Util.* 2020, *42*, 101295.

[201] Sun, H., Wang, J., Zhao, J., Shen, B., Shi, J., Huang, J., et al., Dual functional catalytic materials of Ni over Ce-modified CaO sorbents for integrated CO_2 capture and conversion. *Appl. Catal. B Environ.* 2019, *244*, 63–75.

[202] Jing, J.Y., Liu, L., Xu, K., Li, W.Y., Improved hydrogen production performance of Ni–Al_2O_3/CaO–$CaZrO_3$ composite catalyst for CO_2 sorption enhanced CH_4/H_2O reforming. *Int. J. Hydrogen Energy* 2023, *48*, 2558–2570.

[203] Xie, H., Yu, Q., Zuo, Z., Han, Z., Yao, X., Qin, Q., Hydrogen production via sorption-enhanced catalytic steam reforming of bio-oil. *Int. J. Hydrogen Energy* 2016, *41*, 2345–2353.

[204] Remiro, A., Valle, B., Aramburu, B., Aguayo, A.T., Bilbao, J., Gayubo, A.G., Steam reforming of the bio-oil aqueous fraction in a fluidized bed reactor with in situ CO_2 capture. *Ind. Eng. Chem. Res.* 2013, *52*, 17087–17098.

[205] Xie, H., Yu, Q., Lu, H., Zhang, Y., Zhang, J., Qin, Q., Thermodynamic study for hydrogen production from bio-oil via sorption-enhanced steam reforming: Comparison with conventional steam reforming. *Int. J. Hydrogen Energy* 2017, *42*, 28718–28731.

[206] Soria, M.A., Barros, D., Madeira, L.M., Hydrogen production through steam reforming of bio-oils derived from biomass pyrolysis: Thermodynamic analysis including in situ CO_2 and/or H_2 separation. *Fuel* 2019, *244*, 184–195.

[207] Yan, C.F., Hu, E.Y., Cai, C.L., Hydrogen production from bio-oil aqueous fraction with in situ carbon dioxide capture. *Int. J. Hydrogen Energy* 2010, *35*, 2612–2616.

[208] Parvez, A.M., Afzal, M.T., Victor Hebb, T.G., Schmid, M., Utilization of CO_2 in thermochemical conversion of biomass for enhanced product properties: A review. *J. CO2 Util.* 2020, *40*, 101217.

[209] Nezam, I., Zhou, W., Gusmão, G.S., Realff, M.J., Wang, Y., Medford, A.J., et al., Direct aromatization of CO_2 via combined CO_2 hydrogenation and zeolite-based acid catalysis. *J. CO2 Util.* 2021, *45*, 101405.

[210] Kim, C., Yoo, C.J., Oh, H.S., Min, B.K., Lee, U., Review of carbon dioxide utilization technologies and their potential for industrial application. *J. CO2 Util.* 2022, *65*, 102239.

[211] Ateka, A., Rodriguez-Vega, P., Ereña, J., Aguayo, A.T., Bilbao, J., Kinetic modeling and reactor design of the direct synthesis of dimethyl ether for CO_2 valorization. A review. *Fuel* 2022, *327*, 125148.

[212] Saravanan, A., Senthil kumar, P., Vo, D.V.N., Jeevanantham, S., Bhuvaneswari, V., Anantha Narayanan, V., et al., A comprehensive review on different approaches for CO_2 utilization and conversion pathways. *Chem. Eng. Sci.* 2021, *236*, 116515.

[213] Blumberg, T., Morosuk, T., Tsatsaronis, G., CO_2-utilization in the synthesis of methanol: Potential analysis and exergetic assessment. *Energy* 2019, *175*, 730–744.

[214] Gao, Y., Jiang, J., Meng, Y., Yan, F., Aihemaiti, A., A review of recent developments in hydrogen production via biogas dry reforming. *Energy Convers. Manag.* 2018, *171*, 133–155.

[215] Farooqi, A.S., Yusuf, M., Mohd Zabidi, N.A., Saidur, R., Sanaullah, K., Farooqi, A.S., et al., A comprehensive review on improving the production of rich-hydrogen via combined steam and CO_2 reforming of methane over Ni-based catalysts. *Int. J. Hydrogen Energy* 2021, *46*, 31024–31040.

[216] Zhao, S., Li, H., Wang, B., Yang, X., Peng, Y., Du, H., et al., Recent advances on syngas conversion targeting light olefins. *Fuel* 2022, *321*, 124124.

[217] Lin, T., An, Y., Yu, F., Gong, K., Yu, H., Wang, C., et al., Advances in selectivity control for Fischer-Tropsch synthesis to fuels and chemicals with high carbon dfficiency. *ACS Catal.* 2022, *12*, 12092–12112.

[218] Zhou, W., Cheng, K., Kang, J., Zhou, C., Subramanian, V., Zhang, Q., et al., New horizon in C1 chemistry: breaking the selectivity limitation in transformation of syngas and hydrogenation of CO_2 into hydrocarbon chemicals and fuels. *Chem. Soc. Rev.* 2019, *48*, 3193–3228.

[219] Guilhaume, N., Bianchi, D., Wandawa, R.A., Yin, W., Schuurman, Y., Study of CO_2 and H_2O adsorption competition in the combined dry / steam reforming of biogas. *Catal. Today* 2021, *375*, 282–289.

[220] Charisiou, N.D., Siakavelas, G., Papageridis, K.N., Baklavaridis, A., Tzounis, L., Avraam, D.G., et al., Syngas production via the biogas dry reforming reaction over nickel supported on modified with CeO_2 and/or La_2O_3 alumina catalysts. *J. Nat. Gas Sci. Eng.* 2016, *31*, 164–183.

[221] Al-Nakoua, M.A., El-Naas, M.H., Combined steam and dry reforming of methane in narrow channel reactors. *Int. J. Hydrogen Energy* 2012, *37*, 7538–7544.

[222] Khani, Y., Shariatinia, Z., Bahadoran, F., High catalytic activity and stability of $ZnLaAlO_4$ supported Ni, Pt and Ru nanocatalysts applied in the dry, steam and combined dry-steam reforming of methane. *Chem. Eng. J.* 2016, *299*, 353–366.

[223] Buasuk, N., Saelee, T., Rittiruam, M., Phatanasri, S., Praserthdam, S., Praserthdam, P., Deactivating and non-deactivating coking found on Ni-based catalysts during combined steam-dry reforming of methane. *Top. Catal.* 2021, *64*, 357–370.

[224] Dan, M., Mihet, M., Borodi, G., Lazar, M.D., Combined steam and dry reforming of methane for syngas production from biogas using bimodal pore catalysts. *Catal. Today* 2021, *366*, 87–96.

[225] Kwon, Y., Eichler, J.E., Mullins, C.B., $NiAl_2O_4$ as a beneficial precursor for Ni/Al_2O_3 catalysts for the dry reforming of methane. *J. CO2 Util.* 2022, *63*, 102112.

[226] Baharudin, L., Rahmat, N., Othman, N.H., Shah, N., Syed-Hassan, S.S.A., Formation, control, and elimination of carbon on Ni-based catalyst during CO_2 and CH_4 conversion via dry reforming process: A review. *J. CO2 Util.* 2022, *61*, 102050.

[227] Challiwala, M.S., Ghouri, M.M., Linke, P., El-Halwagi, M.M., Elbashir, N.O., A combined thermo-kinetic analysis of various methane reforming technologies: Comparison with dry reforming. *J. CO2 Util.* 2017, *17*, 99–111.

[228] Guharoy, U., Reina, T.R., Liu, J., Sun, Q., Gu, S., Cai, Q., A theoretical overview on the prevention of coking in dry reforming of methane using non-precious transition metal catalysts. *J. CO2 Util.* 2021, *53*, 101728.

[229] Xia, Y., Lu, N., Li, J., Jiang, N., Shang, K., Wu, Y., Combined steam and CO_2 reforming of CH_4 for syngas production in a gliding arc discharge plasma. *J. CO2 Util.* 2020, *37*, 248–259.

[230] Zhao, S., Cai, W., Li, Y., Yu, H., Zhang, S., Cui, L., Syngas production from ethanol dry reforming over Rh/CeO_2 catalyst. *J. Saudi Chem. Soc.* 2018, *22*, 58–65.

[231] Wang, W., Cao, Y., Combined carbon dioxide reforming with steam reforming of ethanol for hydrogen production: Thermodynamic analysis. *Int. J. Green Energy* 2012, *9*, 503–516.

[232] Bac, S., Keskin, S., Avci, A.K., Recent advances in sustainable syngas production by catalytic CO_2 reforming of ethanol and glycerol. *Sustain. Energy Fuels* 2020, *4*, 1029–1047.

[233] Selcuk, O., Caglayan, B.S., Avci, A.K., Ni-catalyzed CO_2 glycerol reforming to syngas: New insights on the evaluation of reaction and catalyst performance. *J. CO2 Util.* 2023, *67*, 102329.

[234] Oh, G., Park, S.Y., Seo, M.W., Ra, H.W., Mun, T.Y., Lee, J.G., et al., Combined steam-dry reforming of toluene in syngas over CaNiRu/Al_2O_3 catalysts. *Int. J. Green Energy* 2019, *16*, 333–349.

[235] Savchenko, V.I., Zimin, Y.S., Nikitin, A. V., Sedov, I. V., Arutyunov, V.S., Utilization of CO_2 in non-catalytic dry reforming of C_1–C_4 hydrocarbons. *J. CO2 Util.* 2021, *47*, 101490.

[236] Okonkwo, O., Zhang, H., Li, K., Liu, Q., Biswas, P., Thermodynamic analysis of hydrocarbon reforming. *J. CO2 Util.* 2022, *60*, 101998.

[237] Xu, Q., Feng, P., Huang, K., Xin, S., Wei, T., Liao, L., et al., Research of the combined reforming of bio-oil model compound for hydrogen production. *Environ. Prog. Sustain. Energy* 2020, *39*.

[238] Xu, Q., Feng, P., Qi, W., Huang, K., Xin, S., Yan, Y., Catalyst deactivation and regeneration during CO_2 reforming of bio-oil. *Int. J. Hydrogen Energy* 2019, *44*, 10277–10285.

[239] Fu, M., Qi, W., Xu, Q., Zhang, S., Yan, Y., Hydrogen production from bio-oil model compounds dry (CO_2) reforming over Ni/Al_2O_3 catalyst. *Int. J. Hydrogen Energy* 2016, *41*, 1494–1501.

[240] Yao, X., Yu, Q., Xu, G., Han, Z., Xie, H., Duan, W., et al., The characteristics of syngas production from bio-oil dry reforming utilizing the waste heat of granulated blast furnace slag. *Int. J. Hydrogen Energy* 2018, *43*, 22108–22115.

[241] Xie, H., Li, R., Yu, Z., Wang, Z., Yu, Q., Qin, Q., Combined steam/dry reforming of bio-oil for H_2/CO syngas production with blast furnace slag as heat carrier. *Energy* 2020, *200*, 117481.

[242] Yao, X., Yu, Q., Xu, G., Han, Z., Qin, Q., Production of syngas from dry reforming of bio-oil model compound in granulated blast furnace slag. *Korean J. Chem. Eng.* 2019, *36*, 722–728.

[243] Lampropoulos, A., Binas, V., Konsolakis, M., Marnellos, G.E., Steam gasification of Greek lignite and its chars by co-feeding CO_2 toward syngas production with an adjustable H_2/CO ratio. *Int. J. Hydrogen Energy* 2021, *46*, 28486–28500.

[244] Selvatico, D., Lanzini, A., Santarelli, M., Low temperature Fischer-Tropsch fuels from syngas: Kinetic modeling and process simulation of different plant configurations. *Fuel* 2016, *186*, 544–560.

[245] Salaudeen, S.A., Acharya, B., Heidari, M., Arku, P., Dutta, A., Numerical investigation of CO_2 valorization via the steam gasification of biomass for producing syngas with flexible H_2 to CO ratio. *J. CO2 Util.* 2018, *27*, 32–41.

[246] Song, X., Guo, Z., Technologies for direct production of flexible H_2/CO synthesis gas. *Energy Convers. Manag.* 2006, *47*, 560–569.

[247] Cao, Y., Gao, Z., Jin, J., Zhou, H., Cohron, M., Zhao, H., et al., Synthesis gas production with an adjustable H_2/CO ratio through the coal gasification process: Effects of coal ranks and methane addition. *Energy and Fuels* 2008, *22*, 1720–1730.

[248] Hernández, S., Farkhondehfal, M.A., Sastre, F., Makkee, M., Saracco, G., Russo, N., Syngas production from electrochemical reduction of CO_2: current status and prospective implementation. *Green Chem.* 2017, *19*, 2326–2346.

[249] Mosayebi, A., Eghbal Ahmadi, M.H., Combined steam and dry reforming of methanol process to syngas formation: Kinetic modeling and thermodynamic equilibrium analysis. *Energy* 2022, *261*, 125254.

[250] Pashchenko, D., Thermodynamic equilibrium analysis of combined dry and steam reforming of propane for thermochemical waste-heat recuperation. *Int. J. Hydrogen Energy* 2017, *42*, 14926–14935.

[251] Jabbour, K., Tuning combined steam and dry reforming of methane for "metgas" production: A thermodynamic approach and state-of-the-art catalysts. *J. Energy Chem.* 2020, *48*, 54–91.

[252] Soria, M.A., Mateos-Pedrero, C., Guerrero-Ruiz, A., Rodríguez-Ramos, I., Thermodynamic and experimental study of combined dry and steam reforming of methane on Ru/ ZrO_2-La_2O_3 catalyst at low temperature. *Int. J. Hydrogen Energy* 2011, *36*, 15212–15220.

[253] Khor, S.C., Jusoh, M., Zakaria, Z.Y., Hydrogen production from steam and dry reforming of methane-ethane-glycerol: A thermodynamic comparative analysis. *Chem. Eng. Res. Des.* 2022, *180*, 178–189.

[254] Hu, X., Lu, G., Bio-oil steam reforming, partial oxidation or oxidative steam reforming coupled with bio-oil dry reforming to eliminate CO_2 emission. *Int. J. Hydrogen Energy* 2010, *35*, 7169–7176.

[255] Ochoa, A., Bilbao, J., Gayubo, A.G., Castaño, P., Coke formation and deactivation during catalytic reforming of biomass and waste pyrolysis products: A review. *Renew. Sustain. Energy Rev.* 2020, *119*, 109600.

[256] Gao, X., Wang, Z., Ashok, J., Kawi, S., A comprehensive review of anti-coking, anti-poisoning and anti-sintering catalysts for biomass tar reforming reaction. *Chem. Eng. Sci. X* 2020, *7*, 100065.

[257] Argyle, M.D., Bartholomew, C.H., Heterogeneous catalyst deactivation and regeneration: A review. *Catalysts* 2015, *5*, 145–269.

[258] Remiro, A., Arandia, A., Bilbao, J., Gayubo, A.G., Comparison of Ni based and Rh based catalyst performance in the oxidative steam reforming of raw bio-oil. *Energy and Fuels* 2017, *31*, 7147–7156.

[259] Montero, C., Ochoa, A., Castaño, P., Bilbao, J., Gayubo, A.G., Monitoring Ni^0 and coke evolution during the deactivation of a Ni/La_2O_3-αAl_2O_3 catalyst in ethanol steam reforming in a fluidized bed. *J. Catal.* 2015, *331*, 181–192.

[260] He, L., Hu, S., Jiang, L., Syed-Hassan, S.S.A., Wang, Y., Xu, K., et al., Opposite effects of self-growth amorphous carbon and carbon nanotubes on the reforming of toluene with Ni/α-Al_2O_3 for hydrogen production. *Int. J. Hydrogen Energy* 2017, *42*, 14439–14448.

[261] He, L., Hu, S., Jiang, L., Liao, G., Zhang, L., Han, H., et al., Co-production of hydrogen and carbon nanotubes from the decomposition/reforming of biomass-derived organics over Ni/α-Al_2O_3 catalyst: Performance of different compounds. *Fuel* 2017, *210*, 307–314.

[262] Mueanngern, Y., Li, C.H., Spelic, M., Graham, J., Pimental, N., Khalifa, Y., et al., Deactivation-free ethanol steam reforming at nickel-tipped carbon filaments. *Phys. Chem. Chem. Phys.* 2021, *23*, 11764–11773.

[263] He, L., Liao, G., Hu, S., Jiang, L., Han, H., Li, H., et al., Effect of temperature on multiple competitive processes for co-production of carbon nanotubes and hydrogen during catalytic reforming of toluene. *Fuel* 2020, *264*.

[264] He, L., Liao, G., Li, H., Ren, Q., Hu, S., Han, H., et al., Evolution characteristics of different types of coke deposition during catalytic removal of biomass tar. *J. Energy Inst.* 2020, *93*, 2497–2504.

[265] Valle, B., García-Gómez, N., Remiro, A., Bilbao, J., Gayubo, A.G., Dual catalyst-sorbent role of dolomite in the steam reforming of raw bio-oil for producing H_2-rich syngas. *Fuel Process. Technol.* 2020, *200*, 106316.

[266] García-Gómez, N., Valle, B., Valecillos, J., Remiro, A., Bilbao, J., Gayubo, A.G., Feasibility of online pre-reforming step with dolomite for improving Ni spinel catalyst stability in the steam reforming of raw bio-oil. *Fuel Process. Technol.* 2021, *215*, 106769.

[267] Vicente, J., Ereña, J., Montero, C., Azkoiti, M.J., Bilbao, J., Gayubo, A.G., Reaction pathway for ethanol steam reforming on a Ni/SiO_2 catalyst including coke formation. *Int. J. Hydrogen Energy* 2014, *39*.

[268] Montero, C., Remiro, A., Valle, B., Oar-Arteta, L., Bilbao, J., Gayubo, A.G., Origin and nature of coke in ethanol steam reforming and its role in deactivation of Ni/La_2O_3–αAl_2O_3 catalyst. *Ind. Eng. Chem. Res.* 2019, *58*, 14736–14751.

[269] Sehested, J., Larsen, N.W., Falsig, H., Hinnemann, B., Sintering of nickel steam reforming catalysts: Effective mass diffusion constant for Ni-OH at nickel surfaces. *Catal. Today* 2014, *228*, 22–31.

[270] Sehested, J., Four challenges for nickel steam-reforming catalysts. *Catal. Today* 2006, *111*, 103–110.

[271] Sehested, J., Gelten, J.A.P., Helveg, S., Sintering of nickel catalysts: Effects of time, atmosphere, temperature, nickel-carrier interactions, and dopants. *Appl. Catal. A Gen.* 2006, *309*, 237–246.

[272] Sehested, J., Sintering of nickel steam-reforming catalysts. *J. Catal.* 2003, *217*, 417–426.

[273] Sehested, J., Carlsson, A., Janssens, T.V.W., Hansen, P.L., Datyey, A.K., Sintering of nickel steam-reforming catalysts on $MgAl_2O_4$ spinel supports. *J. Catal.* 2001, *197*, 200–209.

[274] Sehested, J., Gelten, J.A.P., Remediakis, I.N., Bengaard, H., Nørskov, J.K., Sintering of nickel steam-reforming catalysts: effects of temperature and steam and hydrogen pressures. *J. Catal.* 2004, *223*, 432–443.

[275] Li, S., Gong, J., Strategies for improving the performance and stability of Ni-based catalysts for reforming reactions. *Chem. Soc. Rev.* 2014, *43*, 7245–7256.

[276] Zhou, J., Zhao, J., Zhang, J., Zhang, T., Ye, M., Liu, Z., Regeneration of catalysts deactivated by coke deposition: A review. *Chinese J. Catal.* 2020, *41*, 1048–1061.

[277] Sharifzadeh, M., Sadeqzadeh, M., Guo, M., Borhani, T.N., Murthy Konda, N.V.S.N., Garcia, M.C., et al., The multi-scale challenges of biomass fast pyrolysis and bio-oil upgrading: Review of the state of art and future research directions. *Prog. Energy Combust. Sci.* 2019, *71*, 1–80.

[278] Zhang, Y., Sun, G., Gao, S., Xu, G., Regeneration kinetics of spent FCC catalyst via coke gasification in a micro fluidized bed. *Procedia Eng.* 2015, *102*, 1758–1765.

[279] Bednarczuk, L., Ramírez de la Piscina, P., Homs, N., Efficient CO_2-regeneration of Ni/$Y_2O_3La_2O_3ZrO_2$ systems used in the ethanol steam reforming for hydrogen production. *Int. J. Hydrogen Energy* 2016, *41*, 19509–19517.

[280] Alenazey, F., Cooper, C.G., Dave, C.B., Elnashaie, S.S.E.H., Susu, A.A., Adesina, A.A., Coke removal from deactivated Co–Ni steam reforming catalyst using different gasifying agents: An analysis of the gas–solid reaction kinetics. *Catal. Commun.* 2009, *10*, 406–411.

[281] Oar-Arteta, L., Remiro, A., Vicente, J., Aguayo, A.T., Bilbao, J., Gayubo, A.G., Stability of $CuZnOAl_2O_3$/HZSM-5 and $CuFe_2O_4$/HZSM-5 catalysts in dimethyl ether steam reforming operating in reaction–regeneration cycles. *Fuel Process. Technol.* 2014, *126*, 145–154.

[282] Arandia, A., Remiro, A., García, V., Castaño, P., Bilbao, J., Gayubo, A.G., Oxidative steam reforming of raw bio-oil over supported and bulk Ni catalysts for hydrogen production. *Catalysts* 2018, *8*, 322.

[283] Wang, C., Wang, Y., Chen, M., Hu, J., Liang, D., Tang, Z., et al., Comparison of the regenerability of Co/sepiolite and Co/Al_2O_3 catalysts containing the spinel phase in simulated bio-oil steam reforming. *Energy* 2021, *214*, 118971.

[284] Remiro, A., Valle, B., Oar-Arteta, L., Aguayo, A.T., Bilbao, J., Gayubo, A.G., Hydrogen production by steam reforming of bio-oil/bio-ethanol mixtures in a continuous thermal-catalytic process. *Int. J. Hydrogen Energy* 2014, *39*, 6889–6898.

[285] Wagenaar, B.M., Kuipers, J.A.M., Prins, W., van Swaaij, W.P.M., The rotating cone flash pyrolysis reactor, in: *Advances in Thermochemical Biomass Conversion*, Springer, Dordrecht, 1993, pp. 1122–1133.

[286] Channiwala, S.A., Parikh, P.P., A unified correlation for estimating HHV of solid, liquid and gaseous fuels. *Fuel* 2002, *81*, 1051–1063.

[287] Fassinou, W.F., Sako, A., Fofana, A., Koua, K.B., Toure, S., Fatty acids composition as a means to estimate the high heating value (HHV) of vegetable oils and biodiesel fuels. *Energy* 2010, *35*, 4949–4954.

[288] Remón, J., Casales, M., Gracia, J., Callén, M.S., Pinilla, J.L., Suelves, I., Sustainable production of liquid biofuels and value-added platform chemicals by hydrodeoxygenation of lignocellulosic bio-oil over a carbon–neutral Mo_2C/CNF catalyst. *Chem. Eng. J.* 2021, *405*, 126705.

[289] Garcia-Perez, M., Chaala, A., Pakdel, H., Kretschmer, D., Roy, C., Characterization of bio-oils in chemical families. *Biomass and Bioenergy* 2007, *31*, 222–242.

[290] Czernik, S., Bridgwater, A. V., Overview of applications of biomass fast pyrolysis oil. *Energy and Fuels* 2004, *18*, 590–598.

[291] Wang, C., Ding, H., Zhang, Y., Zhu, X., Analysis of property variation and stability on the aging of bio-oil from fractional condensation. *Renew. Energy* 2020, *148*, 720–728.

[292] Oasmaa, A., Peacocke, C., Properties and fuel use of biomass-derived fast pyrolysis liquids. A guide, Vuorimiehentie (Finland): Julkaisija-Utgivare, 2010.

[293] Bertero, M., De La Puente, G., Sedran, U., Fuels from bio-oils: Bio-oil production from different residual sources, characterization and thermal conditioning. *Fuel* 2012, *95*, 263–271.

[294] Oasmaa, A., Leppaemaeki, E., Koponen, P., Levander, J., Tapola, E., Physical characterization of biomass-based pyrolysis liquids. Application of standard fuel oil analyses, Vuorimiehentie (Finland): Julkaisija-Utgivare, 1997.

[295] Mohan, D., Pittman, C.U., Steele, P.H., Pyrolysis of wood/biomass for bio-oil: A critical review. *Energy and Fuels* 2006, *20*, 848–889.

[296] Xiu, S., Shahbazi, A., Bio-oil production and upgrading research: A review. *Renew. Sustain. Energy Rev.* 2012, *16*, 4406–4414.

[297] Valle, B., García-Gómez, N., Remiro, A., Gayubo, A.G., Bilbao, J., Cost-effective upgrading of biomass pyrolysis oil using activated dolomite as a basic catalyst. *Fuel Process. Technol.* 2019, *195*, 106142.

[298] Brunauer, S., Emmett, P.H., Teller, E., Adsorption of gases in multimolecular layers. *J. Am. Chem. Soc.* 1938, *60*, 309–319.

[299] Barrett, E.P., Joyner, L.G., Halenda, P.P., The determination of pore volume and area distributions in porous substances. I. Computations from nitrogen isotherms. *J. Am. Chem. Soc.* 1951, *73*, 373–380.

[300] Sing, K.S.W., Everett, D.H., Haul, R.A.W., Moscou, L., Pierotti, R.A., Rouquerol, J., et al., Reporting physisorption data for Gas/Solid systems with special reference to the determination of surface area and porosity. *Pure Appl. Chem.* 1985, *57*, 603–619.

[301] Leofanti, G., Padovan, M., Tozzola, G., Venturelli, B., Surface area and pore texture of catalysts. *Catal. Today* 1998, *41*, 207–219.

[302] Benrabaa, R., Barama, A., Boukhlouf, H., Guerrero-Caballero, J., Rubbens, A., Bordes-Richard, E., et al., Physico-chemical properties and syngas production via dry reforming of methane over $NiAl_2O_4$ catalyst. *Int. J. Hydrogen Energy* 2017, *42*, 12989–12996.

[303] Arandia, A., Remiro, A., Valle, B., Bilbao, J., Gayubo, A.G., Deactivation of Ni spinel derived catalyst during the oxidative steam reforming of raw bio-oil. *Fuel* 2020, *276*, 117995.

[304] Tada, S., Shimizu, T., Kameyama, H., Haneda, T., Kikuchi, R., Ni/CeO_2 catalysts with high CO_2 methanation activity and high CH_4 selectivity at low temperatures. *Int. J. Hydrogen Energy* 2012, *37*, 5527–5531.

[305] Hu, Y., Li, X., Zhang, L., Zhou, M., Wang, G., Zhang, Y., et al., Mesoporous alumina as a solid phase extraction adsorbent for the determination of abamectin and ivermectin in vegetables by liquid chromatography-tandem mass spectrometry. *Anal. Methods* 2014, *6*, 4734–4741.

[306] Ye, R.P., Li, Q., Gong, W., Wang, T., Razink, J.J., Lin, L., et al., High-performance of nanostructured Ni/CeO_2 catalyst on CO_2 methanation. *Appl. Catal. B Environ.* 2020, *268*, 118474.

[307] Hu, X., Zhang, Z., Gholizadeh, M., Zhang, S., Lam, C.H., Xiong, Z., et al., Coke formation during thermal treatment of bio-oil. *Energy and Fuels* 2020, *34*, 7863–7914.

[308] Ochoa, A., Aramburu, B., Ibáñez, M., Valle, B., Bilbao, J., Gayubo, A.G., et al., Compositional insights and valorization pathways for carbonaceous material deposited during bio-oil thermal treatment. *ChemSusChem* 2014, *7*, 2597–2608.

[309] Valle, B., Aramburu, B., Remiro, A., Arandia, A., Bilbao, J., Gayubo, A.G., Optimal conditions of thermal treatment unit for the steam reforming of raw bio-oil in a continuous two-step reaction system. *Chem. Eng. Trans.* 2017, *57*.

[310] Lima Da Silva, A., Müller, I.L., Hydrogen production by sorption enhanced steam reforming of oxygenated hydrocarbons (ethanol, glycerol, n-butanol and methanol): Thermodynamic modelling. *Int. J. Hydrogen Energy* 2011, *36*, 2057–2075.

[311] Li, X., Zhang, Z., Zhang, L., Fan, H., Li, X., Liu, Q., et al., Investigation of coking behaviors of model compounds in bio-oil during steam reforming. *Fuel* 2020, *265*, 116961.

[312] Hu, S., He, L., Wang, Y., Su, S., Jiang, L., Chen, Q., et al., Effects of oxygen species from Fe addition on promoting steam reforming of toluene over Fe–Ni/Al_2O_3 catalysts. *Int. J. Hydrogen Energy* 2016, *41*, 17967–17975.

[313] Montero, C., Oar-Arteta, L., Remiro, A., Arandia, A., Bilbao, J., Gayubo, A.G., Thermodynamic comparison between bio-oil and ethanol steam reforming. *Int. J. Hydrogen Energy* 2015, *40*, 15963–15971.

[314] Xie, H., Yu, Q., Wang, K., Shi, X., Li, X., Thermodynamic analysis of hydrogen production from model compounds of bio-oil through steam reforming. *Environ. Prog. Sustain. Energy* 2014, *33*, 1008–1016.

[315] Vagia, E.C., Lemonidou, A.A., Thermodynamic analysis of hydrogen production via autothermal steam reforming of selected components of aqueous bio-oil fraction. *Int. J. Hydrogen Energy* 2008, *33*, 2489–2500.

[316] Santamaria, L., Lopez, G., Arregi, A., Amutio, M., Artetxe, M., Bilbao, J., et al., Stability of different Ni supported catalysts in the in-line steam reforming of biomass fast pyrolysis volatiles. *Appl. Catal. B Environ.* 2019, *242*, 109–120.

[317] Rodrigues, C.T., Alonso, C.G., Machado, G.D., de Souza, T.L., Optimization of bio-oil steam reforming process by thermodynamic analysis. *Int. J. Hydrogen Energy* 2020, *45*, 28350–28360.

[318] Li, J., Yu, H., Yang, G., Peng, F., Xie, D., Wang, H., et al., Steam reforming of oxygenate fuels for hydrogen production: A thermodynamic study. *Energy and Fuels* 2011, *25*, 2643–2650.

[319] Arregi, A., Lopez, G., Amutio, M., Barbarias, I., Bilbao, J., Olazar, M., Hydrogen production from biomass by continuous fast pyrolysis and in-line steam reforming. *RSC Adv.* 2016, *6*, 25975–25985.

[320] Hernández, L., Kafarov, V., Thermodynamic evaluation of hydrogen production for fuel cells by using bio-ethanol steam reforming: Effect of carrier gas addition. *J. Power Sources* 2009, *192*, 195–199.

[321] Ochoa, A., Valle, B., Resasco, D.E., Bilbao, J., Gayubo, A.G., Castaño, P., Temperature programmed oxidation coupled with in situ techniques reveal the nature and location of coke deposited on a Ni/La_2O_3-αAl_2O_3 catalyst in the steam reforming of bio-oil. *ChemCatChem* 2018, *10*, 2311–2321.

[322] Yang, X., Weng, Y., Li, M., Sun, B., Li, Y., Wang, Y., Enhanced hydrogen production by steam reforming of acetic acid over a Ni catalyst supported on mesoporous MgO. *Energy and Fuels* 2016, *30*, 2198–2203.

[323] Venkataraman, A., Amadi, E.V., Chen, Y., Papadopoulos, C., Carbon nanotube assembly and integration for applications. *Nanoscale Res. Lett.* 2019, *14*, 220.

[324] Ferrari, A.C., Robertson, J., Interpretation of Raman spectra of disordered and amorphous carbon. *Phys. Rev. B* 2000, *61*, 14095–14107.

[325] Li, J., Jia, P., Hu, X., Dong, D., Gao, G., Geng, D., et al., Steam reforming of carboxylic acids for hydrogen generation: Effects of aliphatic chain of the acids on their reaction behaviors. *Mol. Catal.* 2018, *450*, 1–13.

[326] Bokobza, L., Bruneel, J.L., Couzi, M., Raman spectroscopic investigation of carbon-based materials and their composites. Comparison between carbon nanotubes and carbon black. *Chem. Phys. Lett.* 2013, *590*, 153–159.

[327] Choi, Y.C., Min, K.I., Jeong, M.S., Novel method of evaluating the purity of multiwall carbon nanotubes using raman spectroscopy. *J. Nanomater.* 2013, *2013*.

[328] Jorio, A., Saito, R., Raman spectroscopy for carbon nanotube applications. *J. Appl. Phys.* 2021, *129*, 021102.

[329] Schuepfer, D.B., Badaczewski, F., Guerra-Castro, J.M., Hofmann, D.M., Heiliger, C., Smarsly, B., et al., Assessing the structural properties of graphitic and non-graphitic carbons by Raman spectroscopy. *Carbon N. Y.* 2020, *161*, 359–372.

[330] Gayubo, A.G., Vicente, J., Ereña, J., Montero, C., Olazar, M., Bilbao, J., Comparison of Ni and Co catalysts for ethanol steam reforming in a fluidized bed reactor. *Catal. Letters* 2014, *144*.

[331] Koo, K.Y., Lee, S.H., Jung, U.H., Roh, H.S., Yoon, W.L., Syngas production via combined steam and carbon dioxide reforming of methane over Ni-Ce/$MgAl_2O_4$ catalysts with enhanced coke resistance. *Fuel Process. Technol.* 2014, *119*, 151–157.

[332] Van Der Lee, M.K., Van Dillen, A.J., Geus, J.W., De Jong, K.P., Bitter, J.H., Catalytic growth of macroscopic carbon nanofiber bodies with high bulk density and high mechanical strength. *Carbon N. Y.* 2006, *44*, 629–637.

[333] Galetti, A.E., Gomez, M.F., Arrúa, L.A., Abello, M.C., Hydrogen production by ethanol reforming over NiZnAl catalysts. Influence of Ce addition on carbon deposition. *Appl. Catal. A Gen.* 2008, *348*, 94–102.

[334] Kawamoto, H., Murayama, M., Saka, S., Pyrolysis behavior of levoglucosan as an intermediate in cellulose pyrolysis: Polymerization into polysaccharide as a key reaction to carbonized product formation. *J. Wood Sci.* 2003, *49*, 469–473.

[335] Gayubo, A.G., Valle, B., Aramburu, B., Montero, C., Bilbao, J., Kinetic model considering catalyst deactivation for the steam reforming of bio-oil over Ni/La_2O_3-αAl_2O_3. *Chem. Eng. J.* 2018, *332*, 192–204.

[336] Shang, Z., Li, S., Li, L., Liu, G., Liang, X., Highly active and stable alumina supported nickel nanoparticle catalysts for dry reforming of methane. *Appl. Catal. B Environ.* 2017, *201*, 302–309.

[337] Sun, H., Zhang, Y., Wang, C., Isaacs, M.A., Osman, A.I., Wang, Y., et al., Integrated carbon capture and utilization: Synergistic catalysis between highly dispersed Ni clusters and ceria oxygen vacancies. *Chem. Eng. J.* 2022, *437*, 135394.

[338] Hongmanorom, P., Ashok, J., Chirawatkul, P., Kawi, S., Interfacial synergistic catalysis over Ni nanoparticles encapsulated in mesoporous ceria for CO_2 methanation. *Appl. Catal. B Environ.* 2021, *297*, 120454.

[339] Santamaria, L., Lopez, G., Arregi, A., Amutio, M., Artetxe, M., Bilbao, J., et al., Influence of the support on Ni catalysts performance in the in-line steam reforming of biomass fast pyrolysis derived volatiles. *Appl. Catal. B Environ.* 2018, *229*, 105–113.

[340] Anil, S., Indraja, S., Singh, R., Appari, S., Roy, B., A review on ethanol steam reforming for hydrogen production over Ni/Al_2O_3 and Ni/CeO_2 based catalyst powders. *Int. J. Hydrogen Energy* 2022, *47*, 8177–8213.

[341] Guo, Y., Zou, J., Shi, X., Rukundo, P., Wang, Z.J., A Ni/CeO_2-CDC-SiC catalyst with improved coke resistance in CO_2 reforming of methane. *ACS Sustain. Chem. Eng.* 2017, *5*, 2330–2338.

[342] Ochoa, A., Arregi, A., Amutio, M., Gayubo, A.G., Olazar, M., Bilbao, J., et al., Coking and sintering progress of a Ni supported catalyst in the steam reforming of biomass pyrolysis volatiles. *Appl. Catal. B Environ.* 2018, *233*, 289–300.

[343] Alvarez, D., Abanades, J.C., Pore-size and shape effects on the recarbonation performance of calcium oxide submitted to repeated calcination/recarbonation cycles. *Energy and Fuels* 2005, *19*, 270–278.

[344] Chen, Y.-T., Karthik, M., Bai, H., Modification of CaO by organic alumina precursor for enhancing cyclic capture of CO_2 greenhouse gas. *J. Environ. Eng.* 2009, *135*, 459–464.

[345] Giammaria, G., Lefferts, L., Catalytic effect of water on calcium carbonate decomposition. *J. CO2 Util.* 2019, *33*, 341–356.

[346] Chen, K., Zhang, H., Ibrahim, U.K., Xue, W.Y., Liu, H., Guo, A., The quantitative assessment of coke morphology based on the Raman spectroscopic characterization of serial petroleum cokes. *Fuel* 2019, *246*, 60–68.

[347] Cao, K.L.A., Rahmatika, A.M., Kitamoto, Y., Nguyen, M.T.T., Ogi, T., Controllable synthesis of spherical carbon particles transition from dense to hollow structure derived from Kraft lignin. *J. Colloid Interface Sci.* 2021, *589*, 252–263.

[348] Ambriz-Torres, J.M., Lvova, L.D., García, C.J.G., Garnica-González, P., Aguilar-García, O., Contreras-Navarrete, J.J., Characterization and comparison of carbon structures synthesized from rubber waste and naphthalene. *MRS Adv.* 2022, 1–5.

[349] Chen, L., Noreña, L.E., Wang, J.A., Limas, R., Arellano, U., Vargas, O.A.G., Promoting role of amorphous carbon and carbon nanotubes growth modes of methane decomposition in one-pot catalytic approach. *Catalysts* 2021, *11*, 1217.

[350] Cortazar, M., Lopez, G., Alvarez, J., Amutio, M., Bilbao, J., Olazar, M., Behaviour of primary catalysts in the biomass steam gasification in a fountain confined spouted bed. *Fuel* 2019, *253*, 1446–1456.

[351] De Andrés, J.M., Narros, A., Rodríguez, M.E., Behaviour of dolomite, olivine and alumina as primary catalysts in air–steam gasification of sewage sludge. *Fuel* 2011, *90*, 521–527.

[352] Brito, J., Pinto, F., Ferreira, A., Soria, M.A., Madeira, L.M., Steam reforming of biomass gasification gas for hydrogen production: From thermodynamic analysis to experimental validation. *Fuel Process. Technol.* 2023, *250*, 107859.

[353] Dang, C., Xia, H., Luo, J., Cai, W., Dendritic layered Ni/Al_2O_3 derived from $NiAl_2O_4$ as high-performance catalyst for dry reforming of methane. *Fuel Process. Technol.* 2023, *241*, 107615.

[354] Du, J., Gao, J., Gu, F., Zhuang, J., Lu, B., Jia, L., et al., A strategy to regenerate coked and sintered Ni/Al_2O_3 catalyst for methanation reaction. *Int. J. Hydrogen Energy* 2018, *43*, 20661–20670.

[355] Arregi, A., Lopez, G., Amutio, M., Barbarias, I., Santamaria, L., Bilbao, J., et al., Regenerability of a Ni catalyst in the catalytic steam reforming of biomass pyrolysis volatiles. *J. Ind. Eng. Chem.* 2018, *68*, 69–78.

[356] Barbarias, I., Artetxe, M., Lopez, G., Arregi, A., Santamaria, L., Bilbao, J., et al., Catalyst performance in the HDPE pyrolysis-peforming under reaction-regeneration cycles. *Catalysts* 2019, *9*, 414.

[357] Pakhare, D., Spivey, J., A review of dry (CO_2) reforming of methane over noble metal catalysts. *Chem. Soc. Rev.* 2014, *43*, 7813–7837.

[358] Palmer, C., Upham, D.C., Smart, S., Gordon, M.J., Metiu, H., McFarland, E.W., Dry reforming of methane catalysed by molten metal alloys. *Nat. Catal. 2020 31* 2020, *3*, 83–89.

[359] Caravella, A., Brunetti, A., Grandinetti, M., Barbieri, G., Dry reforming of methane in a Pd-Ag membrane reactor: Thermodynamic and experimental analysis. *ChemEngineering* 2018, *2*, 48.

[360] Buelens, L.C., Galvita, V. V., Poelman, H., Detavernier, C., Marin, G.B., Super-dry reforming of methane intensifies CO_2 utilization via le Chatelier's principle. *Science (80-.).* 2016, *354*, 449–452.

[361] Ateka, A., Pérez-Uriarte, P., Gamero, M., Ereña, J., Aguayo, A.T., Bilbao, J., A comparative thermodynamic study on the CO_2 conversion in the synthesis of methanol and of DME. *Energy* 2017, *120*, 796–804.

[362] Vagia, E.C., Lemonidou, A.A., Thermodynamic analysis of hydrogen production via steam reforming of selected components of aqueous bio-oil fraction. *Int. J. Hydrogen Energy* 2007, *32*, 212–223.

[363] Resende, K.A., Ávila-Neto, C.N., Rabelo-Neto, R.C., Noronha, F.B., Hori, C.E., Thermodynamic analysis and reaction routes of steam reforming of bio-oil aqueous fraction. *Renew. Energy* 2015, *80*, 166–176.

Annexes

A. RESULTS OF THE THERMODYNAMIC STUDIES

A.1. Validation of the calculation with ProII software and SRK model

In order to prove the validity of the simulation procedure used, the equilibrium molar flow rates obtained for selected conditions for the SR of acetone were compared with those obtained using other software (DWSIN 6.4.3) and thermodynamic models (Peng-Robinson (PR) and UNIFAC). The differences in the molar flow rates of products obtained using different thermodynamic models (SRK vs PR) with ProII software are shown in Table A.1, whereas the differences in the results calculated with SRK model and different software are gathered in Table A.2. Moreover, Table A.3 gathers the differences in the calculations using DWSIM software and using different thermodynamic models.

Table A.1. Percentage relative error of the equilibrium molar flow rates calculated for the SR of acetone under selected conditions associated with the use of SRK or PR thermodynamic models (ProII software).

T, °C	S/C	H_2	CO	CO_2	CH_4
400	3	0.02	0.03	<0.01	<0.01
400	7	0.01	0.02	0.01	0.01
800	3	<0.01	<0.01	<0.01	0.04
800	7	0.02	0.02	0.05	0.04

Table A.2. Percentage relative error of the equilibrium molar flow rates calculated for the SR of acetone under selected conditions associated with the use of ProII or DWSIM software (SRK thermodynamic model).

T, °C	S/C	H_2	CO	CO_2	CH_4
400	3	2.48	3.30	0.76	0.58
400	7	2.30	3.18	1.07	1.56
800	3	0.41	1.33	1.63	1.83
800	7	0.29	2.67	0.95	0.08

Table A.3. Percentage relative error of the equilibrium molar flow rates calculated for the SR of acetone under selected conditions associated with the use of SRK, PR or UNIFAC thermodynamic models (DWSIM software).

	T, °C	S/C	H_2	CO	CO_2	CH_4
SRK-PR	400	3	<0.01	0.05	0.03	0.05
SRK-PR	400	7	0.01	0.03	0.05	0.03
SRK-PR	800	3	0.05	0.18	0.06	0.38
SRK-PR	800	7	0.02	0.01	0.01	<0.01
SRK-UNIFAC	400	3	0.13	0.07	0.04	0.01
SRK-UNIFAC	400	7	0.13	0.08	0.1	0.08
SRK-UNIFAC	800	3	0.05	0.17	0.07	0.3
SRK-UNIFAC	800	7	<0.01	0.02	<0.01	0.01

A.2. Effect of reaction conditions in the SR of the oxygenates and in the WGS reaction

Figure A.1 shows the effect of the reaction temperature on the relative molar flow rates (referred to a feed of 1 kmol/h of oxygenated compound) of the reaction products in the SR of each oxygenate at a S/C ratio of 5. Moreover, Figure A.2 shows the effect of S/C ratio and temperature on the equilibrium molar flow rates of H_2 (equal to that of CO_2) and CO in the WGS reaction, as it helps understanding the results of the SR of the oxygenates, due to the relevant contribution of WGS reaction to the overall mechanism of SR reactions. The effect of temperature has a similar trend for all oxygenates and is consistent with the results previously reported by Xie et al. [314] for the SR of ethanol, acetic acid, acetone and phenol.

Therefore, maximum H_2 flow rate is obtained at intermediate temperatures (close to 600 °C) in Figure A.1, because the increase in temperature favours the steam reforming reaction (Eq. (1.14)), but it also promotes the reverse-WGS reaction (Eq. (1.15)) (see the decrease in the yields of CO_2 and H_2 with temperature in Figure A.2, in parallel with an increase in CO yield). Similarly, the CO_2 flow rate is maximum at intermediate temperatures, usually 100 °C lower than those

maximising the H_2 flow rate. It is noteworthy that the H_2/CO_2 ratio is almost constant once the maximum H_2 flow rate is reached, whereas this ratio decreases rapidly at lower temperatures, evidencing that decomposition/decarboxylation reactions (Eq. (1.16)) are thermodynamically promoted over steam reforming reaction at low temperatures.

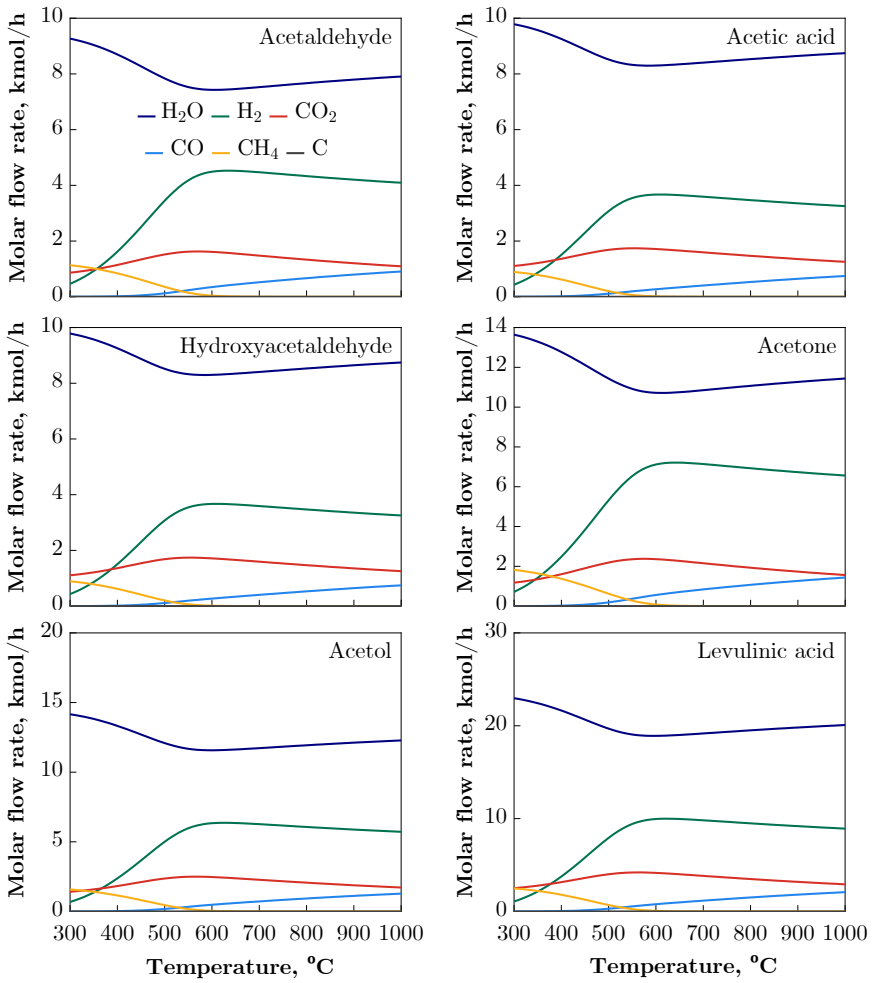

Figure A.1. Evolution with temperature of the molar flow rate of products in the SR of each oxygenate for a S/C ratio of 5.

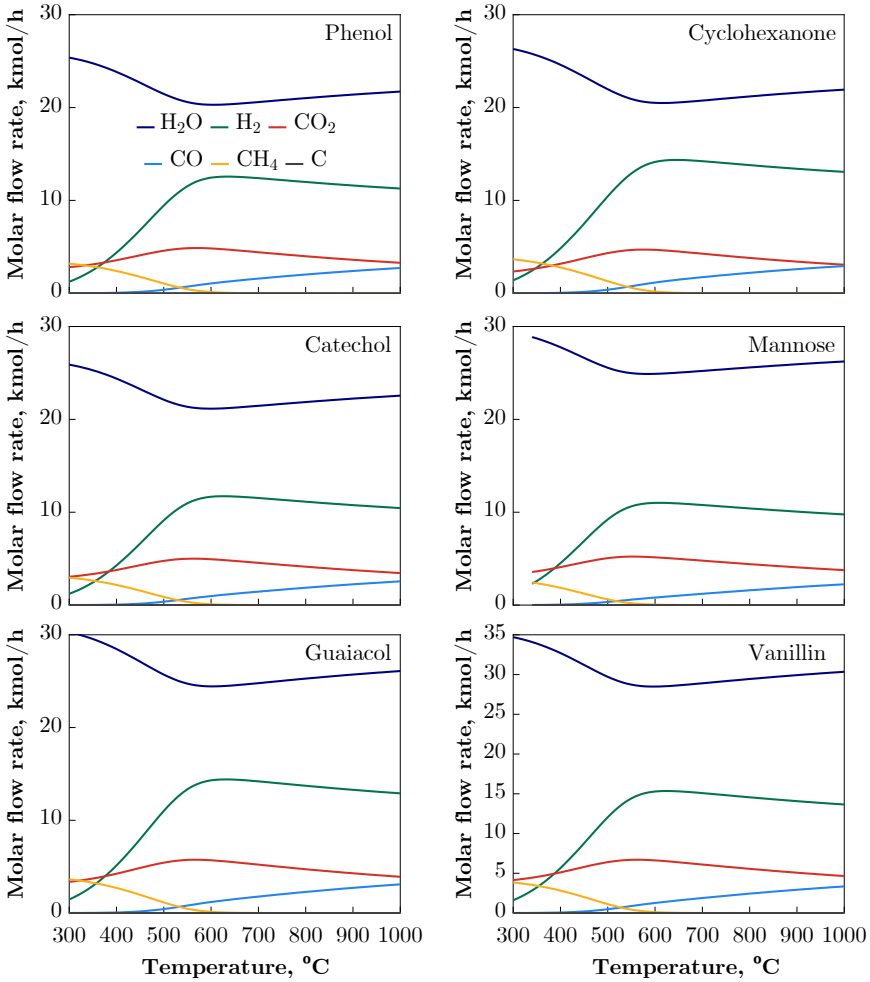

Figure A.1. Continued.

The flow rate of CH_4 is maximum at 300 °C, because methanation reactions are highly promoted at low temperatures, and it decreases steadily with increasing temperature because the extent of methane steam reforming reaction (Eq. (1.17)) is promoted. Conversely, CO flow rate is almost null below 400 °C, the temperature at which methanation reaction (reverse of Eq. (1.17)) and Boudouard reaction (Eq. (1.21)) are favoured, and it increases steadily with temperature due to the promotion first of methane reforming reaction, (Eq. (1.17)), and then (above 600 °C)of the reverse-WGS reaction (Eq. (1.15)). For all of the oxygenates studied, the predicted C-graphite formation is null for the whole

range of temperature at high S/C ratios, in agreement with previous results in the literature [313, 314, 362, 363].

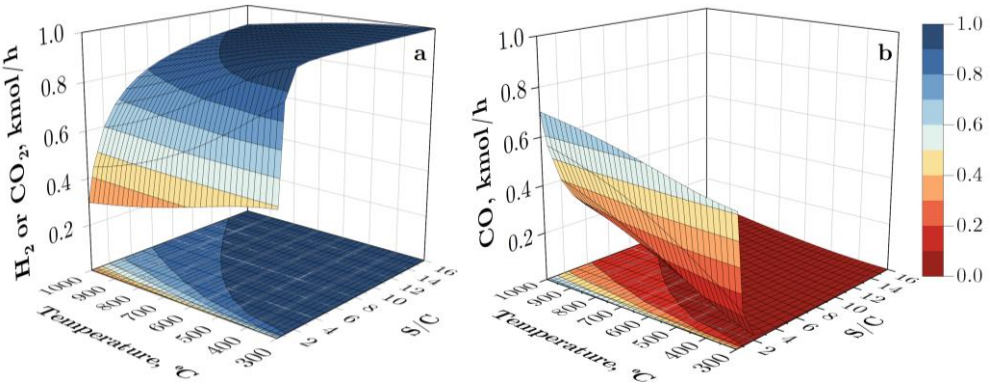

Figure A.2. Effect of temperature and S/C ratio on the equilibrium molar flow rates of the products of WGS reaction.

A.3. Deduction of the correlation for the calculation of the optimum yields and the temperature in the SR of oxygenates

Mathematical correlations (Eqs. (3.1)-(3.5)) of the values in Table 3.1 were sought as a function of both the feed composition (steam/carbon molar ratio) and the composition of the corresponding oxygenate (atomic C/H/O ratios, shown in Table 2.1). For this purpose, the values of the yields of each product and of the temperature were plotted in Figure A.3-Figure A.7 as a function of the H/C, O/C and O/H atomic ratios, respectively. As observed, for any S/C ratio in the feed, the maximum equilibrium H_2 yield increases with increasing H/C, O/C and O/H ratios (Figure A.3), whereas the corresponding values of temperature and yields of carbon by-products do not depend on the H/C ratio, but they show clear trends with the O/C and O/H ratios. In particular, for any S/C ratio in the feed, the temperature (Figure A.4) and the CO yield (Figure A.6) decrease with increasing O/C and O/H ratios, whereas CO_2 yield increases with increasing O/C and O/H ratios (Figure A.5). In the case of CH_4 yield (Figure A.7), the trend with O/C and O/H ratios is different depending on the S/C ratio in the feed. For low S/C

ratios, it increases with increasing O/C and O/H ratios, whereas for S/C ratio ≥5 it decreases with increasing both molar ratios.

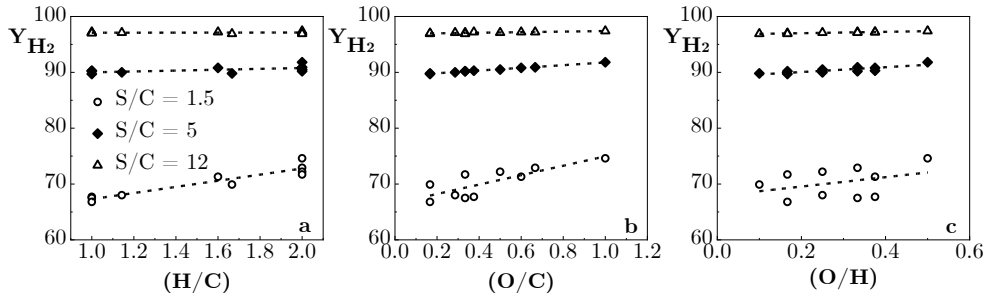

Figure A.3. Evolution of the maximum equilibrium H_2 yield with the H/C (a) O/C (b) and O/H (c) ratios of the oxygenated compounds, for different S/C ratios in the feed.

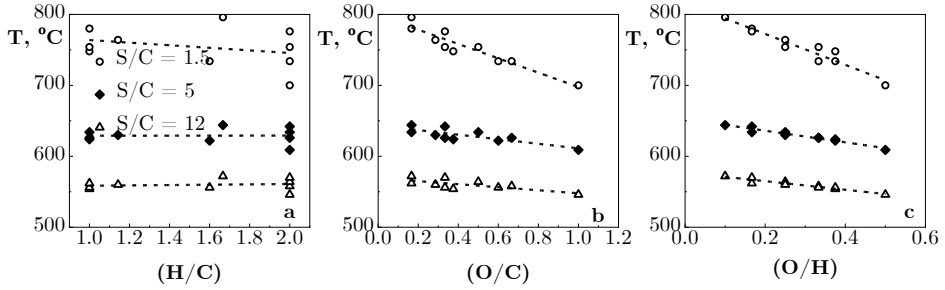

Figure A.4. Evolution of the temperature corresponding to the maximum equilibrium H_2 with the H/C (a) O/C (b) and O/H (c) ratios of the oxygenated compounds, for different S/C ratios in the feed.

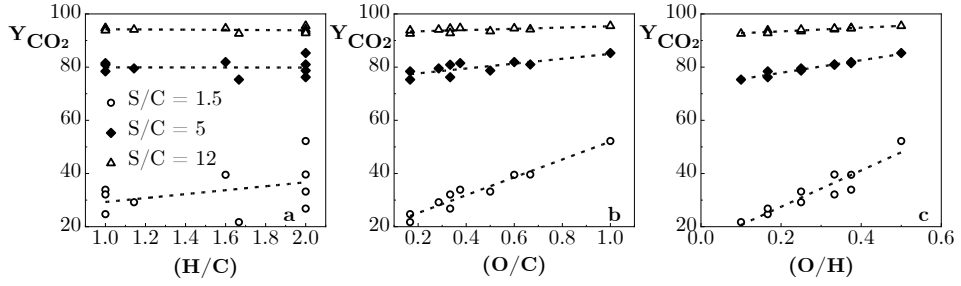

Figure A.5. Evolution of the CO_2 yield corresponding to the maximum equilibrium H_2 yield with the H/C (a) O/C (b) and O/H (c) ratios of the oxygenated compounds, for different S/C ratios in the feed.

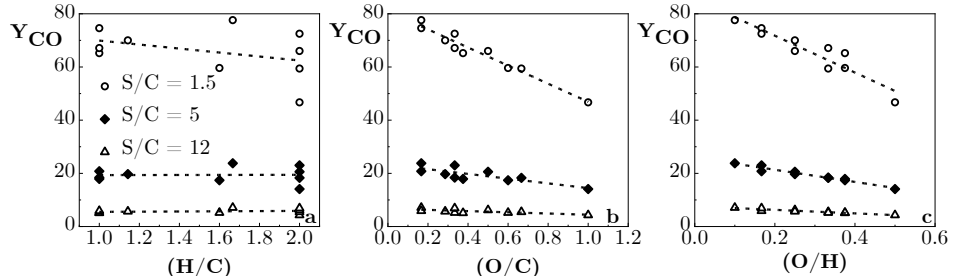

Figure A.6. Evolution of the CO yield corresponding to the maximum equilibrium H_2 yield with the H/C (a) O/C (b) and O/H (c) ratios of the oxygenated compounds, for different S/C ratios in the feed.

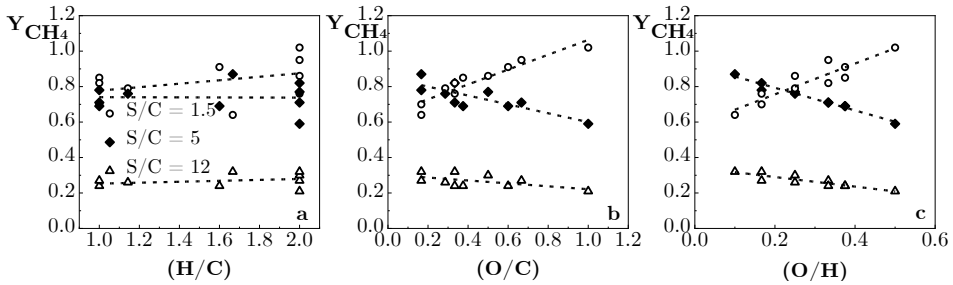

Figure A.7. Evolution of the CH_4 yield corresponding to the maximum equilibrium H_2 yield, with the H/C (a) O/C (b) and O/H (c) ratios of the oxygenated compound for different S/C ratios in the feed.

Based on these general trends, the H_2 yield was related to the sum of all these ratios (H/C+O/C+O/H), whereas temperature and yields of carbon by-products were related to the sum of (O/C+O/H) ratios (Figure A.8). As shown in this figure, linear relationships were obtained in all cases. The values of the ordinate at the origin (O.O) and the slope of the linear fit for each product yield and temperature were in turn correlated with the composition of the feed (Figure A.9). Specifically, both O.O and slope for the yields of H_2, CO and CO_2 and for temperature are a linear function of the carbon/steam (C/S) ratio in the feed (Figure A.9a-Figure A.9d), whereas the values of O.O and slope for CH_4 yield are a second order polynomic function of the C/S ratio in the feed (Figure A.9e).

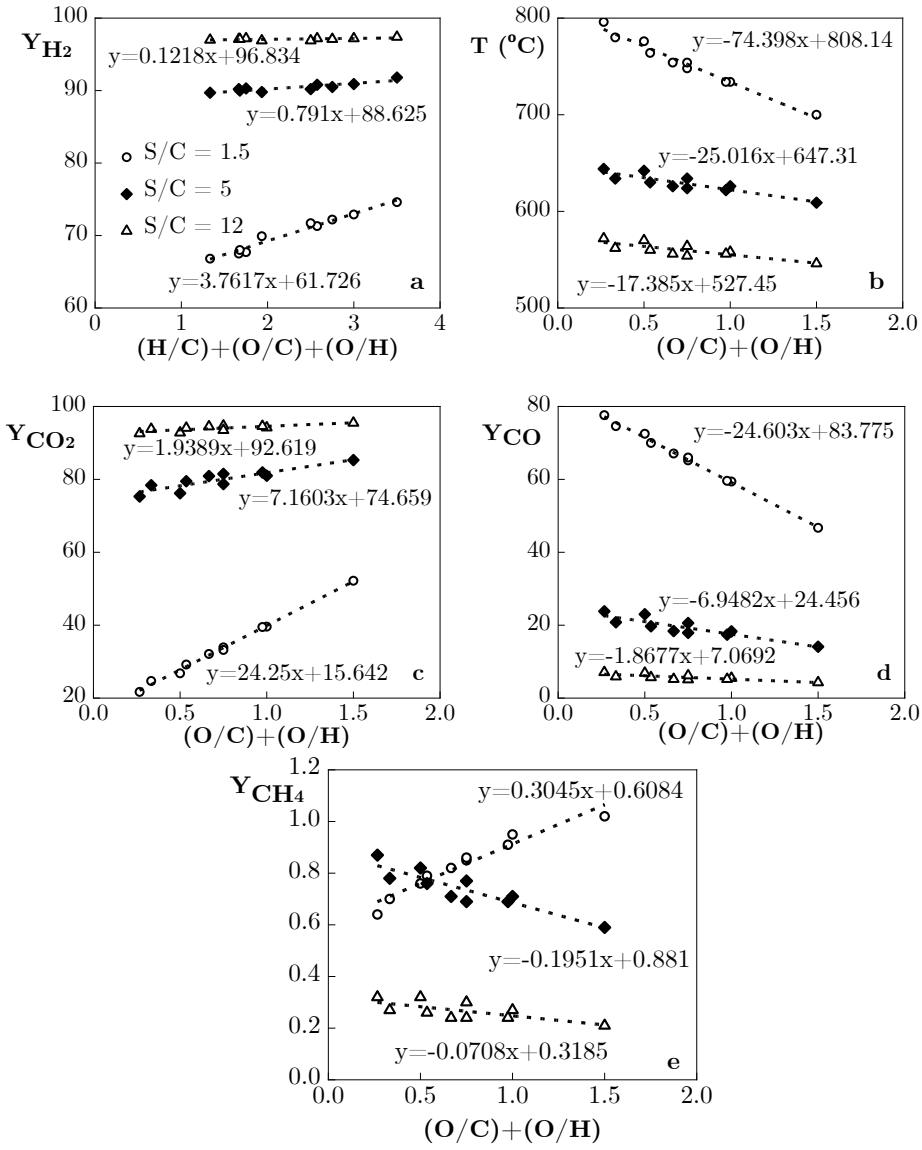

Figure A.8. Dependence of maximum equilibrium H_2 yield (a) and corresponding values of temperature (b) and carbon by-products yields (c-e) on the composition of the oxygenated compound.

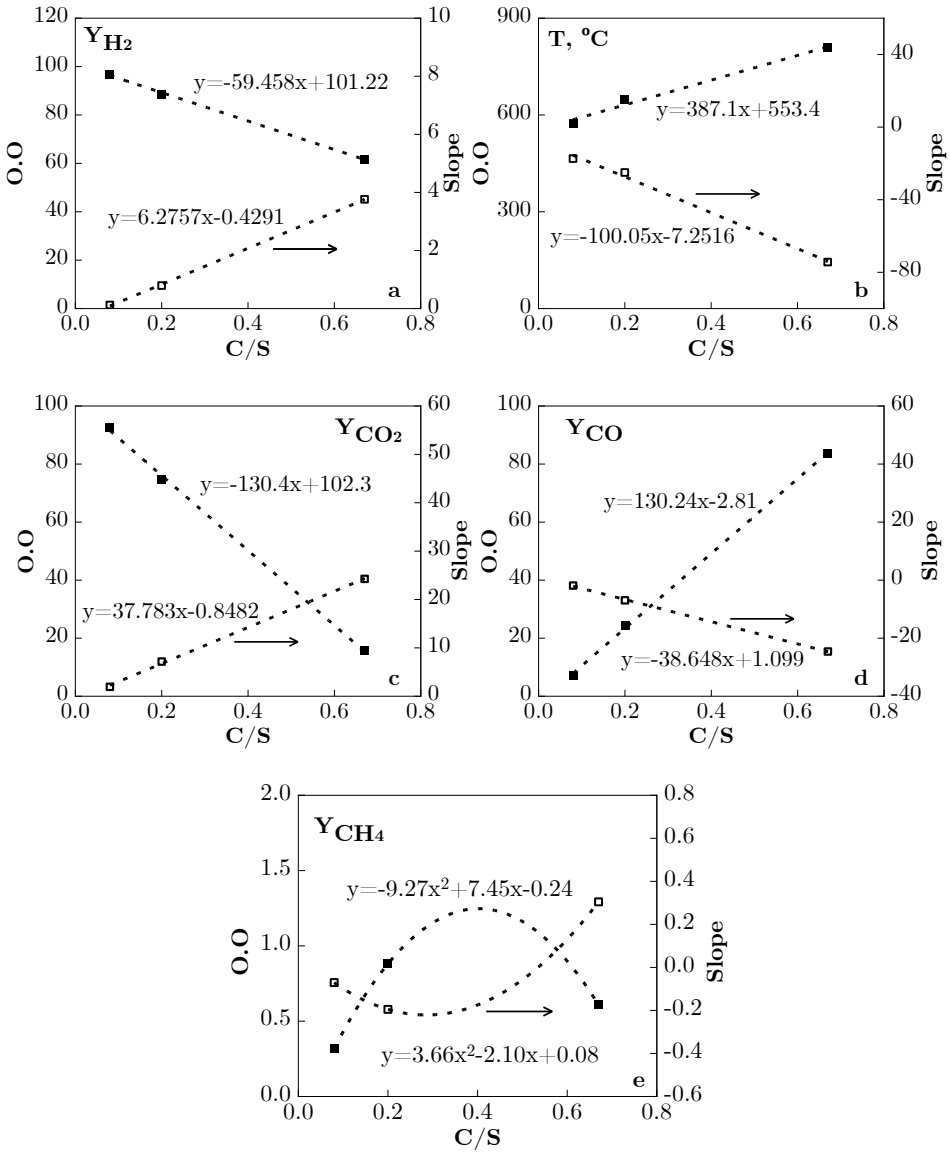

Figure A.9. Correlations of the ordinate at the origin (O.O) and the slopes of the fitting lines of Figure A.3-Figure A.7 as a function of the C/S ratio in the feed.

A.4. Results of the thermodynamic study of the CSDR of simulated bio-oil

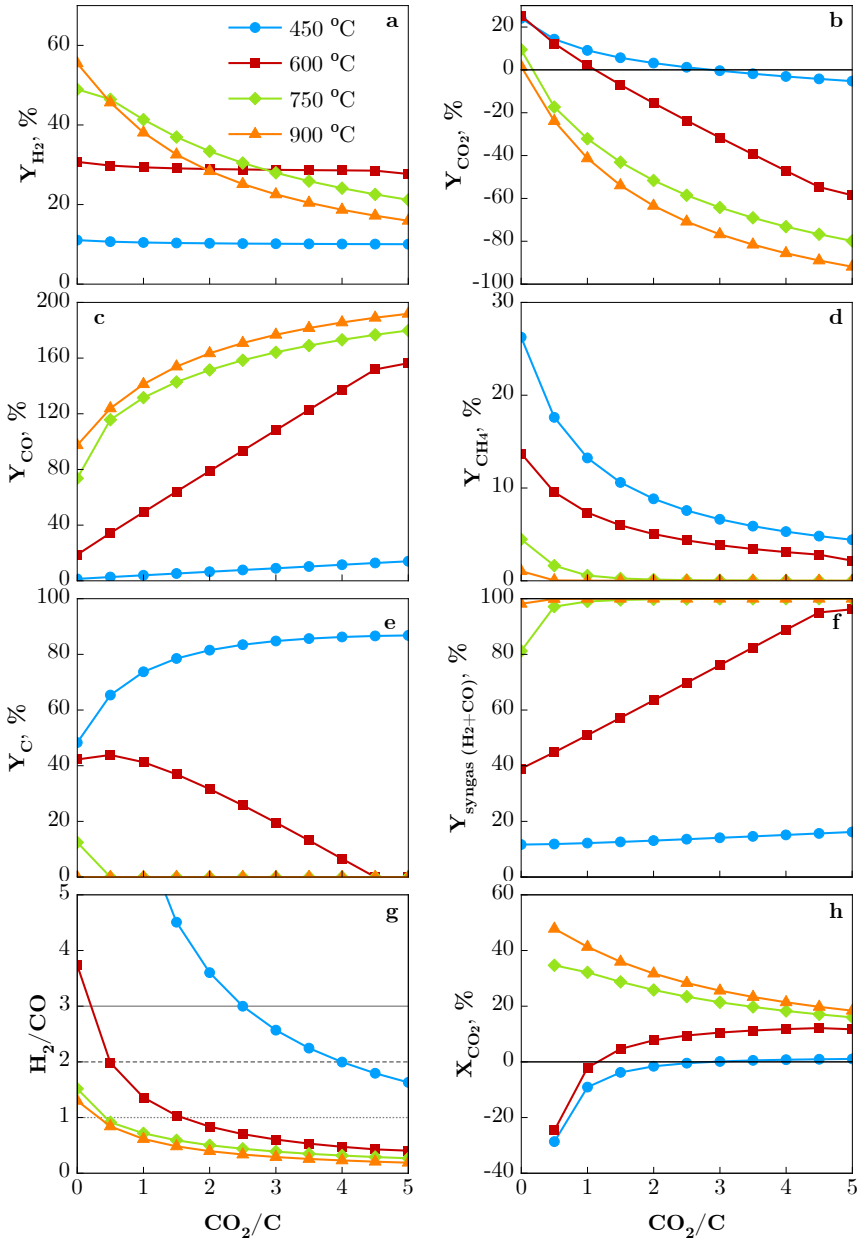

Figure A.10. Effect of CO_2/C ratio on the equilibrium products yields (a-e), syngas yield (f), H_2/CO ratio (g) and CO_2 conversion (h), for different values of temperature. S/C ratio of 0.5.

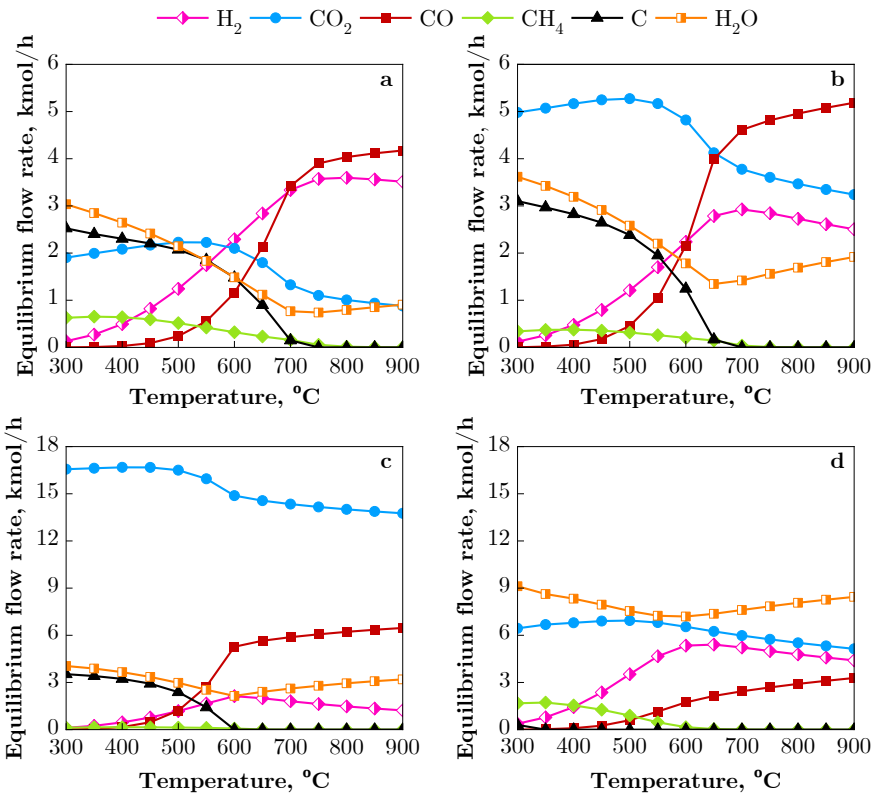

Figure A.11. Effect of temperature on equilibrium molar flow rates of products for a S/C ratio of 0.5 with a CO_2/C ratio of 0.5 (a) and 5 (c), and for a CO_2/C ratio of 1.5 with a S/C ratio of 0.5 (b) and 3 (d).

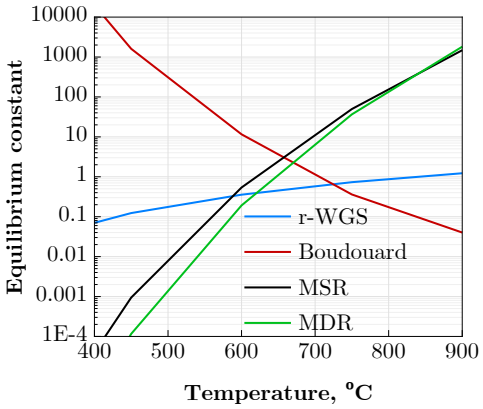

Figure A.12. Effect of temperature on equilibrium constants for the reverse-WGS (r-WGS), Boudouard, methane steam reforming (MSR) and methane dry reforming (MDR) reactions.

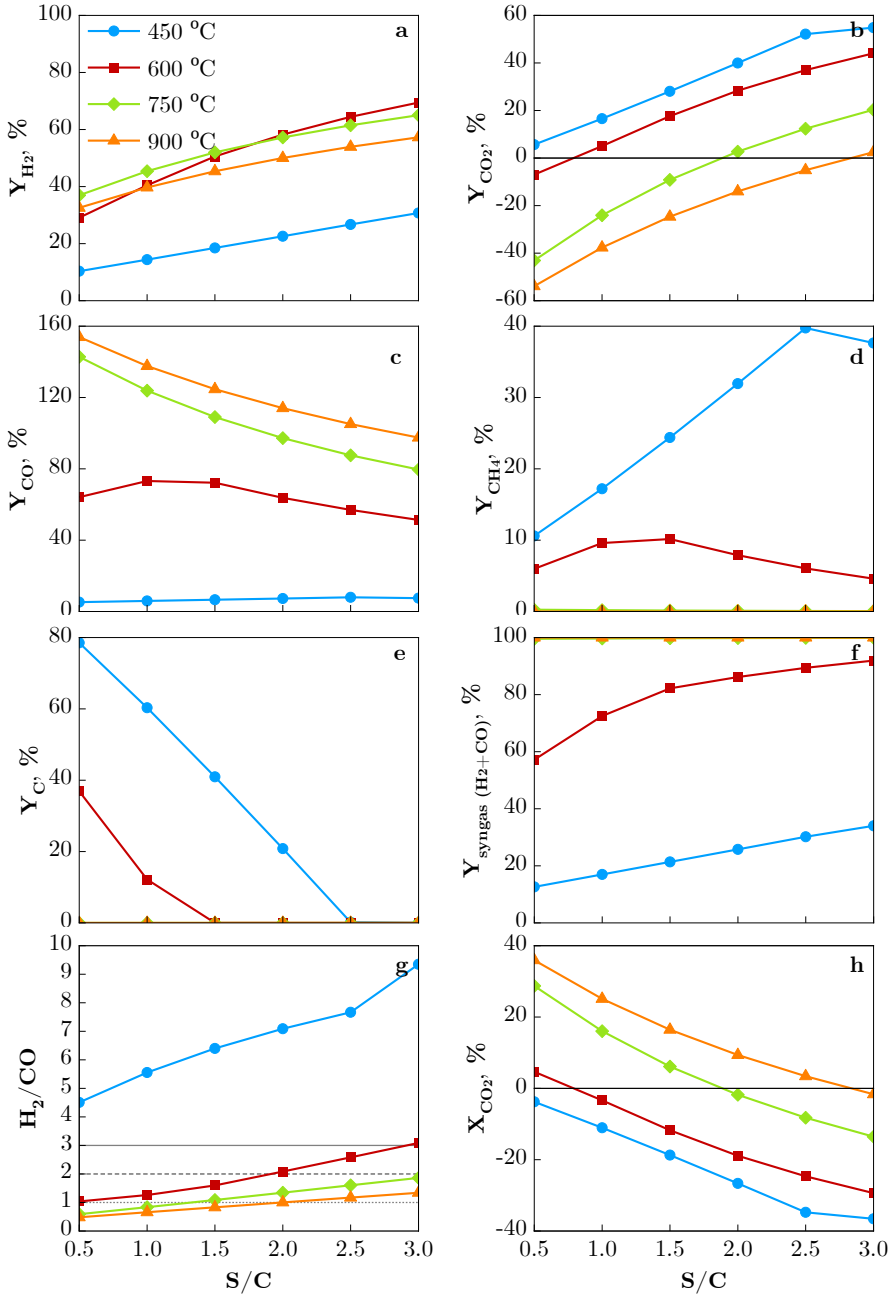

Figure A.13. Effect of S/C ratio on the equilibrium products yields (a-e), syngas yield (f), H_2/CO ratio (g) and CO_2 conversion (h), for different values of temperature. CO_2/C ratio of 1.5.

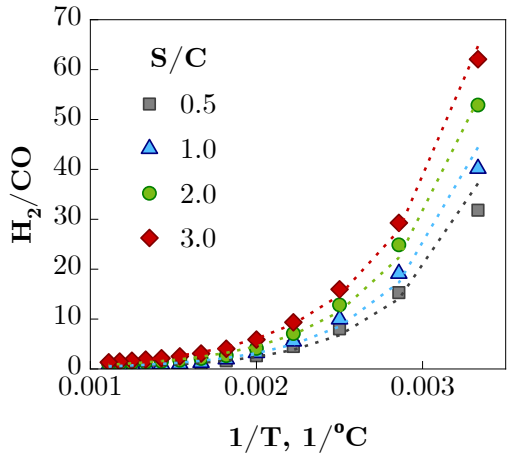

Figure A.14. Trend of H_2/CO ratio with the inverse of the temperature, at different S/C ratios, for a CO_2/C ratio of 1.5.

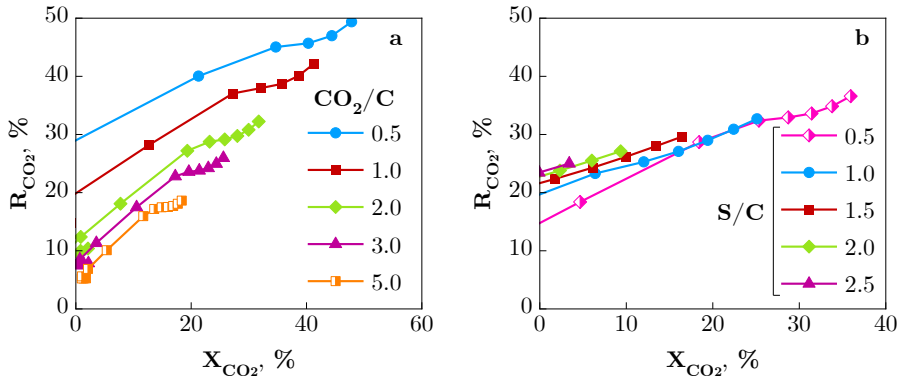

Figure A.15. Correlation between reduction of CO_2 emissions and CO_2 conversion for different values of CO_2/C ratio (a, with S/C ratio of 0.5) and different values of S/C ratio (b, with CO_2/C ratio of 1.5).

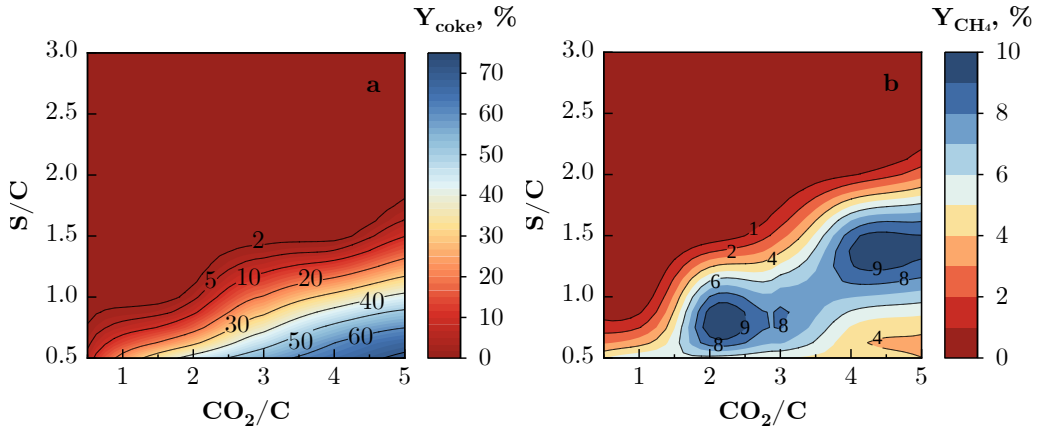

Figure A.16. Coke yield (a) and CH_4 yield (b) when producing a syngas with a H_2/CO ratio of 1, for different S/C and CO_2/C ratios, with the temperature values depicted in Figure 5.8a.

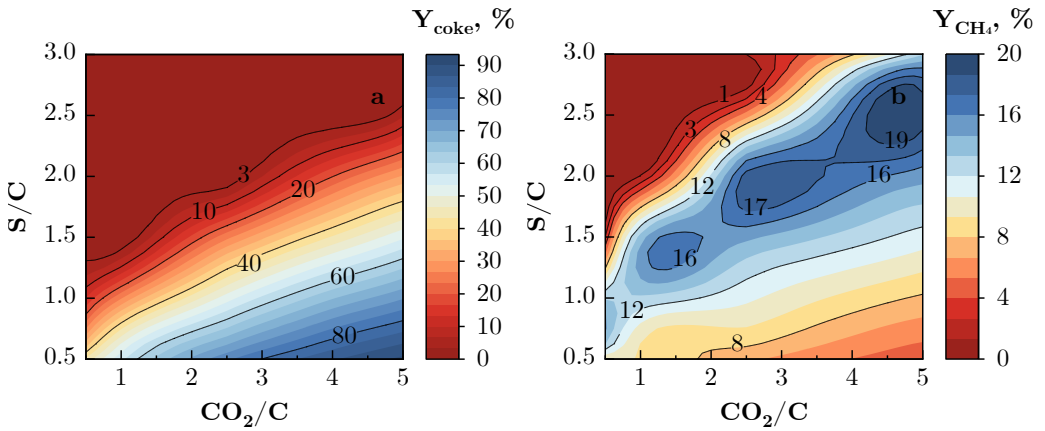

Figure A.17. Coke yield (a) and CH_4 yield (b) when producing a syngas with a H_2/CO ratio of 2, for different S/C and CO_2/C ratios, with the temperature values depicted in Figure 5.9a.

B. CHARACTERIZATION OF USED CATALYSTS AND SORBENTS

B.1. N_2 adsorption-desorption isotherms and pore volume distribution

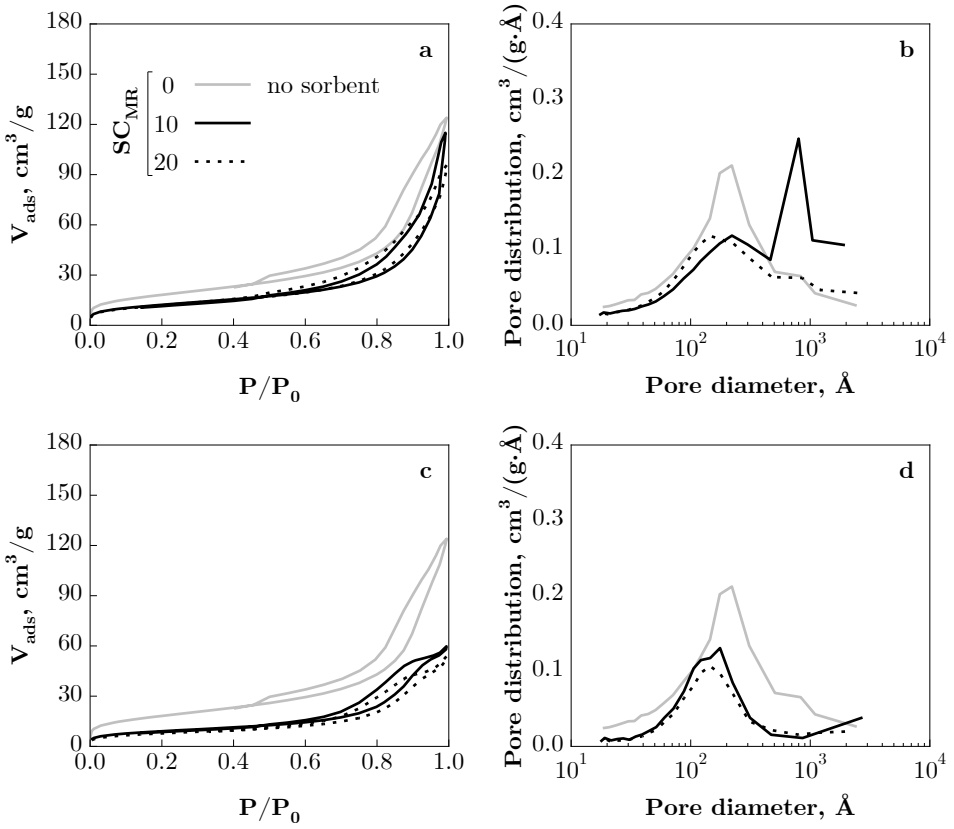

Figure B.1. N_2 adsorption-desorption isotherms (left graphs) and BJH pore volume distribution (right graphs) of Ni/Al_2O_3 catalyst samples used in the SR run and SESR runs with dolomite (a and c) or Ca-M (c and d) as sorbent, under the conditions indicated in Figure 4.1 and Figure 4.3.

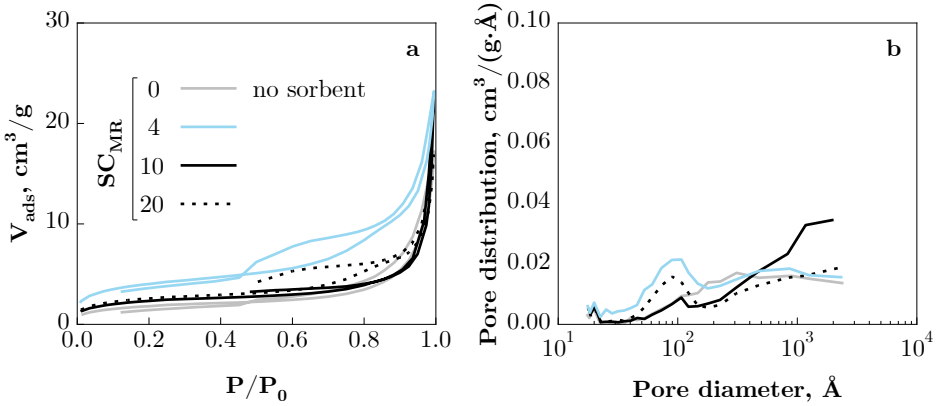

Figure B.2. N_2 adsorption-desorption isotherms (a) and BJH pore volume distribution (b) of Ni/CeO_2 catalyst samples used in the SR run and SESR runs with dolomite as sorbent, under the conditions indicated in Figure 4.5 and Figure 4.6

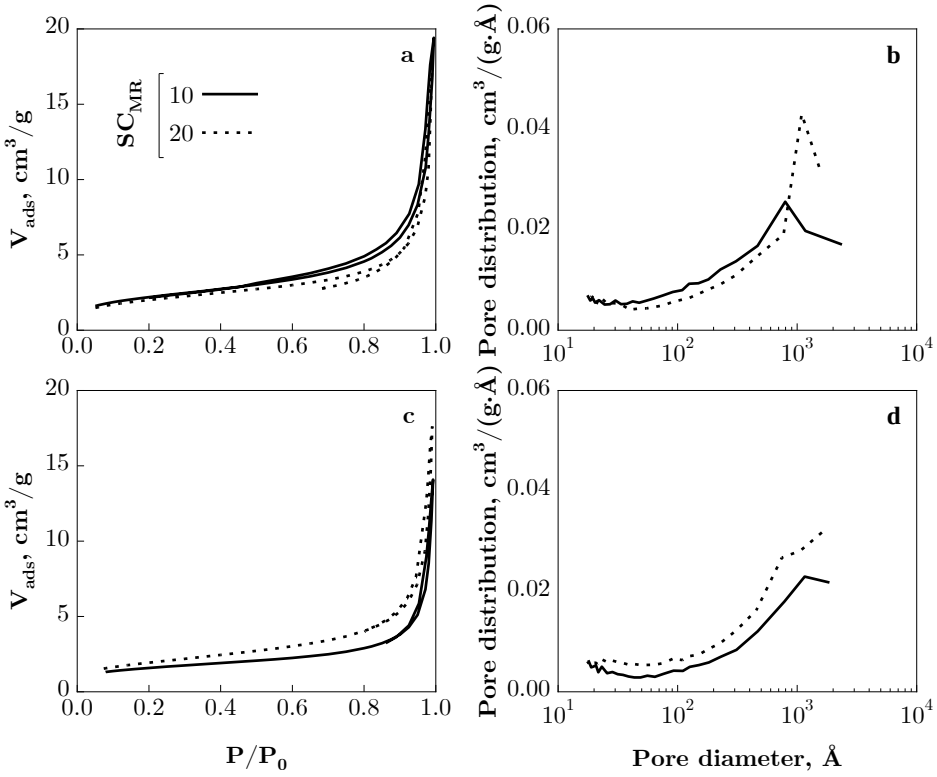

Figure B.3. N_2 adsorption-desorption isotherms (left graphs) and BJH pore volume distribution (right graphs) of the saturated dolomite (a and c) or Ca-M (c and d) sorbents used in the SESR runs with Ni/Al_2O_3 catalyst in the conditions indicated in Figure 4.1 and Figure 4.3.

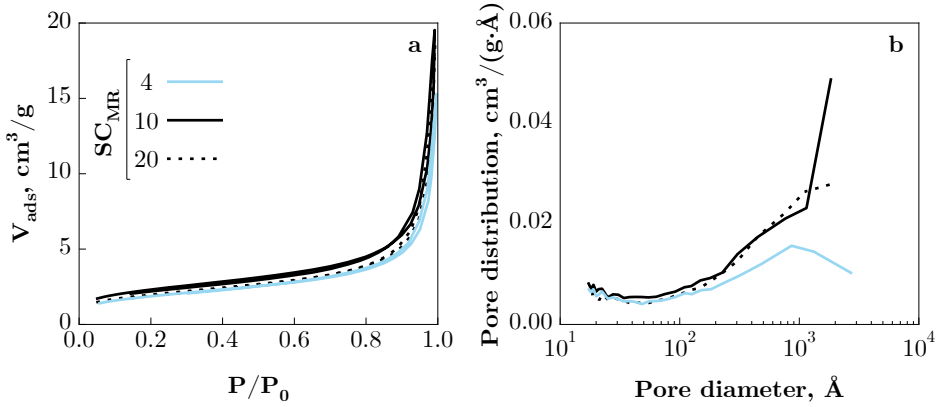

Figure B.4. N_2 adsorption-desorption isotherms (a) and BJH pore volume distribution (b) of the saturated dolomite samples used in the SESR runs with Ni/CeO_2 catalyst under the conditions indicated in Figure 4.5 and Figure 4.6

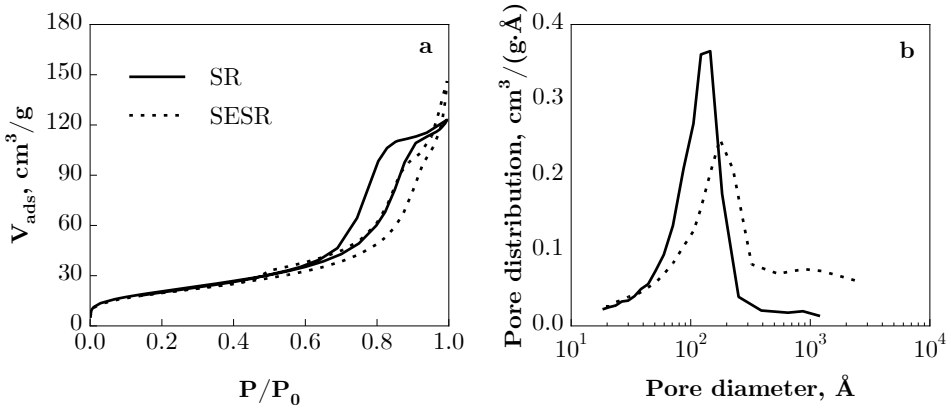

Figure B.5. N_2 adsorption-desorption isotherms (a) and BJH pore volume distribution (b) of Ni/Al_2O_3 catalyst samples used in the SR (no dolomite, solid lines) and SESR (dolomite/catalyst mass ratio of 10, dashed lines) runs with FBR in the conditions indicated in Figure 4.15 and Figure 4.16.

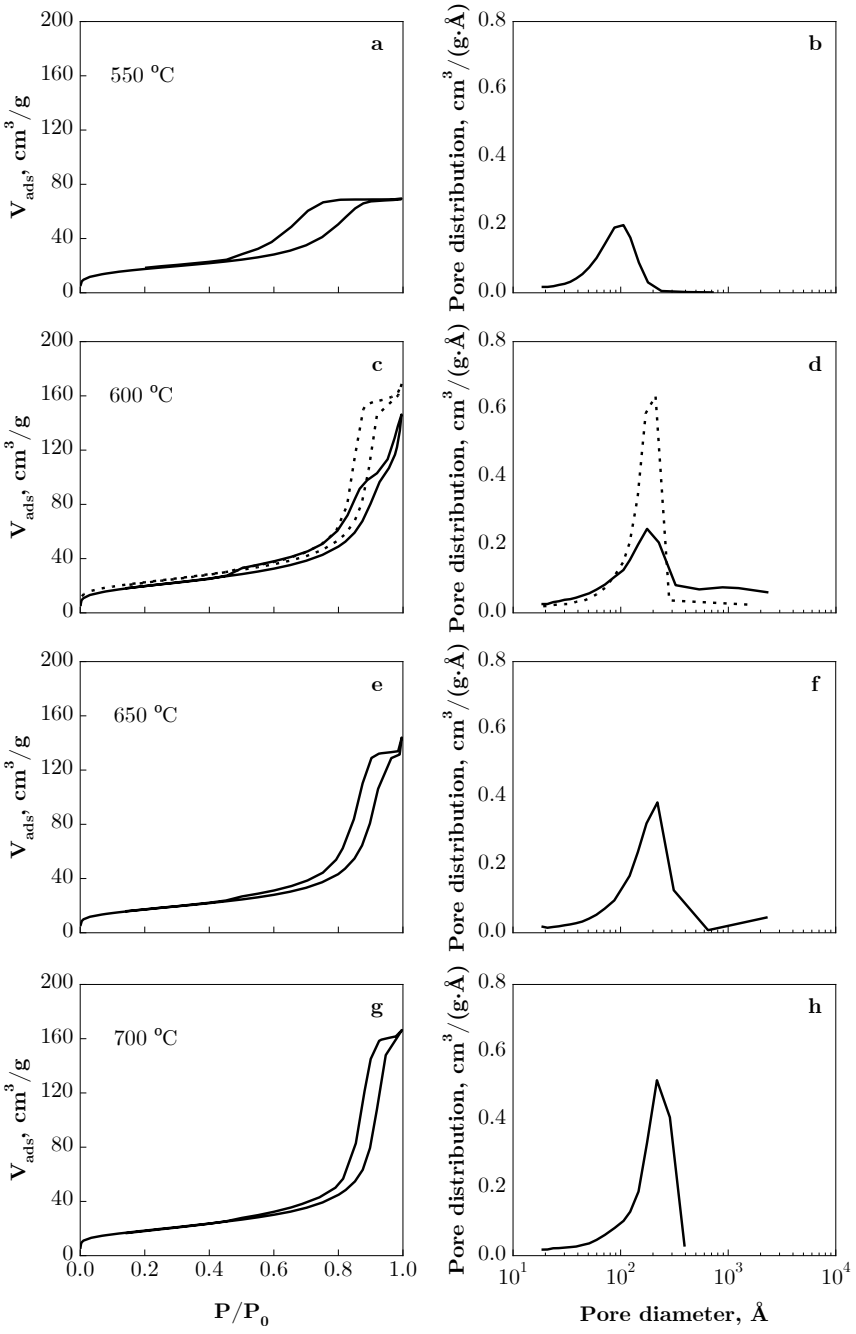

Figure B.6. N_2 adsorption-desorption isotherms (left graphs) and BJH pore volume distribution (right graphs) of Ni/Al_2O_3 catalyst samples used in the SESR runs at different temperatures in the conditions of Figure 4.30 (solid lines) and Figure 4.32 (dashed lines).

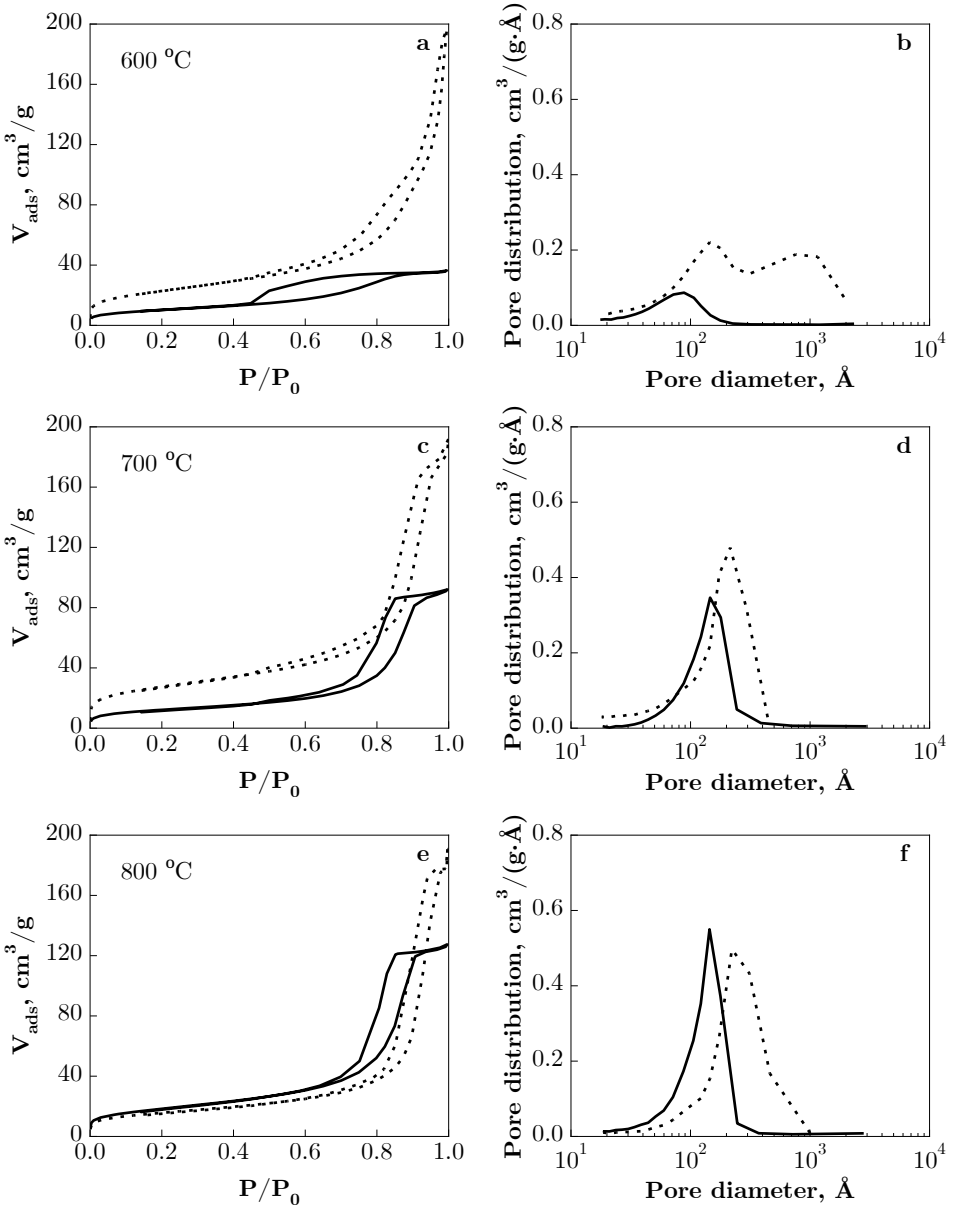

Figure B.7. N_2 adsorption-desorption isotherms (left graphs) and BJH pore volume distribution (right graphs) of Ni/Al_2O_3 catalyst samples used in the CSDR runs at different temperatures for a CO_2/C ratio of 1.1 and S/C ratio-space time ($g_{catalyst}$·h/$g_{oxygenates}$) of 0.5 - 0.125 (solid lines) or 1.7 – 0.250 (dashed lines).

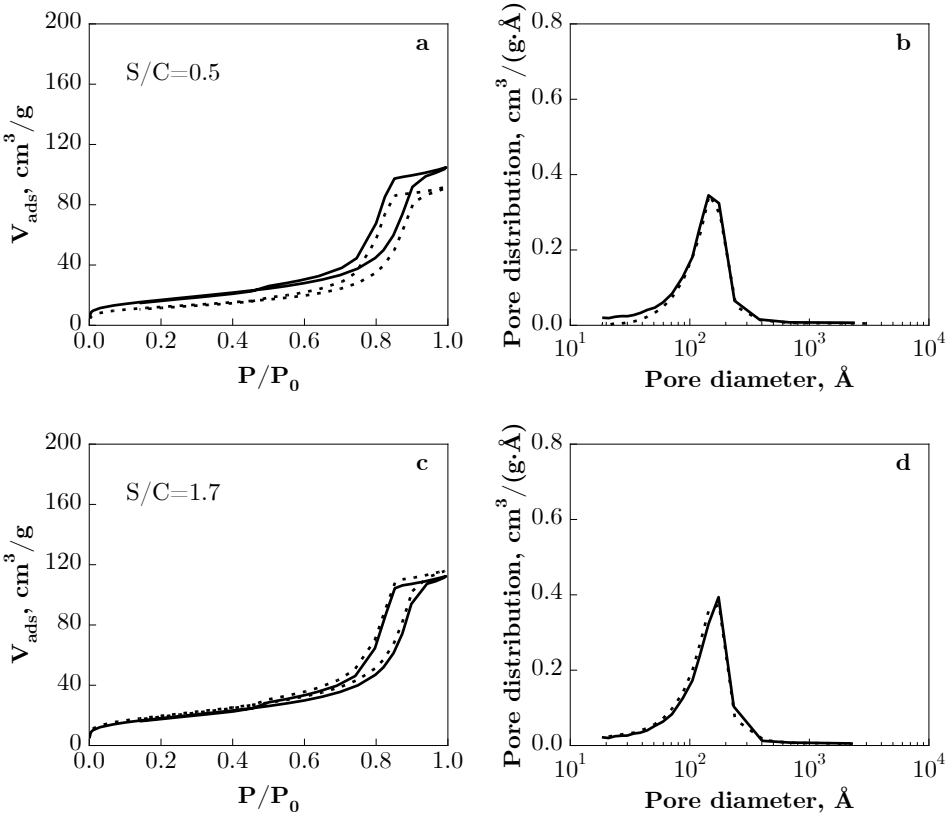

Figure B.8. N_2 adsorption-desorption isotherms (left graphs) and BJH pore volume distribution (right graphs) of Ni/Al_2O_3 catalyst samples used in the CSDR runs at different S/C ratios at 700 °C and space time of 0.125 $g_{catalyst}{\cdot}h/g_{oxygenates}$ with a CO_2/C ratio of 0.6 (solid lines) and 1.1 (dashed lines).

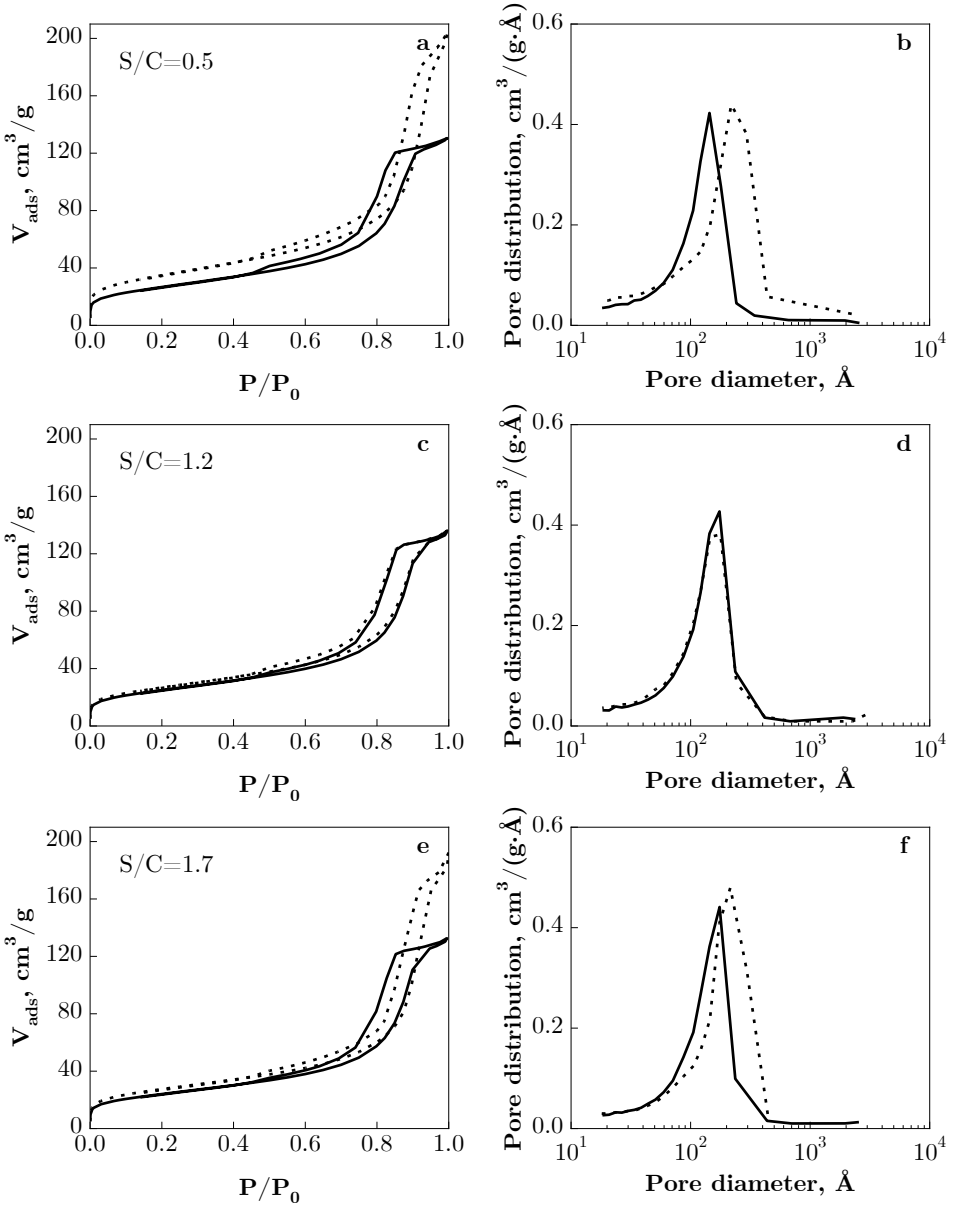

Figure B.9. N_2 adsorption-desorption isotherms (left graphs) and BJH pore volume distribution (right graphs) of Ni/Al_2O_3 catalyst samples used in the CSDR runs at different S/C ratios at 700 °C and space time of 0.250 $g_{catalyst}$·h/$g_{oxygenates}$ with a CO_2/C ratio of 0.6 (solid lines) and 1.1 (dashed lines).

B.2. SE-SEM images of $NiAl_2O_4$ derived catalyst used in SR runs

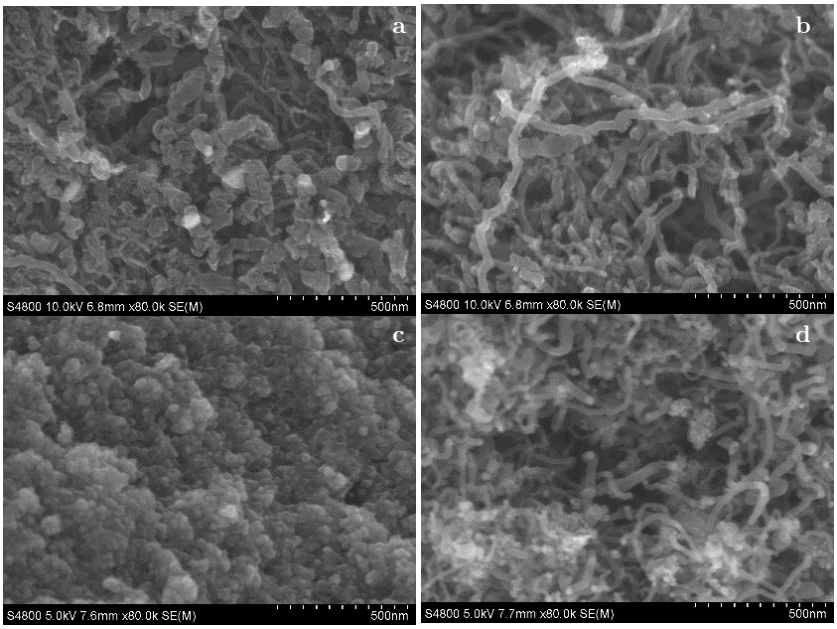

Figure B.10. SE-SEM images of Ni/Al_2O_3 catalyst samples used in the SR of ethanol (a, b) and guaiacol+ethanol (c, d) at 700 °C.

B.3. Results of Raman analysis

Raman spectra (Figure B.11) were deconvoluted (Figure B.12) using Lorentzian bands as commonly described in the literature. Most of the spectra required four Lorentzian bands centred at ~1200 cm^{-1} (possibly assigned to sp^3 hybridized carbons), 1340-1345 cm^{-1} (D band), ~1500 cm^{-1} (assigned to phases of amorphous carbon) and 1577-1600 cm^{-1} (G band) [96]. The spectra of the catalyst used in the SR of ethanol at 700 °C (Figure B.12b) required five Lorentzian bands because of a noticeable band at 1608 cm^{-1}, which appears in carbon nanotubes [328].

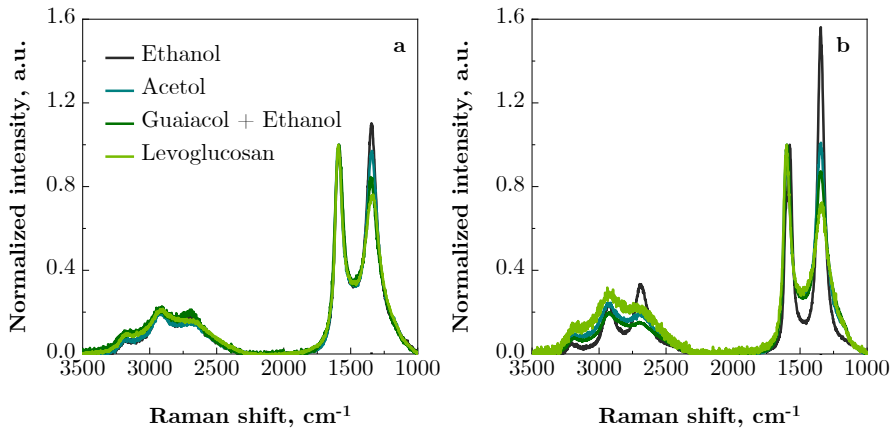

Figure B.11. Raman spectra of Ni/Al_2O_3 catalyst samples used in the SR of ethanol, acetol, guaiacol+ethanol and levoglucosan at 600 °C (a) and 700 °C (b).

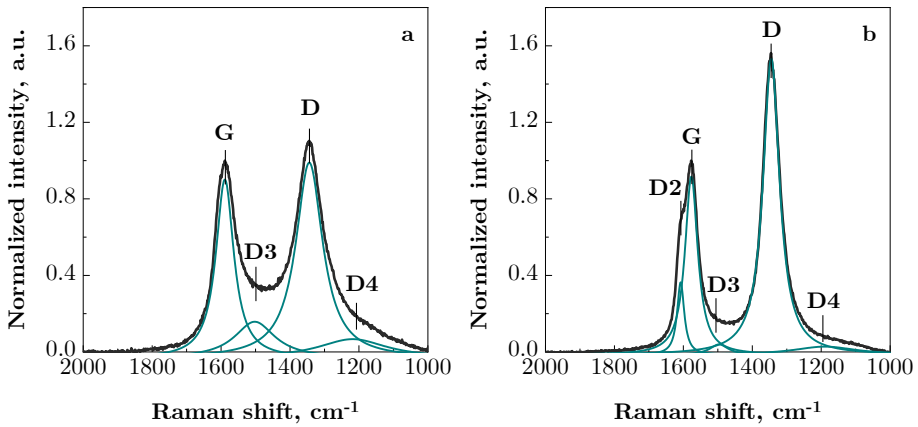

Figure B.12. Deconvoluted Raman spectra of Ni/Al_2O_3 catalyst samples used in the SR of ethanol at 600 °C (a) and 700 °C (b).

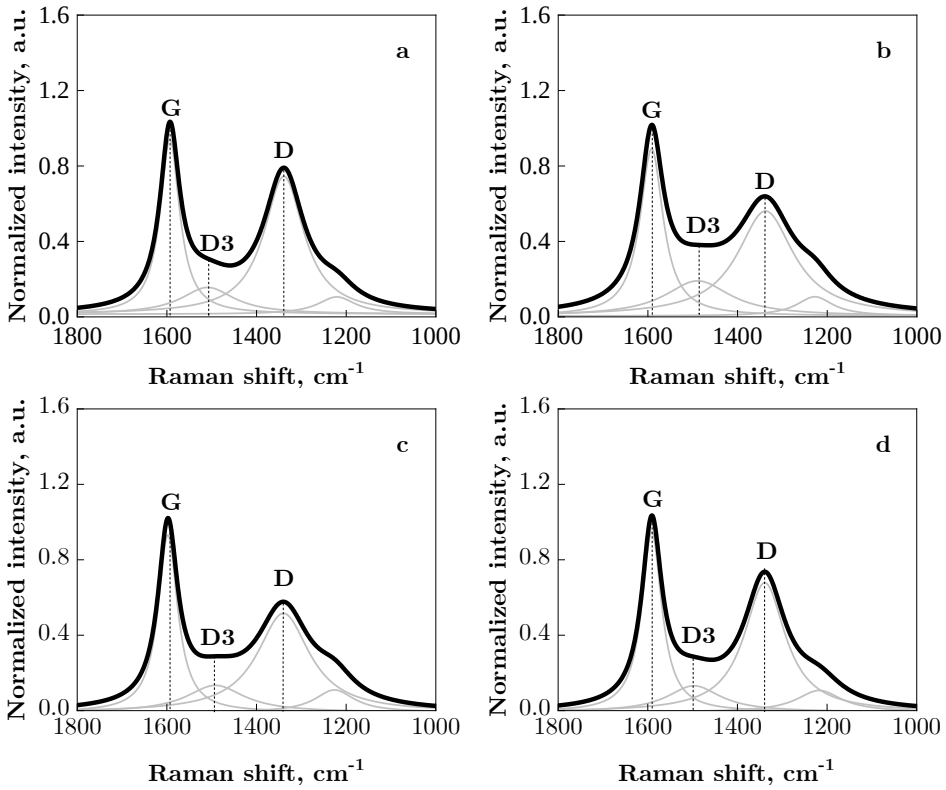

Figure B.13. Deconvoluted Raman spectra of Ni/Al_2O_3 catalyst samples used in the SR (a and b) and SESR (c and d) runs in PBR (a and c) or FBR (b and d).

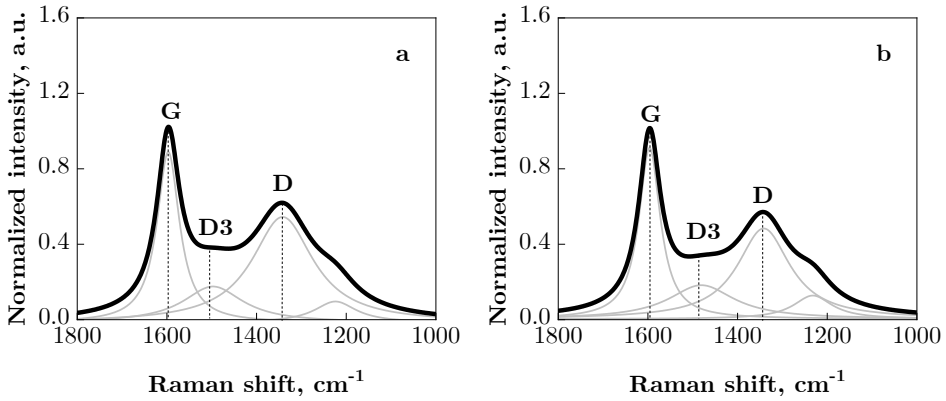

Figure B.14. Raman spectra of dolomite used in the SESR runs in PBR (a) or FBR (b).

B.4. Results of TPO analysis

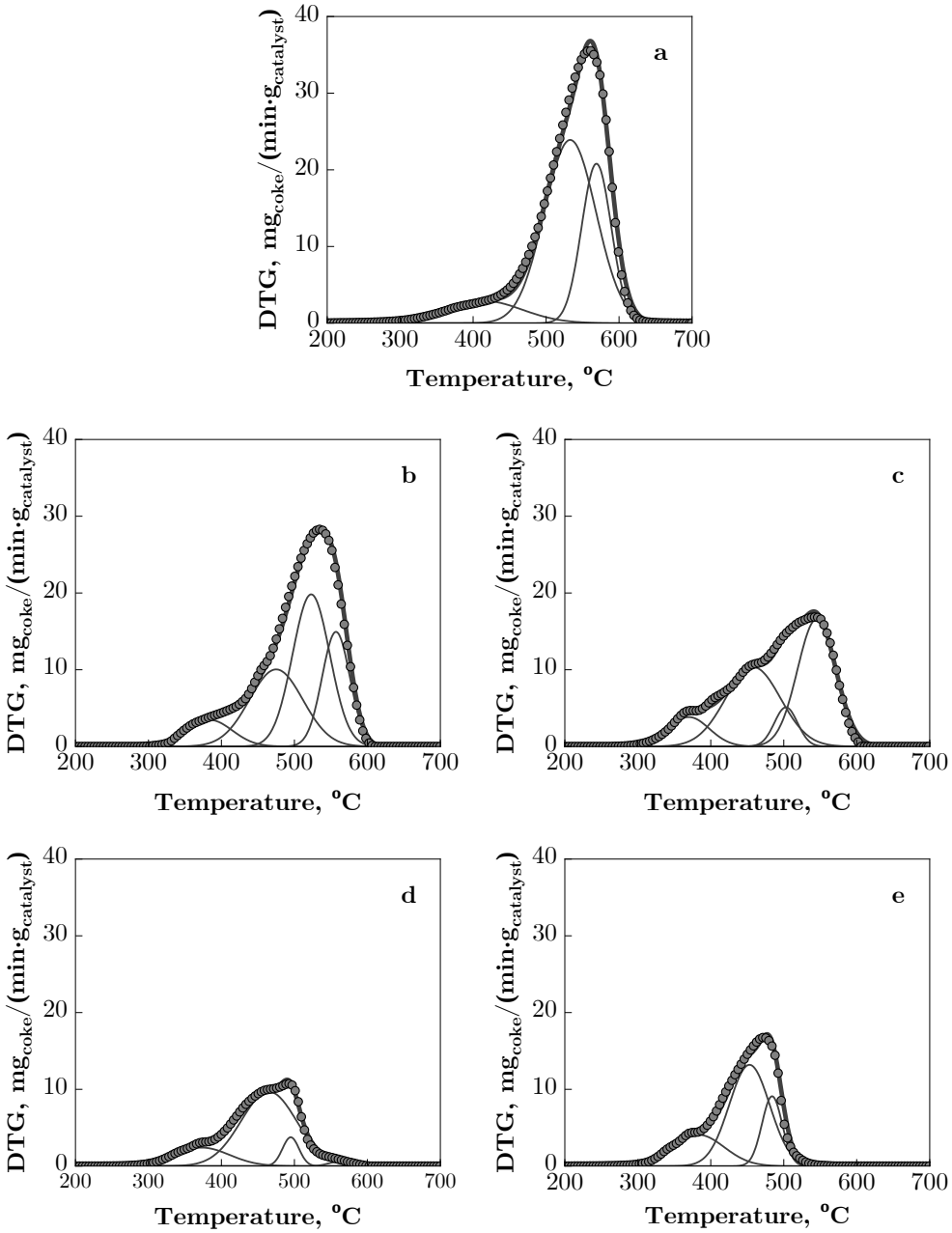

Figure B.15. Deconvolution of the TPO profiles of the coke deposited on Ni/Al_2O_3 catalyst used in the SR run (a) and SESR runs with dolomite (b-c) or Ca-M (d-e) as sorbents for SC_{MR} of 10 (b, d) and 20 (c, e).

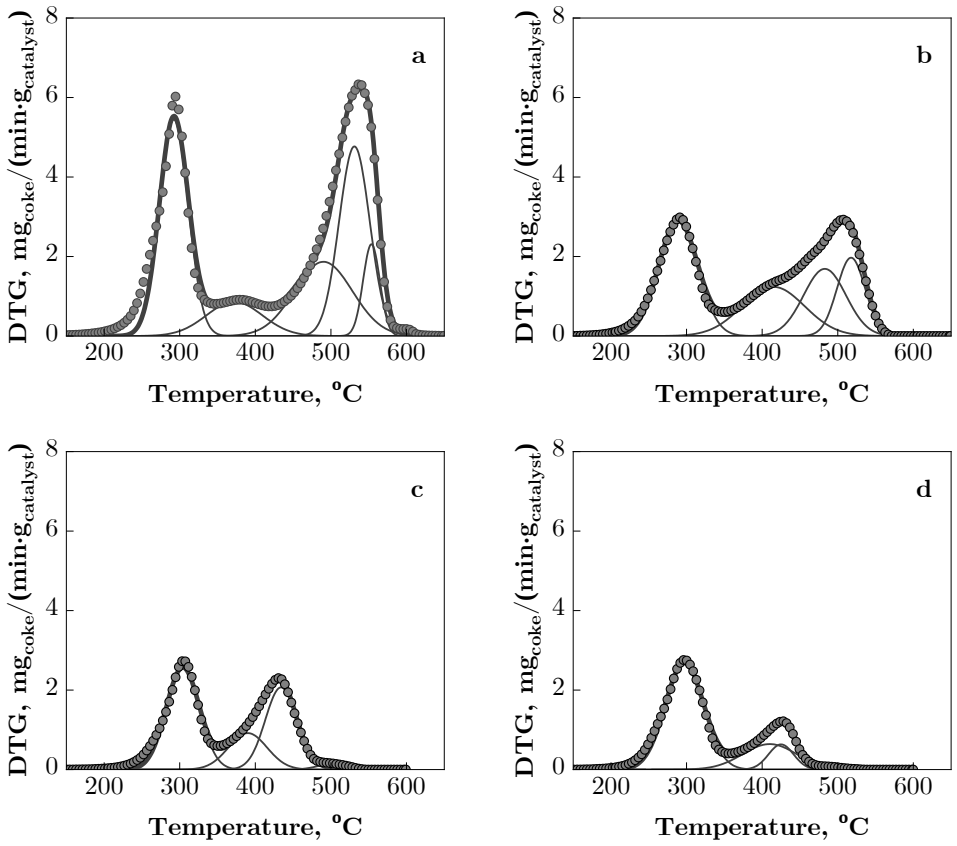

Figure B.16. Deconvolution of the TPO profiles of the coke deposited on Ni/CeO_2 catalyst used in the SR run (a) and SESR runs with dolomite as sorbent for SC_{MR} of 4 (b), 10 (c) and 20 (d).

C. EVOLUTION WITH TOS OF BY-PRODUCTS IN THE CSDR WITH $NiAl_2O_4$ DERIVED CATALYST

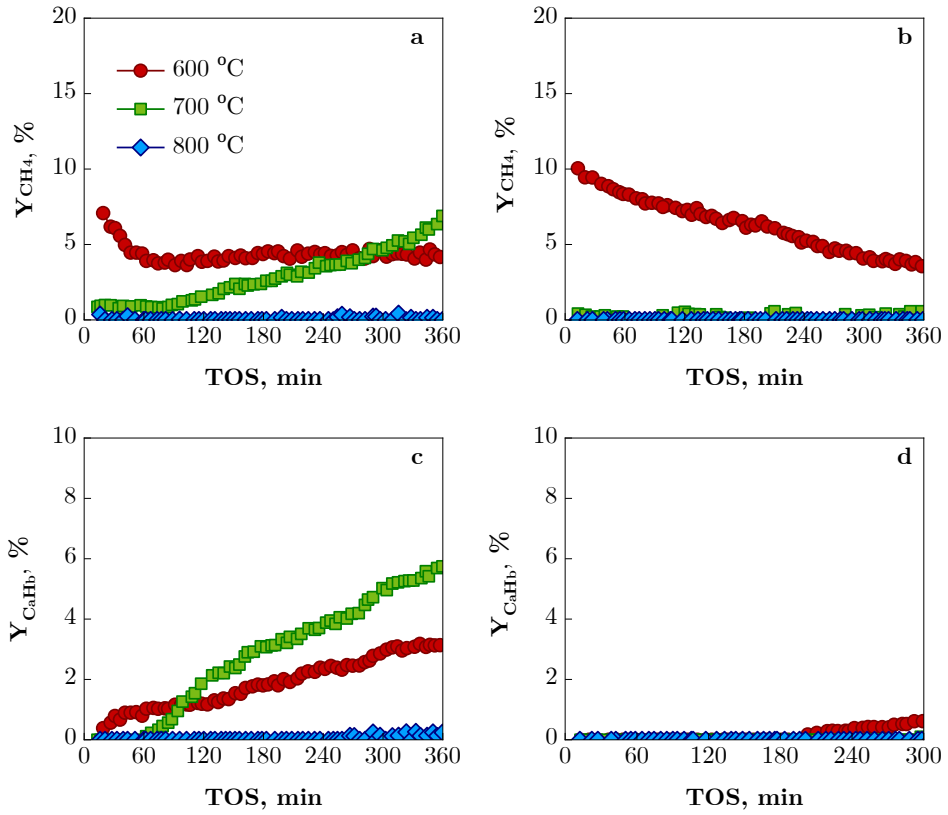

Figure C.1. Effect of temperature on the evolution with TOS of by-product yields: CH_4 (a,b) and light hydrocarbons (c,d) in the CSDR runs for a CO_2/C ratio of 1.1 with S/C ratio of 0.5 and space time of 0.125 $g_{catalyst}$·h/$g_{oxygenates}$ (left graphs) and S/C ratio of 1.7 and space time of 0.250 $g_{catalyst}$·h/$g_{oxygenates}$ (right graphs).

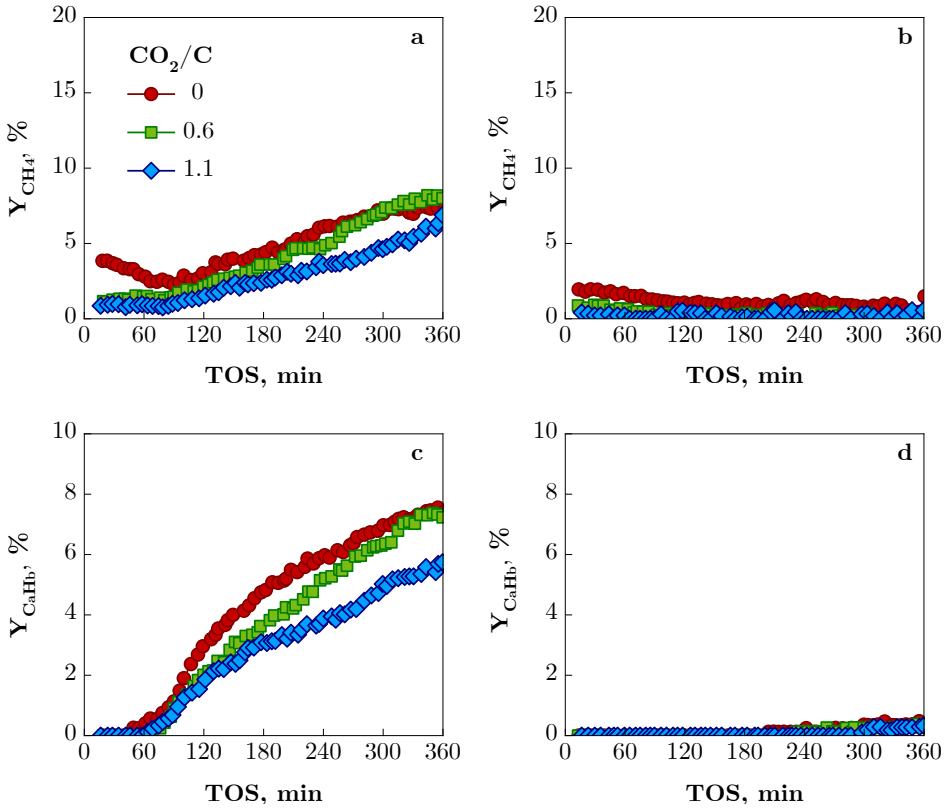

Figure C.2. Effect of CO_2/C ratio on the evolution with TOS of by-product yields: CH_4 (a, b) and light hydrocarbons(c, d) in the CSDR runs at 700 °C with a S/C ratio of 0.5 and space time of 0.125 $g_{catalyst}$·h/$g_{oxygenate}$s (left graphs) and a S/C ratio of 1.7 and space time of 0.250 $g_{catalyst}$·h/$g_{oxygenates}$ (right graphs).

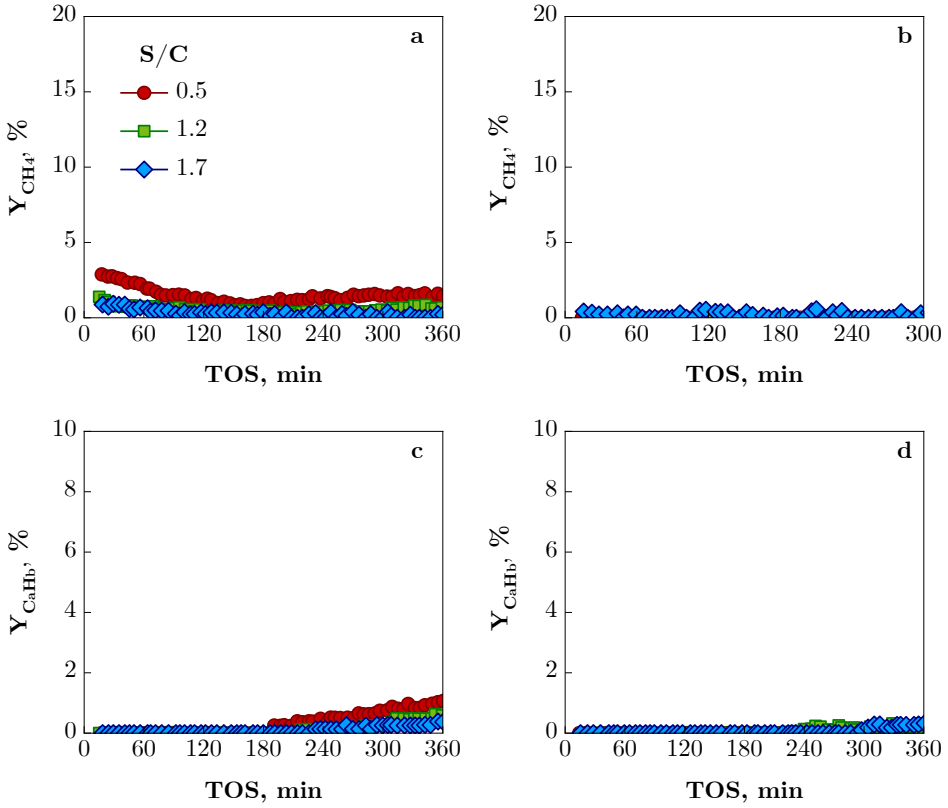

Figure C.3. Effect of S/C ratio on the evolution with TOS of by-product yields: CH_4 (a, b) and light hydrocarbons (c, d) in the CSDR runs at 700 °C and space time of 0.250 $g_{catalyst}{\cdot}h/g_{oxygenates}$ with a CO_2/C ratio of 0.6 (left graphs) and 1.1 (right graphs).

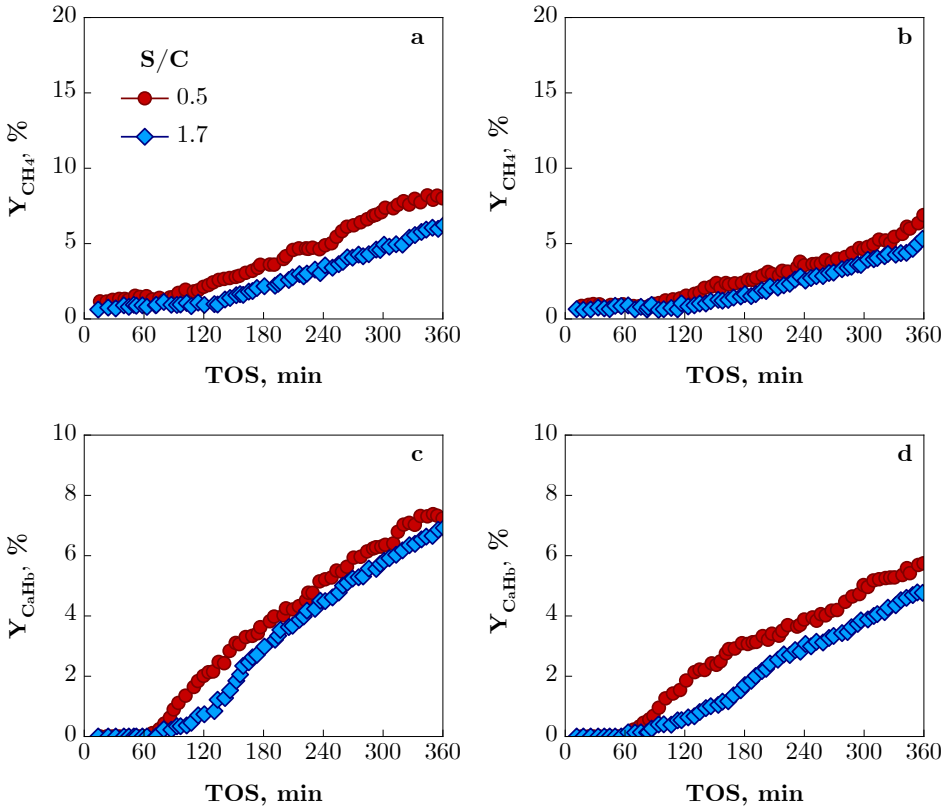

Figure C.4. Effect of S/C ratio on the evolution with TOS of by-product yields: CH_4 (a, b), and light hydrocarbons (c,d) in the CSDR runs at 700 °C and space time of 0.125 $g_{catalyst}{\cdot}h/g_{oxygenates}$ with a CO_2/C ratio of 0.6 (left graphs) and 1.1 (right graphs).